Lacustrine Shale Gas Reservoir Characterization in the Yanchang Formation by Integrated Geological Facies, Geochemistry, Chemostratigraphy, SEM Pore Imaging, Petrography, and Geophysics

Final Report

February 2016

PIs: Tongwei Zhang and Hongliu Zeng, Bureau of Economic Geology (BEG), The University of Texas at Austin, Austin, TX

BEG participants: Bob Loucks, Kitty Milliken, Eric Potter, Steve Ruppel, Harry Rowe, Hongliu Zeng, Sheng Peng, Xun Sun, Patrick Smith, Farzam Javadpour, Ali Afsharpoor, Evan Sivil, Daniel Enriquez, and Tongwei Zhang

Yanchang participants: Chao Gao, Bojian Fan, Ying Shen, Wei Wang, and Jianfeng Zhan

Table of Contents

Executive Summary

Yanchang-BEG Lacustrine Shale Gas Project

During the past 2 years, researchers from the Bureau of Economic Geology (BEG) and Yanchang Petroleum Group (Yanchang) have worked closely to conduct an integrated research project, "Lacustrine Shale Gas Reservoir Characterization in the Yanchang Formation by Integrated Geological Facies, Geochemistry, Chemostratigraphy, SEM Pore Imaging, Petrography, and Geophysics."

On November 8, 2013, a team of executives, led by Dr. Xiangzeng Wang, Vice President and Chief Geologist of the Shaanxi Yanchang Petroleum Company, Ltd., visited the Bureau of Economic Geology (BEG) to sign a 2-year agreement for the project. Project objectives were to provide integrated studies of geological facies, hydrocarbon geochemical characterization, chemical stratigraphy, SEM pore imaging, and detailed petrographic study. These aspects were to be integrated to yield broader concepts about hydrocarbon generation and storage and the distribution of geological facies and fundamental rock attributes. In addition, models were to be developed for evaluating sweet spots for shale gas that can be applied in making economic decisions.

All project tasks have been on schedule, and collaboration between the BEG and Yanchang Petroleum has been very successful. A team of executives, led by Dr. Xiangzeng Wang, Vice President of the Shaanxi Yanchang Petroleum Company, Ltd., traveled to Austin twice in the course of the research project for midterm and final project reviews. The Research Institute of Shaanxi Yanchang Petroleum sent five researchers to the BEG who were involved in specific research tasks, relevant to their research backgrounds and interests. A team of BEG researchers led by Dr. Scott Tinker, BEG Director; Eric Potter, BEG Energy Program Manager; and Drs. Tongwei Zhang and Hongliu Zeng, Principal Investigators (PIs) of the research project, traveled to Xi'an three times to conduct core description, data collection, and sampling. A field trip to Yanchang Formation outcrops took place during one visit, and presentations were given at the year-1 project review meeting and at the final project review meeting. BEG researchers also conducted a series of technology-transfer workshops at The Research Institute of Shaanxi Yanchang Petroleum.

A large amount of new data collection has been conducted during the 2 years of the project. More than 60,000 raw data for 23 new analytical items are summarized in **Table 1**: 15 GB of petrographic data, 25 GB of SEM pore imaging data, and 216 core pictures were collected. Twenty oral presentations, nine poster presentations, three reports, and five abstracts were given in annual and final project review meetings (**Table 2**). Key results will be published in *Interpretation,* in a Special Section titled "Lacustrine shale characterization and shale resource potential in Ordos Basin, China," in May 2017.

The following new and significant discoveries and concepts were produced from this integrated study:

1. A depositional model of the lithofacies of the Triassic Yanchang Formation was established. Four lithofacies, including (1) OM-rich argillaceous mudstone,

(2) OM-lean argillaceous mudstone, (3) quartzose feldspathic arkose (silt and sand), and (4) feldspathic quartzose arkose (silt and sand) were determined for Yanchang Formation based on high-resolution XRF and XRD data. The organic-lean and organic-rich argillaceous mudstones were deposited in a deeper water lacustrine setting during lake highstands. Interbedded with the argillaceous mudstones are argillaceous siltstones that were deposited in shingled turbidites in the distal delta. The sandstone at the top of Chang 7 may have been deposited in a deltaic complex.

2. Four flooding surfaces were defined, each of which represents basin deepening and serves as a possible correlation event. Each event is marked by the superposition of OM-rich mudstones over more proximal arkosic siltstones and sandstones. In addition to the surfaces that form the base and top of Chang 7, two surfaces were defined in Chang 8.

3. General facies types can be interpreted from most wireline logs, but detailed correlations require consideration of all log responses. Variations in organic matter are well defined by density and resistivity wireline logs. The chemostratigraphy and TOC results indicate the significant linkage between TOC and %Al (a proxy for clay content), and the linkage between enhanced TOC with enhanced %S (a proxy for pyrite content). Rock strength correlates closely with clay mineral and organic abundance, i.e., mudstone facies. Because of their high clay mineral content, mudstones are relatively ductile at reservoir depths and are probably poor candidates for hydraulic fracturing.

4. The argillaceous mudstones and siltstones are immature mineralogically. The siltstones are lithic arkoses and/or arkosic litharenites. The high clay-mineral content, generally greater than 40%, in the absence of significant cementation, has promoted extensive compaction of the sediments, occluding nearly all the primary interparticle pores, thus greatly reducing reservoir quality. The high clay-mineral content does not favor hydraulic fracturing of the mudstone reservoir.

5. The dominant diagenetic processes in the mudstones are compaction and organic maturation. Texturally, the mudstones of the Yanchang Formation are silt-bearing and silt-rich argillaceous mudstones. Greater silt content in the mudstones is correlated with the preservation of larger pores. Compositionally, mudstones of the Yanchang Formation are rich in quartz, feldspars, and clay minerals. The Yanchang mudstones have little cement, and the cement that is present is located primarily in anomalously large intragranular pores.

6. The pore network within the mudstones is dominated by intraparticle pores with a lesser abundance of OM-hosted pores. Interparticle pores are rare. Mean GRI porosity is 4.19%. Because the pore network is dominated by intraparticle pores and because the average pore size is very small, permeability is low (GRI estimated geometric mean permeability = 9.86 nd). The dominance of ineffective intraparticle pores creates a very weak correlation between GRI porosity and permeability.

7. Compaction and organic maturation are the main controls on porosity evolution in the lacustrine Yanchang Formation. Texture, as expressed by silt content and size, and OM-content affect the pathways of porosity modification during compaction and

maturation. Silt content is associated with the preservation of intergranular mineral-hosted, larger pores (> 20 nm). OM content, which is higher in relatively silt-poor samples, is associated with the loss of large pores and the generation of very small (< 10 nm), spongy, OM-hosted pores.

8. The OM-rich mudstone is a good-to-excellent source for oil generation potential, and the strong compaction during diagenesis favors petroleum expulsion. Carbon isotope data suggest that mudstones contain primarily aquatic organic matter, whereas arkoses contain terrestrial organic matter. Organic matter type varies in different depositional facies, Organic matter content is dominated by oil-prone Type I and II kerogens in deep lake facies, a mixture of Type II and III kerogens in prodelta facies, and Type III kerogen in delta plain/delta front facies. Its thermal maturity is in the oil window. The lower part of the Chang 7 member, a 25-m-thick organic-rich interval, contains a large amount of free oil and gas. It is the target for shale gas/oil exploration in terms of resources.
9. Models for gas storage in OM-rich mudstones were developed. Both clay minerals and organic matter provide spaces for adsorbed gas and free gas storage in Triassic-aged Yanchang Formation mudstones. The exhumation causes a significant amount of free gas loss, and the extent of gas loss varies with burial depth. The sequential pore fluid removal method provides a method for determining gas, oil and water saturation. The free gas capacity is from 1.75 MMcm to 4.75 MMcm (in per million cubic meters) of the Chang 7 organic-rich mudstone reservoir, which as a 4% total porosity.
10. Pore-network models of Yanchang shale samples were developed to simulate slip-corrected liquid flow and thus to determine apparent fluid permeability. Pore-network simulation results reveal that pore geometry and slip effect play important roles in fluid flow in Yanchang shale samples. If we ignore noncircularity of pores and assume that all pores are circular, our estimates of apparent permeability would be incorrect by factors of 2.5 to 9.0.
11. Field seismic data were reprocessed to fit the needs for high-resolution, high-fidelity prediction of lithology, rock properties, and fracking performance. A novel and creative workflow was adopted to suppress noise and to improve resolution, post and prestack inversion, and microseismic data analysis.
12. Integration of seismic, chemostratigraphy, and lithology from wireline logs was used to predict sweet spots. Seismic amplitude and acoustic impedance can be correlated to log lithology at a resolution approximating 10 m. The Chang 7 member includes three seismic units (from top to bottom): (1) delta plain/delta front (Ch 7-1), (2) prodelta (Ch 7-2), and (3) deep lake (Ch 7-3) facies. The Ch 7-3 mudrock unit is unsuitable for shale-gas drilling and fracking because of its low porosity and permeability, ductile properties, and interbedded sandy/muddy layers, which produce varied frackability (a tunnel effect). The more brittle, sandy Ch 7-2 interval, which thickens to as much as 50 m to the northeast, is recommended as the target zone, with a possible sweet spot to the northeast.

Table 1. Summary of Analytical Items and Raw Data Collection.

Analytical item	Number of samples	Number of measured data points	Number of images	Number of pictures
XRF trace elements	2924	17,544		
XRF major elements	2924	35,088		
Quick XRD	206	2060		
Detailed XRD	58	928		
TOC	635	635		
$\delta^{13}C$ of TOC	635	635		
Bambino Measurement (UCS)	2277	4554		
RockEval	58	522		
Bitumen reflectance	15	15		
Rock-crushed gas composition	58	754		
SARA for EOM	30	120		
Saturate and aromatic GC-MS	30	60		
CH_4 adsorption	7	357		
N_2 adsorption	35	385		
He GRI porosity and permeability	26	52		
Thin section	58		58	
Light microscope	58		116	
Light microscope CL	6		6	
X-ray mapping	58		58	
SEM pore imaging	24		240	
TEM imaging	5		60	
High-resolution SEM imaging	5		60	
Organic petrography images			211	
Core pictures				216
Micro seismic data	5 wells			
Wireline logs	29 wells			
3D seismic data	100 sq km			

Table 2: Summary of Presentations, Reports, and Publications Resulting from This Project.

Oral presentations	10 in annual project review meeting in Xi'an, January 6-7, 2015
	10 in final project review meeting in Austin, December 15-16, 2015
Poster presentations	6 in annual project review meeting in Xi'an, January 6-7, 2015
	3 in final project review meeting in Austin, December 15-16, 2015
Reports	100 pages annual report, delivered in February 2015
	30 pages research progress report, delivered in July 2015
	200 pages final report, delivered in February 2016
Workshops	10 lectures at Research Institute of Shaanxi Yanchang Petroleum
Publications	Five abstracts for AAPG and SEG conferences
	Interpretation Special Section: May 2017
	Lacustrine shale characterization and shale resource potential in Ordos Basin, China

Introduction

Tongwei Zhang, Eric Potter, and Hongliu Zeng[1]

[1]Bureau of Economic Geology, Jackson School of Geosciences, The University of Texas at Austin, Austin, TX

This final report details the 2-year integrated research project, Lacustrine Shale Gas Reservoir Characterization in the Yanchang Formation by Integrated Geological Facies, Geochemistry, Chemostratigraphy, SEM Pore Imaging, Petrography, and Geophysics.

On November 8, 2013, a team of executives led by Dr. Xiangzeng Wang, Vice President and Chief Geologist of the Shaanxi Yanchang Petroleum Company, Ltd., visited the Bureau of Economic Geology (BEG) to sign a 2-year agreement for the project, whose objectives were to provide integrated studies of geological facies, hydrocarbon geochemical characterization, chemical stratigraphy, scanning electron microscopy (SEM) pore imaging, and detailed petrographic study. These aspects were to be related to larger findings on hydrocarbon generation and storage, as well as on the distribution of geological facies and fundamental rock attributes. In addition, models were to be developed for evaluating sweet spots for shale gas that can be applied to economic decisions.

All project tasks are on schedule, and collaboration between the BEG and Yanchang Petroleum has been highly successful. The Research Institute of Shaanxi Yanchang Petroleum sent five researchers to the BEG: Dr. Bojiang Fan worked with Harry Rowe for chemostratigraphy, Dr. Ying Shen worked with Kitty Milliken and Bob Loucks for petrography and pore imaging, Dr. Jianfeng Zhang worked with Tongwei Zhang for gas geochemistry and pore-size distribution, Dr. Chao Gao worked with Hongliu Zeng and Steve Ruppel for well-log calibration, and Dr. Wei Wang worked with Hongliu Zeng for 3D seismic data processing and interpretation.

In early December 2013, a team from the BEG, including Milliken, Rowe, and Zhang, traveled to Xi'an, China, for core description, X-ray fluorescent (XRF) scans, gas sampling, and an outcrop field trip. From two wells (YY1 and YY22), 46 core samples were collected. XRF scanning was performed on 4 cores (YY1, YY22, YY8, YY32), and rock powders taken for X-ray diffraction (XRD) and total organic content (TOC) analyses. XRF data were collected at 2,924 sample sites: 206 samples were collected for XRD data and 565 samples for TOC data. In the course of project operation in 2014, 46 core samples were used for detailed petrography, geochemistry, and pore characterization. See further details in the report that follows.

On January 6–7, 2015, the BEG's Eric Potter, Milliken, Zeng, Rowe, Sivil, and Zhang attended a review meeting at Xi'an, China, and reported research progress with presentations and posters. Potter, Milliken, and Zeng also conducted a half-day workshop, delivering presentations to an audience from the Yanchang Petroleum Group. After the workshop, the BEG team met with 20 researchers from the group—led by Professor Xiangzeng Wang—to discuss the 2015 work plan and research focus. The meeting generated the following comments and suggestions:

- Because lacustrine shale has very strong heterogeneity, and mm-cm scale sandstone and silty sandstone layers exist within the thicker organic-rich layer. Thus, the concept of "interval" should be considered instead of specific lithology units.

- Large-scale layering identification and analysis, and combination of different scales, should also be considered.
- The BEG should take full advantage of the multidisciplinary research team to conduct integrated research.
- Principal Investigator Zhang should follow up on the progress and requirements of each task.

On December 15 and 16, 2015, a team of executives led by Dr. Xiangzeng Wang, Vice President of the Yanchang Petroleum Company, visited the Bureau for final project review. Nine BEG researchers presented their research discoveries in the final review meeting.

On February 29 and March 1, 2016, the BEG's Scott Tinker, Zeng, and Zhang attended a final review meeting at Xi'an, China, and reported research results with presentations to a large group of Yanchang Petroleum Group staff. Dr. Scott Tinker, BEG Director, also conducted a half-day workshop, delivering presentations to an audience from the Yanchang Petroleum Group.

Our results suggest significant differences between the Yanchang Formation and successful U.S. shale plays. This is not surprising and should simply serve as a reminder that lacustrine shales may require different approaches for commercial success. Overall, the Yanchang shales have higher clay content than do U.S. marine shale plays. Organically hosted porosity is present in some Yanchang zones and geographic areas, which is a favorable factor for play success. Lithology is the main control on key shale reservoir properties, such as porosity, permeability, organic matter (OM) abundance, and suitability for hydraulic fracturing. The elements of the research conducted on the Yanchang Formation are presented in six sections.

In the first section, which includes Task 1.1 and Task 1.2, Ruppel and Rowe conducted a detailed characterization of the depositional facies and rock attributes in the Yanchang Formation and provide important insights into their depositional setting and the relationships between rock attributes and wireline logs. Detailed chemostratigraphic analyses included closely spaced measurement of major, minor, and trace element variations through cores using handheld XRF scanners, combined with XRD measurements of mineral abundances, and carbon isotope values. Four major facies were defined, including OM-poor, coarser grained, arkosic sandstones and siltstones and finer grained, OM-bearing mudstones. Variations in OM are well defined by density and resistivity wireline logs, and rock strength correlates closely with clay mineral and organic abundance, that is, mudstone facies.

In the second section, Milliken, Loucks, Sheng, and Ruppel conducted detailed microscopic and SEM studies on lithology, mineralogy, grain assemblage, and diagenesis in the Yanchang Formation and provide important insights about mineral matrix source input, cements, and sedimentary features. In Task 2.1, Loucks and Ruppel described thin sections and identified that the organic-lean and organic-rich argillaceous mudstones with lesser argillaceous siltstones are dominant in the Yanchang Formation. In Task 2.2, Milliken and Sheng conducted detailed microscopic studies using transmitted light microscopy, X-ray elemental mapping, and point-counting of X-ray images. Compositional and textural data from imaging were used to refine the lithologic categories, and comparisons of pore-size distributions from N_2 adsorption were made using those categories. The dominant diagenetic processes in the mudstones are compaction and organic maturation.

In the third section, which includes Tasks 3.1, 3.2, 3.3, and 3.4, pore types, pore-size distribution, and porosity and permeability in the Yanchang Formation were intensively characterized by SEM pore imaging, N_2 adsorption, and GRI PnP measurement. In Task 3.1, Loucks and others conducted detailed field-emission scanning electron microscopy (FE-SEM) imaging of Ar-Ion milled samples to define pore types and pore networks in the Yanchang Formation. The pore network within the mudstones is dominated by intraparticle pores with a lesser abundance of OM pores. Interparticle pores are rare. Mean GRI crushed-rock porosity is 4.19%. In Task 3.2, Zhang and others conducted N_2 adsorption analysis of the samples before and after oil cleaning to characterize the pore size distribution. Pores less than 10 nm in width are dominant in finer-grained and organic-rich mudstones. Pores greater than 20 nm in width are dominant in organic-lean, silt-rich mudstones and sandstones. Compaction and organic maturation are the main controls on porosity evolution in the lacustrine Yanchang Formation. In Task 3.3, Sheng and Zhang conducted porosity and permeability measurement for Yanchang samples using the GRI method. Both the comparison between He and N_2 porosity measurements and the relative permeability analysis have important implications to the relative distribution of residual moisture, oil, and immobile components. In Task 3.4, Patrick and others presented a high-resolution microscopic analysis, including low-voltage scanning electron microscopy (LVSEM) and high-resolution transmission electron microscopy (HRTEM) to image the pores of less than 10 nm size and that have nanoscale OM and clay minerals structures.

In the fourth section, which includes Tasks 4.1, 4.2, and 4.3, OM type, thermal maturity, gas origin, and OM input have been characterized by using organic petrographic analysis, gas chromatography (GC) gas compositional analysis, and residual oil gas chromatography-mass spectrometry (GCMS) analysis. In Task 4.1, Zhang and others conducted gas geochemical characterization of the released gas from rock crushing, TOC and RockEval pyrolysis and documented that the Triassic Yanchang Formation is a “good-to-excellent” source for oil generation potential and that thermogenic gas is main source for shale gas. The lower part of the Chang 7 member, at a 25-m-thick organic-rich interval, contains a significant amount of free oil. The gaseous hydrocarbon content, determined by gas logging, is the target for shale gas/oil exploration in terms of resources. In Task 4.2, Hackley and Zhang measured solid bitumen reflectance, and BRo values ranges from 0.67% to 0.95%, terrestrial vitrinite and inertinite are scarce. In Task 4.3, Sun and Enriquez conducted detailed GCMS biomarker studies, and they documented that OM-type varies in different depositional facies. It is dominated by a mixture of Type II and Type III kerogens in prodelta facies, and Type III kerogen in delta plain/delta front facies.

In the fifth section, which includes Tasks 5.1 and 5.2, gas storage and fluid flow models have been investigated. In Task 5.1, Zhang and Zhang conducted CH_4 adsorption at high pressure and temperature condition. Both clay minerals and OM provide spaces for adsorbed gas and free gas storage in Triassic-age Yanchang Formation mudstones. The sequential pore fluid removal method provides a method for determining gas, oil, and water saturation. The free gas capacity is from 1.75 MMcm to 4.75 MMcm (in per million cubic meters) in the Chang 7 organic-rich mudstone reservoir, which has 4% total porosity. In Task 5.2, Ali and Javadpour conducted fluid flow modeling and developed pore-network models for the Yanchang shale samples to simulate slip-corrected liquid flow and to determine apparent fluid permeability. Pore-network simulation results reveal that pore geometry and slip effect play important roles in fluid flow in Yanchang

shale samples. If we ignore noncircularity of pores and assume that all pores are circular, our estimates of apparent permeability would be erroneous by factors of 2.5 to 9.0.

In the last section, including Tasks 6.1 and 6.2, Zeng and Wang conducted a “sweet spot” prediction by using 3D seismic, well logs, and lithology studies. Field seismic data were reprocessed to fit the needs for high-resolution, high-fidelity prediction of lithology, rock properties, and fracking performance. A novel and creative workflow was adopted to suppress noise; as well as to improve resolution, post, and prestack inversion and to incorporate microseismic data analysis. Seismic amplitude and acoustic impedance can be correlated to log lithology at a resolution approximating 10 m. The Chang 7 member includes three seismic units (from top to bottom): (1) delta plain/delta front (Chang 7–1), (2) prodelta (Chang 7–2) (3) deep lake (Chang 7–3) facies. The Chang 7–3 mudrock unit is unsuitable for shale-gas drilling and fracking because of its low porosity and permeability, ductile properties, and interbedded sandy/muddy layers that result in varied frackability (tunnel effect). The more brittle, sandy Chang 7–2 interval thickens to as much as 50 m to the northeast and is recommended as the target zone, with a possible sweet spot to the northeast.

In summary, an integrated approach involving multidisciplinary research elements is the key to shale gas reservoir characterization. A multidisciplinary research workflow to characterize the lacustrine shale gas system of the Yanchang Formation has been developed in this study. Chemostratigraphic analysis of cores samples using XRF is the first step of the workflow and the basis of further study, including pore characterization and determinations of mineralogy, fluid chemistry, and storage. Assessing TOC, thermal maturity, and OM type are important factors in gas generation, but rock properties (that is, mineralogy, porosity, permeability, brittleness and fractures and others) and gas chemistry are crucial for studying the gas storage and gas-in-place in shale. The combination of depositional facies, OM maturation, diagenesis, and basin thermal history controls the lithological distribution, OM distribution, gas generation, and pore evolution. The linkage of gas storage and gas-in-place to fundamental rock attribute data, distribution of geological facies, and seismic responses is a robust basis for predicting gas and oil sweet spots.

TASK 1.1

Facies, Rock Attributes, Stratigraphy and Depositional Environments: YY1 and YY22 Cored Wells

Stephen C. Ruppel and Harry Rowe[1]

1-Bureau of Economic Geology, Jackson School of Geosciences, The University of Texas at Austin, Austin, Texas

Introduction

Cores recovered from the YY1 and YY22 wells allow detailed characterization of the depositional facies and rock attributes in the Yanchang Formation and provide important insights into their depositional setting and the relationships between rock attributes and wireline logs.

Methods

Facies were investigated using a conventional macroscopic core study combined with thin-section microscopy and chemostratigraphy. A macroscopic study allowed classification of facies by grain size, e.g., Sandstone, Muddy Sandstone, Sandy Mudstone, and Mudstone (**figs. 1 and 2**). This characterization is important for understanding depositional settings and processes but does not provide an understanding of the mineralogical variations that are key to wireline log calibration and correlation. A few volcanic ash beds were also observed macroscopically (for example, see **figs. 1 and 2)**.

Detailed chemostratigraphic analyses included the closely spaced measurement of major, minor, and trace element variations in both cores using handheld X-ray fluorescence (XRF) scanners, combined with X-ray diffraction (XRD) measurements of mineral abundances, and carbon isotope values (see Rowe and others, Task 1.2 of this report). All analytical work was performed by Bureau of Economic Geology scientists and staff of the Research Institute of the Shaanxi Yanchang Petroleum (Group) Co. Ltd., in part in China and in part in Austin, Texas.

Key XRF elements and element ratios were calibrated with XRD data to produce high-resolution depth curves depicting variations in mineral composition throughout the cores. Aluminum abundance serves as a good proxy for clay mineral abundance in these rocks, and the silicon/aluminum ratio gives a reasonable measure of quartz abundance (e.g., **figs. 3 and 4**). Feldspar abundance was defined by integrating closely spaced, semiquantitative XRD analysis with more widely spaced, high-resolution XRD measurements (e.g., **figs. 3 and 4**).

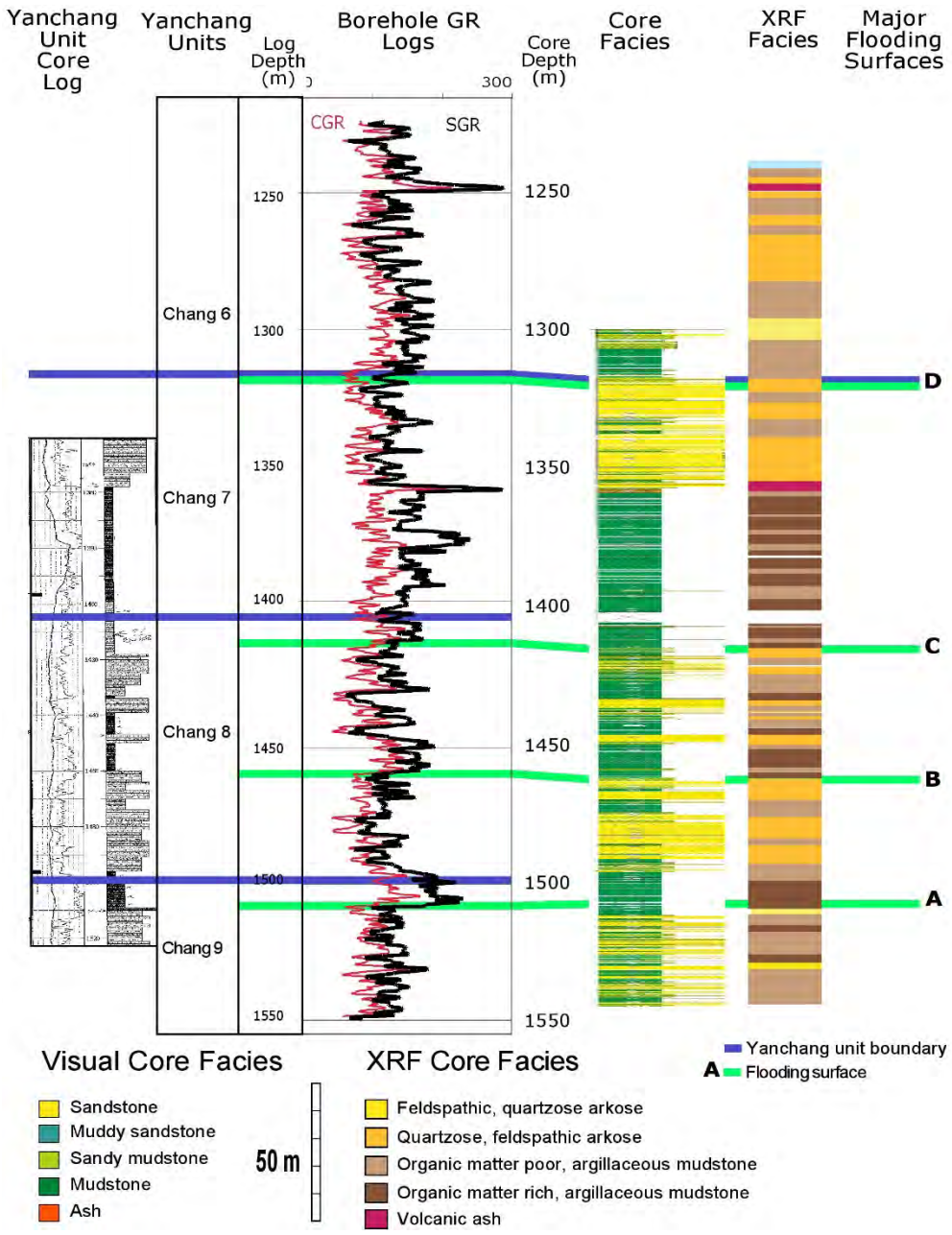

Figure 1. Facies and core/log correlations for the YY1 well. Four major facies can be defined from both visual and chemostratigraphic characterization. Four flooding events have been defined; some match or almost match Chang unit boundaries, but some do not. Location of the cored well is shown in **Figure 7.**

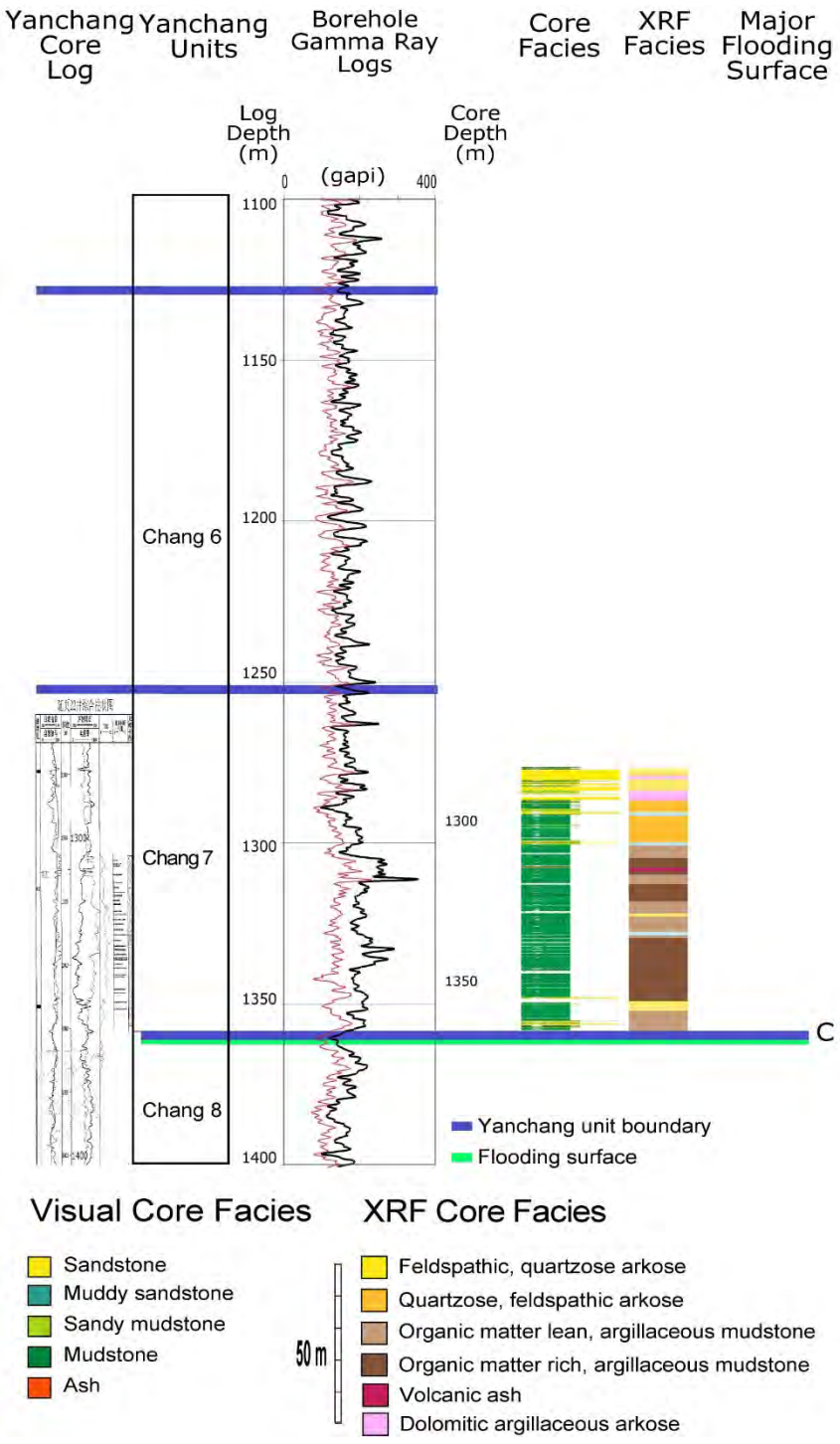

Figure 2. Facies and core/log correlations for the YY22 core. As with the YY1 core, four major facies can be defined from both visual and chemostratigraphic characterization. A single flooding event is definable with cores and logs. Note the close correlations between the Chang 7/8 log pick and the base of the basal Chang 7 flooding event. Location of the cored well is shown in **Figure 7.**

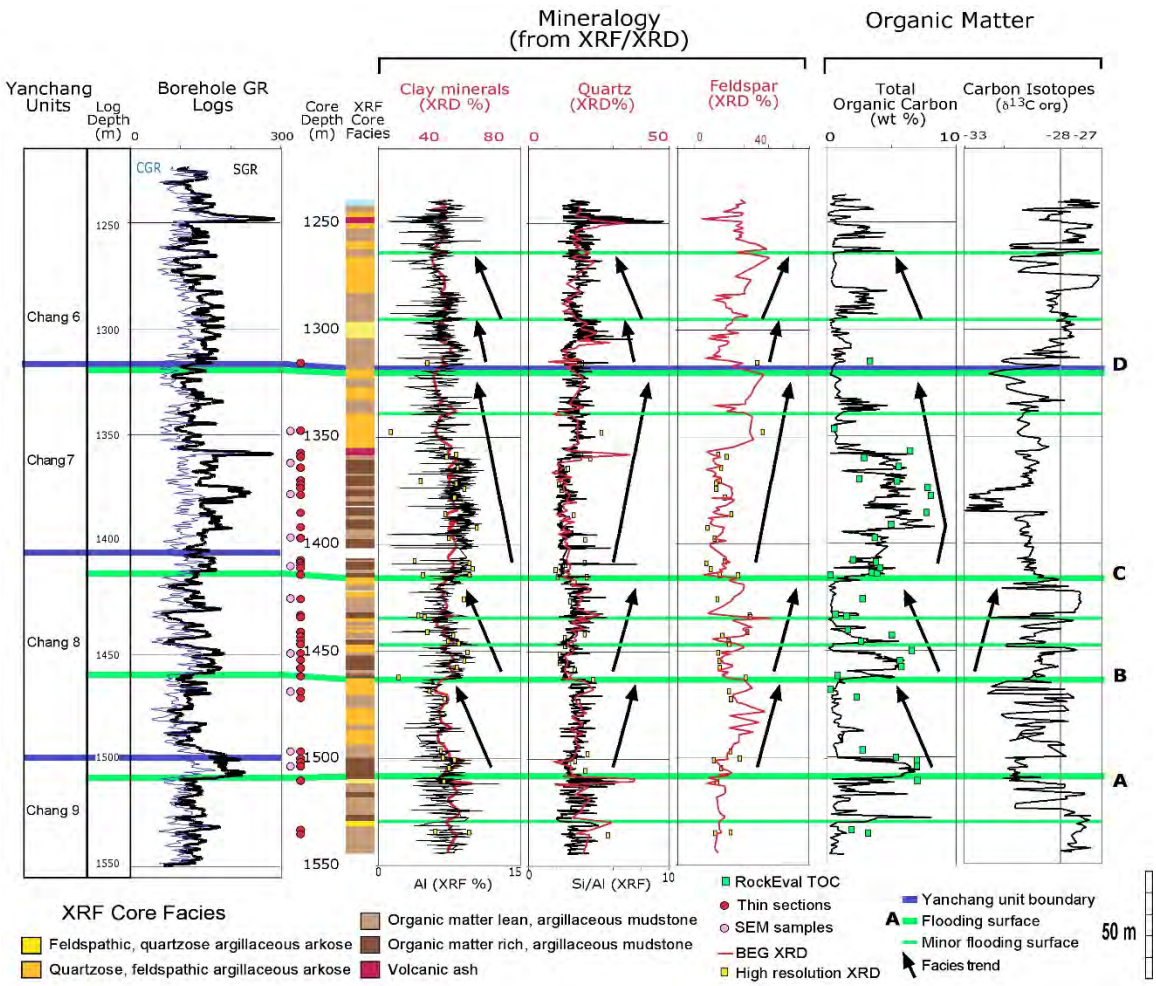

Figure 3. Plots of chemostratigraphic data used to define mineralogical (XRF) facies in the YY1 well. For mineralogy plots, three data types are shown: XRF elemental profiles, high-frequency quick-look XRD data, and higher-resolution XRD sample data. Mineral percentages are calculated by correlating high-resolution XRD (yellow points) data with continuous, semiquantitative XRD data (red curve) and XRF data (black curves). Note that carbon isotopes display generally lower values in mudstones and higher values in arkoses.

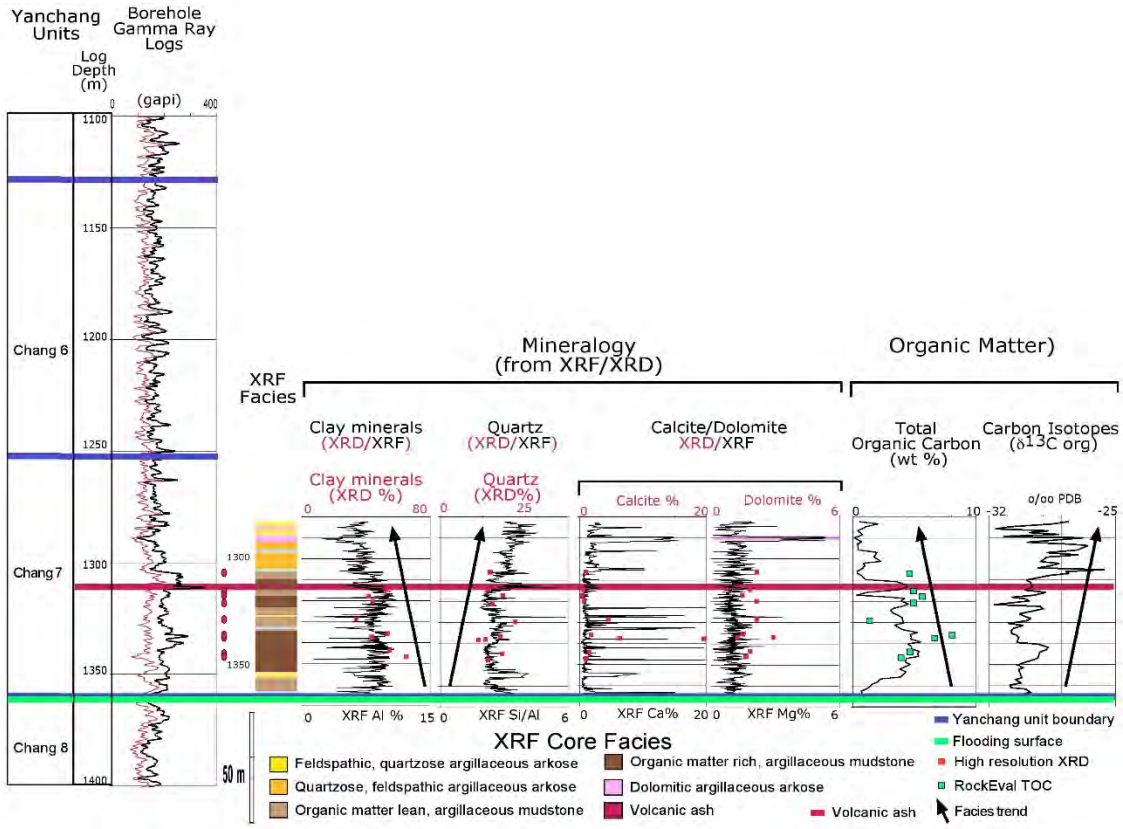

Figure 4. Plots of chemostratigraphic data used to define mineralogical (XRF) facies in the YY22 well. For mineralogy plots, two data types are shown: XRF elemental profiles, high-frequency and high-resolution XRD sample data. Mineral percentages are calculated by correlating high-resolution XRD (yellow points) data with and XRF data (black curves) and by comparisons with relationships defined in the YY1 core. Note that, as observed in the YY1 core, carbon isotopes display strong relationships to facies. Core depths are shifted approximately 5 m relative to log depths.

Organic matter (OM) abundance was measured by conventional laboratory methods and supplemented by measurements made on individual samples by an outside laboratory. OM type is not easily defined in mature rocks like these, but stable carbon isotopes were measured to provide some insight into these variations (e.g., **figs. 3 and 4**).

Rock strength, a measure of potential brittleness and suitability for hydraulic fracturing (hereafter referred to as “fracability”) was measured using a rebound hammer and calibrated to unconfined compressive strength (UCS) (e.g., **fig. 5**). Calibrations of this and other rock attributes were made by direct comparisons of core and log data (e.g., **fig. 5**).

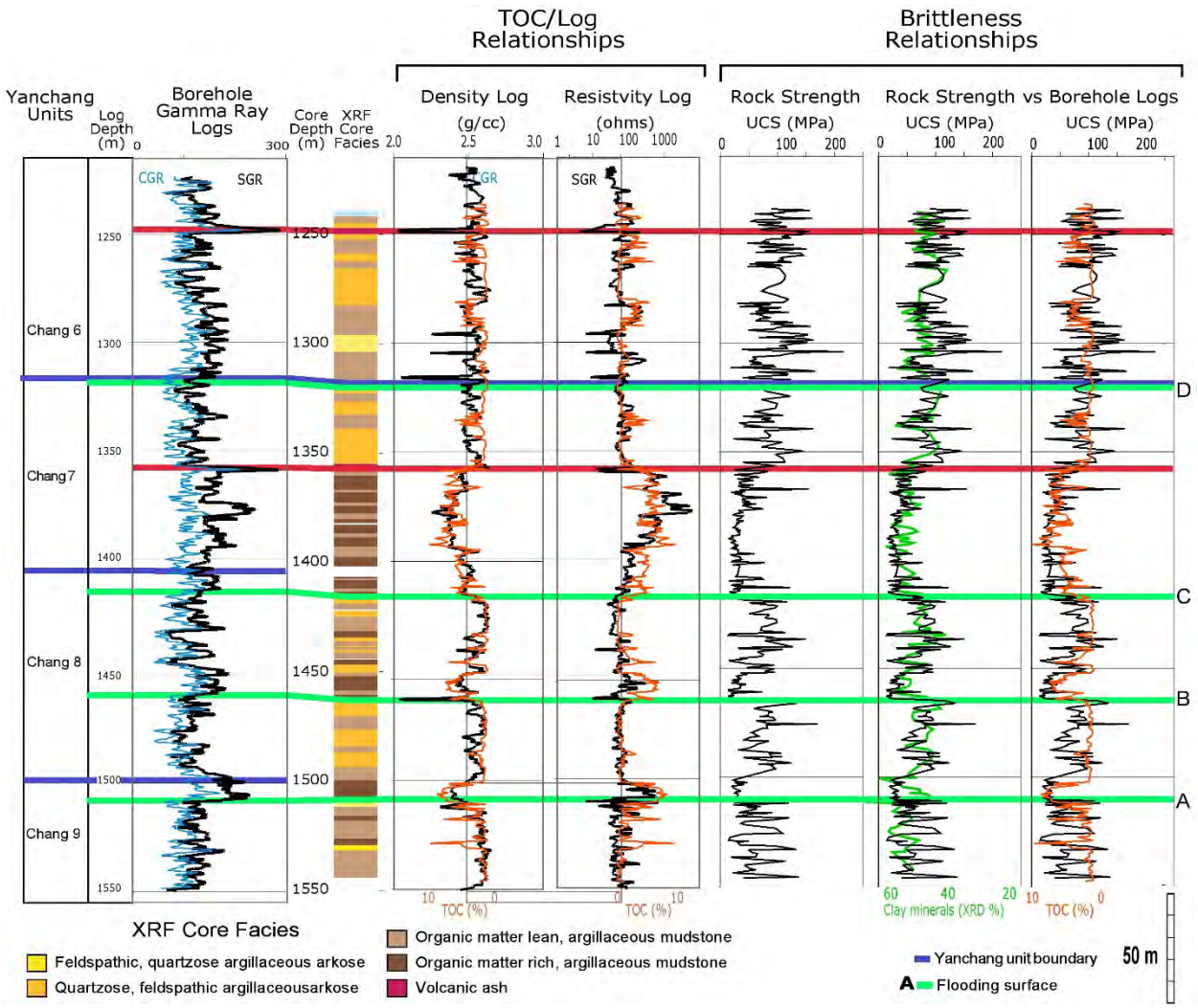

Figure 5. Plots showing relationships between wireline logs and core attributes in the YY1 well. TOC variations correlate well with both the density and resistivity logs but not with the gamma-ray logs. Rock strength correlates closely with clay mineral volume and TOC, although less well with TOC. Gamma-ray logs do not correlate closely with either TOC or rock strength.

Facies

Detailed chemostratigraphic data from both cores was used to define mineralogical facies that are key for defining paleoenvironments and establishing rock/core correlations. Four primary facies were identified on the basis of major element variations and XRD mineralogy: (1) the Quartzose, Feldspathic, and Argillaceous Arkose Facies, (2) the Feldspathic, Quartzose, and Argillaceous Arkose Facies, (3) the Organic-Matter-Lean, Mudstone Facies, and (4) the Organic-Matter-Rich, Mudstone Facies. A fifth facies, apparent volcanic ashes, was indicated by high quartz values and associated high gamma responses (e.g., **fig. 2**). Facies characteristics are subsequently given.

Quartzose, Feldspathic, Argillaceous Arkose Facies

These rocks contain variable amounts of quartz, feldspars, and clay minerals. Feldspars are very abundant, averaging 25% to 40%; quartz averages approximately 20% (**fig. 2**). Clay minerals are also extremely abundant (averaging 40% to 45%). OM in these rocks is extremely low, typically less than 1%. Visual, macroscopic core descriptions show that these rocks, and the Feldspathic, Quartzose, and Argillaceous Arkose Facies subsequently discussed, contain abundant sand-sized grains of quartz and feldspar and are equivalent to Sandstone and Muddy Sandstone lithologies (**fig. 1**). These rocks are common in the upper parts of depositional cycles in Chang 7 and Chang 8 and are dominant in Chang 6 (**fig. 2**). Comparison of chemostratigraphic data with visual, reconnaissance core descriptions shows that these rocks contain abundant sand- and silt-sized grains (that is, sandstones and siltstones; **figs. 6A, B, and C**) and correlate well with rocks defined macroscopically in this study as sandstones (**fig. 1**).

Feldspathic, Quartzose, Argillaceous Arkose Facies

As do the Quartzose, Feldspathic, Argillaceous Arkose Facies, these rocks contain variable amounts of quartz, feldspars, and clay minerals. However, feldspar is much less abundant (average 15% to 20%), and quartz is more abundant in this facies (30% to 40%) (**fig. 2**). Clay mineral volume averages approximately 40%. Also like the Quartzose, Feldspathic, Argillaceous Arkose Facies, these rocks contain little or no OM. This facies is uncommon in the cored intervals. For the most part, it is found in Chang 6 and as thin interbeds in Chang 9 (**fig. 2**).

Organic-Matter-Rich Argillaceous Mudstone Facies

These rocks and the subsequently described Organic Matter Lean Argillaceous Mudstone Facies are characterized by having high levels of clay minerals. In this facies, clay minerals average 60% and quartz and feldspars average 15% to 20% each (**fig. 2**). OM is abundant, typically averaging 4% to 6%, locally ranging up to 9% (**figs. 3 and 4**). These rocks dominate the lower part of Chang 7. They are also found near the base and in the middle of Chang 8, where they define flooding events (**fig. 2**). Visual core descriptions show these rocks to be dark gray to black and massive to weakly laminated (**figs. 6D, E, F, and G**); they are typically referred to macroscopically simply as mudstones (e.g., **fig. 1**).

Organic-Matter-Lean, Argillaceous Mudstone Facies

This facies is similar in mineral composition to the Organic-Matter Rich Argillaceous Mudstone Facies, with which it is commonly interbedded, but it differs in containing less OM (average 2% to 3%). Like the Organic Matter Rich Argillaceous Mudstone Facies, these rocks are most common in the lower part of Chang 7 but also are found in Chang 6, 8, and 9 (**fig. 2**). When viewed macroscopically in core, they are commonly laminated, lighter in color because of the greater abundance of silt- and sand-sized grains (**figs. 6E, F, and G**), and referred to macroscopically as sandy mudstones (e.g., **fig. 1**).

Other Minor Facies

Two other lithologies were identified based on a combination of visual and chemical studies: volcanic ash beds and the Dolomitic Mudrock Facies. Volcanic ash beds were observed in both the YY1 and the YY22 cores (**figs. 1 and 2**). Dolomitic mudstone is characterized by relatively high amounts of dolomite and was found only in the YY 22 core in the upper part of the Chang 7 unit (**fig. 4**).

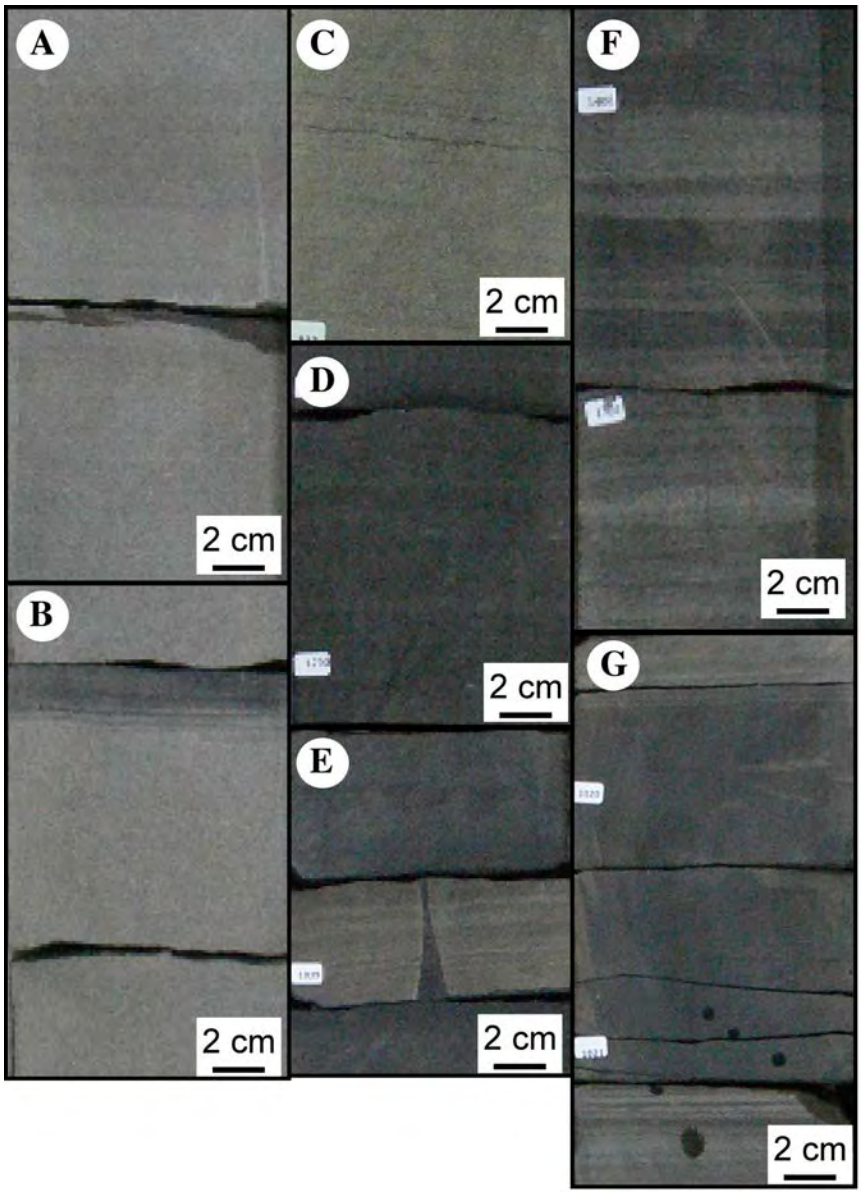

Figure 6. Core slab photographs of typical facies observed in the YY1 core. A. Light-gray, planar laminated sandstone of the Quartzose, Feldspathic, Argillaceous Arkose Facies. Depth: 1,470 m. Upper AB cycle, lower Chang 8 Unit. B. Same facies as A but displaying upward-fining gradation into laminated siltstone/mudstone. Depth: 1,434 m. Middle BC cycle, upper Chang 8 Unit. C. Similar to A but displaying low-angle cross laminations. Depth: 1,346 m. CD cycle, upper Chang 7 Unit. D. Dark gray to black, massive to weakly laminated mudstone of the Organic-Rich, Argillaceous Mudstone Facies. Depth: 1,456 m. Basal BC cycle, upper Chang 8 Unit. E. Interbedded dark gray to black, massive mudstone of the Organic-Matter-Rich, Argillaceous Mudstone Facies and planar laminated, sandy siltstone of the Organic-Matter-Lean, Argillaceous Mudstone Facies. Depth: 1,375 m. CD cycle, lower Chang 7 Unit. F. Thinly interbedded dark gray to black, planar laminated, mudstone of the Organic-Matter-Rich, Argillaceous Mudstone Facies and planar laminated, muddy siltstone of the Organic-Matter-Lean, Argillaceous Mudstone Facies. Depth: 1,406 m. CD cycle, base of Chang 7 Unit. G. Interbedded dark gray, massive mudstone of the Organic-Rich, Argillaceous Mudstone Facies and planar laminated, sandy siltstone of the Organic-Matter-Lean, Argillaceous Mudstone Facies. Note gradational contacts at base and top of Organic-Matter-Rich, Argillaceous Mudstone Facies. Depth: 1,372 m. CD cycle, upper part of lower Chang 7 Unit. Small numbers are XRF scan points.

Depositional Environments

Environments of deposition represented by these rocks are inferred from three primary characteristics: grain size, mineralogy, and OM abundance. Grain size data were obtained from megascopic, visual examination of the cores, supported by thin sections. Mineralogy and OM abundance were defined from chemostratigraphic data (XRF, XRD, RockEval, and isotope data).

All major facies (save the volcanic ashes) comprise four primary components: feldspars, quartz, clay minerals, and OM. Mudstone facies are finer grained and consist of greater volumes of clay minerals and OM, whereas, arkose facies contain higher volumes of quartz and feldspars and a mixture of coarser (that is, sand size) and finer (silt and clay size) particles. OM is common to abundant in the former and rare in the latter. Collectively these attributes indicate that the arkoses represent more proximal (that is, more landward) facies and the mudstone more distal (that is, more basinward) facies.

Previous studies have shown that during the Late Triassic, the Ordos Basin was a lacustrine system fed by marginal fluvial-deltaic complexes. Zhao and others (2015), in an excellent outcrop-based study and summary of earlier research, argued that most sediment was derived from deltas established on the northeast (NE) margin of the basin and braided streams systems to the southwest (SW) (**fig. 7**). Most sediment-transport models have interpreted the coarser grained sediment (that is, lithic sandstones, arkoses, and siltstones) to be associated with fluvial and proximal delta deposition, whereas finer grained sediments (mudstones) represent distal deposition in a prodelta (**fig. 8**) or central lake basin setting.

The major facies identified in this study are generally consistent with the previously summarized depositional models. However, the overall abundance of clay minerals in all facies, including the coarser grained arkoses, suggests that the depositional setting of the YY1 and YY22 cored wells during deposition of the Yanchang Formation was more distal than proximal. Although arkosic sandstones and siltstones are present, especially in the upper Chang 7 and in Chang 9 (**fig. 1**), they are muddy sandstones and siltstones (that is, argillaceous arkoses). This suggests that they were deposited in lower energy settings either in distal subaqueous delta margin or in proximal prodelta environments. The absence of OM in these rocks is a function of sediment dilution caused by rapid sediment influx and probably well-oxygenated conditions in these environments. The presence of cross laminations (**fig. 6C**) and local burrows in these rocks is additional evidence in support of this interpretation. However, more specific determination of the depositional processes and environments represented by these rocks was outside the scope of this study and requires a more detailed investigation of these and other coarse clastic facies.

The mudstone facies, which contain very high levels of clay minerals and significant amounts of OM, reflect deposition in low-energy, low-sediment accumulation rate settings distal to clastic input source areas. The Organic-Matter-Rich Argillaceous Mudstone Facies contains the highest levels of OM and probably represents deposition in the most distal parts of the lake in conditions of very low sediment-accumulation rate, lowest energy, and highest degree of anoxia. Lower levels of OM in the Organic-Matter-Lean, Argillaceous Mudstone Facies, coupled with lower volumes of clay minerals and higher levels of silt and sand-sized quartz and feldspar, suggest that these rocks accumulated during times of higher sediment flux than existed during deposition of the Organic-Matter-Rich Argillaceous Mudstone Facies with which they are interbedded.

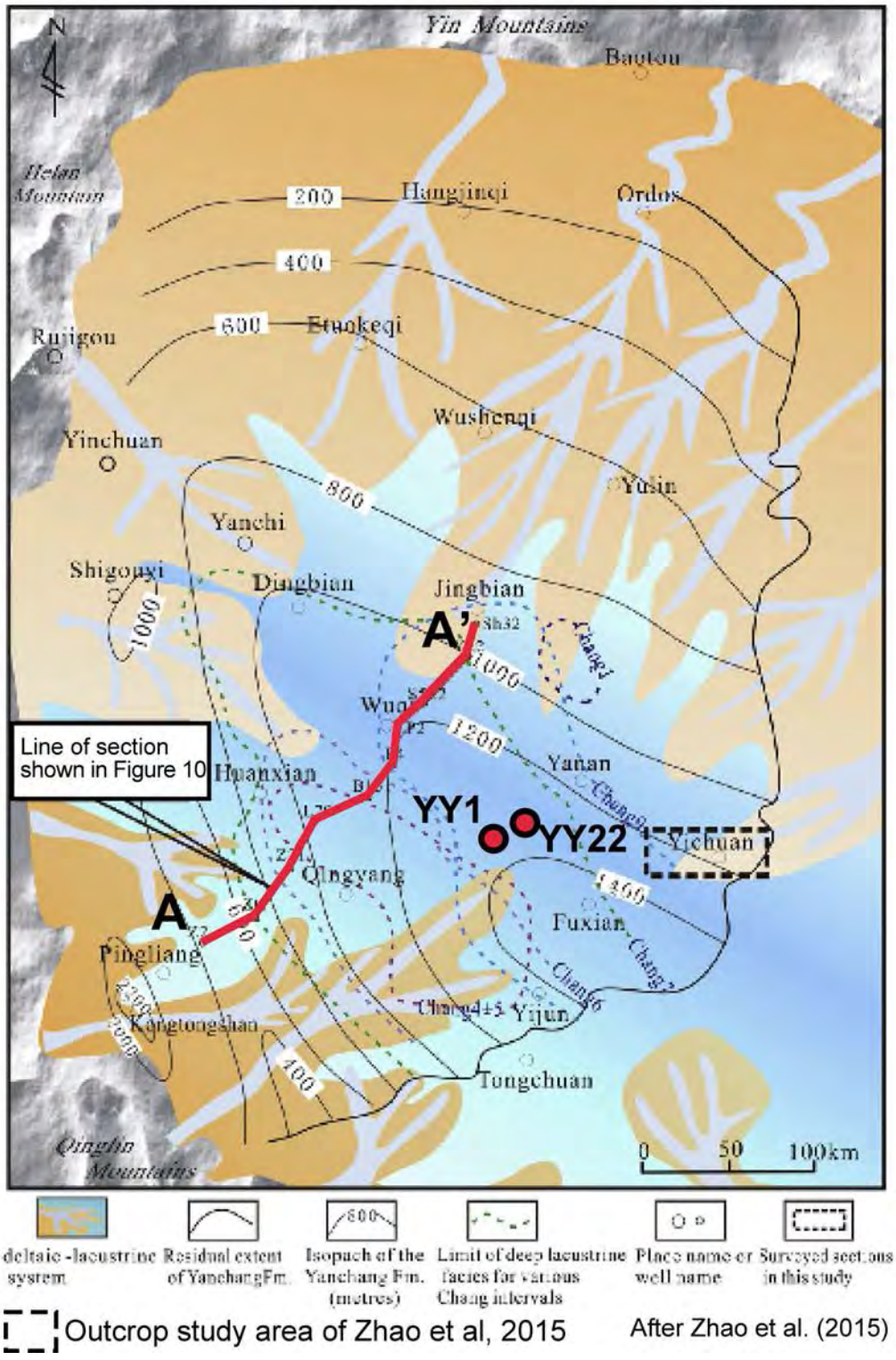

Figure 7. Map depicting general thickness trends and paleogeography of the Yanchang Formation in the Ordos Basin showing the location of the YY1 and YY22 cored wells.

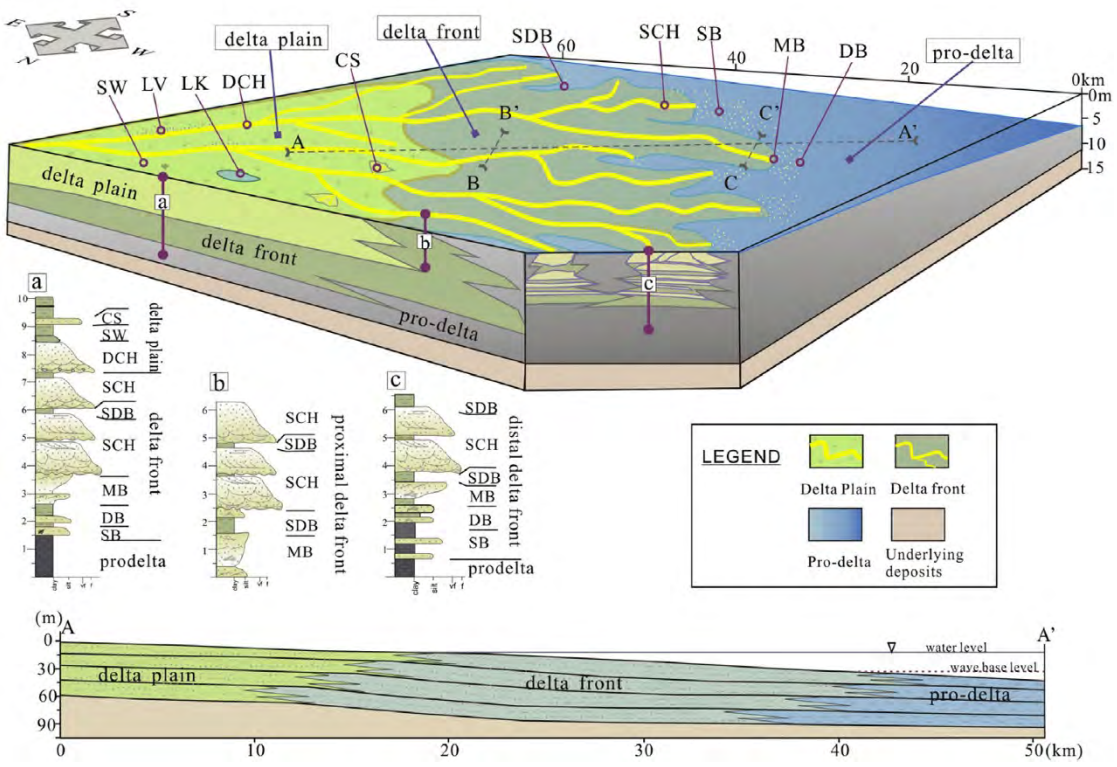

Figure 8. Model of depositional processes in the Ordos Basin. From Zhao (2015). Although representative of more proximal settings, this model does not completely characterize the facies and environments observed in the YY1 and YY22 cores.

These rocks may represent episodes of progradation during which more proximal sediments (that is, quartz and feldspars) were carried further into the basin, or they may document gravity-transport deposition. Determination of which mechanism is responsible was outside the scope of this study and requires a more detailed study of the quartz- and feldspar-dominated facies (that is, arkosic sandstones, and siltstones).

Figure 9 portrays the likely interrelationships of these facies along a depositional dip, assuming a simple punctuated progradation model of deposition. The Quartzose, Feldspathic Argillaceous Arkose Facies and Feldspathic, Quartzose, Argillaceous Arkose Facies were deposited in relatively proximal settings, most likely in the outer delta or proximal prodelta environments. Lower levels of clay minerals in the latter suggest more proximity to land or to distributary channels. The Organic-Matter-Rich Argillaceous Mudstone Facies and Organic-Matter-Lean, Argillaceous Mudstone Facies accumulated in much more distal settings in which the former most likely represent an extreme distal lake environment and the latter represents minor episodes of higher sediment flux, possibly related to gravity transport.

Isotope data obtained from OM carbon provide insights into changes in OM type consistent with interpretations of depositional environments. Isotopes show close relationships to facies: mudstones typically display lighter $\delta^{13}C$ values (< -30% PDB); whereas, arkoses exhibit much

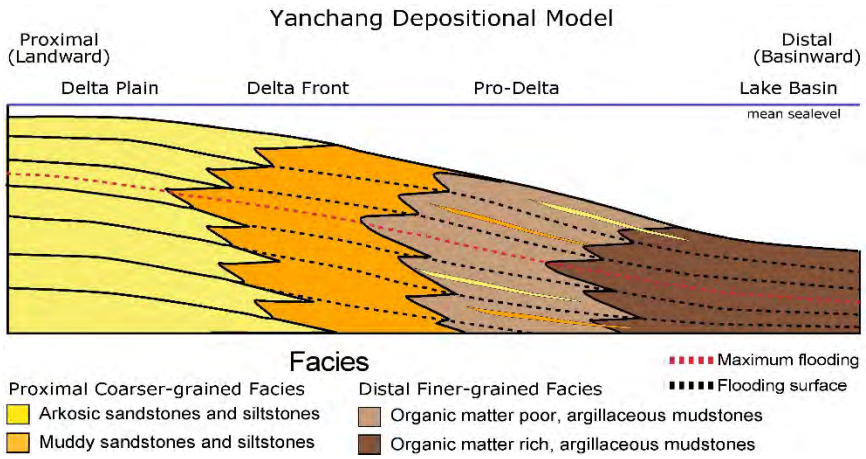

Figure 9. Diagrammatic cross section depicting general settings of primary facies types in the Yanchang Formation in the Ordos Basin along depositional dip. Facies observed in the YY1 and YY2 cores primarily represent deposition in prodelta and central lake basin settings. Note that thin interbeds observed in many intervals may be the result of episodic gravity transport of coarser grained facies into more distal (that is, downdip) areas.

heavier values of -27% to -28% δ^{13}C (fig. 2). This suggests the possibility that arkoses, which represent sediment flux from landward areas, may contain OM that is extremely different from that in the more distally deposited mudrocks. As in marine systems, proximal sediment flux is often associated with terrestrial OM, whereas distal environments are dominated by aquatic OM. Although both aquatic and terrestrial sources of OM in lacustrine systems commonly have similar carbon isotope values (at approximately -28% δ^{13}C) under some conditions isotopes from aquatic plankton can be shifted to much lighter values (Lewan, 1986). The relationships observed in the YY1 core suggest this strong possibility.

Cycle Stratigraphy

Vertical patterns of upward-coarsening facies in the YY1 core define several depositional cycles. Each of these cycles is marked by having OM-bearing mudstone facies at its base and more arkosic facies at its top (**figs. 1 and 2**). Because the mudstone facies that comprise the basal facies of each cycle represent the most distal (or downdip) facies in this system, the contact between these mudstones and the underlying arkoses can be considered flooding (or deepening) surfaces (that is, surfaces A, B, C, and D, **figs. 1 and 2)**. These surfaces define complete cycles: cycle AB and BC comprise Chang 8, and cycle CD comprises the entire Chang 7 unit (**fig. 2)**. [Note that the contacts defined for these cycles in this study approximate but do not precisely match previously picked boundaries for Chang 8 and 7 (e.g., **fig. 2**).] Definition of three of these flooding surfaces (A, B, and C) is apparent from OM abundance and type trends as well as from mineralogy trends. In contrast, surface D (the base of Chang 6) is defined on the basis of mineralogy alone (**fig. 2**). Cycles AB and BC are approximately 50 m thick, whereas cycle CD is twice that. Other, thinner (average 20-m) cycles are suggested by vertical variations in rock properties in Chang 6 and 8; however, more core control is needed to define their significance more precisely.

Previous studies (including that by Zhao and others, 2015, summarized herein) have recognized that the Yanchang Formation records several episodes of lake expansion and filling caused

primarily by varying rates of fluvial-deltaic and/or braided steam sediment influx and subsidence. They also argued that these alternations in sediment flux represent four depositional sequences and that the dominance of mudstone facies in the Chang 7 and Chang 9 units marks these intervals as times of major transgression and accumulation of organic-rich mudstone, whereas Chang 8 defines a period of progradation (**fig. 10**). Our studies of the Chang 7 unit are consistent with these ideas. However, facies stacking patterns in Chang 8 and Chang 9 in the YY1 cored well are more consistent with the former, representing a period of deepening compared with the latter. This is suggested OM and type trends from Chang 9 upward into Chang 8 (**fig. 2**). The stratigraphic succession characterized by YY1 and YY22 wells suggests the beginning of local transgression during the upper Chang 9, continued transgression during Chang 8, maximum flooding during the lower Chang 7 followed by the beginning of regression and progradation during upper Chang 7 and into Chang 6 (**fig. 2**).

Differences in depositional history and sequence definitions proposed by Zhao and others (2015) and our study may have several causes. First, it may be that the trends apparent in the YY1 and YY22 cores represent only local variations in regional trends. Second, these "patterns" may document differences in sedimentary architecture caused by significant subregional patterns of sediment flux. It is noteworthy that there is a major shift in feldspar abundance that begins in Chang 8 cycle tops and continues to increase upsection into Chang 6 (**fig. 2**). This change was also noted by Zhao and others, (2015) and may document a shift in a source area from fluvial deltaic sources to the northeast to more immature, lithic, feldspathic sandstones derived from braided stream complexes at the southwest margin of the basin (**fig. 7**). Third, wireline logs, like those used by Zhao and others (2015) to interpret regional patterns, may be insufficient to provide accurate measures of facies changes (see discussion of log/core relationships in a subsequent section). Resolution of these questions of facies architecture requires additional detailed studies of cored wells.

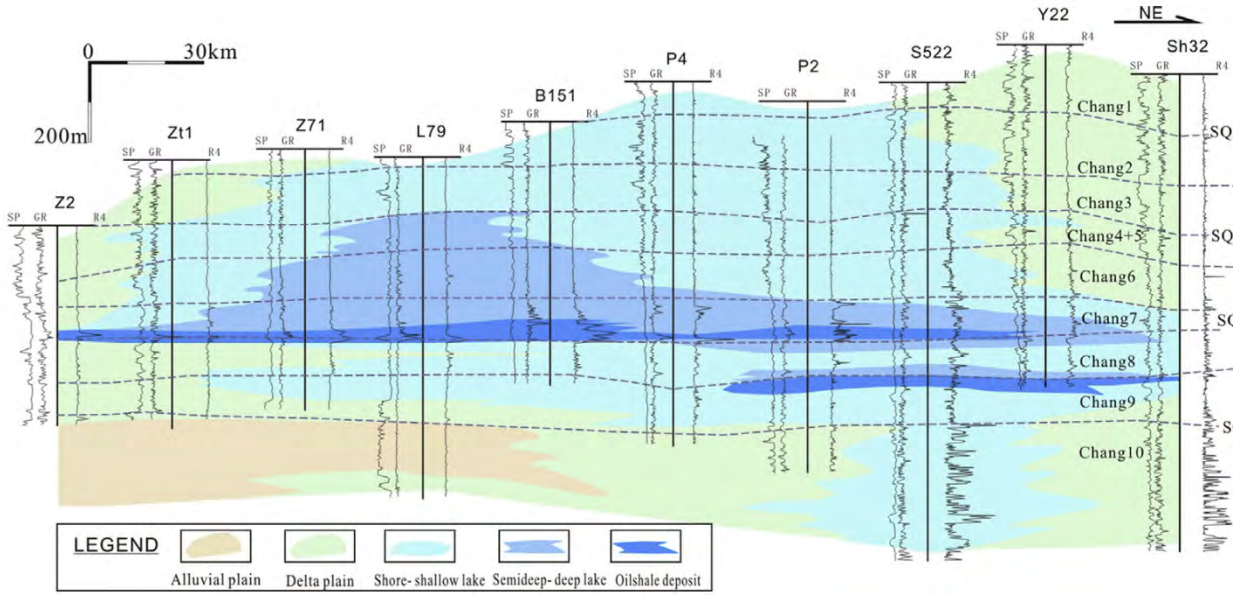

Figure 10. Regional cross section depicting the general facies architecture of the Yanchang Formation in the Ordos Basin. Modified from Zhao (2015).

Rock Strength and Brittleness

Wireline Log Relationships

For the facies and other rock attributes defined in the YY1 and YY22 cores to be of broader value in determining regional and subregional patterns of facies and reservoir development, it is important that they can be identifiable on wireline logs. In all subsurface successions, log calibration to cores is crucial to an accurate interpretation and correlation of facies distribution and rock properties. Some facies characteristics key to defining depositional environments are not definable from logs, especially sedimentary structures, such as burrows, laminations, grain-size variations, and floral and faunal content. In some cases, facies and depositional environments can be inferred from vertical and horizontal stratal relationships (e.g., thickness trends, vertical facies stacking patterns)—*if* well logs can be tied to cores *and* correlated confidently. General facies characters can, however, in many cases be interpreted from wireline logs based on mineralogical and elemental variations. In the Yanchang Formation, OM and clay mineral abundance are key rock attributes that can potentially be defined.

Defining Rock Attributes

Comparison of core-based measurements of OM with YY1 wireline logs shows that both density and resistivity logs display very good relationships to OM (**fig. 5**). Relationships are best in OM-matter-rich intervals such as Chang 7 and Chang 8 but are weaker in more arkosic intervals (that is, Chang 6). The neutron log acquired in the YY22 well also shows a very good correlation to OM abundance (**fig. 12**). Other logs (e.g., gamma-ray and acoustic logs) show general but far less accurate correlations to OM (**fig. 5**).

Clay mineral abundance is well defined by XRD and XRF measurements taken on core (**figs. 3 and 5**). As previously described, there is a close correlation to rock strength and OM matter abundance (**fig. 5**). However, ties to wireline logs are rather weak. Spectral gamma-ray logs, especially the computed gamma-ray log (K+Th), provide a general estimate. However, a better indicator of clay mineral variations is the density log, which ties closely to OM content and thus to clay mineral abundance in at least some parts of the core.

Interwell Correlations

Although only a short core was taken in the YY22 well, some observations can be made about the correlatability of facies and rock attribute data between YY1 and YY22. General recognition and correlation of the organic-rich mudstones that compose the lower part of the Chang 7 unit is possible using gamma-ray logs. However, precise correlation of this interval is best achieved with density and/or resistivity logs (**fig. 11**). These correlations are supported by ties to core-defined TOC and by signs of a large volcanic ash bed observed in both cores (**fig. 11**). Bases (flooding surfaces) of cycles A, B, and C can also be defined and correlated with gamma-ray logs. However, correlations of the upper Chang 7 Unit and Chang 6 are less clear. Some of the apparent ash beds in this part of the section appear to be continuous, thus offering insights into correlation.

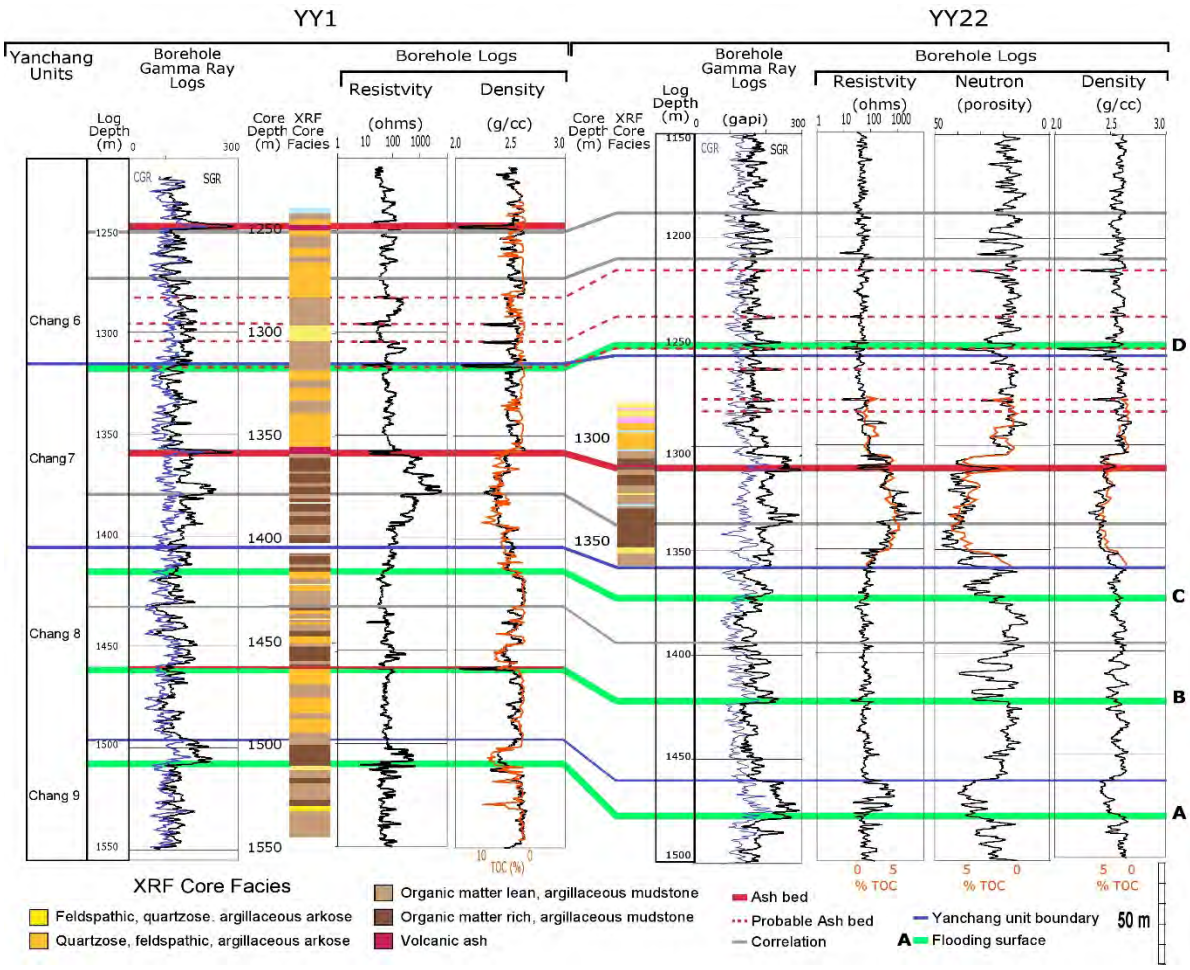

Figure 11. Cross section showing correlations between YY1 and YY22. Locations of wells are shown on **Figure 7.**

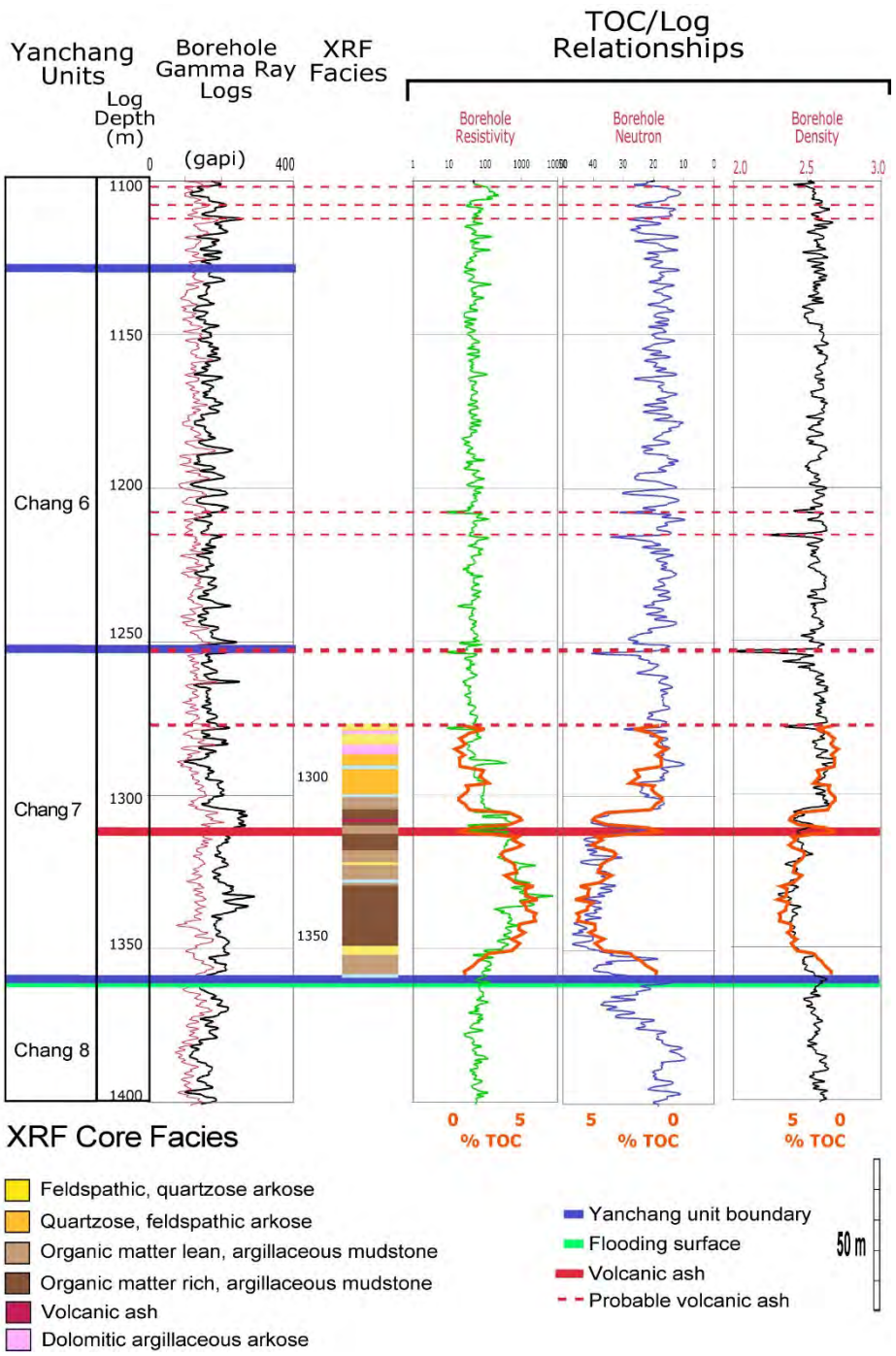

Figure 12. Plots showing relationships between wireline logs and core attributes in the YY22 well. TOC variations correlate well with both the density and resistivity logs but not with the gamma-ray logs.

Discussion

As previously discussed, the facies defined from integrated chemostratigraphic study of the YY1 and YY22 cores are indicative of deposition in a distal setting, i.e., close to the lake center where muddy, organic-matter-rich facies are most abundant. This finding is consistent with the position of these wells near the middle of the lake basin as defined by Zhao and others (2015) (**fig. 7**). However, Yanchang rocks in YY1 and YY22 do not fit the basic model of delta to prodelta deposition proposed by these authors (**fig. 8)** but instead represent mostly prodelta to lake center settings (**fig. 9)**. It is obvious, however, by the cyclic nature of finer and coarser clastics in Yanchang rocks that conditions of sediment supply and water depth have fluctuated because of changes in lake levels. This has been shown by previous authors and by the cycles defined in this study (e.g., **fig. 1)**. The range of water depths caused by these fluctuations is impossible to define in the YY1/YY22 area, however, using past or present studies. This determination requires a more detailed study of the coarse-grained facies, their sedimentary structures and textures, and fabrics. It seems likely from reconnaissance examination of these features in the YY1 core that many of the coarser grained intervals in the lower Chang 7 unit may be gravity flow deposits that reflect episodic transport of these more proximal sediments into deeper, more distal environments. Ripples and cross laminations present along with burrows in some of the arkosic sandstones and siltstones, especially in the upper Chang 7 and in Chang 6, do suggest shallowing and more proximal deposition. But again, validation of such interpretations must await further detailed core study.

The accommodation patterns depicted by our analysis of the YY1 and YY22 cores are in part in disagreement with those of previous authors. Our studies do support the idea that parts of the Chang 7 represent maximum deepening and expansion of the lake. However, stacking patterns suggest that Chang 8 represents part of the progressive deepening that culminated in deposition of Chang 7 organic rich facies rather than being part of a major progradation and shallowing of the basin. This difference could be a function of differential sediment input from the two dominant sources areas. Most other studies have been in the northern and eastern parts of the basin, where sediment flux was probably dominated by the fluvial-deltaic system to the northeast (see **fig. 7)**. The YY1 and YY22 wells are actually closer to the braided-stream delta system that dominated the southwestern part of the basin (**fig. 7)**. The abundance of feldspars in these two cores is consistent with sourcing from these braided streams, which apparently flowed from uplifted mountains just to the southwest (Zhao and others, 2015). Sediment flux from these two sources may not have been synchronous, thus producing different accommodation and facies stacking patterns in areas dominated by each system. If so, correlation of regional expressions of deepening and shallowing, as well as of individual formations and time lines, may be more difficult than has been inferred.

Wireline log correlations between YY1 and YY22 are reasonably straightforward (**fig. 11)**. But, this is, in part, because cores are available for both wells and, in part, because they are close to one another. All logs define mudstone-dominated intervals, the lower Chang 7 mudstone interval being the easiest to identify. However, correlations with gamma ray alone are not always straightforward because of the interbedding of facies. Correlation of flooding surfaces is even more problematic because of lateral changes in thickness and abundance of both clay minerals and OM. Because these surfaces provide the best indicators of at least subregional temporal

correlation it is critical that their correlation be based on all available logs. Most logs demonstrate some degree of accuracy of correlation with TOC abundance (**figs. 5**). Because TOC primarily varies closely with clay mineral abundance, logs can also be used to define general variations in clay mineral abundance. Comparison of these relationships suggest that density, resistivity, and in some cases neutron, logs are best for this purpose (**fig. 11**). The presence of volcanic ash beds in some areas can also help constrain correlations between wells. A few ash beds were observed in reconnaissance study of cores—the thickest and most obvious of which includes one at the top of the lower Chang 7 in cycle CD and one near the top of the top of the YY1 core in Chang 6 (**fig. 11**). Examination of log responses to these known ash beds suggests that others can be defined from logs. Typical log responses include high spikes in gamma-ray logs and low spikes in density and resistivity logs (**fig. 2**). Similar log responses suggest the presence of several thin ash beds in Chang 6, in addition to the thick one observed in core (**fig. 11**).

Measurements of rock strength show a close correlation with clay mineral and OM abundance (**fig. 5**). The high levels of clay minerals in mudstones indicate that they are likely to be poor candidates for hydraulic fracturing. Arkosic facies also have relatively high clay mineral contents (as much as 40%), but they display much higher rock strength, thereby suggesting they can develop and transmit fractures well.

Characterizing OM types is difficult in rocks that have reached even modest levels of thermal maturation. However, carbon isotope values measured from OM in the YY1 core provide possible clues to variations in the types present in Yanchang facies in this area. Carbon isotope values of lake aquatic and terrestrial OM are similar (at approximately -28% $\delta^{13}C$). However, aquatic macerals are characteristically more subject to methanogenic degradation than is less reactive land-derived OM (Meyer and Ishiwadari, 1993). Methanogenesis can produce substantially depleted $\delta^{13}C$ values, like those seen in Yanchang OM-rich facies. Recycling of this $\delta^{13}C$ depleted CO_2 by aquatic plankton can thus result in very light depleted $\delta^{13}C$, values such as those seen in Yanchang 7 mudstones. Lewan (1986) argued that these conditions are common in shallow lacustrine lake basins where the water mass is highly stratified. Thus, the close correlation between OM-rich facies, which are interpreted to have accumulated in environments distal to terrestrial source areas, and depleted isotope values (**fig. 5**) is consistent with a model of land-derived OM dominance in more arkosic facies and aquatic dominated OM in distal mudrocks.

Summary and Key Findings

Our integrated chemostratigraphic studies of the YY1 and YY22 cores are the first conducted on the Yanchang Formation and, as such, provide important new insights into the facies, depositional environments, rock attributes, and wireline log relationships of the succession. Key findings include the following:

- Integrated, high-resolution XRF and XRD data provide the first detailed analysis of mineralogical facies variations in the Chang 6 through 9 members.
- Four major facies can be defined, including OM-lean, coarser grained, arkosic sandstones and siltstones, and finer grained, OM-bearing mudstones.

- The abundance of clay minerals in all facies indicates that the YY1 and YY22 wells are located in a relatively distal part of the lake basin compared to previously studied areas.
- Carbon isotope data suggest that mudstones contain primarily aquatic OM; whereas arkoses contain terrestrial OM.
- Facies stacking patterns define four flooding surfaces, which form the basis of major cycles or sequences that are key correlation events.
- General facies types can be interpreted from most wireline logs, but detailed correlations require consideration of all log responses.
- Variations in OM are well defined by density and resistivity wireline logs.
- Rock strength correlates closely with clay mineral and organic abundance, that is, with mudstone facies.
- Because of their high clay mineral content, mudstones are relatively ductile at reservoir depths and probably poor candidates for hydraulic fracturing.
- Volcanic ash beds, which are locally common and can, in some cases, be defined by log responses, thereby, making them possible aids in interwell correlation.

References

Lei, Y., Luo, X., Wang, X., Zhang, L., Jiang, C., Yang, W., Yu, Y., Cheng, M., and Zhang, L., 2015, Characteristics of silty laminae in Zhangjiatan Shale of southeastern Ordos Basin, China: Implications for shale gas formation: AAPG Bulletin, v. 99, p. 661–687.

Lewan, M.D., 1986, Stable carbon isotopes of amorphous kerogens from Phanerozoic sedimentary rocks: Geochimica et Cosmochimica Acta, v. 50, p. 1583–1591.

Loucks, R., and Ruppel, S., Thin-Section Description of Lithofacies of the Late Triassic Yanchang Formation (Chang 7, 8, and 9 Members) Lacustrine System in the Yanchang Petroleum Group YY1 and YY22 Wells, Southeastern Ordos Basin, China: This volume Task 2.1.

Meyers, P.A., and Ishiwatari, R., 1993, Lacustrine organic geochemistry: an overview of indicators of organic matter sources and diagenesis in lake sediments: Organic. Geochemistry, v. 20, no. 7, p. 867–900.

Rowe, R., Zhang, T., Milliken, K., Ruppel, S., Loucks, R., and Sivil, E., 2016, Mineralogy, Chemostratigraphy, and Isotope Stratigraphy of the Triassic Yanchang Formation, Ordos Basin, China: This volume, Task 1.2.

Yuan, X., Lin, S., Liu, Q., Yao, J., Wang, L., Guo, H., Deng, X., and Cheng, D., 2015, Lacustrine fine-grained sedimentary features and organic rich shale distribution pattern: A case study of Chang 7 Member of Triassic Yanchang Formation in Ordos Basin, NW China: Petroleum Exploration and Development, v. 42, p. 37–47.

Zhao, J., Mountney, N.P., Liu, C., Qu, H., and Lin, J., 2015, Outcrop architecture of a fluvio-lacustrine succession: Upper Triassic Yanchang Formation, Ordos Basin, China: Marine and Petroleum Geology, v. 68, p. 394–413.

TASK 1.2

Mineralogy, Chemostratigraphy, and Isotope Stratigraphy of the Triassic Yanchang Formation, Ordos Basin, China

Harry Rowe[1], Stephen C. Ruppel[1], and Bojiang Fan[2]

[1]Bureau of Economic Geology (BEG), Jackson School of Geosciences, The University of Texas at Austin, Austin, TX
[2]Shaanxi Yanchang Petroleum (Group) Co. Ltd., Xi'an, Shaanxi, China

Background

The Yanchang Formation of North-Central China represents a large (370,000 km^2), long-lived (>20 million years) fluvio-lacustrine system of Late Triassic age. The current understanding of the tectonic and climatic history during Yanchang deposition indicates a complex syn- and post-depositional compressional tectonic setting (Liu and others, 2013; Bao and others, 2014), with a temperate-humid climate (**fig. 1**, Liu, 1998; Zhao and others, 2010). The potential exists for the Yanchang Formation to be used as a depositional and hydrocarbon reservoir analogue of overlying Jurassic-aged strata in the Ordos Basin, and the may be analogous to other fluvio-lacustrine systems developed in overall compressional tectonic regions.

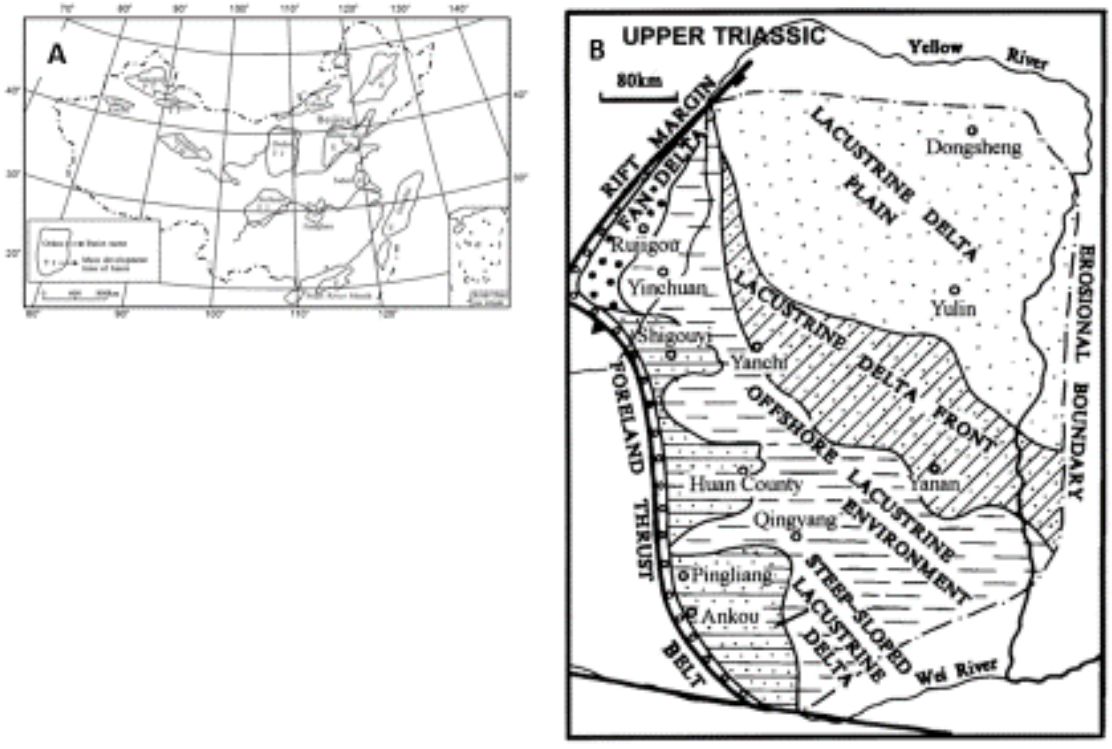

Figure 1. Location map of major structural basins in China (A, Zhao and others, 2010), and the Ordos Basin of North-Central China (Liu, 1998).

With varied success chemostratigraphic studies continue to be integrated with more traditional evaluations of drill core (e.g., Nance and Rowe, 2015; Fairbanks and others, 2016). A primary reason for taking core during the drilling process is for the stratigraphic succession and the sedimentary materials from which it is taken can be observed. The sedimentary facies definition is one of the most fundamental methods of describing a drill core. Thus, to optimize the understanding of a chemostratigraphic variability, geochemical data must be collected on the scale of facies variability. This has been accomplished for the Yanchang Formation, and the outcome yields a much more quantitative perspective of facies variability. Moreover, petrophysical properties can be compared with highly resolved chemostratigraphic results to better understand the linkages between mineralogical and rock physics variability.

X-ray fluorescence (XRF) and x-ray diffraction (XRD) analyses constrain stratigraphic changes in mineralogy and provide insights into the conditions under which organic matter accumulated. Measurements of total organic carbon (TOC) reveal strong mineralogical controls on organic matter accumulation. The chemostratigraphic study of a 300-meter-long core from near the central axis of the Ordos depocenter reveals intervals (<10 m to 65 m thick) of fine-grained lacustrine strata, interpreted to represent a deep-water lacustrine deposition, interspersed with thick (10 to 30 m) intervals of arkosic sandstones, reflective of deltaic deposition during lake lowstands. Along with elevated concentrations of %Al, a proxy for clay content, maximum TOC values in the deep-water lacustrine facies reach 8%, with average values of ~3%. The fine-grained, organic-rich facies is also characterized by elevated sulfur concentrations (up to 6%), a proxy for pyrite, and an indicator of more reducing conditions in the deep water mass of the lake during highstand intervals (representing times of the highest lake levels). Concentrations of %P are also elevated in the deep-water facies, indicating enhanced preservation of phosphorus, probably from fish bones, teeth, and scales. Most redox-sensitive trace element (RSTE) concentrations are only mildly elevated in the deep-water lacustrine facies, especially zinc (Zn), vanadium (V), and uranium (U); however, U concentrations are punctuated in thin intervals within the deep lacustrine facies, suggesting episodes of enhanced suboxia/anoxia during lacustrine highstands.

The stable isotopic composition of total organic carbon ($\delta^{13}C_{org}$) in the succession varies from approximately -34% to -26% (an 8% range). Most values of the ratio of total organic carbon (TOC) to nitrogen (C/N) fall below 10, suggesting the dominance of algal and microbial sources, which are also supported by the overall depleted $\delta^{13}C_{org}$ values. Higher C/N values are reflective of either greater terrestrial inputs or differential remineralization of N with respect to C—a process that is very common in both lacustrine and marine environments. Overall, the bulk organic characteristics point toward algal and/or microbial sources for the primary organic matter.

Although dramatic shifts between delta and deep lacustrine deposition are recorded in the Yanchang strata, no evidence indicates the lacustrine system ever built up appreciable salt concentration (Ji and others, 2010), thereby suggesting that an outlet was maintained throughout the depositional history. Some geochemical evidence supports the idea that the overall climate was humid (Qiu and others, 2015), but additional results that help provide constraints on water balance are lacking.

The following questions are posed in this study, and answers to these questions are expected to refine our understanding of bulk rock properties, paleoenvironmental conditions, and stratigraphic architecture—all relating to the heterogeneity of facies.

1) What is the stratigraphic variability in the bulk elemental composition of the Yanchang Formation?
2) How does the inorganic elemental composition relate with the organic content?
3) How does the bulk elemental composition compare to the mineralogical composition, as inferred using X-ray diffraction techniques?
4) What can be said about the evolution of fluvio-lacustrine deposition, as preserved in cores from the Yanchang Formation?

Sampling

Drill cores of the Yanchang Formation were sampled for their bulk inorganic elemental geochemistry (XRF chemostratigraphy), mineralogy (X-ray diffraction), and TOC during November and December 2013. **Table 1** lists the number of XRF, XRD, and TOC/$\delta^{13}C_{org}$ analyses for the YY1 (YY1112), YY22 (YY1133), YY8, and YY32 cores. The sampling strategy focused on the entire succession (sandstones, siltstones, and mudrocks), with an emphasis on the clay- and TOC-rich mudrock intervals.

Table 1. Tally of XRF, XRD, and TOC analyses for all sampled cores.

Core	XRF Samples	XRD Samples	TOC/$\delta^{13}C_{org}$ Samples
YY1112	2207	206	458
YY1133	577	X	72
YY0000	83	X	19
YY0001	57	X	16

Methods

X-ray fluorescence analysis was undertaken on the cleaned slab face of the four cores previously mentioned using two Bruker TRACER III-V XRF units. Each stratigraphic interval was analyzed for major (Na, Mg, Al, Si, P, S, K, Ca, Ti, Mn, and Fe) and trace (Ba, V, Cr, Co, Ni, Cu, Zn, As, Ga, Pb, Th, U, Rb, Sr, Y, Zr, Nb, and Mo) elements for 60 seconds. Raw X-ray spectra were calibrated using well-defined calibration reference materials (Rowe and others, 2012). The sampling interval varied slightly but was generally 10 cm.

Sample powders for XRD and TOC were drilled from the back of the slabbed core at a variable interval that attempted to capture the variability in facies but also to maintain a level of continuity. For the YY1112 core, the sampling interval for XRD analyses had an average of 11 m. XRD analyses were undertaken with an Olympus BTX diffractometer, with Cu K-alpha radiation, and a scan range of 2 to 55°. Sample spectra were used with mineral libraries (PDF-2 library) to define sample mineralogies using XPowder, yielding a semiquantitative data set. These data were supplemented with high-end quantitative XRD results obtained from KT Geoservices (see Ruppel and Rowe, Task 1.1 of this volume).

For TOC samples, the average sampling interval was 4 m. TOC samples were analyzed using a Costech Analytical ECS-4010 combustion unit coupled by way of a Conflo-IV device to a ThermoFinnigan Delta V isotope ratio mass spectrometer. TOC values were calibrated with an acetanilide standard. Values of the stable isotopic composition of a TOC ($\delta^{13}C_{org}$) were calibrated with internationally accepted standards (National Institute of Standards [NIST] and International Atomic Energy Agency [IAEA]) and in-house reference materials (glutamic acid).

In an effort to develop traceable (repeatable), multielement-defined sample groupings, the statistical technique of hierarchical cluster analysis (HCA) was undertaken using the XRF chemostratigraphy data as input. Provided that sufficient insight can be gained regarding the elemental signatures and relative rankings of elemental concentrations within the groupings, known in statistical terms as *clusters*, chemically defined facies, or *chemofacies*, can be developed. Specifically, the Ward's Method of HCA was used with all elemental values recalculated on a scale from 0 to 1. All major elements were input as weight percent. No trace elements were used in the analysis, but their concentrations and enrichments were tallied for each cluster. The major elements used in the HCA were: carbonate-related elements (Ca, Mn, and Mg), siliciclastic-dominated elements (Al, Ti, K, and Si), pyrite-related elements (S and Fe), and phosphate-related elements (P). Evaluation of the sample dendrogram created during the HCA process indicated that an initial choice of seven clusters provided significant subdivision of the data set. Following the definition of the clusters, the average elemental concentration was calculated for each cluster, and elemental rankings were calculated for each cluster by dividing the elemental averages within each cluster by the elemental averages of the entire data set. These enrichment rankings collectively form a partition index table (Phillips, 1991) that can be used to assess elemental enrichments in each cluster and their linkages to mineralogical and/or phase abundances.

Results

The dominant minerals observed in core materials are quartz, calcite, ankerite, illite, albite (bulk feldspars), kaolinite, pyrite, and apatite (minor). As noted, the feldspars were lumped under the "albite" heading because of the semiquantitative nature of the XRD system type used. Additional work using higher-end instrumentation better elucidates the breakdown of the feldspars, which is of greater importance in the Yanchang Formation because the dominant lithologies are arkosic (see Ruppel and Rowe, Task 1.1 of this volume).

Because of the primary need to understand the origin, stratigraphic location, and fate of organic matter in this study, the XRF chemostratigraphy is placed in the context of TOC. **Figure 2** shows the TOC content (in weight percent) for the YY1112 core. Yellow shading denotes the organic-rich intervals. It is noted that high values of TOC are coincident with %Al enrichment. In most mudrock successions, the %Al content is generally an indicator of the clay content (Algeo and Maynard, 2004). Although a significant portion of the aluminum-bearing mineral matrix is composed of feldspars (see XRD mineralogy), it is still the case that the %Al is higher in the TOC-rich intervals because of the clay content. Thus, %Al is used as an indicator of clay content in the mudrocks.

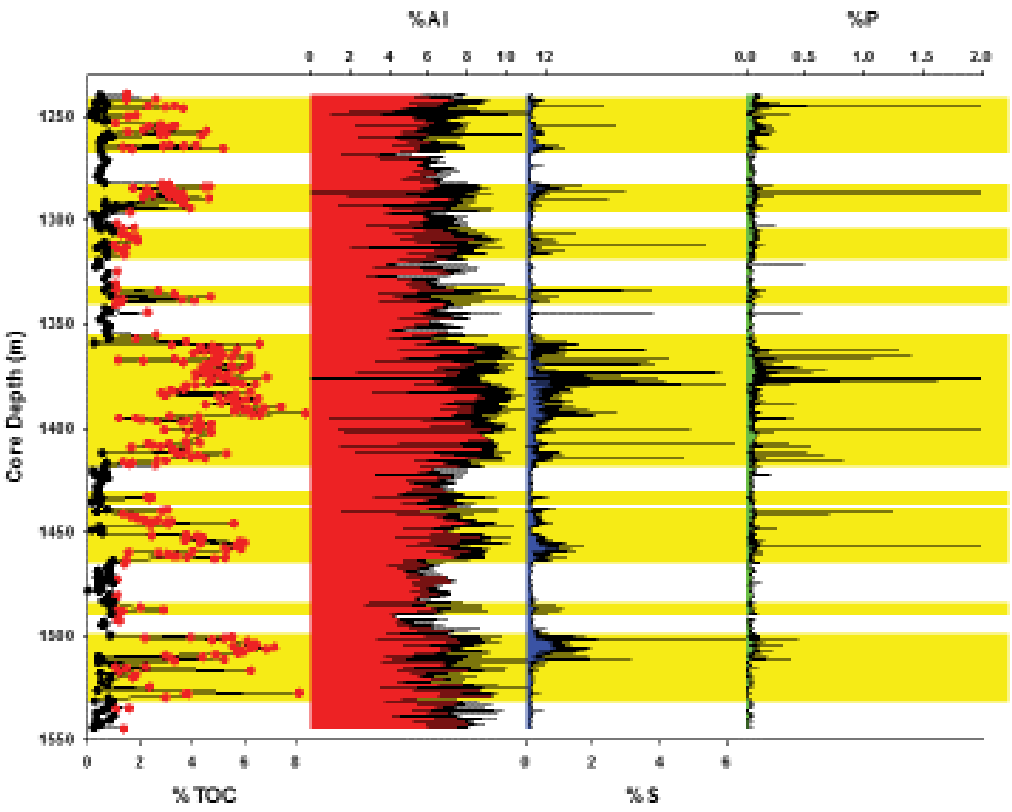

Figure 2. Chemostratigraphic data for YY1112 (YY1) core: %TOC (organic matter proxy), %Al (clay content), %S (pyrite proxy), and %P (fish bones, productivity proxy). Although a dramatic range in elemental composition is observed, the results can be simplified into TOC-rich (red circles, >1%), and TOC-poor (black circles, <1%). High TOC intervals are also elevated in clay (%Al), pyrite (%S), and apatite (%P). The yellow-shaded intervals are used simply to draw the eye to the proxy relationships with %TOC.

It is also observed that the %S is enriched in the TOC- and clay-rich intervals. Mineralogical analysis (XRD) indicates that pyrite is the dominant sulfur-bearing mineral phase in the succession, and thus, it is inferred that %S is a proxy for pyrite. And, the %S is well correlated to the %TOC, with some scatter. The linkage between %S and pyrite is also supported by the arsenic (As) content (**fig. 3**), because As is incorporated into the pyrite mineral structure. Furthermore, the phosphorus content (%P, **fig. 2**) tends to be enriched but compositionally erratic in the TOC-, clay-, and pyrite-rich intervals. Apatite was determined to be the P-bearing mineral of greatest abundance in the succession, thus, the %P is inferred to be a proxy for apatite, the concentration of which is generally assumed to reflect variations in the concentration of fish bones, teeth, and the like.

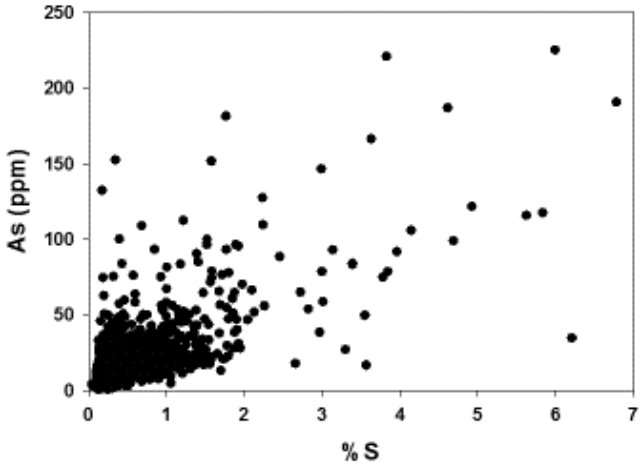

Figure 3. Cross-plot of %S and As (ppm), indicating their general positive relationship and defining their affinity in pyrite.

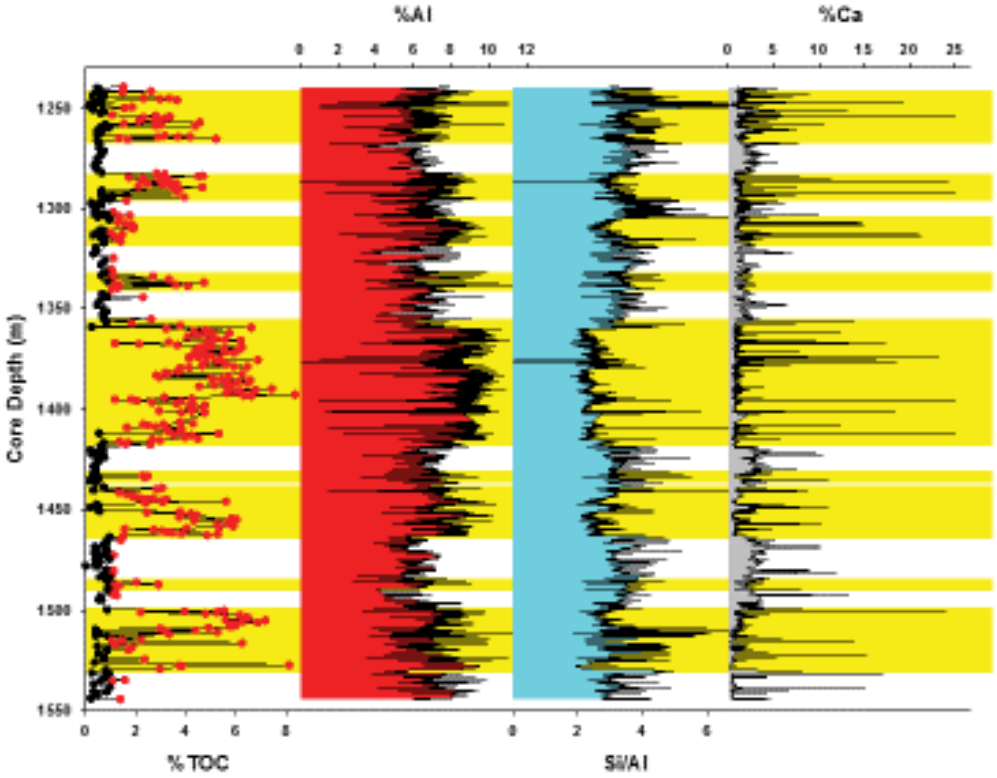

Figure 4. Same as **Figure 2**, except demonstrating the Si/Al (proxy for quartz/clay in mudrocks) and %Ca (proxy for calcite) in the context of organic content (%TOC) and clay content (%Al). Both quartz and calcite are enriched in the coarser-grained, fluvio-deltaic facies intervals.

Figure 4 demonstrates the variable controls that Si/Al (a proxy for quartz) and %Ca (a proxy for calcite) have in the Yanchang chemostratigraphy. Note that the Si/Al is generally higher in the low-%Al (low clay) intervals. Furthermore, the %Ca is highest (but compositionally erratic) in

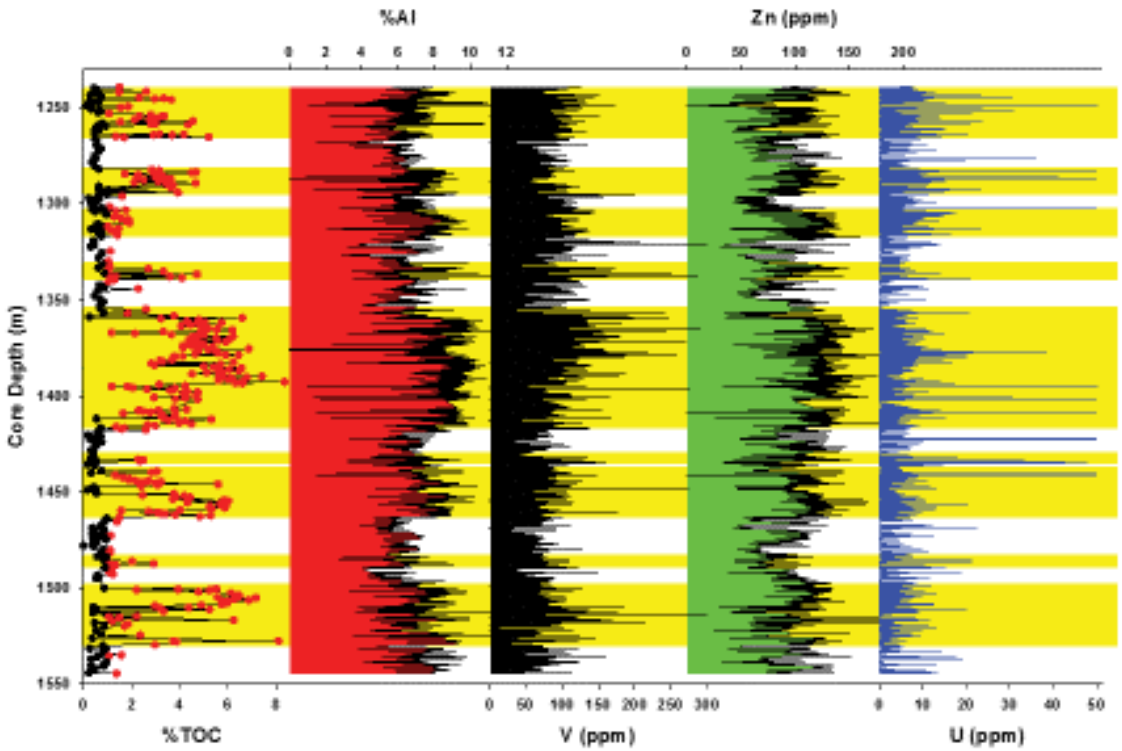

Figure 5. The redox-sensitive elements (V, Zn, U), demonstrating that only a mild enrichment of these elements occurs, and in general, higher values occur in the clay-rich, TOC-rich intervals.

the low-clay intervals. Thus, quartz and calcite are more abundant in the low-TOC, low-clay, low-pyrite, low-apatite intervals. Elemental concentrations of three of the redox-sensitive elements (e.g., V, Zn, and U) are observed in the Yanchang succession (**fig. 5**). Their concentrations are generally low, and with respect to U, are often at or just above the limit of detection. Unfortunately, uranium is a very difficult element to measure using the energy-dispersive XRF technique; therefore, the data are rather "jumpy." Similarly, values of other redox-sensitive elements (e.g., Mo, Ni, and Co) are quite low.

Figure 6 demonstrates that the semiquantitative XRD work undertaken on the core materials largely supports the high-resolution XRF results. Note that the TOC- and %Al-rich intervals are also enriched in the XRD-determined clay minerals and pyrite. And, the coarser-grained intervals that lack clay minerals are enriched in quartz.

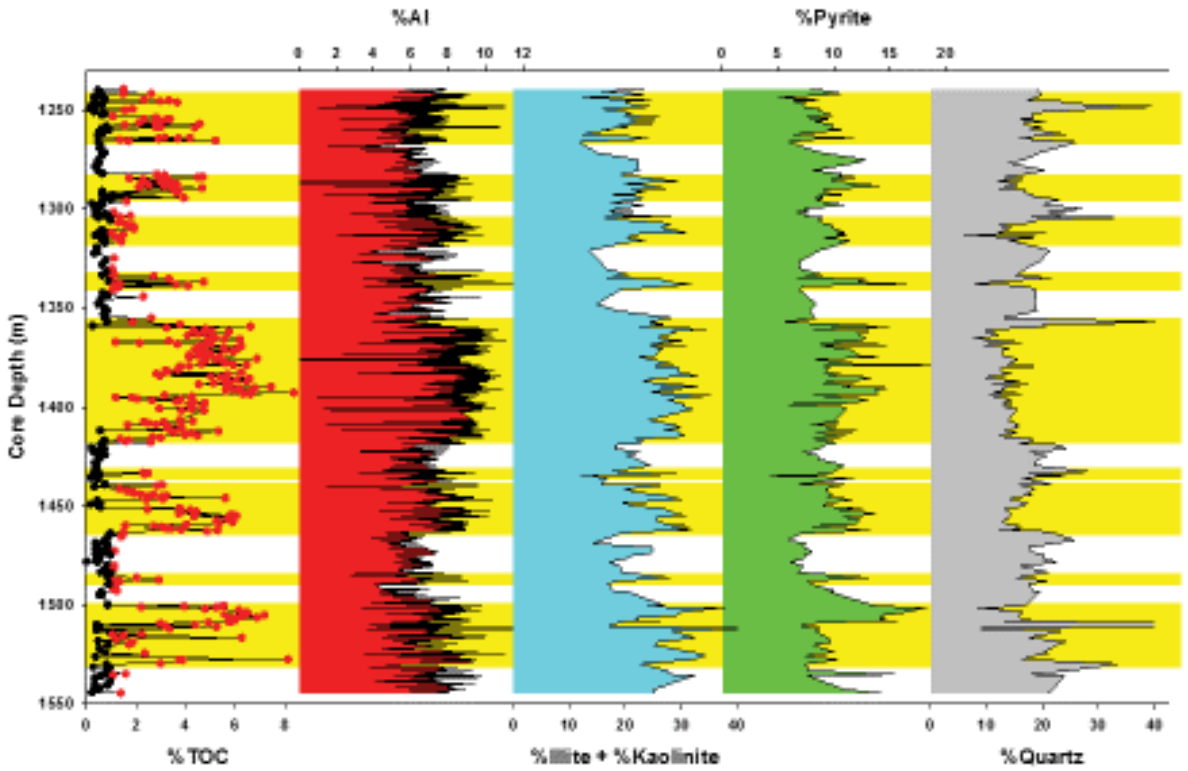

Figure 6. Chemostratigraphy and mineralogy (from XRD) linkages. The high-TOC and high-%Al intervals (determined using XRF) are the same intervals that are high in the clay minerals and pyrite, and low in quartz, as determined using XRD.

The outcomes of the hierarchical cluster analysis, elemental ranking through the use of a partition index table (**Table 2**), and the expression of the resulting chemofacies are plotted in stratigraphic order in **Figure 7**, and the relative abundance of the chemofacies are shown in **Figure 8**. These chemofacies are subsequently discussed and more deeply interpreted.

Table 2. Partition index table for the YY1112 core XRF-defined chemostratigraphic data. Each value represents the average concentration of an element within the HCA-defined cluster divided by the average concentration of that element in the entire data set. The calculation represents an estimate of elemental enrichment (or depletion) within each cluster, which is related to the sample mineralogy (primary and diagenetic phases) and the organic matter. Carbonate-dominating elements (Ca, Mg, and Mn) are shown in blue. Elements that generally act as proxies for clay content (Al, Ti, and K) are in green. Silicon (Si) is yellow to demonstrate relative ranking in quartz. Elements largely associated with pyrite (Fe and S) are red, and phosphorus (proxy for phosphates) is gray. Although sodium (Na) was not used in the cluster analysis (it is not an easily measured element with XRF), its average abundances were calculated and tallied along with the other elements. The "HCA-defined Chemofacies Assignment" given to each cluster is based both on the elemental ranking and on previous knowledge of the lithostratigraphy. Ss = sandstone, ss = siltstone, and mS = mudstone.

Element	Clust-0	Element	Clust-1	Element	Clust-2	Element	Clust-3	Element	Clust-4	Element	Clust-5	Element	Clust-7
n=	246	n=	378	n=	58	n=	706	n=	20	n=	24	n=	775
%Ca	1.55	%Ca	1.19	%Ca	4.05	%S	1.25	%P	70.08	%S	9.05	%K	1.27
%Mn	1.09	%Si	1.15	%Mn	1.55	%Mn	1.17	%Ca	10.57	%Mg	1.84	%Al	1.15
%Na	1.07	%Ni	1.00	%Ni	1.08	%Fe	1.12	%S	3.24	%Fe	1.49	%Ti	1.08
%Fe	1.00	%Mn	0.88	%Mg	0.84	%Ti	1.11	%Mg	3.03	%P	1.42	%Mg	1.03
%Ni	0.94	%Al	0.85	%P	0.78	%Mg	1.10	%Fe	0.80	%Al	1.08	%Si	1.03
%Si	0.88	%K	0.79	%Si	0.70	%Al	1.05	%Mn	0.73	%Ti	1.02	%Na	1.02
%Mg	0.80	%Fe	0.77	%Fe	0.69	%Si	0.98	%Na	0.65	%Si	0.89	%Fe	1.01
%Al	0.77	%Ti	0.77	%Ti	0.58	%Na	0.97	%Ti	0.56	%K	0.88	%S	0.88
%K	0.75	%Mg	0.74	%Al	0.55	%K	0.96	%Al	0.35	%Mn	0.68	%Mn	0.87
%S	0.52	%S	0.55	%S	0.55	%Ca	0.74	%Si	0.34	%Na	0.63	%Ca	0.52
%P	0.33	%P	0.33	%K	0.51	%P	0.41	%K	0.29	%Ca	0.44	%P	0.30
HCA-defined Chemofacies Assignment	(Clayey) SS, sS		(Clayey) SS, sS		Calc-cemented SS, sS		Pyrite mS		P-Carb SS, sS		Pyrite-Mg mS		Silty mS

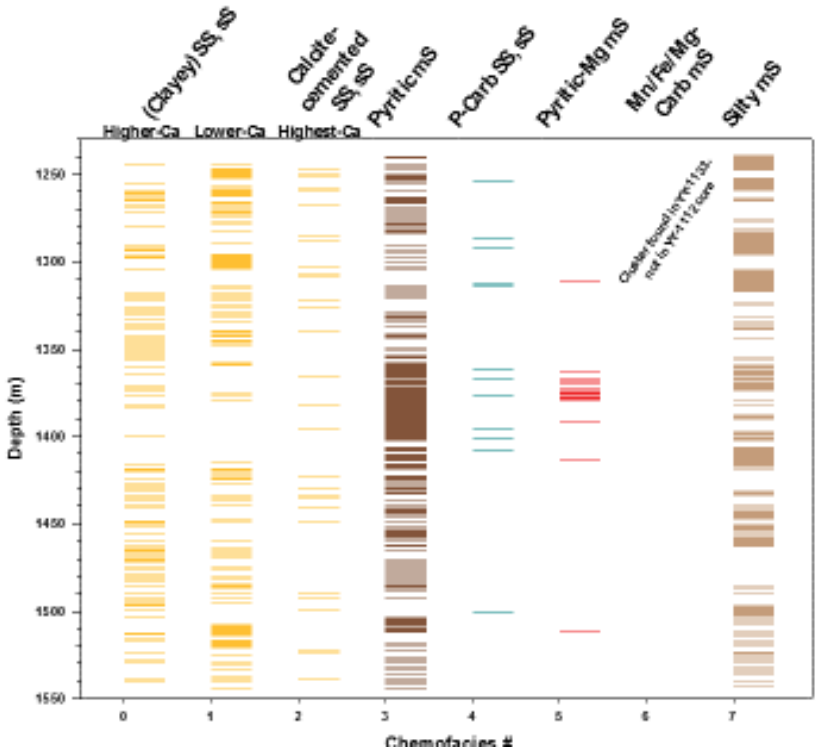

Figure 7. Stratigraphic designation of the chemofacies defined using hierarchical cluster analysis (HCA) of XRF samples from the YY1112 core. The dominant chemofacies designations, based on elemental enrichments, have been color coded to match XRF, XRD, and visually defined lithofacies assigned by Ruppel (this volume). Chemofacies 0 through 2 are all sandstones, reflective of the Feldspathic/quartzone and Quartzone/feldspathic argillaceous arkose facies defined by Ruppel and Rowe (this volume). These chemofacies are herein termed sandstones (Ss) and siltstones (sS), and they are largely separated according to the amount of %Ca (a proxy for calcite) in each sample. Chemofacies 3 is herein termed a pyritic mudstone (mS).

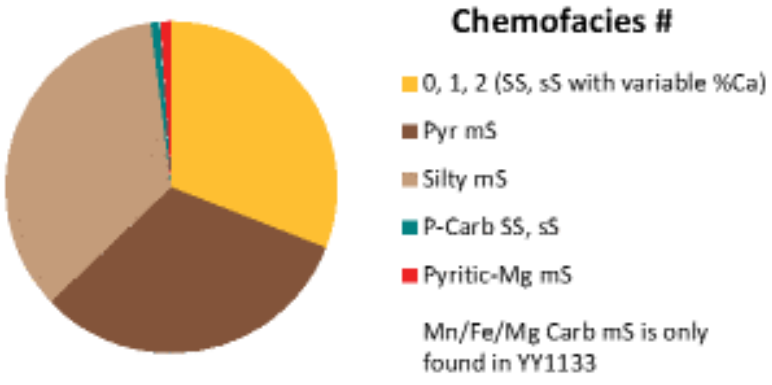

Figure 8. A pie chart demonstrating the relative abundances of the XRF-based, HCA-defined chemofacies in the YY1112 core. Note the subequal nature of sandstone/siltstone, pyritic mudstone, and silty mudstone chemofacies. Chemofacies designations are the same as in **Figure 7.**

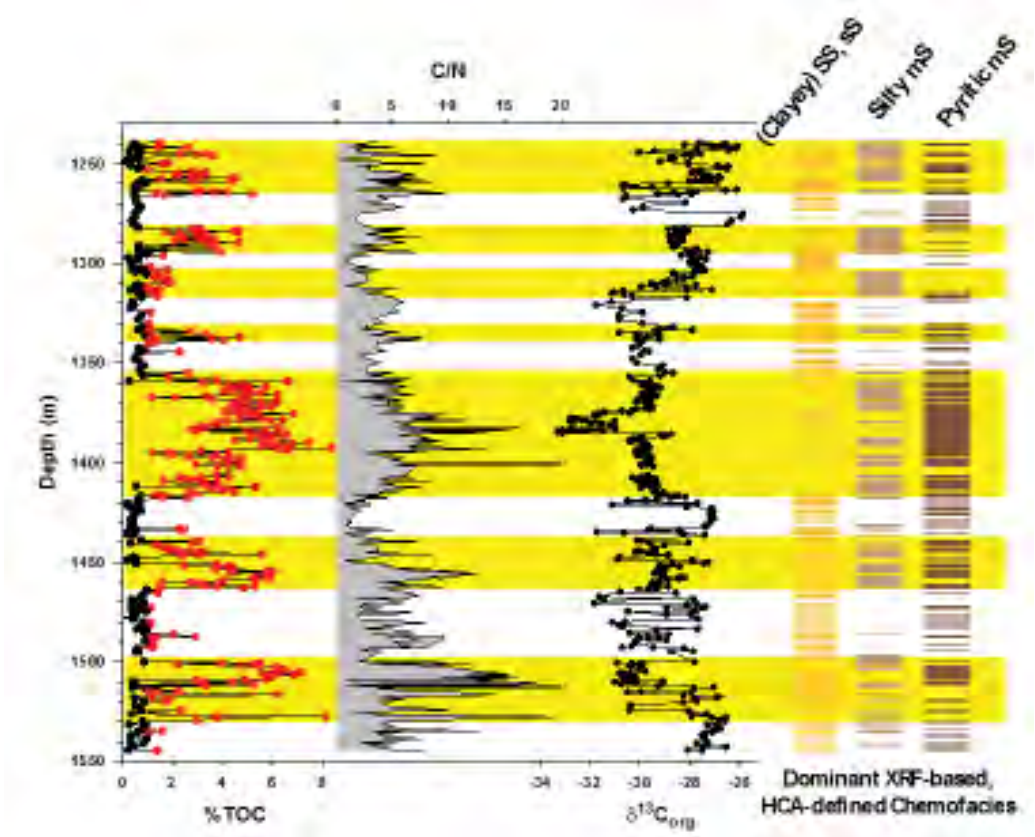

Figure 9. Bulk organic parameters (%TOC, C/N, and $\delta^{13}C_{org}$) for the YY1112 core compared with the stratigraphic shifts in chemofacies defined using HCA.

Figure 9 illustrates changes in the C/N ratio (organic carbon over total nitrogen ratio) and the stable isotope composition of organic carbon ($\delta^{13}C_{org}$). The C/N ratio has been used as a first-order indicator of the type of organic matter (Meyers, 2003), and has been used in lacustrine systems along with $\delta^{13}C_{org}$ to indicate variable inputs of algal, microbial, and higher plant material, as well as to define a degradation trend in algal materials by microbial decay (e.g., Rowe and others, 2002). These organic proxies are plotted along with the dominant chemofacies defined for YY1112, demonstrating the stratigraphic evolution of organic content and the largely mineralogically driven shifts in lithology, as defined by elemental proxies.

Figure 10 demonstrates how the HCA-defined chemofacies based on XRF results largely reproduce the visual lithofacies and XRF facies defined through non-HCA methods (Ruppel and Rowe, Task 1.1 of this volume). The main point is to observe the similarities of the findings of the techniques and to understand how clustering of samples may be used to gain a higher resolution perspective on lithological variability.

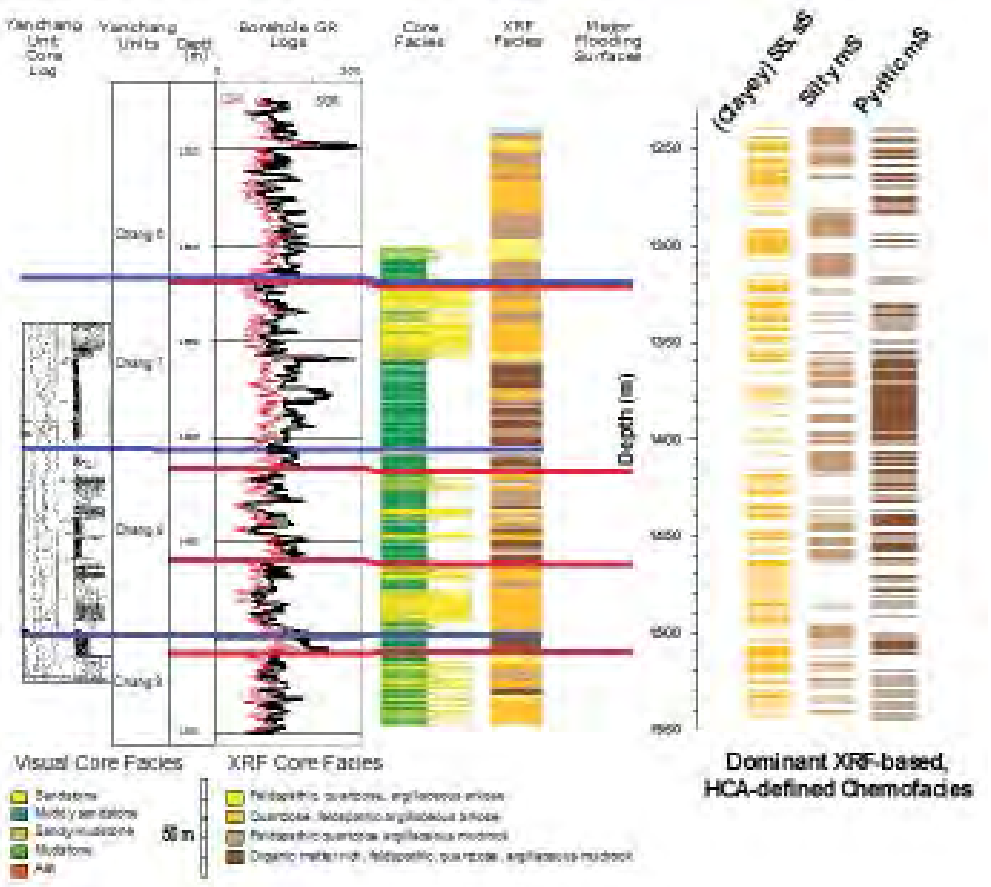

Figure 10. An integration of core and well log results (Ruppel and Rowe, this volume) with the XRF-based HCA-defined chemofacies.

Discussion

The fluvio-lacustrine system represented by the lithofacies of the Yanchang Formation is interpreted to have been dominated by deltaic sedimentation, punctuated by deeper water lacustrine accumulation (e.g., Liu and others, 2015). Adding to the dynamic environment was the complex orogenic history around the North China Block before, during, and after the Yanchang deposition. The overall goals of the geochemical portion of the study are to understand mineralogical changes in the Ordos Basin and to infer changes in the circulation, stratification, oxygenation, and salinity of the lake water mass, thereby leading to a better understanding of facies distribution and organic accumulation.

Stratigraphic and mineralogical variability as inferred from XRF elemental chemistry and X-ray diffraction

Bulk elemental variations in the Yanchang Formation are dominated by shifts in %Al (**fig. 2**), illustrating the oscillation between clay-rich mudstone facies and clay-poor arkosic sandstone/siltstone facies. The %Al ranges from 3% to 6% in the clay-poor coarse-grained

lithologies (arkoses) to 6% to 10% in the mudstone lithologies. The dominant clay mineral is illite, although minor amounts of kaolinite are reported. The clay-rich intervals are also characterized by relatively higher S and P concentrations—indicative of increases in pyrite and apatite, respectively. The clay-poor intervals are characterized by higher Si concentrations, which suggest higher quartz and feldspar content (**figs. 4 and 6**).

Although developing a diagenetic history of the Yanchang succession is probably best evaluated using SEM techniques, the bulk geochemical analysis of %Ca may provide a stratigraphic understanding of which coarse-grained facies (arkoses) possess variable amounts of secondary calcite cement. The concentration of Ca in the succession is generally low, and whereas %Ca is punctuated in the argillaceous, high-TOC mudstones, it shows an overall increased concentration in the arkosic facies (**fig. 4**).

Relationship between the inorganic elemental composition and TOC

The clay content and the organic content of the Yanchang Formation are intimately linked (**fig. 2**). TOC is highest in the clay-rich facies (mudstones) and can range up to 8% in the most argillaceous intervals. **Figure 9** demonstrates that, in general, the thicker TOC-rich intervals are also characterized by higher C/N ratios, which can suggest either (1) inputs of higher plant materials (which have more N-poor components like cellulose and lignin) or (2) a microbially degraded algal source, whereby the N has been preferentially removed over C, leaving the residual organic matter with a higher C/N ratio. We suggest that the higher C/N ratios are caused by microbial degradation, as the C/N peaks tend to occur within the clay-rich (mudstone) facies that are thought to be indicative of lacustrine highstand phases. Low-energy hydrographic conditions during these intervals would generate the least likely setting for transporting higher plant (terrestrial or aquatic macrophyte) materials to the deep parts of the basin. The stable carbon isotope composition of organic matter, which possesses an 8% range in the YY1112 core, is highly variable stratigraphically (**fig. 9**). Much of the argillaceous facies have lighter isotopic values, and many of the arkosic facies have heavier values. This relationship is not universal, though, and it may suggest that the controls on the evolution of organic matter are complicated by differential degradation of algal material by microbial activity and/or by differential inputs of higher plants—although the latter has not proven to be a dominant process.

The evolution of fluvio-lacustrine deposition as preserved in cores from the Yanchang Formation

In essence, the simple fluvio-lacustrine setting for the Yanchang Formation described in the literature (Zhou and others, 2010; Zhou and others, 2012; Liu and others, 2015) can be inferred using the previous information: 1) lake highstand conditions brought about the deposition of fine-grained facies (dominated by lake clays) caused by lower energy conditions, and 2) lake lowstand conditions yielded coarser-grained facies (fluvial-deltaic deposits) caused by higher energy and a more mixed water column. The increase in TOC in the lake clay facies is caused by a higher organic productivity and/or an increased preservation potential stemming from a deeper water mass with more sluggish vertical circulation (lower oxygenation caused by less equilibration with the atmosphere). The more sluggish vertical circulation of the lake under highstand conditions is also supported by the increased %S (and As) in the lake clay facies—pyrite would not precipitate, unless suboxic/anoxic conditions prevailed during deposition.

The %P record (fish bone proxy) suggests that the lake may have had higher productivity during highstands.

The low abundance of redox-sensitive trace elements suggests the lake water mass was not particularly enriched in trace elements (probably quite fresh lake waters), and perhaps only during deep water mass stagnation did these elements fall out of solution and sorb onto organic particles (Tribovillard and others, 2006, Algeo and Rowe, 2012). That being said, it appears that uranium (U) is the most responsive to inferred redox changes.

Conclusions

Depositional cycles preserved in the Yanchang Formation elucidate our understanding of lowstand, coarse-grained fluvio-deltaic deposition dominated by accumulation of sand-sized quartz and feldspars, and highstand, fine-grained, deeper-water lacustrine deposition dominated by accumulation of clays, organic matter, pyrite, and biological debris. The TOC values reach as high as 8% in thin intervals, but, on average, reach 3% to 6% in the lacustrine facies. In general, TOC values are much lower (~<1%) in the fluvio-deltaic facies. The chemostratigraphy and TOC results indicate the significant linkage between TOC and %Al (a proxy for clay content), and the linkage between enhanced TOC with enhanced %S (a proxy for pyrite content). Thus, organic matter was best preserved during episodes of fine-grained mineral deposition, most probably defining lacustrine highstands. It can be inferred from this that the intervals with the richest TOC content also have the least fracable (clay) content, when compared to the low-TOC, high-quartz/feldspar content of the intervening coarse-grained units.

References

Algeo, T.J., and Maynard, J.B., 2004,Trace element behavior and redox facies in core shales of Upper Pennsylvanian Kansas-type cyclothems: Chemical Geology, v. 206, p. 289–318.

Algeo, T.J., and Rowe, H.D., 2012, Paleoceanographic applications of trace-metal concentration data: Chemical Geology, v. 324–325, p. 6-–8.

Bao, C., Chen, Y., Li, D., and Wang, S., 2014, Provenances of the Mesozoic sediments in the Ordos Basin and implications for collision between the North China Craton (NCC) and the South China Craton (SCC): Journal of Asian Earth Sciences, v. 96, p. 296–307.

Fairbanks, M., Ruppel, S.C., and Rowe, H.D., 2016. High-resolution stratigraphy and facies architecture of the Upper Cretaceous (Cenomanian–Turonian) Eagle Ford Group, Central Texas: AAPG Bulletin, in press.

Ji, L.-M., Yan, K., Meng, F.-W., and Zhao, M., 2010, The oleaginous Botryococcus from the Triassic Yanchang Formation in Ordos Basin, Northwestern China: Morphology and its paleoenvironmental significance: Journal of Asian Earth Sciences, v. 38, p. 175–185.

Liu, S., 1998, The coupling mechanism of basin and orogen in the western Ordos Basin and adjacent regions of China: Journal of Asian Earth Sciences, v. 16, no. 4, p. 369–383.

Liu, S., Su, S., and Zhang, G., 2013, Early Mesozoic basin development in North China: Indications of cratonic deformation: Journal of Asian Earth Sciences, v. 62, p. 221–236.

Liu, Z., Shen, F., Zhu, X., Li, F., and Tan, M., 2015, Formation conditions and sedimentary characteristics of a Triassic shallow water braided delta in the Yanchang Formation, Southwest Ordos Basin, China: PLoS ONE 10(6): e0119704. doi:10.1371/journal.pone. 0119704.

Meyers, P.A., 2003, Applications of organic geochemistry to paleolimnological reconstructions: a summary of examples from the Laurentian Great Lakes: Organic Geochemistry, v. 34, p. 261–289.

Nance, H.S., and Rowe, H.D., 2015, Eustatic controls on stratigraphy, chemostratigraphy, and water mass evolution preserved in a Lower Permian mudrock succession, Delaware Basin, west Texas, USA: Interpretation, v. 3, no. 1, p. SH11–SH25, http://doi.org/10.1190/INT-2014-0207.1.

Phillips, N.D., 1991, Refined subsidence analyses as a means to constrain Late Cenozoic fault movement, Ventura Basin, California: The University of Texas at Austin, Master's thesis, 545 p.

Qiu, X., Liu, C., Mao, G., Deng, Y., Wang, F., and Wang, J., 2015, Major, trace and platinum-group element geochemistry of the Upper Triassic nonmarine hot shales in the Ordos basin, Central China: Applied Geochemistry, v. 53, p. 42–52.

Rowe, H.D., Dunbar, R.B., Mucciarone, D., Seltzer, G.O., Baker, P.A., and Fritz, S., 2002, Insolation, moisture balance and climate change on the South American Altiplano since the last glacial maximum: Climatic Change, v. 52, p. 175–199.

Rowe, H.D., Hughes, N., and Robinson, K., 2012, The quantification and application of handheld energy-dispersive x-ray fluorescence (ED-XRF) in mudrock chemostratigraphy and geochemistry: Chemical Geology, v. 324-325, p. 122–131.

Tribovillard, N., Algeo, T.J., Lyons, T.W., and Riboulleau, A., 2006, Trace metals as paleoredox and paleoproductivity proxies: an update: Chemical Geology, v. 232, p. 12–32.

Zhao, W., Wang, H., Yuan, X., Wang, Z., and Zhu, G., 2010, Petroleum systems of Chinese nonmarine basins. Basin Research, 22, 4–16.

Zou, C., Zhang, X., Luo, P., Wang, L., Luo, Z., and Liu, L., 2010. Shallow-lacustrine sand-rich deltaic depositional cycles and sequence stratigraphy of the Upper Triassic Yanchang Formation, Ordos Basin, China. Basin Research, v. 22, p. 108–125.

Zou, C., Zhang, X., Luo, P., Wang, L, Luo, Z., and Liu, L., 2012, Deep-lacustrine transformation of sandy debrites into turbidites, Upper Triassic, Central China: Sedimentary Geology, v. 265–266, p. 143–155.

TASK 2.1

Thin-Section Description of Lithofacies of the Late Triassic Yanchang Formation (Chang 7, 8, and 9 Members) Lacustrine System in the Yanchang Petroleum Group YY1 and YY22 Wells, Southeastern Ordos Basin, China

Robert Loucks and Stephen Ruppel[1]

[1]Bureau of Economic Geology, Jackson School of Geosciences, The University of Texas at Austin, Austin, TX

Introduction

The major goal of this section is to provide a brief description of the thin sections that were prepared for the Yanchang project. The descriptions are of thin section taken from the YY1 and YY2 wells. These descriptions will help in defining and documenting the facies descriptions provided in other parts of the report. Forty-one thin sections were described using a standard petrographic microscope equipped with reflected light. The major objectives were to: (1) define grain types including intrabasinal and extrabasinal grains, (2) describe sedimentary features, and (3) and summarize lithofacies seen in thin sections.

Nonbiota-Related Grains

Sand-Sized Terrigenous Grains

Very fine to fine-grain-sized quartz was the major sand-sized grain recognized in thin section. Only rare feldspars were noted, even though XED and SEM analysis shows that they are very common (as much as or more than quartz). The lack of recognition of feldspars may be related to fact the thin sections were not stained for plagioclase or K-spar. Sand-sized mica and chlorite were also noted.

Silt-Sized Terrigenous Grains

Very fine to coarse-silt-sized grains are very common. Similar to the sand-sized grains, most of them appear to be quartz, but again as with the sand-sized grains the feldspars were probably not recognized because thin sections were not stained.

Clay-Sized Terrigenous Grains

Clay-sizes grains are very common, and from SEM analysis they range in mineralogy from quartz, plagioclase, and K-spar to different clay minerals (mainly mixed layered, illite, and chlorite). Much of the clay-sized particles were deposited as aggregates of silt-sized peloids, which are discussed below.

Biota-Related Grains

Peloids

It is interesting to note that the most common grains seen in thin sections are argillaceous peloids (**Fig. 1**). Peloids are defined here as circular to irregular shaped grains composed predominantly

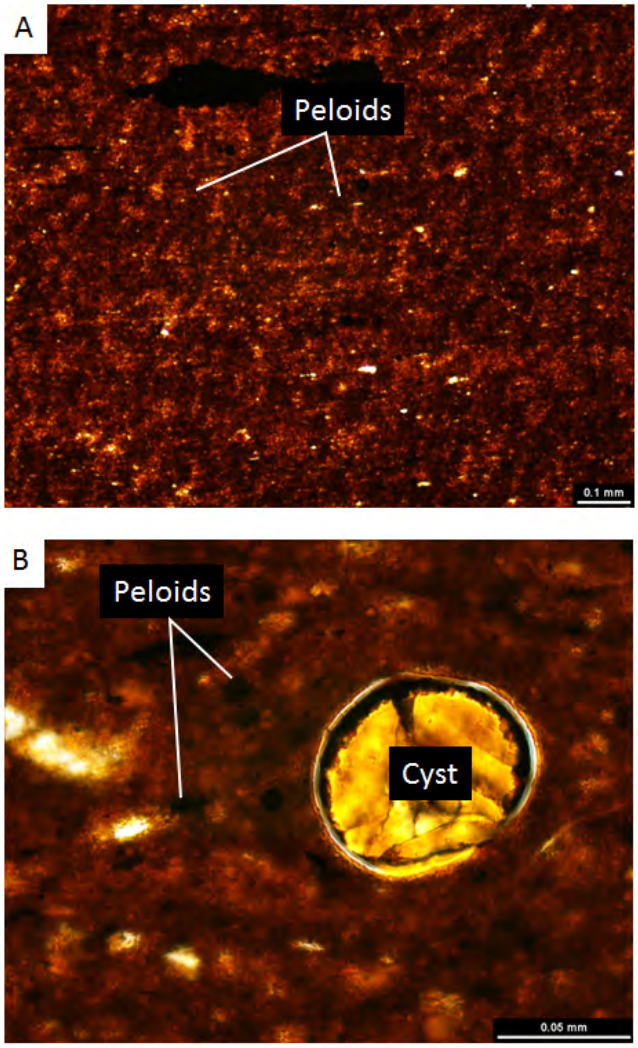

Figure 1. Peloidal fabric. (A) Argillaceous peloids ranging from 10 to 50 micrometers. YY1-1359.66 m. (B) Peloids mixed with algal cyst. YY1-1409.26 m.

of clay-sized material (mineral and organics). In thin section they appear dark and opaque. They range in size from 10 to 50 micrometers (mm). Their origin is unclear, but it may be related to one of two processes: (1) lacustrine snow and/or (2) biota waste products. Marine snow is a common and well-known process in the marine environment. Clay-sized material flocculates together near the surface of the water column by chemical and biological processes and sinks to the ocean bottom and accumulates. A similar process can occur in lakes, as clays and organics can flocculate in fresh water. The second origin is related to fecal pellet production by animals in the water column and at the lake bottom.

It is important to recognize the role of peloids in deposition. The clays were not deposited as single grains but as peloids that could act hydraulically similar to silt-sized grains. Therefore, the peloids would have had hydrological properties different from those of the individual clay particles. Also, these soft peloids must have formed in the basin under lower energy conditions because they would not have survived the higher energy conditions within the fluvial-deltaic complex.

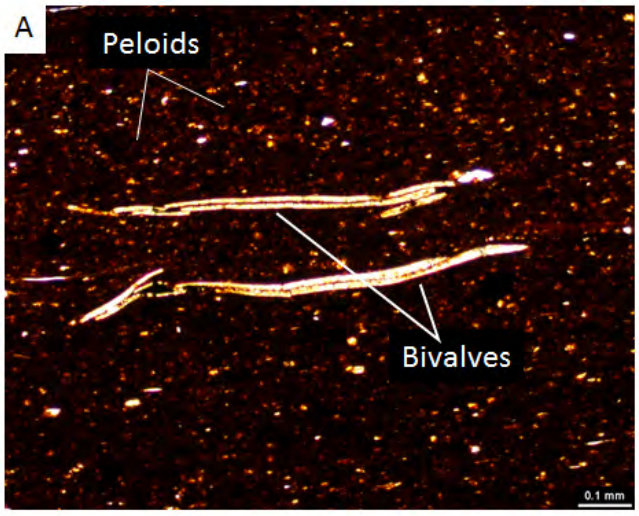

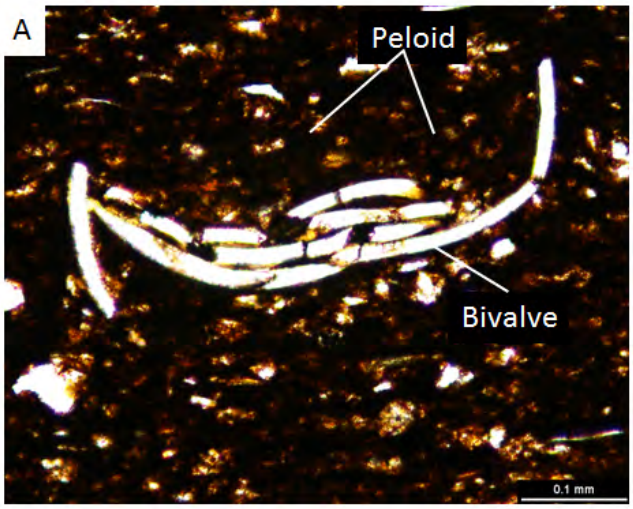

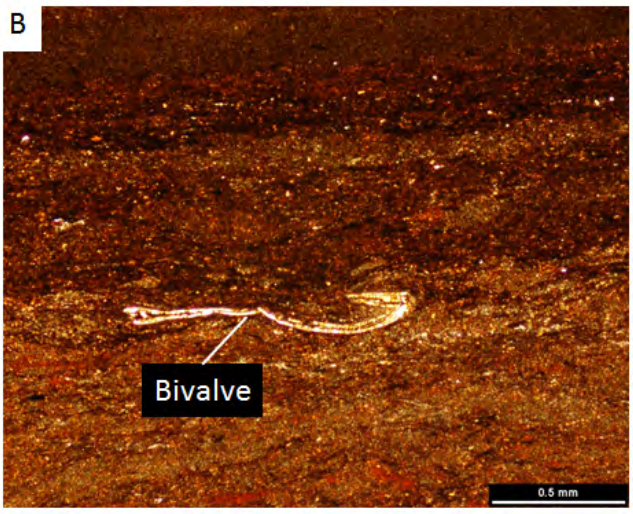

Figure 2. Mollusks. (A) Compacted and broken thin-walled calcite mollusk. YY1-1315.72 m. (B) Compacted and broken thin-walled calcite mollusk.YY1-1370.77 m.

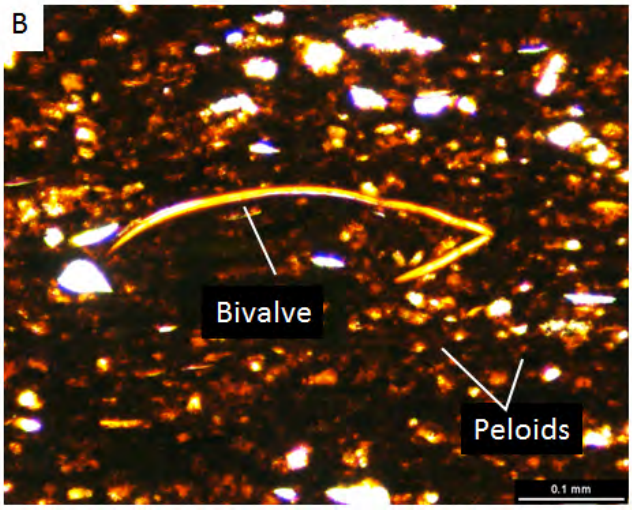

Figure 3. Mollusks. (A) Calcite mollusk that was deposited whole was crushed by compaction. YY1-1358.66 m. (B) Near phosphate mollusk. YY1-1358.66 m.

Fossils

Fossils are not common in the Yanchang sediments. We have recognized bivalve and algal cysts. Another grain described below is listed as unidentified. We are unsure if the grain (or grains) is organic or mineral related.

***Bivalves*:** Many of the bivalves were preserved whole, but because they were thin and fragile, they were crushed by compactional processes (**Figs. 2, 3**). Most of the bivalves were carbonate, but some appear to have been phosphate (**Fig. 3B**). The deposition of whole fragile bivalves suggests a low-energy, quiet-water bottom setting.

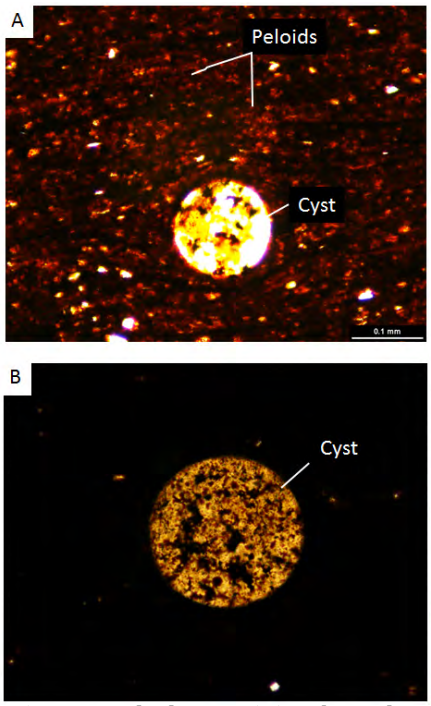

Figure 4. Algal cysts. (A) Spherical algal cyst in a peloidal argillaceous mudstone. YY1-1374.44 m. (B) Spherical algal cyst filled with organic matter. YY1-1392.75 m.

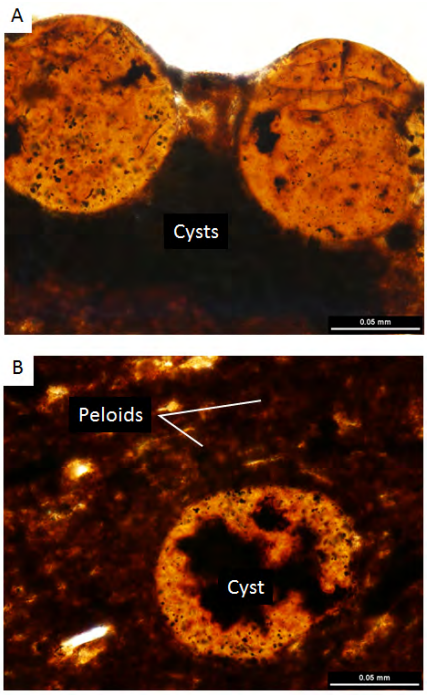

Figure 5. Algal cysts. (A) Spherical algal cysts. YY1-1359.66 m. (B) Spherical algal cyst filled with organic matter and pyrite. YY1-1359.66 m.

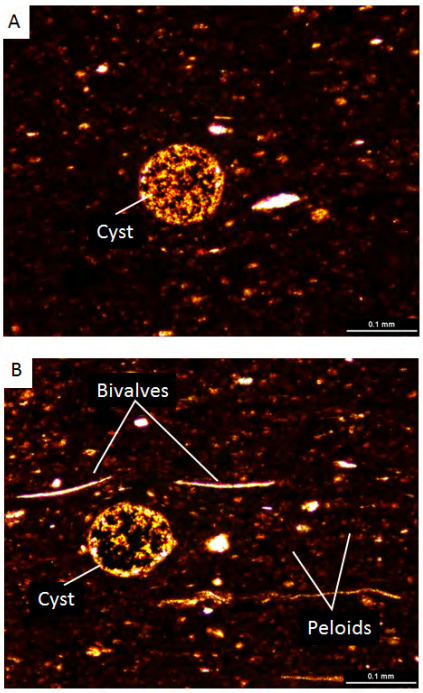

Figure 6. Algal cysts. (A) Spherical algal cyst in peloidal mudstone. YY1-1315.72 m. (B) Spherical algal cyst and mollusk fragments in mudstone matrix. YY1-1315.72 m.

***Algal Cysts*:** Algal cysts (**Figs. 4, 5, 6**) are present but not common. They are round and have a thin wall. They lived near the surface and settled to the bottom after death. Their interiors are now filled by mud, phosphate, pyrite, or organic matter.

Kerogen

***Type III Kerogen (Wood)*:** Woody kerogen was recognized in several thin sections (**Fig. 7**). The wood pieces are black and elongate, and they show intense distortion by compaction processes (**Fig. 7B**). SEM analysis also revealed common Type III fragments that generally have no organic-matter pores.

***Type II Kerogen (Algal)*:** Algal kerogen in thin section is difficult to see because it is generally in the low micrometer-range in size. Numerous black specks occur in the thin sections and are interpreted as organic matter. This observation is supported by the fact that TOC is generally between 3% and 8%, and therefore organic carbon should be common.

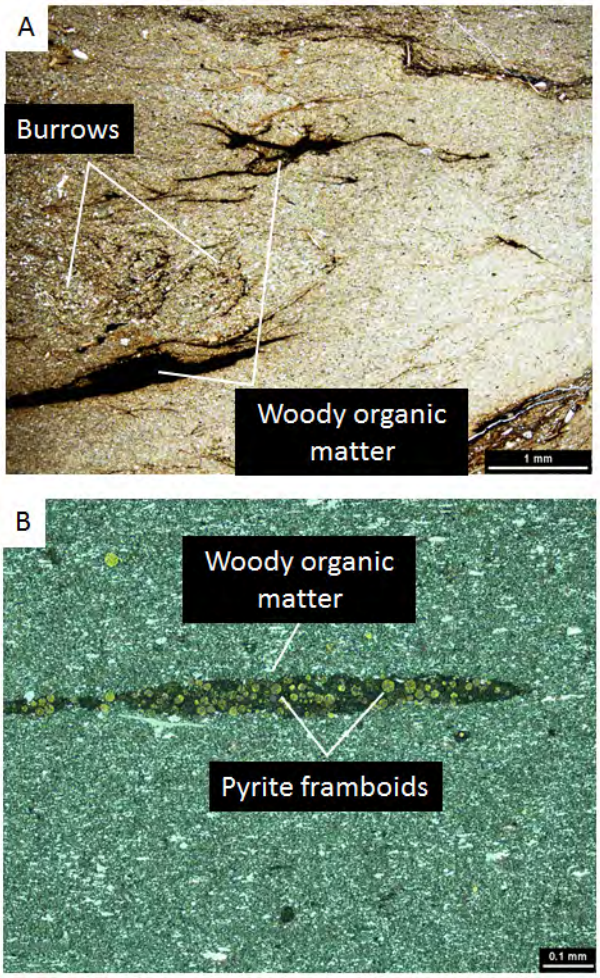

Figure 7. Organic matter. (A) Distorted Type III woody organic matter. The mudstone in bioturbated. YY1-1356.26 m. (B) Organic matter replaced by abundant pyrite framboids. YY1-1358.56 m.

Grains of Unknown Origin

Relatively conspicuous isolated grains seen in the thin section are of unknown origin (**Figs. 8 to 22**). These grains may have more than one origin, but overall they look somewhat similar. Many appear to be a single crystal of calcite. The shape of the grains ranges from a circular form with an irregular outline to a hexagonal form with relatively straight edges. Most have a yellowish center or a yellowish ring in the center. The other layer is a whitish cream color. Some of the grains have a yellow or white rim outlining the grain. The outer layer suggests a bladed to fibrous crystal structure perpendicular to the rim. The grains were rigid at the time of deposition, as noted by compaction of finer sediments around the grains; observers would need reflected light to observe this phenomenon (**Figs. 8B, 16B**).

These grains have been shown to several petrographic experts with experience in paleontology and volcanology. No positive identification was proposed. Possible origins include (1) replacement by some sort of algal cyst, such as a charophyte, (2) another unknown biological form, or (3) a volcanic ash grain.

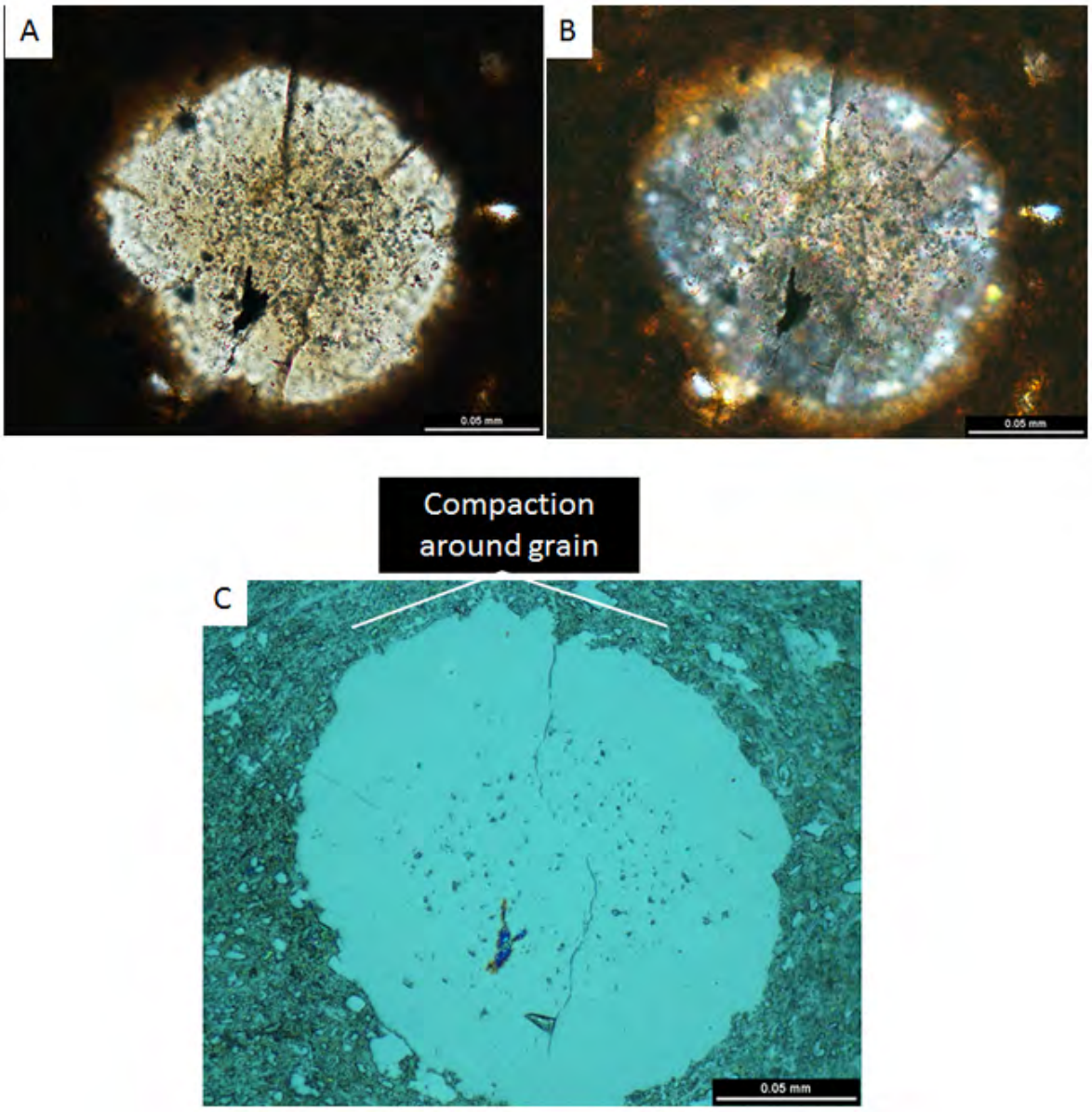

Figure 8. Unidentified grain. YY22-1409.26 m. (A) Unidentified grain with dark center composed of calcite. Plane light. (B) Same as A but under cross polarized light. Note outer rim. (C) Same as A but with reflected light. Note that the grain was rigid and the mud particles compacted around the grain.

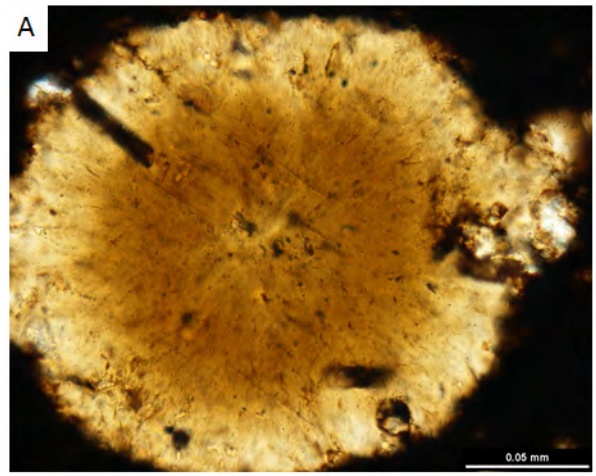

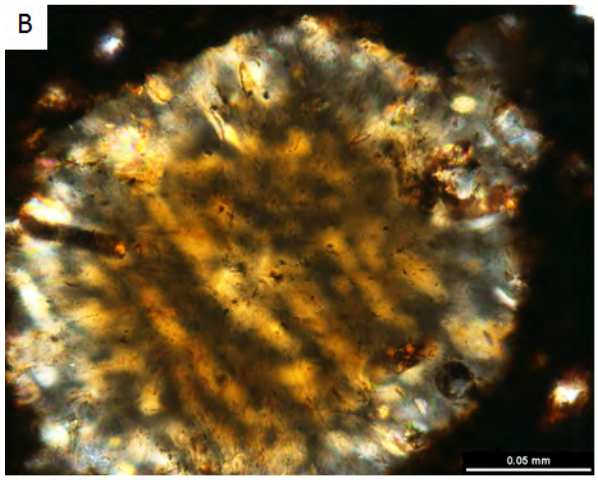

Figure 9. Unidentified grain. YY1-1501.31 m. (A) Unidentified grain with dark center. Grain appears to have a radial structure. Grain also has slight hexagonal structure. Plane light. (B) Same as A but under cross polarized light. Note outer rim.

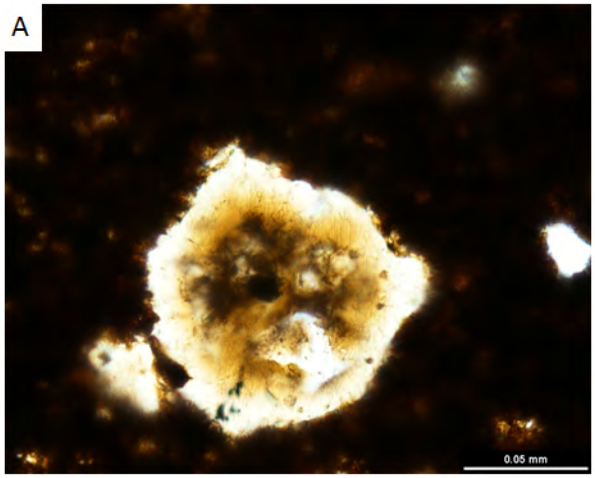

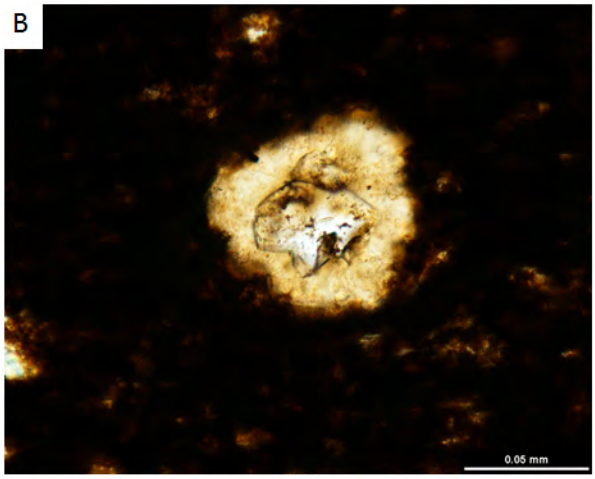

Figure 10. Unidentified grain. YY1-1538.38 m. (A) Unidentified grain with dark center. Grain appears to have a radial structure. Grain also has a poorly developed hexagonal structure. Plane light. (B) Unidentified grain with dark center. Grain appears to have a radial structure.

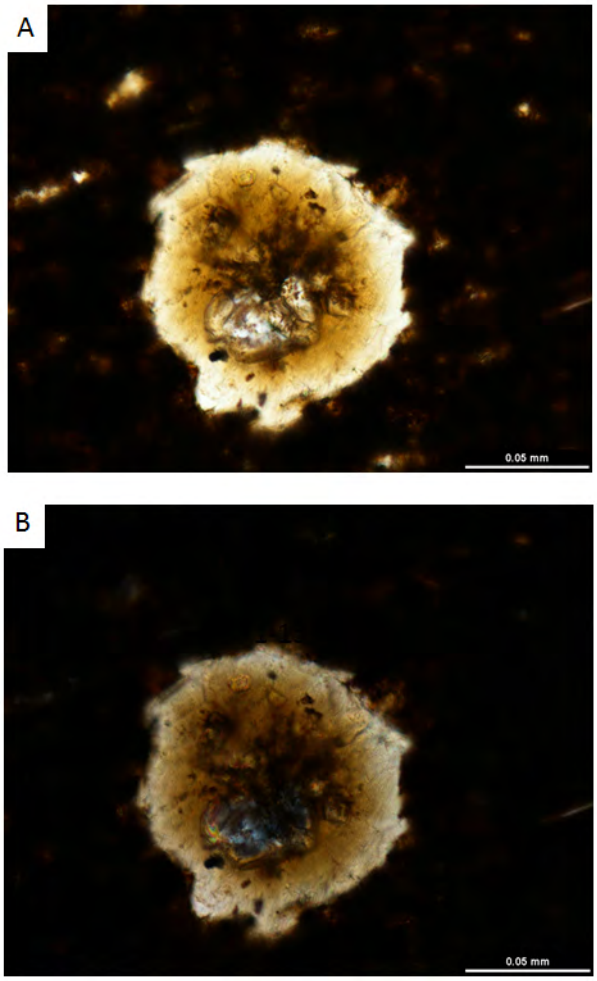

Figure 11. Unidentified grain. YY1-1538.38 m.
(A) Unidentified grain with dark center. Plane light.
(B) Same as A, but under cross polarized light.

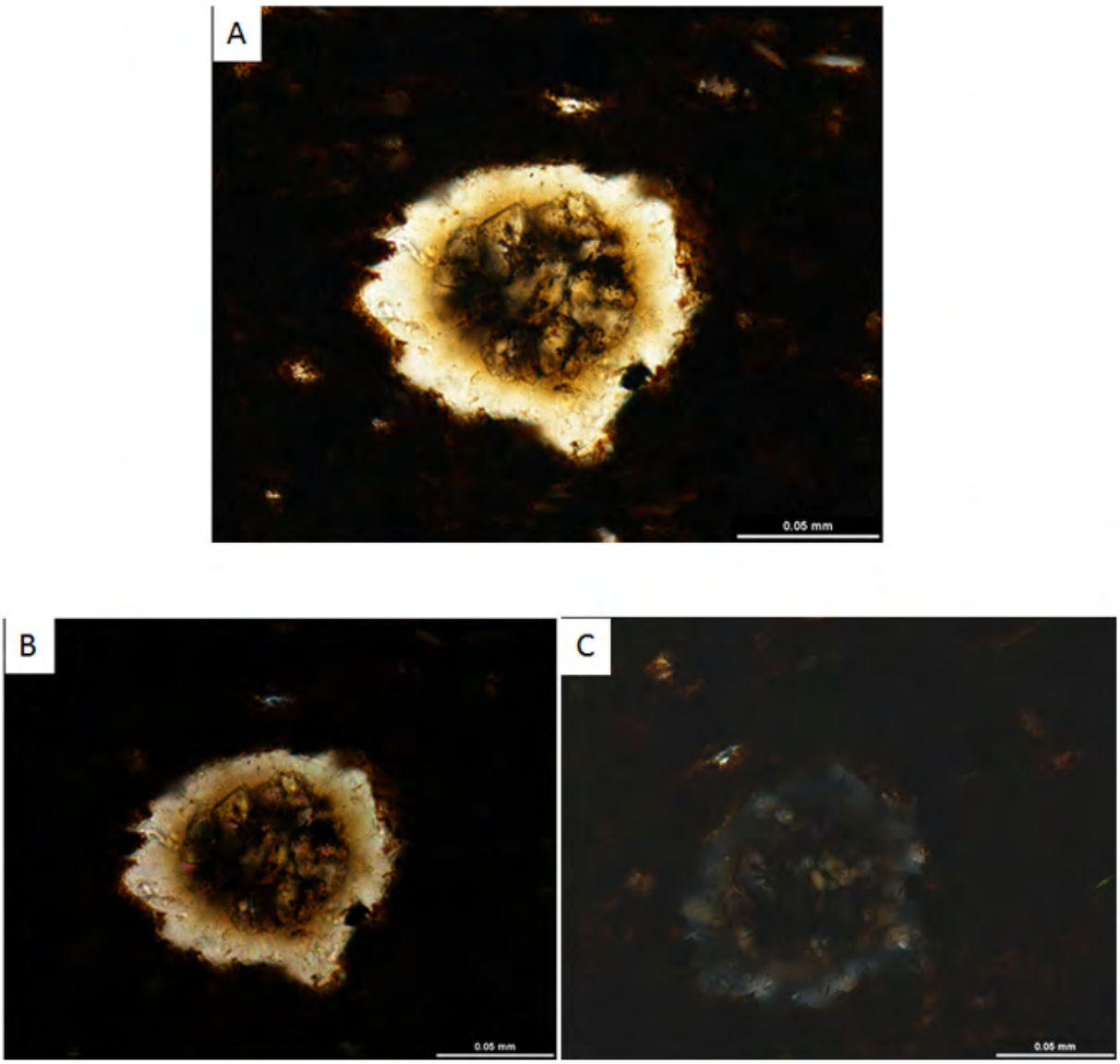

Figure 12. Unidentified grain. YY1-1538.38 m. (A) Unidentified grain with distinct dark center. Grain is a single crystal of calcite. Plane light. (B) Same as A, but under cross polarized light. (C) Same as A, but under cross polarized light at 45 degrees of rotation from B.

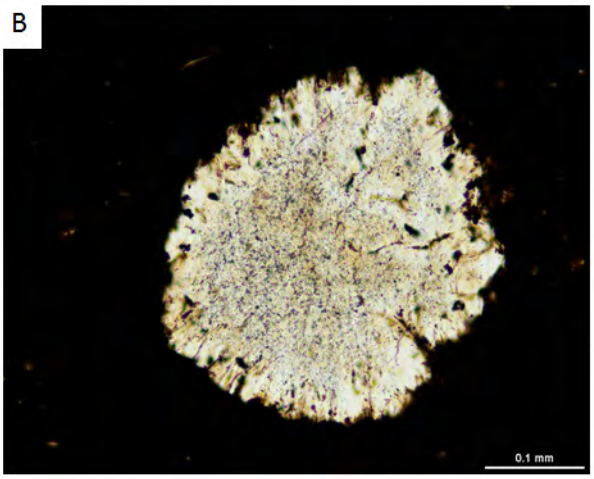

Figure 13. Unidentified grains. (A) Unidentified grain with very irregular outline but showing some planar surfaces. Grain is a single crystal of calcite. Plane light. YY1-1454.82 m. (B) Unidentified grain indicative of radial structure, and the grain has a very irregular border. Plane light. YY22-1329.17 m.

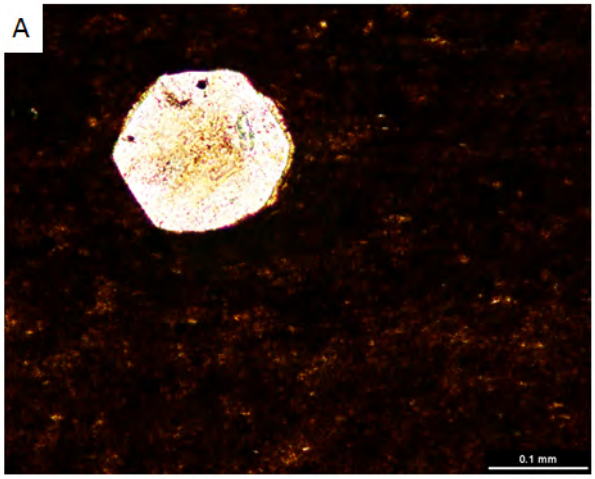

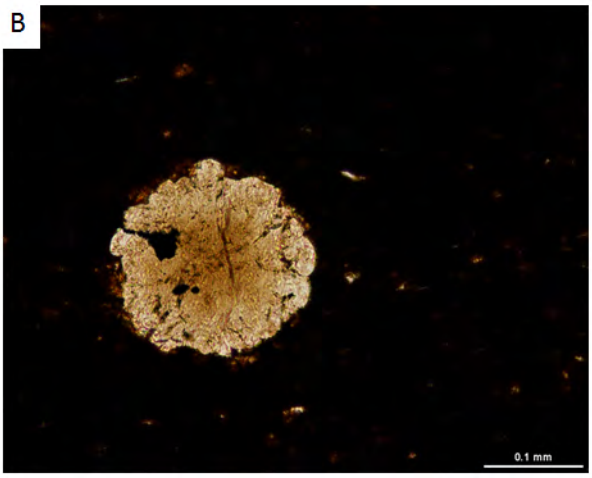

Figure 14. Unidentified grains. (A) Unidentified grain with dark center and well-developed hexagonal outline. Note a remnant of an outer rim. Plane light. YY1-1364.69 m. (B) Unidentified grain with very irregular outline and dark center. Plane light. YY1-1364.69 m.

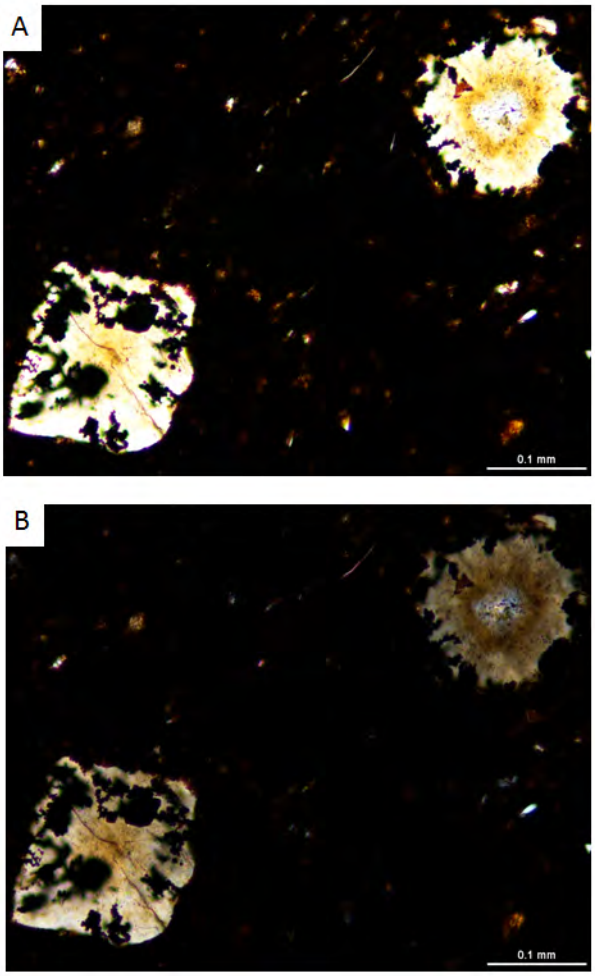

Figure 15. Unidentified grains. YY1-1504.28 m. (A) Unidentified grain (upper right) with dark ring in center and very irregular outline. Unidentified grain (lower left) with polyhedral crystal line. Plane light. (B) Same as A, but under cross-polarized light.

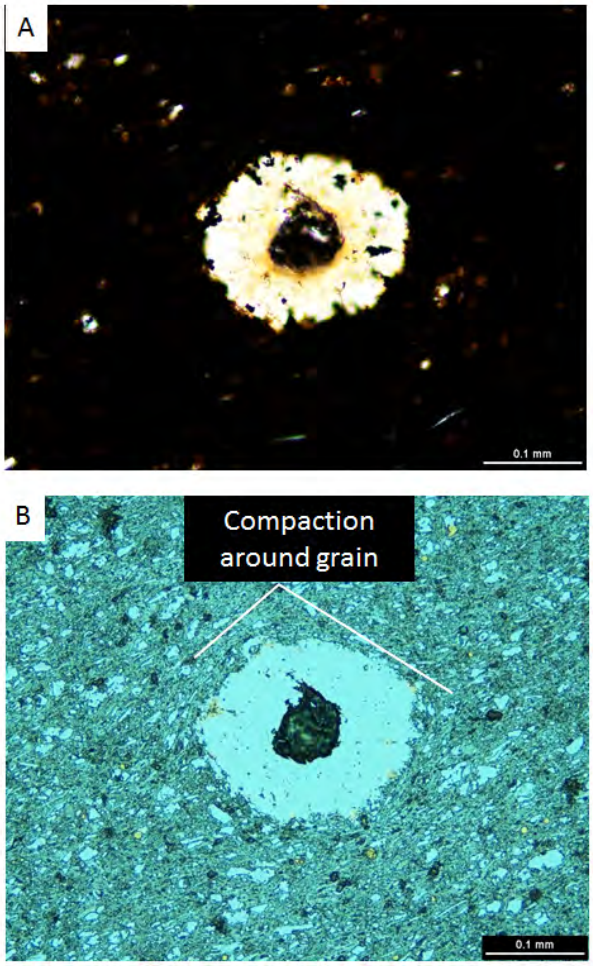

Figure 16. Unidentified grain. YY1-1504.28 m. (A) Unidentified grain with very irregular outline, and it has a possible radial structure. Plane light. (B) Same as A, but under reflected light. The grain must have been rigid before compaction started, as the mud particles compact around the grain.

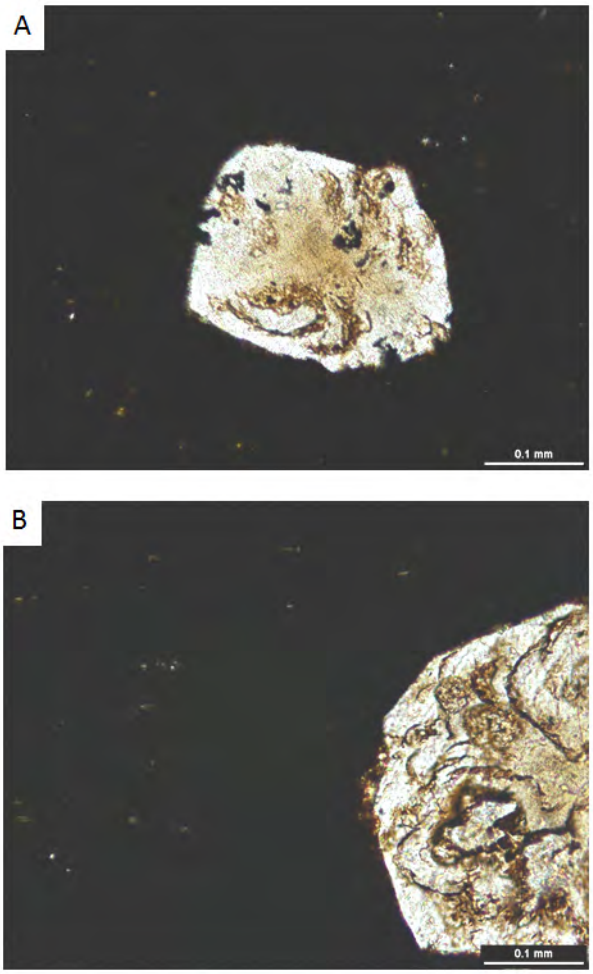

Figure 17. Unidentified grains. YY22-1329.17 m.
(A) Unidentified grain with complex internal structure. Note that the grain has an anhedral crystal outline.
(B) Unidentified grain with complex internal structure. Note that the grain has an anhedral crystal outline.

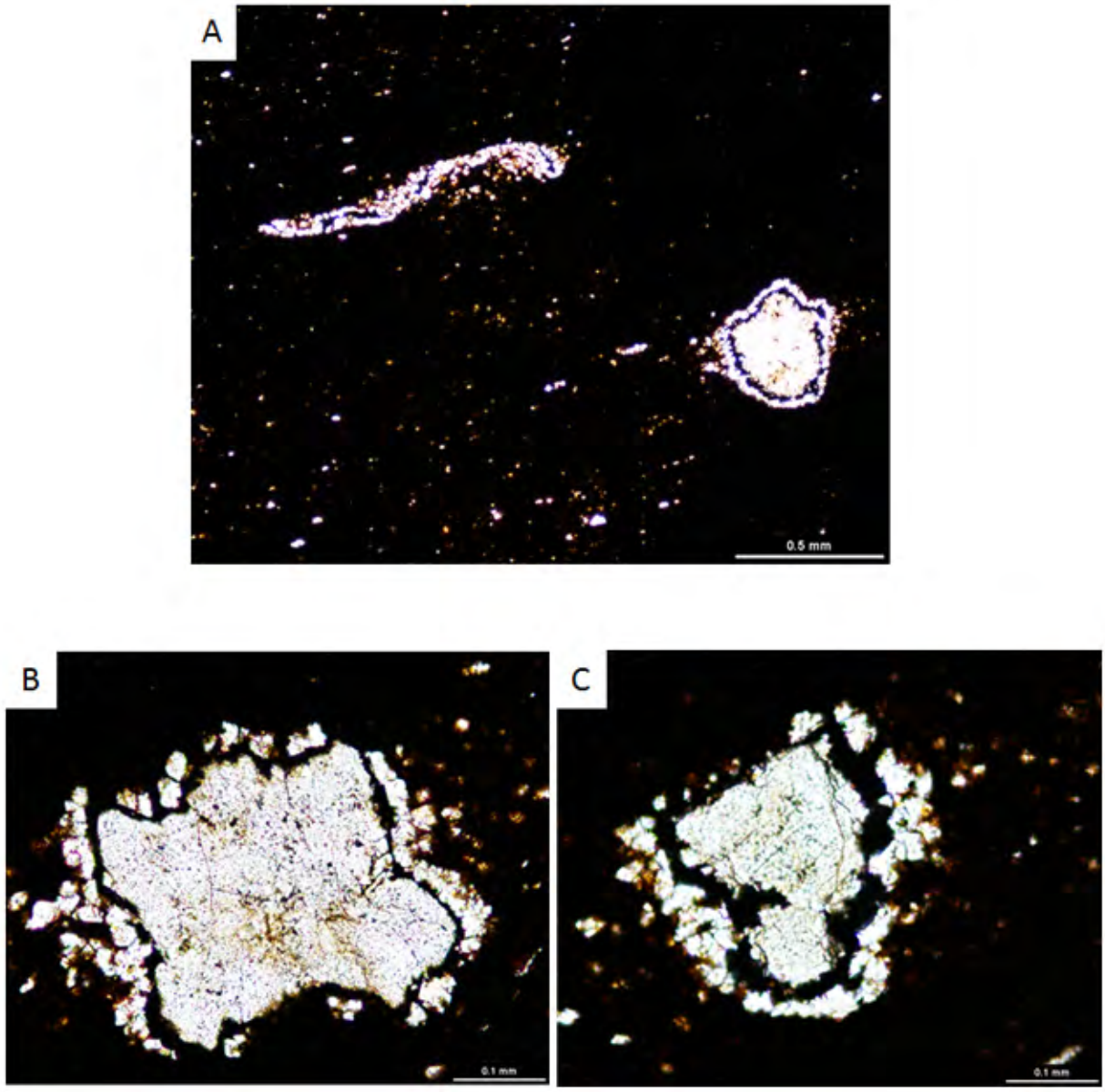

Figure 18. Unidentified grains. YY1-1378.50 m. (A) Unidentified grains. Grain on right shows large calcite crystal in center followed by black zone and rimmed by numerous calcite crystals. The grain in the upper left only displays the numerous calcite crystal outline. The dissimilarity between the two grains suggests that the large crystal in the center of the grain on the right is a cement fill and inhibited the grain from collapsing. The grain on the left without the large crystal-cement fill collapsed during compaction. Plane light. (B) Similar to grain on right in A. (C) Similar to grain on right in A.

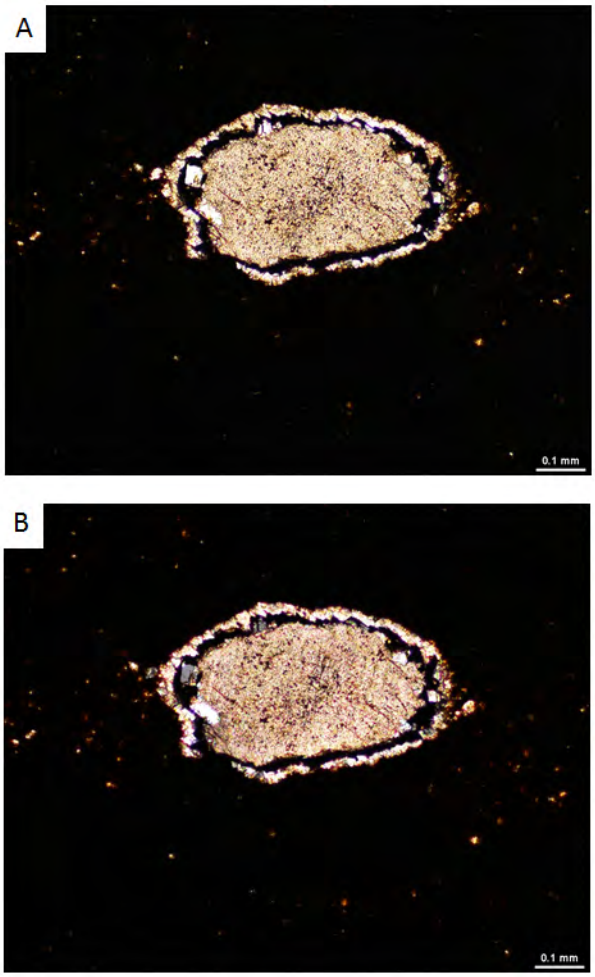

Figure 19. Unidentified grain. YY1-1378.50 m. (A) Unidentified grains. Grain shows large calcite crystal in center followed by black zone and rimmed by numerous calcite crystals. The dark band may be a dissolution zone with some precipitation of later fine crystals. (B) Same as A but under cross-polarized light.

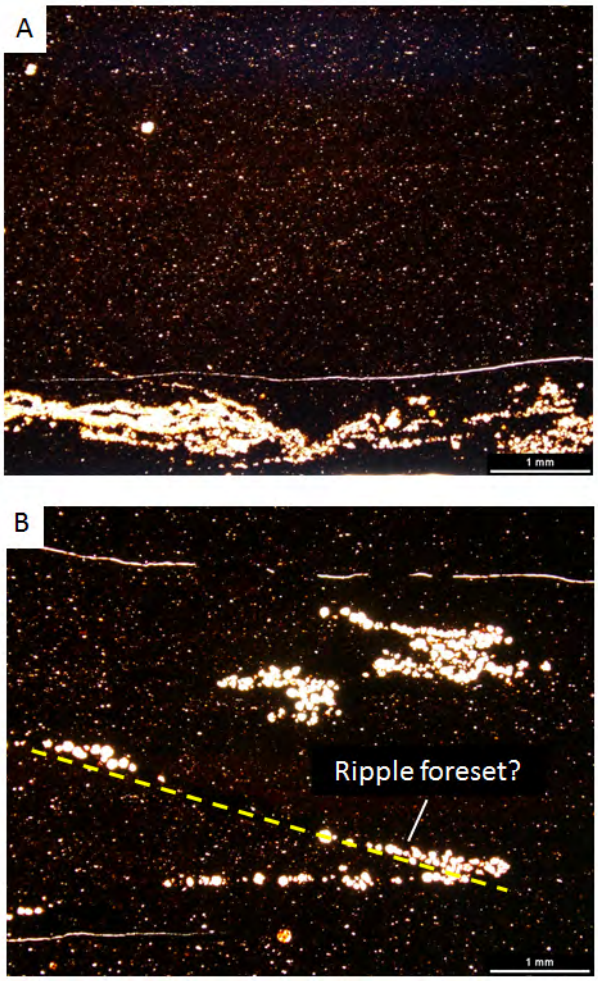

Figure 20. Unidentified grains. (A) Layer of unidentified grains. This layer may be a placer deposit. YY1-1364.69 m. (B) Layers and clusters of unidentified grains. One layer is at an angle that may suggest the foreset of a ripple. YY1-1374.44 m.

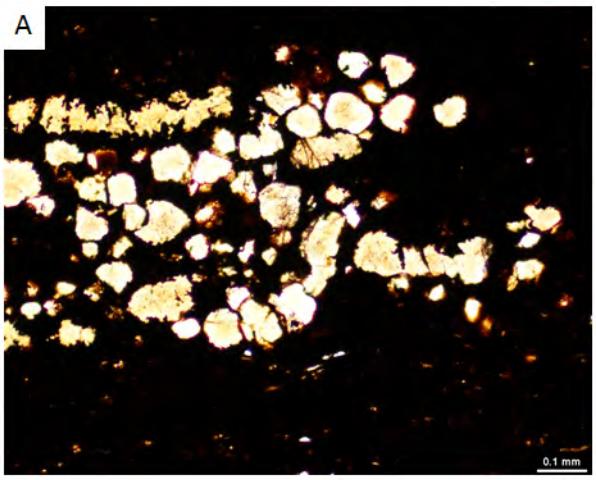

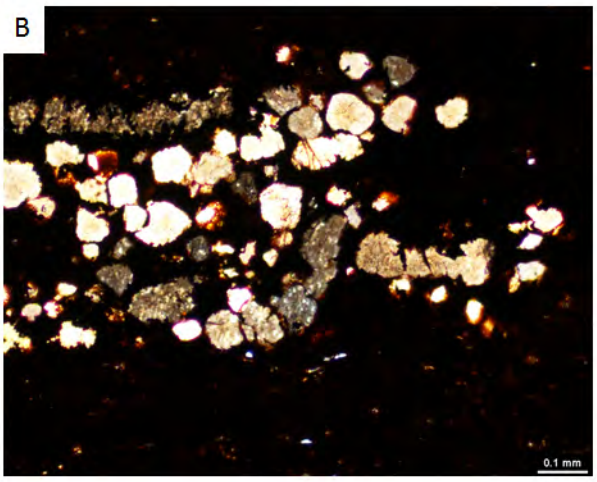

Figure 21. Unidentified grains. YY1-1374.44 m. (A) Cluster of unidentified grains. (B) Same as A but under cross-polarized light.

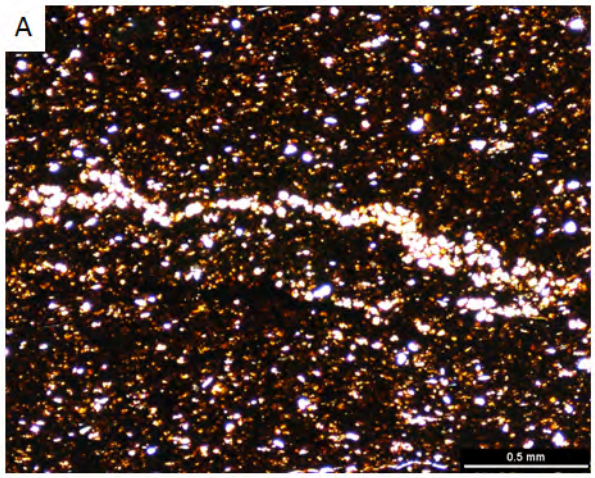

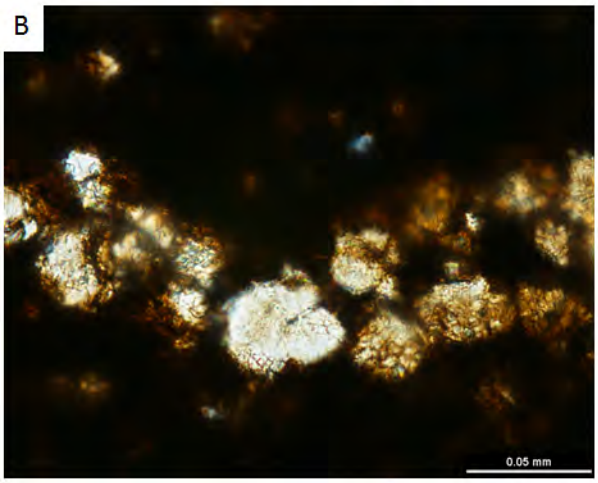

Figure 22. Unidentified grains. YY22-1320.84 m. (A) Irregular stringer of unidentified grains. (B) Closeup of grains shown in A.

Diagenetic Grains

Pyrite

Small pyrite framboids are relatively common and occur mostly as replacement of organic material (**Fig. 7B**). Reflected light is needed to identify the pyrite easily. Other forms exist, such as disseminated grains and euhedral crystals.

Phosphate

A few phosphate grains were noted but were not common. Some of the phosphate is bone material. Other modes of occurrence include fill within algal cysts. (**Fig. 5A**)

Bioturbation

Some thin sections show evidence of bioturbation (**Fig. 7A**). The burrows are commonly at the thick-laminae scale and others are larger but still can be seen in a single thin section.

Sedimentary Features

The two predominant sedimentary features seen in thin section are laminations and small ripples (**Figs. 23 to 27**). The laminations range from faint to well developed (**Figs. 23, 24**). Thickness varies. Some may be suspension laminations, whereas other laminations are event beds indicated by upward-fining grain size created by a waning current (**Fig. 26A**), a distinct unit of silt-/sand-rich grains (**Figs. 24B, 25A**), or by scour surfaces at the base of the laminations (**Fig. 26A**). A few thin sections show low-relief ripples composed of quartz silt and peloids (**Fig. 26A**).

Ash Layers

Some ash layers contain what appears to be flat, compacted fine wood fragments (**Fig. 28**). Several thin sections (**Fig. 28**) are composed of what are interpreted as ash layers or layers of ash rip-up clasts (**Figs. 29, 30**). In thin section the ash layers are tan to brown and are only as much as a millimeter in thickness. The clasts have high birefringence (**Figs. 29, 30**).

Thin-Section Artifact Microfractures

Sharp controversy exists about the presence of microfractures in mudrocks. By microfractures we mean Mode 1 fractures a few tens of micrometers wide and several tens of millimeters long. Our experience is that natural microfractures in mudrocks are rare because the high mineral-clay content of mudrocks is not conducive for fractures.

In the Yanchang thin sections, numerous microfractures appear, but all are artifacts related to thin-section preparation or to earlier desiccation and shrinkage of the mudrock (**Figs. 31, 32, 33**). We did not see any natural microfractures in the Yanchang mudrocks, and thus they should not be counted on to enhance permeability in these tight mudstones.

Figures 31 and 32 show horizontal microfractures that are discontinuous. **Figure 33** is an example of an artifact microfracture that at first appears to have cementation within the microfracture, which would be evidence that the microfracture was natural. However, the

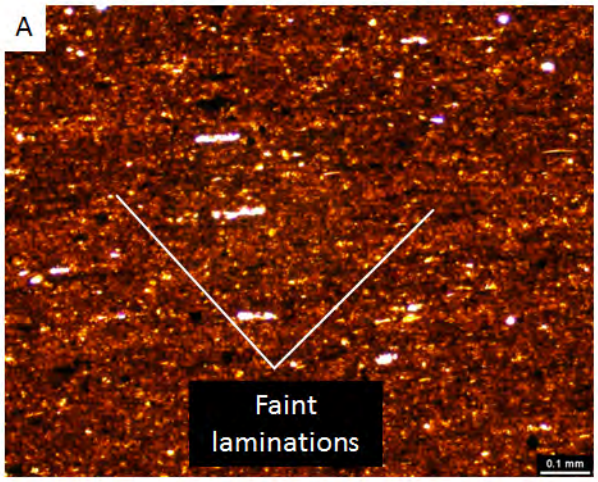

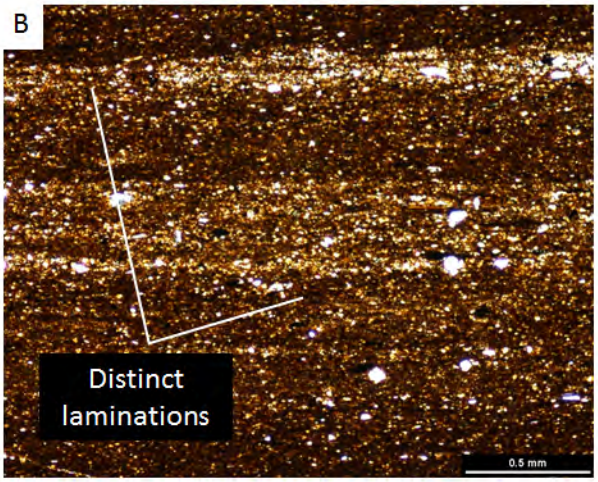

Figure 23. Peloidal organic-lean argillaceous mudstones. (A) Faintly laminated, peloidal organic-lean argillaceous mudstone. TOC = 2.76%. YY1-1497.07 m. (B) Well-laminated, peloidal slightly silty, organic-lean argillaceous mudstone. TOC = 2.72%. YY1-1426.15 m.

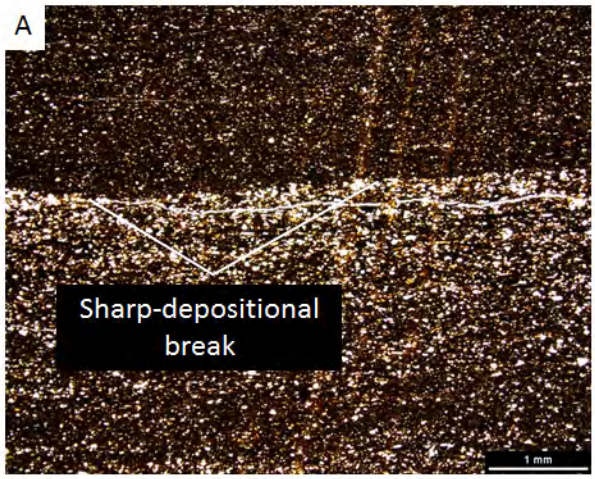

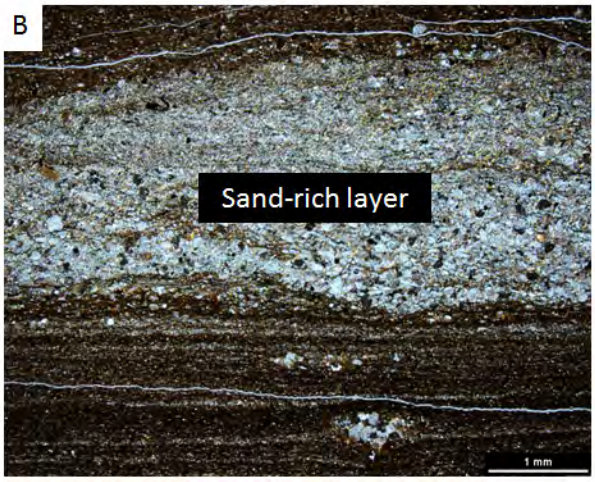

Figure 24. Peloidal organic-lean argillaceous mudstones. (A) Strong depositional break between very silty, peloidal organic-lean argillaceous mudstone (below) and slightly silty, peloidal organic-lean argillaceous mudstone (above). TOC = 2.86%. YY1-1446.86 m. (B) Sandy layer in well-laminated, peloidal slightly silty, organic-lean argillaceous mudstone. TOC = 2.85%. YY1-1445.72 m.

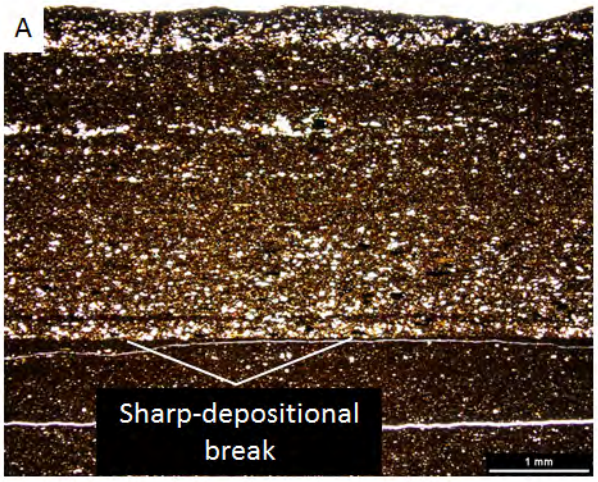

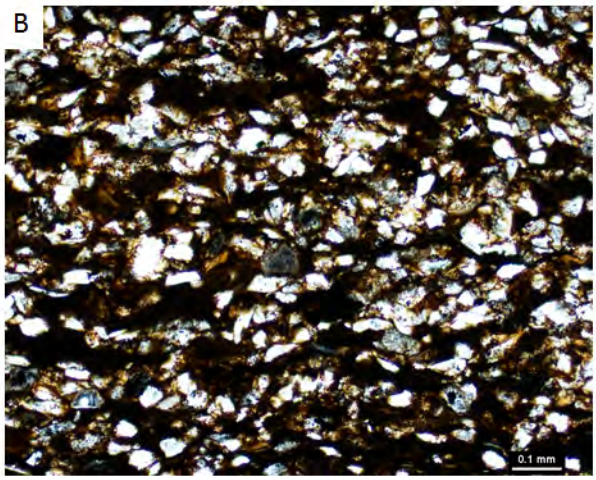

Figure 25. Peloidal organic-rich argillaceous mudstones. (A) Strong deposition break between well-laminated, very silty peloidal organic-rich argillaceous mudstone (above) and slightly silty peloidal organic-rich argillaceous mudstone (below). TOC = 3.25%. YY1-1414.76 m. (B) Sandy layer in well-laminated, peloidal organic-lean slightly silty argillaceous mudstone. TOC = 3.79%. YY1-1397.66 m.

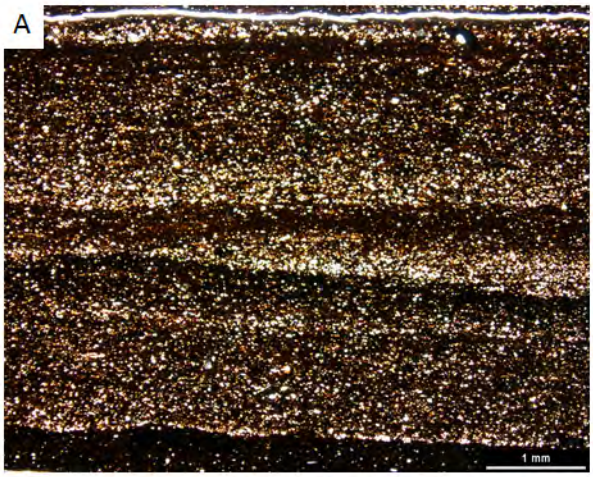

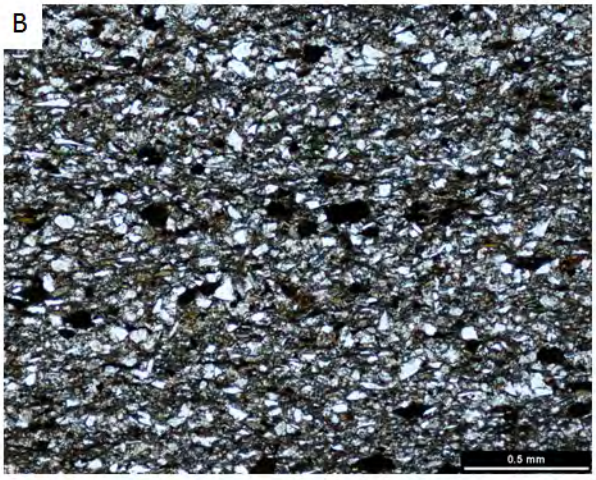

Figure 26. Argillaceous mudstone and siltstone. (A) Rippled, very silty, very peloidal organic-rich argillaceous mudstone. TOC = 3.91%. YY22-1346.87 m. (B) Argillaceous siltstone with dark peloids. TOC = 0.44%. YY1-1414.86 m.

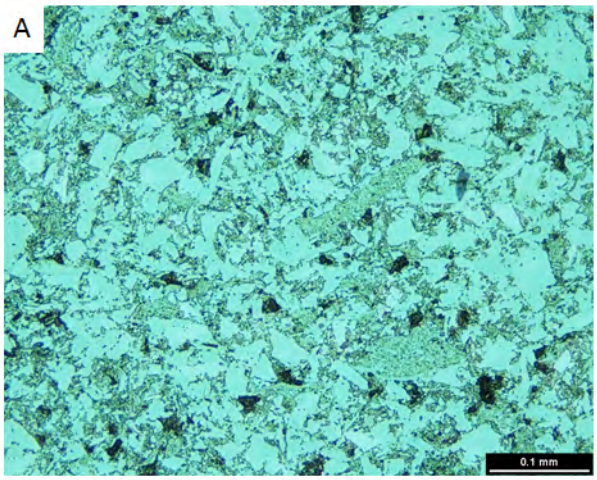

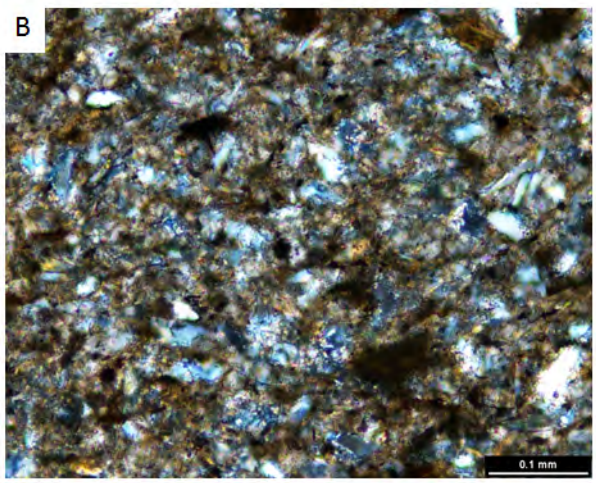

Figure 27. Argillaceous siltstone. YY1-1469.08 m. (A) Argillaceous siltstone. TOC = 0.39%. (B) Same as B but under cross-polarized light. Grains appear to be quartz, rock fragments, mica, and argillaceous peloids.

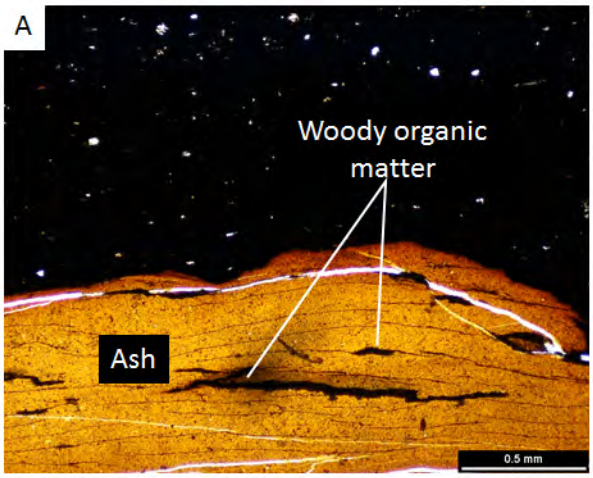

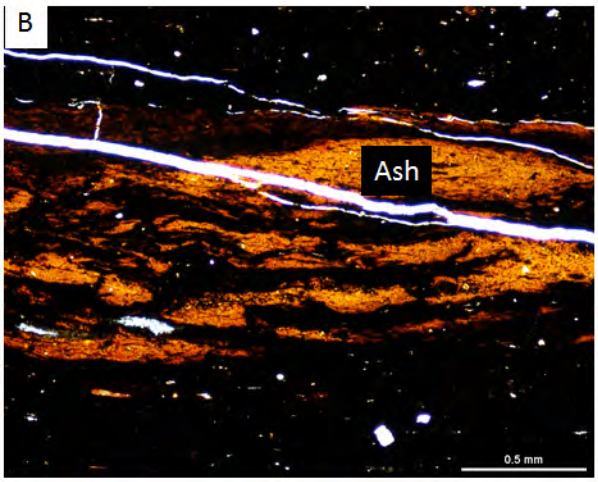

Figure 28. Ash bed. YY1-1359.66 m. (A) Millimeter-thick ash layer. (B) Disrupted ash layer.

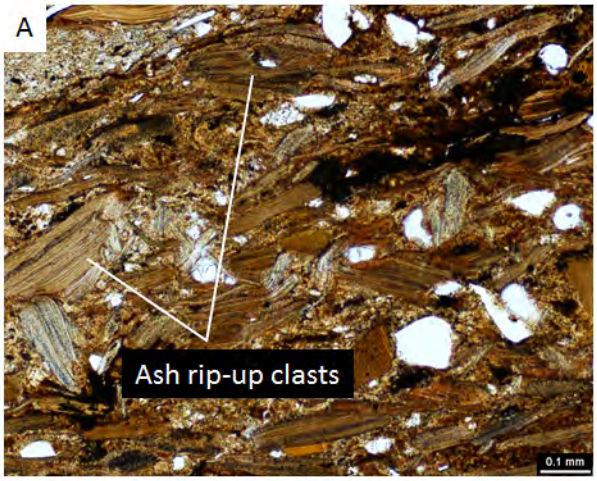

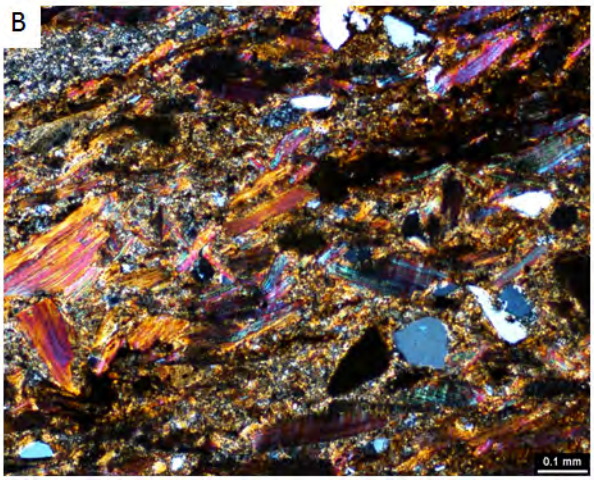

Figure 29. Ash bed. YY1-1335.26 m. (A) Transported volcanic ash rip-up clasts that may now be mica. Silt and sand grains are also present. (B) Same as A, but under cross-polarized light.

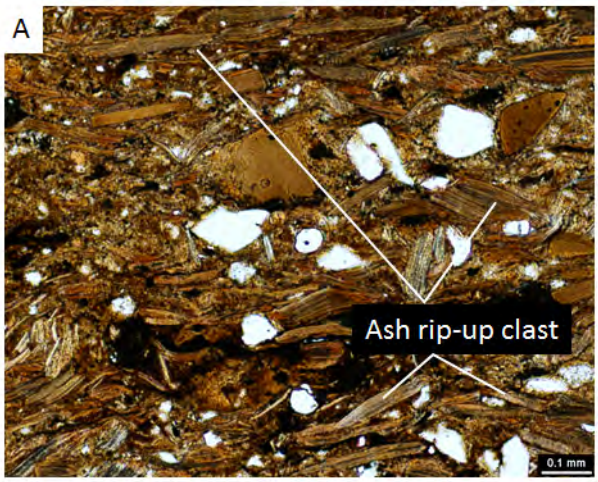

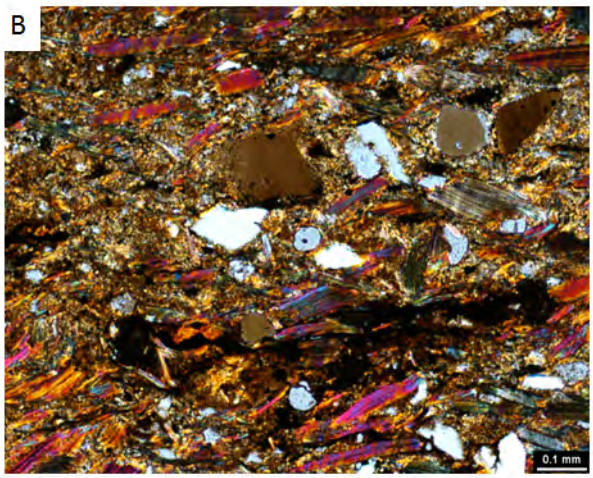

Figure 30. Ash bed. YY1-1535.26 m. (A) Transported volcanic ash rip-up clasts that may now be mica. Silt and sand grains are also present. (B) Same as A, but under cross-polarized light.

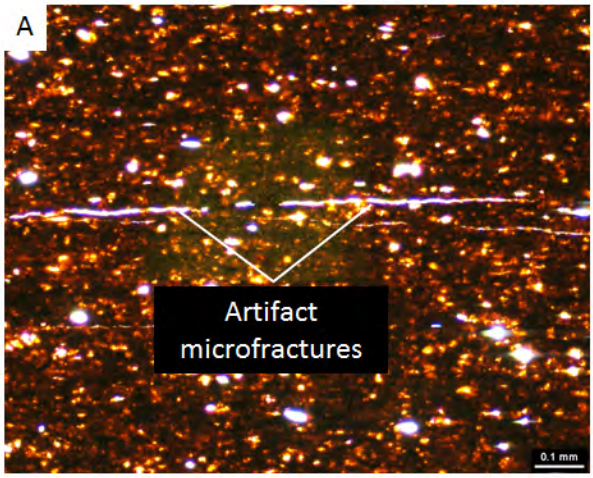

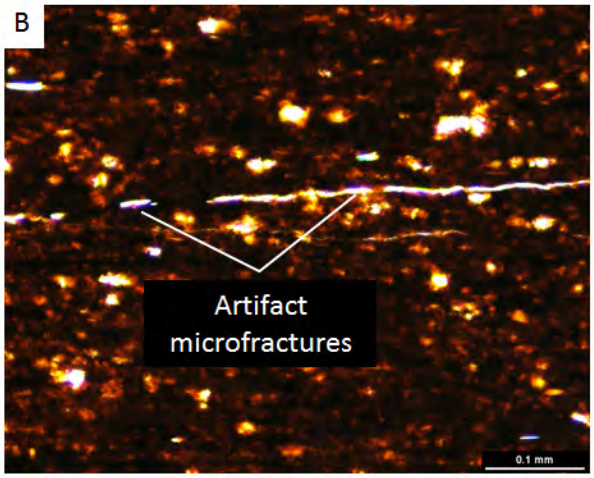

Figure 31. Artifact microfractures. YY1-1451.02 m. (A) Discontinuous horizontal microfractures. (B) Closeup of A.

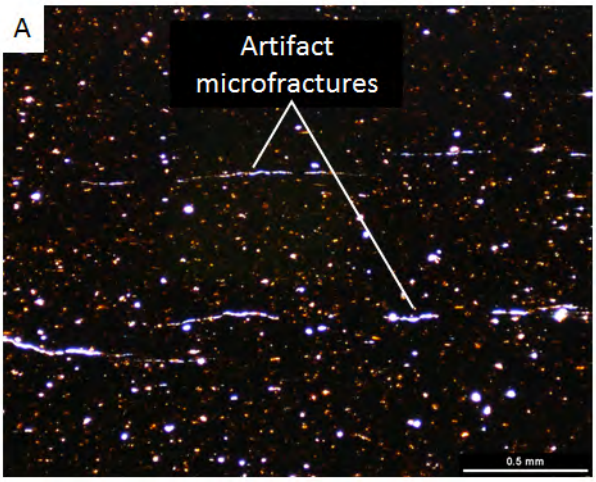

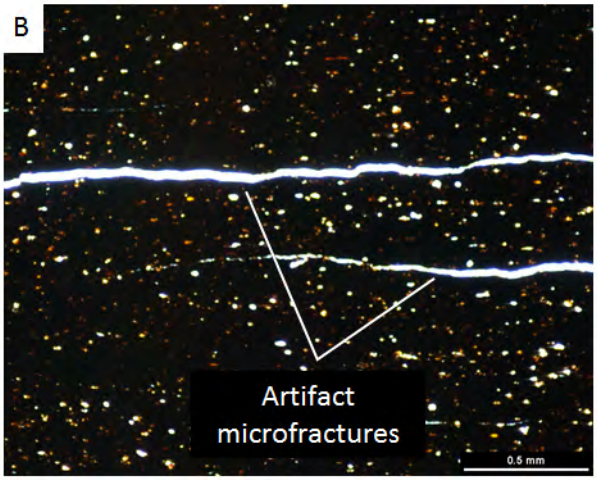

Figure 32. Discontinuous artifact microfractures related to sample preparation or desiccation. YY1-1448.05 m. (A) Discontinuous horizontal microfracture. (B) Discontinuous horizontal microfracture.

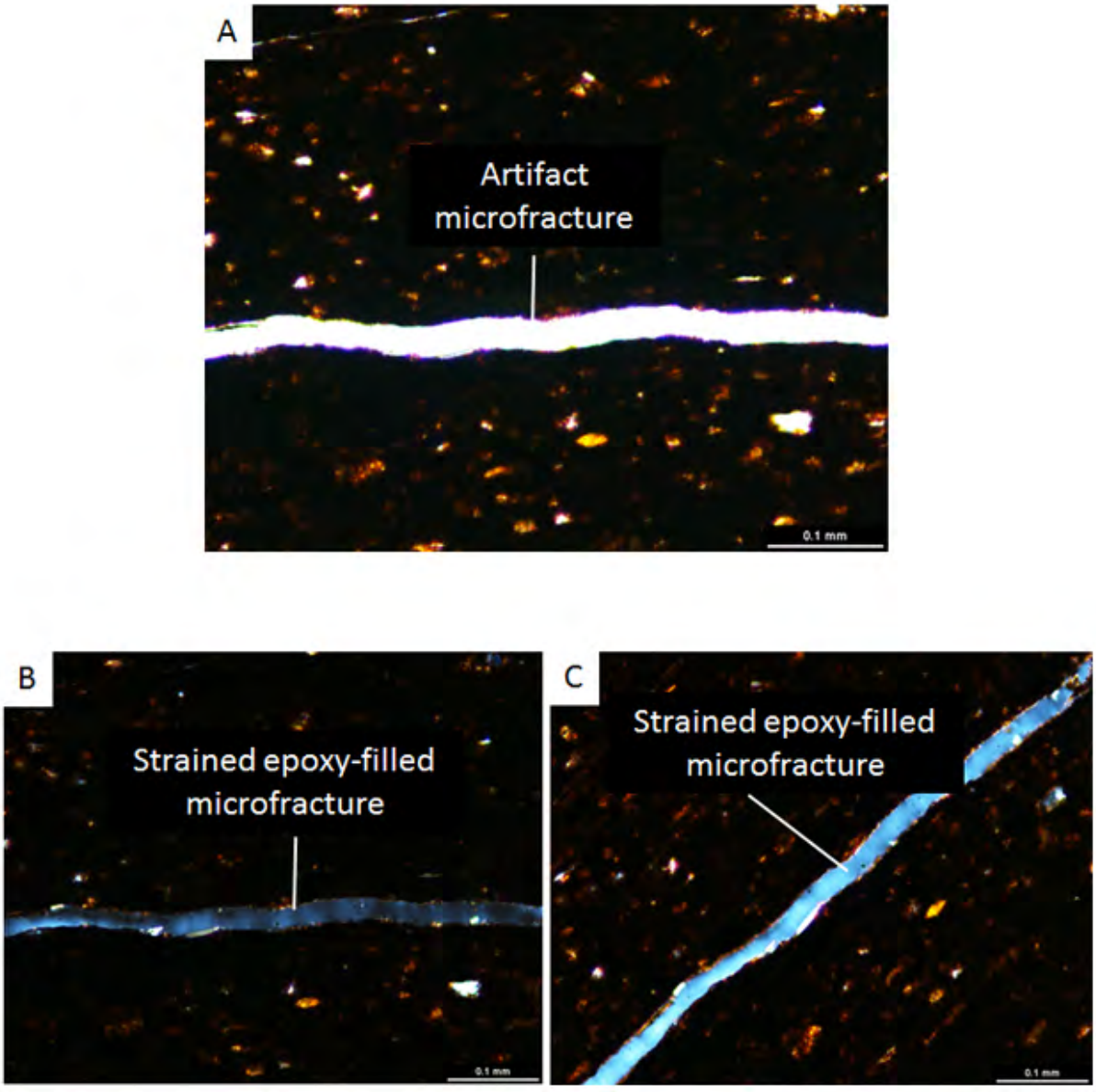

Figure 33. Artifact microfractures filled with birefringent epoxy. YY1-1448.05 m. (A) Discontinuous horizontal fracture. (B) Discontinuous horizontal fracture filled with birefringence strained epoxy that could be mistaken for cement. (C) Same as B but turned 45 degrees.

material in the microfractures is not cement; it is strained-hardened epoxy. The stained epoxy produces birefringence (**Fig. 33B, C**) that can be mistaken for cement.

Lithofacies

Three general lithofacies based on grain size, mixtures of silt- and clay-sized particles, and TOC were recognized: (1) argillaceous siltstone (**Figs. 26B, 27**), (2) organic-lean argillaceous mudstone (**Figs. 23, 24**), and (3) organic-rich argillaceous mudstone (**Figs. 25, 26A**). No sandstones were observed. The difference between organic-lean and organic-rich mudstone is that the former has less than 3% TOC and the latter has as much as or more than 3% TOC.

***Argillaceous Siltstone*:** The argillaceous siltstones generally have greater than 63% percent silt-sized grains and have low TOC. Sedimentary structures include ripples, laminations, upward-fining sequences, scour surfaces, and burrows. Argillaceous peloids are common. The argillaceous siltstones contain the following mean values: quartz = 22.5%, feldspar = 26.4%, phyllosilicates = 32.1%, and TOC = 1.35%. The argillaceous siltstones have the highest amount of quartz and feldspar by a few percent and the least amount of phyllosilicates and TOC (**Table 1**).

***Organic-Lean Mudstone*:** The organic-lean mudstones contain abundant argillaceous peloids and have less than 3% TOC. Most common sedimentary structures are faint to well-developed laminations. Rare, small burrows may be present. Silt- and sand-sized grains range from a few percent to approximately 50%. Individual sand- and silt-layer punctuate the mudstones. The organic-lean mudstones contain the following mean values: quartz = 20.5%, feldspar = 22.1%, phyllosilicates = 47.2%, and TOC = 2.36%. The organic-lean mudstones have intermediate amounts of quartz, feldspar, phyllosilicates, and TOC relative to the siltstones and organic-rich mudstones (**Table 1**).

***Organic-Rich Mudstone*:** The organic-rich mudstones contain abundant argillaceous peloids and have 3% or more TOC. They contain similar sedimentary features as the organic-lean mudstones. The organic-rich mudstones contain the following mean values: quartz = 16.6%, feldspar = 15.7%, phyllosilicates = 57.3%, and TOC = 5.76%. The organic-rich mudstones have the lowest amount of quartz and feldspar by a few percent, and they have the highest amount of phyllosilicates and TOC (**Table 1**).

Table 1. Descriptive statistics for lithofacies as shown by XRD and Rock Eval. All values are in percent (%).

	Quartz	Feldspar	Phyllosilicates	TOC
Argillaceous siltstone	22.5	26.4	32.1	1.35
Organic-lean argillaceous mudstone	20.5	22.1	47.2	2.36
Organic-rich argillaceous mudstone	16.6	15.7	57.3	5.76

Conclusions

The lithofacies in the Yanchang Formation, as seen in the YY1 and YY22 cores, are predominantly organic-lean and organic-rich argillaceous mudstones, with lesser argillaceous siltstones (**Appendix A**). Argillaceous peloids are probably the most common grain type, along with quartz and feldspar. Overall the mineral composition is that of very immature rocks; therefore, the lithofacies was mechanically and chemically unstable at the time of deposition, and it later underwent extensive compaction and diagenesis.

Appendix A

Well and Code	Depth (m)	General texture	TOC %	Description	Quartz %	Feldspar %	Phyllo-silicates %	Notes
YY1-43-1-68-62	1315.72	Argillaceous mudstone	No TOC	Poorly laminated, thin-shelled-mollusk-bearing, very peloidal, slightly silty argillaceous mudstone	20.9	37.8	37	
YY1-68-1-24-19	1358.56	Organic-rich argillaceous mudstone	6.7	Laminated, very peloidal, slightly silty and sandy argillaceous mudstone with some fish bones and organic or algal cysts	20.4	14.5	58.4	
YY1-68-2-37-26	1359.66	Organic-lean argillaceous mudstone	2.69	Poorly laminated, extremely peloidal, slightly silty argillaceous mudstone	24.2	19.7	51.2	Very distinct peloidal texture
YY1-71-1-81-73	1364.69	Organic-rich argillaceous mudstone	5.84	Poorly laminated, very peloidal, slightly silty and sandy argillaceous mudstone with a few sand stingers and some sort of algal cysts	15.5	16.2	59.5	Very peloidal, some sort of algae
YY1-71-1-51-43	1370.77	Organic-lean argillaceous mudstone	2.44	Thickly laminated, burrowed, slightly silty (very fine), argillaceous mudstone with few skeletal grains	14.7	15.6	32	Burrows within laminae
YY1-75-2-81-74	1372.07	Organic-rich argillaceous mudstone	5.43	Laminated, very peloidal, very silty and sandy argillaceous mudstone	12.1	13.3	58.7	
YY1-77-1-47-40	1374.44	Organic-rich argillaceous mudstone	7.94	Poorly laminated, slightly burrowed, very peloidal, slightly silty argillaceous mudstone with rare skeletal fragments and possible algal cysts	13.1	13.4	64.5	Unidentified groups of calcite crystals; may be related to algae or volcanic ash
YY1-79-1-96-86	1378.5	Organic-rich argillaceous mudstone	8.2	Slightly burrowed, very peloidal, slightly silty argillaceous mudstones	15.1	18.7	57.3	Unidentified groups of calcite crystals: algal or volcanic ash
YY1-83-2-87-78	1386.35	Organic-rich argillaceous mudstone	7.8	Poorly laminated, very peloidal, silty argillaceous mudstone with common mica	17.7	22.4	50.5	Unidentified groups of calcite crystals: algal or volcanic ash
YY1-87-1-39-31	1392.75	Organic-rich argillaceous mudstone	5.06	Very dark, slightly laminated, peloidal, very slightly silty argillaceous mudstone	13.1	8.2	73.7	Unidentified groups of calcite crystals; calcite crystals in layers: probably algal
YY1-90-1-64-56.1	1397.66	Organic-rich argillaceous mudstone	3.79	Poorly laminated, very peloidal, very silty argillaceous mudstone with few skeletal grains and ostracods	22.1	12.4	53	Very peloidal
YY1-94-1-69.7-61.2	1408.26	Argillaceous siltstone	2.19	Rippled bedded, peloidal, argillaceous sandy siltstone with abundant mica	22	18.6	27.5	Deposited by flow. Peloids are clay
YY1-94-2-69.7-76.8	1409.26	Organic-rich argillaceous mudstone	3.98	Well laminated, very peloidal, silty argillaceous mudstone with large, very flat thin bivalves	14.7	7.4	68.3	Good example of a large flat bivalve that could be misidentified as a horizontal microfracture.
YY1-97-1-78-70	1414.76	Organic-rich argillaceous mudstone	3.25	Well laminated, very peloidal, silty and sandy argillaceous mudstone with some sandy laminae	11.6	15.4	68.3	Some fining up stringers of sand: turbidites
YY1-104-1-67.5-60.5	1414.86	Argillaceous siltstone	0.44	Poorly laminated with some burrows(?), sandy argillaceous siltstone(?) with mud clasts	22.8	26.6	33.8	Flow
YY1-108-1-52-34	1426.15	Organic-lean argillaceous mudstone	2.72	Well laminated, very peloidal, slightly silty, argillaceous mudstone	16.4	14	64.3	
YY1-112-2-81-72	1434.28	Rippled argillaceous siltstone	1.43	Rippled, very peloidal argillaceous siltstone	22.8	33.9	34.9	Peloids acted as silt grains to form ripples
YY1-113-1-58-49	1441.48	Organic-lean argillaceous mudstone	1.66	Laminated and slightly burrowed, very peloidal, silty argillaceous mudstone	22	32.1	37	
YY1-114-2-38-27.5	1443.13	Organic-rich argillaceous mudstone	5.35	Slightly burrowed, very peloidal, slightly silty and sandy argillaceous mudstone	14.3	16.9	56.3	
YY1-115-1-62-55	1445.72	Organic-lean sandy argillaceous mudstone	2.85	Slightly burrowed, very peloidal, very silty and sandy argillaceous mudstone with layer of sand.	16.7	20.7	52.3	Sand layer composed of quartz and altered VRFs(?) with clay rims
YY1-117-2-15-9	1446.86	Organic-lean sandy argillaceous mudstone	2.66	Thickly laminated (very thin bedded), slightly burrowed, very peloidal, very silty to sandy argillaceous mudstone	14.5	21.2	60.4	Very small burrows
YY1-119-2-8-0	1451.02	Organic-rich argillaceous mudstone	6.62	Faintly laminated, very peloidal, silty argillaceous mudstone containing compacted very thin mollusk.	12.4	14.6	66.8	
YY1-121-1-43.7-37.5	1454.82	Organic-rich argillaceous mudstone	5.82	Faintly laminated, very peloidal, silty (minor sand) argillaceous mudstone containing some phosphate peloids	12.4	15.2	64.6	
YY1-123-2-45-37	1458.05	Organic-rich argillaceous mudstone	5.86	Faintly laminated, very peloidal, silty (minor sand) argillaceous mudstone	18.1	15.5	58.8	Good example of artifact fractures
YY1-129-1-98-84	1469.08	Argillaceous siltstone	0.39	Massive bedded, argillaceous siltstone with few peloids	20.4	20.9	38.5	Best siltstone so far; check on depth
YY1-142-1-87.5-82	1472.64	Organic-lean argillaceous mudstone	2.39	Faintly laminated, burrowed(?) extremely peloidal, silty argillaceous mudstone	19.6	22.3	50.2	Peloidal siltstone
YY1-144-1-54-45	1497.07	Organic-lean argillaceous mudstone	2.76	Clay-rich peloidal mudstone with silt/sand stringer.	23.1	21.9	47.1	Clays aligned and rotate to extinction
YY1-145-1-61-55	1500.38	Organic-rich argillaceous mudstone	5.43	Faintly laminated, burrowed(?) very peloidal, silty argillaceous mudstone	18.4	27.5	48.6	
YY1-146-2-34.3-27	1501.31	Organic-rich argillaceous mudstone	7.17	Faintly laminated, very peloidal silty argillaceous mudstone with clay clasts (ash?) and few sand grains.	16	11.9	57.3	Plankton of some type; algal cysts?
YY1-147-2-63-53	1504.98	Organic-rich argillaceous mudstone	7.08	Faintly laminated, very peloidal silty argillaceous mudstone.	22.2	16.3	53.4	Artifact fractures and epoxy with extinction
YY1-150-1-96.5-87	1511.42	Organic-rich argillaceous mudstone	7.08	Faintly laminated, very peloidal silty argillaceous mudstone with clay layers. Possible ash?	27.2	13.8	49.5	Contains clay layer type from which the mud clasts above are derived: ash beds
YY1-163-2-30-22.5	1535.26	Organic-lean argillaceous mudstone	2.08	Disturbed fabric, clay-clast-bearing sandy argillaceous mudstone (ash?). Layer of clay clasts, ash	30.9	22.1	43.1	Organic-rich with type III
YY22-14-1-77.5-64	1306.89	Organic-rich argillaceous mudstone	3.4	Laminated, fine peloidal clay-mineral-rich argillaceous mudstone with some algal cysts and flat thin bivalves	15.2	10.1	57	Clays aligned to extinction
YY22-18-2-67.8-56.7	1315.22	Organic-rich argillaceous mudstone	4.93	Laminated and microburrowed (?), fine very peloidal silty argillaceous mudstone with some algal cysts and flat thin bivalves	14.5	20.3	55.8	
YY22-20-1-52.7-41.8	1317.88	Organic-rich argillaceous mudstone	5.64	Laminated, fine very peloidal silty argillaceous mudstone with some algal cysts and flat thin bivalves	18.8	26.7	42.2	
YY22-22-1-7.8-0	1320.84	Organic-rich argillaceous mudstone	4.93	Laminated, fine very peloidal silty argillaceous mudstone with some algal cysts and flat thin bivalves	15.6	7.8	45.7	
YY22-26-1-86.5-76.5	1329.17	Organic-lean argillaceous mudstone	1.36	Laminated, fine very peloidal silty argillaceous mudstone with some algal cysts	22.7	31.2	33.9	Algal or volcanic ash grain
YY22-30-1-33.2-27.2	1336.03	Organic-rich argillaceous mudstone	8.07	Laminated, fine very peloidal silty argillaceous mudstone with algal cysts	18.1	15	57	
YY22-34-2-71.5-64	1344.07	Organic-rich argillaceous mudstone	4.65	Slightly laminated, in very peloidal silty argillaceous mudstone with few flat bivalves	18.6	11.3	58.4	
YY22-36-1-57.5-47.5	1346.87	Organic-rich argillaceous mudstone	3.91	Well laminated, very peloidal, silty argillaceous mudstone	14.5	4.4	69.8	Well laminated

TASK 2.2

Assessment of Detrital Grain Assemblages and Diagenetic Components by Light Microscopy, X-ray Mapping and Scanned Cathodoluminescence Imaging

Kitty L. Milliken[1] and Ying Shen[2]

[1]Bureau of Economic Geology, Jackson School of Geosciences, The University of Texas at Austin, Austin, Texas
[2]Shaanxi Yanchang Petroleum (Group) Co. Ltd., Xi'an, Shaanxi, China

This report expands upon the year-end report of 2014. Five additional samples from the YY1 well and 12 new samples of variable maturities from several different wells have been documented using transmitted light microscopy, X-ray elemental mapping, and point-counting of X-ray images. Compositional and textural data from imaging have been used to refine the lithologic categories for the samples and comparisons of pore-size distributions have been made (from N-adsorption) based on those categories.

Background

Primary detrital grain assemblages in conventional sandstone reservoirs are a key control on the evolution of porosity and other bulk properties in the subsurface (e.g., Ajdukiewicz and Lander, 2010; Lander and Walderhaug, 1999; Pittman and Larese, 1991).The chemical and mechanical reactivity of carbonate grains similarly control the diagenetic evolution of limestones (e.g., Bathurst, 1975; Flügel, 2004). Current understanding of the diagenetic impact of grain assemblage composition in mudrocks is less refined, but it is clear that mudrock diagenesis entails processes such as compaction (Velde, 1996) and cementation (Milliken and Day-Stirrat, 2013) that, in sandstones and limestones, are strongly influenced by grain composition. It is also well-established that compositional variation of grain assemblages in mudrocks is large (Milliken, 2014) for both marine and lacustrine mudstones, leading to the expectation that the evolution of bulk mudrock properties in the subsurface will follow diverse pathways. Development of predictive models for mudrock property evolution in diagenesis depends upon observational studies of contrasting grain assemblages to document their particular chemical and mechanical responses to changing conditions in the subsurface. Triassic lacustrine basin sediments of the Ordos Basin provide an important data point for understanding the diagenetic behavior of mudrock systems.

In productive organic-rich mudrocks examined to date, grain assemblages include a substantial component of intrabasinal grains that impart reactivity that results in early cementation. For example, in the Barnett Shale in the Fort Worth Basin, abundant grains of biogenic opal have reacted in early diagenesis to yield matrix-dispersed microquartz (**Figure 1A**) that plays an important role in the generation of brittle mechanical properties (Milliken et al., 2012). In the Eagle Ford Formation in South Texas, reaction of coccolithic debris and other unstable biogenic carbonate grains yields calcite cementation (**Figure 1B**) that causes substantial lithification

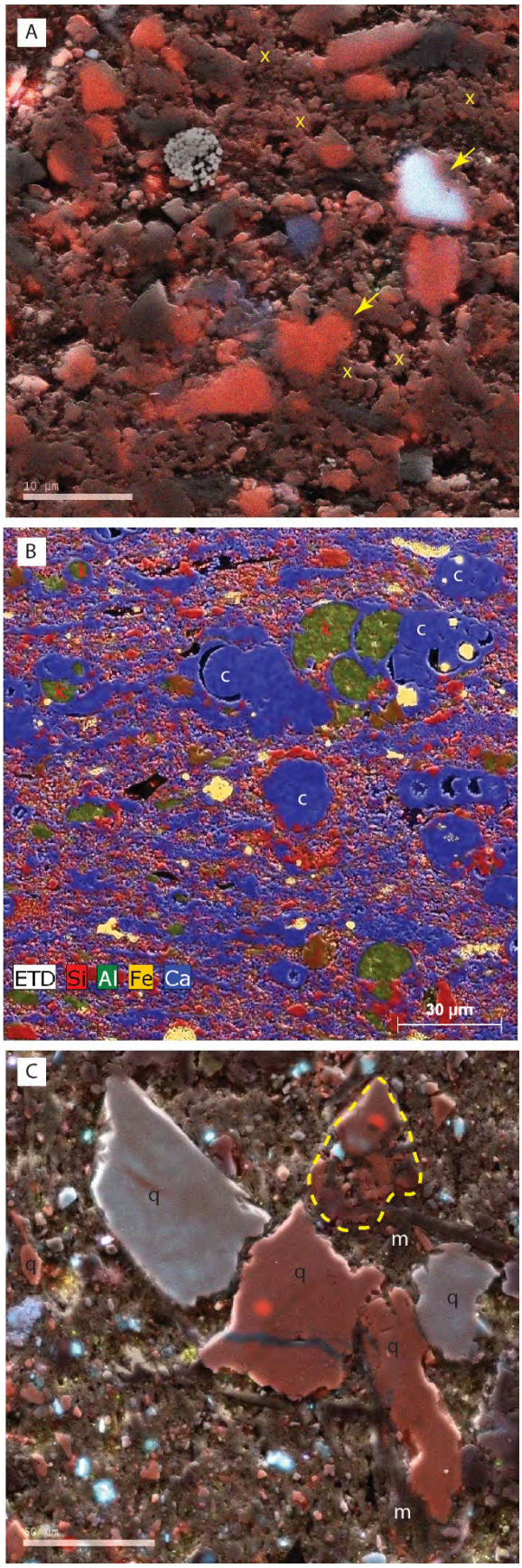

Figure 1. Petrographic character of sarl, carl, and tarl. (A) Sarl with abundant matrix-dispersed authigenic microquartz (yellow Xs). Arrows indicate authigenic microquartz that has nucleated on extrabasinal detrital quartz grains. Cathodocluminescence image. Barnett Shale, Fort Worth Basin. (B) **X-ray map. Eagle Ford Formation, Maverick Basin.** Carl with a diverse authigenic pore-filling minerals including calcite (c), kaolinite (k), and authigenic microquartz replacing skeletal grains and dispersed in the matrix (red). (C) **Tarl with detrital quartz (q), detrital mica (m), a lithic fragment (dashed yellow outline) and a near-total lack of quartz cement.** Matrix of this rock is entirely detrital clay and possibly, clay cements that are too fine to image at this scale. Note that the clay-size quartz that is distributed through the matrix has the same CL brightness and color variations as the silt-size quartz and is therefore also interpreted as extrabasinal detrital material. Cathodoluminescence image. Wilcox Formation, Gulf of Mexico Basin.

(Pommer and Milliken, 2015). Mudrocks lacking in significant intrabasinal grains, for example, the thick marine Cenozoic mudrocks of the Gulf of Mexico basin are dominated by the products of continental weathering and, do not, in general contain substantial organic matter nor manifest early cementation (**Figure 1C)** (Day-Stirrat et al., 2010b; Milliken, 2004; Milliken and Land, 1993; Milliken et al., 1989). Mudrocks dominated by extrabasinal debris and which are also organic-matter-rich, exist, but have been less studied in terms of their lithification history. Examples of these include marine shales such as the Kimmeridge Clay (Jurassic) (Fishman et al., 2012), the lower Paleozoic shales of Poland (klm personal observations), as well as lacustrine examples such as Wealden Shale (Cretaceous) of the Saxony basin (klm personal observations).

Task 2 Goals

Main: What is the composition of detrital grain assemblages in the mudrocks of the lacustrine Triassic Yanchang Formation? How do these grain assemblages compare to those in other lacustrine and marine mudrock units? Secondary: What diagenetic features are observed in the Yanchang Formation mudrocks? Answers to these questions are sought to refine our understanding of diagenetic controls on bulk rock properties in the Yanchang Formation. Data on detrital and authigenic components are used in the final section of this report to assess processes of porosity evolution.

Sampling

Thirty-three mudstone samples were obtained from the YY1 well and 8 mudstone samples from the YY22 well (**Table 1**). An addition four sandstone samples from YY1 were obtained for comparative purposes. Two cone-in-cone calcite samples were obtained; the cone-in-cone specimen in YY1 was also used as a mudstone sample. Sandstones, with their larger intergrain pore spaces, allow easier observation of cementation processes that, potentially, also take place in associated mudstones. Grain alteration processes in particular are known to occur in comparable type and abundance in sandstones and associated mudrocks. Diagenetic features, in particular carbonate precipitates such as concretions, although volumetrically minor, may provide key information about the chemistry of depositional fluids and about the conditions of early diagenesis, and thus, are of interest for understanding the overall conditions of organic matter deposition, preservation, and alteration.

Table 1. Point-count results and other comparative data.

Refer to accompanying Excel file

Methods

Several petrographic methods have been integrated for characterization of grain assemblages and diagenetic features. Polished thin sections were prepared by Spectrum Petrographics. To achieve better textural preservation during mechanical polishing, the sections were treated by surface

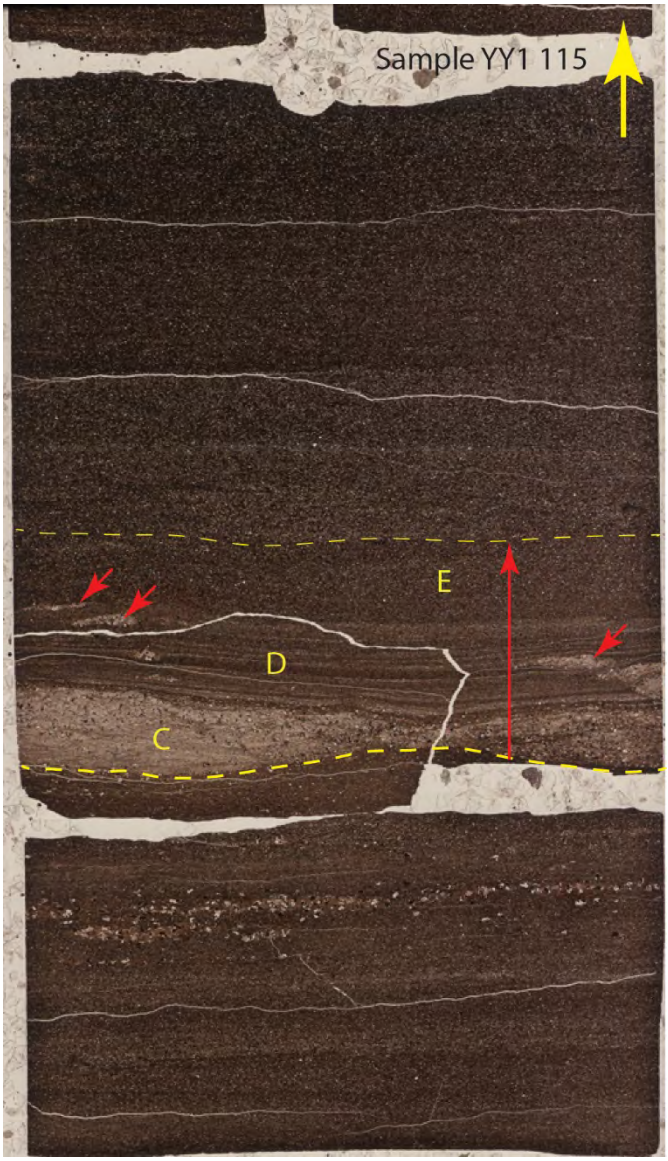

Figure 2. Scan of whole thin section. Original pixel resolution is 5515 x 3226. Such images can be used to observe the tiny sedimentary structures that form in fine-grained sediments. In this image the heavy dashed line denotes the scoured base of an upward-fining (possible partial Bouma sequence, red arrow) that includes a rippled base of coarse silt to very fine sand (C), a parallel-laminated interval of coarse silt and clay (D), and an upper layer of structureless silty mud (E). Small burrows (small red arrows) mix sand from layer C into layer D.

impregnation with a low-viscosity medium. After curing of the medium, polishing was accomplished within the impregnated surface layer.

Light microscopy: A whole-thin-section transmitted-light image was created using a high-resolution scanner (Nikon Coolscan 5000) to provide an overview of the sample fabric and for referencing further imaging (**Figure 2**). Each sample was then observed using a conventional petrographic microscope in both transmitted (plane- and cross-polarized light) and reflected light modes (**Figure 3**). Images were captured (Nikon DS-Ri1) to illustrate the overall sample fabric and also any notable biogenic or diagenetic features.

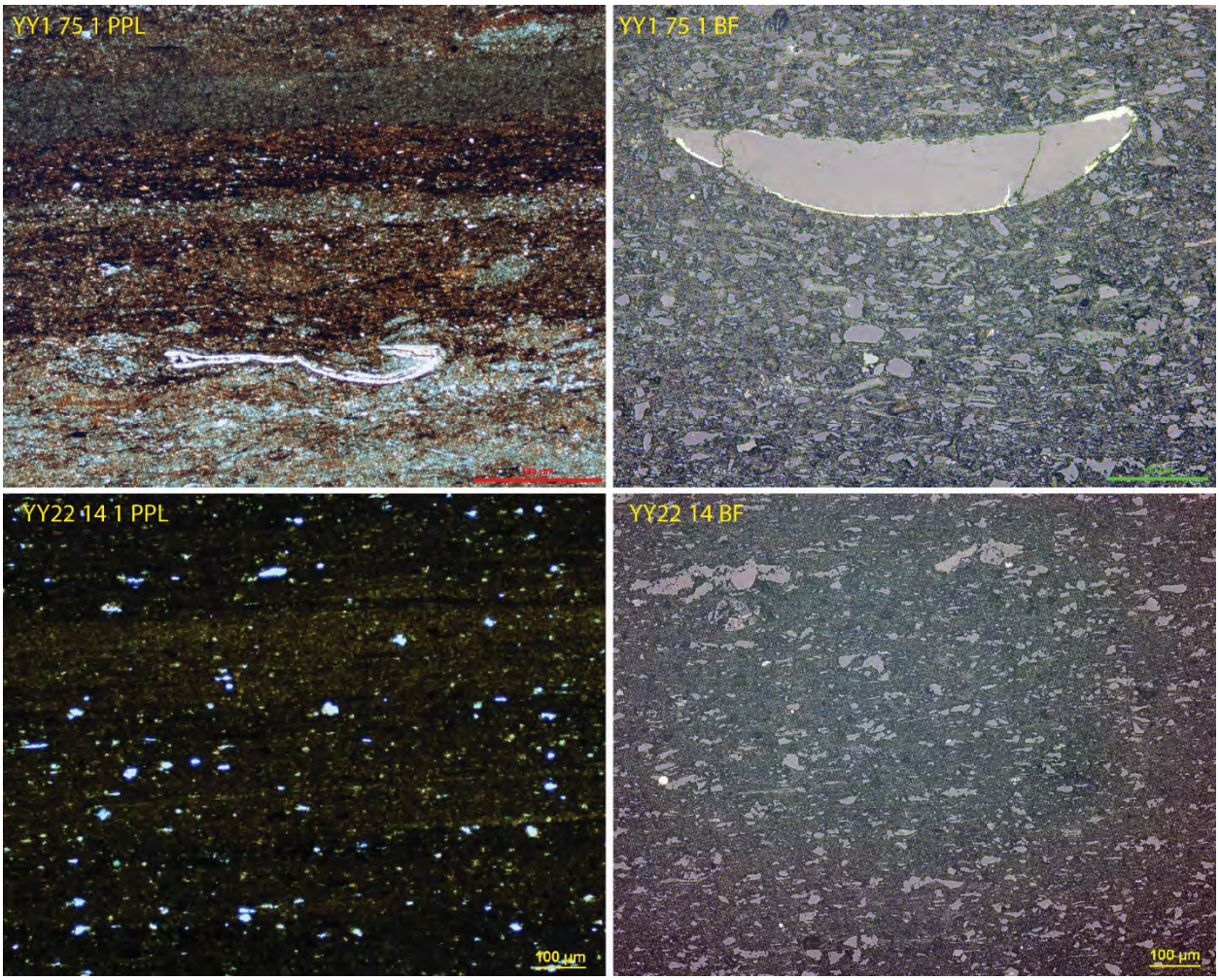

Figure 3. Transmitted (plane-polarized light, PPL) and reflected light microscopy (bright-field, BF) of two samples with contrasting silt content. Top images are Sample YY1 71 1, which contains only 22 percent clay matrix. Lower images are Sample YY22 14, which contains 71 percent clay matrix.

X-ray mapping: The thin sections were coated with 25 nm of carbon (as measured against the color of a polished brass standard) using a Ladd Vacuum Evaporator. Imaging was performed on an FEI NovaNanoSEM and the X-ray signal was captured with twin 30 mm^2 Bruker X-flash Energy Dispersive Spectroscopy (EDS) X-ray detectors. Imaging conditions for X-ray mapping require an accelerating voltage (15 KV) high enough to excite the characteristic X-ray signal from inner shell electrons of the light to intermediate elements of interest and a sufficient sample current (spot size of "5", about 90% of maximum for the instrument, and a 50 µm column aperture) to generate a strong X-ray signal. Elements of interest were selected to highlight particular mineral phases known to be present based upon light microscope observations. X-ray maps were combined with the secondary electron signal to produce a multi-channel image that features greater edge sharpness on crystal components that is possible with the X-ray signals alone. Under the conditions for X-ray mapping and on a flat specimen (no topography), much of the contrast "seen" by the secondary electron detector actually arises from a back-scattered

electron component.of the total electron signal. Thus, extremely heavy and light components (e.g., pyrite and organic matter) can be readily discriminated. To allow systematic comparisons of the samples, X-ray maps were collected at routine machine magnifications of 1000x and 3000x. Particular features of interest were mapped at a variety of magnifications.

Producing a clear and easily interpretable X-ray map depends upon selecting element combinations that highlight minerals with unique or nearly-unique X-ray signals. For example, Al is of little utility because it co-occurs in similar, moderate amounts in plagioclase, K-feldspar, micas, and clays. Although Si co-occurs in numerous mineral species, the highest Si signal can be confidently attributed to quartz (100% SiO_2). Si is, however, of little utility for discriminating other silicate phases, which in many cases can be better discriminated without the complicating addition of the Si signal. For example, K co-occurs in K-feldspar and in K-clays and micas, although in different amounts (14, 6, and 10 percent K, respectively). The sizes and shapes of these minerals further aid in their discrimination.

Elements, their assigned colors, and intended mineral targets were mapped as follows (**Figure 4**): C (orange, organic matter), Si (red, quartz), Na (aqua, Na-feldspar), Mg (fuchsia, dolomite, chlorite) K (yellow, K-feldspar, muscovite, and K-clay), Ca (blue, calcite), Fe (yellow, pyrite, biotite). In special cases P, Ba, Ti, and other elements were mapped to delineate local occurrences of other detrital or authigenic minerals. Six particular element combinations (combined with the SE signal) were routinely saved (**Table 2**).

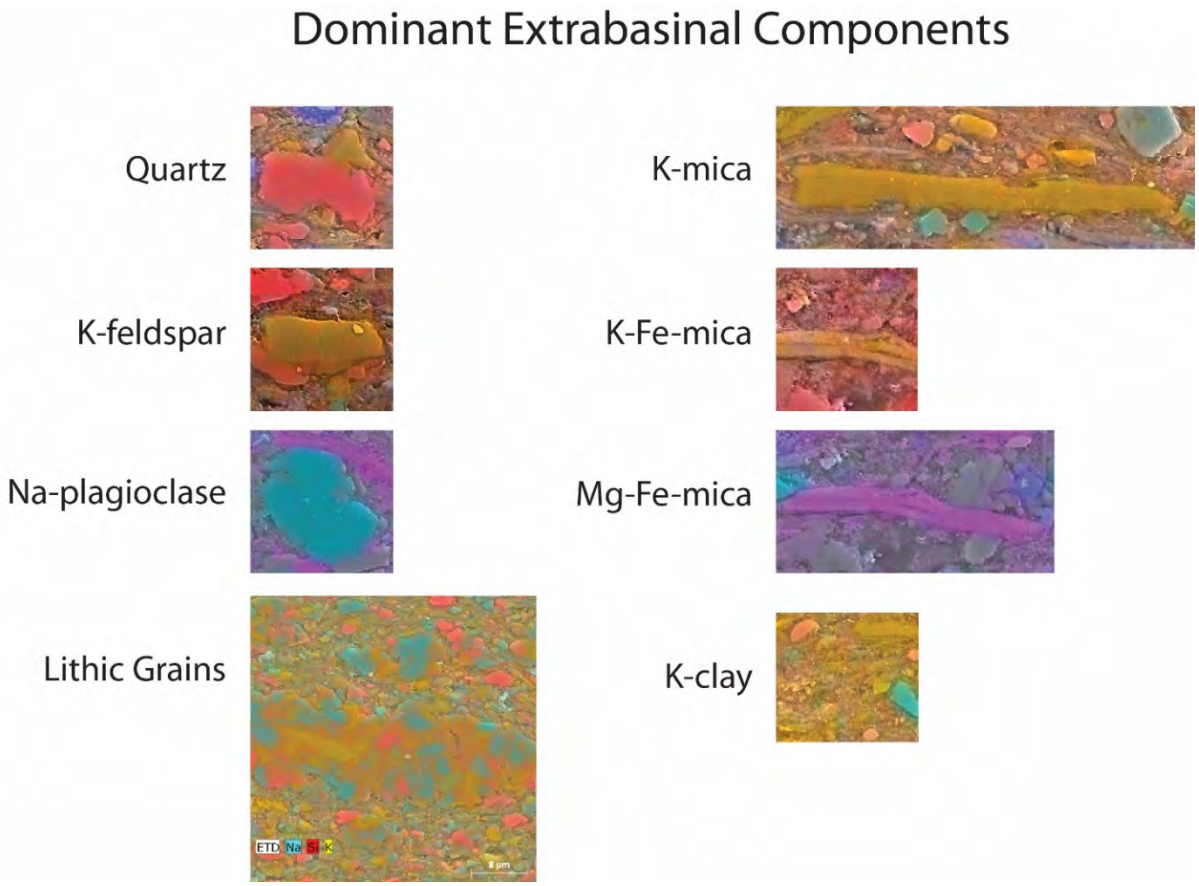

Figure 4. False color scheme used to discriminate the key extrabasinal components in X-ray mapping.

Table 2. Color scheme for X-ray mapping mineral identification.

1. Na, Si, Ca—maps detrital quartz, Na-feldspar, and carbonate minerals that dominate the silt fraction without the confusing addition of strong color to the clay mineral-dominated clay-size fraction
2. Na, Si, K, Ca— maps as above with the addition of K-feldspar, K-micas, but with the addition of color to the clay mineral-dominated clay-size fraction. This is the mix used primarily for point-counting.
3. Na, Si, Ca, Fe— highlights pyrite, Fe-bearing dolomite, and biotite
4. Na, Mg, Ca— highlights the carbonate minerals and discriminates calcite from dolomite, shows the Mg-micas, and leaves a portion of the silicate silt fraction (Na-feldspars) clearly visible
5. Na, Mg, K, Ca —highlights the carbonate minerals and also the feldspars plus K-mica and K-clay, while still leaving a portion of the silicate silt fraction visible.
6. Na, Mg, Ca, Fe— highlights the carbonate minerals and also pyrite and any Fe-micas, while still leaving a portion of the silicate silt fraction visible.

Cathodoluminescence imaging: CL imaging was performed under the same beam conditions as X-ray mapping using a Gatan Chroma CL detector. Fields of view were first mapped by EDS, and then regions containing abundant quartz were imaged in CL, the main goal being to inspect the samples for possible authigenic quartz. Most CL images are in the range of 2000x to 5000x machine magnification.

Point-counting: Modal data based on 200 random points were obtained from the 600x or 1000x X-ray maps using JMicrovision (Roduit, 2008). Point-counting at this magnification allows ready identification of silt-size components, but discrimination of non-clay minerals in the clay-size fraction is limited. Categories of detrital and authigenic components together with point-count results and certain bulk rock properties are shown in **Table 1**. Point-counting was carried out with multiple element combination maps layered within JMicrovision so that different element combinations could be queried for component ID. For example, a mica grain with both Fe and K is biotite, K alone is muscovite, Fe and Mg denote chlorite.

Results

X-ray mapping

Textural grain assemblages

Mudrock samples from wells YY1 and YY22 can be divided into two broad textural groups based on the sizes of the contained silt fraction and the ratio of silt-size particles to clay-size matrix. All the samples contain significant silt-size particles (28 to 77 volume percent) **(Figure 5)**. By the classification of Macquaker and Adams (2003), samples with < 50% silt are called silt-bearing-mudstones, whereas those with >50% silt are silt-rich mudstones. In the case of the present sample set however, the additional factor of silt-size can be taken into account (**Figure 6**). Near the 50% silt boundary silt size as well as silt abundance clearly plays a role in affecting bulk rock properties (discussed further below). Thus, some samples containing silt in amounts slightly greater than 50 percent, yet of very fine silt size (e.g., YY1 144, depth = 1500.38, 52.6 percent silt) are classed with the silt-bearing mudstones.

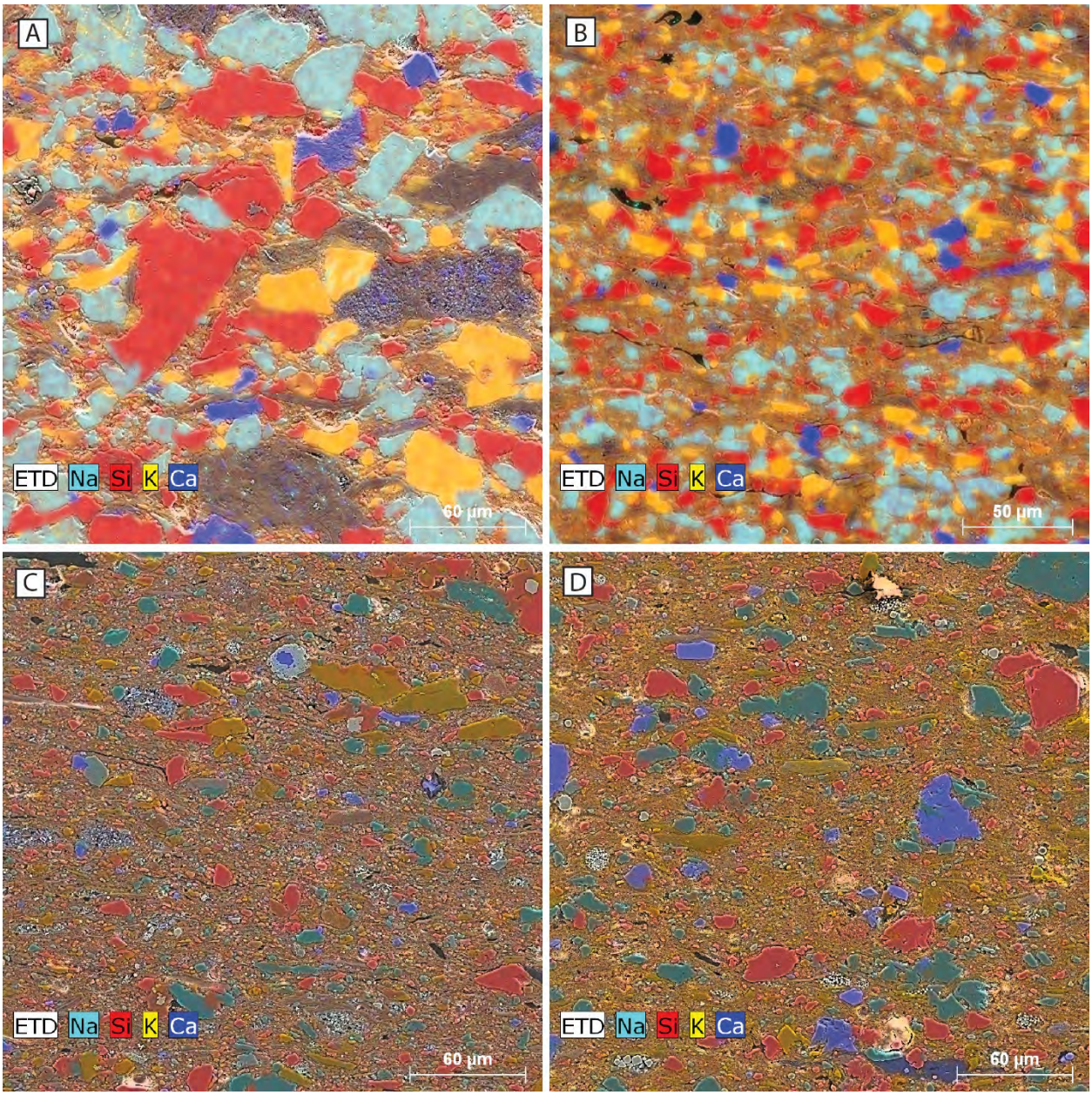

Figure 5. Textural variations as seen in X-ray maps. All images are at the same magnification. The total sample set includes large variations in both silt/clay ratio and the size of the silt component. (A) Sample YY1 112 2, depth 1441 m, 73.5% silt. Silt is in the upper range of silt size and a few particles are in the range of very fine sand. (B) Sample YY1 115 1, depth 1446 m, 54.5 % silt. Silt is in the mid-range of silt-size. (C) Sample YY1 771, depth 1374 m, 47.2 % silt. Silt size ranges from medium silt to fine silt. (D) Sample YY1 146 2, depth 1504 m, 38.4 % silt. Silt size ranges from medium silt to fine silt.

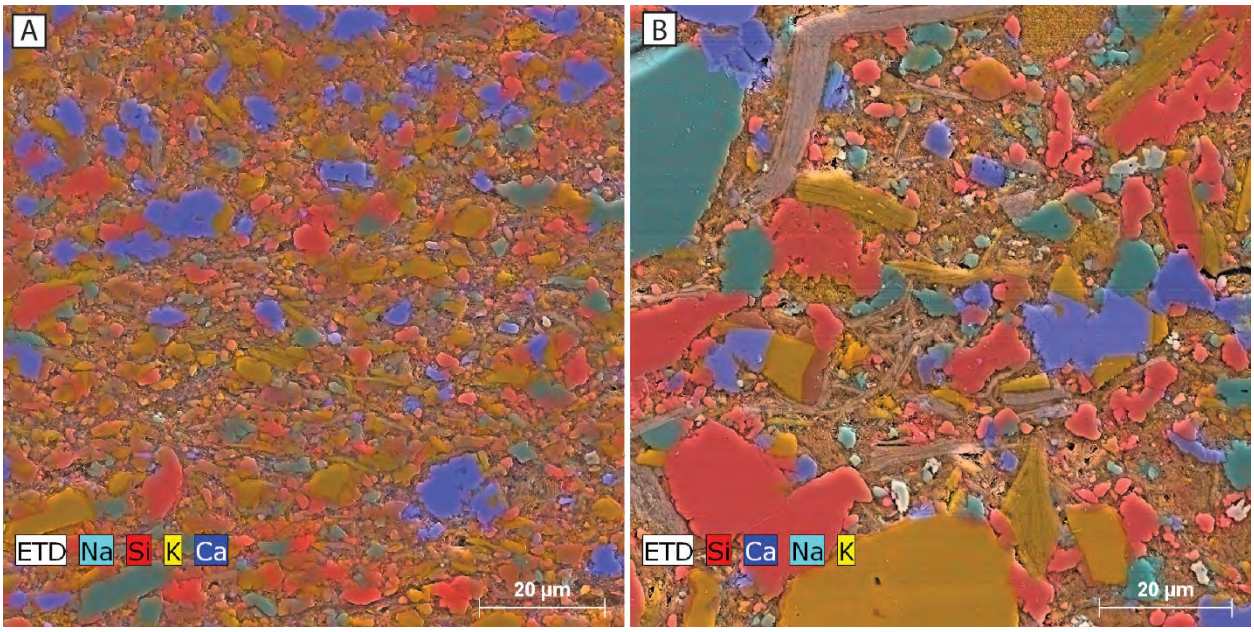

Figure 6. Textural variations within the population of silt-rich mudstones. X-ray maps. Both images are at the same magnification. (A) Sample YY1 75 1, depth 1370 m, 77.2% silt. Silt here is dominated by particles that are near the lower end of the silt-size range. (B) Sample YY1 104 1, depth 1426, 73.2% silt. Silt in this sample is in the mid-range of silt size. Note the abundance of micas.

Silt content among the 12 variable maturity samples is generally lower than in wells YY1 and YY22. Only one of those samples is a silt-rich mudstone (depth = 1248) and three of the samples approach clay-dominated texture (>90 percent clay-size matrix). It is important emphasize that the textural category of "clay-size matrix" is not equivalent to the mineralogical category of "clay" as assessed by the XRD bulk mineralogical analysis. Textural clay-size matrix includes micas, quartz, feldspar, and other non-clay minerals in addition to detrital clay minerals.

Compositional grain assemblages

Overall, the grain assemblage is dominated by extrabasinal grains (**Figure 7**). Monocrystalline detrital feldspar (plagioclase + K-feldspar) is the most abundant component in the silt-size fraction, averaging 21.3 volume percent (by point-count). Total feldspar averages 20.4 weight percent by XRD. Silt-size feldspar ranges from 3.0 volume percent in a clay-dominated sample to 52.3 percent in a silt-rich mudstone. Monocrystalline detrital quartz is the second most abundant silt-size component, averaging 13.2 volume percent by point-count). Total quartz averages 19.9 percent by XRD. Silt-size quartz ranges from 2.5 volume percent in a clay-dominated sample to 29.5 percent in a silt-rich mudstone.

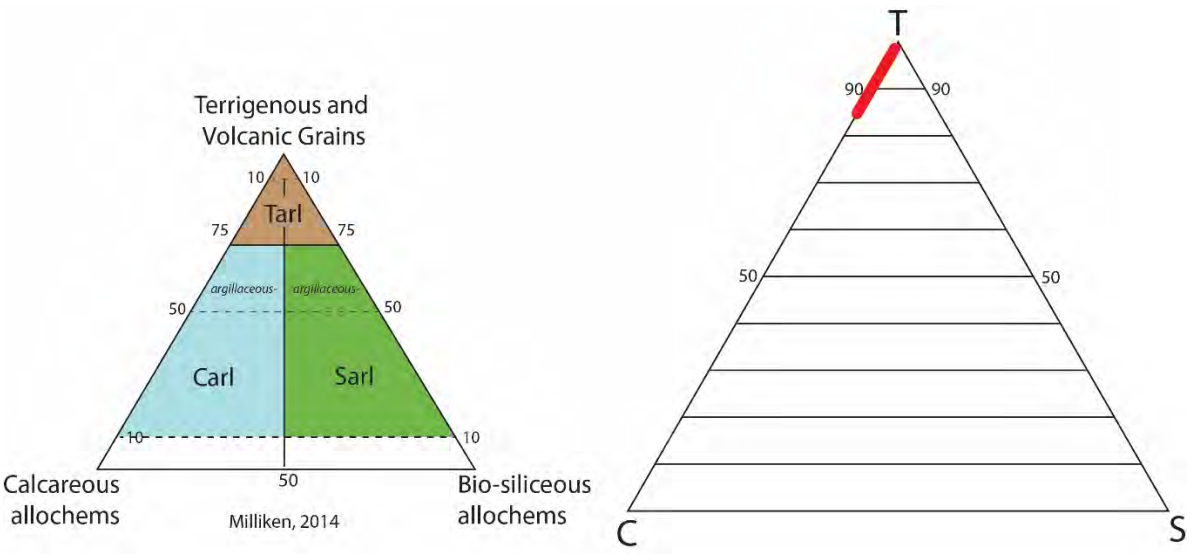

Figure 7. Compositional classification of Milliken (2014) applied to the Yanchang mudrock samples from wells YY1, YY22, and the 12 variable-maturity samples. Containing greater than 85% by volume of extrabasinal grains, all of the samples plot as tarls.

In higher magnification images, feldspar and quartz also are clearly visible in the coarser clay-size fraction, but these minerals in this size fraction have not been quantified. Comparison of average point-counted silt abundance versus XRD mineral-abundances suggests that clay-size quartz is more abundant than clay-size feldspar.

Grains of mica, including muscovite, biotite, and chlorite, are the third most abundant silt-size components, averaging 6.0 percent and ranging from 0.5 to 20.6 percent. Lithic fragments (polymineralic aggregates) are interpreted as volcanic rock fragments, average 0.60 percent and range from 0 to 6.5 percent.

Intrabasinal grains, those grained formed inside the basin of deposition either in the water column on by benthic processes, are minor constituents overall, averaging 4.2 volume percent and ranging from 0.5 to 15.1 percent. Only 3 samples contain greater than 10 volume percent intrabasinal grains and in each case the intrabasinal component is dominated by grains of dolomite (interpreted as syn-sedimentary). Other intrabasinal grain types include phosphatic grains from fish (teeth, scales, and bones), minor carbonate skeletal debris, and silt-size organic matter fragments, and sediment aggregates (interpreted as pellets) (**Figure 8**).

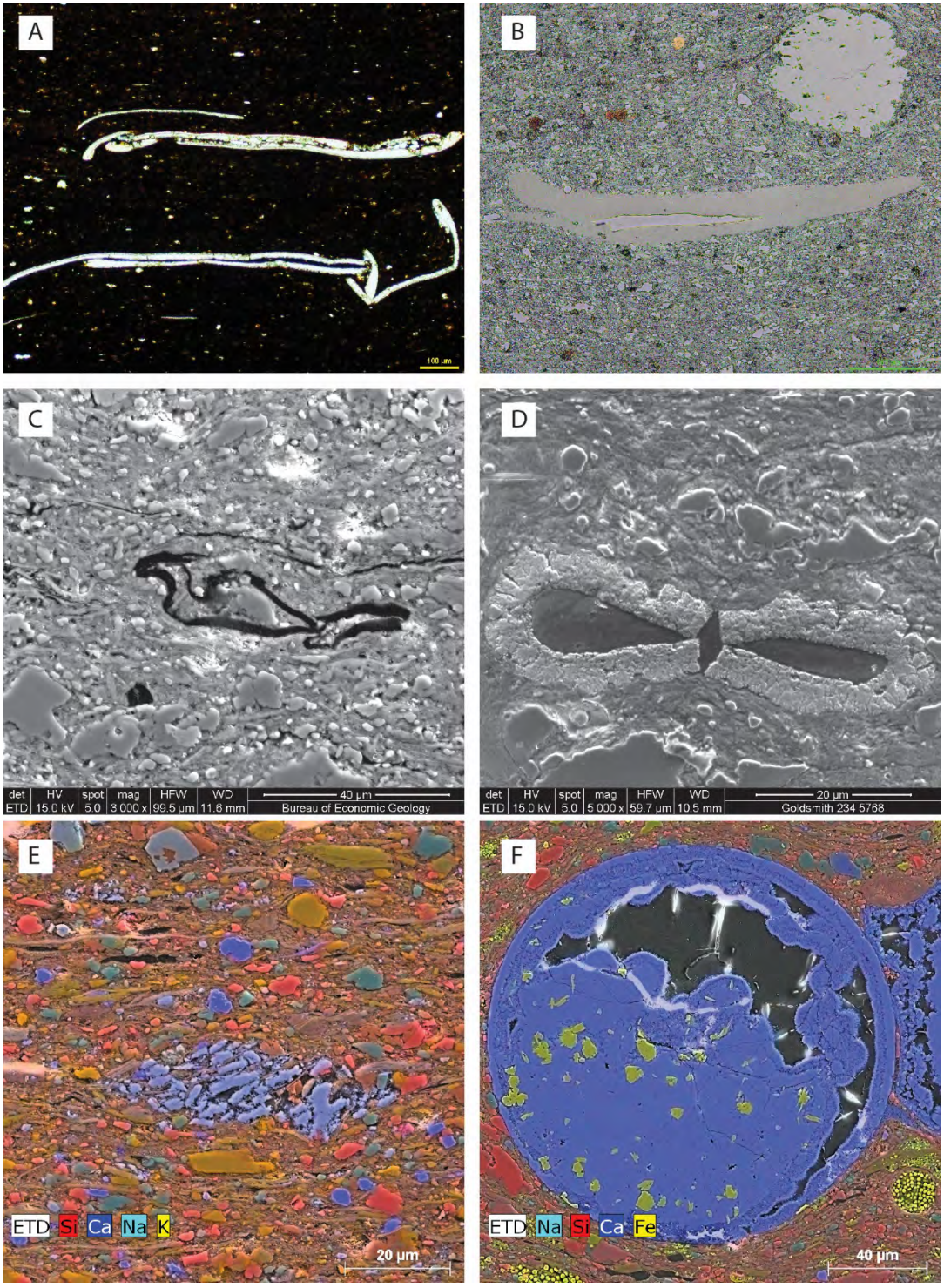

Figure 8. Examples of intrabasinal grains. (A) Thin walled calcitic skeletal fragments, possible mollusks. YY1 43 1 Plane-polarized light. (B) Bone fragment (center) and possible spore (upper right). YY1 71 1 Bright-field reflected light. (C) Possible collapse organic spore case. YY1 90 1 Secondary electron/back-scattered electron image. (D) Unknown collapsed calcitic skeletal fragement. YY1 121 1 Secondary electron/back-scattered electron image. (E) Aggregate of ferroan calcite fragments, possible pellet of a water-column feeder. YY1 77 1 X-ray map. (F) Phosphatic skeletal fragment filled with authigenic Ca- phosphate. YY1 77 1 X-ray map.

In general, the TOC of the silt-bearing mudstones is greater than that of the silt-rich mudstones and sandstones (**Figure 9A**), consistent with the positive co-variation between TOC and bulk clay minerals (**Figure 9B**) and the negative co-variation of TOC with respect to silt-associated minerals such as plagioclase (**Figure 9C**). Organic matter as detected in images, however, is only a fraction of the total organic content (TOC). In silt-bearing mudstones of YY1 and YY22 there is an average of 0.94 volume percent organic matter measured by point-counting, in silt-rich mudstones organic matter averages 0.68 volume percent. Assuming that TOC volume percent has a value of around 2x the weight percent, this means that only about 9 percent of TOC is detected in X-ray maps of the silt-bearing mudstones and around 13 percent of the TOC is detected in silt-rich mudstones. This suggests that TOC in the silt-rich mudstones contains a somewhat greater fraction of particulate organic matter.

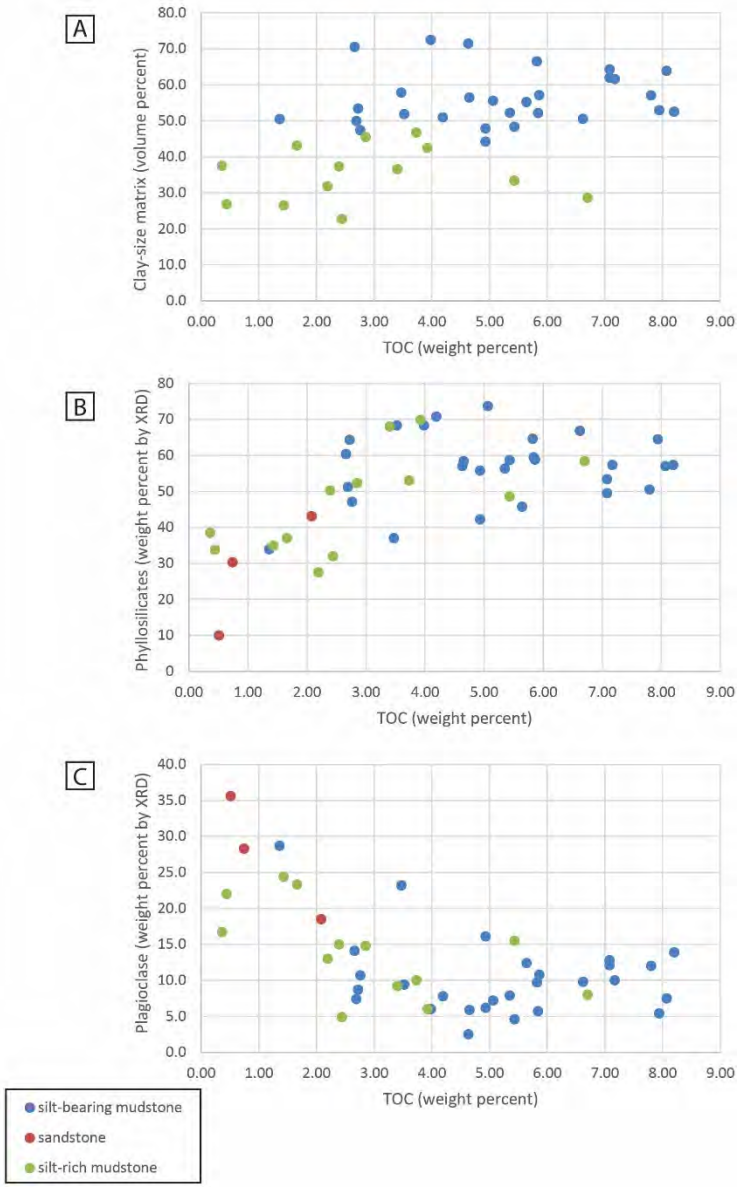

Figure 9. Relationships between TOC and texture and grain composition. (A) TOC versus the content of clay-size matrix. Although there is overlap, in general, coarser, silt-rich mudstones (green dots) have a lower range of TOC. (B) TOC versus total phyllosilicate content by XRD. It is important to note that phyllosilicate as determined by XRD includes clay-size detrital clay minerals, silt-size micas, and authigenic clay minerals. In general, because of the dominance of clay-size detrital clay minerals in the total phyllosilicate fraction, there is a positive co-variation displayed in this plot. Finer-grained samples contain greater amounts of clay and organic matter. (C) TOC versus plagioclase as determined by XRD. Because plagioclase is dominantly associated with the silt-size fraction, there is a negative co-variation with TOC.

Diagenetic Features

Diagenetic features evident in X-ray mapping include pore-filling precipitates in anomalously large intragranular pores (**Figure 10A**), replacement of possible skeletal debris (**Figure 10B**), replacement of feldspar grains (**Figure 10C**), pyrite framboids (**Figure 10D**), and cone-in-cone structures (**Figure 11**).

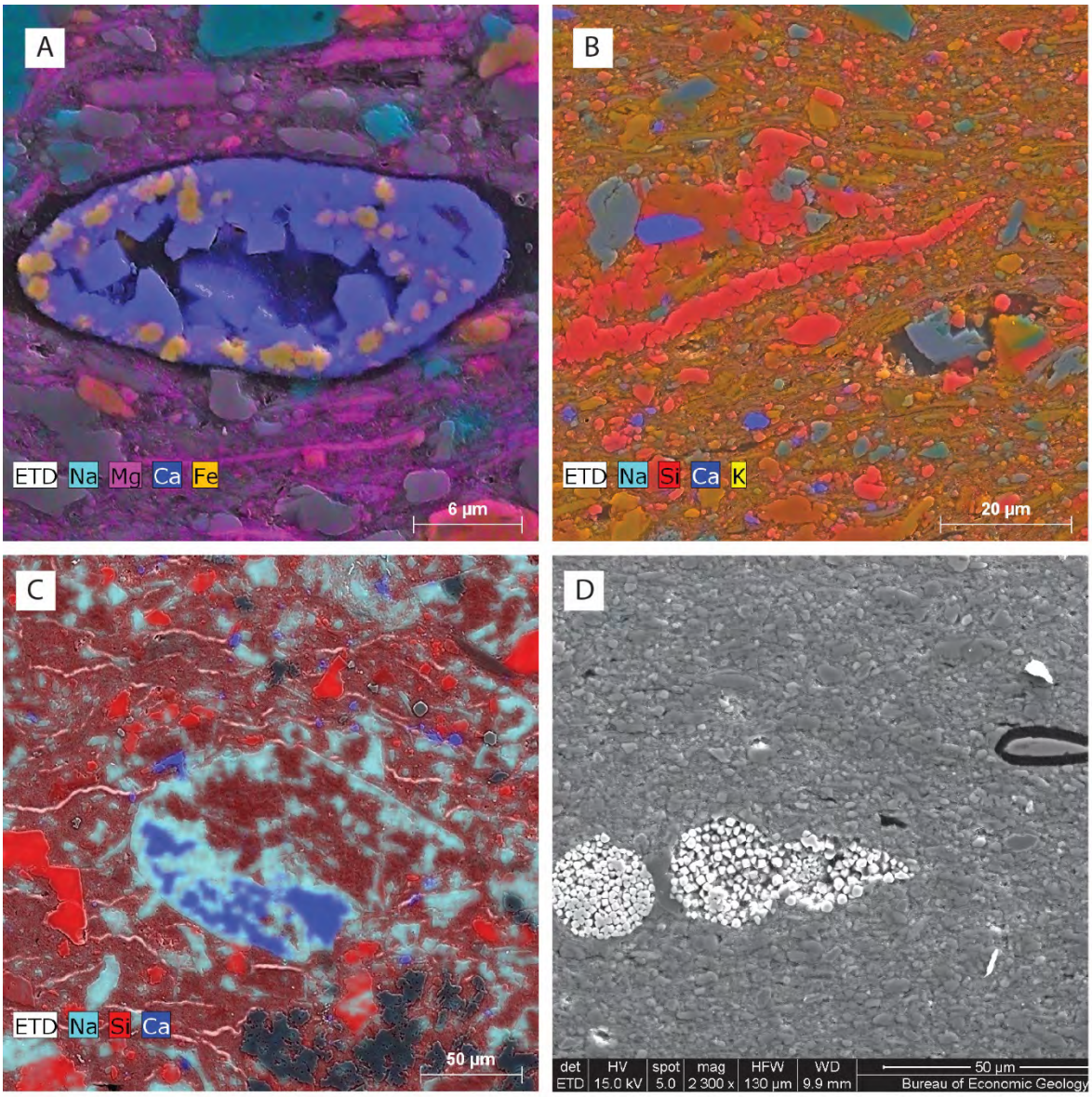

Figure 10. Diagenetic features. (A) Ca-phosphate (blue) and pyrite (orange) filling an organic-walled structure. YY1 71 1 X-ray map. (B) Quartz-replaced skeletal fragment. YY1 43 1 X-ray map. (C) Calcite (blue) replacing Na-feldspar that is also partly filled with K-clay. YY1 115 1 X-ray map. (D) Pyrite framboids (white) in silty mudstone. YY1 68 2 Secondary electron/back-scattered electron image.

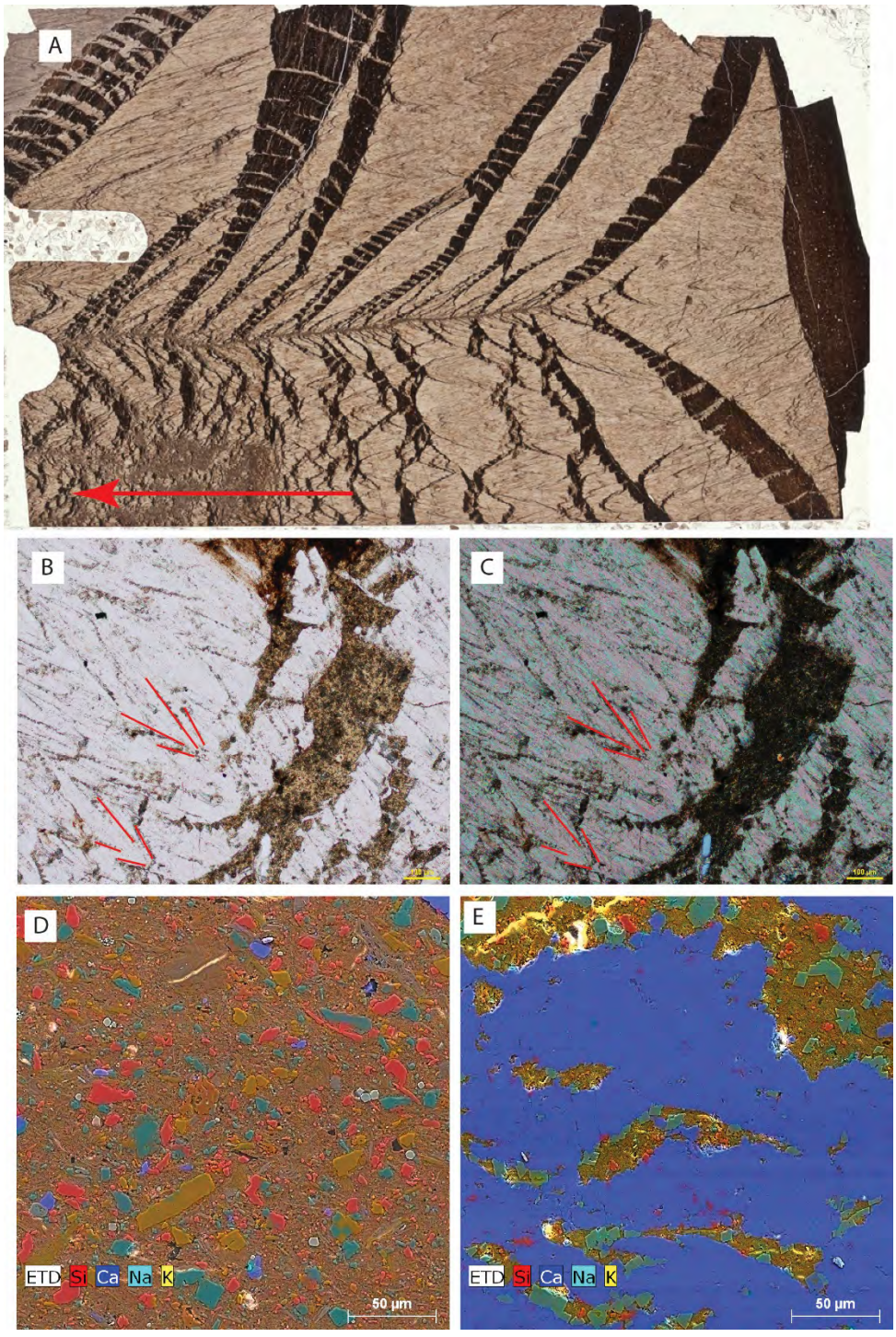

Figure 11. Cone-in-cone structures. (A) Thin section scan of Sample YY 22 30 2. Dark areas are the mudrock host rock that has been displacively disrupted by the growth of the calcite. (B) Nested cones (red lines) that are characteristic of cone-in-cone calcite. Sample YY1 96 1. Plane-polarized light. (C) Nested cones (red lines) characteristic of cone-in-cone calcite. Same field of view as image C. Sample YY1 96 1.Cross-polarized light. (D) Host rock that contains the cone-in-cone calcite is one of the more clay-rich lithologies. Sample YY1 96 1.X-ray map. (E) Cone-in-cone calcite (blue) does not manifest any zoning that can be detected by EDS. Note the dolomite that has nucleated on the edges of the calcite. Sample YY1 96 1.X-ray map.

CL imaging

Quartz grain assemblages

Detrital quartz in the sample set appears to be exclusively of extrabasinal origin, as denoted by its general bright CL and variable CL colors and fabrics (**Figure 12**).

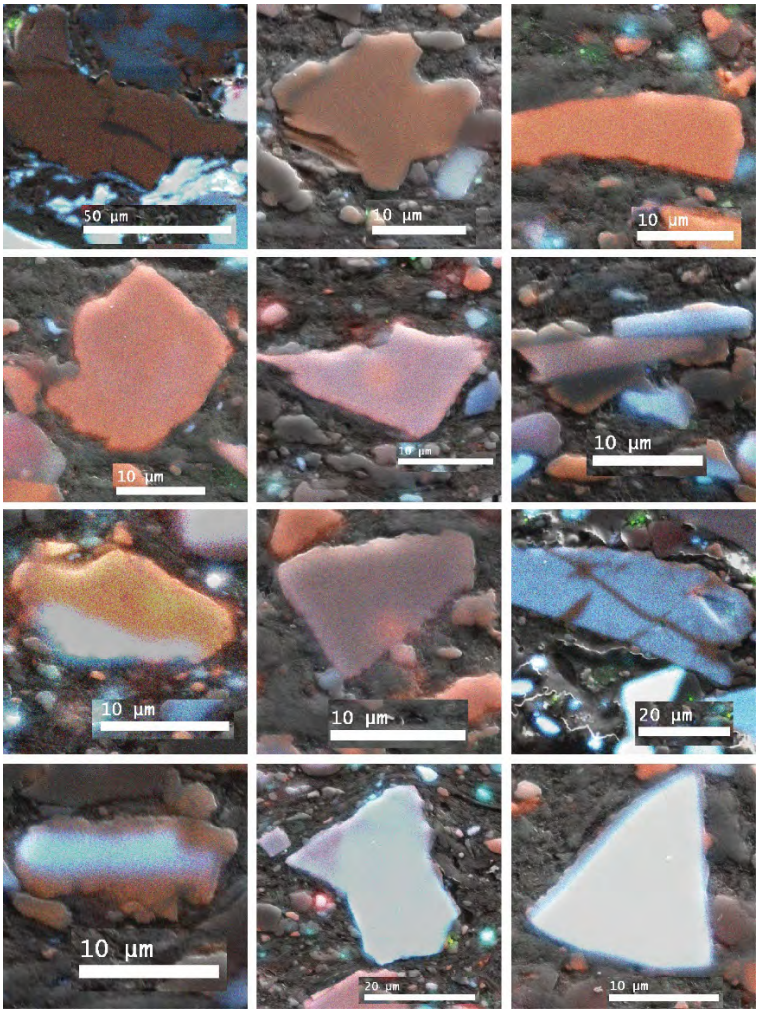

Figure 12. Examples of detrital quartz grains ranging in CL color and brightness from dark red to bright blue. Most common colors for silt-size quartz are seen in the top row center and right. In addition to variations in color and intensity, some grains display fabrics such as quartz-filled fractures and overgrowths inherited from the source rocks.

Quartz cement

For the most part, detrital clays appear to have compacted fully onto quartz grain surfaces, leaving no appreciable nucleation surface for the growth of quartz cement (**Figure 13A**). Only minor amounts of quartz cement are observed very locally at contacts between quartz grains, where packing flaws appear to have preserved small pores (**Figure 13B**). Matrix-dispersed authigenic microquartz as illustrated in **Figure 1A** is not observed.

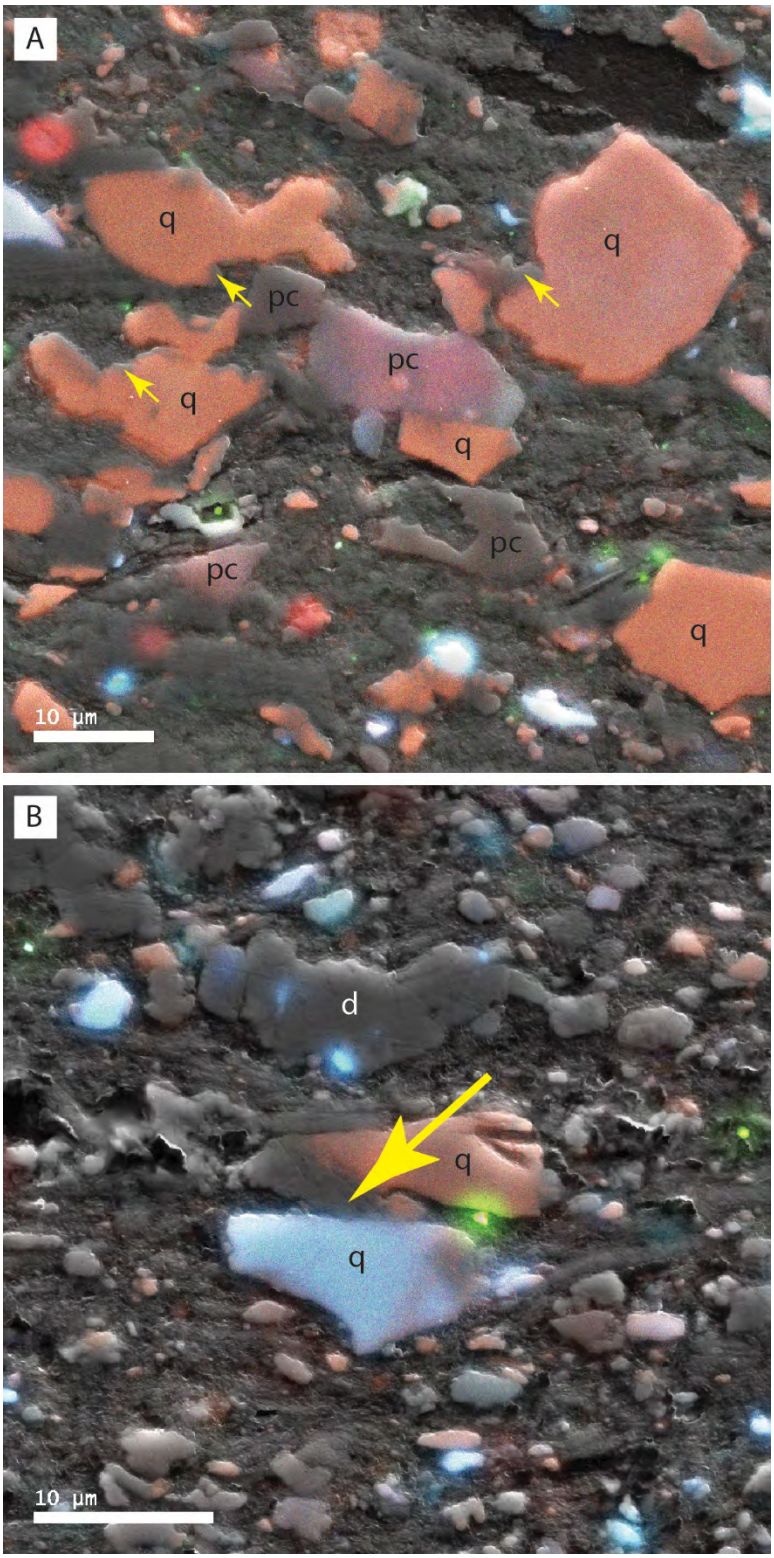

Figure 13. CL evidence of quartz cementation and the overall lack thereof. (A) Most surfaces of the reddish quartz grains (q) here lack evidence of associated dark-luminescing quartz cement. A few possible examples of mostly sub-micron overgrowths are indicated by the yellow arrows. Plagioclase grains (pc) are also abundant in the field of view. Sample YY1 163 2. (B) Convincing quartz overgrowths are found mostly between adjacent quartz grains (q). Dolomite is labeled d. Sample YY1 79 1.

Comparison of Mudrock Texture and Pore-size Distributions (N-adsorption)

Texture, as expressed by the silt-clay ratio, appears to be a key control on pore-size distribution (PSD, reported by Zhang et al., this volume) in the sample set. A plot of clay-matrix volume versus the percent of pores >10 nm in the total pore population (wells YY1 and YY22) shows that larger pores are preferentially associated with coarser samples (one outlier, sample 94-2, depth = 1409) (**Figure 14A**). Among samples containing less than 4 weight percent TOC, silt-bearing mudstone samples have a greater proportion of small pores (< 5 nm) than do silt-rich mudstones (**Figure 14B**). In silt-bearing mudstones containing 4 weight percent or greater TOC **(Figure 14B**) there is a strong positive covariation with the abundance of the smallest pores, suggesting that addition of very small pores with increasing organic content may be balancing destruction of intermineral pores by kerogen compaction and bitumen filling (see reports by Loucks and others, and by Hackley, this volume).

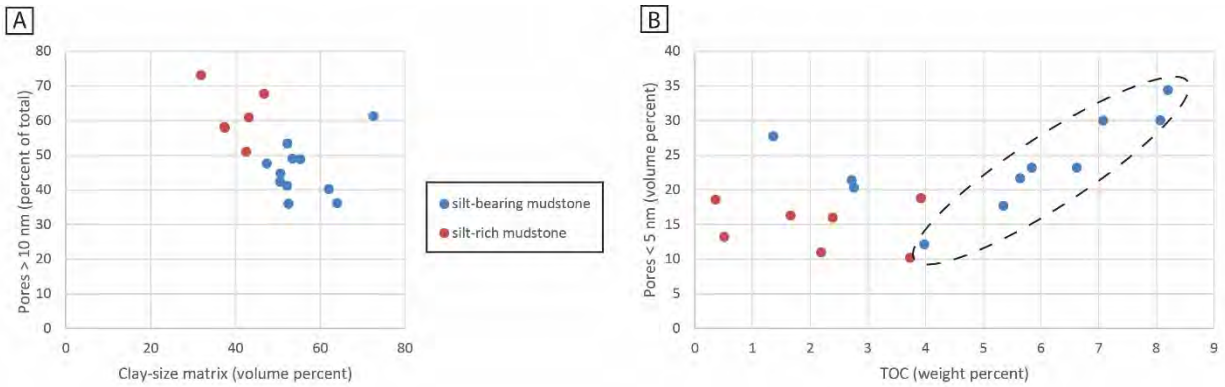

Figure 14. Textural and compositional controls on pore size. Pore sizes determined from N-adsorption (Zhang and others, this report). (A) Pores > 10 nm (percent of total pore population) versus texture. Silt-rich samples contain a greater proportion of larger pores. (B) Pores < 5 nm (percent of total pore population) versus TOC. In At lower TOC contents (< 4 weight percent), there is no particular trend between these two parameters, but finer-grained samples mostly have more of the very small pores. At higher TOC there is a positive co-variation between TOC and the abundance of small pores---suggesting that small pores within organic matter contribute additional small pores at the higher TOCs.

The overall shape of the PSD as measured by the N-adsorption data has clear contrasts related to silt content (**Figure 15**). In silt-bearing mudstones, which, overall, contain more clay-mineral-rich matrix and higher TOC, are concentrated in sizes smaller than 10 nm and have prominent modes in the range of 4 to 5 nm (**Figure 15A**). Siltier silt-bearing mudstones (shown in yellow in **Figure 15A**), contain a greater proportion of pores in the range of 6 to 15 nm. Pores above 30 nm are very rare in the silt-bearing mudstones. In silt-rich mudstones and in a sandstone sample, the modes at 4 to 5 nm are much reduced in comparison to the silt-bearing mudstones. The coarsest samples (plotted in yellow) have fewer pores at the 4-5 nm mode. In the silt-rich mudstones pores in the range of 10 to 30 nm are far more abundant within the pore population (**Figure 15B**) than is true for the less silty mudstones. Pores greater than 30 nm are about twice as abundant in silt-rich as opposed to silt-bearing mudstones (**Figure 15 B**).

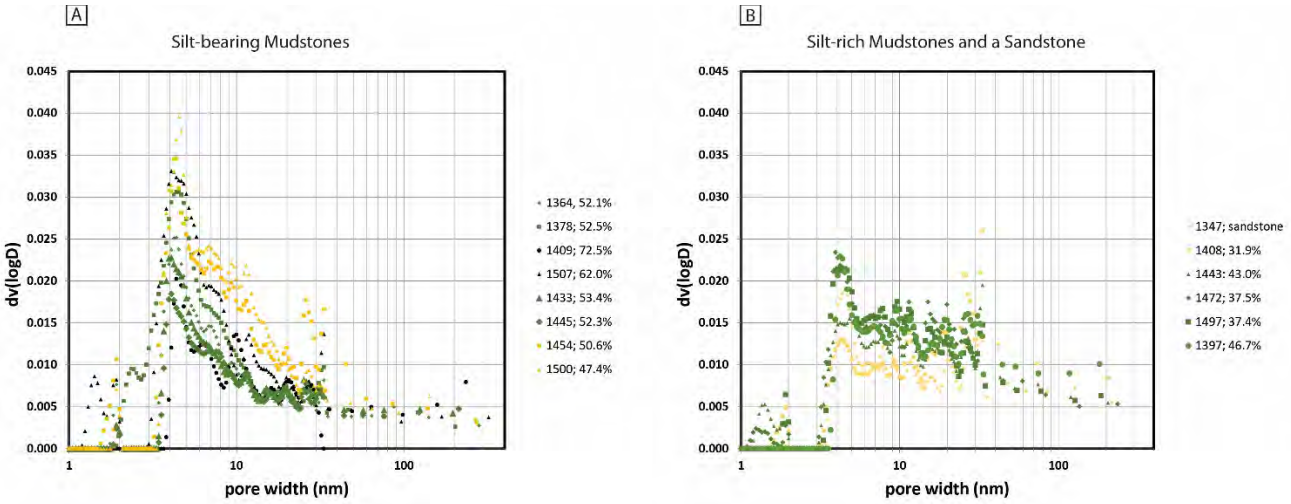

Figure 15. Pore-size distributions (PSDs) from N-adsorption (Zhang and others, this report) compared across mudrocks of contrasting texture. Numbers in legend are depths (m) and the volume percent of clay-size matrix. See text for further discussion. (A) PSDs of silt-bearing mudstones. In yellow are the two coarsest (siltiest) samples). Sample 1500 m is plotted with the silt-bearing mudstones because its silt particles are nearly clay-size. (B) PSDs of silt-rich mudstones and one sandstone.

The lower maturity samples from the new sample set provide an interesting comparison of PSD (**Figure 16**) that places constraints on the timing of pore loss in the Yanchang Formation. At lower maturity, silt-bearing mudstones preserve pore sizes that are similar to those observed in the silt-rich mudstones of wells YY1 and YY22 (**Figure 16**). This contrast in pore size distribution indicates that pore loss continued through the early to middle stages of oil maturation. The relative roles of compaction versus pore filling by bitumen (Loucks, this volume) in this latter stage of pore loss is uncertain.

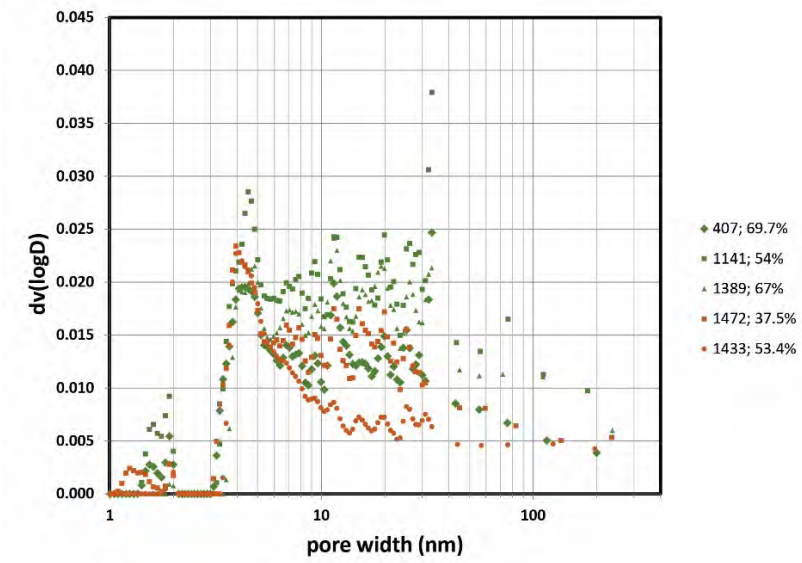

Figure 16. Pore-size distributions (PSDs) of three low-maturity samples (R_o estimated as 0.7 or less, in green) contrasted with two samples from well YY1 (maturity in the range of R_o 0.9, in orange). Sample YY1 1433 (orange dots) is a silt-bearing mudstone. Sample YY1 1472 (orange squares) is a silt-rich mudstone. The low maturity samples are silt-bearing mudstones, yet display porosities greater than that of the silt-rich mudstones at higher maturity. The contrast between the low-maturity samples and Sample YY1 1433 suggests the magnitude of porosity decline across the maturity range from R_o 0.7 to 0.9.

Discussion

The mudstones of the Yanchang Formation are tarls, with grain assemblages generally containing more than 90 percent grains of extrabasinal derivation. There is a substantial volcanogenic component, and, based on the ratio of detrital quartz, detrital feldspar, and lithic fragments (QFL ratio), the silt fraction is arkosic. Like other tarls (Milliken et al., 1989; Milliken and Land, 1993; Day-Stirrat et al., 2010b) the samples manifest little evidence of early cementation and essentially no evidence of cementation in intergranular pores.

In the absence of cements, and in the presence of very low overall porosities (Loucks and others, this volume), it can be concluded that compaction is the dominant diagenetic process, together with pore-filling by mobilized diagenetic hydrocarbon (bitumen; see the pore imaging report by Loucks, this volume). Silt content in the early diagenesis of muds is documented to preserve larger pores through packing flaws and sheltering of intergranular pores from compaction (Day-Stirrat et al., 2010a; Milliken et al., 2012; Milliken and Reed, 2010; Oertel, 1983; Schneider et al., 2011). In contrast, in the Barnett Shale of Texas, at somewhat higher thermal maturity, the lithologies are sarls and argillaceous sarls that contained primary assemblages of very high reactivity, and as a consequence, diagenesis by combined cementation and compaction has erased the effects of primary texture on porosity and other bulk rock properties (Milliken et al., 2012). In the tarls of the Yanchang Formation, with no significant early cementation and a compaction-dominated diagenetic system, textural controls on bulk rock properties are still evident. Higher porosity (and, very likely, higher permeabilities) are expected in the siltier tarls of the delta front and prodelta successions. The strong compactional aspects of the diagenetic system will help to ensure that organic-rich mudstones in this unit are effective source rocks, whereas low porosities and the lack of cement-generated brittle properties work against the development of mudrock reservoirs. Yanchang Formation mudrocks, from a more basinward position, further removed from sources of extrabasinal influx, would be interesting to assess to determine if there are more detrital and diagenetic components more favorable to preservation of unconventional reservoir quality.

Conclusions

1. Texturally, the mudstones of the Yanchang Formation are silt-bearing and silt-rich mudstones.
2. Although all the samples are of very low porosity, greater silt content in the mudstones is correlated with the preservation of larger pores.
3. Compositionally, mudstones of the Yanchang Formation are tarls that contain an arkosic silt fraction.
4. Like other tarls, the Yanchang mudstones have little cement, and the cement that is present is located primarily in anomalously large intragranular pores.
5. The dominant diagenetic processes in these mudstones are compaction and organic maturation.

References

Ajdukiewicz, J.M., and Lander, R.H., 2010, Sandstone reservoir quality prediction: state of the art: AAPG Bulletin, v. 94, p. 1082–1091.

Bathurst, R.G.C., 1975, Carbonate Sediments and their Diagenesis: Amsterdam, Elsevier Scientific Publishing Company, 658 p.

Day-Stirrat, R.J., Milliken, K.L., Dutton, S.P., Loucks, R.G., Hillier, S., Aplin, A.C., and Schleicher, A.M., 2010, Open-system chemical behavior in deep Wilcox Group mudstones, Texas Gulf Coast, USA: Marine and Petroleum Geology, v. 27, p. 1804–1818.

Fishman, N.S., Hackley, P.C., Lowers, H.A., Hill, R.J., Egenhoff, S.O., Eberl, D.D., and Blum, A.E., 2012, The nature of porosity in organic-rich mudstones of the Upper Jurassic Kimmeridge Clay Formation, North Sea, offshore United Kingdom: International Journal of Coal Geology, v. 103, p. 32–50.

Flügel, E., 2004, Microfacies of Carbonate Rocks: Berlin, Springer, 976 p.

Lander, R.H., and Walderhaug, O., 1999, Predicting porosity through simulating sandstone compaction and quartz cementation: AAPG Bulletin, v. 83, p. 433–449.

Milliken, K.L., 1992, Chemical behavior of detrital feldspars in mudrocks versus sandstones, Frio Formation (Oligocene), South Texas: Journal of Sedimentary Petrology, v. 62, p. 790–801.

Milliken, K.L., 2004, Late diagenesis and mass transfer in sandstone-shale sequences, *in* Mackenzie, F.T., ed., Sediments, Diagenesis, and Sedimentary Rocks, Volume 7: Treatise on Geochemistry: Oxford, Elsevier-Pergamon, p. 159–190.

Milliken, K.L., 2014, A compositional classification for grain assemblages in fine-grained sediments and sedimentary rocks: Journal of Sedimentary Petrology, v. 84, p. 1185–1199.

Milliken, K.L., and Day-Stirrat, R.J., 2013, Cementation in mudrocks: Brief review with examples from cratonic basin mudrocks, *in* Chatellier, J.-Y., and Jarvie, D.M., eds., Critical Assessment of Shale Resource Plays, Volume 103: Memoir: Tulsa, Oklahoma, USA, American Association of Petroleum Geologists, p. 133–150.

Milliken, K.L., Esch, W.L., Reed, R.M., and Zhang, T., 2012, Grain assemblages and strong diagenetic overprinting in siliceous mudrocks, Barnett Shale (Mississippian), Fort Worth Basin, Texas, U.S.A.: AAPG Bulletin, v. 96, p. in press.

Milliken, K.L., and Land, L.S., 1993, The origin and fate of silt-sized carbonate in subsurface Miocene-Oligocene mudrocks, South Texas Gulf Coast: Sedimentology, v. 40, p. 107–124.

Milliken, K.L., Land, L.S., and McBride, E.F., 1989, Numerical assessment of dissolution versus replacement in the subsurface destruction of detrital feldspars, Oligocene Frio Formation, South Texas: Journal of Sedimentary Petrology, v. 59, p. 740–757.

Pittman, E.D., and Larese, R.E., 1991, Compaction of lithic sands: experimental results and applications: American Association of Petroleum Geologists Bulletin, v. 75, p. 1279–1299.

Pommer, M., Milliken, K.L., and Ozkan, A., 2015, Pore types and pore-size distributions across thermal maturity, Eagle Ford Formation, South Texas: AAPG Bulletin, v. 98, in press.

Velde, B., 1996, Compaction trends of clay-rich deep sea sediments: Marine Geology, v. 133, p. 193–201.

TASK 3.1

Pore Types, Pore-Network Analysis, and Pore Quantification using FE-SEM Imaging of Ar-Ion Milled Samples of the Late Triassic Yanchang Formation (Chang 7, 8, and 9 Members) Lacustrine System in the Yanchang Petroleum Group YY1 and YY22 Wells, Southeastern Ordos Basin, China

Robert Loucks, Stephen Ruppel, Lucy Ko, Patrick Smith, Sheng Peng, and Tongwei Zhang[1]

[1]Bureau of Economic Geology), Jackson School of Geosciences, The University of Texas at Austin, Austin, TX

Abstract

The continental Upper Triassic Yanchang "black shales" in the Ordos Basin have proved to be unconventional gas reservoirs and are still in the stage of exploitation. The organic-lean and organic-rich argillaceous mudstones that form the reservoirs were deposited in a deeper water lacustrine setting during lake highstands. In the stratified lake, the bottom waters were dysaerobic to anoxic. This low-energy and low-oxygen lake-bottom setting allowed Type II and Type III organic matter to accumulate. Interbedded with the argillaceous mudstones are argillaceous siltstones that may have been deposited by gravity-flow processes (turbidites).

The 14 studied Ar-ion-milled samples from the Yanchang YY1 and YY22 Chang 7 to 9 members are very immature mineralogically. The mineral grains are composed predominantly of relatively equal proportions of quartz and feldspar. Acidic extrusive and metamorphic rock fragments are also present. The high clay content, generally greater than 40%, has promoted extensive compaction of the sediments, and this content permitted the ductile material to deform and occlude the primary interparticle pores. Also, the high clay content does not favor induced hydraulic fracturing of the mudstone reservoir.

The pore network within the mudstones is dominated by intraparticle pores with a lesser abundance of organic matter (OM) pores. Interparticle pores are rare. Mean GRI crushed-rock porosity is 4.19%. Because the pore network is dominated by ineffective intraparticle pores, permeability is very low (GRI-estimated geometric mean permeability = 9.86 nd). Also, the dominance of intraparticle pores creates a very poor correlation between GRI porosity and permeability.

Several methods of porosity analysis (GRI crushed-rock, nitrogen adsorption, and point count) were conducted on each of the 14 samples, and the results were compared). There is no significant correlation between the three methods of analysis, thereby indicating that each method must be measuring either different pore sizes or types. Also, there is no relationship between reservoir quality and total organic content (TOC). Much of the OM is nonporous, which suggests it is Type III. Most of the OM pores are in migrated solid bitumen.

Overall, the samples analyzed in the Yanchang Chang 7 to 9 members are of low reservoir quality. Even though the organic-rich mudstones are in the peak oil window, the mudstones appear to be too tight to produce oil, but they may be adequate for gas production. The less argillaceous-rich siltstones and sandstones within the systems may be potential carrier beds for the hydrocarbons forming a hybrid shale reservoir.

Introduction

Continental Upper Triassic Yanchang "black shales" in the Ordos Basin of north central China (**figs. 1 and 2**) have proved to be unconventional gas reservoirs (that is, Wang, 2012, Wang and others, 2015). Several studies have attempted to characterize the mudrocks within the system (that is, Wang, 2012, Tang and others, 2014, Gao and others, 2014, 2015, Yao and others, 2014, Wang and others, 2015, and Zhao and others, 2015) and several studies have commented on the pore networks and reservoir quality (that is, Wang, 2012, Tang and others, 2014, Gao, 2015, Wang, X. and others, 2015, and Wang, Y. and others, 2015). This present investigation concentrates on the nanopore to micropore networks as seen using ion-milled samples viewed on a field-emission scanning electron microscope (FE-SEM).

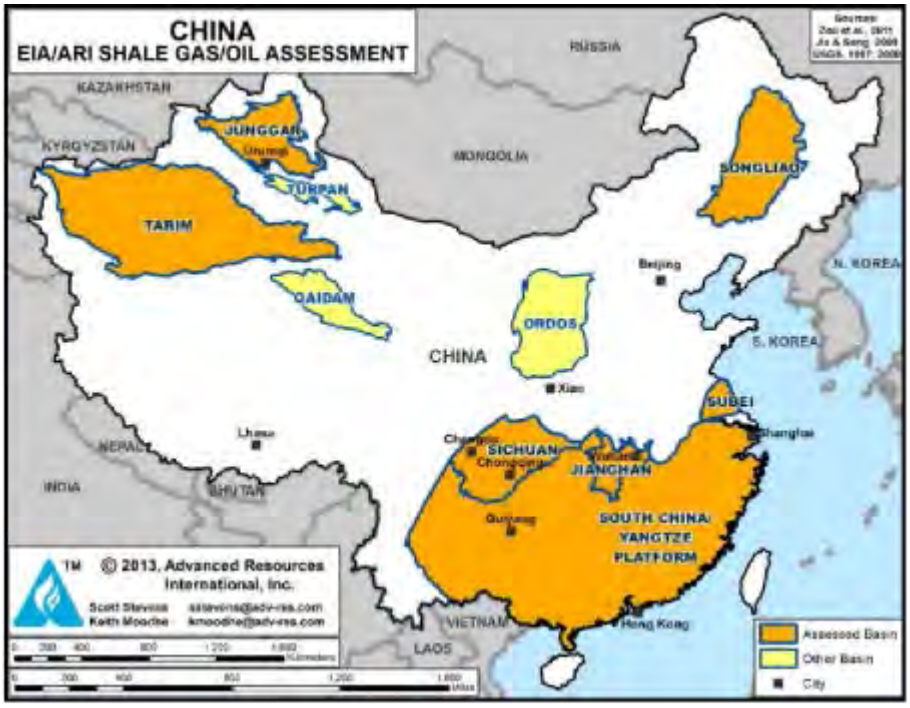

Figure 1. Map of China showing the seven most prospective shale gas and shale oil basins. The Ordos Basin is located in north central China. Map from Advance Resources International, Inc. (2013).

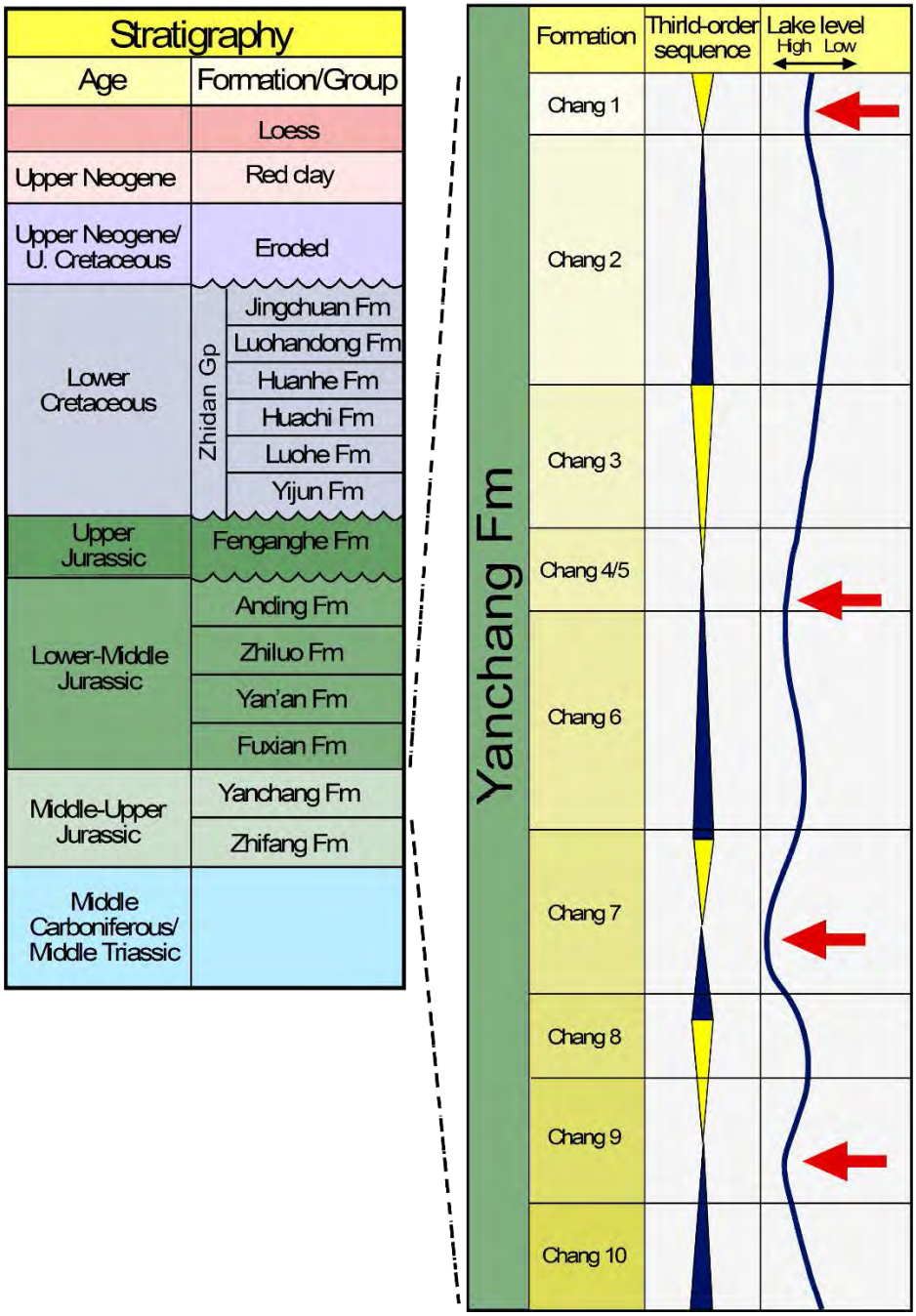

Figure 2. General stratigraphic section of the Ordos Basin with the detailed section of the Yanchang Formation showing the 10 members. Zhoa et al. (2015) defined four third order sequences reflecting rise and fall of lake level. Red arrows indicate periods of maximum transgression or periods of highest lake levels. Note that both the Chang 7 and 9 Members correspond to the highest lake levels. Modified from Zhao et al. (2015).

The major goal of this investigation is to character the pore network in the Yanchang YY1 and YY22 cores (**fig. 3**). Specific objectives are as follows:

(1) Describe general texture, fabric, and mineralogy of the argillaceous siltstones and silty argillaceous mudstones at the micrometer level.
(2) Present pore types present in each rock type.
(3) Discuss in-place (depositional) OM versus migrated OM.
(4) Quantify pore networks through point-counting SEM images taken at 15000X.
(5) Compare point-count porosity to GRI crushed-rock porosity and nitrogen-adsorption porosity.

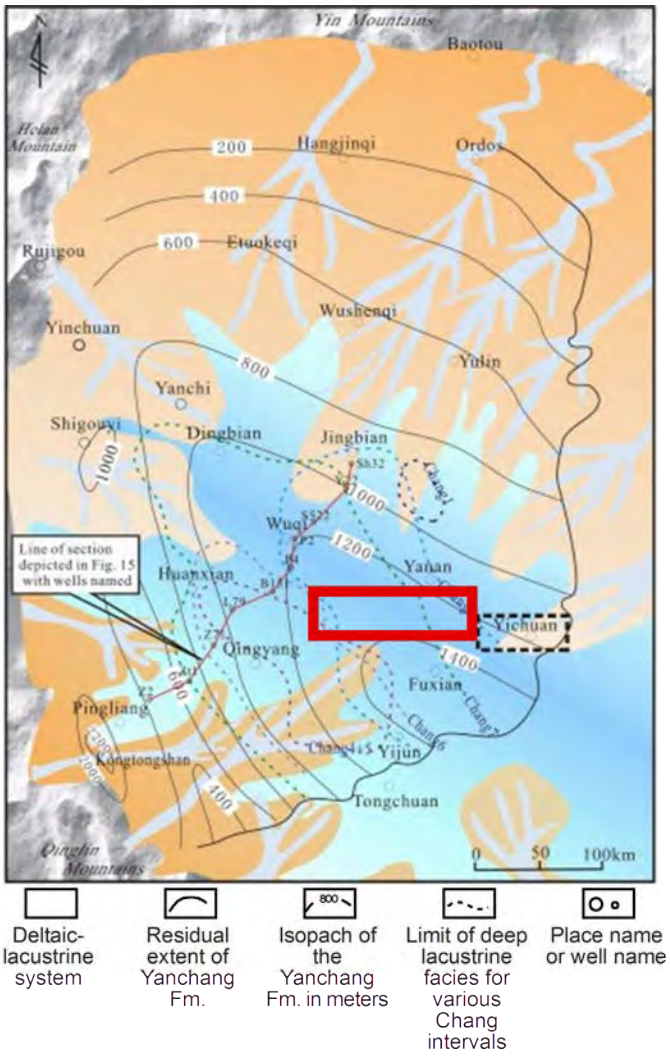

Figure 3. General paleogeographic and isopach map of the Yanchang Formation in the Ordos Basin. The Yanchang Group YY1 and YY22 cored wells are within the area of the red box. Map from Zhao et al. (2015).

Data and Methods

The basic data for this investigation are cores from the Yanchang YY1 and YY22 wells (**fig. 3**). Several core samples from other wells were also obtained. The cores were described for general lithofacies by Kitty Milliken at the Bureau of Economic Geology (BEG). More detailed lithofacies were defined for the samples selected for pore-network analysis using core, thin-section, X-ray diffraction (XRD), and TOC data (**Table 1**). Samples were selected for thin-section, XRD, Rock Eval, GRI crushed-rock porosity, and nitrogen-adsorption porosity analyses (**Table 2**). Fourteen samples were selected from the Yanchang YY1 and YY22 cores to prepare ion-milled scanning electron microscopy (SEM) samples (**Table 2**). Several ion-milled samples from several other wells were also produced. The 14 samples were selected to cover a range (0.36% to 8.20%) of TOC and the full length of the core (**fig. 4**). XRD analysis was done by K-T GeoServices (Gunnison, CO) and Rock Eval was completed by GeoMark (Houston, TX) on the ion-milled-related samples. GRI crushed-rock porosity analysis was completed by Sheng Peng, and the nitrogen-adsorption porosity was completed by Tongwei Zhang in the BEG laboratories.

Table 1. General lithofacies.

Member	Depth (m)	General lithofacies	TOC (%)	Clay (%)
Chang 7	YY1-1347.96	Organic-poor, low-angle cross-bedded argillaceous siltstone	0.51	10
Chang 7	YY1-1364.69	Organic-rich, poorly laminated, silty very argillaceous mudstone	5.84	59.5
Chang 7	YY1-1378.51	Organic-rich, poorly laminated, silty very argillaceous mudstone	8.2	57.3
Chang 7	YY1-1397.66	Organic-rich, laminated, silty very argillaceous mudstone	3.79	53
Chang 8	YY1-1409.26	Organic-rich, laminated, silty very argillaceous mudstone	3.98	68.3
Chang 8	YY1-1426.15	Organic-lean, laminated, silty very argillaceous mudstone	2.72	64.3
Chang 8	YY1-1451.02	Organic-rich, poorly laminated, silty very argillaceous mudstone	6.62	66.8
Chang 8	YY1-1469.08	Organic-poor, laminated, argillaceous siltstone	0.39	38.5
Chang 8	YY1-1497.07	Organic-lean, poorly laminated, silty very argillaceous mudstone	2.76	47.1
Chang 9	YY1-1504.98	Organic-rich, poorly laminated, silty very argillaceous mudstone	7.08	53.4
Chang 7	YY22-1317.88	Organic-rich, laminated, silty very argillaceous mudstone	5.64	42.2
Chang 7	YY22-1329.17	Organic-lean, laminated, silty argillaceous mudstone	1.36	33.9
Chang 7	YY22-1336.34	Slighty organic-rich, laminated, silty argillaceous mudstone	8.07	57
Chang 7	YY22-1346.87	Organic-rich, laminated, silty very argillaceous mudstone	3.92	69.8

Table 2. Analyzed samples from the YY1 and YY22 cores.

Member	Depth (m)
Chang 7	YY1-1347.96
Chang 7	YY1-1364.69
Chang 7	YY1-1378.51
Chang 7	YY1-1397.66
Chang 8	YY1-1409.26
Chang 8	YY1-1426.15
Chang 8	YY1-1451.02
Chang 8	YY1-1469.08
Chang 8	YY1-1497.07
Chang 9	YY1-1504.98
Chang 7	YY22-1317.88
Chang 7	YY22-1329.17
Chang 7	YY22-1336.34
Chang 7	YY22-1346.87

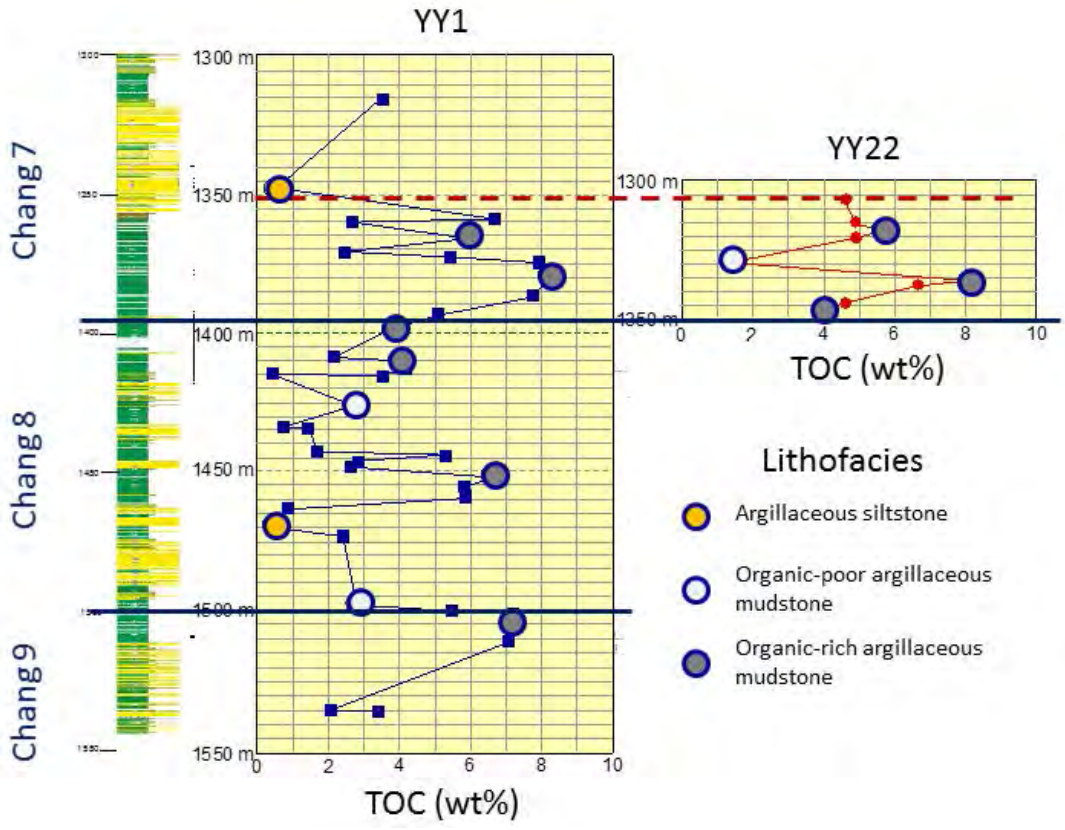

Figure 4. General YY1 core description and plots of TOC analyses from the YY1 and YY22 cores. The 14 analyzed Ar-ion-milled samples are circled and the samples are color coded by general lithofacies.

The samples were viewed using an FEI Nova NanoSEM 430 at The University of Texas at Austin by Patrick Smith, Lucy Ko, and Robert Loucks. Use of this field-emission scanning electron microscope (FE-SEM) equipped with in-lens secondary electron detectors provided greatly increased detail of nanometer-scale features. Lower accelerating voltages (1 to 10 kilovolts [kV]) were generally used on these samples to prevent beam damage, and working distances were 3 to 7 millimeters (mm). Ar-ion milled samples (see Loucks and others, 2009 for discussion of description and preparation of Ag-ion milled samples) are excellent for observing a flat surface without any irregularities related to differential hardness. These samples also allow three-dimensional (3D) viewing because the samples are not impregnated with epoxy. Energy-dispersive X-ray microanalysis (EDXA) mapping was also performed on the samples, which provided elemental analysis at the microscale and facilitates mineral identification.

Quantifying pore types in mudrocks is very time consuming and expensive (SEM time and Ar-ion milling preparation). Ar-ion milled samples are needed to image nano-size pores. The ion-milled sample surface provides a relatively limited area for investigation (**fig. 5**). A well-prepared sample provides a viewing area of 2 mm by 0.5 mm. To best quantify the sample, five photomicrographs were taken at equal intervals perpendicular to bedding along the milled surface (**fig. 5**). Each of the photomicrographs recorded an area of 20 µ by 20 µ. The magnification of the photomicrographs were 15000×. At this magnification, pores down to ~10 nanometer (nm) can be identified.

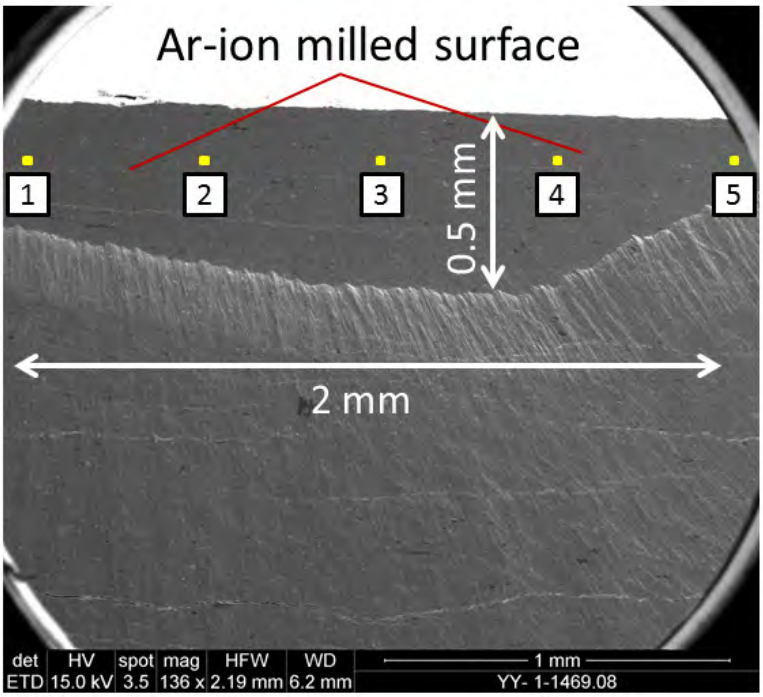

Figure 5. Example of an Ar-ion-milled sample with dimensions. The sampling strategy of selecting five photomicrographs for quantitative point counting of pores are shown by the yellow squares. The photomicrographs are taken at 15,000× and the yellow squares are approximately 20 × 20 micrometers.

Once the photomicrographs are collected, they are analyzed using JMicroVision to point count the pore types. The photographs are taken at a magnification of 15000×. On JMicroVision, four views were analyzed (**fig. 6**). The point counts are done on the image to the right of the left panel (**fig. 6**). This image can be enlarged to where pores in the range of 10 nm to 15 nm can be counted. The image on the far left (**fig. 6**) shows the whole photograph, and each point records a counted position, and the point is color coded as to pore type or composition. Five categories were recorded: (1) mineral, (2) organic matter, (3) OM pore, (4) intraparticle pore, and (5) interparticle pore. The two microphotographs on the right are EDAX maps of selected elements (left) and a carbon-element map (right) (**fig. 6**). These elemental maps help to decide where the pore is located (interparticle or intraparticle) and if the pore is associated with OM. One-thousand points are counted for each photograph. Therefore, for each Ar-ion milled sample, five photomicrographs are point counted. With 1,000 points per photomicrograph, a total of 5,000 points are counted for each sample. This count provides precise statistical accuracy of percentages of pore types.

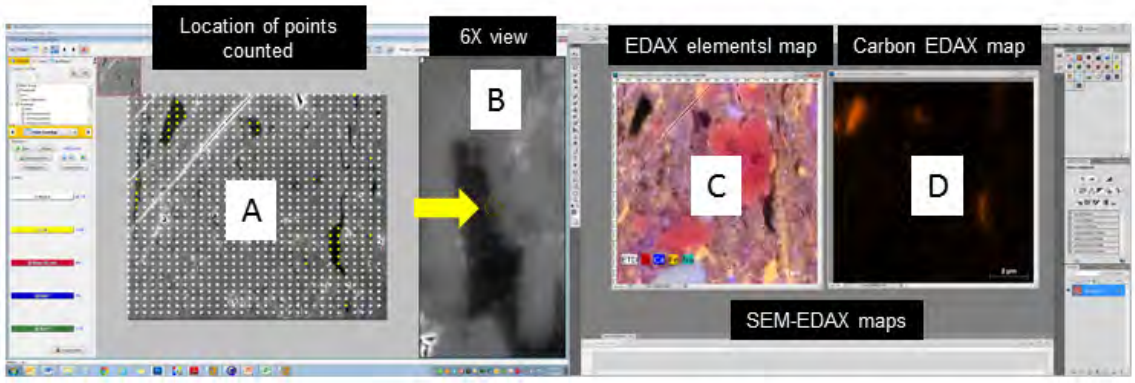

Figure 6. Screen shot of JMicroVison software display and associated SEM photomicrographs. Photomicrograph A shows the locations of the 1000 point counts. Photomicrograph B is an enlargement of A that allows close up observation of the decision-spot to help define the category. Yellow arrow shows point to be defined. Photomicrograph C is an EDAX elemental map that helps define pore types and relationship to minerals. Photomicrograph D is a carbon-element EDAX map that help define organic matter and associated pores.

Regional Geology, Stratigraphy, Mineralogy, and Lithofacies

This section presents background data to help understand the geologic setting and rock types in the Upper Triassic Yanchang strata. One can refer to the literature for a more detailed analysis of these geologic parameters (that is, Yao, 2009, Wang, 2012, Tang and others, 2014, Gao and others, 2014, 2015, Yao and others, 2014, Wang and others, 2015, and Zhao and others, 2015).

Regional Geology

The Triassic Ordos Basin is an intracratonic sedimentary basin that is ~260,000 km^2 in area located in the central part of the North China Plate (Yang and others, 2005, Tang and others, 2014, Sun and others, 1989, and Zhao and others, 2015) (see **fig. 1**). The basin is a large

asymmetrical syncline with the eastern limb dipping to the west and the western limb steeply dipping east. The center of the basin forms the Tianhuan Sag (Ding and others, 2013). According to Zhao and others (2015) the basin contains 800 meters (m) to 1,500 m of the Yanchang Formation (see **fig. 3**) composed of sandstone and silty sandstone interbedded with silty and argillaceous mudstones. Zou and others (2010) and Yu and others (2013) proposed the sediment source of the Yanchang Formation was the Palaeo-Yin Mountains to the north and the Qinling orogenic belt to the south. Since deposition, portions of the Yanchang Formation have been buried to depths of approximately 2,600 m by early Late Cretaceous time and then uplifted during Late Cretaceous time and at its present depth of burial since the beginning of Tertiary time (Wang, X. and others, 2015) (**fig. 7**).

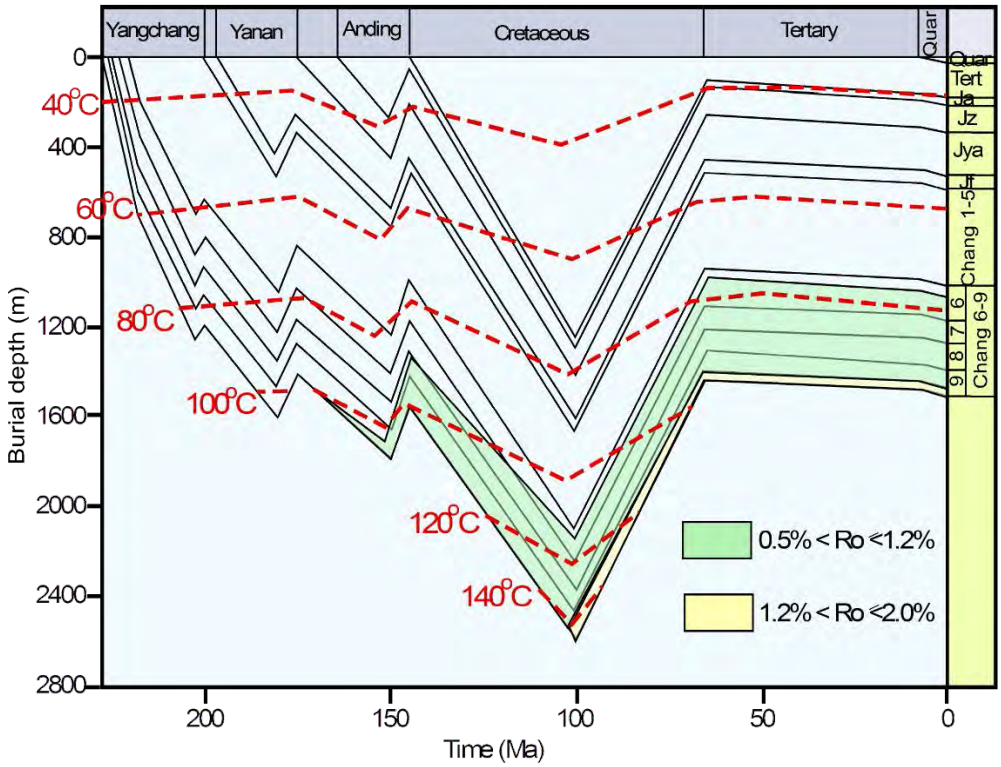

Figure 7. Burial and thermal history of Y2 in the Ordos Basin. Diagram from Wang, X. et al. (2015).

Stratigraphy

Figure 2 from Zhao and others (2015) shows the stratigraphic section of the Yanchang Formation within a generalized stratigraphic column for the Ordos Basin. The Yanchang Formation is the Upper Tertiary in age and occurred between the Carnian stage to Norian stage (237.0 millennia ago (Ma) to 208.5 Ma) (Zhao and others, 2015). The formation is divided into 10 members recording 4 major lacustrine transgressive-regressive cycles (Yao and others, 2009, and Zhao and others, 2015). Zhao and others (2015) interpreted that maximum transgressions or the deepest lake levels occurred during the Chang 7 and 9 deposition (**fig. 2**).

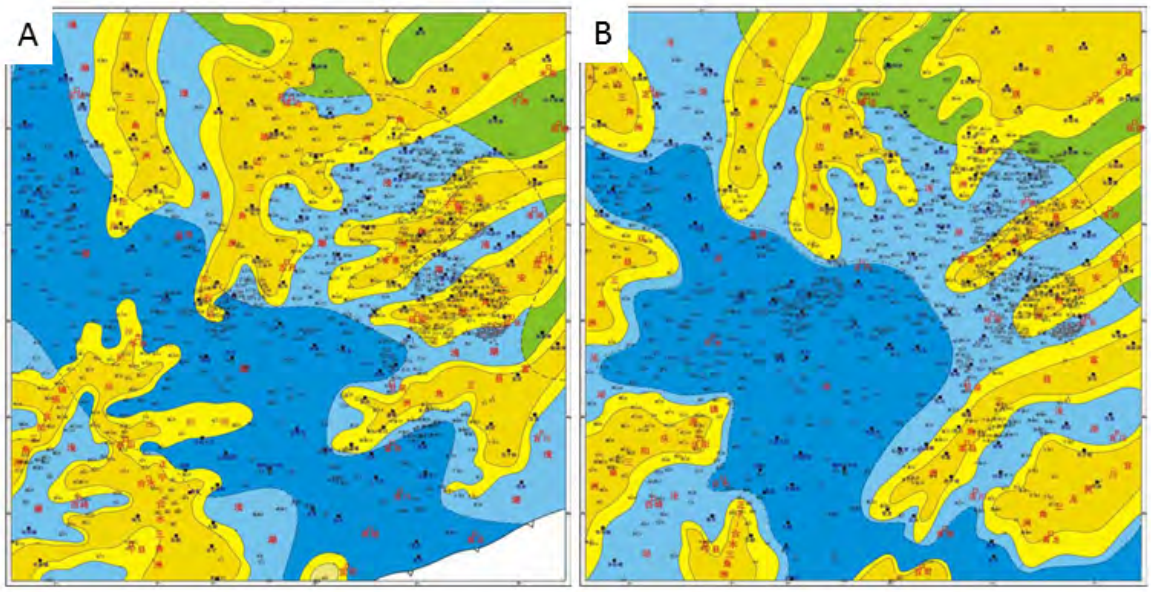

Figure 8. Paleogeographic maps of the Yanchang Formation. (A) Paleographic map of Chang 7 Member. (B) Paleographic map of Chang 9 Member.

Depositional Setting and Depositional Systems

The general depositional setting of the Yanchang Formation is lacustrine within a closed basin (Deng and others, 2011, Wang, 2012, Guo and others, 2014, Tang and others, 2014, and Zhao and others, 2015). Guo and others (2014) provided a summary of the depositional history of the Yanchang Formation. Chang 10 and 9 members, the lowest members, were deposited during the early expanding stage or deepening of the semi-enclosed lake. In the middle of the Chang 9, the first of four maximum floods occurred (see **fig. 2**). This deep water setting produced an anoxic condition and allowed the accumulation of organic-rich muds (Guo and others, 2014). This condition was followed by a lowering of the lake level reaching its maximum low level during the Chang 8 sedimentation. Another maximum flood occurred during the Chang 7 deposition and again anoxic condition, and allowed the accumulation of organic-rich muds. During a deposition of the Chang 6, 5, and 4, the lake leveled and remained relatively low except for a slight deepening at the base of the Chang 5. Guo and others (2014) noted that the lake was dominated by deltaic deposits during the Chang 3, 2, and 1 deposition.

The edges of the basin were dominated by deltaic/fluvial sedimentation and the center of the basin by lacustrine deposits (Wang, 2012, and Zhao and others, 2015) (**figs. 3 and 8**). Paleogeographic maps by Wang (2013) (**fig. 8**) showed elongate deltas prograding out into the basin. The lake was a fresh water-to-brackish (Yao and others, 2014) system that would have produced Gilbert-type deltas. The characteristic of the lake-center deposits would have depended on the depth and circulation of the lake. The dominant sediment would have been silty and/or argillaceous muds. Mud and silt deposition into the lake center would have been by turbidity currents, sandy debris flows, and hyperpycnal mud plumes (Wang, 2012, Yao, 2014, and Zhao, 2015). Also, river-discharge with sediment would have been denser than the lake water, and this

density would have allowed hypopycnal sediment plumes to carry mud and silt into the center of the lake basin. Whether laminated or burrowed sediment would characterize the lake-center deposits would have depended on the oxygenation state of the bottom environment. If oxygenated, burrowing would mix the sediments and destroy any hydrologic sedimentary features, whereas, if anoxic, the sediment may show laminations, ripples, etc. Anoxia would suggest a stratified water column that did not allow circulation of oxygenated waters to reach the bottom on a regular basis.

Several studies have suggested that the deep lake was anoxic and allowed the accumulation of abundant organic-rich mud that produced a source rock in the Chang 7 and 9 members (Guo and others, 2014, Tang and others, 2014, and Rowe and others, 2015). As subsequently discussed, the high TOC measurements in the Chang 7 and 9 members, as well as laminated mudstones, support a stratified, anoxic bottom-water column at least during some parts of the deposition of these units. As previously noted, the Chang 7 and 9 members correspond to maximum flooding or deepest lake levels in the basin (see **fig. 2**).

Mineralogy

Many studies have presented data relative to the mineralogy of the Yanchang sediments (Wang, 2012, Guo and others, 2014, Tang and others, 2014, Yao and others, 2014, and Rowe, 2014). The brittle minerals are predominantly quartz and feldspar (K-spar and plagioclase), and the clay minerals are composed of mixed-layer clay, illite and mica, chlorite, and kaolinite. Many of the sand-sized grains are acidic extrusive and metamorphic rock fragments. The sandstones would plot in the sandstone classification of Folk (1974) in the lithic arkose or arkosic litharenite area. Diagenetic minerals include carbonate (calcite, Fe-calcite, dolomite, and siderite), albite, and pyrite. Examples of the mineralogy of the Yanchang rock are shown in the section on General Lithofacies and summarized in **Appendix A**.

XRD analysis was completed on each of the Ar-ion-milled samples from the YY1 and YY22 cores, and the results are plotted on a mineralogical stability/brittleness ternary diagram (**fig. 9, Appendix A**). Many of the samples are clay-mineral rich (>40% clay) and relatively quartz poor. The high clay content supports greater compaction and a less brittle rock. The extensive compaction of ductile grains tend to destroy primary interparticle pores.

The level of brittleness of shale-gas or shale-oil mudstones is important because it influences the ability of the rock to either fracture naturally or by artificial hydraulic fracturing. The rocks from the present study appear to be poor candidates for fracking because of their high clay-mineral mineral content (**fig. 9**). Other studies of the rock in the Yanchang Formation describe similar mineralogies to those presented in this study (Guo and others, 2014, and see **fig. 5**). Guo and others (2014) present a mineral composition ternary plot showing 23 XRD samples from the Chang 7 and 9 members. All the samples contain greater than 40% clay minerals.

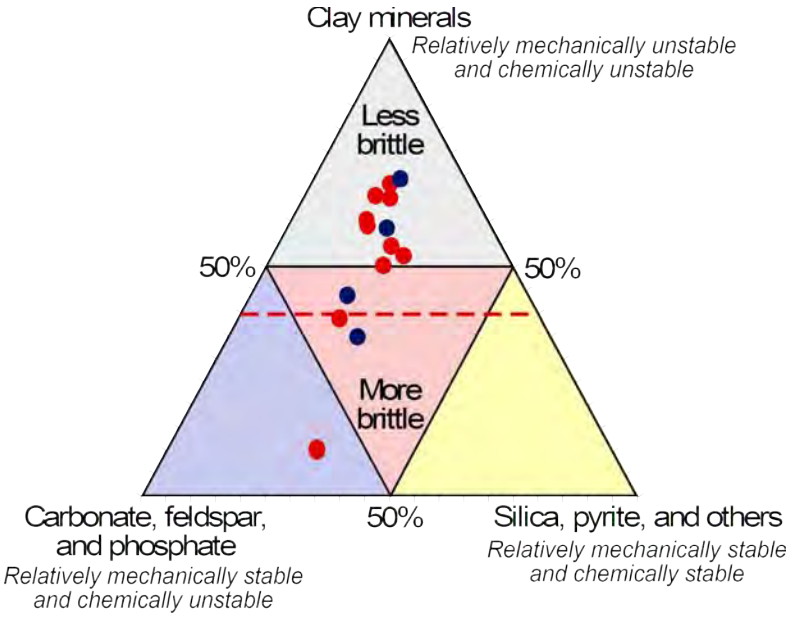

Figure 9. Mineralogy stability/brittleness ternary diagram showing XRD analysis of the 14 samples color coded by well. The ternary diagram emphases the mechanical and chemical stability relative to mineral composition. Samples plotting above 40 percent clay minerals (red horizontal line) tend to have low brittleness. Diagram developed by Loucks et al. (2012).

One would think this amount of clay content would lower the potential for hydraulic fracking of the reservoir, however, several studies have provided evidence that fracking is feasible (Gao and others, 2015). Gao and others (2015) presented several sets of data to suggest the rocks in the Chang 7 member are conducive to hydraulic fracturing because of their brittleness. They show a plot of Young's modulus and Poisson's ratio (see **fig. 3**) that indicates half their samples are brittle. They also developed their own rock brittleness classification (their **Table 6**) that concludes the rocks are brittle to highly brittle.

General Lithofacies

The YY1 and YY22 cores were not described in detail for lithofacies in this investigation of pore networks. Instead, three general lithofacies were defined for the 14 Ar-ion-milled samples using core photographs, thin sections, SEM photomicrographs, and XRD and TOC analyses (see **Table 1**). The three lithofacies are as follows:

> *Argillaceous siltstone* (**fig. 10**): This lithofacies has an average of 24.3% clay minerals and 0.45% TOC (range = 0.39% to 0.51%). Sedimentary features seen in core and thin section consist of low-angle cross bedding and laminations. This lithofacies was probably deposited in an environment where there was periodic induction of silt, such as in the prodelta or in a deeper water gravity-flow deposit. The low TOC content indicates an aerobic depositional setting.

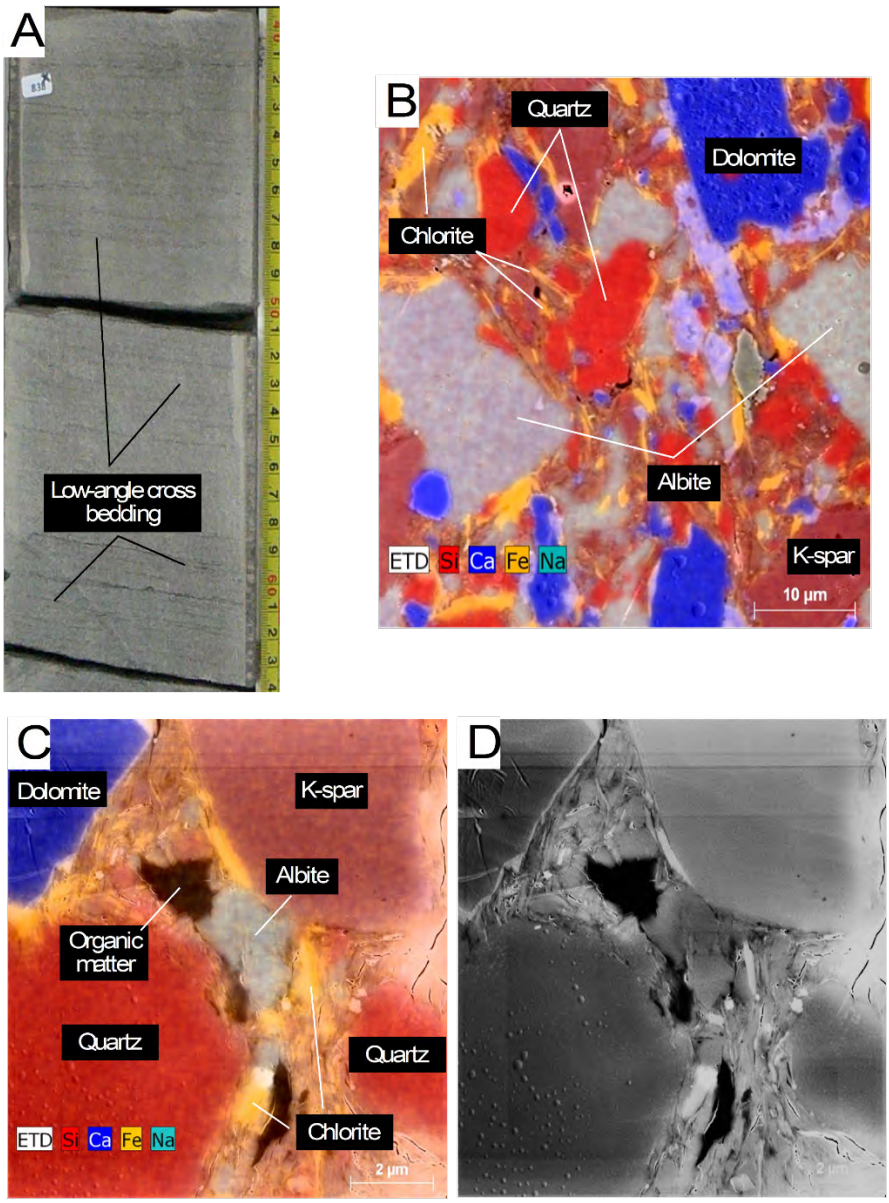

Figure 10. Example of argillaceous siltstones. (A) Core slab showing low-angle cross stratification. Clay-mineral content is 10 percent. YY1-1347.96 m. (B) SEM/EDAX photomicrograph of argillaceous siltstone showing argillaceous matrix. YY1-1469.08 m. (C) SEM/EDAX photomicrograph of argillaceous siltstone showing argillaceous matrix and organic matter. YY1-1469.08 m. (D) SEM backscattered photomicrograph of photomicrograph C.

Organic-lean argillaceous mudstone (**fig. 11**): Clay minerals averaged 48.4% and TOC averaged 2.28% (range = 1.36% to 2.76%). Most samples contained some silt. Sedimentary features included common lamination (poorly to well developed). The average TOC content of 2.28% is relatively high and indicated a dysaerobic to anoxic deeper lake-bottom setting, and the laminations indicated the lack of burrowing fauna. The difference between the organic-lean and organic-rich argillaceous mudstones may reflect dilution by clays or changes in surface productivity.

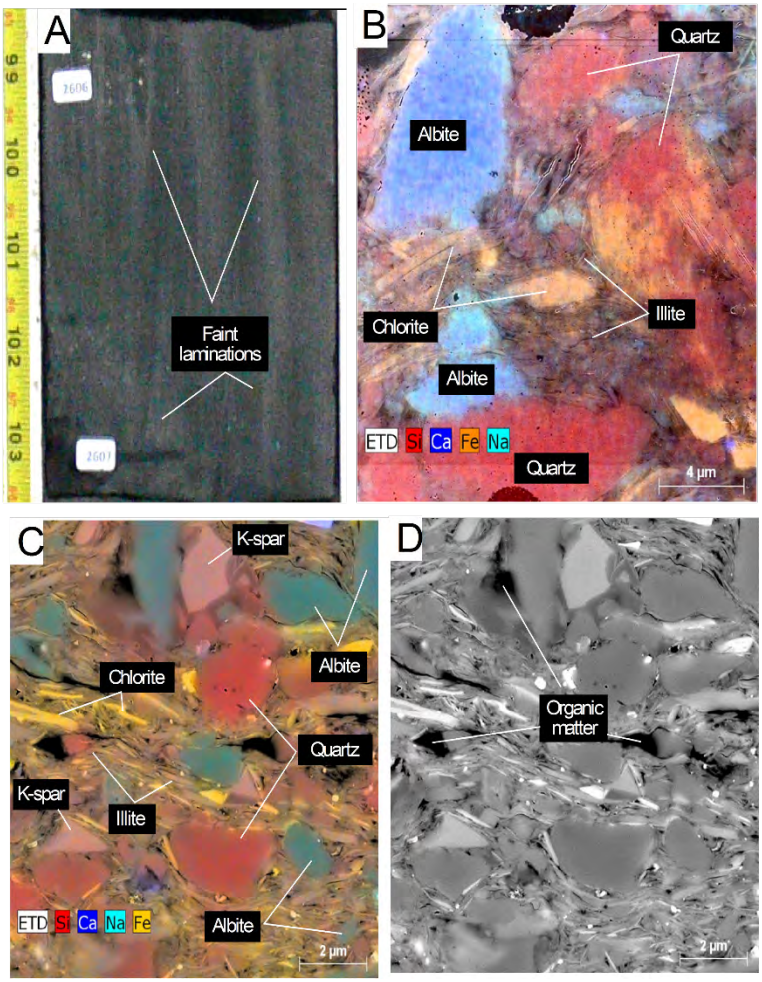

Figure 11. Example of organic-lean argillaceous mudstone. (A) Core slab showing very faint laminations. YY22-1329.17 m. (B) SEM/EDAX photomicrograph of organic-lean argillaceous mudstone. Clay minerals are illite and chlorite. Also, albite and quartz appear as clay-size grains. YY22-1329.17 m. (C) SEM/EDAX photomicrograph of organic-lean argillaceous mudstone. Clay minerals are illite and chlorite. Also albite, quartz, and K-spar appear as clay-size grains. YY1-1426.15 m. (D) SEM backscattered photomicrograph of photomicrograph C. Organic matter is noted.*Organic-rich argillaceous mudstone* (**fig. 12**): Clay minerals averaged 58.6% and TOC averaged 6.0% (range = 3.79% to 8.07%). The mudrock contained very faint laminations. The high TOC content and faint laminations suggested a deeper water, very low-energy, anoxic deposition setting in a deep lake during maximum transgression.

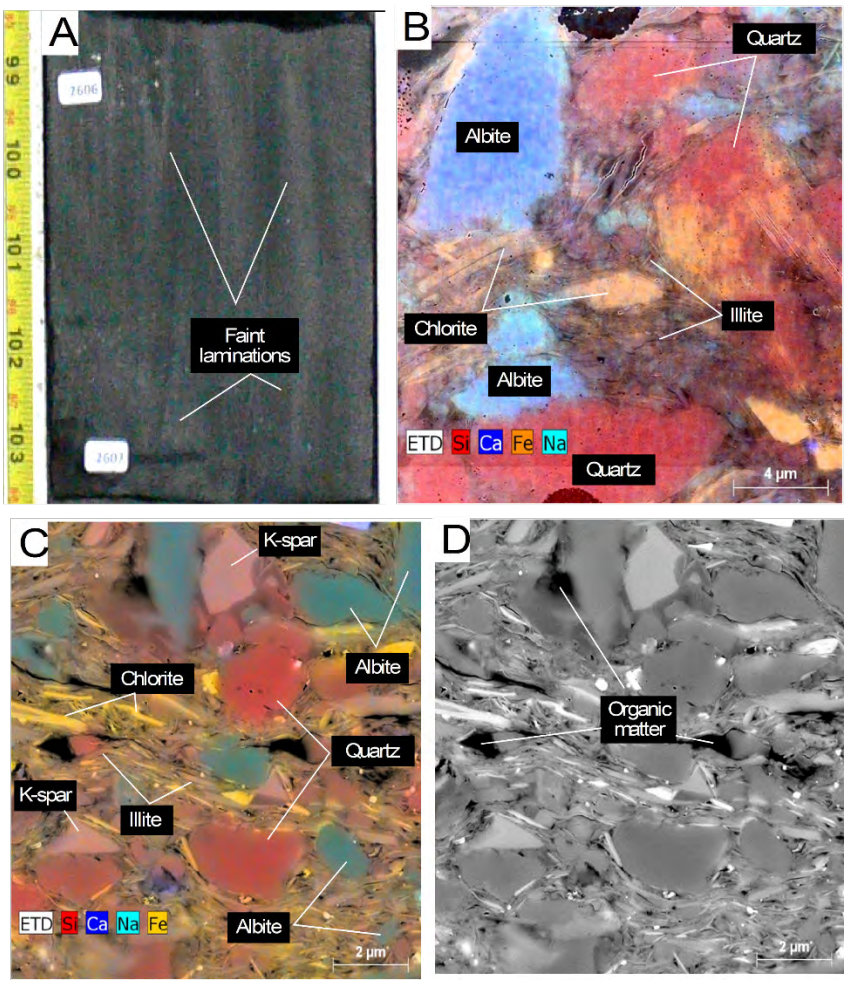

Figure 12. Example of organic-rich argillaceous mudstone. (A) Core slab showing very faint laminations. YY1-1364.69 m. (B) SEM backscattered photomicrograph showing organic-rich argillaceous mudstone. Quartz and albite clay-sized grains in clay-mineral matrix. Large pieces of organ matter may be Type III. YY1-1364.69 m. (C) SEM/EDAX photomicrograph of organic-rich argillaceous mudstone. Quartz and albite clay-sized grains in clay-mineral matrix. Large pieces of organ matter may be Type III. YY22-1317.88 m. (D) SEM backscattered photomicrograph of area shown C.

These general lithofacies are fairly similar to those described by other authors (Wang 2012). However, no sandstones or clean siltstones were in the samples collected from the cores. This is not a limitation to this pore network investigation because the major goal was to describe pore networks in the mudstones, not the sandstones.

Organic Matter

The Yanchang Chang 7 and 9 are well documented as rich source rocks (Wang, 2012, Guo and others, 2014, and Tang and others, 2014). For this investigation, a Rock Eval analysis was completed on each Ar-ion-milled sample. It is important to know the kerogen-matter type, TOC, and R_o because each of these parameters have an effect on pore development and pore types (Loucks and others, 2012, and Wang and others, 2015).

In general, the literature shows the TOC of the Yanchang organic-rich shales to have variable TOC content. Tang and others (2014) measured TOC values of 0.16 wt.% to 6.9 wt.% with an average of 2.18% for the Chang 9 member and 0.49 wt.% to 6.08 wt.% with an average 2.74 wt.% for the Chang 7 member in the southeastern part of the Ordos Basin. This is similar to what was measured in the YY1 and YY22 samples (**figs. 4 and 13A**). A plot of S1 and S1+S2 versus TOC derived from Rock Eval analysis is shown in **Figure 14**. The plot shows all the samples to be a good to excellent source of rock samples.

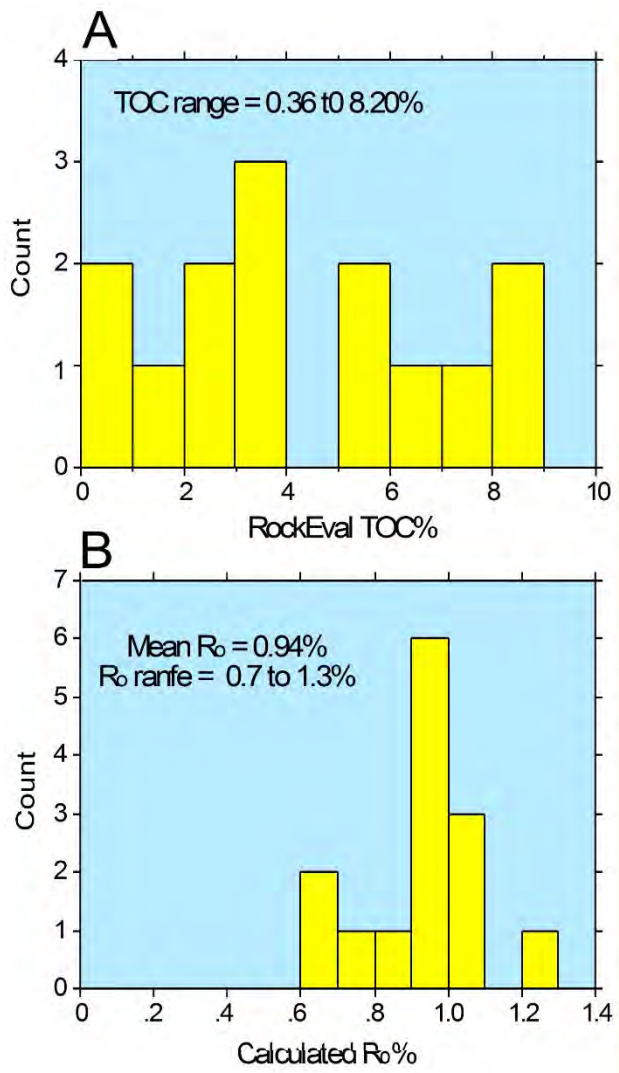

Figure 13. TOC and R_o histograms based on Rock-Eval analysis. (A) Histogram of Rock-Eval TOC. (B) Histogram of Rock-Eval calculated R_o.

Rock Eval calculated R_o from the present investigation provides a range from 0.7% to 1.3% (**fig. 13B**) with a mean of 0.94%. This R_o puts the studied samples in the peak oil generation range. As pointed out by Wang (2012) and as shown in the burial history plot in **Figure 7**, the samples have been buried deeper than their present depth.

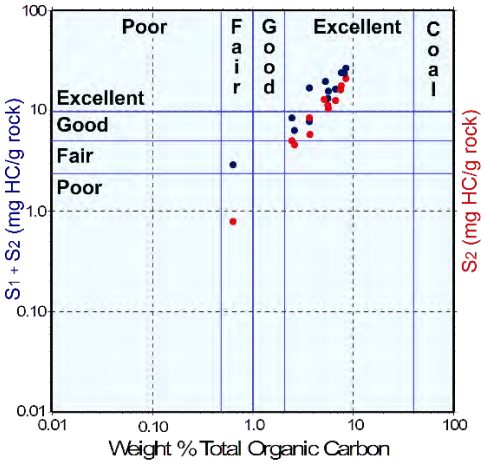

Figure 14. Plot of total weight percent TOC versus S1 and S1+ S2 from Rock-Eval analysis. The analyses plot in the good to excellent source rock range. For details about his type of plot see Dembicki (2009).

Several studies have published on the kerogen types with the analyses based on Rock Eval. Tang and others (2014) described the kerogen as Type II (either II1 or II2) and Guo and others (2014) described it as Type II2. Neither author noted any Type III woody kerogen. Our thin-section analysis showed many large pieces of flattened and chucky, nonporous kerogen several tens of micrometers long (**figs. 15A and B**). We suggested these larger pieces of kerogen are actually Type III. This is important because Type III kerogen commonly does not produce organic-matter pores (Loucks and Reed, 2014).

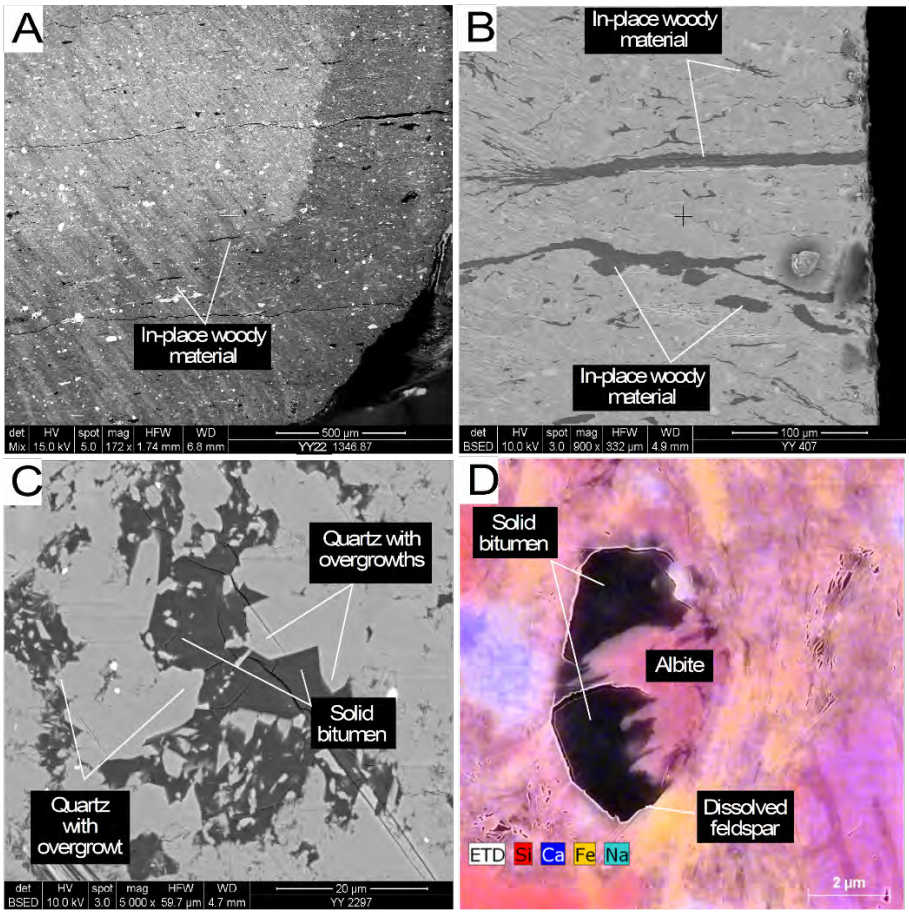

Figure 15. Examples of in-place kerogen and migrated solid bitumen. (A) In-place flakes of woody organic matter in organic-rich argillaceous mudstone. YY22-1346.87 m. (B) Late pieces of in-placed compacted woody material. YCDT-407 m. (C) Large interparticle pore space with quartz overgrowth followed by emplacement by bitumen (now solid bitumen). WCYWV-2297.05 m. (D) Mold of a dissolved feldspar that was partly replaced by albite is filled with migrated solid bitumen. YY1-1409.26 m.

An important observation of the OM in the Ar-ion-milled samples is that the OM occurs in two general forms: (1) original depositional kerogen (**figs. 15A and B**), and (2) migrated solid bitumen (**figs. 15C and D**). This is significant because as Loucks and Reed (2014) pointed out, the kerogen is commonly and sparsely disseminated throughout the matrix, and the pores that form in the kerogen may not be well connected to the effective porosity network, whereas, the bitumen is expelled into many of the original interparticle and intraparticle pores during hydrocarbon generation, and the pores in this material are more abundant and better connected to the effective pore network. Criteria for documenting migrated bitumen were developed by Loucks and Reed (2014). In the Yanchang samples, solid bitumen is recognized by the bitumen occurring in pore spaces following the precipitation of grain overgrowths, such as quartz and carbonate (**fig. 15C and D**). Also, the pores in the solid bitumen is extremely "spongy" (this pore texture is subsequently described).

Pore Types and Pore Networks

The major goals of this investigation were to document visible pore types using Ar-ion-milled samples on the scanning electron microscope and define the major pore networks. Several recent articles have addressed the pores in the Yanchang Chang 7 and 9 members, including SEM, nitrogen adsorption, high-pressure mercury injection (HPMI), and GRI crushed-rock analyses (Wang, X., 2012, Tang and others, 2014, Wang, X. and others, 2015, and Wang, Y. and others, 2015).

Pore Types

Several type pores occur within the Yanchang samples, including (1) interparticle, (2) intraparticle, and (3) organic-matter OM pores (**fig. 16**). We use the pore classification constructed by Loucks and others (2012). The relative abundance of pore types are plotted on the ternary diagram (**fig. 16**) following the Loucks and others (2012) classification. Quantifying the different pore types are subsequently discussed. The following pore types are described as follows in order of abundance.

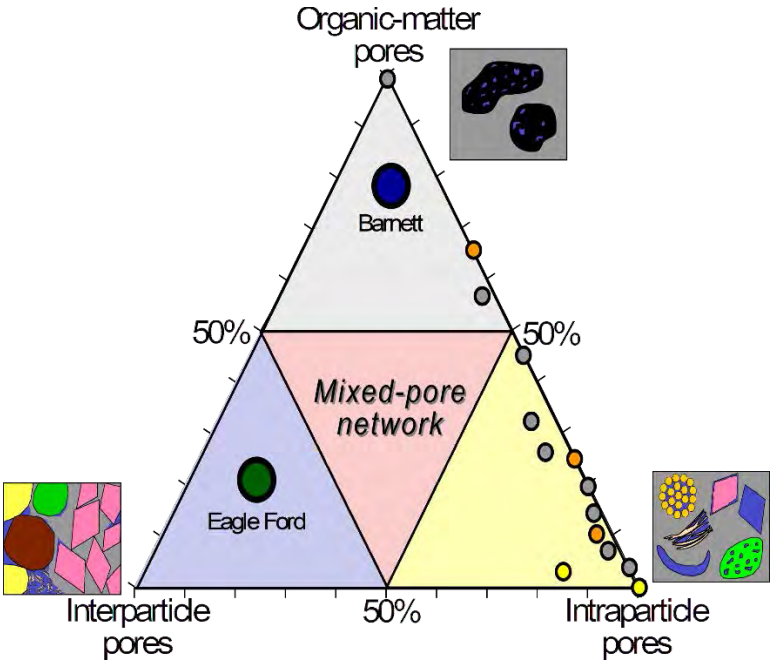

Figure 16. Relative abundance of pore type using the pore classification of Loucks et al. (2012). General relative pore abundances are also shown on ternary diagram.

Intraparticle pores (**fig. 17**): This is the most common pore type (**fig. 16**). The majority of intraparticle pores are within clay floccules (**figs. 17A and B**) and distorted mica books. Other intraparticle pores are by grain dissolution (**fig. 17C**) and as fluid inclusion within feldspar crystals (**fig. 17D**). Intraparticle pores within clay floccules are the most common. These pores occur in local domains and may not be well connected to the effective pore network and therefore do not contribute much to permeability.

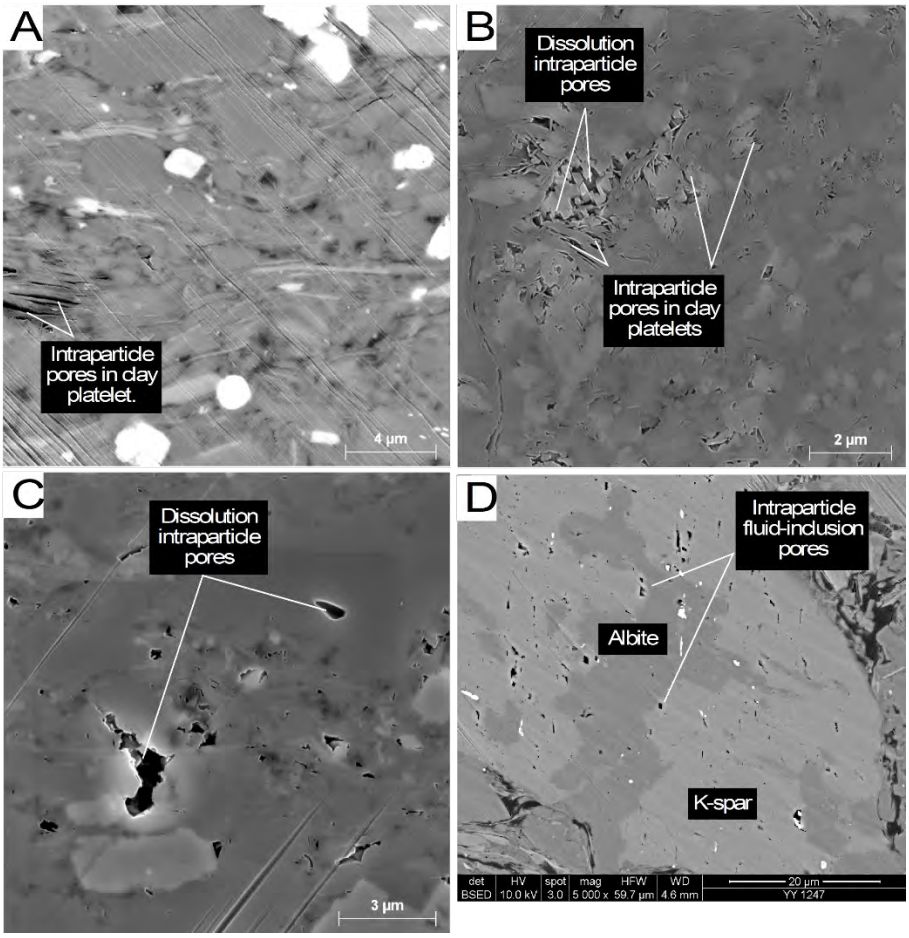

Figure 17. Intraparticle pores. (A) Intraparticle pores in clay flocculate created by distortion of clay platelet. YY1-1346.87 m. (B) Pore network of intraparticle pores in clay platelets and secondary dissolution pores. YY1 1347.96 m. (C) Dissolution pores within grains. YY1-1397.66 m (D) Intraparticle fluid inclusion pores with K-feldspar grain partly replaced by albite. YCWV-1247 m.

Organic-matter pores (**fig. 18**): This is the second most common pore type but is not very common. OM pores are primarily from solid bitumen (**fig. 18**) that has migrated into original primary pore spaces, but some may form in the original in-place kerogen. The pores occur as bubble pores (generally in the several hundred nanometer-size range) (**fig. 18B**) and spongy pores (generally in the tens of nanometer size range) (**fig. 18**) as defined by Loucks and Reed (2014) and Ko and others (in review). The bubble pores form when the bitumen migrates into a pore containing water. Most of the water is pushed out of the pore, but, some may be trapped within the bitumen and forms a bubble. Also, some bubbles may form when the bitumen cracks to oil or gas. The oil or gas may concentrate in a bubble form. Spongy pores form during maturation of the bitumen and generally consists of a large population of nanopores (**fig. 18**). These OM pores form permeability pathways as shown by Ambrose and others (2010) and Sondergeld and others (2010).

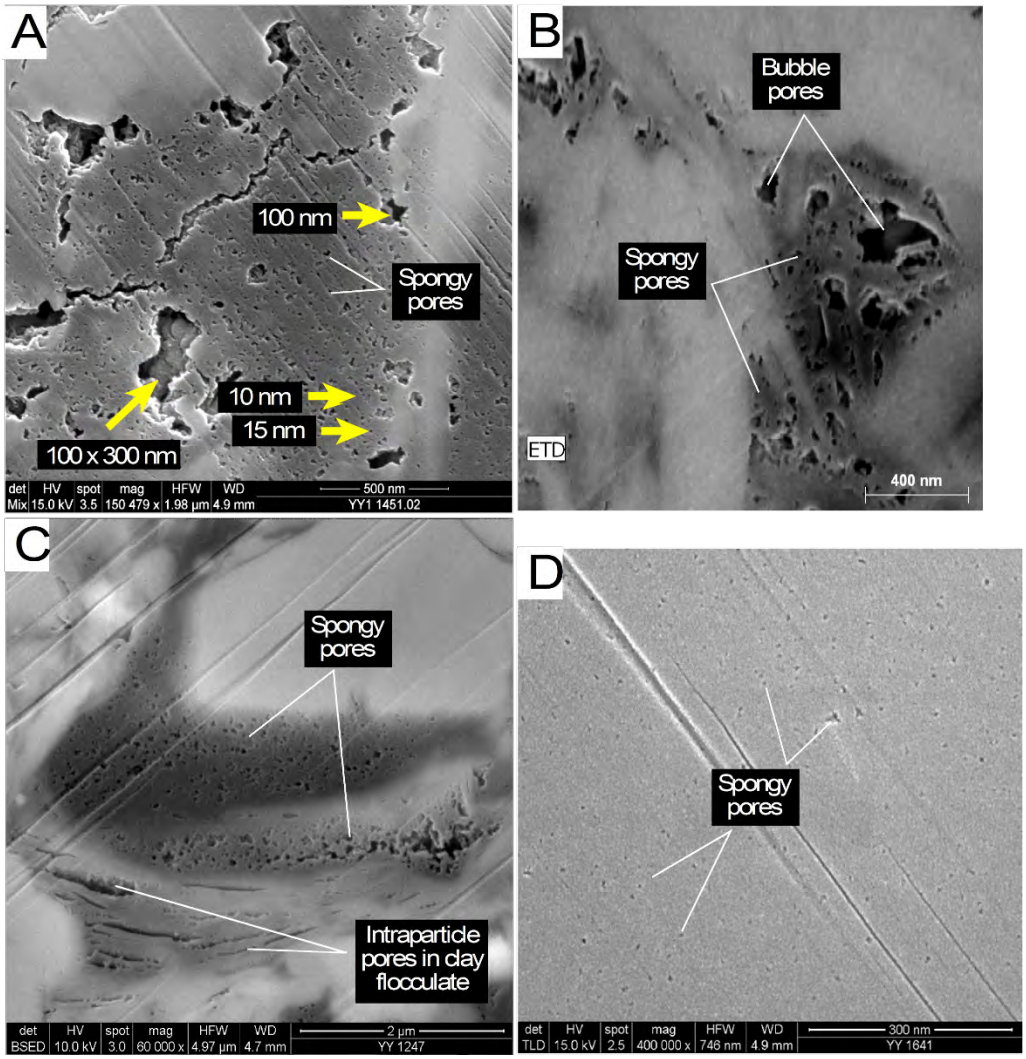

Figure 18. Organic matter pores. (A) OM pores of various sizes in transported solid bitumen. YY1=1451.02 m. (B) Spongy and bubble pores in transported solid bitumen. YY1 1497 m. (C) Spongy OM pores in migrated solid bitumen and intraparticle pores in clay platelet. YCWV 1149-1247 m. (D) Very small spongy nanopores in low nanometer-size range (< 5nm). YCYV 1123-1614 m.

Also, it is important to note that even at magnifications as high as 180000×, no pores can be seen in some OM (**fig. 19**). Therefore, one must recognize that not all organic material contains OM pores. We think this OM is Type III, which is generally nonporous. Therefore, it is important to note that most of the OM in the YY1 and YY22 cores do not contain OM pores.

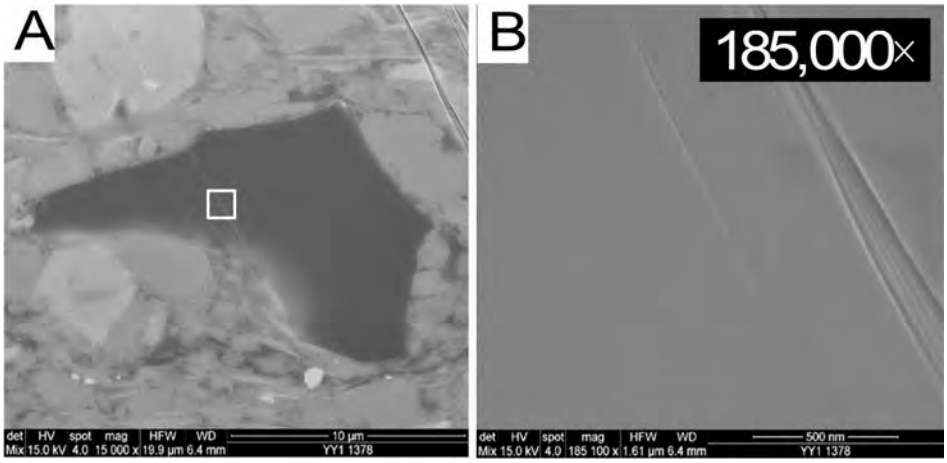

Figure 19. Example of kerogen without OM pores. (A) Large piece of kerogen without OM pores. White outlined box shows area of photomicrograph shown in B. YY1-1378 m. (B) Close up of A showing kerogen without OM pores.

Interparticle pores (**fig. 20**): Interparticle pores are relatively uncommon. They occur as original pores between grains and are generally partly occluded with clay (**figs. 20A and B**). This pore type in rocks of other formations (that is, Eagle Ford, Pommer and Milliken, 2014) are the best connected and generally forms interconnected flow pathways, however, in the Yanchang samples, they are too sparse to contribute to an effective pore network.

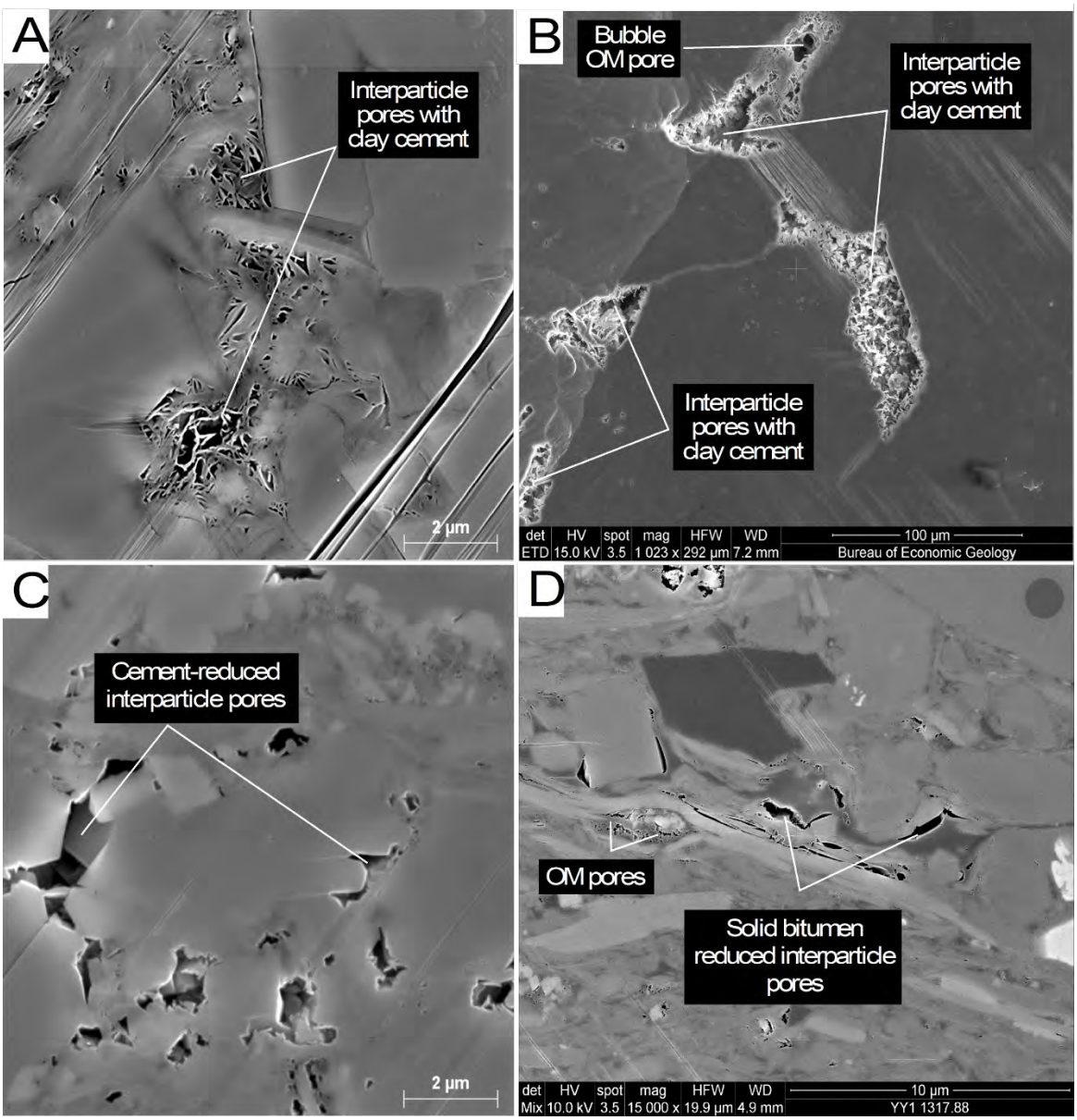

Figure 20. Interparticle pores. (A) Interparticle pore reduced by quartz cement and clay. YY1-1347.96 m. (B) Interparticle pore reduced by clay. YY1-1347.96 m. (C) Cement-reduced interparticle pore. YY1-1397.66 m. (D) Interparticle pore nearly totally cemented by solid bitumen. The reopening of the interparticle pore probably developed by shrinkage of the bitumen. YY1-1317.88 m.

Other studies have noted the same pore types (Guo and others, 2014, Wang, X. and others, 2015, and Wang, Y., 2015). However, Wang, Y., and others (2015) incorrectly identified interparticle pores in clay flocculates that are actually intraparticle pores. Therefore, their conclusion that interparticle pores are common is misleading.

Quantification of Pore Types

The general pore types in the 14 Yanchang Ar-ion-milled samples were quantified by point counting SEM photomicrographs using JMicroVision as discussed in the Data and Method section. As already noted, five subareas of each samples were photographed at 15000×, and 1,000 points were counted on each photomicrograph. Therefore, 5,000 points were collected for each sample. Results for subsample and total sample are presented in Appendix A. The mean point-count porosity is 2.23% with a range from 0.06% to 7.58% (**fig. 21**). The histogram presented in **Figure 21A** indicates that 10 of the 14 samples have SEM point-count porosity of less than 2%. Therefore, these samples have very little porosity related to pores larger than 10 nm.

A

	Point-count porosity	GRI crushed-rock porosity	Nitrogen-adsorption porosity
Mean porosity	2.227	4.188	4.831
Standard deviation	2.386	1.322	1.167
Count	14	12	14
Minimum	0.06	2.10	3.02
Maximum	7.58	6.22	7.06

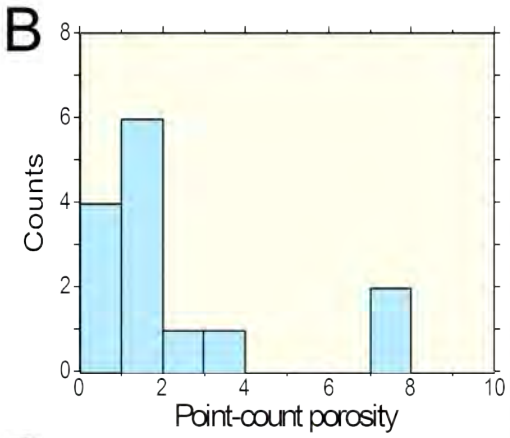

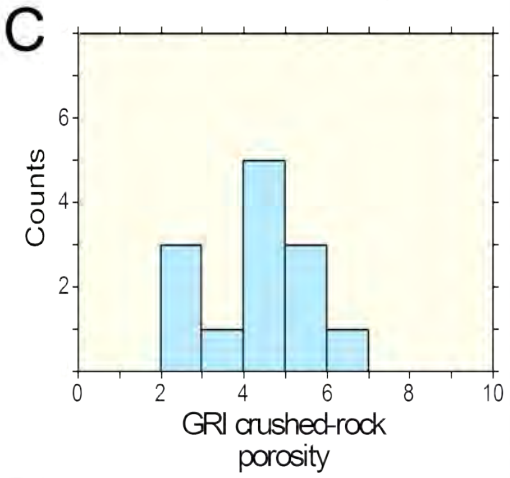

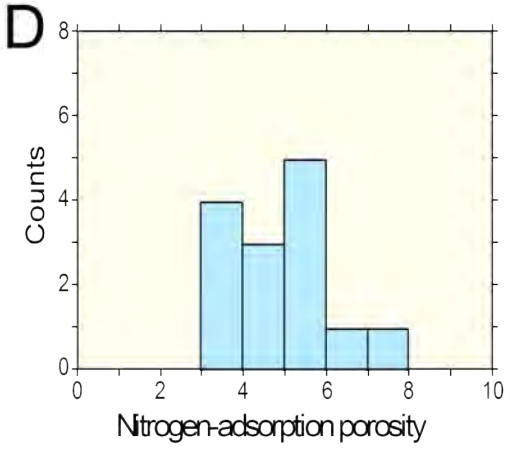

Figure 21. Comparison of results from different porosity measurement types. (A) Table of descriptive statistics. (B) Histogram of porosity values from point-count analysis. (C) Histogram of porosity values from GRI crushed-rock analysis. (D) Histogram of porosity values from nitrogen-adsorption analysis.

At 15000×, pores as small as ~10 nm can be recognized. However, as noted in the literature, many of the pores are less than 10 nm in the Yanchang Formation (Wang, X., 2012, and Guo and others, 2014). Therefore, the photomicrographs analyzed at 15000× do not point count the smallest pores, but we believe the larger pores (> 10 nm) are the most important, and these pores determine reservoir quality. Smaller pores down to 2 nm to 5 nm can be point counted if magnifications of greater than 150000× are used. However, larger magnifications greatly reduce the area analyzed. A photomicrograph at 150000× has only 1% of the area of a photomicrograph at 15000×. Therefore, a magnification of 15000× was chosen for optimum area coverage and speed of point counting.

To test for a significant difference between the porosity recorded at 15000× and porosity recorded at higher magnifications, a sample (YY1-1497.7 m) with abundant porosity was selected to be analyzed at a 150000× magnification. Four exact areas photographed at 15000× and 150000× were point counted to compare porosity results (**fig. 22**). The results appear to be quite similar (**fig. 23**). Even though the photomicrographs taken at 150000× can resolve pores as fine as 2 nm, whereas, the photomicrographs taken at 15000× are limited to defining pores greater than ~10 nm, measurements appear to be similar. The reason for the similarity is that the finest nanopores begin to blend together at the 15000× scale (**figs. 22A, B, and 24**), thereby creating what appears to be a larger coalesced pore. However, analysis at 15000× misses the pores less 10 nm (**figs. 22B and 24A**). It is important to note that much of the OM material commonly is OM pore free as noted in the example shown in **Figure 19**. Therefore, all examples need to be checked at a high magnification to ensure that finer pores are not being neglected. As an example, one sample required a magnification of 400000× to resolve some very fine nanopore in the range of 2 nm to 5 nm (see **fig. 18D**).

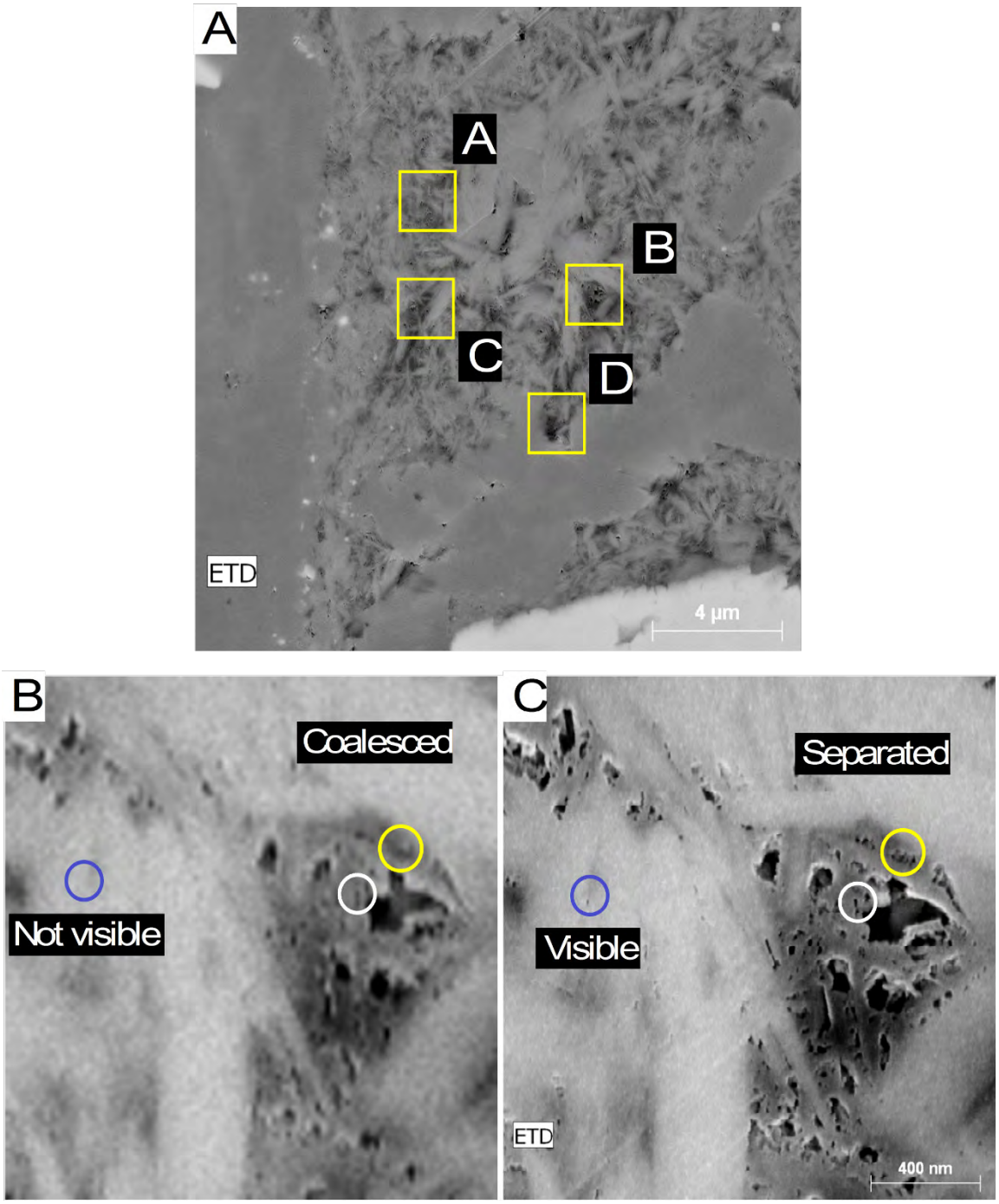

Figure 22. Test of the effect of magnification on pore resolution. Four areas of this porous sample were used to test measure point-count porosity between photomicrographs taken at 15,000× and 150,000×. (A) Photomicrograph with abundant OM pores showing four area athat were compared for pore resolution. YY1-1497.07 m. (B) Photomicrograph taken at 15,000×. (C) Photomicrograph taken at 150,000×.

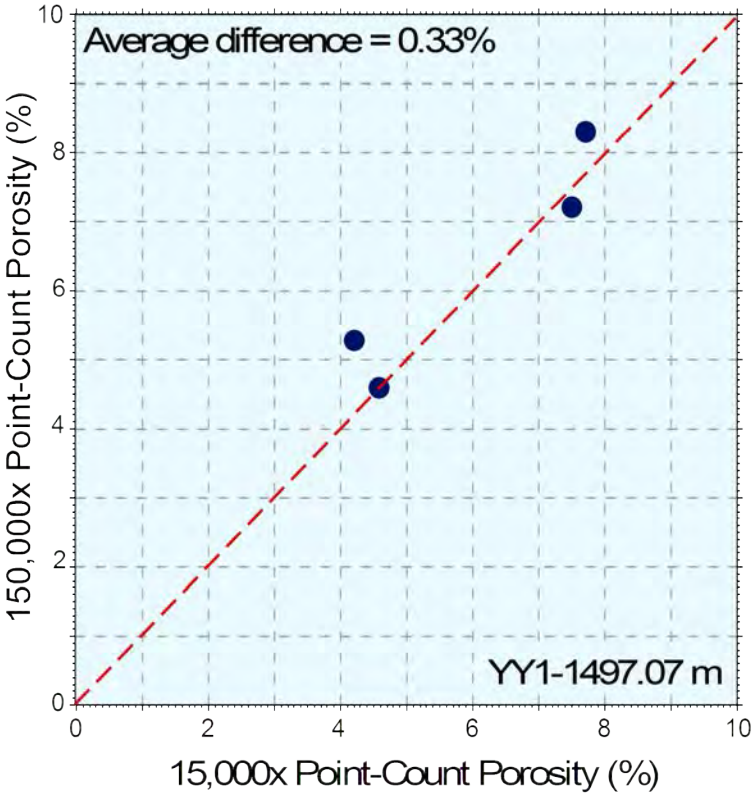

Figure 23. Plot showing comparison of point-count porosity measured at 15,000× and 150,000×. Values between the two photomicrograph magnifications for point-counting porosity are very similar.

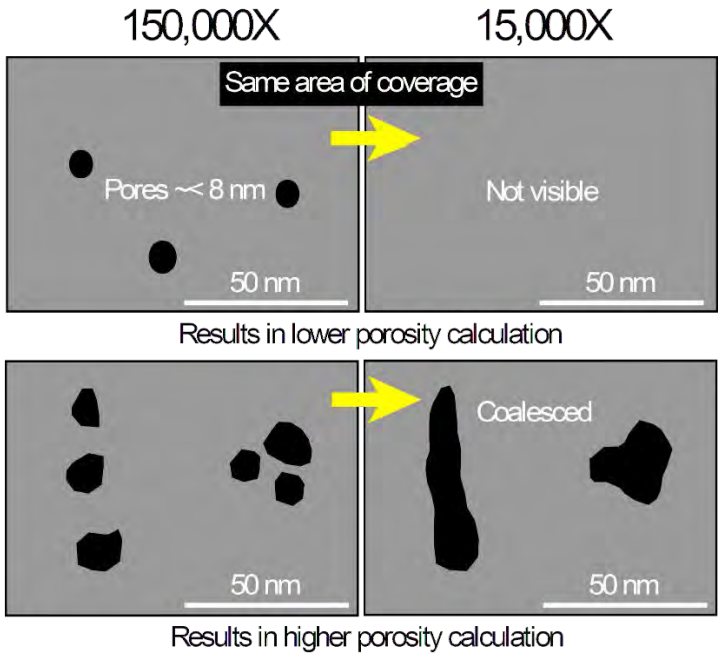

Figure 24. Schematic diagram showing errors of point counting at too low of a magnification. (A) Pores that are visible at 150,000× may not be visible at 150,000×. (B) Individual pores visible at 15,000× may coalesce to appear as a single pore at 15,000×.

Pore Networks

A pore network is the sum of the pore types and how these different pore types connect together. If the pores are few and scattered, they do not form an effective pore network, whereas, if the pore are abundant and connected, they form an effective pore network. Also, the larger the proportion of intraparticle pores, the lower the effectiveness of the pore network. As shown in **Figure 16**, the predominant pore type is intraparticle with OM pores being secondary. Interparticle pores are relatively rare. The abundance of pores in the Yanchang samples is low, and the preponderance of intraparticle pores produces a low-quality matrix pore network. This is reflected in the low-mean porosities calculated by SEM point-count (2.23%), GRI crushed-rock (4.12%), and nitrogen-adsorption (4.8%) methods (see **Fig. 21A**).

Comparison of Methods of Calculating Reservoir Quality

Reservoir quality is a product of porosity (storage), permeability (ability to flow fluids), and reservoir thickness and lateral continuity (reservoir volume). In this study to help understand reservoir quality, pore types and point-count porosity were determined. Several other methods of porosity and permeability were also completed (GRI crushed-rock porosity and permeability [Peng] and nitrogen-adsorption porosity [Zhang]). Each of these methods must be considered to understand reservoir quality.

Comparison of Porosity Calculation Methods

Based on our experience, measuring porosity in mudrocks is difficult, expensive, and time consuming. Also, different methods provide different values for the same sample suggesting that different porosity measurements may not be measuring the same population of pores. In this section, we compare porosity derived from different methods, including SEM-point counting, GRI crushed-rock, and nitrogen-adsorption analyses. A summary of each of these analyses is presented in **Figure 21**.

GRI crushed-rock porosity and permeability is the standard reservoir quality analysis method for industry. **Figure 25** shows the cross plot of GRI crushed-rock porosity versus GRI crushed-rock permeability. In this plot, the permeability value had to be adjusted to fit the GRI values produced by commercial service laboratories. As seen in the figure, there is a relatively poor correlation between porosity and permeability. The r^2 is 0.09, indicating almost no relationship.

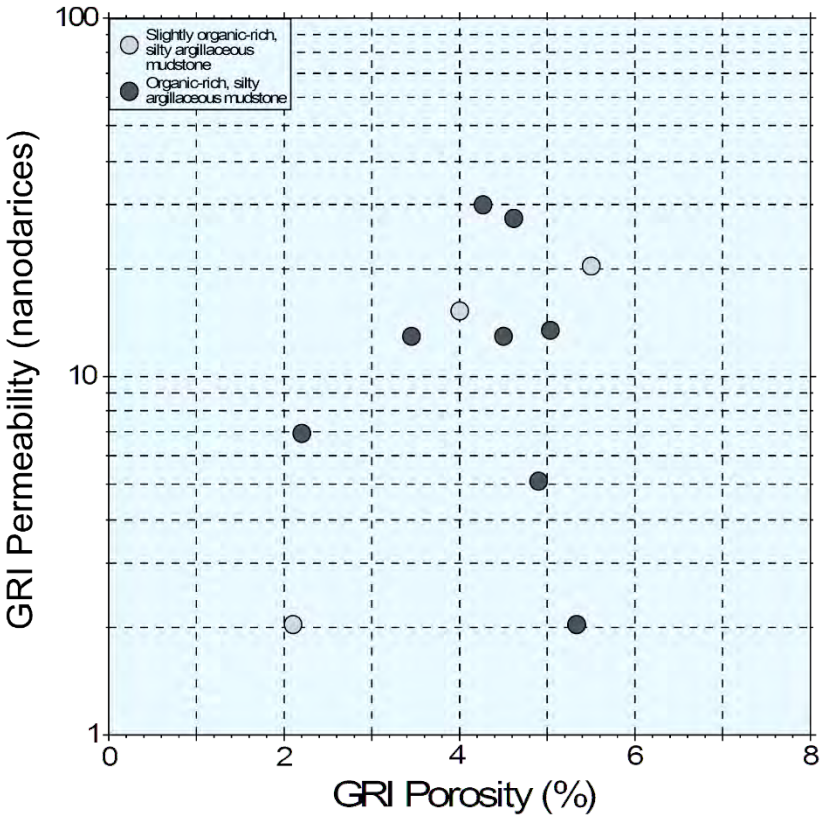

Figure 25. GRI crushed-rock porosity versus permeability.

Figure 26 shows the comparison of the different porosity measurement methods. GRI crushed-rock porosity has a weak ($r^2 = 0.33$) correlation with nitrogen-adsorption porosity (**fig. 26A**). Ten out of the 14 samples show that the nitrogen-adsorption porosity is higher than the GRI porosity. Nitrogen-adsorption porosity measures pore diameters down into the angstrom range. It is assumed that the GRI porosity calculation method is not recording these angstrom-size pores. Also, these angstrom-size pores most likely do not add much to reservoir quality because they would not be large enough to allow hydrocarbons to flow in a reasonable time frame.

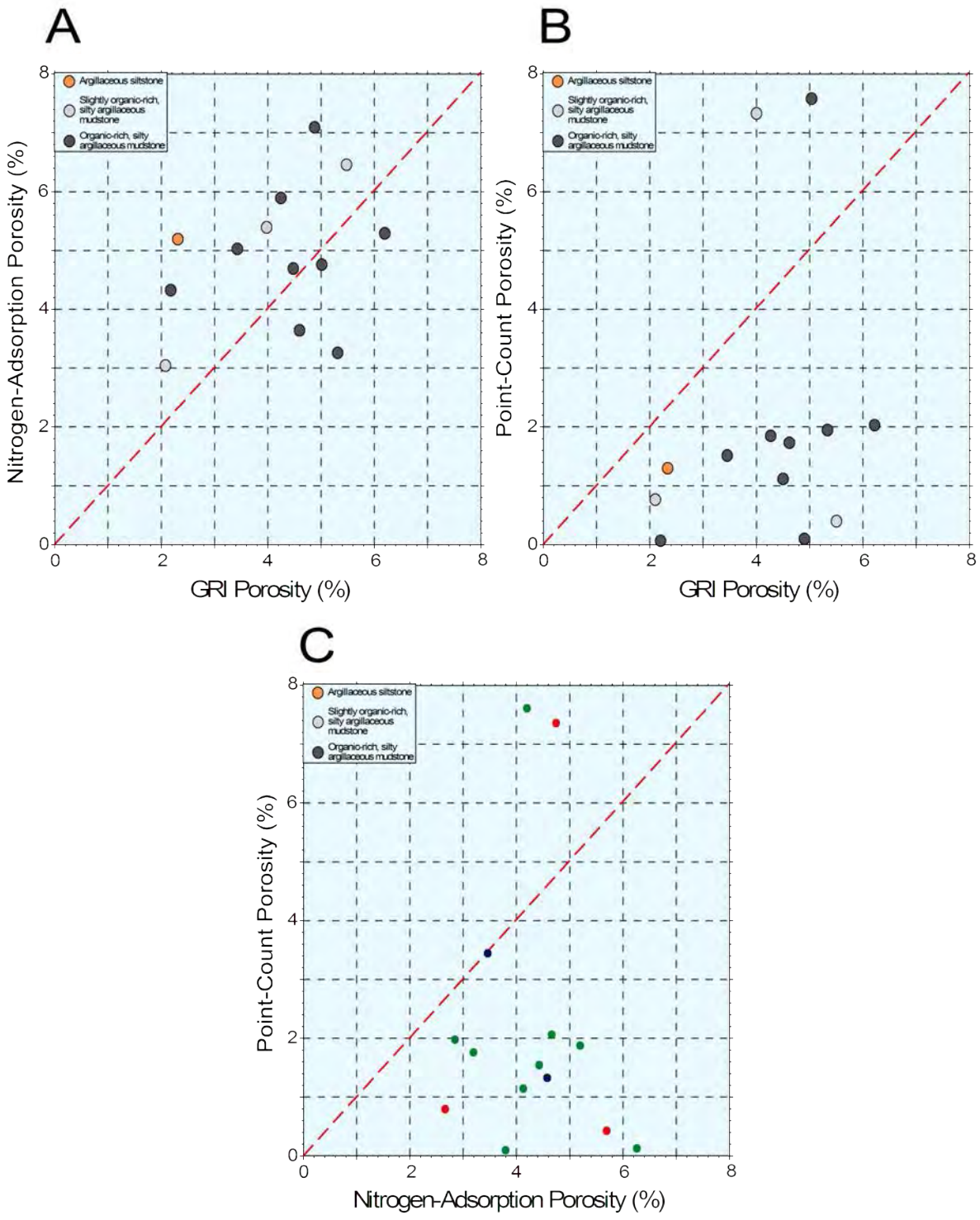

Figure 26. Comparison of porosity measurements by different analysis methods. (A) GRI crushed-rock porosity versus nitrogen-adsorption porosity. (B) GRI crushed-rock porosity versus point-count porosity. (C) Nitrogen-adsorption porosity versus point-count porosity.

GRI crushed-rock porosity has no relationship ($r^2 = 0.04$) (**fig. 26B**) with point-count porosity. All but two of the GRI porosity measurements are higher than the point-count porosity measurements. As noted earlier, point-count porosity only records pores greater than 10 nm, and the sample area is very small. The other option has the GRI porosity measuring a broader pore-size range (micrometer size) and as well as measuring a larger volume of sample. We recognized that GRI porosity is more accurate, but it does not reveal any information about pore types or pore distribution.

Nitrogen-adsorption porosity is also generally greater than point-count porosity, and the correlation between the two measurements is extremely poor ($r^2 = 0.08$) (**fig. 26C**). Again, as previously mentioned, nitrogen-adsorption porosity measures pores down into the angstrom-size range, whereas, the lower limit of point-count porosity is approximately 10 nm. Also, nitrogen-adsorption porosity has an upper limit of pore-recognition size at approximately 200 nm, whereas, the point-count porosity method can record the pores into the micrometer range.

We also compared the mean porosities analyzed by the different method to lithofacies. GRI crushed-rock and point-count mean porosities are the same for the argillaceous siltstones (2.34% and 2.36%, respectively). The nitrogen-adsorption porosity for the argillaceous siltstones (4.5%) is twice that of the previous two methods. This higher value for the nitrogen-adsorption porosity is probably related to the fact that the nitrogen-adsorption method measures smaller pores than the other two methods. Different mean values were derived for the organic-lean argillaceous mudstones by the three porosity calculation methods. The nitrogen-adsorption method has a mean porosity of 4.9%, the GRI crushed-rock method has a mean porosity of 3.87%, and the point-count method has a mean porosity of 3.8%. For the organic-rich argillaceous mudstones, the GRI crushed-rock and nitrogen-adsorption methods provide similar mean porosities (4.5% and 4.8%, respectively). Point-count porosity is much lower at 2.0%. Again, point-count porosity is low, because the method does not resolve the many smaller pores (< 10 nd) that are common in the Yanchang mudstones.

Different information can be gleaned from each method. The GRI crushed-rock method provides both porosity and permeability value. The nitrogen-adsorption porosity provides data on the smallest pore sizes (into the angstrom range). The point-count porosity provides information on pore types, shapes, distribution, and mineral and organic-matter relationships. Therefore, each measure method provide information and because we collect more data sets in which all three measurement types are collected, we are able to better integrate the combined information to provide a fuller characterization of reservoir quality.

Comparison GRI Crushed-Rock Permeability to Porosity Calculation Methods

As previously mentioned, GRI crushed-rock permeability is poorly correlated to GRI crushed-rock porosity ($r^2 = 0.09$) (**fig. 25**). The point-count porosity has a weak correlation ($r^2 = 0.24$) (**fig. 27A**) with GRI permeability as does the nitrogen-adsorption porosity ($r^2 = 0.20$) (**fig. 27B**). The overall pore correlation between permeability and porosity is that much of the porosity is not effective porosity because the pores are not well connected. Because this investigation has been documented, the predominant pore type is intraparticle. Intraparticle pores are generally not well connected and thus provide little permeability per porosity unit. As Lucia (1995) pointed out in

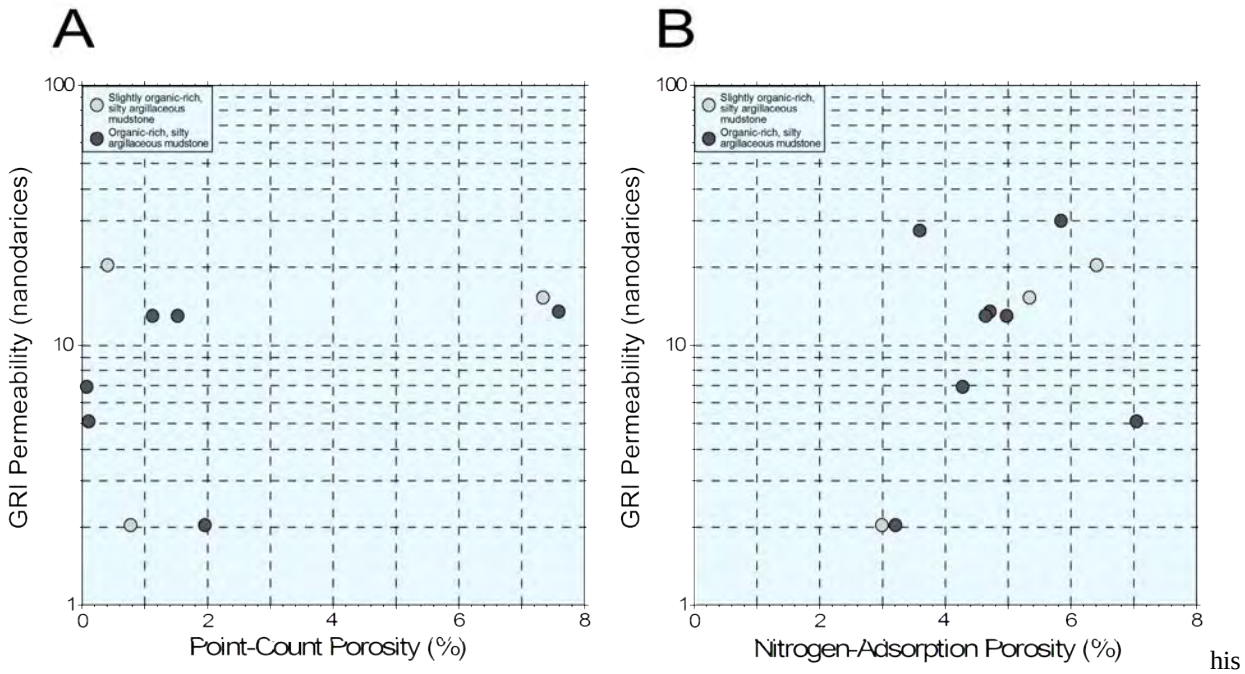

Figure 27. Comparison of permeability to porosity measurements by different analysis methods. (A) Point-count porosity versus GRI crushed-rock permeability. (B) Nitrogen-adsorption porosity versus GRI crushed-rock permeability.

his

studies of porosity to permeability relationships, permeability correlates strongly to interparticle pores, but not to intraparticle pores.

The GRI crushed-rock estimated permeability is very similar between the organic-lean and organic-rich argillaceous mudstones (12.55 nd and 13.90 nd, respectively). This close comparison of permeability values correlate with the similarities between the porosity values for the organic-lean and organic-rich argillaceous mudstones (3.87% and 4.50%, respectively).

Comparison of TOC to Porosity

In many mudstones, porosity correlates with the amount of OM as pores commonly form in OM during maturation (Loucks and others, 2009). Two total organic carbon analyses types were completed for this investigation: (1) point-count TOC and (2) Rock Eval TOC. **Figure 28** is a cross plot of Rock Eval versus point-count TOC. There is only a weak relationship between the two methods ($r^2 = 0.33$) and Rock Eval TOC is higher in 10 out of the 14 analyses. The reason for this is that Rock Eval measured a greater volume of sample, and the Ar-ion-milled samples deliberately avoided larger pieces of OM. Therefore, Rock Eval TOC is considered the more accurate method for measuring TOC.

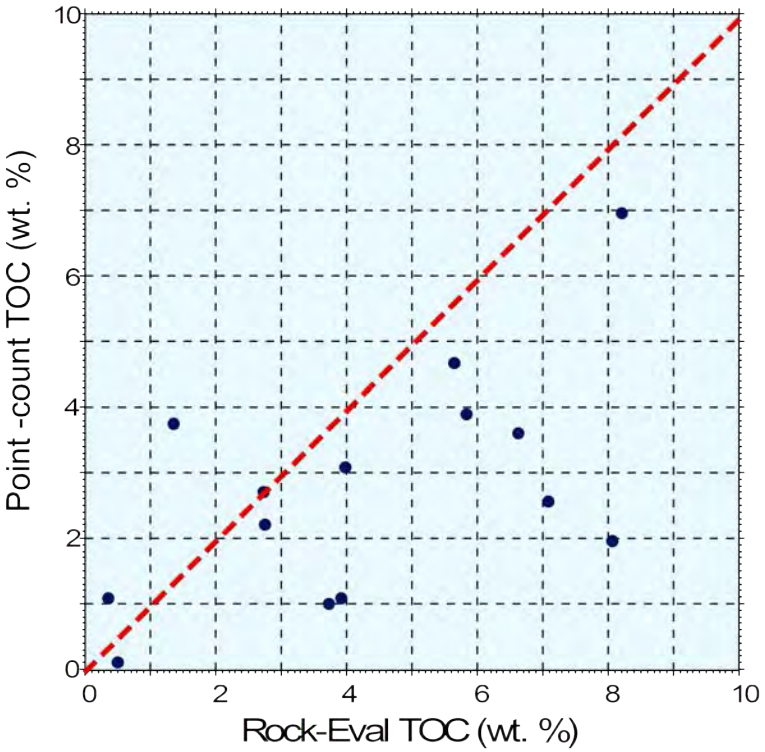

Figure 28. Rock-Eval TOC versus point-count TOC.

Both GRI crushed-rock porosity and permeability have almost no correlation to Rock Eval TOC (**fig. 29**). The r^2 between TOC and porosity is 0.09 and between TOC and permeability is 0.03. The reason for the extremely poor correlation with porosity and permeability is that much of the OM in the Yanchang samples contains no pores. This may be related to the composition of the kerogen types. The kerogen is a mixture of Type II and III as previously noted. Type III kerogen generally does not produce pores during hydrocarbon maturation (Loucks and Reed, 2014). Plotting Rock Eval TOC with nitrogen-adsorption porosity and point-count porosity also produced no relationship between TOC and porosity. The r^2 between TOC and nitrogen-adsorption porosity is $3.9x10^5$ and between TOC and point-count porosity is 0.06.

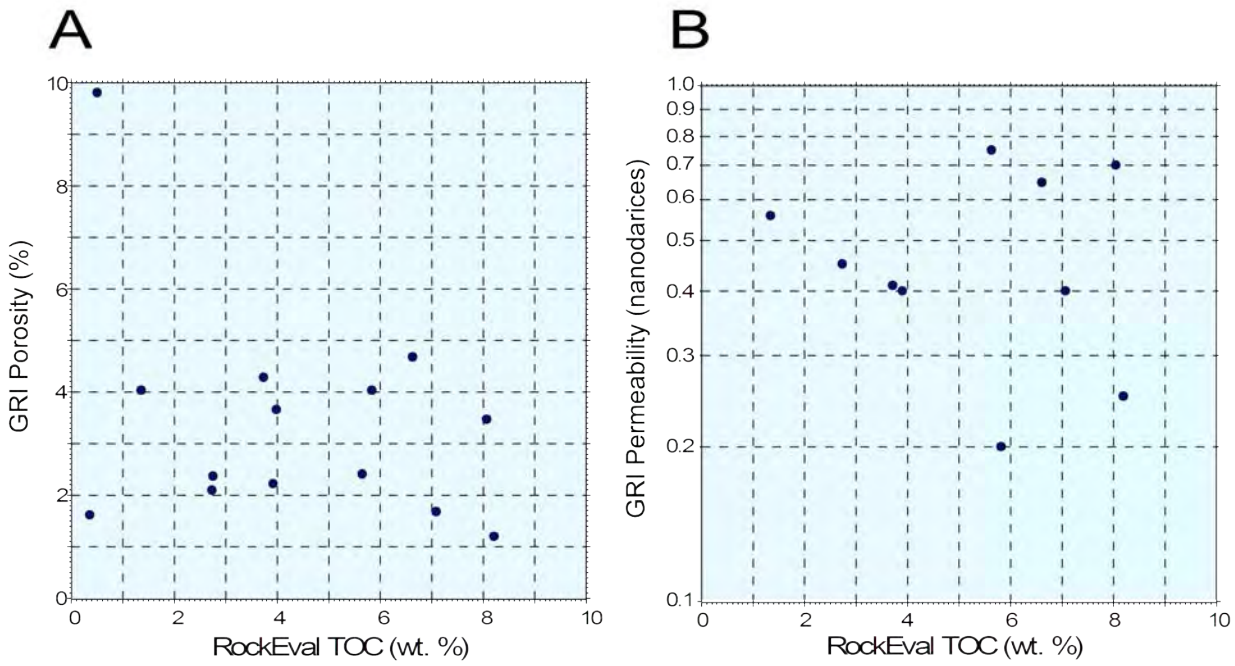

Figure 29. Rock-Eval TOC versus GRI crushed-rock porosity and permeability. (A) Rock-Eval TOC versus GRI crushed-rock porosity. (B) Rock-Eval TOC versus GRI crushed-rock permeability.

Reservoir Quality

The overall reservoir quality in the 14 Yanchang analyzed sample is low for mudrocks. Mean GRI porosity is 4.19% (range = 2.10% to 6.22%), mean estimated GRI permeability is 13.52 nd (range = 2.03 nd to 30.19 nd), and geometric mean estimated GRI permeability is 9.86 nd. Wang, X. (2012) noted the mode of porosity to be 6% to 7%, Wang, Y. and others (2015) mentioned that mercury porosimetry analysis gave a mean porosity of 5.27% and a range between 1.93 and 7.65%, and Tang and others (2014) calculated acoustic logging porosities ranging between 3% and 8% for the C9 shale interval and 3% and 6% for the C7 shale interval. All three of these published porosity calculations are in relative agreement with the mean porosity and range of porosity presented in the present investigation.

Permeability analyses were presented by Wang, X. (2012) and Tang and others (2014). Wang, X. (2012) calculations show the Yanchang samples to have a mean permeability of 7.2 nd, which is relatively consistent with our mean permeability of 13.2 nd. However, Tang and others (2014) show a permeability range between 1,000 nd and 10,000 nd (0.001 md and 0.01 md). This appears very high and may be related to the siltstones and sandstones in the Yanchang Formation.

Separating reservoir quality by lithologies using the GRI crushed-rock analyses, the argillaceous siltstones appear to have the poorest quality (mean porosity = 2.34%, permeability is not available). The organic-lean and organic-rich argillaceous mudstones have a slightly better

reservoir quality with a mean porosity of 3.85% and 4.50% and estimated mean permeability of 12.55 nd and 13.90 nd. Overall, each of these lithofacies have a low reservoir quality.

Yang and others (2013) and Tang and others (2014) commented on the reservoir quality in the adjacent sandstone in the Chang 7 member. They noted that the interbedded sandstones have a very low reservoir quality and are considered tight oil sandstones. Sandstones porosity ranges between 0.8% and 12% and permeability averages 0.18 nd. Even with the relatively low permeabilites of the sandstone, they could be the carrier beds for the oil or gas in the adjacent organic-rich mudstones. This would set up a hybrid shale-gas/shale-oil system. Wang, X. and others (2015) also concluded the Chang 7 and 9 members can form a hybrid system in which the interbedded siltstones are the carrier beds.

Conclusions

The continental Upper Triassic Yanchang “black shales” in the Ordos Basin have proved to be unconventional gas reservoirs and are still in the stage of exploitation. This present investigation was conducted to examine the mudrocks for pore types and relative pore-type abundances to characterize the pore networks in the Yanchang Chang 7 to 9 members as seen in the YY1 and YY22 cores. Fourteen Ar-ion milled samples were examined using an FE-SEM. Several other samples from other Yanchang cores were also available for examination.

The organic-lean and organic-rich argillaceous mudstones were deposited in a deeper water lacustrine setting during lake highstands. In the stratified lake, the bottom waters were dysaerobic to anoxic. This low-energy and low-oxygen lake-bottom setting allowed Type II and Type III OM to accumulate. Interbedded with the argillaceous mudstones are argillaceous siltstones that may have been deposited by gravity-flow processes (turbidites). The argillaceous siltstones are very low in TOC.

The studied samples are very immature minerlogically. The siltstones are either lithic arkoses or arkosic litharenites. The high clay content, generally greater than 40%, has promoted extensive compaction of the sediments, and this allowed the ductile material to deform and occlude the primary interparticle pores, thus greatly reducing reservoir quality. Also, the high clay-mineral content does not favor induced hydraulic fracturing of the mudstone reservoir.

The pore network within the mudstones is dominated by intraparticle pores with a lesser abundance of OM pores. Interparticle pores are rare. The mean GRI porosity is 4.19%. Because the pore network is dominated by intraparticle pores, permeability is low (GRI-estimated geometric mean permeability = 9.86 nd). Also, the dominance of ineffective intraparticle pores creates a very poor correlation between GRI porosity and permeability.

Several methods of porosity analysis (GRI crushed-rock, nitrogen-adsorption, and point-count) were conducted on each of the 14 samples, and the results were compared. There is no significant correlation between the three method of analysis indicating that each method must be measuring different pore sizes or types. However, a comparison of the three porosity calculation methods does enhance the understanding of pore types, distribution, and abundance.

There is no relationship between reservoir quality and TOC. Much of the OM is nonporous because it is Type III. Most of the OM pores are in migrated solid bitumen that had filled the earlier formed interparticle and intraparticle pores.

Overall, the samples analyzed in the Yanchang Chang 7 to 9 members are of low reservoir quality. Even though the organic-rich mudstones are in the peak oil window, the mudstones appear to be too tight to produce oil, but they may be adequate for gas production. The less argillaceous-rich siltstones and sandstones within the systems may be potential carrier beds for the hydrocarbons forming a hybrid shale reservoir.

Acknowledgments

We want to express our appreciation to Yanchang Petroleum for supporting this project. Amanda R. Masterson edited this manuscript, and Jamie H. Coggin provided formatting and layout. We thank them for their efforts.

References

Advanced Resources International, Inc., 2013, XX China: in EIA/ARI World Shale Gas and Shale Oil Resource Assessment, prepared for the U.S. Energy Information Administration, U.S. Department of Energy, p. xx-1–xx–58.

Ambrose, R.J., Hartman, R.C., Diaz-Campos, M., Akkutlu, I.Y., and Sondergeld, C.H., 2010, New pore-scale considerations for shale gas in place calculations, in Proceedings, SPE Unconventional Gas Conference, Pittsburgh, Pennsylvania, 23–25 February, SPE-131772, 17 p.

Dembicki, H., 2009, Three common source rock evaluation errors made by geologists during prospect or play appraisals: AAPG Bulletin, v. 93, p. 341–356.

Ding, W.L., Zhu, D.W., Cai, J.J., Gong, M.L., and Chen, F.Y., 2013, Analysis of the developmental characteristics and major regulating factors of fractures in marine-continental transitional shale-gas reservoirs: a case study of the Carboniferous-Permian strata in the southeastern Ordos Basin, Central China: Marine Petroleum Geology, v. 45, p. 121–133.

Folk, R.L, 1974, Petrology of sedimentary rocks: Austin, Texas, Hemphill, 182 p.

Gao, R., Wang, X., and Jing, F., 2015, Fracability evaluation of lacustrine shale in the Yanchang Formation of southeastern Ordos Basin: Energy Exploration and Exploitation, v. 33, p. 363–374.

Guo, H., Jia, W., Peng, P., Lei, Y., Luo, X., Cheng, M., Wang, X., Zhang, L., and Jiang, C., 2014, The composition and its impact on the methane sorption of lacustrine shales from the Upper Triassic Yanchang Formation, Ordos Basin, China: Marine and Petroleum Geology, v. 57, p. 509–520.

Ko, L., Tongwei, T., Loucks, R.G., Ruppel, S.C., and Shao, D., in review, Pore evolution of Upper Cretaceous Eagle Ford organic-rich mudstones–Results from gold-tube pyrolysis experiments, AAPG Bulletin.

Loucks, R.G., and Reed, R.M., 2014, Scanning-electron-microscope petrographic evidence for distinguishing organic-matter pores associated with depositional organic matter versus migrated organic matter in mudrocks, GCAGS Journal, v. 3, p. 51–60.

Loucks, R.G., Reed, R.M., Ruppel, S.C., and Hammes, U., 2012, Spectrum of pore types and networks in mudrocks and a descriptive classification for matrix-related mudrock pores, AAPG Bulletin, v. 96, no. 6, p. 1071–1098.

Loucks, R.G., Reed, R.M., Ruppel, S.C., and Jarvie, D.M., 2009, Morphology, genesis, and distribution of nanometer-scale pores in siliceous mudstones of the Mississippian Barnett Shale. Journal of Sedimentary Research, v. 79, p. 848–861.

Lucia, F.J., 1995, Rock-Fabric/Petrophysical Classification of Carbonate Pore Space for Reservoir Characterization: AAPG Bulletin, v. 79, p. 1275–1300.

Pommer, M., and Millken, K., 2014, Pore types and pore-size distributions across thermal maturity, Eagle Ford Formation, southern Texas: AAPG Bulletin, v. 99, p. 1713–1744.

Rowe, H., Wang, X., Fan, B., Zhang, T., Milliken, K., Shen, Y., and Zhang, J., 2015, Chemostratigraphy of the Triassic Yanchang Fluvio-Lacustrine Succession, Ordos Basin, Shaanxi Province, China, AAPG Annual Convention and Exhibition, Denver, CO., abstract.

Sondergeld, C.H., Ambrose, R.J., Rai, C.S., and Moncrieff, J., 2010, Micro-structural studies of gas shales, in Proceedings, SPE Unconventional Gas Conference, February 23–25, Pittsburgh, Pennsylvania, SPE 131771, 17 p.

Tang, X., Zhang, J., Wang, X., Yu, B., Ding, W., Xiong, J., Yang, Y., Wang, Lo, and Yang, C., 2014, Shale characteristics in the southeastern Ordos Basin, China, Implications for hydrocarbon accumulation conditions and the potential of continental shales: International Journal of Coal Geology, v. 128–129, p. 32–46.

Wang, Xiangzeng, 2012, The exploration discovery and key technologies of continental shale gas, Yanchang Petroleum, http://www.uschinaogf.org/Forum12/pdf/21%20-%20Xiangzeng%20-%20Shaanxi%20Yanchang%20Petroleum-EN.pdf (referenced November 7, 2015).

Wang, X., Zhang, L.,Jiang, C., and Fan, B., 2015, Hydrocarbon storage space within lacustrine gas shale of the Triassic Yanchang Formation, Ordos Basin, China, Interpretation, v. 3, p SJ15–SJ23.

Wang, Y., Zhu, Y., Wang, H., and Feng, G., 2015, Nanoscale pore morphology and distribution of lacustrine shale reservoirs, Examples from the Upper Triassic Yanchang Formation, Ordos Basin: Journal of Energy Chemistry, v. 4, p. 512–519.

Yao, S.P., Zhang, K., Hu, K.X., Fang, H.F., and Jiao, K., 2009, Sedimentary organic facies of the Triassic Yanchang Formation in the Ordos Basin: Oil & Gas Geology, v. 30, p. 74–84 (in Chinese with English abstract).

Yao, Z., Yang, Y., Ying, H., and Dong, Y., 2014, Mineral characteristics and their geological significance of black shales in southeastern Ordos Basin by X-ray diffraction analysis: China Journal of Geochemistry, v. 33, p. 119–124.

Yang, H., Li, S.X., and Liu, X.Y., 2013, Characteristic and resource prospects of tight oil and shale oil in Ordos Basin: Acta Petrolei Sinica, v. 34, p. 1–11.

Yang, Y., Li, W., and Ma, L., 2005, Tectonic and stratigraphic controls on hydrocarbon systems in the Ordos basin, A multicycle cratonic basin in central China: AAPG Bulletin, v. 89, p 255–269.

Yu, X., Li, S., Tan, C., Xie, J., Chen, J., and Yang, F., 2013, The response of deltaic systems to climatic and hydrological changes in Daihai Lake rift basin, Inner Mongolia, northern China: Journal of Paleogeography, v. 2, p. 41–55.

Zhao J., Mountney, N.P., Liu, C., Qu, H., and Lin, J., 2015, Outcrop architecture of a fluvio-lacustrine succession, Upper Triassic Yanchang Formation, Ordos Basin, China: Marine and Petroleum Geology, v. 68, p. 304–413.

Zou, C., Zhang, X., Lou, X., Lang, L., Lou, Z., and Liu, L., 2010, Shallow–lacustrine sand–rich deltaic depositional cycles and sequence stratigraphy of the Upper Triassic Yanchang Formation, Ordos Basin, China: Basin Research, v. 22, p. 108–125.

TASK 3.2

Pore-Size Distribution of Triassic Organic-Rich Yanchang Formation by Using N_2 Adsorption Isotherms

Tongwei Zhang[1], Jianfeng Zhang[2], and Kitty Milliken[1]

[1]Bureau of Economic Geology[1], Jackson School of Geosciences, The University of Texas at Austin, Austin, TX
[2]Shaanxi Yanchang Petroleum (Group) Co. Ltd., Xi'an, Shaanxi, China

Problem Statement and Objectives

Pore type, size, structure, and connectivity within shales are critically important characteristics for understanding shale's potential for oil and gas storage, flow, and productivity. Work to date at the Bureau of Economic Geology (BEG) reveals that the dominant pore system in many gas shales resides within the organic matter, and these pores extend into sizes below available imaging resolution (around 7 nm by field-emission SEM imaging on Ar-ion milled surfaces). It has been repeatedly observed that, in many shales, most of the pores are too small to be seen. Recent research has indicated the shale matrix predominantly consists of both micropores (<2-nm diameter) and mesopores (2-nm to 50-nm diameter), which are below available imaging resolution of 57-nm for traditional scanning electron microscopy (SEM) methods (Kuila and Manika, 2011). The use of adsorption and desorption isotherms allows determination of pores in the range of 0.38 nm to 300 nm, yielding both a total surface area (BET) and a pore size distribution (PSD). The hysteresis loop (the gap between the adsorption and desorption lines) provides crucial information about pore shapes (Hu and others, 2015). In addition to quantifying the smallest pores, high-resolution adsorption/desorption analysis is also a tool that can assess network effects (that is, constrictions and connections) within the shales. Cross comparisons with pore sizes determined by SEM imaging can provide critical information for the assessment of both pore-size distribution methods.

The presence of oil and moisture pore fluids can greatly affect the measurement of porosity and pore-size distribution of oil-bearing mudrocks. The pore-fluid removal method was applied sequentially to exposure pores filled by moisture, mobile oil, and asphaltane-dominated residual oil. Clay- and organic-rich mudrocks from the Triassic Lacustrine Yanchang Formation, Ordos Basin, China, were used in this study. The PSD values of as-received, dried, pentane-extracted, and CH_2Cl_2-extracted four aliquots of the same sample were determined by using N_2 adsorption isotherms, and the comparison of PSD among four aliquots reveals pore fluid distribution corresponding to the different sizes of the pores.

Effect of the grain size of mineral matrix on pore size distribution was investigated by combining N_2 PSD characterization and grain-size SEM imaging. As a result, the effect of geological facies on pore development was investigated.

Samples and Methods

Physisorption of Gases

This technique exposes a solid sample (~0.5g) to the gas (adsorptive) in an evacuated tube held at low temperature (77 K for N_2) through a series of pressures, ranging from $P/P_o < 1 \times 10^{-7}$ to 0.999. As the pressure increases, the amount of gas adsorbed onto the surface of the sample increases, until reaching equilibrium. During the course of this process, the micropores are filled first (at very low pressures), after which the free surface becomes covered with a monolayer of the adsorbate gas. Finally, the larger pores are filled until there is an even multilayer of adsorbate on the surface of the sample **(fig. 1**). Similarly, for the desorption process, the pressure is systematically reduced to release the adsorbed molecules from the surface. Together, these sets of data produce a complete adsorption–desorption isotherm. The Brunauer-Emmett-Teller (BET) equation, the Barrett-Joyner-Halenda (BJH) equation, and density functional theory (DFT) are used for BET surface area and PSD analysis (Thommes, 2010).

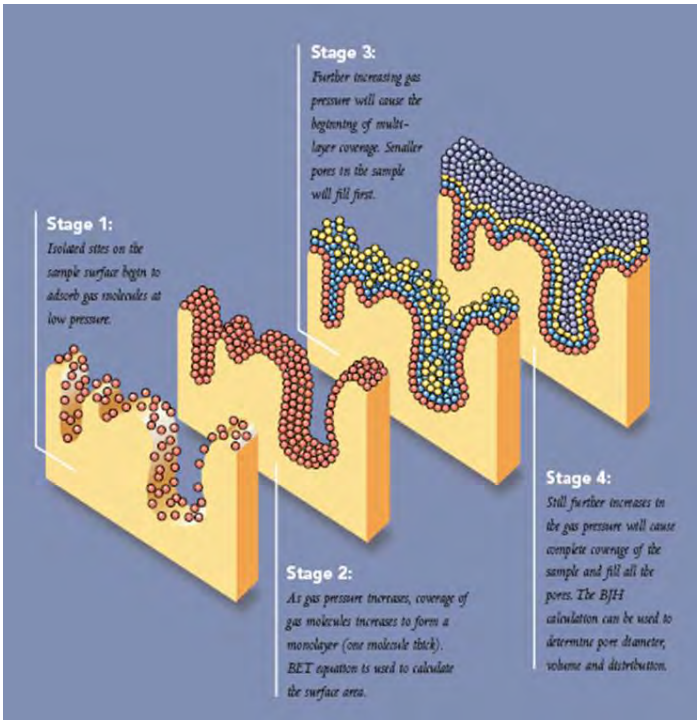

Figure 1. Steps of gas sorption in porous material. (Source: *http://www.micromeritics.com/Repository/Files/Gas_Sorption.pdf*)

N_2 Adsorption and Desorption Isotherms and PSD of Organic-Rich Shales

After oil was removed by CH_2Cl_2 solvent extraction, total pore volume (in ml/g rock), PSD, and BET surface area were determined by N_2 adsorption isotherms. The results show that lithologic variation greatly affects pore size distribution. N_2 gas adsorption and desorption isotherms measured from samples of the Yanchang Formation at 77 K show typical Type IV isotherms

and Type H3 hysteresis loops, thereby indicating aggregates of nonrigid plate-like particles creating slit-shaped pores. The Type H3 hysteresis loop is associated with capillary condensation in mesopore walls (International Union of Pure and Applied Chemistry [IUPAC], 1994). Adsorption isotherms obviously show larger pore volumes in organic-rich mudstone than in silty sandstone and silty mudstone at a relative pressure lower than 0.1, indicating that mesopores 2 nm to 10 nm in width develop abundantly.

The distribution of pore volume with respect to pore size is called pore size distribution. The "open" hysteresis loops between adsorption and desorption isotherms for Yanchang organic-rich mudstones exist because of the irreversible uptake of N_2 molecules in pores of about the same width as that of an adsorptive molecule. An interpretation of desorption isotherms showing low-pressure hysteresis is difficult, and an accurate pore size analysis is no longer possible. Therefore, the adsorption branch was taken for calculation of the pore-size distribution. The BJH method was used for pore-size distribution calculation based on the adsorption branch. The BJH method does not give a realistic description of the filling of micropores and even narrow mesopores, which leads to an underestimation of pore sizes. The DFT provides a much more accurate approach for pore-size analysis and bridges the gap between the molecular-level and macroscopic approaches. A combination of PSD from the BJH method and DFT method was used to achieve pore-size distribution in the 0.35-nm to 300-nm range. The ASiQWin software includes a number of kernels consisting of individual (P/Po and W) isotherms derived for nitrogen-carbon systems by the nonlocal DFT computer simulation.

Organic-rich mudstones in Chang 7, 8, and 9 members in the YY1 well show a similar pattern of pore size distribution (**fig. 2**): 2-nm to 10-nm pores dominate pore-size distribution, with small peaks of 1-nm 2-nm pores and 20-nm to 40-nm pores. Three samples with high TOC content represent organic-rich mudstones in Chang 7, 8, and 9 members. PSD for pores < 35 nm in width is calculated from the adsorption branch based on the DFT method; PSD for pores > 35 nm in width, from the adsorption branch based on the BJH method. The combination of pore-size distribution from DFT and BJH methods provides a way to determine the size distribution of 0.35-nm to 300-nm pores by means of N_2 adsorption isotherms.

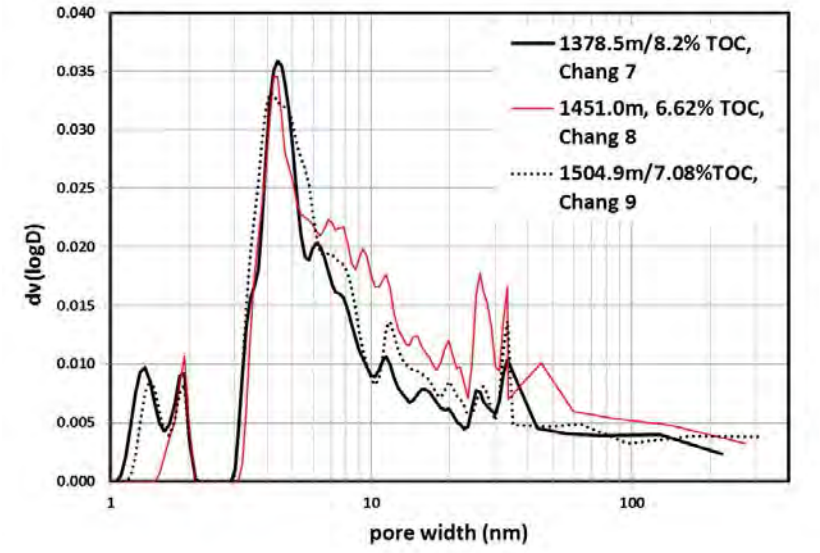

Figure 2. Similar pore size distribution observed for organic-rich mudrocks of Chang 7, 8, and 9 members.

It is worth noting that the pore-size distribution calculated from N_2 desorption branch can largely overestimate the proportion of the pores in the width of 3–5-nm pores because of the surface tension effect, showing a significant adsorbed nitrogen drop in the desorption branch when a relative pressure reaches approximately 0.48 (P/P_o). As the pressure reaches 0.45, the surface tension between the gas phase and the liquid phase breaks, and all the nitrogen filled in irregular pores, which includes bottle-ink pores and neck pores, is released. The empty pore volume is assumed to be the pores within the width range of 3 nm to 5 nm, resulting in the overestimation. The surface area value obtained from the adsorption branch is obviously larger than the desorption branch value, and the difference is attributed to the overestimation of 3 nm- to 5-nm pores with a desorption branch.

Another interesting point is the separation between the desorption branch and the adsorption branch when the relative pressure P/P_o is less than 0.48. This phenomena is called the "swelling effect." Most samples from the Yanchang Formation show this "swelling effect," suggesting that gas filled in the small pores cannot be released even if the pressure is low.

After grouping pores into two families, < 10 nm and > 20 nm in width, we saw that the volume of pores > 20 nm in width remains almost constant in a wide range of TOC content from 0.35% to 8.2%, suggesting that pores > 20 nm in width are dominated by mineral-hosted pores. In contrast, the pores < 10 nm in width vary significantly with TOC content and increase with the rise of TOC when TOC content is greater than 6% (**fig. 3**). The BET-surface area, which is mainly composed of the pores < 10 nm in width, is much larger for samples with a high TOC content (**fig. 3**). Pores < 10 nm, mainly related to OM-hosted pores, account for more than 60% of total porosity in organic-rich mudstones. The porosity of Triassic Yanchang lacustrine mudstones in the YY1 well ranges from 3 to 6.9%, with an average value of 4.8%.

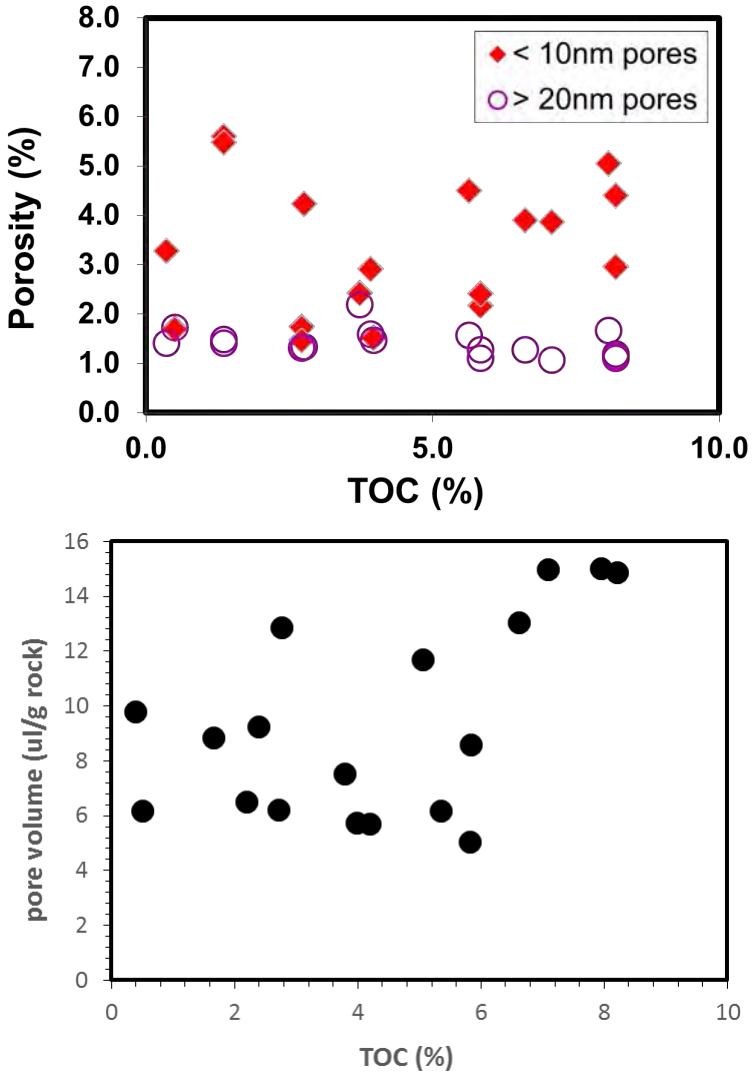

Figure 3. Correlation of pore volume and BET surface area with TOC content.

Effect of Lithology Variation on PSD

Integration of the pore-size distribution and mineralogical study allows the identification of the main controls on pore evolution. Grains are mainly transported from an extrabasinal source, based on light-microscope imaging and petrographic study of the Yanchang Formation. Point counting based on X-ray mapping provides a method to quantify the proportion of extrabasinal and intrabasinal source minerals. **Figure 4** shows the thin-section and X-ray mapping for three samples from the YY1 well, which represents silt-rich mudstone, silt-bearing mudstone, and organic-rich mudstone. Mineralogy of the silt-rich mudstone (1408.26 m) is composed of 22% quartz, 19% K-feldspar + plagioclase, 29% dolomite, 11.6% illite + mica, 3.4% chlorite, 9.9% I/S mixture, and 2.6% kaolinite. Mineralogy of silt-bearing mudstone (1397.7 m) is 22.1% quartz, 12.4% K-feldspar + plagioclase, 11.8% carbonate (dolomite + calcite + siderite), 26.5% illite + mica, 3.3% chlorite, 21.5% I/S mixture, and 1.7% kaolinite. Mineralogy of

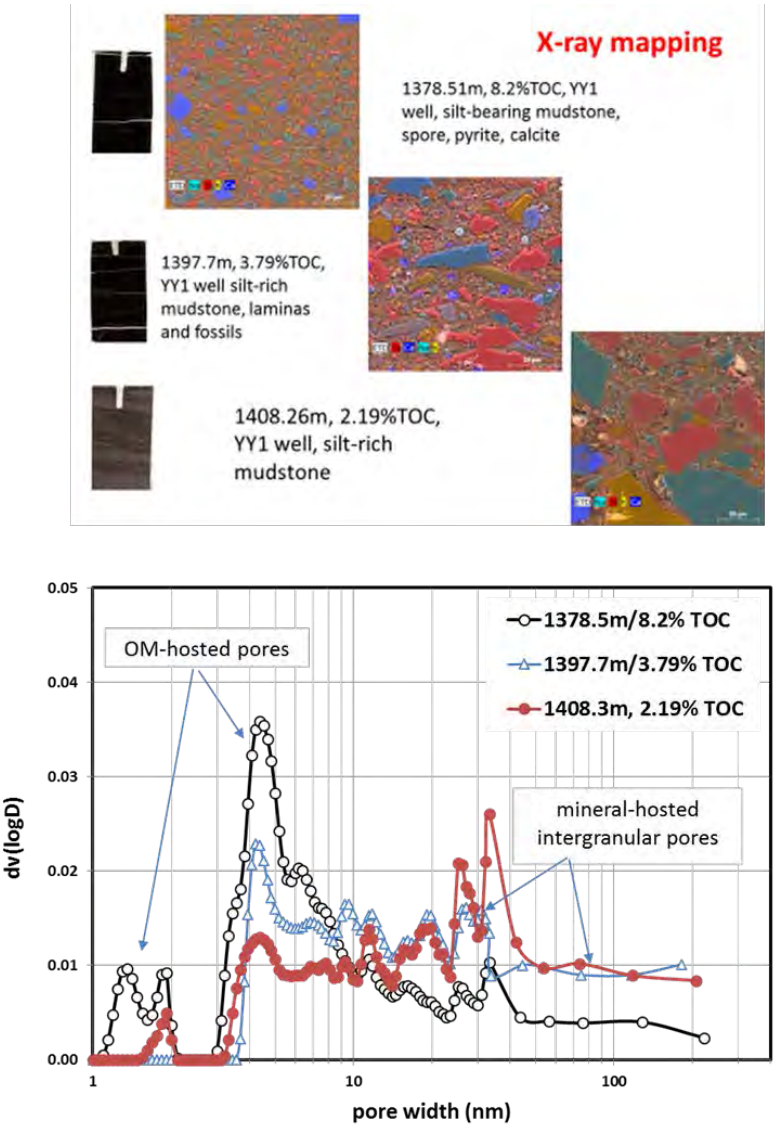

Figure 4. TOC and rock-grain assemblage are the main controls on pore-size distribution in the mudstones of the lacustrine Yanchang Formation. The upper graph is an X-ray map showing grain assemblage in silt-rich mudstone, silt-bearing mudstone, and organic-rich mudstone of the Yanchang Formation; the lower graph shows pore-size distribution from N_2 adsorption.

organic-rich mudstone (1,378.51 m) is 15.1% quartz, 18.7% K-feldspar + plagioclase, 7.2% carbonate (dolomite + calcite + siderite), 25.5% illite + mica, 4.2% chlorite, 25.2% I/S mixture, and 2.4% kaolinite. Grain-assemblage texture from silt-rich mudstone to silt-bearing mudstone to organic-rich mudstone tends to be finer (**fig. 4**), and clay mineral content increases.

Pore size distribution in the previous three samples displays a distinctive pattern and closely corresponds to lithology variation (**fig. 4**). Four peaks of organic-rich mudstone appear in PSD: 1 nm to 2 nm, 3 nm to 5 nm, 6 nm to 10 nm, and 20 nm to 70 nm. The 3 nm to 5 nm pores are dominant in organic-rich mudstone. Three peaks of silt-bearing mudstone appear in PSD: 4 nm to 5 nm, 6 nm to 10 nm, and 30 nm to 70 nm. Pores of 6 nm to 10 nm and 30 nm to 70 nm are dominant in silt-bearing mudstone. Three peaks of 1 nm to 2 nm, 4 nm to 5 nm, and 10 nm to 70 nm appear in PSD of silt-rich mudstone; 10-nm to 70-nm pores are dominant. Therefore, we infer that pores with different sizes represent different origins. Pores of 1 nm to 2 nm and 3 nm to 5 nm are associated with OM-hosted pores, pores of 6 nm to 10 nm with mineral-hosted intergranular pores and OM-hosted pores, and pores of 20 nm to 70 nm with mineral-hosted intergranular pores.

Extrabasinal source minerals constitute more than 90% of the fine-grain and coarse-grain supply in the Yanchang Formation; intrabasinal source minerals are minor. Therefore, compaction could be the key diagenetic factor in porosity reduction in organic-rich mudstone. OM-hosted pores are present but are dominated by < 10-nm pores, and increases with TOC content (**fig. 5**). It is expected that OM-hosted pores can be more abundant at a high-thermal maturity when burial temperature is hot enough for oil cracking to gas to take place. We need samples covering a wide range of thermal maturity to constrain the main controls to porosity development in the organic-rich mudstone of the Yanchang Formation.

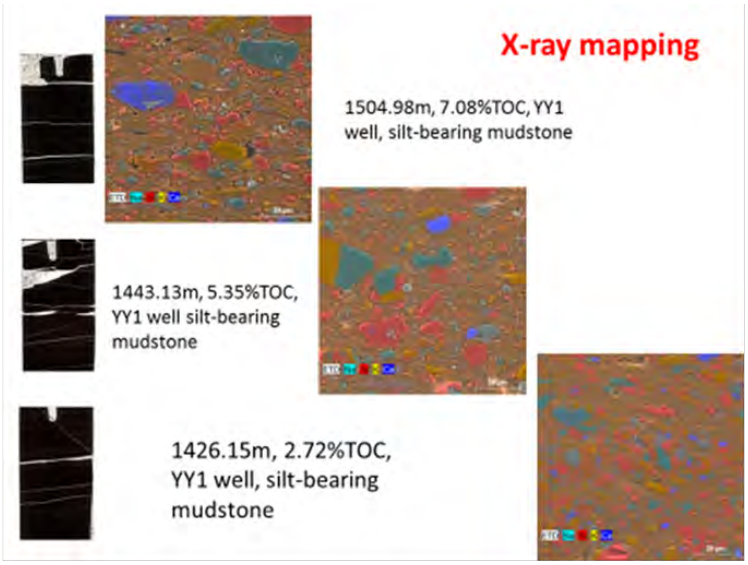

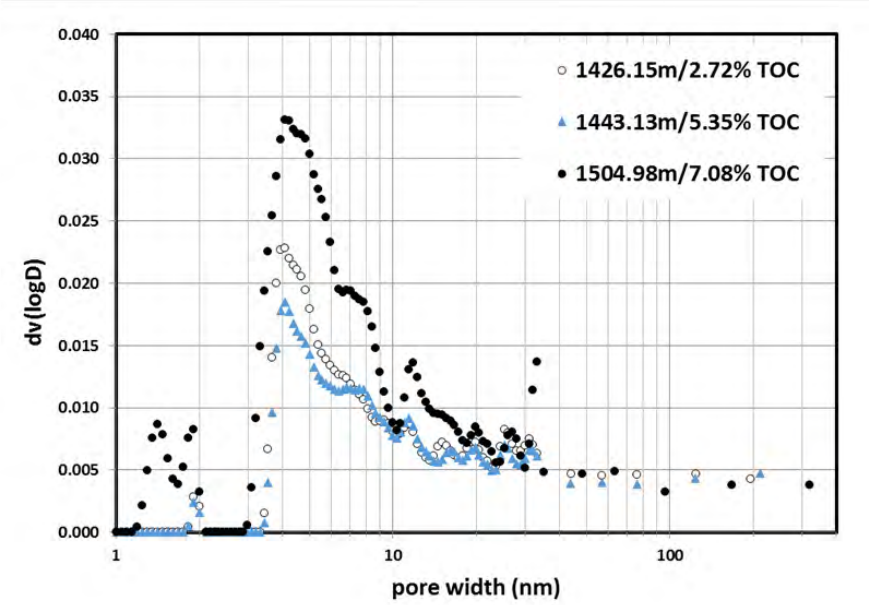

Figure 5. OM-hosted pores are dominated by < 10-nm pores as shown in silt-bearing mudstones with similar grain assemblage (X-ray mapping) but varied TOC contents in the YY1 well.

Effect of TOC Variation in Silt-Bearing Mudrocks on PSD

TOC variation in silt-bearing mudrocks affects the pore-size distribution. The silt-bearing mudstones with similar rock texture are shown in **Figure 5**. As TOC content varies from 2.72% to 7.08%, the PSD shows a similar pattern and dominates in OM-hosted pores (< 10-nm pores), further indicating that < 10-nm pores are mainly developed in organic matter particles. In contrast, the proportions of > 20-nm pores are almost equivalent to the decrease of TOC content, suggesting that mineral-hosted intergranular pores are dominated by the pores larger than 20 nm. Mineral-hosted intergranular pores are related to the primary grain assemblage.

An interesting observation is that organic-rich mudstones with abundant silt grains still contain intergranular mineral-hosted pores. The organic-rich sample at 1392.75-m depth has an abundant proportion of the pores greater than 10 nm in width, which are mineral-hosted intergranular pores. Larger than 5-um sized mineral grains, including quartz, feldspar, and even clay minerals, are composed of the rock texture, as shown in **Figure 6**. The organic-rich sample at 1451.02 m depth has a peak of PSD from 20- to 70-nm mineral-hosted intergranular pores. Larger than 20-μm sized mineral grains, including quartz feldspars, are abundant. The organic-rich sample at 1374.44 m has two minor peaks of PSD at 10-nm to 20-nm pores and 30-nm to 40-nm pores. Larger than 5-um sized mineral grains, including quartz and feldspar, are present in moderate amounts. These results clearly show that mineral-hosted intergranular pores are associated with primary grain assemblage, the more abundant, bigger grains, and the greater proportion of the mineral-hosted intergranular pores. We infer that compaction plays an important role in mineral-hosted intergranular pores.

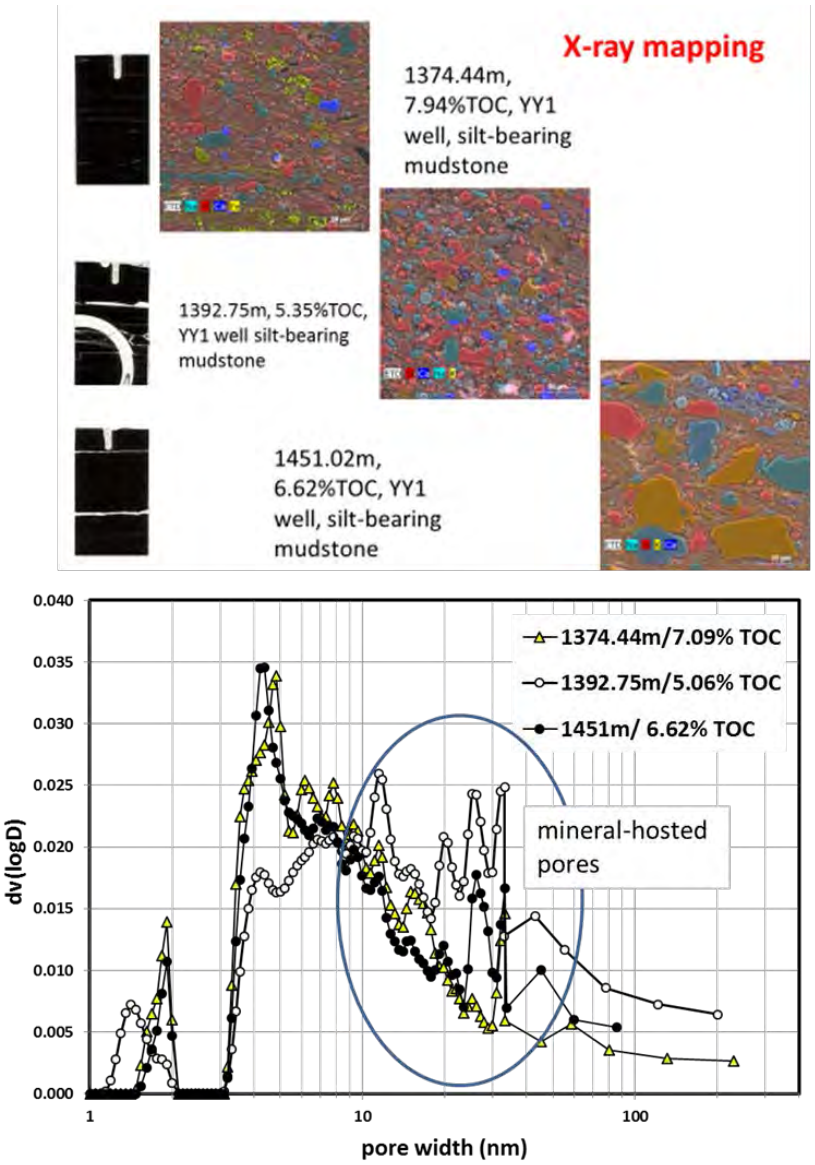

Figure 6. TOC variation in lacustrine argillaceous mudrocks, based on pore-size distribution in the YY1 well.

Effect of Oil Presence in Argillaceous Mudrocks on PSD

Study of pore-size distribution of 12 organic-rich argillaceous mudrock samples before and after oil cleaning with CH_2Cl_2 extraction was conducted, and the results of pore characterization for these 12 samples before and after oil cleaning are summarized in **Table 1**. Pore volume is obviously larger for the extracted samples than the unextracted ones; a similarly increased trend exists for BET surface area. As shown in **Figure 7**, the increased pore volume is mainly contributed by < 30-nm pores, but 30- to 300-nm pores make a minor contribution. We divided pores into four groups based on the pore size—< 10 nm, 10 nm to 20 nm, 20 nm to 30 nm, and 30 nm to 300 nm. Then we compared the increased pore volume in response to the pore size. The increased pore volumes for both < 10-nm pores and 10-nm to 20-nm pores are much higher than

the remaining two groups after oil cleaning, thereby suggesting that oil primarily stores in the less than 20-nm pores.

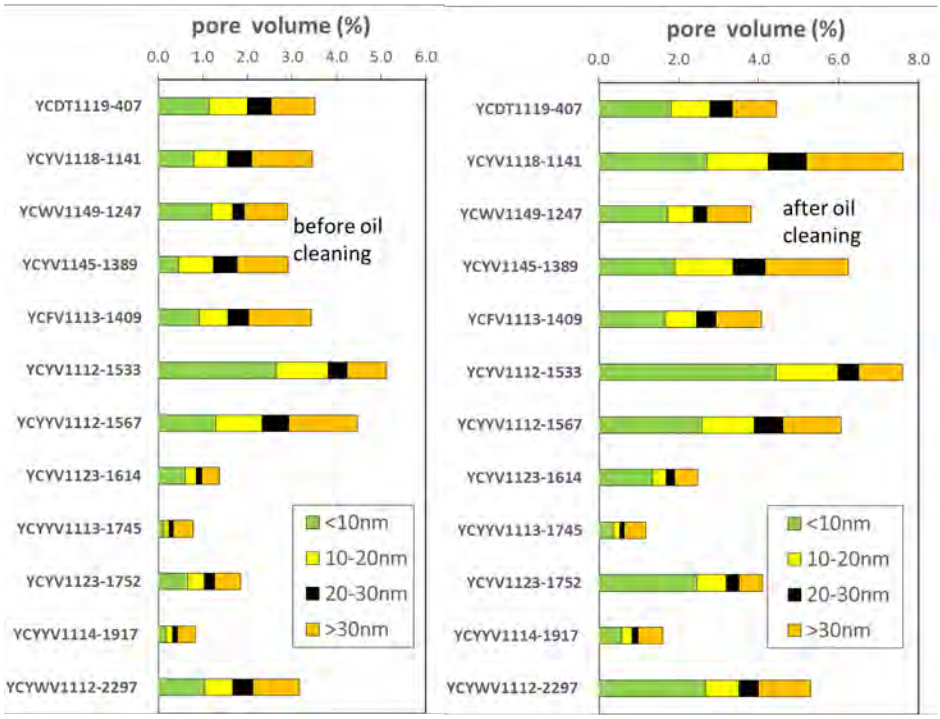

Figure 7. Comparison of pore volume change before and after oil cleaning with a CH_2Cl_2 extraction.

Table 1. Pore characterization of 12 organic-rich argillaceous mudrock samples from the Yanchang Formation before and after oil cleaning with CH_2Cl_2 extraction.

Sample ID	depth	BET surface	average pore	total pore volume	pore volume to different range of pore width (%)							
	m	area /m^2/g	diameter /nm	(%)	< 5nm	5-10nm	10-15nm	15-20nm	20-25nm	25-30nm	30-35nm	35-300nm
YCDT1119-407 no oil extraction	407.00	5.866	9.3	3.25	0.45	0.69	0.42	0.43	0.26	0.28	0.15	0.83
YCYV1118-1141 no oil extraction	1141.0	3.776	13.6	3.23	0.15	0.65	0.38	0.38	0.24	0.29	0.09	1.27
YCWV1149-1247 no oil extratction	1248.0	5.178	8.3	2.72	0.38	0.82	0.27	0.20	0.13	0.13	0.05	0.90
YCYV1145-1389 no oil extraction	1389.0	2.534	16.8	2.68	0.00	0.47	0.38	0.39	0.24	0.29	0.08	1.06
YCFV1113-1409 no oil extraction	1409.5	4.247	11.3	3.07	0.26	0.67	0.34	0.30	0.21	0.26	0.10	1.30
YCYV1112-1533 no oil extraction	1533.0	10.436	7.5	4.80	0.64	2.01	0.76	0.40	0.21	0.21	0.07	0.81
YCYYV1112-1567 no oil extraction	1567.0	5.68	11.7	4.14	0.29	0.99	0.55	0.49	0.26	0.34	0.13	1.41
YCYV1123-1614 no oil extraction	1614.1	2.821	7.6	1.33	0.21	0.40	0.15	0.09	0.06	0.06	0.01	0.39
YCYYV1113-1745 no oil extraction	1745.0	0.732	17.3	0.72	0.03	0.10	0.06	0.06	0.05	0.05	0.03	0.42
YCYV1123-1752 no extraction	1752.0	2.548	10.6	1.73	0.09	0.57	0.21	0.16	0.11	0.12	0.01	0.57
YCYYV1114-1917 no extraction	1917.0	0.87	14.6	0.78	0.06	0.13	0.06	0.09	0.05	0.06	0.02	0.39
YCYWV1112-2297 no oil extraction	2297.0	5.153	9.3	4.71	0.38	0.66	0.32	0.31	0.21	0.24	0.12	0.92
YCDT1119-407	407.00	9.30	7.60	4.16	0.80	1.00	0.57	0.41	0.26	0.29	0.17	0.95
YCYV1118-1141	1141.0	13.213	8.5	6.85	1.13	1.57	0.81	0.72	0.44	0.52	0.30	2.11
YCWV1149-1247	1248.0	8.153	6.9	3.51	0.78	0.95	0.37	0.27	0.14	0.18	0.11	0.99
YCYV1145-1389	1389.0	8.968	10.5	5.74	0.58	1.33	0.78	0.67	0.39	0.41	0.22	1.86
YCFV1113-1409	1409.5	7.288	8.4	3.88	0.57	1.09	0.42	0.35	0.23	0.26	0.11	1.03
YCYV1112-1533	1533.0	19.365	6.1	7.09	1.59	2.85	1.00	0.54	0.27	0.25	0.12	0.97
YCYYV1112-1567	1567.0	12.135	7.5	5.60	1.05	1.53	0.73	0.56	0.32	0.39	0.18	1.27
YCYV1123-1614	1614.1	10.334	6.2	3.99	0.60	0.76	0.20	0.13	0.08	0.13	0.04	0.55
YCYYV1113-1745	1745.0	2.174	9.2	1.13	0.09	0.28	0.09	0.08	0.05	0.06	0.01	0.53
YCYV1123-1752	1752.0	10.334	6.4	4.11	0.90	1.56	0.46	0.28	0.13	0.18	0.05	0.54
YCYYV1114-1917	1917.0	2.873	8.7	1.52	0.15	0.43	0.15	0.10	0.06	0.09	0.02	0.60
YCYWV1112-2297	2297.0	14.395	5.6	4.91	1.57	1.10	0.46	0.38	0.24	0.25	0.17	1.13

The increased volume of 0.35-nm to 300-nm pores shows a good linear correlation with the increased BET surface area after oil cleaning with CH_2Cl_2 extraction (**fig. 8a**). The pores smaller than 10 nm make the major contribution to BET surface area, and the increased BET surface after oil cleaning indicates that the < 10-nm pores were exposed. Linear correlation between the increased BET surface area and the increased pore volume provides further evidence that the < 10-nm pores play an important role in oil storage in the organic-rich argillaceous mudrocks of the Yanchang Formation.

The increased volume of 0.35-nm to 300-nm pores shows a positive correlation with the amount of extracted organic matter with CH_2Cl_2 (**fig. 8b**). Given a density of 0.85 g/ml for the extracted organic matter (EOM), the calculated volume of EOM for our studied samples ranges from 3.7- to 13.5-ul/g rock, which is similar to the measured values of the increased pore volume (3.1- to 15.4-ul/g rock). This consistency provides a cross-check for the reliability of our pore volume and PSD measurement using the N_2 adsorption method.

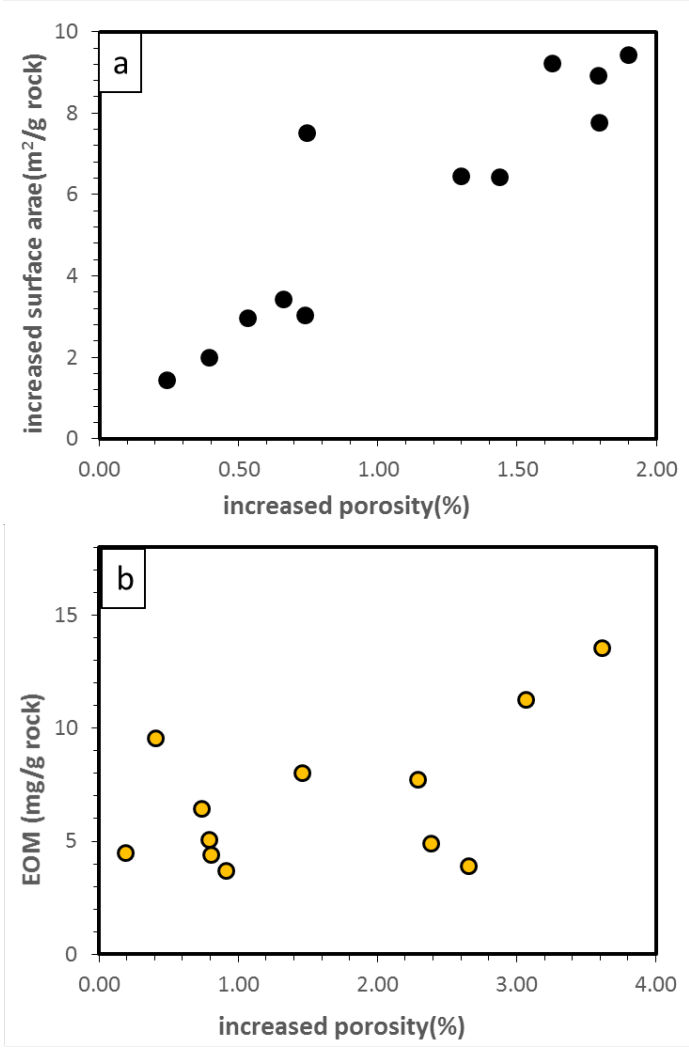

Figure 8. Relationship between increased pore volume and increased BET surface area (a), and amount of extracted organic matter (b) after oil cleaning with CH2Cl2 extraction.

Pore Fluids Storage with Respect to Pore-Size Distribution

The 20 to 50 mesh-sized oil-bearing samples were initially dried at 110°C for 12 hours under vacuum conditions and then extracted by pentane to remove mobile oil, which is composed of saturate and aromatic fractions. They were subsequently extracted by CH_2Cl_2 for asphaltane removal. The PSD of the as-received, dried, pentane-extracted, and CH_2Cl_2-extracted four aliquots of the same sample was determined by using N_2 adsorption isotherms. Comparison of PSD among the four aliquots reveals pore fluid distribution corresponding to the different sizes of pores.

Total pore volume and BET surface area are the lowest for moisture-containing samples; however, both values significantly increase after the samples were dried at 110°C (**Table 2**). The increased pore volume is mainly attributed to the exposed pores with less than 10 nm in width when comparing the PSD before and after the sample was dried (**fig. 9a and 9b**). The exposed pores after drying could be partially filled with connate water residual and moisture adsorption from air in post-coring storage, and those pores could also be storage spaces for gas and light oil volatiles that escaped after coring. Our results suggest that the less than 10-nm sized pores, mainly hosted in clay minerals and organic matter, play an important role in connate water storage in Triassic clay- and organic-rich lacustrine Yanchang mudstones. Less than 10-nm sized pores might be available spaces for oil and gas storage when gas/oil saturations are high. The wettability of less than 10-nm sized pores tends to be water wet even in the presence of oil.

Table 2. Pore characterization of three organic-rich argillaceous mudrocks from the Yanchang Formations under four different conditions.

Sample ID	depth (m)	sample treament condition	BET surface area m^2/g rock	average pore diameter /nm	total pore volume (%)	pore volume to different range of pore width (%)							
						< 5nm	5-10nm	10-15nm	15-20nm	20-25nm	25-30nm	30-35nm	35-300 nm
YY1-1070	1378.5	as received (moisture+oil)	1.765	10.6	1.16	0.13	0.27	0.11	0.08	0.07	0.07	0.01	0.48
		dry with oil	8.835	6.07	3.25	0.54	1.44	0.33	0.19	0.10	0.08	0.00	0.63
		after pentane extraction	12.293	6.05	4.46	1.13	1.83	0.39	0.24	0.12	0.14	0.04	0.56
		after CH_2Cl_2 extraction	17.853	5.38	5.69	1.79	2.04	0.49	0.30	0.16	0.18	0.11	0.82
YY1-2103	1504.98	as received (moisture+oil)	1.579	10.1	1.00	0.12	0.20	0.06	0.12	0.05	0.05	0.01	0.42
		dry with oil	8.53	6.07	3.23	0.61	1.34	0.33	0.19	0.11	0.09	0.00	0.62
		after pentane extraction	12.847	6.3	4.83	0.61	1.34	0.33	0.17	0.13	0.09	0.11	0.47
		after CH_2Cl_2 extraction	15	5.5	4.96	1.57	1.56	0.44	0.28	0.16	0.16	0.10	0.98
YCYYV1112-1567	1567	as received (moisture+oil)	1.96	12.5	1.56	0.08	0.35	0.20	0.18	0.13	0.12	0.05	0.52
		dry with oil	3.749	12.04	2.84	0.17	0.69	0.41	0.34	0.21	0.24	0.11	0.91
		after pentane extraction	6.775	9.4	3.98	0.45	1.12	0.56	0.44	0.25	0.27	0.11	1.16
		after CH_2Cl_2 extraction	9.573	8.3	4.90	0.77	1.26	0.65	0.51	0.30	0.31	0.18	1.47

Total pore volume and BET surface area increase after cleaning oil with a solvent extraction, and 2 to 300-nm sized pores were largely exposed and made a dominant contribution to the increased pore volume (**fig. 9c and 9d**). Less than 2-nm sized pores were exposed, in particular after dichloromethane extraction, indicating that asphaltane-heavy molecules can be adsorbed on the surface of tiny pores with the width equivalent to asphaltane molecular size (0.5 to 3 nm). Compared with dried samples without oil cleaning, the increased pore volume of pentane-extracted and CH_2Cl_2-extracted samples is mainly contributed by the < 20-nm pores, suggesting that oil mainly stores in pores of less than 20 nm in Triassic clay- and organic-rich lacustrine Yanchang mudstones.

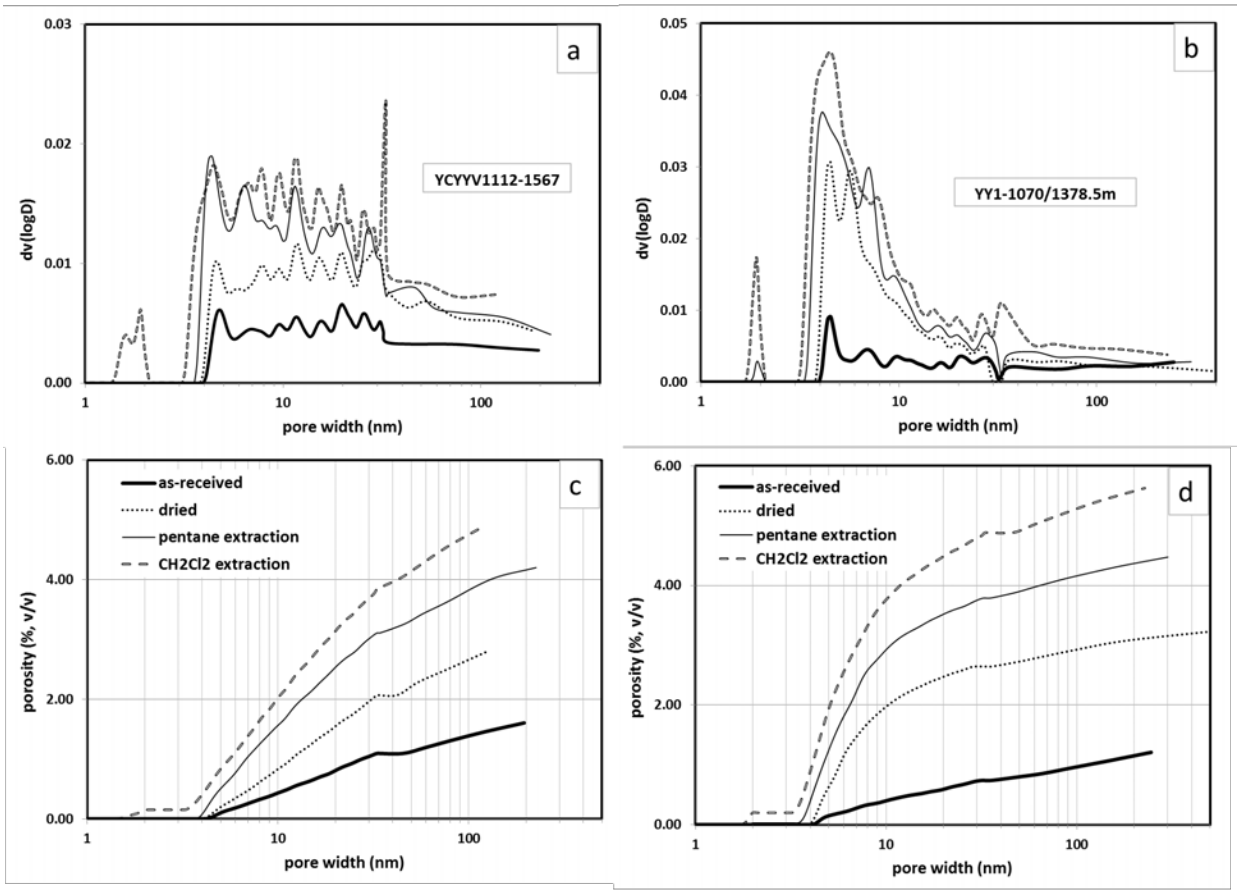

Figure 9. Comparison of PSD and pore volume in the four aliquots of the same sample, including as-received, dried, pentane-extracted and CH_2Cl_2 extracted. Two samples are YCYYV1112-1567 (a, c), YY1-1070 (b, d).

The sequential pore-fluid removal method was applied to estimate pore-fluid distribution and fluid saturation. For an as-received core sample, the pores are filled with connate water and residual oil and air. The air-filled pores of an as-received sample were occupied by gas and light oil under a reservoir condition; the oil escaped from degassing during and after coring. At the beginning of N_2 adsorption, approximately 0.5 g to 1.0 gas-received core sample is exposed to a high-vacuum condition and all the air-filled pores are emptied and ready for gas filling in the course of N_2 adsorption. Therefore, gas/light oil-filled porosity can be determined with an as-received core sample. The better the core sample is preserved, the more reliable the gas-filled porosity or gas saturation is expected to be. Core sample preservation is the key to obtaining a reliable fluid-saturation measurement. A wax-seal core plug is the correct solution for core preservation or drill cuttings. The difference in pore volumes between dried and as-received aliquots of the same sample represents the pore volume occupied by connate water or moisture, which can be used to determine water saturation. Similarly, the difference in pore volumes between dried and CH_2Cl_2-extracted aliquots of the same sample represents the pore volume occupied by both mobile oil and asphaltane, which can be used to determine oil saturation. The obvious advantage of the sequential pore fluid removal method not only provides fluid saturation, but also reveals pore fluid distribution with respect to pore size.

Figure 10 shows a method for determining gas, water, and oil saturation by N_2 adsorption with sequential fluid removal. TOC content values for YCYYV1112-1567 and YY1-1070 are 4.52% and 8.2%, respectively. Gas saturation values are 31% and 19%, and YCYYV1112-1567 is approximately 10% higher. Water saturation are 26% and 36%, and YCYYV1112-1567 is approximately 10% smaller. Oil saturations are 44% and 45%, and both samples are similar. The uncertainty about the fluid saturation is mainly attributable to the condition of core preservation. If well-preserved core sample is available, gas, water, and oil saturation can be reasonably determined. The method also can use drill cuttings if the drill cuttings are carefully preserved with the wax-seal approach. Comparison studies by using core samples and drill cuttings are needed for assessing the reliability of fluid saturation measurement by using drill cuttings. Our studies clearly demonstrate that the presence of pore fluids can make a significant difference in porosity measurement; therefore, consistency in sample pretreatment should be applied when comparing porosity using different methods.

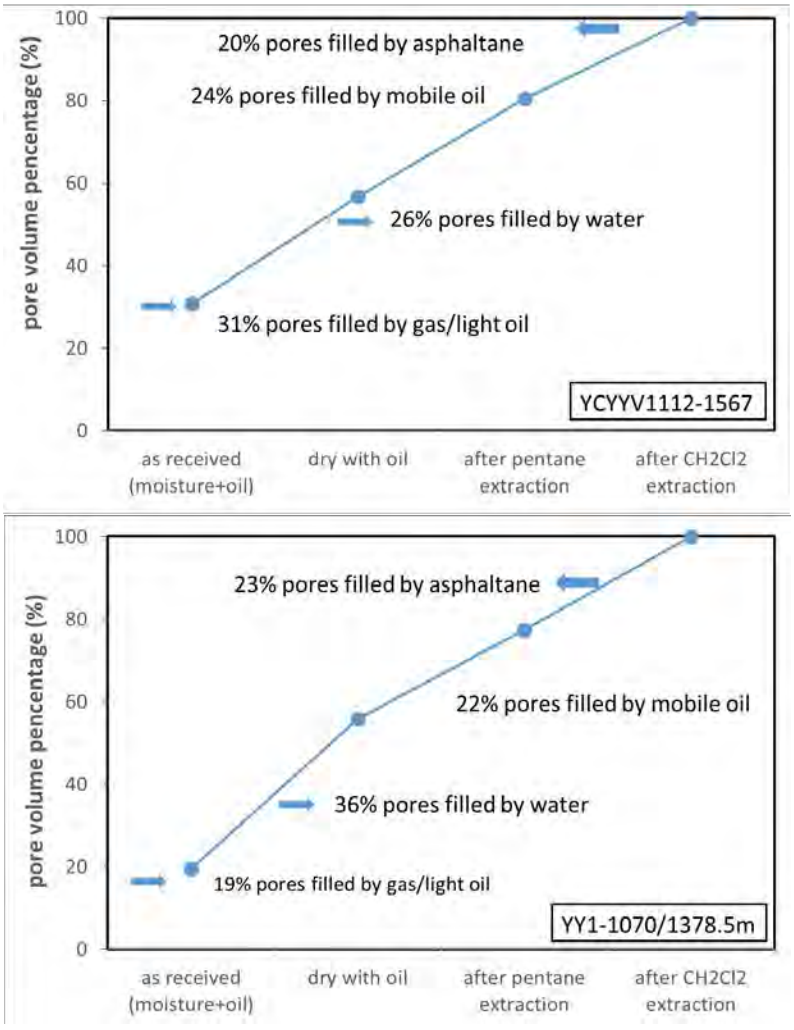

Figure 10. Two examples showing to determine gas, water and oil saturation by N2 adsorption with sequential fluid removal method. The two samples are YCYYV1112-1567 (upper graph), YY1-1070 (lower graph).

The difference in gas saturation and water saturation between YCYYV1112-1567 and YY1-1070 may be attributable to the textural difference. The main textural difference is the silt size. The 1567 sample has silt that ranges from very fine to coarse (almost sand size), whereas the 1070 sample has silt that is much finer (nearly clay-size). Such contrasts in the size of the silt can lead to significant differences in bulk properties, as was demonstrated by the saturations and pore sizes reported herein.

Conclusions

1. In the absence of cementation (Milliken report, this volume), compaction and organic maturation are the main controls on porosity evolution in silt-bearing mudstones of the lacustrine Yanchang Formation.

2. Texture, as expressed by silt content and size, and OM-content affect the pathways of porosity modification during compaction and maturation. Silt content is associated with the preservation of larger pores. OM content, which is higher in relatively silt-poor samples, is associated with the loss of large pores and the generation of very small OM-hosted pores.

3. Pores less than 10 nm in width are dominant in finer-grained and organic-rich mudstones of the Triassic lacustrine Yanchang Formation. Pores greater than 20 nm in width are dominant in organic-lean, silt-rich mudstones and sandstones.

4. The increased pore volume observed after solvent extraction is attributed to pores of all sizes. However, in OM-rich, finer-grained lithologies, the pores opened by extraction are primarily less than 20 nm, thereby suggesting that these pores are contained within OM.

5. The sequential pore fluid removal method provides a way to determine gas, oil, and water saturation, as well as pore fluid distribution with respect to pore size.

References

Hu, H., Zhang, T., Wiggins-Camacho, J.D., Ellis, G.S., Lewan, M.D., and Zhang, X., 2015, Experimental investigation of changes in methane adsorption of bitumen-free Woodford Shale with thermal maturation induced by hydrous pyrolysis: Marine and Petroleum Geology, v. 59, p. 114–128.

IUPAC (International Union of Pure and Applied Chemistry), 1994, Physical Chemistry Division Commission on Colloid and Surface Chemistry, Subcommittee on Characterization of Porous Solids: Recommendations for the characterization of porous solids (Technical Report): Pure and Applied Chemistry, v. 66, no. 8, p. 1739–1758.

Kuila, U., and Manika, P., 2011, Surface area and pore-size distribution in clays and shales: Society of Petroleum Engineers, Paper No. SPE-146869, 13 p.

Longman, Mark, and Kocman, Katie, 2014, Petrography of the Bakken black shales in the eastern Williston Basin: invited talk presented at Bakken/Three Forks/Plus Emerging Plays AAPG Geosciences Technology Workshop, Green Center, Colorado School of Mines, Golden, CO, 17–-19 November 2014.

Thommes, M., 2010, Physical adsorption characterization of nanoporous materials: Chemie Ingenieur Technik, v. 82, p. 1059–1073.

Zhang, T., 2014, Hydrocarbon geochemistry and pore characterization of the Bakken Formation and implication for oil migration and oil saturation: invited talk presented at Bakken/Three Forks/Plus Emerging Plays AAPG Geosciences Technology Workshop, Green Center, Colorado School of Mines, Golden, CO, 17–19 November 2014.

TASK 3.3

Porosity and Permeability Measurement for Yanchang Samples Using the GRI Method

Sheng Peng and Tongwei Zhang[1]

[1]Bureau of Economic Geology, Jackson School of Geosciences, The University of Texas at Austin, Austin, TX

Problem Statement and Objectives

Porosity and permeability are two of the most important petrophysical parameters for reservoir characterization. This task aims to measure porosity and permeability with crushed samples using the GRI method. Samples with different pretreatments were used to investigate the influence of residual moisture and oil on porosity and permeability. Specifically, the objectives are to 1) measure porosity and permeability for oven-dried and cleaned crushed samples and 2) measure porosity and permeability for samples with residual moisture and/or oil to investigate the influence of residual moisture, oil, and immobile components on porosity and permeability, and their implications to fluid storage.

Samples and Methods

A total of 26 samples from YY1 and YY2 were used for clean and dry porosity and permeability measurement. The samples as-received were crushed to 20/50 meshes (0.3 mm to 0.85 mm) and cleaned with pentane and dichloromethane extractions. The cleaned samples were then oven-dried under a vacuum at 110°C for 24 hours. Approximately 10 to 30 gram samples were used for the measurement.

Sample YY1567 was selected for different pretreatment analysis. As-received samples were subdivided into four sets. One set was kept as as-received. The other three were pretreated by oven-drying at 110°C for 24 hours, pentane extraction and oven-drying, dichloromethane extraction and oven-drying, respectively.

Bulk density was calculated through volume and mass measurement for bulk samples. Bulk volume was measured using a laser scanner (NextEngine 3D Scanner) with a resolution of 0.1 mm and a measurement error of less than 0.1% for a standard volume of 51.48 cm^3. Bulk density was then calculated with oven-dry mass and bulk volume. These bulk-density values were in turn used to calculate bulk volume for the crushed samples, based on the crushed sample mass.

The GRI method (Luffel and Hopkins, 1993; Guidry and others, 1995; Cui and others, 2009) was used to measure porosity and permeability in this study. No plug samples were available from the cores, and thus, no plug permeability was measured. The GRI permeability method has been increasingly applied because it has a simple experimental setup and is considerably faster than the traditional steady-state or pulse-decay methods. No requirement for intact plug sample is also an advantage in many cases.

An experimental setup for the GRI method is shown in Figure 1. Helium is provided with a high-pressure gas tank and is directed to the reference cell. After gas pressure stabilizes in the reference cell, the valve between the tank and reference cell is closed, helium is then introduced to the core holder by opening the connecting valve. At first, helium occupies the dead volume in the sample cell and subsequently penetrates into the sample particles. After the gas-expansion experiment, initial pressure and equilibrium pressure in the sample cell are used to calculate the porosity based on Boyle's law, as introduced in Cui and others (2009):

$$V_g = \frac{V_s\left(\frac{P_e}{Z_e}-\frac{P_0}{Z_0}\right)-V_r\left(\frac{P_{r0}}{Z_{r0}}-\frac{P_e}{Z_e}\right)}{\frac{P_e}{Z_e}-\frac{P_0}{Z_0}} \quad (1)$$

$$\emptyset = 1 - \frac{V_g}{V_b} \; or \; \emptyset = 1 - \frac{\rho_b}{\rho_g} \quad (2)$$

where V_g, V_b is grain and bulk volumes, respectively, V_s and V_r is sample cell volume and reference volume, respectively, and P_e, P_0, P_{r0} is equilibrium pressure, initial pressure at sample cell, and initial pressure at reference cell. ϕ is porosity, Z is compressibility factor, which can be approximated as one in a low-pressure range (0 to 200 psi).

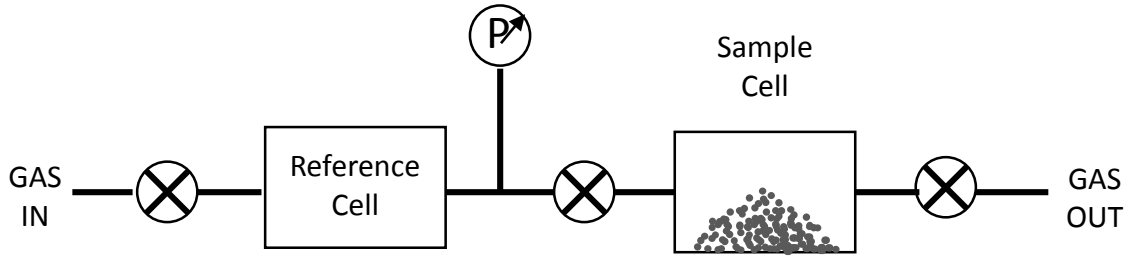

Figure 1. Schematic experimental setup for the GRI method.

By considering that density is a function of pressure, the gas flow model is as follows:

$$\phi \frac{1}{P}\frac{\partial P^2}{\partial t} = \frac{k}{\mu}\frac{1}{r^2}\frac{\partial}{\partial r}\left(r^2\frac{\partial P^2}{\partial r}\right) \quad (3)$$

Profice and others (2011) provided a form of analytic solution of P for (**Equation 3**):

$$P(t) = \sqrt{\frac{3\gamma K}{3\delta K {r_0}^2 + {r_0}^3} + \frac{2}{r_0}\sum_m \frac{\gamma K exp(-\frac{{\varepsilon_m}^2 Kt}{{r_0}^2})\sin(\varepsilon_m)}{r_0(\delta K \varepsilon_m \cos(\varepsilon_m)+(r_0+2\delta K)\sin(\varepsilon_m))} + {P_0}^2} \quad (4)$$

with:

$$\gamma = \delta {r_0}^2 (P_0^2 - P_i^2) \quad (5)$$

$$\delta = \frac{\mu(V_r+V_d)/P}{A_{ex}k} \quad (6)$$

$$K = \frac{k}{\phi\mu/P} \quad (7)$$

A_{ex} is the total particle exchange area, which is approximated as $V_s \cdot 3/r_0$ by assuming a spherical shape of the particles, and V_s is m/ρ_b (total particle mass over bulk density). The ε_m are the roots of the following:

$$\tan(\varepsilon_m) = \frac{\varepsilon_m}{1+\frac{\delta K \varepsilon_m{}^2}{r_0}} \tag{8}$$

This analytic solution, as well as (**Equations 4 through 7**), is obtained based on the assumption of the spherical shape of the crushed-sample particles and constant compressibility, which may lead to a slight deviation with the measured value. To better reflect the shape of the pressure drop, a linear transformation of the measured pressure is made by the following:

$$P_r = \frac{P-P_e}{P_i-P_e} \tag{9}$$

and the curve fitting is conducted on the P_r-t data set based on (**Equations 4 through 9**). All the calculations with above equations are based on standard metric units and permeability is converted to and reported in unit of nD.

Results and Discussion

Porosity and Permeability for Clean Samples

Figure 2 shows a typical pressure drop curve and the fitting using Profice's analytical solution. Using the initial and equilibrium pressures, porosity can be calculated based on **Equations 1 and 2**. Permeability can be calculated based on **Equations 3 through 9**. **Table 1** includes all the results.

Table 1. GRI porosity and permeability. Nitrogen porosity is also included for comparison.

Well name	Sample ID	Depth (m)	He porosity	N_2 porosity (%)	He permeability (nD)	Estimated Core Lab perm (nD)
YY1	838	1347.96	9.6	3.9	NA	NA
YY1	934	1364.69	4.9	7.1	0.2	5.1
YY1	1070	1378.51	2.2	4.3	0.3	6.9
YY1	1257	1397.66	5.0	4.7	0.4	13.4
YY1	1418	1409.26	5.3	3.2	0.1	2.0
YY1	1610	1426.15	2.1	3.0	0.1	2.0
YY1	1775	1451.02	6.2	5.3	0.7	24.9
YY1	1907	1469.08	2.3	5.2	0.1	2.0
YY1	2037	1497.07	4.0	5.4	0.5	15.2
YY1	2103	1504.98	3.5	5.0	0.4	13.0
YY22	2560	1317.88	4.3	5.9	0.8	30.2
YY22	2676	1329.17	5.5	6.4	0.6	20.4
YY22	2746	1336.03	4.6	3.6	0.7	27.5
YY22	2858	1346.87	4.5	4.7	0.4	13.0
YCYV1112-1533	1112	1533	1.7	7.5	0.1	1.8
YCYYV1112-1567	1112	1567	5.7	5.6	0.6	20.9
YCYWV1112-2297	1112	2297	7.2	4.8	0.7	28.6
YCFV1113-1409	1113	1409	4.8	3.8	0.3	8.8
YCYYV1113-1745	1113	1745	4.2	1.1	0.2	3.8
YCYYV1114-1917	1114	1917	3.6	1.5	0.1	2.0
YCYV1118-1141	1118	1141	9.7	6.7	0.9	38.5
YCDT1119-407	1119	407	5.7	4.1	0.4	11.3
YCYV1123-1614	1123	1614	2.8	4.0	0.1	2.9
YCYV1123-1752	1123	1752	0.5	4.3	0.1	0.8
YCYV1145-1389	1146	1389	5.2	5.8	0.7	28.6
YCWV1149-1247	1149	1247	2.7	3.5	0.2	6.6

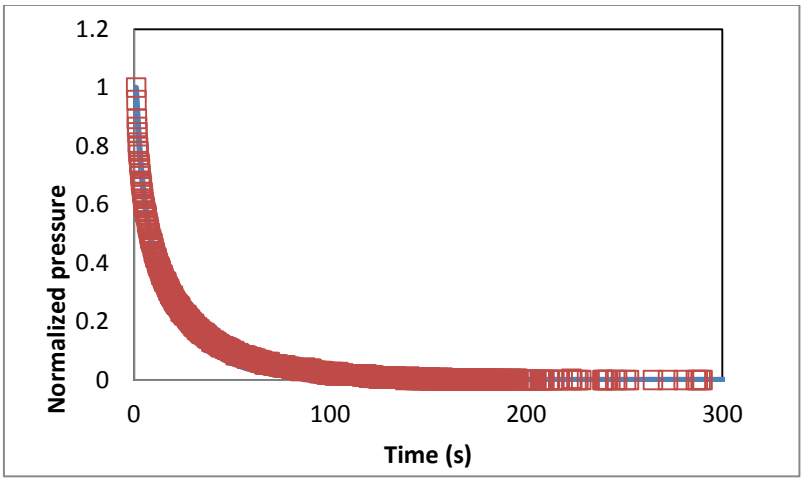

Figure 2. A typical pressure-drop curve in GRI measurement. Red square is measured data, blue curve is the fitting using Profice's solution.

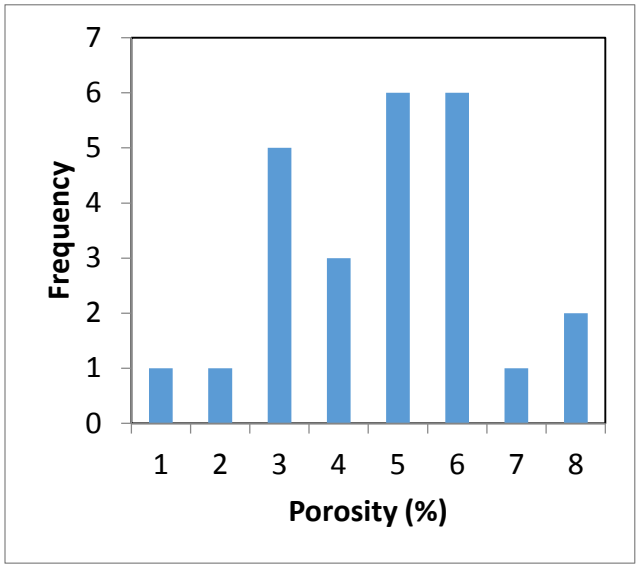

Figure 3. Frequency histogram of porosity.

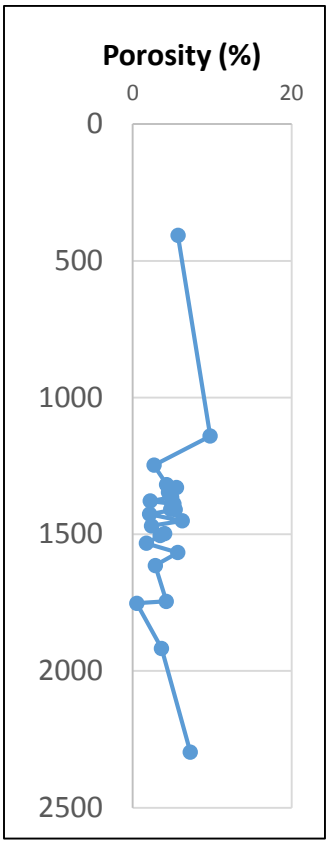

Figure 4. Porosity along the depth (m).

Observation of **Figure 3** reveals that most of the porosity ranges from 2% to 6%. This range is in relative agreement with that from the literature (Tang and others, 2012; Wang and others, 2015). Tang and others (2014) calculated acoustic logging porosities ranging between 3 and 8% for the C9 shale interval and 3 and 6% for the C7 shale interval, and Wang and others (2015) mentioned

that mercury porosimetry analysis gave a mean porosity of 5.27% and a range between 1.93% and 7.65%. The distribution of porosity along depth is shown in **Figure 4**. It can be seen that the porosity distribution has some "Z" shaped pattern between the depths of 1,200 m to 2,000 m.

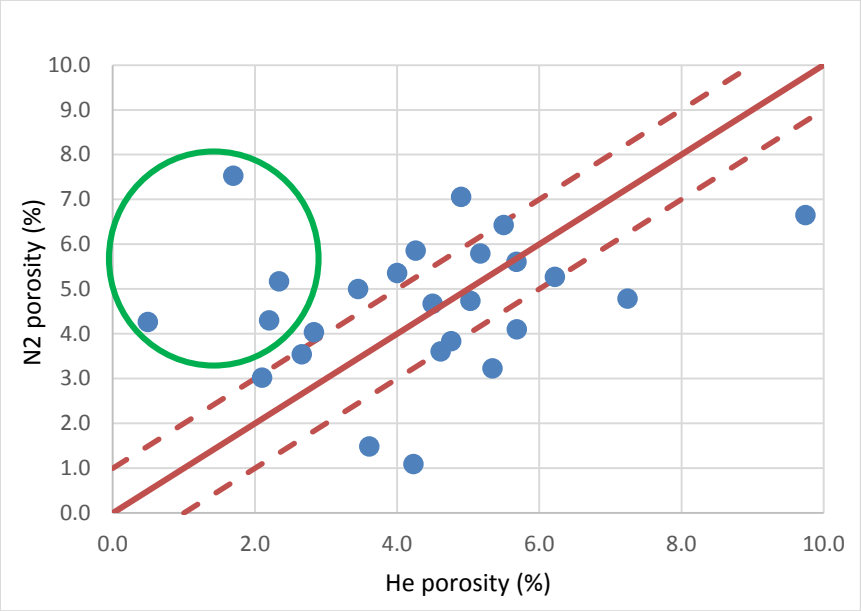

Figure 5. Comparison between He porosity and N_2 porosity. Solid red line is 1:1 line. Upper dash red line denotes He porosity = N_2 porosity – 1%, lower dash red line denotes He porosity = N_2 porosity + 1%.

Helium porosity is also compared with porosity measured from nitrogen adsorption. A major part of the samples lies around or within the two red dash lines, indicating similar He and N_2 porosity. Because the N_2 adsorption method cannot measure pores larger than approximately 200 nm, it is expected that He porosity is larger than N_2 porosity for samples with substantial > 200 nm pores, as shown by the data points at the right lower side of the lower red dashed line. There are some samples showing larger N_2 porosity, as those in the circle, however, this should be related to the sample representativeness. Approximate 0.5-g samples are used in N_2 adsorption experiment, whereas 10-g to 30-g samples are used in GRI porosity. Therefore, the small amount of samples used in N_2 adsorption experiment may not be adequate to reflect the overall porosity.

Permeability values from the Yanchang samples are generally low. GRI permeability using Profice's solution ranges from 0.1 nD to 0.7 nD. The pressure-drop data were also estimated through Core Lab's permeability software. The results are from 0.8 nD to 38.5 nD (Table 1). The results from Profice's solution and CoreLab's estimation can be used as the range of the permeability for the Yanchang samples. The relative wide range of the permeability for each sample also highlights the uncertainty in permeability measurement for the mudrock samples.

Porosity and Permeability for Samples with Different Pretreatments

Sample YY1567 was subdivided into four sets, each with a different pretreatment, as previously mentioned. An oven-dried sample contains no moisture, but a pentane-extracted and dried sample does not have residual oil (mobile oil) and moisture, and the CH_2Cl_2 extracted and dried sample contains no residual heavy oil (asphaltenes), light oil, and moisture. Figure 6 shows the porosity measurement results. It can be seen that He porosity increases with further extraction of residual oil and moisture. From the difference between the measured He porosity and the adjacent pretreatment, residual water saturation is calculated as 29.8%, which is equal to (4.5 to 2.6)/6.4. Similarly, residual oil saturation is 7.8%, whereas the immobile component (asphaltenes) saturation is 20.3%.

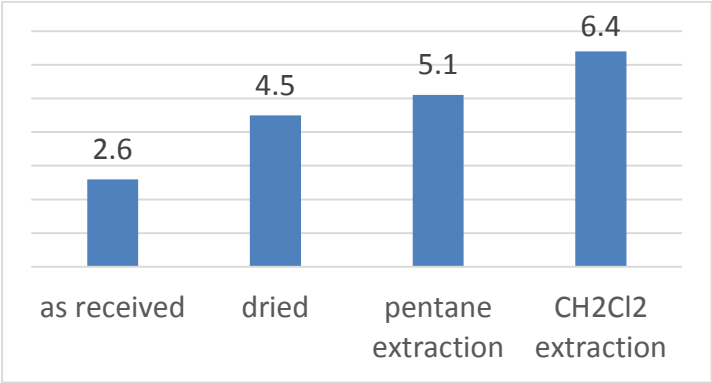

Figure 6. Porosity (percent) for YY-1567 with four different pretreatments.

Nitrogen porosity was also measured for YY-1567 after four different pretreatments. Comparison of the nitrogen and helium porosity is shown in Figure 7. He porosity is consistently larger than N_2 porosity for this sample, and the difference is consistently at approximately 1.5%. This indicates that 1) YY-1567 has substantial pore volume with pores larger than 200 nm, and the porosity of the pores larger than 200 nm is 1.5%, which is 30% of the total porosity, and 2) most of the residual moisture, oil, or immobile components are contained in pores smaller than 200 nm. In other words, for YY-1567, the > 200-nm pores are more likely to be occupied by either water or light oil (under in-situ conditions), which was removed by evaporation during the process of core drilling and sample preparation.

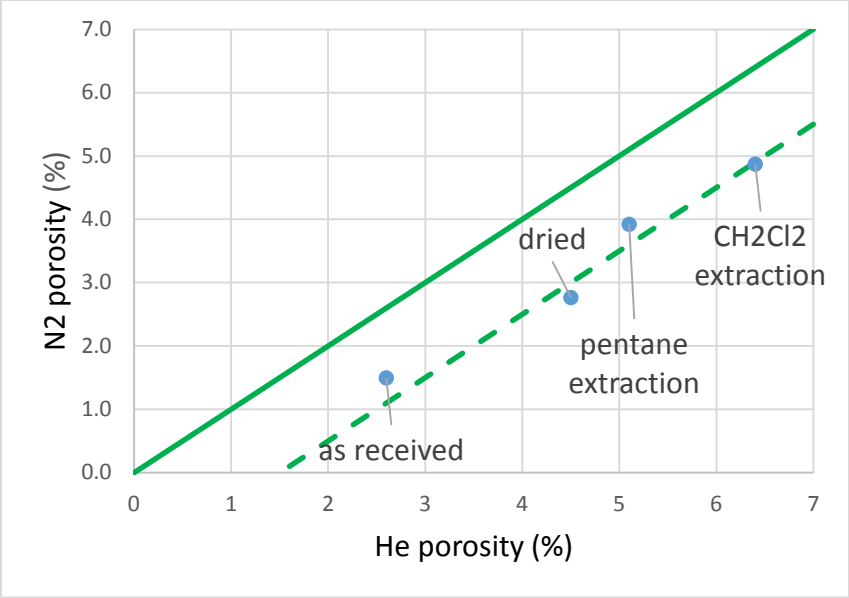

Figure 7. He and N_2 porosity comparison for YY-1567 with four different pretreatments.

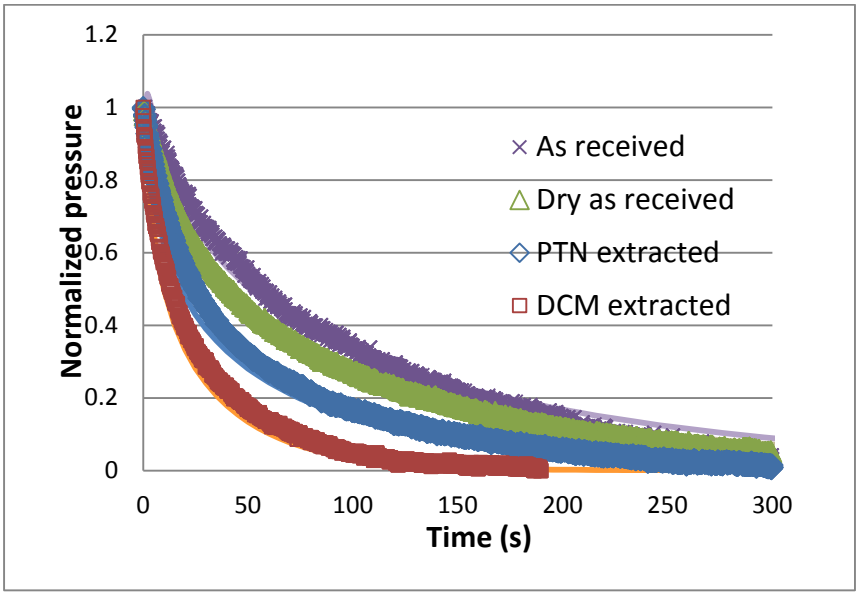

Figure 8. Pressure drop curves for YY-1567 with four different pretreatments.

Permeability was also measured for YY-1567 with four different pretreatments. **Figure 8** shows the pressure-drop curves. A faster drop of pressure indicates higher permeability, therefore, the trend of permeability increase is consistent with increased He porosity.

The relative distribution of residual moisture, oil, and immobile components provides a path for relative permeability analysis. Relative permeability (K_r) is calculated as permeability at different pretreatment status divided by the clean-and-dry permeability. **Figure 9** shows the relation between the relative permeability and gas saturation. Oak and others (1990) proposed an empirical equation to describe relative permeability as follows:

$$K_r = \frac{(S-S_r)}{(1-S_r)^b} \quad (10)$$

where S is the gas saturation, S_r is the minimum moisture and oil saturation. S_r is determined as 30 percent. The best fit of Equation 10 to the measured data results in a b value of 2.46.

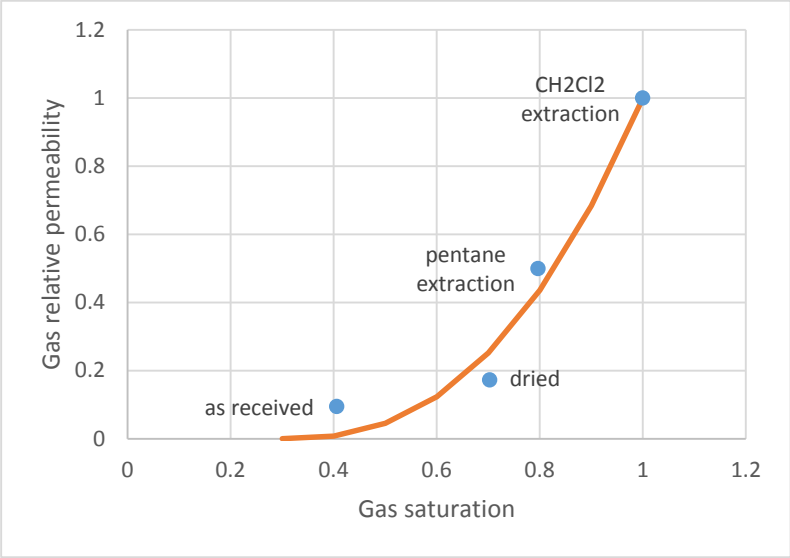

Figure 9. Relationship between relative gas permeability and gas saturation.

Observation of **Figure 9** reveals a few important implications on relative distribution of the residual moisture, oil, and immobile components. From an as-received to a dried sample, there is a relatively large porosity increase, which is caused by the removal of residual water in the sample, and it accounts for 30% of the porosity. However, the permeability does not increase proportionally. Instead, only a small amount of permeability increase is observed. This indicates that the residual water is primarily distributed in the pores that do not contribute significantly to the flow. These pores should be hydrophilic pores for water to not be stored, and thus most likely are mineral pores. The slight contribution of these pores to the permeability then suggests that the mineral pores are not well connected with the main percolating pore network.

In contrast, when comparing a dried sample with a pentane extracted sample, it can be seen that a relatively small increase of porosity leads to a substantial permeability enhancement. This indicates that the residual oil occupies pores that contribute dominantly to the flow. Further, after the immobile components (asphaltenes) are removed, although the porosity increase is moderate, a significant increase of permeability is produced. This indicates that the immobile components, that is, asphaltenes, lie in locations that are well connected to the dominant percolating pore network. The removal of such components then opens up many additional flow paths, which lead to a significant permeability increase. Because oil and immobile components are more likely located in organic matter, it is speculated that organic matter pores are more important for flow for this sample.

Conclusions

Porosity and permeability were measured through the GRI method with crushed samples for 26 Yanchang samples. Porosity for these samples has a range of 2% to 6%. Permeability, although with uncertainties, is generally low, ranging from 0.1 nD to 38 nD.

Comparison between He and N_2 porosity measurements and the relative permeability analysis have important implications on relative distribution of residual moisture, oil, and immobile components. Pores larger than 200 nm should contain minimum immobile components, that is, asphaltenes, under an in-situ condition. Residual moisture primarily lies in mineral pores that are not well connected to the dominant percolating pore network, whereas residual oil and immobile components are located in the dominant pore network.

References

Cui, X., Bustin, A.M.M., and Bustin, R.M., 2009, Measurements of gas permeability and diffusivity of tight reservoir rocks: different approaches and their applications: Geofluids, 9, 208–223 (2009). doi: 10.1111/j.1468-8123.2009.00244.x

Guidry, K., Luffel, D., and Curtis, J., 1995, Development of laboratory and petrophysical techniques for evaluating shale reservoirs, final report: Des Plaines, IL, Gas Technology Institute, GRI-95/0496, 304 p.

Luffel, D.L., and Hopkins, C.W., 1993, Matrix permeability measurement of gas productive shales: SPE Annual Technical Conference and Exhibition, SPE 26633, p, 261–270.

Oak, M.J., Baker, L., and Thomas, D., 1990, Three-phase relative permeability of Berea Sandstone. SPE. Journal of Petroleum Technology, p. 1054–1061.

Profice, S., Lasseux, D., Jannot, Y., Jebara, N., and Hamon, G., 2011, Permeability, porosity and Klinkenberg coefficient determination on crushed porous media. SCA2010-32, 12 p., presented at the International Symposium of the Society of Core Analysts, Austin, TX, 18–21 September 2011.

Tang, X., Zhang, J., Wang, X., Yu, B., Ding, W., Xiong, J., Yang, Y., Wang, Lo., and Yang, C., 2014, Shale characteristics in the southeastern Ordos Basin, China: Implications for hydrocarbon accumulation conditions and the potential of continental shales: International Journal of Coal Geology, v. 128–129, p. 32–46.

Wang, Y., Zhu, Y., Wang, Y., and Feng, G., 2015, Nanoscale pore morphology and distribution of lacustrine shale reservoirs: Examples from the Upper Triassic Yanchang Formation, Ordos Basin, Journal of Energy Chemistry, 2015, v. 4, p. 512–519.

TASK 3.4

High-Resolution Microscopic Analysis of Mineral and Organic-Matter Components in Lacustrine Yanchang Formation, Southeastern Ordos Basin, China

Patrick Smith, Lucy Tingwei Ko, and Tongwei Zhang[1]

[1]Bureau of Economic Geology, Jackson School of Geosciences[2], and The University of Texas at Austin, Austin, TX

Abstract

One of the major issues confronting researchers when studying porosity in gas shales is reconciling the disconnection between indirect and direct pore-measurement methodologies. The pore systems from the Yanchang Formation reservoirs were investigated by the integration of scanning electron microscopy (SEM) imaging and nitrogen gas adsorption. Gas adsorption and GRI helium porosity data suggest that most of the porosity on these samples was contributed by pore size less than 10 nanometers (nm), and these pores are not easily resolved by conventional field-emission SEM (FE-SEM) imaging. In this study, we investigated this disconnection by leveraging two microscopic methodologies with the potential for nanoscale spatial resolutions: (1) a Zeiss Gemini 500 SEM in low-voltage mode (LVSEM), and (2) JEOL high-resolution transmission electron microscope (HRTEM). Using their unique microanalysis capabilities, the in-situ distribution and character of the organic-matter (OM) pores, and pore networks can be clearly determined at the nanometer scale. Results revealed that LVSEM was able to resolve pore sizes down to 5 nm with very good image quality. Pore size less than 5 nm becomes increasingly interpretative and hard to quantify. HRTEM greatly improved our understanding of the distribution and structure of organic-matter pores in these shales, and their contribution to porosity and permeability.

Introduction

Microfabric signatures preserved in fine-grained sediments and rocks can be used to identify sedimentary environments and processes. Conventional field-emission scanning electron microscopy (FE-SEM) of cross-sectional Ar-ion-milled samples has been routinely used by investigators to characterize the evolution of texture, fabric, and pore structures in unconventional reservoirs of mudstones (e.g., Loucks and others, 2009; Loucks and others, 2012). This two-dimensional (2D) surface methodology can, under the right circumstances, resolve features as small as 2 nm. However, in reality, routine analysis at this resolution is very difficult because of the preparation artifacts, instrument limitations, and complexities of the sample. Any features less than 10 nm are often subjected to qualitative interpretation. It is critical for any quantitative analysis in shales to have the ability to clearly image all the pore sizes in a viewed area, especially when other measurement techniques, such as nitrogen gas adsorption and GRI helium porosity, suggest that a significant proportion of porosity is contributed by pore sizes less than 10 nm. Understanding nanostructures of organic matter (OM) and OM pores is important in estimating oil and gas storage—both adsorbed gas and free gas. Studies have

demonstrated the value of HRTEM as an important technique to describe organic carbon hydrocarbon trapping layer structures in relation to maturation and nano porosity (Oberlin and others, 1980; Boulmier and others, 1982; Oberlin, 1989; Rouzaud and Oberlin, 1989). A recent study using HRTEM in combination with Raman Micro-spectroscopy and low-pressure, gas-adsorption analyses showed a positive correlation between surface areas of mesopores (pores of approximately 2 to 50 nm diameter) and maturity levels (Romero-Sarmiento and others, 2014).

The primary goal of this study is to reconcile the disconnection between indirect adsorption measurements and direct SEM and TEM imaging on the same aliquot of samples to reach the spatial resolution for more accurate quantification.

Samples and Methods

Sample Sets

Five Yanchang samples of the Chang 7, 8 and 9 members in YY1, YCYYV1112, and YCYYV1113 wells were selected for this study (**Table 1**). Samples were selected based on their unique nitrogen-gas adsorption -size distribution pattern.

Table 1: Geochemical characteristics of studied samples.

properties	YY1-1378 TEM/LVSEM	YY1-1451 LVSEM	YY1-1504 LVSEM	YCYYV1112-1567 TEM/LVSEM	YCYYV1113-1745 TEM/LVSEM
Formation	Chang 7	Chang 8	Chang 9	Chang 7	Chang 7
Depth (m)	1378.5	1451.0	1504.9	1567.0	1745.3
TOC (%)	8.2	6.62	7.08	4.52	10.1
Bitumen R_o (%)	0.93	0.89	0.94	0.95	0.87
T_{max} (°C)	447	455	455	457	443
S_1/TOC (mg/g)	64	86	60	85.8	29.4
Quartz (%)	15.1	12.4	22.2	23	24.2
Clay (%)	57.3	66.8	53.4	40.4	26.1
Calcite (%)	7.2	4.5	5	10.9	8.7
K-feldspar (%)	4.8	4.8	3.5	7.7	18.2
Plagioclase (%)	13.9	9.8	12.8	17	21

Ten 10 x 10 mm cube samples were prepared using a standard cross-sectional Ar-ion milling technique (Loucks and others, 2009). Five of these samples were coated with 5 nm of iridium, and then, analyzed using an FEI Nova NanoSEM 430 (FESEM) fitted with energy-dispersive spectrometer (EDS) at the Bureau of Economic Geology (BEG). The remaining five uncoated,

prepared samples were then shipped for analysis to the Zeiss demonstration laboratory in Pleasanton, California. Analyses were performed in the Zeiss Gemini 500 SEM in low-voltage mode, with a focus on high-resolution imaging of the organic component. Three HRTEM samples from the uncoated group were prepared and imaged at the Cerium laboratories in Austin, Texas. Samples were mounted on SEM stubs and then prepared in an FEI XL830, XL835 Dual-Beam system using the focused-ion beam (FIB) slice-extraction technique (**fig. 1**) (Lee and others, 2003). The extracted slices (lamella) were then transferred to a JEOL 2010F for observation (Smith and others, 2001; Thompson and others, 2006).

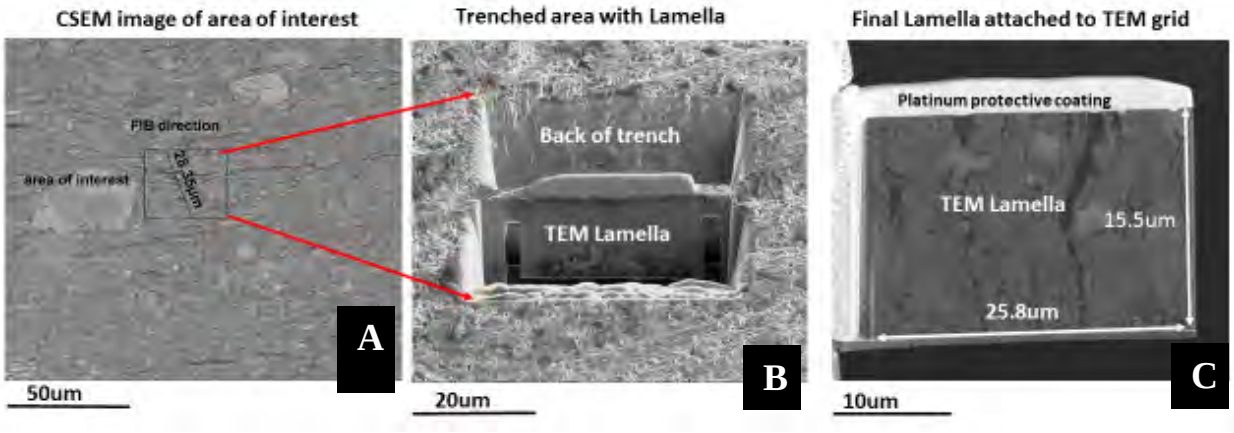

Figure 1. Diagram showing TEM specimen preparation process using focus ion beam (FIB) method. (A) Area of interest was selected from conventional SEM photomicrograph. (B) Focus ion beam (FIB) was used to cut two trenches, one from each side, leaving a thin TEM lamella. (C) Lamella was removed directly from the trench area and attached to a TEM grid

High-resolution imaging techniques

Zeiss Gemini 500 Low-voltage SEM (LVSEM)

The Zeiss Gemini is a standard SEM two-dimensional imaging system capable of producing high-resolution images with eV beam energies. This modality theoretically allows observations of near-surface features of 2 nm. A low-voltage electron beam has many advantages when studying these fine-grained mudrocks. Because the interaction volume is small (within 1 to 2 nm), all features can be observed at or very near the surface of the material. A low-energy beam mode in the Gemini is engineered to generate a relatively small scanning probe; therefore, the resolution can be improved significantly. With operating conditions under (1) 600 to 900 accelerating voltage, (2) in-lens working distances of 1 to 2 mm, and (3) uncoated samples viewed in high-vacuum mode, the potential for nanometer resolution improves because Gemini is specifically designed to capture the low-energy signal generated from the sample.

JEOL high-resolution transmission electron microscope (HRTEM)

HRTEM is a 3D (volumetric) technique in which a high-energy electron beam is transmitted through a thin sample (100-nm in thickness) and projected onto a CCD camera. The way the electron beam is either scattered or diffracted within the sample volume dictates image formation. The resolution with this technique is 0.2 nm (the distance between atoms).

Results

Characteristics of the Yanchang Lacustrine Shales

The dominant minerals in the studied lacustrine shale samples are clay minerals (e.g., chlorite), quartz, albite, calcite, plagioclase, and feldspars (**fig. 2**). The present-day TOC values range from 4.52 to 10.1 wt%. The Rock-Eval Tmax and bitumen reflectance measurement indicate that studied samples all reached oil window maturation (Xun and others and Hackley and others, Tasks 4.1 and 4.2, this volume).

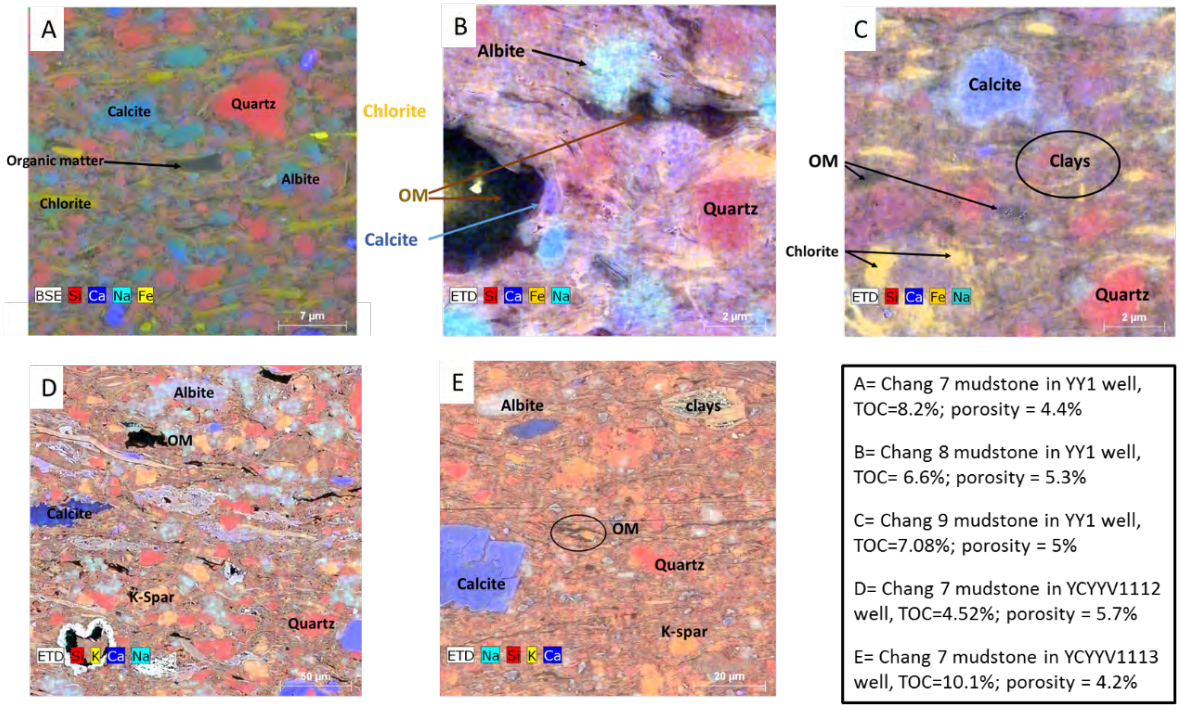

Figure 2. Pictures showing mineralogical components in five Yanchang samples. (A) Quartz, albite, calcite, chlorite, and organic matter are major components in the Chang 7 member, YY1 well. (B) Quartz, albite, calcite, chlorite, and organic matter are major components in the Chang 8 member, YY1 well. (C) Quartz, calcite, chlorite, and organic matter are major components in the Chang 9 member, YY1 well. (D) Quartz, albite, feldspar, calcite, chlorite, and organic matter are major components in the Chang 7 member, YCYYV 1112 well. (E) Quartz, albite, feldspar, calcite, chlorite, and organic matter are major components in the Chang 7 member, YCYYV1113 well.

Pores from SEM, LVSEM, and N_2-adsorption

The size of OM spongy pores is, in general, smaller than OM spongy pores in the marine depositional environment (e.g., Eagle Ford, Barnett, and Woodford Shales). Most of the OM pores are in the range of a few to tens of nanometers in size (**figs. 3 and 4**). It is difficult to image and quantify those OM spongy pores using a conventional SEM setting. **Figure 3** compares the OM spongy pores using conventional SEM and the Zeiss high-resolution low-voltage mode SEM. Although there is not much difference resolving mineral grains and texture information in LVSEM, the size, shape, and morphology of the OM spongy pores can be assessed within the 5-nm range. The significantly improved image quality using LV-SEM on the uncoated samples enables us to compare pore sizes in SEM images with pore-size distribution obtained from low-pressure nitrogen adsorption techniques, especially for pore sizes less than 10-nm (**fig. 4**).

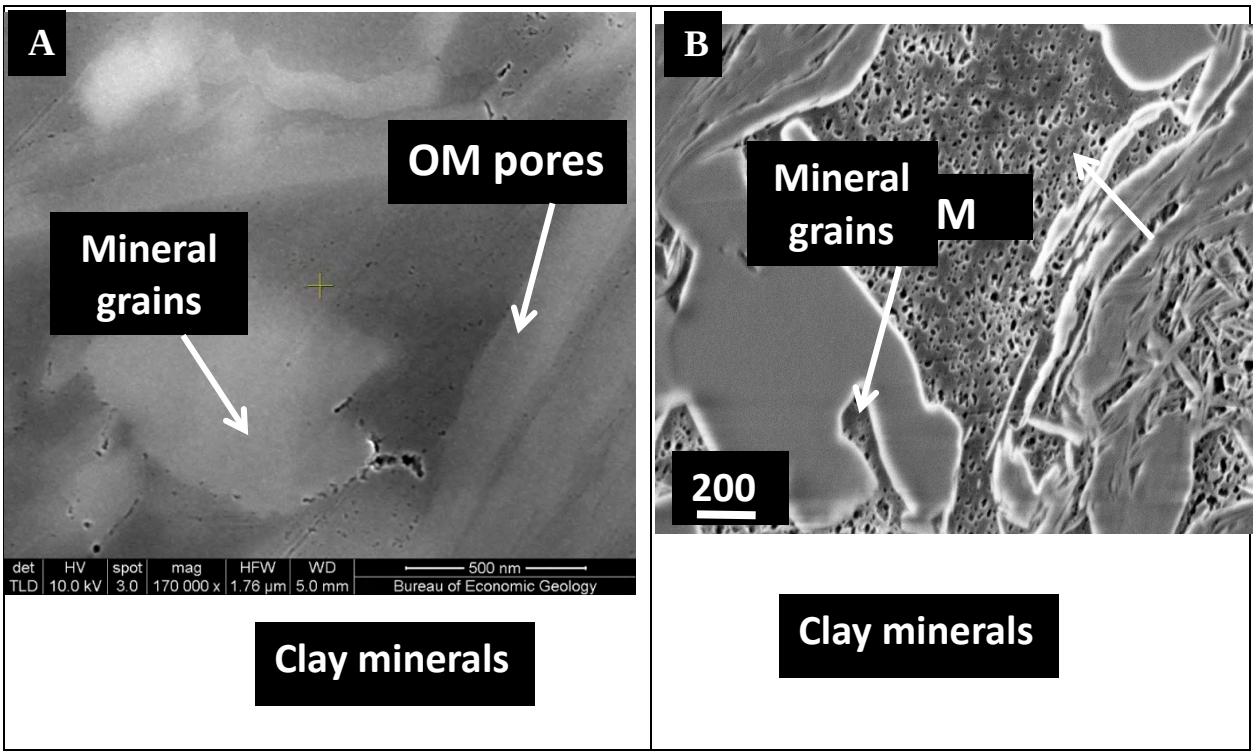

Figure 3. Pictures showing imaging capabilities of (A) conventional SEM and (B) low-voltage mode SEM (LVSEM). Both images showing clear texture and fabric information, but it is apparent that the LVSEM images the OM pores better. Samples are organic-rich mudstone at depth of 1378.51 m in the Chang 8 member, YY1 well.

The extremely low porosity in sample YCYYV1113 1745 from absorption data was confirmed with LVSEM images. The direct LVSEM image of sample YCYYV1112 1567 shows almost no pores developed in OM, similar to indirect measurement from nitrogen adsorption.

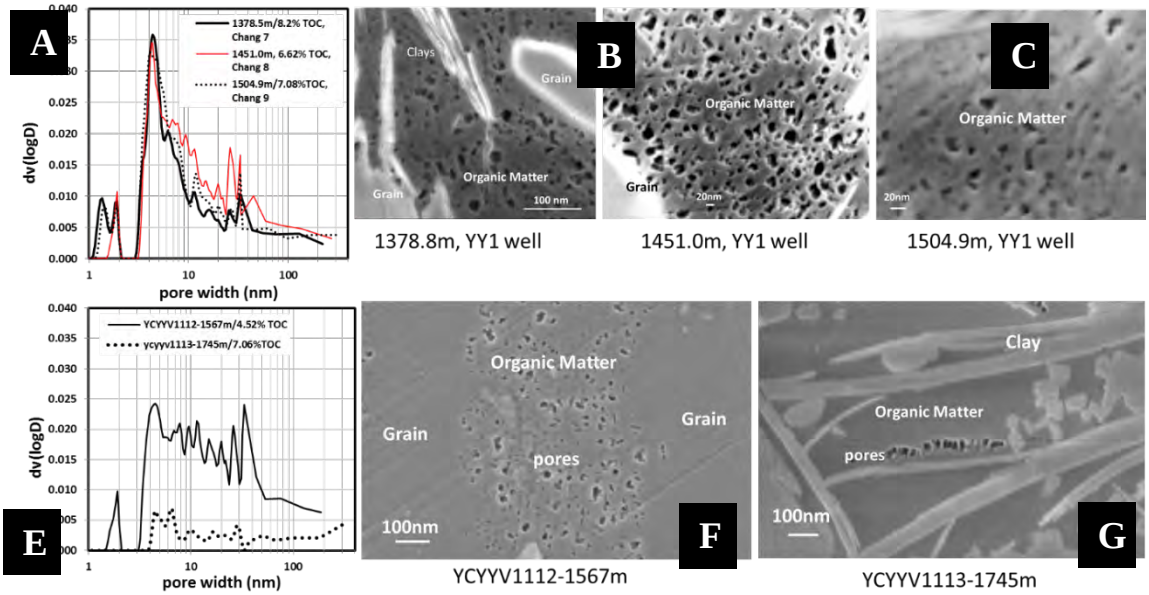

Figure 4. Diagrams and pictures showing the comparison of pore-size distribution (PSD) patterns by N_2 gas adsorption and LVSEM images for all samples. (A) Pore-size distribution at depth of 1378.8 m, 1451.0 m, and 1504.9 m, YY1 well. (B, C, D) OM pores in samples in the YY1 well. (E) Pore-size distribution at depth of 1567 m in the YCYYV1112 well and 1745 m in the YCYYV1113 well. (F, G) YCYYV1113-1745 have almost no pores in N_2 adsorption that were confirmed by using LVSEM.

Observations of Pores Using TEM

OM spongy pores were investigated using high-resolution TEM on three selected samples YY1-1378, YCYYV1112-1567, and YCYYV1113-1745 (**Table 1**). HRTEM allows imaging of the nanoscale polyaromatic layers as dark fringes in the carbon nanostructure and the mutual orientation of these layers, which reveal the 3D structures of the OM (**fig. 5**).

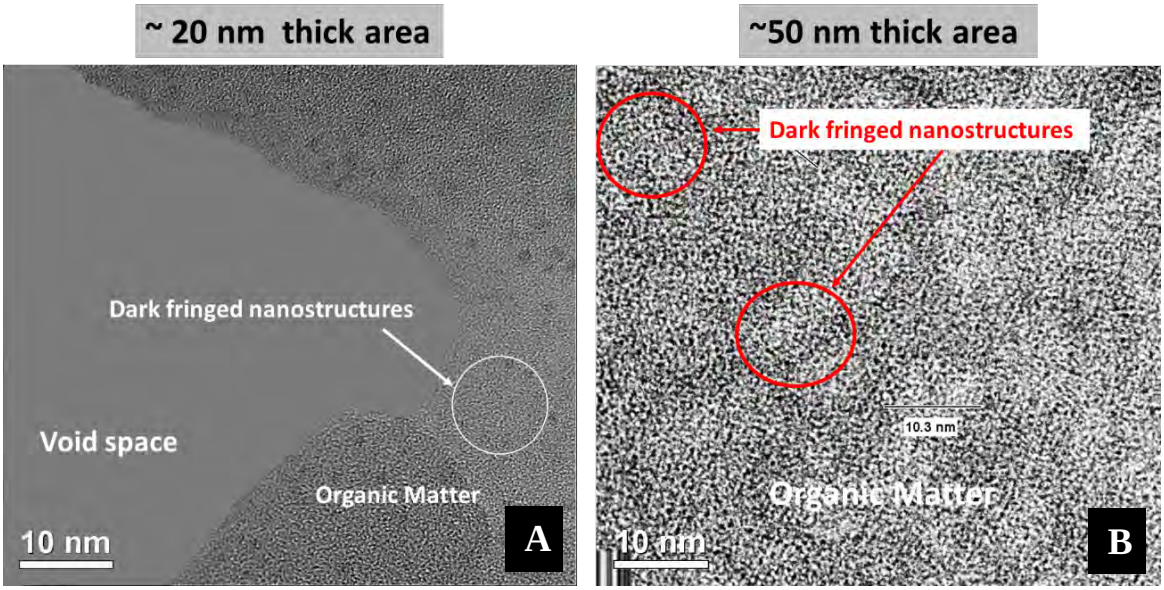

Figure 5. Two images illustrating the nano-layering structures found in the organic component of the sample at 1378.8 m depth in the YY1 well. The brightness and contrast in these images are due to the diffraction of the electron beam due to mass differences as it travels through the sample.

Thermal maturation affects the structure of the OM (Hunt, 1995). The maturity continuum starts with quasi-amorphous, immature OM. The immature OM layers are very small (< 1 nm). With increased thermal maturity, OM becomes organized, causing an increased occurrence of nanometer-sized polyaromatic layers, which are stacked by 2 or 3 to form nano-scaled structural units within the OM structure. Our mature oil-window samples show local parallel stacks and large, oval-based structural units (pores) from a nanometer to micron scale (**fig. 5**). These nanometer pores and aromatic layer structures might explain the less than 5 nm pores in the N_2 absorption data.

A high-resolution TEM is a volumetric-imaging technique, different from two-dimensional (2D) LVSEM surface-imaging (**fig. 6**). Depending on the thickness of the lamella, the orientation and dimension of the imaged objects, size and shape of the mineral grains, and voids/pores can be well captured in the 3D sense. **Figure 6** shows some examples of OM and OM pores (bubble clusters) imaged by high-resolution TEM and SEM. Both **Figures 6A** and **6E** show OM, but the former figure has texture within OM, and the latter figure does not. When compared with corresponding LVSEM images, the former figure shows OM spongy pores in the OM, and the latter figure does not have any OM spongy pores visible. The OM spongy pores are viewed in a 2D surface in **Figures 6B** and **6D,** but their oval and circular shapes can be seen in a 3D volumetric scale using TEM (**fig. 6C**). Some OM pores form localized coalescing strings or clusters within the body of the OM. As shown in **Figure 7** for the YY1-1378.8-m sample, the combination of conventional SEM, LVSEM, and HRTEM imaging techniques can be better characterized in OM-hosted pores.

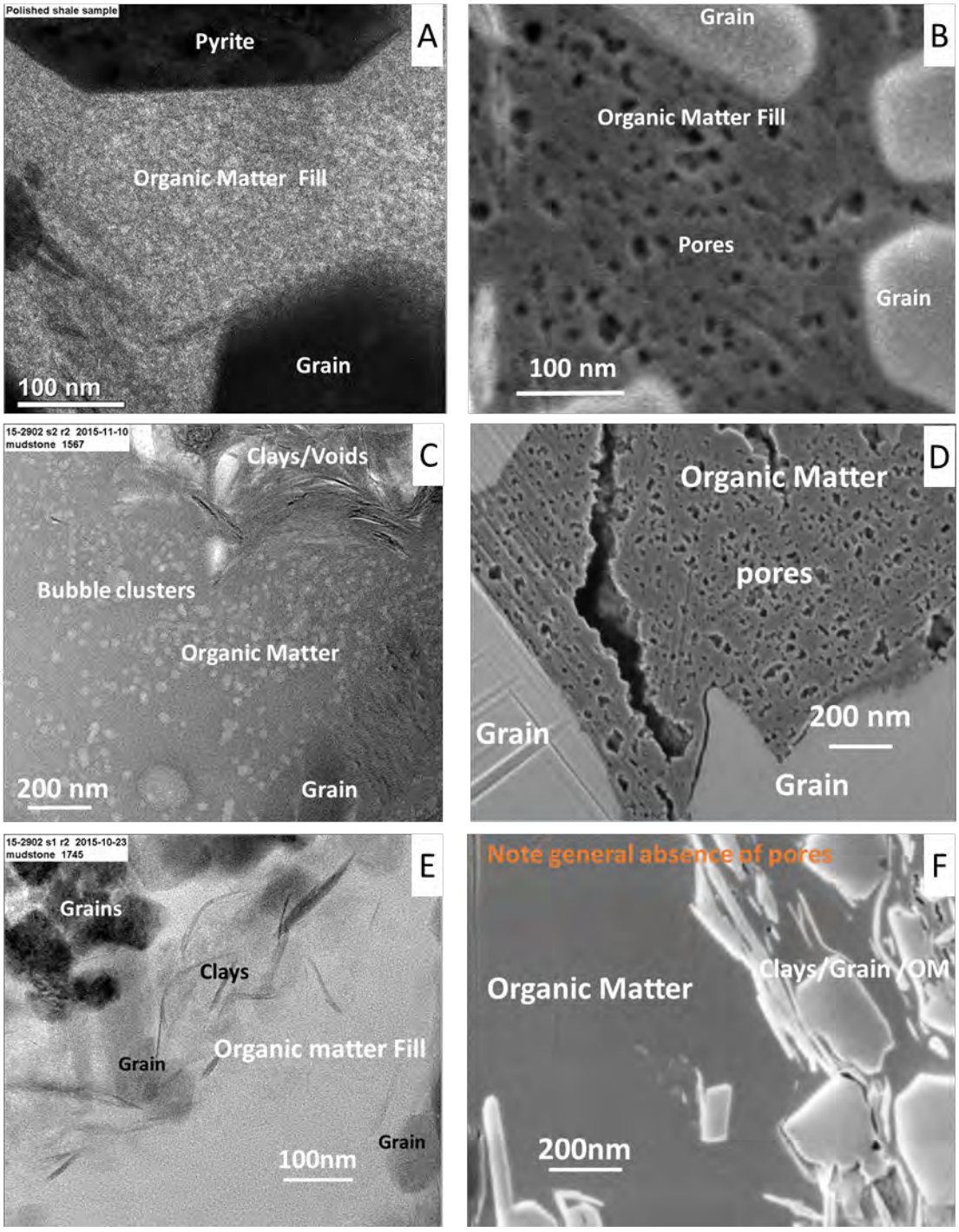

Figure 6. Images from HRTEM and LVSEM. (A) TEM image at the depth of 1378.8 m, YY1 well. (B) LVSEM image at the depth of 1378.8 m, YY1 well. (C) TEM image at the depth of 1567 m, YCYYV1112 well. (B) LVSEM image at the depth of 1567 m, YCYYV1112 well. TEM is a volume technique, whereas LV SEM is a near-surface imaging methodology.

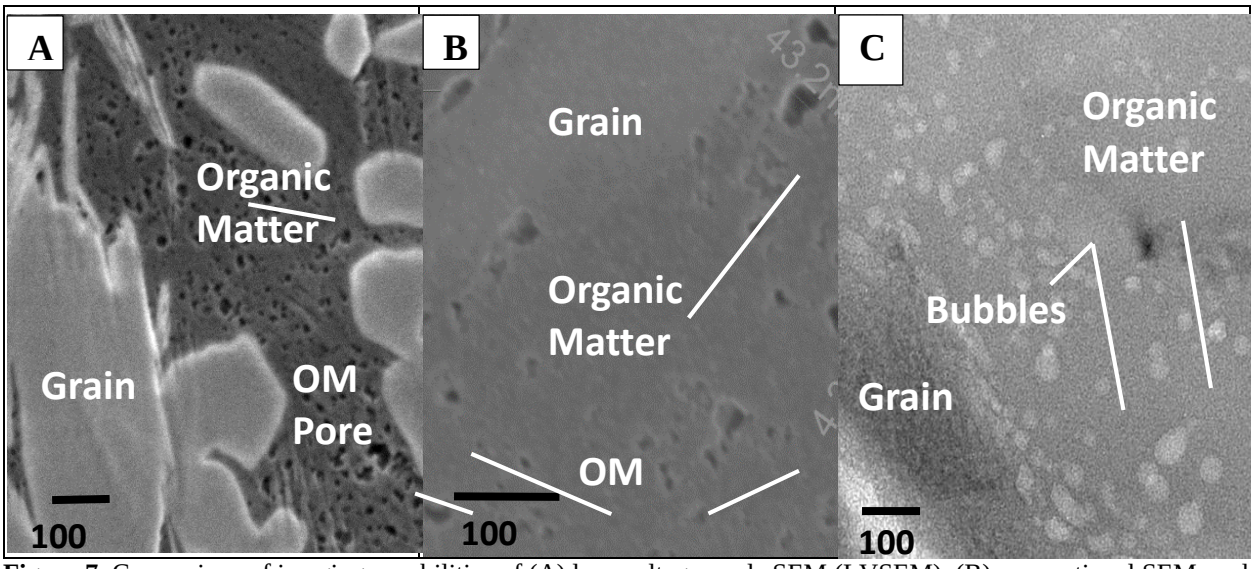

Figure 7. Comparison of imaging capabilities of (A) low-voltage mode SEM (LVSEM), (B) conventional SEM, and (C) HRTEM.

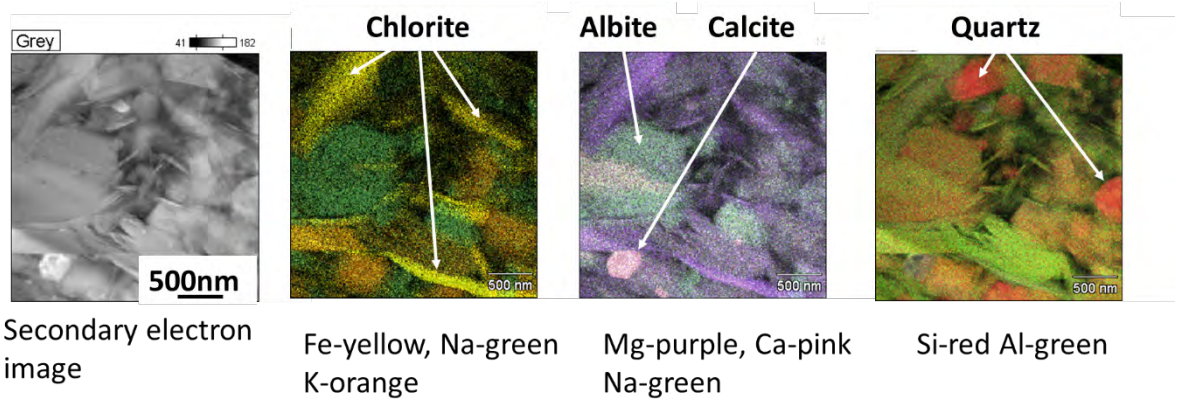

Figure 8. High-resolution mineral identification capabilities of TEM EDS. TEM images for the sample at 1378.8 m in the YY1 well.

Compositional information can also be obtained from HRTEM EDS. Stacked elemental maps demonstrate the nanometer-resolution capability of this technique (**fig. 8**). The mineralogical suite is reflective of earlier SEM EDS scans.

Pores in Lacustrine versus Marine Mudstones

Our studied Yanchang lacustrine mudstones show smaller pore sizes and a low porosity when compared to that of marine mudstones such as the Marcellus and Eagle Ford in the United States. **Figure 9** demonstrates that with a similar TOC content, OM-hosted pores are small, and OM porosity in the lacustrine mudstones is lower than that of the Marcellus and Eagle Ford formations. From nitrogen-adsorption measurement and high-resolution imaging techniques, we now understand that this low-OM porosity resulted from relatively small sizes of OM spongy

pores in the lacustrine mudstones. To characterize these OM pores better, improved imaging techniques are required.

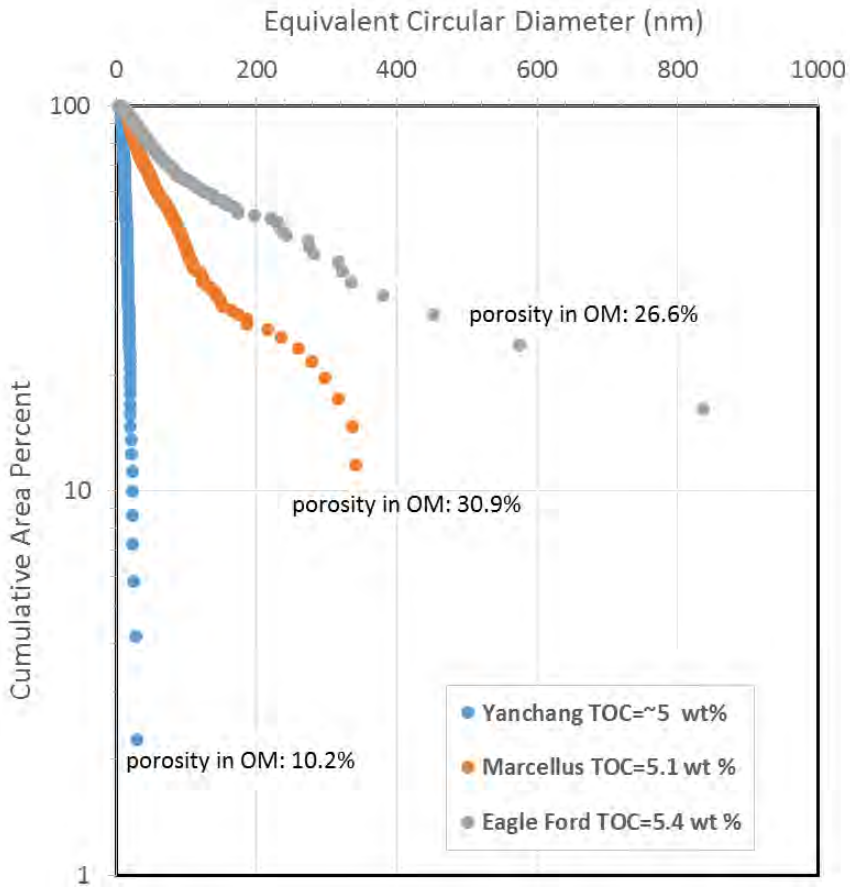

Figure 9. Comparison of OM-hosted porosity in Yanchang lacustrine mudstone to the Marcellus and Eagle Ford marine mudstones using a point count method of LVSEM images.

Mixed structure of clay and organic matter

The morphology of the clay mineral and OM mixture is an important feature for understanding oil generation and expulsion in clay- and organic-rich mudstones. Deformed clays, bent and delaminated clays, and nanoscaled OM and clay mixtures can be clearly imaged in a 3D volumetric TEM technique (**fig. 10**). Both thermal maturation- and compaction-forced OM were redistributed and injected into the clay minerals matrix assemblage, filling the heterogeneous mineral matrix and fractures (**fig. 10**). HRTEM images show local concentric parallel aromatic layer structures associated with gas maturity, as seen by Romero-Sarmiento and others (2014), and some OM/mineral associated pores (**fig. 10**). The overall lack of OM pores might relate to the properties of host OM material, clay mineral matrix, and compaction.

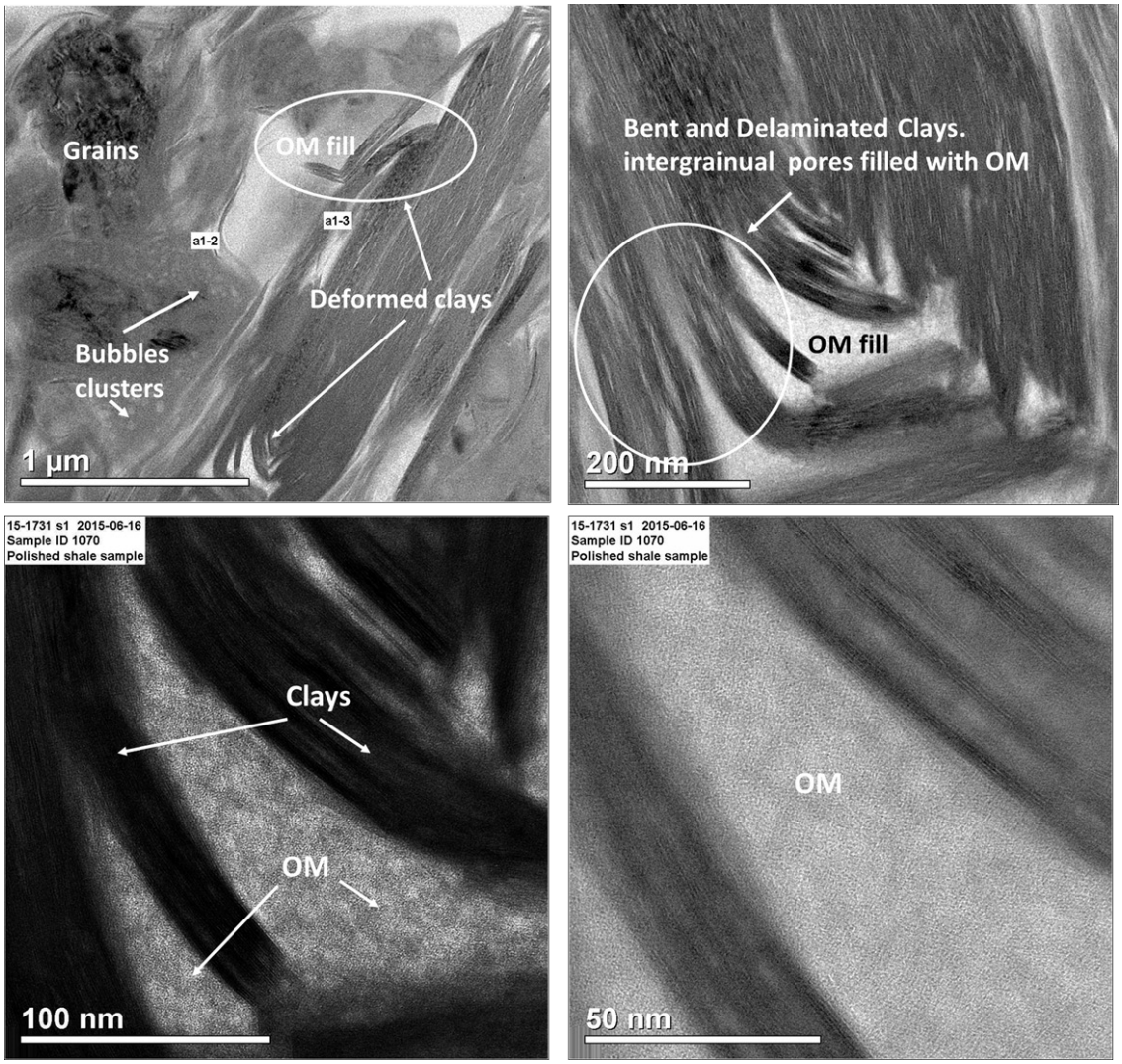

Figure 10. Illustration of mixing between organic matter and clay fabric at the nanometer scale. TEM images of the sample at 1378.8 m depth in the YY1 well.

Conclusions

High-resolution, low-voltage, scanning microscopy combined with high-resolution transmission electron microscopy was useful for imaging OM, OM pores, and mineral fabrics in the lacustrine mudstone samples because of their extremely small sizes. The following preliminary conclusions were made on the basis of the limited Yanchang Formation sample sets.

1. LVHRSEM is well suited to analyze near-surface features less than 5 nm in the organic component of these rocks.
2. LVSEM was able to resolve pore sizes to approximately 5 nm with high image quality. However, features with less than a 5-nm size resolution require increasing amounts of interpretation.
3. HRTEM demonstrated its value as a unique imaging technique for describing in situ organic carbon nanostructures ($\geq$ 0.2 nm).
4. HRTEM is limited as a direct pore measurement tool, because it has difficulty resolving less than 10-nm pores in a 100-nm-thick volume. In addition, only small (μm) regions can be investigated.

References

Baker, J.C., and Mackinnon, I.D.R., 2010, High-resolution transmission and analytical electron microscopy of smectite to illite transition in Australian mudrock: Clay Mineral Society 28th annual meeting, June 2010, p. 300–314.

Bernard, S., Benzerara, K., Beyssac, O., Brown, G.E., Stamm, L.G., and Duringer, P., 2009, Ultrastructural and chemical study of modern and fossil sporoderms by scanning transmission X-ray microscopy (STXM): Review of Palaeobotany and Palynology, v. 156 (1–2), p. 248–261.

Ho, J.H., and Peacor, D. R., 1989, Illite/smectite from Gulf Coast shales: a reappraisal of transmission electron microscopic images: Clay and Clay Minerals, v. 37, p. 542–546.

Lee, M.R., Bland, P.A., and Graham, G., 2003, Preparation of TEM samples by focused ion beam (FIB) techniques: applications to the study of clays and phyllosilicates in meteorties: Mineralogical Magazine, v. 67, no. 2, p. 581–592.

Loucks, R.G., and Reed, R.M., 2014, Scanning-electron-microscope petrographic evidence for distinguishing organic-matter pores associated with depositional organic matter versus migrated organic matter in mudrocks: GCAGS Journal, v. 3, p. 51–60.

Loucks, R.G., Reed, R.M., Ruppel, S.C., and Hammes, U., 2012, Spectrum of pore types and networks in mudrocks and a descriptive classification for matrix-related mudrock pores: AAPG Bulletin, v. 96, no. 6, p. 1071–1098.

Loucks, R.G., Reed, R.M., Ruppel, S.C., and Jarvie, D.M., 2009, Morphology, genesis, and distribution of nanometer-scale pores in siliceous mudstones of the Mississippian Barnett Shale: Journal of Sedimentary Research, v. 79, p. 848–861.

Oberlin, A., 1989, High-resolution TEM studies of carbonization and graphitization. In: Thrower, P.A. (Ed.), Physic and Chemistry of Carbon, vol. 22. Marcel Dekker, New-York, p. 1–143.

Oberlin, A., Boulmier, J.L., and Villey, M., 1980, Electron microscopic study of kerogen microtexture. In: Durand, B. (Ed.), Kerogen: Technip, p. 191–241.

Petersen, H.I., Schovsbo, N.H, and Nielsen, A.T., 2013, Reflectance measurements of zooclasts and solid bitumen in Lower Paleozoic shaless, southern Scandinavia: Correlation to vitrinite reflectance, International Journal of Coal Geology, v. 114, p. 1–18.

Riediger, C.L., 1993, Solid bitumen reflectance and Rock-Eval T_{max} as maturation indices: an example from the "Nordegg Member," Western Canada Sedimentary Basin: International Journal of Coal Geology, v. 22, p. 295–315.

Romero-Sarmiento, M., Rouzaud, J., Bernard, S., and Deldicque, D., 2014, Evolution of Bernett Shale organic carbon structure and nanstructure with increasing maturation: Organic Geochemistry, v. 71, p. 7–6.

Schoenherr, J., Littke, R., Urai, J. L., Kukla, P.A., and Rawahi, Z., 2007, Polyphase thermal evolution in the Infra-Cambrian Ara Group (South Oman Salt Basin) as deduced by maturity of solid reservoir bitumen: Organic Geochemistry, v. 38, p. 1293–1318.

Smith, A.J., Munroe, P.R., Tran, T., and Wainwright, M.S., 2001. FIB preparation of a sensitive porous catalyst for TEM elemental mapping at high magnifications: Journal of Materials Science, v. 36, no. 14, p. 3519–3524.

TASK 4.1

Organic Matter and Gas Geochemical Characterization of Gas Origin, Gas Storage

Tongwei Zhang[1], Xun Sun[1], Daniel Enriquez[1], and Jianfeng Zhang[2], Chao Gao[2]

Bureau of Economic Geology[1], Jackson School of Geosciences, The University of Texas at Austin, Austin, TX
Shaanxi Yanchang Petroleum (Group) Co. Ltd.[2], Xi'an, Shaanxi, China

Problem Statement and Objectives

The Triassic Yanchang Formation was deposited in a fluvio-lacustrine environment and is dominantly distributed in the Shanbei Slope southeast of the Ordos Basin. Its current burial depth ranges from 500 m to 1800 m. Three organic-rich layers (the Chang 7, 8, and 9 members) are considered to be the main sources of oil accumulation in the sandstone reservoirs, which are interbedded with clay-mineral and organic-matter-rich shale layers. The deliverability of shale gas and oil from a lacustrine shale system containing high clay-mineral content remains a debated issue (Zhang and others, 2012): What are the main controls of gas content in organic-rich lacustrine mudstones? Are there major differences in mineralogy, diagenesis, pore types, organic-matter (OM) properties (abundance, type, and thermal maturity), and oil-expulsion efficiency in a lacustrine shale system as compared with a marine shale system?

Specific research questions include: (1) Are OM properties favorable to oil and gas generation? (2) What is the range of thermal maturity? (3) Is it favorable to the generation of oil, gas, or both? (4) Is there a difference in petroleum expulsion for thick- and thin-layer source rocks? If yes, what is the critical, or effective, thickness of source rocks for petroleum expulsion? (5) Is it possible to identify oil and gas saturation zone(s) within a thick interval of source rocks by using geochemical evidence and the signal of wire logging?

Samples and Methods

This study used 46 core samples: 37 from the YY1 well and 9 from YY22 wells. Details of core samples have been described in Tasks 1 through 3. TOC and Rock-Eval analysis, gas yield and compositional analysis of gases released from rock crushing, residual oil solvent extraction, and SARA quantification have been conducted for the core samples.

This study also used 12 core samples from 12 wells with different thermal maturity, and those samples cover a wide burial depth range from 407 m to 2,297.05 m. There were 10 samples from Chang 7 members and 2 samples from Chang 9 members.

Workflow for gas and oil analysis of core samples in this study is shown in **Figure 1**. Well-preserved wax-coated plugs of fresh core samples can be used for the determination of gas, oil, and water saturation, as well as for the determination of as-received porosity, dry porosity, and permeability. Dips and coatings are used when cores are not tested within a few hours or days

and when the material is to be transported over long distances. Dip coatings can also be used with plastic laminates to add mechanical integrity. (Detailed procedures for dips and coatings and core-plug drilling are available in a different document, which has been provided to Yanchang Petroleum Company.). We will sample the wax-coated cores as part of our ongoing 2016 research plan. Yanchang researchers will be in charge of collecting wax-coated core samples, and the Bureau of Economic Geology (BEG) will provide the name of commercial laboratories for conducting core analysis.

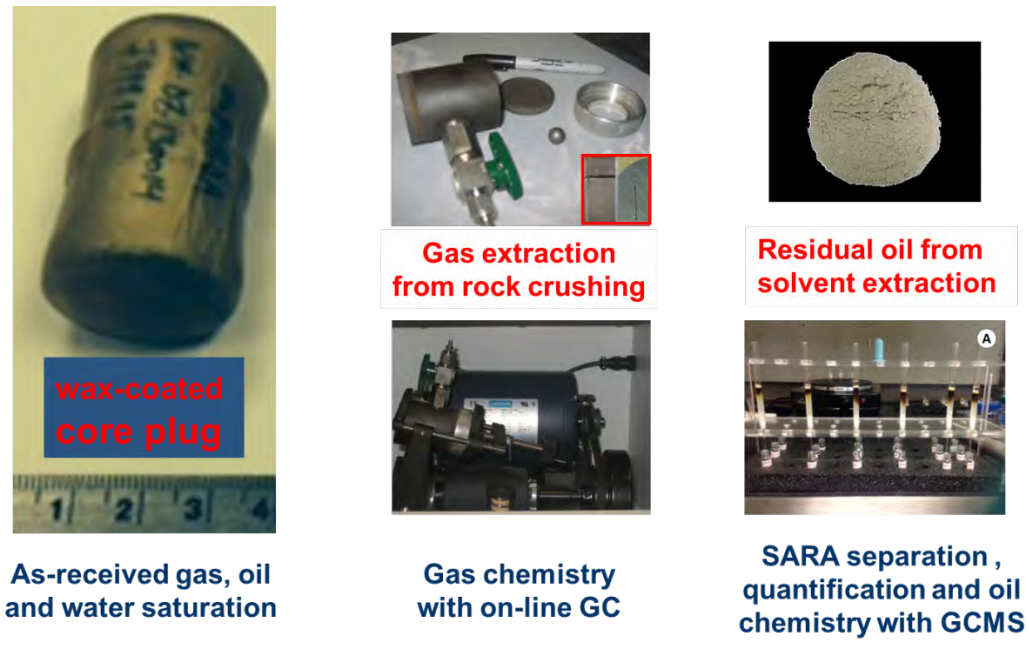

Figure 1. Workflow for gas and oil analysis of core samples in this study.

TOC and Rock-Eval analysis:

GeoMark conducted TOC content and Rock-Eval analysis; the results for YY1 and YY22 wells are shown in **Table 1**; the results for 12 core samples before and after CH2Cl2 extraction are shown in **Table 2**.

Table 1. Rock-Eval analyses for source rock from YY1 and YY22 wells (source: GeoMark)

Table 1 RockEval analyses for Source Rock from YY1 and YY22 Wells

Rock ID	Upper Depth (m)	Percent Carbonate (wt%)	Leco TOC (wt%)	Rock-Eval-2 S1 (mg HC/g)	Rock-Eval-2 S2 (mg HC/g)	Rock-Eval-2 S3 (mg CO2/g)	Rock-Eval-2 Tmax (°C)	Calculated %Ro (RE TMAX)	Hydrogen Index (S2x100/TOC)	Oxygen Index (S3x100/TOC)	S2/S3 Conc. mg HC/mg CO2	S1/TOC Norm. Oil Content	Production Index (S1/(S1+S2)	Experimental Notations
YY1-687	1315.72	4.47	3.47	2.15	5.85	0.40	450	0.94	169	12	15	62	0.27	Low Temp S2 Shoulder
YY1-838	1347.96	15.96	0.51	2.14	0.80	0.38	453	0.99	158	75	2	424	0.73	Low Temp S2 Shoulder
YY1-879	1358.56	9.86	6.70	2.63	12.58	0.54	449	0.92	188	8	23	39	0.17	Low Temp S2 Shoulder
YY1-890	1359.66	7.61	2.69	1.65	4.66	0.43	450	0.94	173	16	11	61	0.26	Low Temp S2 Shoulder
YY1-934	1364.69	10.36	5.84	2.22	11.10	0.61	451	0.96	190	10	18	38	0.17	Low Temp S2 Shoulder
YY1-992	1370.77	36.10	2.44	3.37	5.03	0.66	428	0.54	206	27	8	138	0.40	Low Temp S2 Shoulder
YY1-1005	1372.07	9.27	5.43	4.09	10.20	0.78	445	0.85	188	14	13	75	0.29	Low Temp S2 Shoulder
YY1-1030	1374.44	7.28	7.94	5.59	17.70	0.63	448	0.90	223	8	28	70	0.24	Low Temp S2 Shoulder
YY1-1070	1378.51	26.08	8.20	5.28	20.44	0.68	447	0.89	249	8	30	64	0.21	Low Temp S2 Shoulder
YY1-1145	1386.35	6.01	7.80	7.06	16.41	0.73	452	0.98	210	9	22	91	0.30	Low Temp S2 Shoulder
YY1-1209	1392.75	3.56	5.06	6.09	13.14	0.60	451	0.96	260	12	22	120	0.32	Low Temp S2 Shoulder
YY1-1257	1397.66	15.01	3.79	7.56	8.53	0.60	434	0.65	225	16	14	199	0.47	Low Temp S2 Shoulder
YY1-1408	1408.26	16.21	2.19	4.16	3.77	0.72	453	0.99	172	33	5	190	0.52	Low Temp S2 Shoulder
YY1-1418	1409.26	4.67	3.98	3.20	6.86	0.71	456	1.05	172	18	10	80	0.32	Low Temp S2 Shoulder
YY1-1447	1411.92	5.04	4.19	3.50	7.80	0.65	454	1.01	186	16	12	84	0.31	Low Temp S2 Shoulder
YY1-1476	1414.76	4.62	3.52	2.27	5.99	0.64	455	1.03	170	18	9	64	0.27	Low Temp S2 Shoulder
YY1-1559	1414.86	16.01	0.44	0.16	0.24	0.50	466	1.23	54	113	0	36	0.40	
YY1-1610	1426.15	4.40	2.72	0.86	4.05	0.51	453	0.99	149	19	8	32	0.18	Low Temp S2 Shoulder
YY1-1616	1433.68	6.49	0.74	5.34	0.93	0.55	415	0.31	126	74	2	723	0.85	Low Temp S2 Shoulder
YY1-1663	1434.28	10.23	1.43	1.85	2.02	0.62	459	1.10	141	43	3	129	0.48	Low Temp S2 Shoulder
YY1-1671	1441.48	8.58	1.66	1.94	2.79	0.79	452	0.98	168	48	4	117	0.41	Low Temp S2 Shoulder
YY1-1698	1443.13	6.70	5.35	4.43	9.79	0.77	448	0.90	183	14	13	83	0.31	Low Temp S2 Shoulder
YY1-1711	1445.72	9.44	2.85	1.95	3.68	0.85	459	1.10	129	30	4	68	0.35	Low Temp S2 Shoulder
YY1-1739	1446.86	5.25	2.66	5.59	4.87	0.70	454	1.01	183	26	7	210	0.53	Low Temp S2 Shoulder
YY1-1775	1451.02	6.08	6.62	5.71	11.47	0.69	455	1.03	173	10	17	86	0.33	Low Temp S2 Shoulder
YY1-1807	1454.82	4.61	5.82	2.73	7.94	0.74	453	0.99	136	13	11	47	0.26	Low Temp S2 Shoulder
YY1-1856	1458.05	5.37	5.86	2.65	8.32	0.60	456	1.05	142	10	14	45	0.24	Low Temp S2 Shoulder
YY1-1895	1462.67	20.60	0.86	4.10	1.59	0.78	414	0.29	186	91	2	480	0.72	Low Temp S2 Shoulder
YY1-1907	1469.08	19.46	0.39	0.25	0.20	0.62	468	1.26	52	160	0	64	0.56	
YY1-2005	1472.64	8.31	2.39	2.60	3.42	0.54	455	1.03	143	23	6	109	0.43	Low Temp S2 Shoulder
YY1-2037	1497.07	5.33	2.76	2.48	4.17	0.88	456	1.05	151	32	5	90	0.37	Low Temp S2 Shoulder
YY1-2055	1500.38	4.82	5.43	4.16	9.12	0.79	451	0.96	168	15	12	77	0.31	Low Temp S2 Shoulder
YY1-2083	1501.31	9.35	7.17	4.10	13.23	0.78	456	1.05	185	11	17	57	0.24	Low Temp S2 Shoulder
YY1-2103	1504.98	10.70	7.08	4.24	12.77	0.71	455	1.03	180	10	18	60	0.25	Low Temp S2 Shoulder
YY1-2143	1511.42	6.10	7.08	4.38	12.45	0.77	448	0.90	176	11	16	62	0.26	Low Temp S2 Shoulder
YY1-2244	1534.86	5.62	2.08	0.58	1.63	0.64	466	1.23	78	31	3	28	0.26	
YY1-2248	1535.26	2.05	3.40	1.88	4.12	0.64	460	1.12	121	19	6	55	0.31	Low Temp S2 Shoulder
YY22-2447	1306.89	22.64	4.63	4.26	11.00	1.04	437	0.71	238	22	11	92	0.28	Low Temp S2 Shoulder
YY22-2532	1315.22	9.87	4.93	2.79	9.23	1.18	447	0.89	187	24	8	57	0.23	Low Temp S2 Shoulder
YY22-2560	1317.88	5.89	5.64	5.28	10.10	1.02	441	0.78	179	18	10	94	0.34	Low Temp S2 Shoulder
YY22-2591	1320.84	10.80	4.93	5.82	11.16	1.02	440	0.76	226	21	11	118	0.34	Low Temp S2 Shoulder
YY22-2676	1329.17	82.26	1.36	1.90	2.60	1.04	448	0.90	191	76	3	140	0.42	Low Temp S2 Shoulder
YY22-2746	1336.03	2.28	8.07	7.59	21.20	0.91	451	0.96	263	11	23	94	0.26	Low Temp S2 Shoulder
YY22-2761	1337.52	9.00	6.67	7.38	15.26	0.90	445	0.85	229	13	17	111	0.33	Low Temp S2 Shoulder
YY22-2829	1344.07	9.05	4.65	5.25	10.15	1.00	447	0.89	218	22	10	113	0.34	Low Temp S2 Shoulder
YY22-2858	1346.87	11.21	3.92	3.51	7.88	0.95	451	0.96	201	24	8	90	0.31	Low Temp S2 Shoulder

Table 2. Rock-Eval analyses for 12 core samples before and after CH2/Cl2 extraction (source: GeoMark)

Well ID	FM	Sample #	Depth (m)	TOC (wt%)	S1 (mg HC/g)	S2 (mg HC/g)	S3 (mg CO2/g)	Tmax (°C)	Roc %	HI	OI	S2/S3	S1/TOC	PI (S1/(S1+S2)
with oil	Chang 7	YCDT 1119	407.00	14.70	3.54	43.84	1	442	0.80	298.23	5.71	52.19	24.08	0.07
	Chang 7	YCYV 1118	1141.0	5.19	7.44	10.47	0.43	444	0.83	201.73	8.29	24.35	143.35	0.42
	Chang 7	YCWV 1149	1248.0	4.08	2.26	7.45	0.55	454	1.01	182.60	13.48	13.55	55.39	0.23
	Chang 7	YCYV 1145	1389.0	4.33	4.90	10.79	0.66	442	0.80	249.19	15.24	16.35	113.16	0.31
	Chang 7	YCFV 1113	1409.5	1.93	2.06	2.82	0.66	448	0.90	146.11	34.20	4.27	106.74	0.42
	Chang 9	YCYV 1115	1533.0	4.48	3.84	9.22	0.63	453	0.99	205.80	14.06	14.63	85.71	0.29
	Chang 7	YCYYV 1112	1567.0	4.52	3.88	6.08	0.66	457	1.07	134.51	14.60	9.21	85.84	0.39
	Chang 7	YCYV 1123	1614.1	4.94	2.24	7.58	0.95	450	0.94	153.44	19.23	7.98	45.34	0.23
	Chang 7	YCYYV 1113	1745.3	10.90	3.20	52.95	0.73	450	0.94	485.78	6.70	72.53	29.36	0.06
	Chang 9	YCYV 1123	1752.8	3.94	2.67	5.83	0.52	458	1.08	147.97	13.20	11.21	67.77	0.31
	Chang 7	YCYYV 1114	1917.2	7.06	2.95	24.70	0.71	450	0.94	349.86	10.06	34.79	41.78	0.11
	Chang 7	YCYWV 1112	2297.1	3.71	1.92	7.60	0.58	459	1.10	204.85	15.63	13.10	51.75	0.20
no oil	Chang 7	YCDT 1119	407.00	8.62	0.78	25.30	0.42	439	0.74	293.50	4.87	60.24	9.05	0.03
	Chang 7	YCYV 1118	1141.00	4.25	0.20	5.67	0.30	450	0.94	133.41	7.06	18.90	4.71	0.03
	Chang 7	YCWV 1149	1247.98	3.28	0.12	4.88	0.32	451	0.96	148.78	9.76	15.25	3.66	0.02
	Chang 7	YCYV 1145	1389.00	3.81	0.16	6.50	0.36	444	0.83	170.60	9.45	18.06	4.20	0.02
	Chang 7	YCFV 1113	1409.50	2.07	0.19	2.58	0.35	450	0.94	124.64	16.91	7.37	9.18	0.07
	Chang 9	YCYV 1115	1533.00	4.53	0.19	6.72	0.22	453	0.99	148.34	4.86	30.55	4.19	0.03
	Chang 7	YCYYV 1112	1567.00	4.13	0.17	3.92	0.34	457	1.07	94.92	8.23	11.53	4.12	0.04
	Chang 7	YCYV 1123	1614.05	4.79	0.18	6.59	0.49	454	1.01	137.58	10.23	13.45	3.76	0.03
	Chang 7	YCYYV 1113	1745.32	10.10	0.18	39.53	0.59	443	0.81	391.39	5.84	67.00	1.78	0.00
	Chang 9	YCYV 1123	1752.80	3.47	0.18	4.42	0.21	458	1.08	127.38	6.05	21.05	5.19	0.04
	Chang 7	YCYYV 1114	1917.20	6.70	0.18	19.78	0.40	447	0.89	295.22	5.97	49.45	2.69	0.01
	Chang 7	YCYWV 1112	2297.05	2.97	0.15	4.65	0.27	458	1.08	156.57	9.09	17.22	5.05	0.03

X-ray mineralogy analysis: A bulk and clay (<4 micron) XRD analysis involves semiquantitative (weight percent) determination of all rock-forming and clay/phyllosilicate minerals. Also included is determination of mixed-layer clay types, ordering, and percent expandable interlayers (if any). Bulk and detailed clay XRD analyses of our 46 samples was conducted by K-T Geoservices, Inc., of Gunnison, Colorado.

Gas yield and compositional analysis of gases released from rock crushing: BEG has developed a new method of releasing gases from rocks by crushing under vacuum conditions using the Spex 8000M Mixer/Mill ball mill (Zhang and others, 2014). Released gases from rock grinding under vacuum conditions were directly introduced into the gas chromatograph for gas-compositional analysis. Approximately 10 g of gravel-sized rock sample was loaded into a standard 65-milliliter (mL) hardened steel grinding vial. The vial containing the sample was evacuated overnight through a connection to the gas-chromatograph vacuum gas injection line. After evacuation of the vial, samples were milled for 5 minutes, and the released gas was introduced for analysis to online gas chromatography under a vacuum sample injection mode. Identification and quantification of individual hydrocarbon and nonhydrocarbon gas components was conducted using a two-channel Agilent 7890 Series Gas Chromatograph (GC) custom-configured by Wasson ECE Instrumentation (Fort Collins, CO). The GC was fitted with two capillary columns, six packed columns, a flame ionization detector (FID), and two thermal conductivity detectors (TCD). The GC oven was initially held at 85°C for 5 minutes and then heated to 180°C at 15°C minute^{-1}, where it was held for 10 minutes. The FID signal was recorded on Channel 1 while both TCD signals were collectively monitored on Channel 2. The chromatogram was then integrated using Chemo software. Detector responses have been

calibrated using certified gas standards from Airgas, Inc., at a precision of ±1 mol% for each compound.

- *Residual oil-solvent extraction and quantification:* About 3 g to 5 g of powdered samples were loaded into thimbles and extracted for 4 hours with dichloromethane using Foss Soxtec. The extraction procedure is as follows: (1) Emerge thimbles into a 200 ml aluminum baker loaded with 45 ml CH_2Cl_2 solvent, and boil for 3 hours at 85C°; (2) lift thimbles to an upright position and resin for 50 minutes with CH_2Cl_2; (3) close cooling circulator value and blow with air to dry thimbles for 10 minutes; (4) remove thimbles from extraction system, leave in fume hood and allow to dry completely; (5) leave aluminum cup with extracts in fume hood and weigh cup after it is completely dry; (6) transfer extracts to 2-ml plastic vials; (7) centrifuge plastic vials to precipitate asphaltenes, using pentane at room temperature; and (8) collect pentane solution for column separation after removing asphaltane fraction.
- *SARA fractions separation and quantification:* Small-scale columns were prepared in disposable 5.0-ml serological pipettes by filling with silica gel, which was activated at 120°C for overnight. Saturated hydrocarbons were eluted using 1.8 ml of pentane; aromatic hydrocarbons were eluted using 1.8 ml of 7:3 pentane/dichloromethane mixtures, and the polar eluted using a 9:1 dichloromethane/methanol mixture. Asphaltane fraction, saturate, and aromatic and polar elutes were dried out in fume hood and then weighed with balance.

Organic-Matter Properties of Yanchang Formation

Organic-matter properties include total organic compounds (TOC) content, OM type, and thermal maturity. TOC content ranges from 0.39% to 8.2%, with an average of 4.2% for 46 core samples from YY1 and YY22 wells. Four intervals with TOC > 4% were identified in the YY1 well, from top to bottom: 1,372 m to 1,397 m, 1,409 m to 1,414 m, 1,451 m to 1458 m, and 1,500 m to 1,511 m. High TOC intervals correspond to Chang 7, 8, and 9 members, which are potential sources for oil accumulation in adjacent sandstones. One interval with TOC > 4% in the YY22 well is from 1,315 m to 1347 m; it is stratigraphically equivalent to the Chang 7 member, as in the YY1 well. High TOC intervals also have high oil potential, which is indicated by the S_2 peak of Rock-Eval pyrolysis (**fig. 2**). Oil potential is greater than 5 mg HC/g rock for the samples of TOC >4%, suggesting them as good to excellent source rocks.

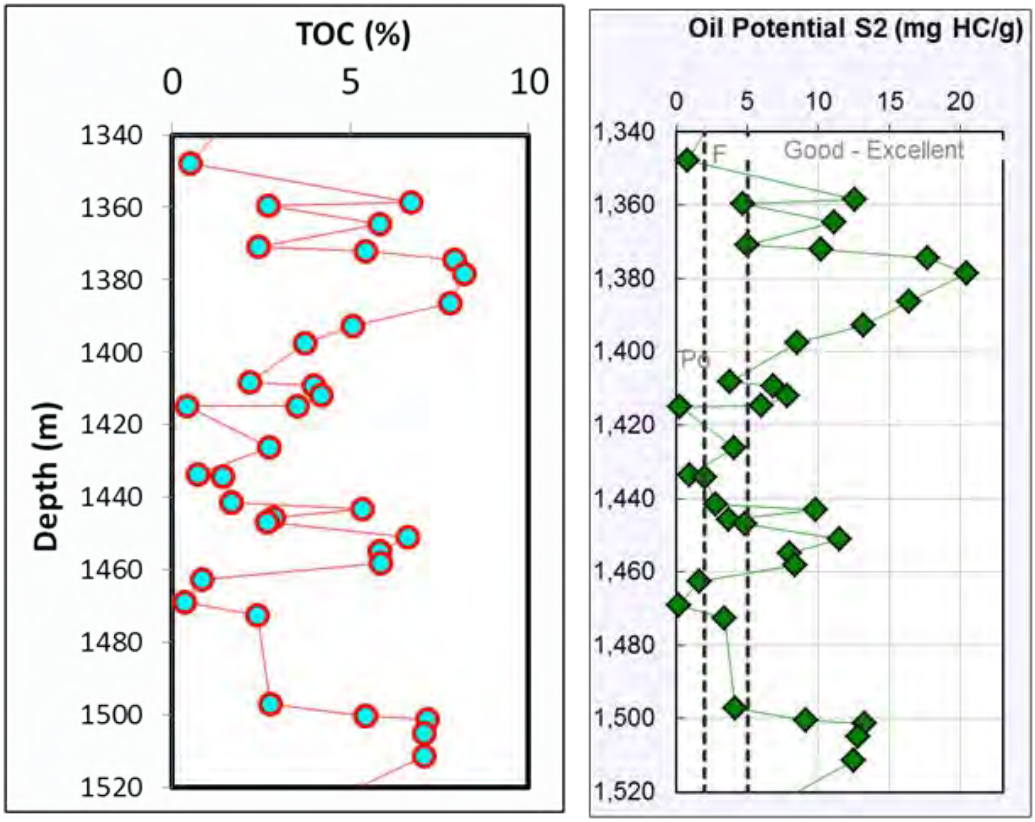

Figure 2. Variation of TOC content and oil potential S_2 in the YY1 well.

The production index, a ratio of S_1 to (S_1+S_2), is a measure of free oil in source rocks and an indicator of migrated oil in sandstones. In the plot of $S_1/(S_1+S_2)$ versus TOC, a very narrow change in the production index appeared for the samples with TOC > 2%; in contrast, a significant increase in the production index appeared for the samples with TOC < 2% (**fig. 3**). The lower the TOC content, the greater the production index, suggesting the presence of migrated oil in sandstones with low TOC content. In some samples with moderate TOC contents (1.5% to 3.5%), a production index that is higher than the high TOC intervals might be attributed to migrated oil or less petroleum expulsion efficiency, or probably a result of the difference in OM type. Oil characterization with gas chromatography-mass spectrometry (GCMS), part of ongoing research work, might provide more evidence to identify the source of free oil in the samples of moderate TOC content.

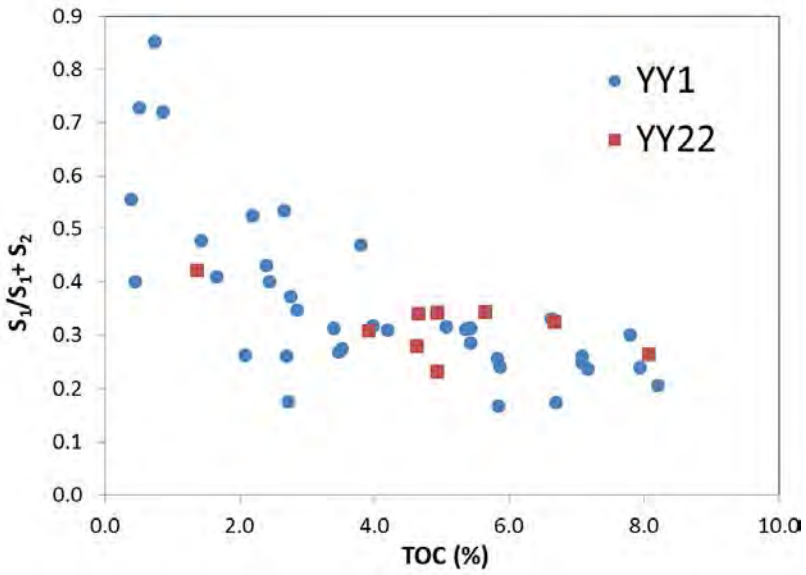

Figure 3. Plot of production index (S_1/S_1+S_2) vs. TOC content. High production index in sandstones with low TOC content is a result of migrated oil.

OM type can be identified from the plot of hydrogen index versus oxygen index if source rocks are immature or in an oil window. We divided all samples into three groups based on TOC content: <2% TOC, 2% to 4% TOC, and >4% TOC. The samples with >4% TOC follow the lines of Type I and Type II kerogen, suggesting that those are good to excellent oil-prone source rocks (**fig. 4**). The samples with <2% TOC follow on the Type III kerogen line, and the samples with moderate TOC content (2% to 4%) are distributed in the area between Type II and Type III kerogen lines. The lower the TOC content, the higher the oxygen index values. Except for two samples with low and high oxygen index, the hydrogen index does not vary significantly as the oxygen index increases. This might be because of the nature of difference in OM type, or the effect of the presence of NSO compounds or asphaltane from migrated oil (Tissot and Welte, 1984). Therefore, a comparison of Rock-Eval pyrolysis for solvent extracted samples is needed to rule out the possibility of a migrated-oil effect.

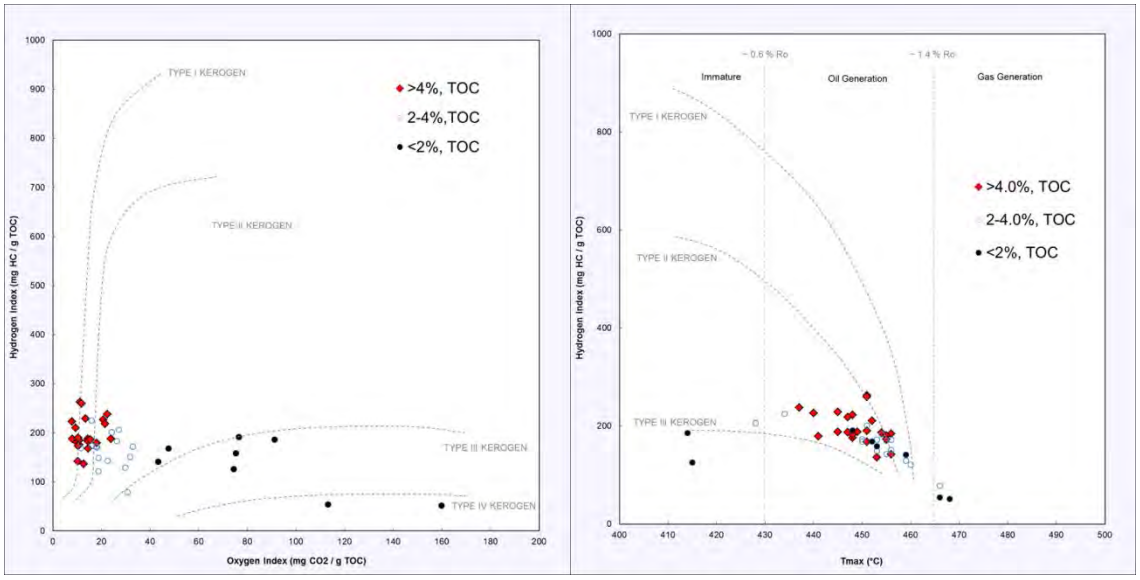

Figure 4. Plots of hydrogen index vs. oxygen index (left) and hydrogen index vs. T_{max} (right).

T_{max}, the temperature at which the maximum release of hydrocarbons from cracking of kerogen occurs during pyrolysis (top of S_2 peak), is an indication of the stage of maturation of the organic matter. The plot of hydrogen index versus T_{max} is normally used to determine the thermal maturity. T_{max} values show a wide range, but mainly fall in the oil-generation range (**fig. 4**). The wide distribution of T_{max} values might also be caused by the presence of large molecular bitumen, which results in low temperature shoulder(s) of S_2 peak. The samples with TOC >4% mainly follow Type II kerogen lines, and it is reasonable to assume that OM type is dominated by Type II kerogen (**fig. 4**). Therefore, we can use T_{max} to calculate the vitrinite reflectance based on the samples with TOC >4%. T_{max} ranges from 437° to 456°C, with an average of 449°C, and the calculated R_o% values are from 0.71 to 1.05, with an average of 0.92%. Hydrogen index values are from 138 mg to 263 mg HC/g TOC, with an average of 199 mg HC/g TOC. The combination of T_{max} values and hydrogen index for the samples with TOC >4% suggests that the thermal maturity of our studied samples is in the oil window.

The thermal maturity versus current burial depth is shown in **fig. 5.** The thermal maturity ranges from 0.74% to 1.08% Roc calculated from T_{max} values based on the equation from Jarvie and others (2005), and the measured bitumen reflectance value by visual kerogen maceral analysis ranges from 0.67% to 0.95%. Indicating organic matter enters the peak of oil generation and the early of oil cracking for the Yanchang Formation in our studied area.

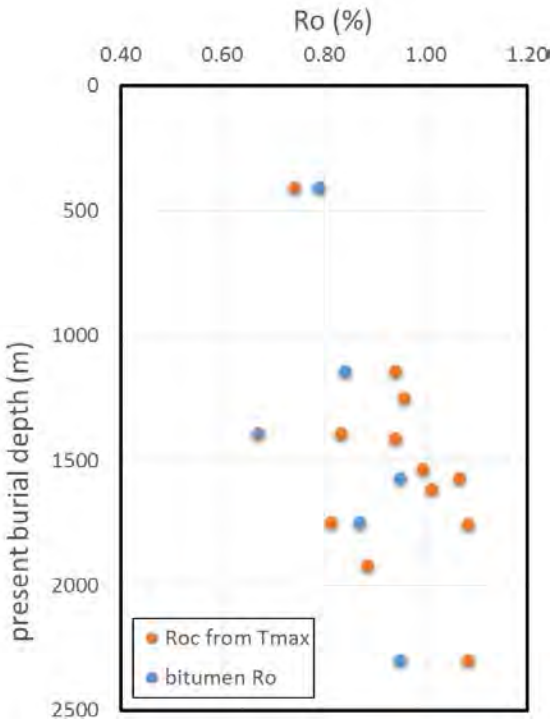

Figure 5. Plot of thermal maturity vs. the present burial depth of the Yanchang Formation.

Thermal maturity in oil window is also supported by gas dryness and residual oil Scanning, Analysis, Response, and Assessment (SARA) compositional fractions. Dryness (C_1/C_{1-5}) of gases released from sandstones ranges from 0.70 to 0.83, with an average of 0.73. The high percentage of NSO polar compounds and asphalting fraction in residual oil extracted from organic-rich mudstones is consistent with the nature of oil generation at oil window. Multiple parameters from different methods of determining thermal maturity can be cross-checked to test the reliability of each.

Geochemical Evidence of Oil Generation, Expulsion in the Yanchang Formation

Total hydrocarbon concentration from gas logging in the YY1 well is shown in **Figure 6.** The thickness of Chang 7 argillaceous mudstone interval is approximately 50 m in the YY1 well. The lower part of the OM rich argillaceous mudrock interval of Chang 7 member has much higher total hydrocarbon concentration than the upper part of Chang 7 organic-rich mudrock. And the thickness of Chang 8 and Chang 9 OM rich argillaceous mudrock is approximately 10 m to 12 m, which is much thinner than the Chang 7 member. Both Chang 8 and Chang 9 organic-rich argillaceous mudrock has much less total hydrocarbon contents than that of the low part of Chang 7 organic-rich argillaceous mudrock. Hydrocarbon content in feldspathic, quartzose, argillaceous arkose intervals that are overlapped just above OM rich argillaceous mudrock are all high, thereby indicating near-source hydrocarbon migration from OM rich argillaceous mudrock and oil/gas charging in argillaceous arkose. Another interesting observation in the lower part of Chang 7 OM rich argillaceous mudrock is that the variation of hydrocarbon content corresponds to mudrock facies, high in OM rich argillaceous mudrock but low in OM lean one.

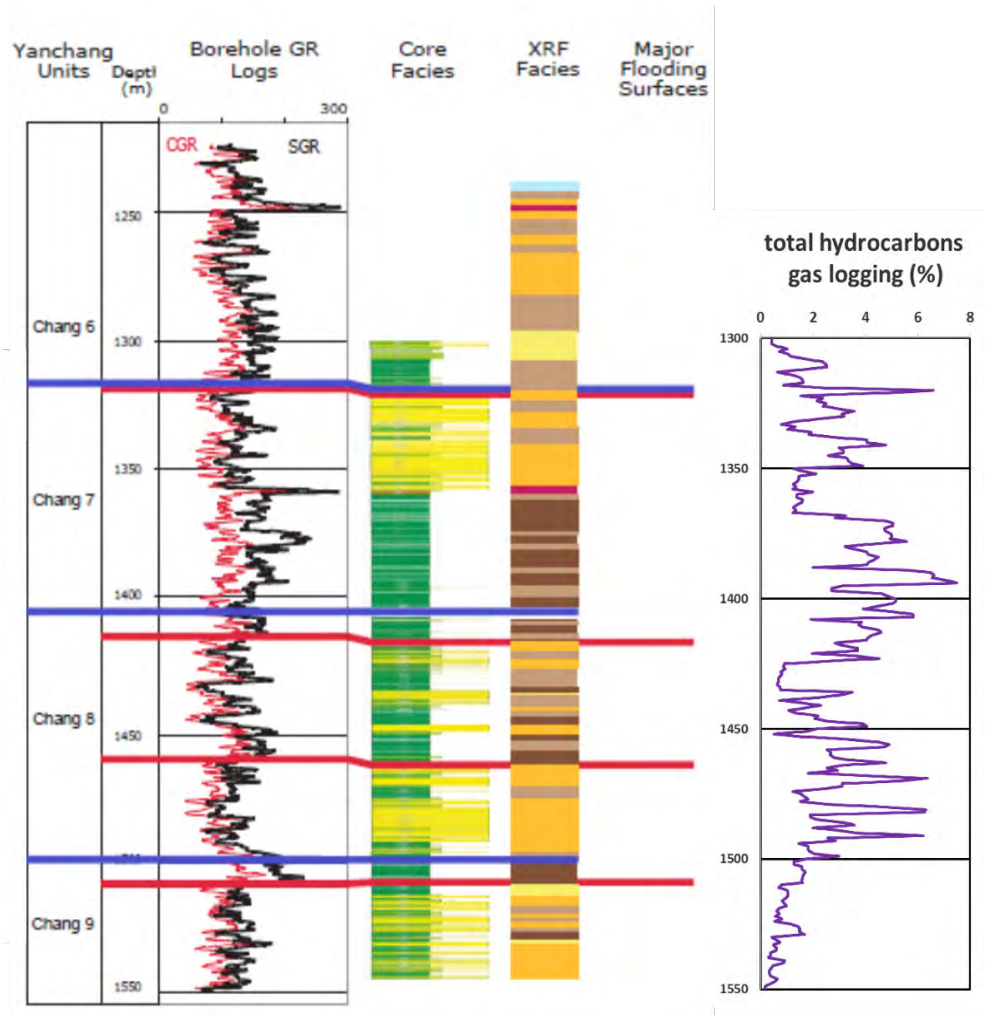

Figure 6. Total hydrocarbons concentration from gas logging in YY1 well.

Free oil (S_1 peak) from Rock-Eval pyrolysis, chemical composition of gases released by rock crushing, and SARA fractions of residual oils extracted from rocks have been investigated in the YY1 well. In **Figure 7**, we highlighted four zones in yellow and one zone in red; all five zones have a high TOC content, but show a highly significant difference in free-oil content and methane concentration.

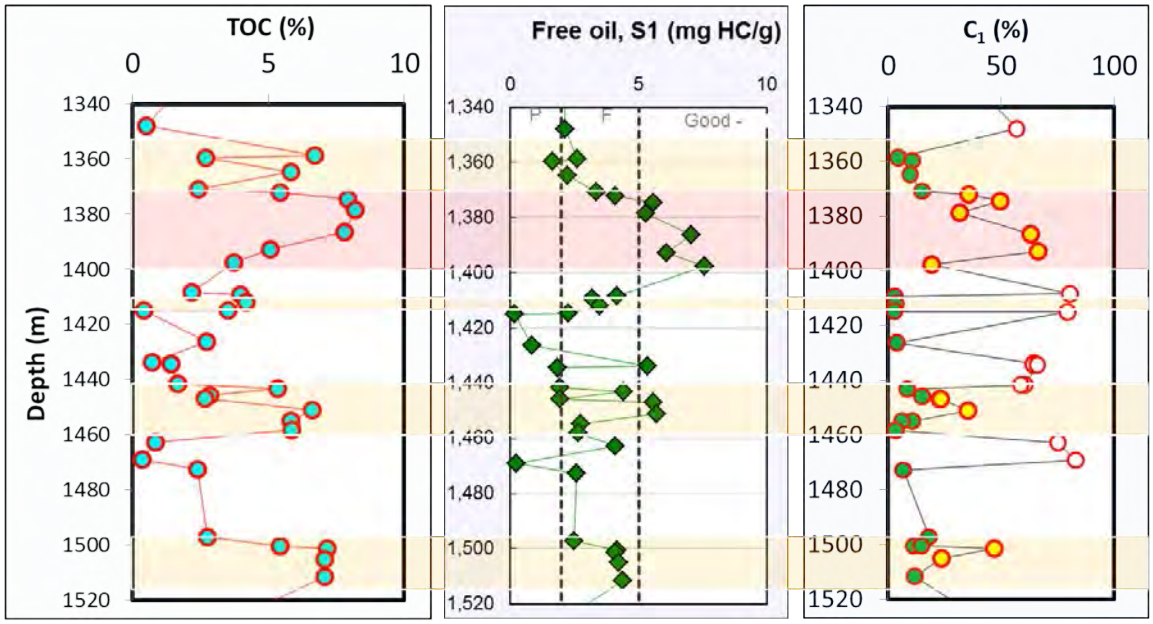

Figure 7. Vertical variation of TOC, free oil (S_1 peak), and methane concentration of gas released from rock crushing in the YY1 well.

Free-oil content in the four zones highlighted in yellow is varied and obviously lower than content in the zone highlighted in red. Five zones highlighted in **Figure** 7 are dominated by OM rich, feldspathic, quartzose argillaceous mudrock. The variation in free-oil content in high TOC zones is mainly related to the difference in petroleum expulsion efficiency. The organic-rich Chang 7 interval can be divided into three parts based on free-oil content. Both the upper and lower parts of the Chang 7 member (1,358 m to 1,371 m and 1,409 m to 1,415 m) have the lowest free-oil content, but the middle part of the Chang 7 member (1,372 m 1,398 m) shows the highest free-oil content among the five highlighted zones. Lithological variation and the thickness of the OM layer play important roles in the free-oil variation in organic-rich layer(s). For the lower part of the Chang 7 member, the organic-rich thin layer (6-m thick from 1,409 m to 1,415 m) is sandwiched by siltstone and sandstone, which is a perfect lithology assemblage for petroleum expulsion. Generated oil in the organic-rich thin layer expelled and migrated in adjacent siltstone and sandstone, which have higher porosity and permeability. Better petroleum expulsion also occurred in the organic-rich interval from 1,358 m to 1,371 m, which is the upper part of the Chang 7 member and approximately 13-m thick. In contrast, the middle part of Chang 7 (26-m thick organic-rich layer) has less petroleum expulsion because of the absence of siltstone and sandstone layers. High free-oil content in the middle of the thick organic-rich Chang 7 mudstone layer suggests that oil saturation is great because of less or absent petroleum expulsion.

The variation in free-oil content in the Chang 7 member is matched with total gaseous hydrocarbons content from gas logging. Both the upper and lower parts of the Chang 7 member (1,358 m to 1,371 m and 1,409 m to 1,415 m) have low gaseous hydrocarbons content, but the

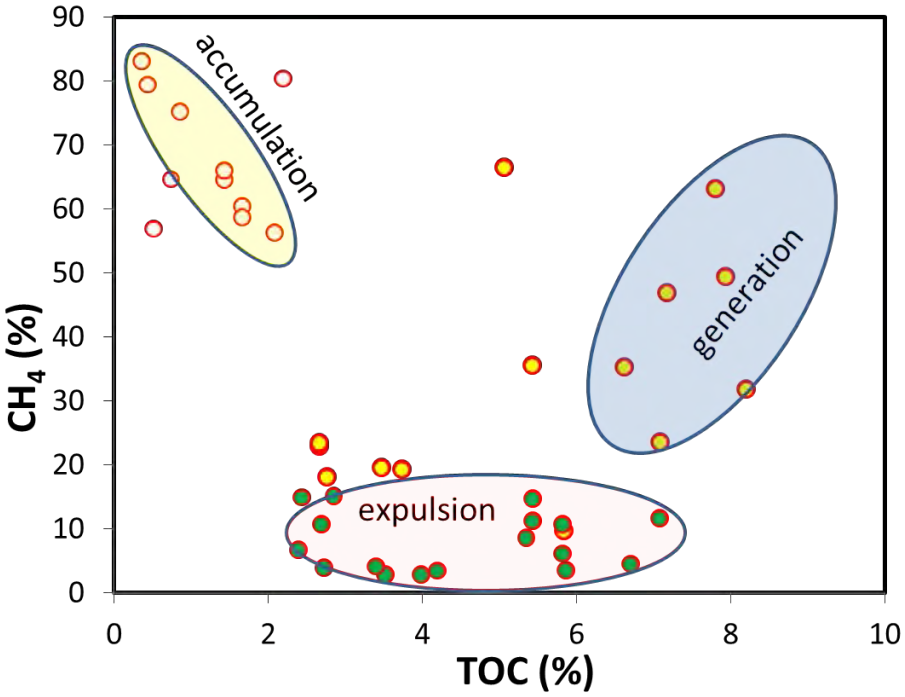

Figure 8. TOC–CH_4 plot for identifying oil generation, expulsion, and accumulation in the Yanchang Formation.

middle part of the Chang 7 member (1,372 m to 1,398 m) shows the highest gaseous hydrocarbons content among the 5 highlighted zones. The organic rich argillaceous mudstone of the Chang 9 member (1,497 m to 1,511 m) has the lowest gas content among 5 highlighted zones, and the gaseous hydrocarbons content of the argillaceous arkose just above the Chang 9 OM rich mudrock is high. It is reasonable to conclude that near-source oil migration occurs and oil charges into adjacent argillaceous arkose reservoirs. The consistence between free-oil and gaseous hydrocarbons content suggests that gas hydrocarbons logging is a reliable tool to determine oil and gas saturation in organic-rich argillaceous mudrock in our studied area.

The chemical composition of gases released from rock crushing shows a dramatic difference between high TOC intervals that experienced different extents (lesser or stronger) of petroleum expulsion. As shown on the right side of **Figure 8**, three groups can be identified based on the percentage of methane concentration. Although green points and yellow points are all in organic-rich mudrocks, methane concentration is obviously different. Open red circles are all sandstone layers; herein, methane concentration is high, above 65%. Green points show low methane concentration (<10%) and represent the organic-rich mudrock layers, which have experienced strong petroleum expulsion, resulting in less free oil and free gas being retained. Gas is mainly dissolved in oil; the dissolved gas can be degassed from oil during rock crushing under vacuum conditions. Gas composition in oil-dissolved gas is dominated by heavier gaseous components (propane, butane, and pentane). In contrast, yellow points show high methane concentration (>15%) and represent the organic-rich mudstone layers, which have experienced less petroleum expulsion. In particular, methane concentration in the middle part of the Chang 7 member is obviously higher than that in both the upper and lower parts of the member. Less or no petroleum

expulsion in the middle part of the Chang 7 results in high methane concentration similar to that in sandstone.

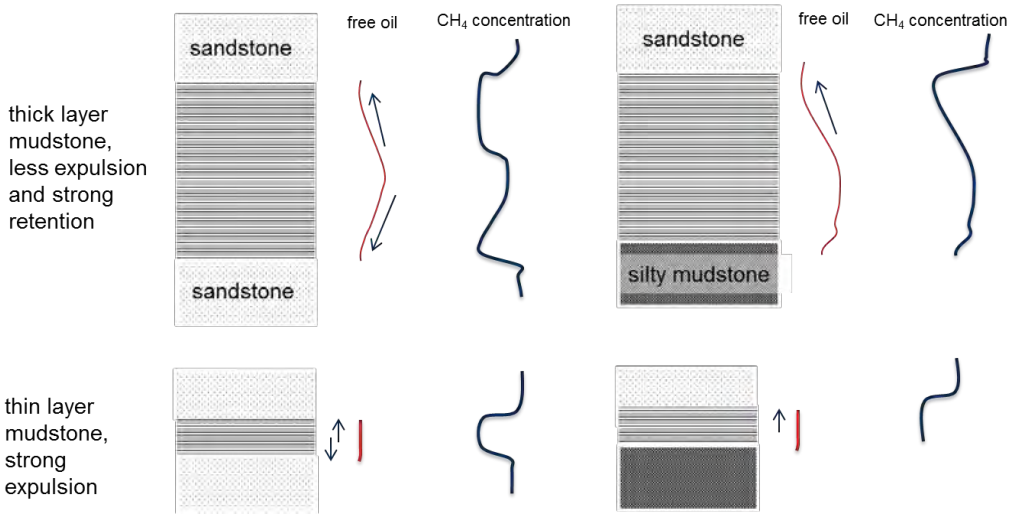

Figure 9. Conceptual model of oil expulsion from OM-rich layers.

Petroleum expulsion in Yanchang lacustrine shale commonly occurs in this sandstone/mudstone interbedded system. It is crucial for us to identify petroleum generation, expulsion, and accumulation by examining the hybrid system as a whole. A CH_4–TOC plot is useful for identifying generated gas in source rocks, retained gas in source rocks after expulsion, and migrated gas in sandstones from source-rock expulsion. CH_4 concentration is high in TOC at less than 2% intervals where siltstone and sandstone are dominant (**fig. 9**). Gas in low-TOC sandstone and siltstone layers mainly derives from migrated gas from source-rock petroleum expulsion. The generated gas in organic-rich mudstones with less or no petroleum expulsion also shows high concentration of CH_4; in contrast, the retained gas in organic-rich mudstones after petroleum expulsion displays very low CH_4 concentration. The wide-ranging variation of CH_4 concentration in organic-rich source rocks reflects the extent of petroleum expulsion. The greater the extent of petroleum expulsion, the lower the concentration of CH_4 in the released gas from rocks.

From our observations, we proposed a conceptual model for oil expulsion from OM-rich layers (**fig. 9**), considering two settings. One setting is the thick mudstone layer with less petroleum expulsion and strong retention. If the thick organic-rich layer is sandwiched by sandstone layers with high porosity and permeability, petroleum-expulsion efficiency toward the boundary of sandstone/mudstone is the highest, decreasing in the middle of the thick mudstone layer. As a result, a decreased concentration gradient in free oil from the middle to the edge of the thick mudstone layer appears, as we observed in the Chang 8 organic-rich interval from 1,451 m to 1,458 m in the YY1 well. CH_4 concentration in gas retained after petroleum expulsion is low and dominated by oil-dissolved gas. If the thick organic-rich layer is sandwiched by a sandstone

layer on its top and silty mudstone on its bottom, petroleum-expulsion efficiency toward the boundary of sandstone/mudstone is high, but low in the middle and lower parts of the thick mudstone layer. The other setting is the thin mudstone layer with strong petroleum expulsion. A sandstone/thin organic-rich mudstone/sandstone- or silty-mudstone pattern is a perfect hybrid system for petroleum expulsion. The thickness for effective source rock, about 10 m to 12 m in the Yanchang Formation, might vary with lithology assemblage.

Possible Petroleum-Expulsion Mechanism

Lithology variation can greatly affect the gas chemical compositions of the migrated gas from source rocks and the retained gas in organic-rich shale. A hand core sample is composed of clay-rich mudstone in the upper portion and carbonate with cone-in-cone structure in the lower portion (**fig. 10**). Chemical compositions of gases released from lithologically different portions are obviously themselves different. Propane, butane, and pentane are dominating components in clay- and organic-rich shale; in contrast, methane and ethane are dominant in cone-in-cone carbonate. The ratios of iC_4/nC_4 and iC_5/nC_5 in organic-rich shale are slightly higher than those in cone-in-cone carbonate, while C_1/C_2 and C_2/C_3 ratios are much smaller in organic-rich shale than those in cone-in-cone carbonate. Oil and gas in cone-in-cone carbonate is most likely from the expelled oil of the organic-rich shale. Migrated gas contains more methane and ethane than the gas retained in the organic-rich shale after oil expulsion.

Gas composition (%)

	C_1	C_2	C_3	iC_4	nC_4	iC_5	nC_5
c-i-c	62.7	18.3	7.6	2.9	4.4	2.3	1.7
shale	2.9	7.0	22.2	24.3	20.1	15.3	7.9

Gas yield (μl/g rock)

	C_1	C_2	C_3	iC_4	nC_4	iC_5	nC_5
c-i-c	25.3	7.4	3.1	1.2	1.8	0.9	0.7
shale	0.7	1.7	5.4	5.9	4.9	3.7	1.9

Gas Ratios

	C_1/C_2	C_2/C_3	iC_4/nC_4	iC_5/nC_5
c-i-c	3.13	1.07	1.32	2.30
shale	0.42	0.31	1.21	1.93

Figure 10. Lithology variation can greatly affect migrated and retained gas compositions.

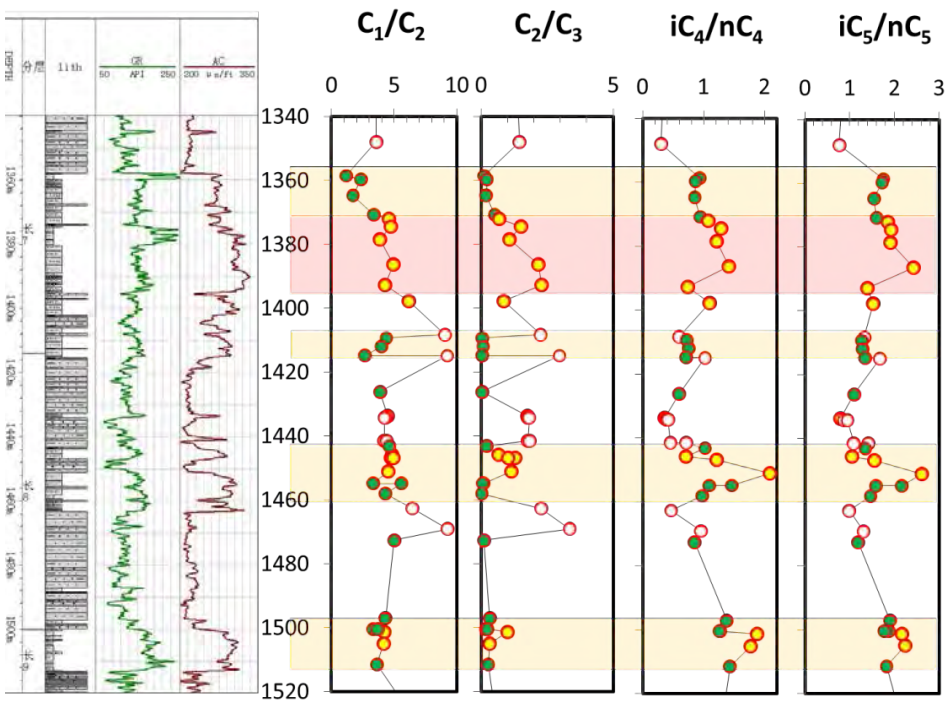

Figure 11. Difference in chemical compositions of generated, migrated, and retained gas in the YY1 well.

The difference in chemical composition between migrated gas and retained gas is also observed from a core study of the YY1 well. In **Figure 11**, green points represent the intervals of retained gas after strong petroleum expulsion; open red circles, the migrated gas from organic-rich mudstone intervals stored in sandstones; and yellow points, the generated gas in organic-rich intervals with less petroleum expulsion. The C_1/C_2 and C_2/C_3 ratios of retained gas in organic-rich mudstone intervals after strong petroleum expulsion are obviously smaller than those of the migrated gas expelled from organic-rich mudstone intervals and stored in sandstones, indicating a strong retention of large gas molecules in organic-rich shales (**fig. 11**). The C_1/C_2 and C_2/C_3 ratios of accumulated gas in sandstones are slightly larger than those of the generated gas in the organic-rich source, possibly suggesting that bulk-fluid migration driven by pressure difference dominates in primary petroleum expulsion. The increasing sequence of iC_4/nC_4 and iC_5/nC_5 ratios is: generated gas > retained gas > accumulated gas, indicating that a preferential retardation of branched compounds to normal ones results from the geo-chromatographic fractionation through the matrix pore system and along migration pathways in organic and clay-rich source rocks.

A correlation of free oil and the SARA fractions of residual oil shows that free oil is mainly composed of saturate and aromatics. Free oil is the volatile oil that refers to the S_1 peak of Rock-Eval pyrolysis at a temperature below 350°C. It has a linear correlation with the sum of saturate and aromatic fractions (**fig. 12**), which are mobile fractions in oil. Most of our samples follow a 1:1 ratio line of free oil and the sum in weight of saturate and aromatic fractions in rocks, thereby indicating that free oil is mainly composed of saturate and aromatic fractions, which are less viscous. In contrast, no correlation exists between free oil and the sum in weight of NSO polar

compounds and asphalting fractions, which have larger molecular weight, strong affinity, and great retardation in organic-rich and clay-rich source rocks. As a result, expelled oil from source rocks enriches in saturate and aromatic fractions.

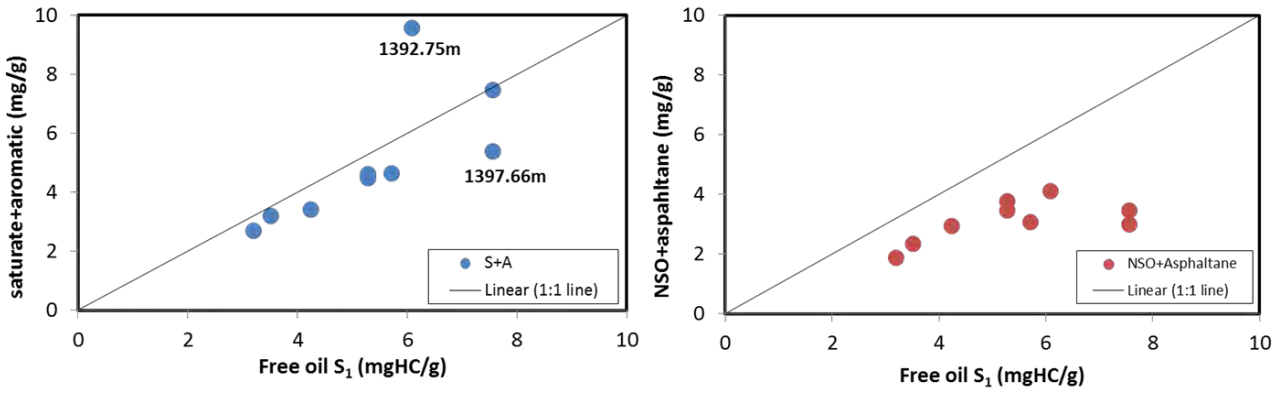

Figure 12. Correlation of free oil and SARA fractions of residual oil in mudstones.

Pore Connectivity and Released Gas Yield from Rock Crushing

Released gas yields from rock crushing under vacuum conditions could be used as a proxy of the pore connectivity in mudstones (Zhang and others, 2014). The yield of gas released from rock crushing can be affected by mineralogy, in particular carbonate content, pore connectivity, and petroleum expulsion efficiency. In general, sandstones contain a high carbonate content (15 wt% to 35 wt%), but total yield of $C_{1\text{-}5}$ released from sandstone crushing is obviously lower than in the organic-rich mudstone intervals with strong petroleum expulsion. Carbonate contents vary slightly in organic-rich mudstone intervals with less or strong petroleum expulsion. Carbonate contents in rocks is not the main factor in determining the variation of retained gas yield.

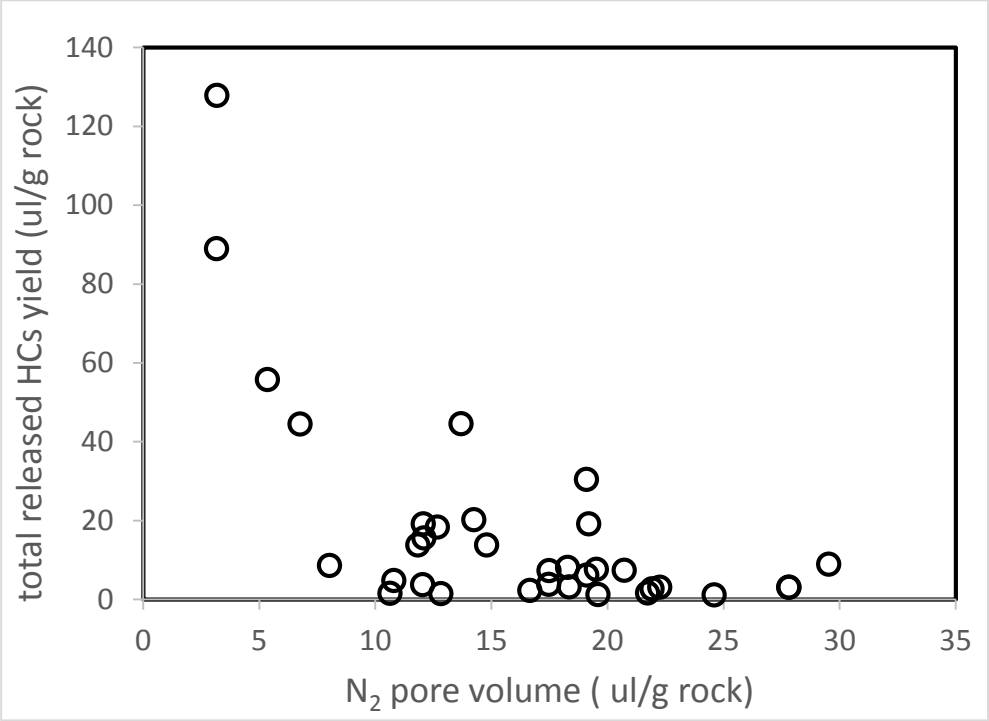

Figure 13. Correlation of total yield of $C_{1\text{-}5}$ retained in isolated pores with rock porosity measured by N_2 porosimetry.

The isolated pores of organic-rich mudstone intervals have a varied gas yield. The greater the pore connectivity, the less the proportion of the isolated pores to total rock porosity (Kitty and others, 2012, 2013). As a result, less gas is blocked in unconnected or isolated pores. A rapid decreasing trend in total yield of $C_{1 \text{ through } 5}$ exists from gas retained in organic-rich mudstones with the rock porosity possibly indicating an increase in pore connectivity (**fig. 13**). Better pore connectivity might exist in the intervals where total porosity is high.

Conclusions

1. TOC content is high and ranges from 0.39% to 8.20%, with an average of 4.2% for the Triassic Yanchang Formation.
2. The Triassic Yanchang Formation is a good-to-excellent source for oil generation potential. Organic matter is dominated by oil-prone Type II kerogen, and its thermal maturity is in the oil window.
3. The lower part of the Chang 7 member, at a 25-m-thick organic-rich interval, contains a significant amount of free oil, and gaseous hydrocarbons content is high based on gas logging. It is the target for shale gas/oil exploration in terms of resources.
4. Gas and oil expulsion occurred for the upper part of the Chang 7 member, and for both of the Chang 8 and Chang 9 members. Near-source oil migration and charging model can be applied to oil and gas accumulation in the argillaceous arkose reservoirs.
5. Bulk-fluid migration driven by pressure difference dominates in primary petroleum expulsion. The induced microfracture in petroleum generation is likely a path for migration.

References

Milliken, K., Esch, W.L., Reed, R.M., and Zhang, T., 2012, Grain assemblages and strong diagenetic overprinting in siliceous mudrocks, Barnett Shale (Mississippian), Fort Worth Basin, TX: AAPG Bulletin, v. 96, no. 8, p. 1553–1578.

Milliken, K., Rudnicki, M., Awwiller, D.N., and Zhang, T., 2013, Organic matter-hosted pore system, Marcellus Formation (Devonian), PA: AAPG Bulletin, v. 97, no. 2, p. 177–200.

Tissot, B.P., and Welte, D.H., 1984, Petroleum formation and occurrence, 2nd ed., New York: Springer-Verlag, 702 p.

Zhang, T., Ellis, G.S.; Ruppel, S.C., Milliken, K., and Yang, R., 2012, Effect of organic-matter type and thermal maturity on methane adsorption in shale-gas systems: Organic Geochemistry, v. 47, p. 120–131.

Zhang, T., Yang, R., Milliken, K., Ruppel, S.C., Pottorf, R.J., and Sun, X., 2014, Chemical and isotopic composition of gases released by crush methods from organic rich mudrocks: Organic Geochemistry, v. 73, p. 16–28.

TASK 4.2

Organic Petrology of Peak Oil Maturity Triassic Yanchang Formation Lacustrine Mudrocks, Ordos Basin, China

Paul C. Hackley[1]

[1]*U.S. Geological Survey, MS 956 National Center, 12201 Sunrise Valley Dr, Reston VA*

Abstract

Organic petrology evaluation and determination of solid bitumen reflectance (BR_o) were completed for Triassic Yanchang Formation mudrocks (n=15) from the Ordos Basin, north-central China, as part of a larger investigation of "shale gas" resources. These data were integrated with information from Rock-Eval pyrolysis to show that samples are in the peak oil window of thermal maturity and that organic matter (OM) is dominated by solid bitumen with minor amounts of Type III kerogen (vitrinite and inertinite) from vascular land plants. Describing a "kerogen Type" for these rocks based strictly on parameters determined from pyrolysis is inappropriate and misleading because the original OM has converted to hydrocarbons (present as solid bitumen), some of which has been expelled into adjacent reservoir facies. However, on the basis of comparison to immature-early mature lacustrine mudrock (Garden Gulch Member of Green River Formation) and marine shale (Boquillas Formation), we suggest that original OM may have been Type I/II with HI values of greater than 700 mg HC/g TOC.

Introduction

Unconventional gas resources in lacustrine shale and mudrock in the continental basins of northern China have received significant attention in the last years following successful development of unconventional marine "shales" in North America (Lin and others, 2013). In China, it is estimated that >85% of hydrocarbon reserves are sourced from lacustrine settings with notable differences in petroleum system characteristics compared to marine systems, e.g., thick, areally-limited source rock presence with poor connectivity to higher porosity reservoir facies, and a generation of highly viscous waxy hydrocarbons (Katz and Lin, 2014). Lacustrine mudrocks in China also are characterized by higher clay concentrations and lower thermal maturity than the majority of North American shale gas systems (Tang and others, 2013a, b). Despite widespread international interest and government promotion of shale petroleum systems, development has thus far been limited; only 22 wells were completed in shale by 2011 (Luo and Zhao, 2012), compared to >10,000 wells spudded in 2011 in the North American unconventional plays (IHS Energy Group, 2015).

The Ordos Basin in north-central China (**fig. 1**) is a flexural sag basin, developed on cratonic rocks when far-field compressive stresses deformed the north and south margins of the China tectonic block (Ritts and others, 2004; Zhao and others, 2006). The Upper Triassic Yanchang Formation is a lacustrine unit consisting of repetitive transgressive-regressive sequences of fluvial, shoreface and deep water sediments deposited in fluvio-lacustrine settings (Zhao and others, 2015). It has been divided into 10 members, called Chang 1 through Chang 10, from

oldest to youngest, respectively. The Chang 7 member, composed of interbedded dark shale, sandy shale, and mudstone, is the primary source rock interval in the Yanchang Formation (Wu and others, 2015; Zhang and others, 2015; Yang and others, 2016). Deposition of Chang 7 represents the period of greatest lake expansion (~85,000 km^2, Zhao and others, 2010). Previous work suggested deep water deposition of algal-rich organic matter occurred in stratified low-salinity waters under reducing conditions (Yang and Zhang, 2005; Yuan and others, 2015). Analytical results from rock-focused studies and burial history modeling show that conditions of oil window thermal maturity were reached in the Early Cretaceous (Zhao and others, 1996; Ren and others, 2007) and hydrocarbon expulsion and primary migration occurred because of volume expansion associated with kerogen cracking (Zhang and others, 2006). Reservoir facies in adjacent delta-front and prodelta Chang 6 and Chang 8 tight sandstones were charged by short- distance hydrocarbon migration from Chang 7 mudrocks (Yao and others, 2013).

Previous studies of OM facies in oil mature Yanchang Chang 7 mudrocks reported Type I-II kerogen (Hanson and others, 2007; Wang and others, 2013; Lin and others, 2013; Tang and others, 2013a, b; Guo and others, 2014). The kerogen typing has been based primarily on pyrolysis classification, although summarized results from organic petrography were reported (Hanson and others, 2007; Wang and others, 2013; Guo and others, 2014). Several studies reported vitrinite reflectance results (Lin and others, 2013; Tang and others, 2013a, b) but did not include descriptions of organic petrographic character. Additional studies on kerogen "Type" of Yanchang Formation strata (cited in Lin and others, 2013; Yao and others, 2013) are in Chinese and largely inaccessible to Western researchers. Here, we observe that kerogen typing from programmed pyrolysis reflects the present-day organic composition of the sample, which, as we subsequently show, is not kerogen. Instead, in the oil window thermal maturity samples examined herein the OM consists almost entirely of solid bitumen. However, previous workers described organic material in similar oil window mature (R_o 0.9–1.1%) Yanchang Formation as "kerogen," present in a "kerogen network" (e.g., Yao and others, 2013). "Solid bitumen" is used by organic petrographers to describe OM representing secondary products of hydrocarbon generation from kerogen (Cardott and others, 2015). This term is not in exact correspondence to the geochemists' definition of "bitumen," which is the organic material removed from rock samples by typical organic solvents, such as or dichloromethane (Durand, 1980; Vandenbroucke and Largeau, 2007). For thermally mature systems, such as the Yanchang mudrocks, the two terms describe in part the same material because what is extracted by organic solvents primarily is extracted from solid bitumen (because solid bitumen is the only labile OM present).

As part of a larger study of the petroleum geology of the Yanchang Formation, we present in this contribution the organic petrology and solid bitumen reflectance values (BR_o) of peak oil mature Chang 7 and other Yanchang mudrocks and integrate this data with the results from Rock-Eval pyrolysis. Further, we compare our data to previous studies of organic facies and thermal maturity in the Yanchang Chang 7, discuss implications with respect to prospectivity for unconventional oil and gas resources, and make comparison to North American marine shales and other prospective lacustrine mudrocks.

Materials and Methods

Samples (n=15) were received at the U.S. Geological Survey (USGS) for organic petrography analysis as small core chips of 3 g to 5 g mass identified by formation/member, well name, and

depth (Table 1). Samples were crushed with mortar and pestle to ~1 mm top size and prepared in 1-inch circular thermoplastic mounts via ASTM D2797 (ASTM, 2015a) for organic petrographic analysis. The mounts were imaged under oil immersion on a Zeiss AxioImager in white and blue incident light. Solid bitumen reflectance analyses (n=14) were conducted according to ASTM D7708 (ASTM, 2015b). A Leica DM4000 microscope equipped with LED illumination and monochrome camera detection was used for reflectance analysis with the computer program DISKUS-FOSSIL by Hilgers Technisches Buero using a Klein and Becker YAG calibration standard (0.908% R_o). Two samples (YCDT 1119 407 m, YCYYV 1113 1,745.32 m) were imaged by way of SEM at USGS in secondary and back-scattered electron mode, generally at 3 kV to 5 kV, 5 mm to 6 mm w.d., and magnifications of 100–15,000x, to observe OM textures. Rock-Eval pyrolysis and total organic carbon (TOC) content were determined in a commercial laboratory (Geomark) by typical methods (Espitalié and others, 1977, Peters, 1986). A select group of samples (**Table 1**) were extracted by way of Soxhlet with dichloromethane (DCM) according to typical procedures at the Bureau of Economic Geology (BEG) before Rock-Eval pyrolysis.

Table 1: Sample identification, lithology, Rock-Eval and reflectance data for Yanchang samples.

	FM	Sample ID	Depth (m)	TOC (wt%)	S1 (mg HC/g)	S2 (mg HC/g)	S3 (mg CO2/g)	T_{max} (°C)	R_o(ca) (%)	BR_o(m) (%)	HI	OI
unextracted	Chang 7	YCDT 1119	407.00	14.70	3.54	43.84	0.84	442	0.80	0.79	298	6
	Chang 7	YCYV 1118	1141.0	5.19	7.44	10.47	0.43	444	0.83	0.84	202	8
	Chang 7	YCYV 1145	1389.0	4.33	4.90	10.79	0.66	442	0.80	0.67	249	15
	Chang 7	YCYYV 1112	1567.0	4.52	3.88	6.08	0.66	457	1.07	0.95	135	15
	Chang 9	YCYV 1123	1752.8	3.94	2.67	5.83	0.52	458	1.08	n.d.	148	13
	Chang 7	YCYWV 1112	2297.1	3.71	1.92	7.60	0.58	459	1.10	0.95	205	16
	Chang 7	YCYYV 1113	1745.32	10.90	3.20	52.95	0.73	450	0.94	0.87	486	7
after Soxhlet extraction	Chang 7	YCDT 1119	407.00	8.62	0.78	25.30	0.42	439	0.74		294	5
	Chang 7	YCYV 1118	1141.00	4.25	0.20	5.67	0.30	450	0.94		133	7
	Chang 7	YCYV 1145	1389.00	3.81	0.16	6.50	0.36	444	0.83		171	9
	Chang 7	YCYYV 1112	1567.00	4.13	0.17	3.92	0.34	457	1.07		95	8
	Chang 9	YCYV 1123	1752.80	3.47	0.18	4.42	0.21	458	1.08		127	6
	Chang 7	YCYWV 1112	2297.05	2.97	0.15	4.65	0.27	458	1.08		157	9
	Chang 7	YCYYV 1113	1745.32	10.10	0.18	39.53	0.59	443	0.81		391	6
unextracted	Chang 7	YY1-1070	1378.51	8.20	5.28	20.44	0.68	447	0.89	0.93	249	8
	Chang 7	YY1-1209	1392.75	5.06	6.09	13.14	0.60	451	0.96	0.95	260	12
	?	YY1-1257	1397.66	3.79	7.56	8.53	0.60	434	0.65	0.93	225	16
	Chang 8	YY1-1775	1451.02	6.62	5.71	11.47	0.69	455	1.03	0.89	173	10
	Chang 9	YY1-2103	1504.98	7.08	4.24	12.77	0.71	455	1.03	0.94	180	10
	Chang 7	YY22-2560	1320.84	4.93	5.82	11.16	1.02	440	0.76	0.73	226	21
	Chang 7	YY22-2746	1336.03	8.07	7.59	21.20	0.91	451	0.96	0.81	263	11
	Chang 7	YY22-2858	1346.87	3.92	3.51	7.88	0.95	451	0.96	0.84	201	24

FM, formation; TOC, total organic carbon; HC, hydrocarbon; R_o(ca), calculated vitrinite reflectance (0.018*T_{max} - 7.16; Jarvie et al., 2001); B
HI, hydrogen index (mg HC/g TOC); OI, oxygen index (mg CO_2/g TOC); PI, production index; n.d., no data.

S2/S3	S1*100/TOC	PI [S1/(S1+S2)]
52.19	24.08	0.07
24.35	143.35	0.42
16.35	113.16	0.31
9.21	85.84	0.39
11.21	67.77	0.31
13.10	51.75	0.20
72.53	29.36	0.06
60.24	9.05	0.03
18.90	4.71	0.03
18.06	4.20	0.02
11.53	4.12	0.04
21.05	5.19	0.04
17.22	5.05	0.03
67.00	1.78	0.00
30.06	64.39	0.21
21.90	120.36	0.32
14.22	199.47	0.47
16.62	86.25	0.33
17.99	59.89	0.25
10.94	118.05	0.34
23.30	94.05	0.26
8.29	89.54	0.31

R_o (m), measured bitumen reflectance;

Results

Rock-Eval pyrolysis and TOC

TOC concentrations range 3.7 to 14.7 wt.% (avg. 6.4 wt.%) for Yanchang mudrocks, the highest TOC content occurring in Chang 7 (**Table 1**). These results are similar to prior reports for oil window mature Yanchang samples (e.g., Lin and others, 2013). Rock-Eval results show average S1 and S2 concentrations of 4.9 and 16.3 mg HC/g, respectively. Average HI value is 233 mg HC/g TOC and average S1/TOC is 89.8 mg HC/g TOC. T_{max} values range from 434° to 459°C and PI values average 0.28. Solvent-extracted samples show an average decrease of 21% for TOC, 93% for S1, 35% for S2, and 21% for HI. Average T_{max} is incrementally lower by 0.1% in extracted samples, whereas average PI is decreased by 89%.

Solid bitumen reflectance

Measured solid bitumen reflectance (BR_o) values range from 0.67% to 0.95% (n=14, **Table 1**), within the range of 0.52% to 1.52% R_o reported by Wang and others (2013). BR_o histograms are illustrated in **Figures 2 and 3**. We elected to measure and report BR_o as opposed to vitrinite reflectance because vitrinite is sparse, absent, or difficult to identify with confidence in the samples examined herein. BR_o is interpreted to be a good proxy for vitrinite reflectance in the peak oil window based on previous studies that compared the two thermal maturity parameters (Jacob, 1989; Landis and Castaño, 1994). Further, we elected not to apply a conversion to BR_o to obtain vitrinite reflectance equivalent values (e.g., Petersen and others, 2013) as recent interlaboratory studies have suggested, these empirical conversion schemes should be treated with caution (Hackley and others, 2015), and perhaps used only in the strata where derived. Measured BR_o values range from 0.15% less than 0.28% greater in reflectance than R_o values calculated from T_{max} (Jarvie and others, 2001), 11 of 14 measured BR_o values are lower than calculated R_o values, averaging 0.1% lower. BR_o values show poor correlation to present-day burial depth (r^2=0.19), as do calculated R_o values (r^2=0.31).

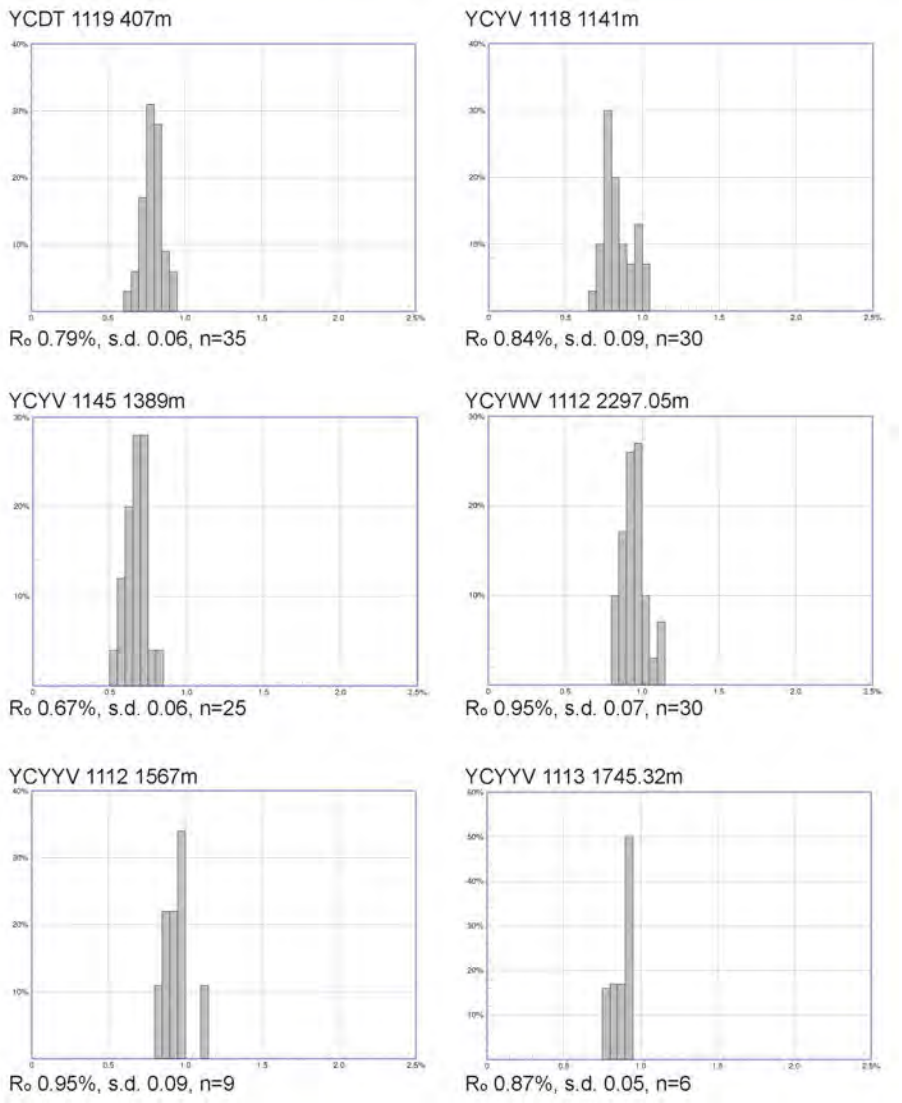

Figure 1. Solid bitumen reflectance (BR_o) histograms for samples from widely dispersed areas. See Table 1 for additional sample information. Abbreviations: s.d., standard deviation, n, number of measurements. For two samples the number of measurements was not compliant with ASTM D7708 (ASTM, 2015b) due to low solid bitumen abundance or because solid bitumen was finely dispersed into the mineral matrix. The abscissa scale is the same in all histograms; the ordinate scale varies according to the total number of measurements and their standard deviation.

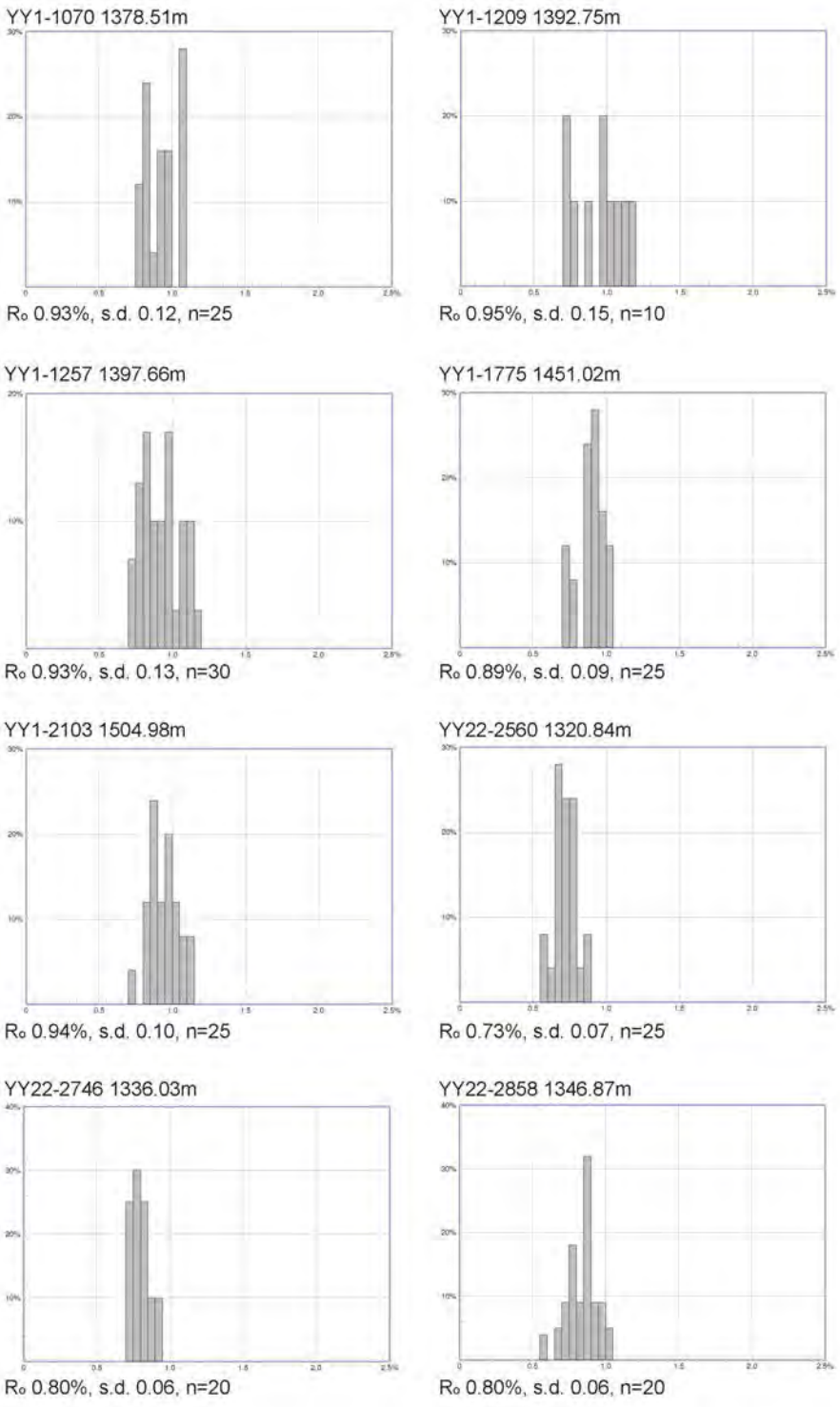

Figure 2. Solid bitumen reflectance (BR_o) histograms for samples from the YY1 and YY22 wells. See Table 1 for additional sample information. Abbreviations: s.d., standard deviation, n, number of measurements. For one sample (YCYV 1118 1141m) the number of measurements was not compliant with ASTM D7708 (ASTM, 2015b) due to low solid bitumen abundance or because solid bitumen was finely dispersed into the mineral matrix. The abscissa scale is the same in all histograms; the ordinate scale varies according to the total number of measurements and their standard deviation.

Organic facies

Organic matter in Chang 7 samples is constituted almost exclusively of solid bitumen, visually estimated as ~95 vol.% of the total OM content. Solid bitumen is present in a continuum of morphologies, ranging between: 1. groundmass or "network" (**fig. 3A**), 2. void- and pore-filling (**fig. 3B**), 3. vein- and fracture-filling (**fig. 3C**), 4. interlayered on bedding planes (**fig. 3D through F**), 5. interleaved with clays (**fig. 4A and B**), and 6. finely dispersed in mineral interstices (**fig. 4C**). Solid bitumen was generated and/or emplaced coevally with authigenic carbonate precipitation as evidenced by frequent contact on euhedral crystal terminations (**fig. 4D**) or adjacent to growth zoned crystals (**figs. 4E through F**). Solid bitumen is present with orange-reddish fluorescence grading to nonfluorescent (**figs. 5A and B**). BR_o measurements were determined on nonfluorescent solid bitumen, which is the dominant occurrence. Solid bitumen was present in all samples; however, in Chang 9 sample YCYV 1123 1752.8 m (TOC 3.95 wt.%) it occurred in mineral interstices generally <5 μm in size (**fig. 4C**), preventing measurement of BR_o.

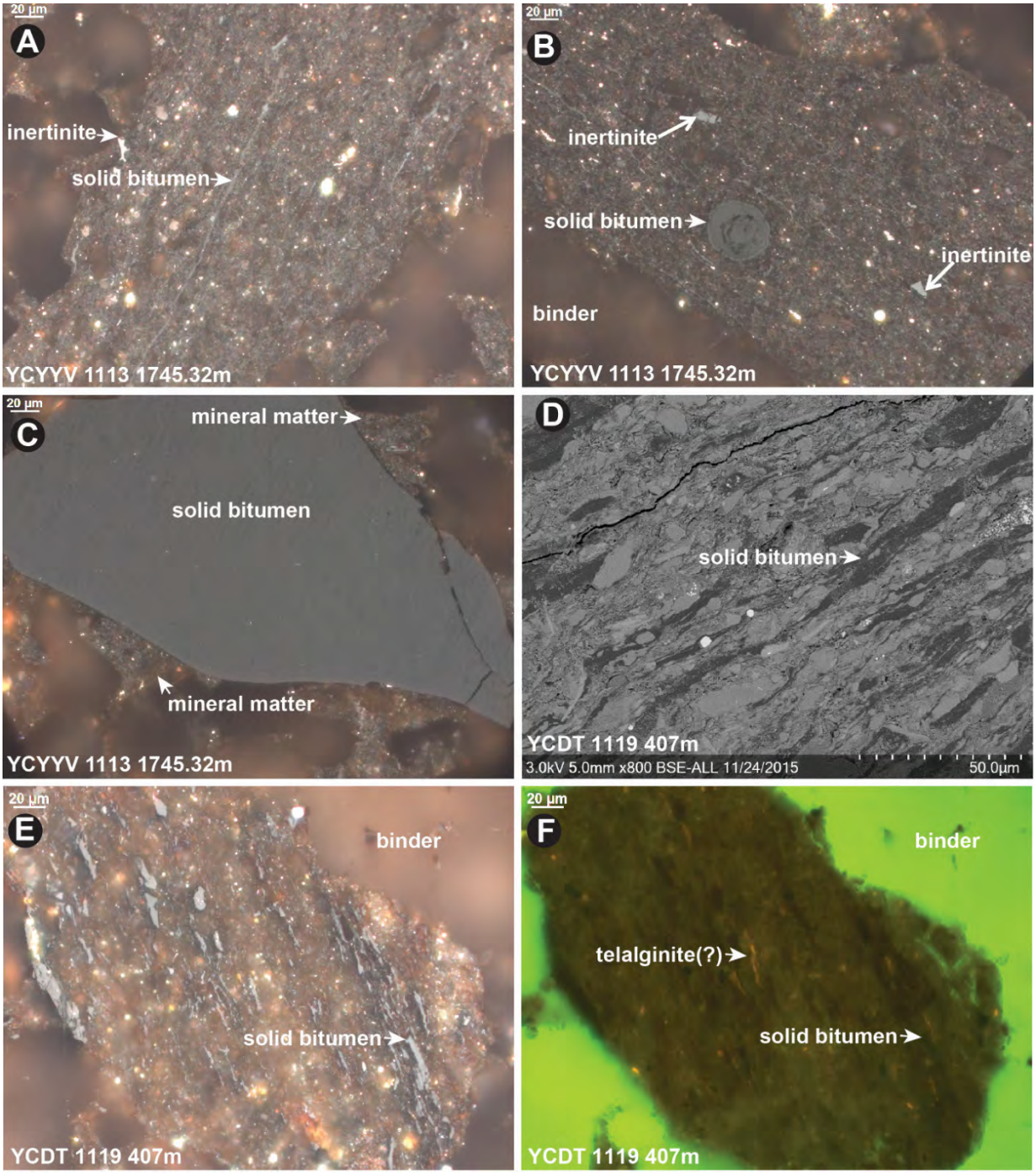

Figure 3. A. Solid bitumen occurring as groundmass in sample YCYYV 1113 1745.32m. Solid bitumen occurs a thin (0-10 µm) discontinuous lens running diagonal from upper right to lower left and grading into the rock mineral matrix. B. Pore-filling solid bitumen in sample YCYYV 1113 1745.32 m. C. Fracture-filling solid bitumen in sample YCYYV 1113 1745.32m. Mineral matter adheres to edges of bitumen fragment. D. Bedding parallel solid bitumen layering in sample YCDT 1119 407 m. E. Bedding parallel solid bitumen layering in sample YCDT 1119 407m. F. Same field as E illuminated with blue light to illustrate fluorescence of kerogen (telalginite) and solid bitumen. A-C, E in white light under oil immersion, D from SEM (conditions labeled at base of image, mechanically polished surface).

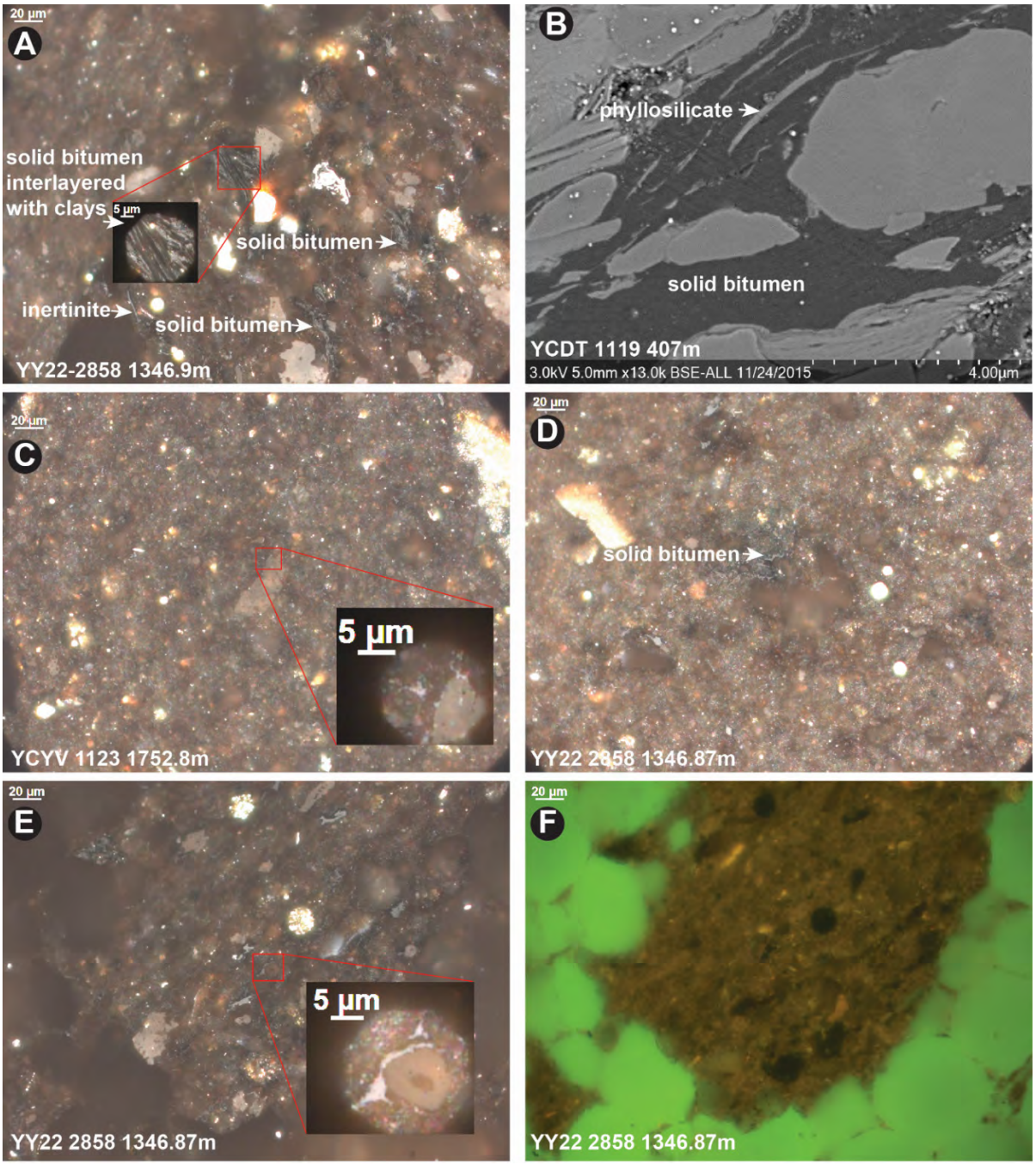

Figure 4. A. Solid bitumen interleaved with clays in sample YY22-2858 1346.9m. Inset shows high magnification (1000x) view where solid bitumen is the whitish gray material. Elongate inertinite lath also present in field. B. Solid bitumen interleaved with clays in sample YCDT 1119 407m (SEM image, conditions labeled at base of image, mechanically polished surface). C. Finely disseminated solid bitumen in sample YCYV 1123 1752.8 m. Inset shows solid bitumen (whitish gray) in mineral interstices adjacent to authigenic carbonate. D. Solid bitumen embayed against euhdedral carbonate in sample YY22 2858 1346.87m. E. Solid bitumen coeval with zoned carbonate in sample YY22 2858 1346.87m. Inset shows 1000x view of solid bitumen (whitish gray) against carbonate overgrowth. F. Same field as E illuminated with blue light to show fluorescence of clay matrix. A, C-E in white light under oil immersion.

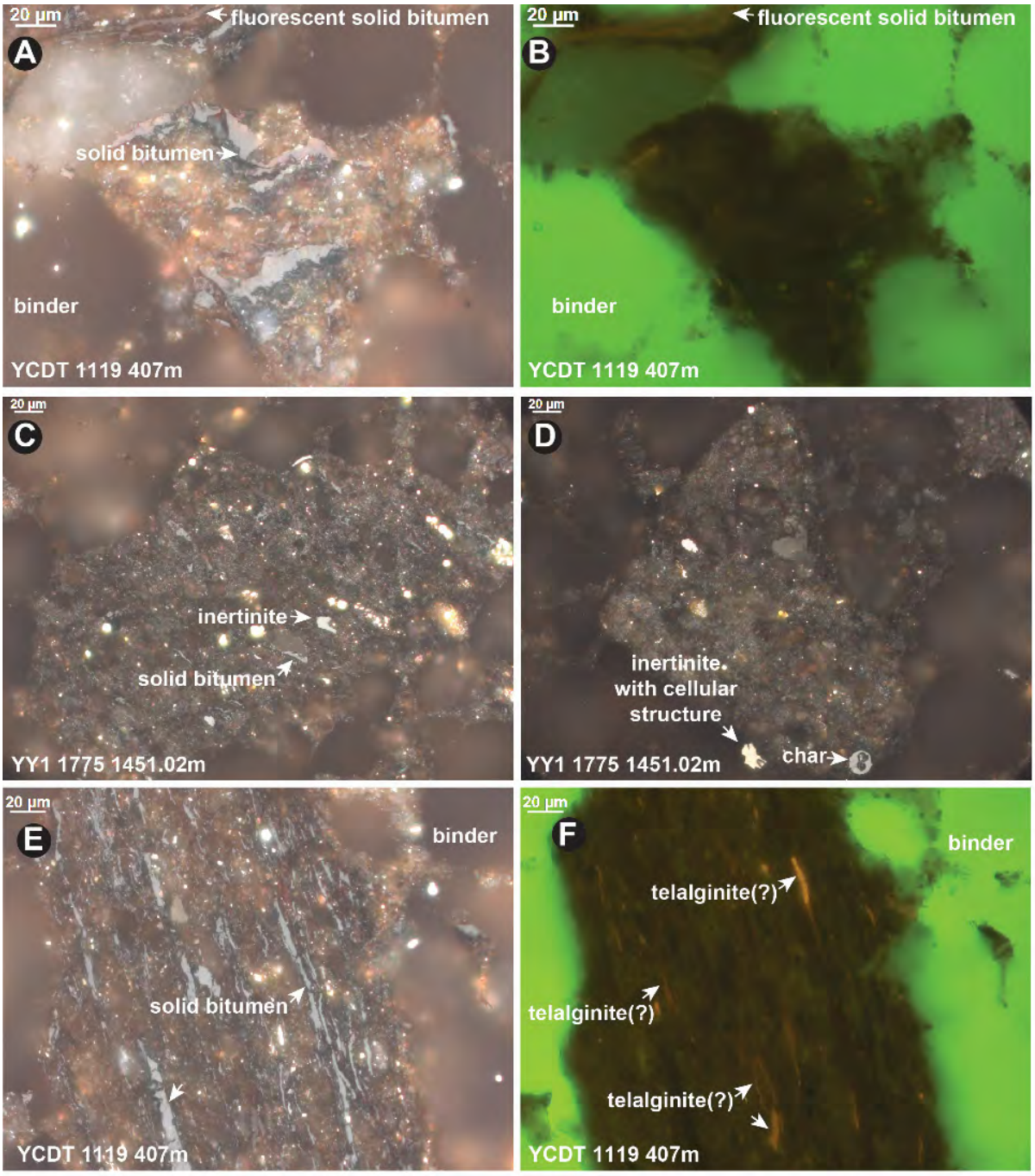

Figure 5. A. Fluorescent and non-fluorescent solid bitumen in sample YCDT 1119 407m. BR_o is determined on non-fluorescent bitumen. The fluorescent solid bitumen is demonstrably coeval with carbonate as demonstrated by the euhedral carbonate included within the solid bitumen vein (arrow). B. Same field as A illuminated with blue light showing fluorescence of solid bitumen. C. Inertinite with arcuate cellular structure adjacent to solid bitumen in sample YY1 1775 1451.02 m. D. Inertinite with partial cell lumen adjacent to char spherule in sample YY1 1775 1451.02 m. E. Solid bitumen (weakly fluorescent) aligned with bedding in sample YCDT 1119 407 m. F. Same field as E illuminated with blue light to show fluorescent degraded telalginite remnants. All images under oil immersion; A, C-E are under white incident light; B and F are under blue incident light.

Dominance of solid bitumen is corroborated by pyrolysis results of pre- and post-Soxhlet extracted samples that show reductions of ~90% in S1 and PI. Reductions in S2 and TOC are less extreme but nonetheless suggest that organic carbon is dominated by an extractable material, that is, solid bitumen. **Figure 6A** illustrates conceptually the volume percentage of solid bitumen and kerogen present in Yanchang samples at oil window thermal maturity, whereas, **Figure 6B** is the geochemical corroboration, showing average reduction in S1 caused by Soxhlet extraction with DCM.

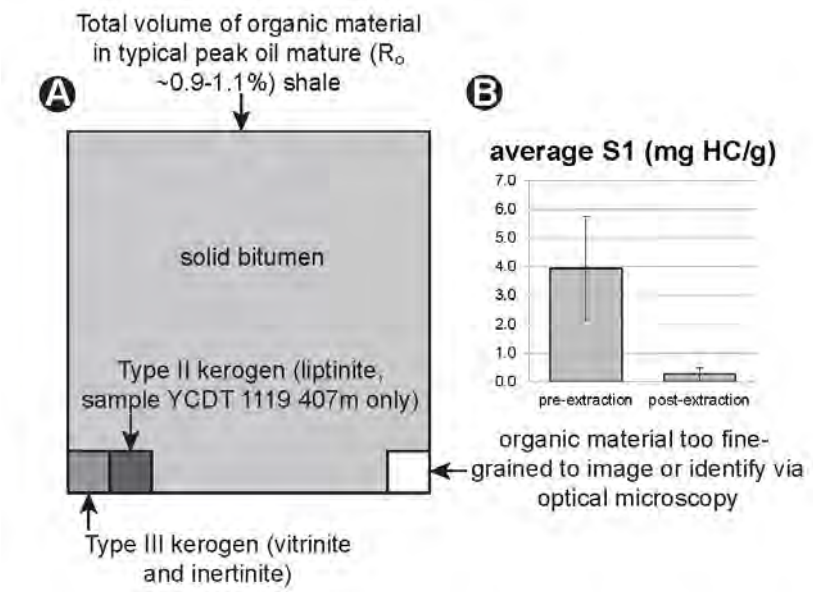

Figure 6. A. Conceptual volume of total organic material in Yanchang samples occupied by solid bitumen, Type III kerogen (vitrinite and inertinite), Type II kerogen (telalginite, sample YCDT 1119 407 m only, see text), and material too fine-grained to be resolved by optical microscopy. B. S1 values of pre- and post-extracted Yanchang samples. Error bars show one standard deviation.

Minor Type III kerogen is present as small dispersed fragments of inertinite and vitrinite, visually estimated as <1 vol.% of the total OM present. Vitrinite and inertinite fragments are lath-shaped to equant and typically 5 µm to 20 µm in diameter (see **figs. 4A and 5C**). A rare relict cellular structure from the original plant precursor is present; char fragments also were rare (**fig. 5D**). Liptinite was observed as relict amorphous kerogen suggestive of "telalginite" in only one sample (YCDT 1119 407 m), where it occurs as a rare lamellar lens up to 100 µm in length and generally <10 µm in width (**figs. 5E and 5F**). These telalginites have no contrast to the mineral matrix in white light (**fig. 5E**), but they are obvious in fluorescence illumination (**fig. 5F**). Some is degraded to a wispy porous groundmass evident only by its weak fluorescence. The presence of rare waxy terrestrial liptinite was suggested by one observation of leaf exine cutinite but this identification is tentative.

Discussion

Thermal maturity and hydrocarbon exploration

The measured BR_o values of 0.67% to 0.95% suggest conditions of early to peak oil thermal maturity (e.g., Dembicki, 2009), if BR_o is considered a good proxy for vitrinite reflectance at this thermal maturity. Work compiled by Robert (1988) indicated that BR_o is lower than R_o until approximately 1.0% R_o (see also Jacob, 1989; Mählmann and Frey, 2012), after which BR_o becomes ≈ R_o. Work by Landis and Castaño (1994) suggested that BR_o is always lower than R_o. Considering that all the prior studies have found BR_o lower than R_o at thermal maturities of R_o<1.0%, we observe that measured BR_o values reported herein probably slightly underestimate thermal maturity. Corroborating this observation, calculated R_o values from T_{max} average 0.1% higher than measured BR_o values (Table 1). Nevertheless, both calculated R_o and measured BR_o values indicate that Yanchang samples examined in this study are thermally mature for oil generation, with most samples showing peak oil window thermal maturity (0.8% to 1.0% BR_o).

Hydrocarbon prospectivity from Chang 7 mudrocks usually is characterized as "shale gas" exploration (Wang and others, 2013; Tang and others, 2013b, Guo and others, 2014). As previously stated, thermal maturity of Yanchang Formation samples studied herein is in the peak oil window and appropriate for production of volatile oil to early wet gas and condensate hydrocarbon products. Exploration for "shale gas" from Chang 7 mudrocks at similar peak oil window thermal maturity is perhaps more a function of governmental incentives and directives to promote shale gas (Guo and Zhao, 2012), according to the state "Twelfth 5-Year Plan" for energy development. Further, a generation of long-chain waxy oils from lacustrine kerogen (e.g., Katz, 1990), and poor permeability in Chang 7 mudrocks (Li and others, 2015; other studies in this volume) may limit oil expulsion from source beds of large thickness.

"Kerogen" typing

Solid bitumen is the secondary product of hydrocarbon generation from kerogen in the peak oil mature Yanchang Formation samples examined herein. Therefore, reporting a kerogen "Type" from pyrolysis is inappropriate and misleading for these samples because the organic material present is not kerogen. Type II kerogen, by definition, contains cyclic aliphatic and aromatic hydrocarbons, associated organic sulfur and yields moderate length n-alkanes ($<C_{25}$) upon extraction, whereas Type I kerogen is highly aliphatic, yielding long-chain *n*-alkanes (up to $>C_{40}$) in oils and rock extracts, indicating accumulation and/or selective preservation of lipid-rich material (summarized in Vandenbroucke and Largeau, 2007). Presence of a Type I versus Type II kerogen may imply specific depositional characteristics; that is, for Type I: photic zone accumulation of lipid-rich bacterial biomass, such as in a microbial mat, and for Type II: accumulation and preservation of planktonic algal kerogen in anoxic marine sulfate-rich waters. However, in the Yanchang samples examined herein, the HI index, which is a proxy for H/C information, revealed by Rock-Eval pyrolysis specifies the composition of the solid bitumen present, not the composition of original kerogen present in the samples prior to catagenesis. Nevertheless, considering poor permeability reported for Yanchang mudrocks (Li and others, 2015; other studies in this volume), we presume that solid bitumen was generated in situ and has

experienced little migration fractionation or oxidation by way of hydrothermal fluids. However, we have no means to quantify potential compositional evolution caused by hydrocarbon devolatilization or other processes, e.g., gas flushing. H/C compositions determined by way of pyrolysis may reflect original kerogen composition, in part, less the most volatile components that have been expelled.

Some workers have used pyrolysis data to back-calculate original TOC and HI values (e.g., Jarvie and others, 2007). However, this approach relies on using visual kerogen data from immature samples, which are not available for the Yanchang Chang 7. Based on geological data that constrain Chang 7 deposition to deep-water facies (e.g., Zhao and others, 2015; other studies in this volume), we surmise that original sedimentary kerogen was constituted by planktonic algae and derivative products (e.g., fecal pellets) that were incorporated into sediments from the overlying water column as a "lacustrine snow," in much the same mechanism as the well-described marine snow (Macquaker and others, 2010). Therefore, original HI values may not have been as high as a true Type I lipid-rich microbial mat facies from a photic zone system, such as the Green River Mahogany Ledge (e.g., HI>800; Hackley and others, 2015). Instead, original kerogen may have contained moderate length *n*-alkanes ($<C_{25}$), more similar to Type I/II planktonic kerogens, such as in the Boquillas Formation (early mature Eagle Ford equivalent) of West Texas (HI>700; Hackley and others, 2015).

Comparison to previous petrographic studies

Hanson and others (2007) reported geochemical analysis of a biodegraded low-maturity solid bitumen vein cross-cutting Jurassic strata in the Ordos Basin, suggesting that it was derived from pre-Jurassic source rocks, possibly the Yanchang, with terrestrial OM input. Their report included petrographic analyses of Yanchang and other source rock strata of the Ordos Basin; however, solid bitumen was not included in the identified organic components. We note that they reported "amorphous kerogen" present in Yanchang Formation rocks at maturity of R_o 1.15%; other petrographic analyses in their report indicated "herbaceous plant" debris at lower maturity (R_o 0.60%). We assume that by "herbaceous plant" debris the authors meant "non-woody" material, that is, liptinite macerals including sporinite (pollen and spores), cutinite (leaf exine), and resinite (resins), all of which may persist as distinct and identifiable entities into the early- to mid-oil window (e.g., Hackley and others, 2009). However, "amorphous kerogen" would have been converted to hydrocarbons at the early wet gas thermal maturity conditions indicated by 1.15% R_o (Taylor and others, 1998). Lacustrine palynofacies were not identified in any of the Yanchang petrographic analyses reported in Hanson and others (2007).

The study by Wang and others (2013) on samples of oil window thermal maturity (R_o 0.52-1.25%) reported "sapropelinite" (>50 vol.%), vitrinite (~20 vol.%), and inertinite (~15 vol.%), and considered that the organic assemblage was dominated by Type II kerogen with a small component of Type I. We observe that "sapropelinite" (as defined by Mukhopadhyay and others, 1985, and used by Mukhopadhyay, 1989) refers to biodegraded algal kerogen. The term is synonymous with the "amorphous kerogen" identified by Hanson and others (2007), and its identification is permitted only in rocks of low thermal maturity (<0.6% R_o). Therefore, identification of "sapropelinite" in oil window mature Yanchang samples by Wang and others (2013) is mistaken, unless the identification applies only to samples of <0.6% R_o. We speculate that the "sapropelinite" observed by these workers may in fact be solid bitumen degraded by

kerogen concentration. This observation particularly applies to the higher maturity samples of their study.

Guo and others (2014) examined kerogen concentrates by way of optical microscopy, observing the dominant presence of “amorphinite” with subordinate vitrinite and inertinite. Again, we note that “amorphinite” (defined by van Gijzel, 1982) also is synonymous with “amorphous kerogen” and its presence cannot be reconciled with oil window thermal maturity (R_o 0.7–1.2%) reported by Guo and others (2014). Therefore, we speculate that the “amorphinite” is, rather, misidentified solid bitumen.

Xiong and others (2016) characterized kerogen as Type I-II by way of pyrolysis in thermally mature Chang 7 and Chang 9 mudrocks from the Yanchang Formation. They performed solvent extractions and thereafter noted increased organic porosity in extracted mudrocks by way of gas sorption experiments. The organic porosity was contained in “residual bitumen.” No organic petrography was performed in their study; we assume by “residual bitumen” they meant the solid bitumens noted in this study. As noted previously, significant solid bitumen is extractable by DCM, reducing TOC by ~20%. Extraction of the more aliphatic and aromatic portions of solid bitumen by DCM or other solvents may result in increased organic porosity in the more polar-rich residue, as observed by other studies in this volume.

In summary, previous work reporting organic petrography of Yanchang Formation mudrocks contained observations difficult to reconcile with reported thermal maturity. The earlier reports that described “amorphous kerogen,” “sapropelinite,” and “amorphinite” in peak oil window thermal maturity samples appear to have been in error, and we speculate that these petrographic studies may have misidentified or overlooked solid bitumen.

Comparisons to organic petrography of other lacustrine mudrocks

Organic petrographic studies of immature to early oil window Permian Lucaogou Formation mudrocks from the lacustrine Santanghu and Junggar Basins of northwest China indicated amorphous kerogen and lamellar alginite dominate (oil-prone Type I kerogen), with some planktonic Prasinophyte green algae and terrestrial Type III kerogens present in low abundance (Tao and others, 2012; Xie and others, 2015; Hackley and others, in prep.). With other influences considered equal, presence of significantly higher plant debris in Permian Lucaogou mudrocks relative to Yanchang strata may imply either: (1) more distal deposition for Yanchang mudrocks, or (2) a lower component of vascular vegetative debris in delivered sediments. However, because the two sedimentary systems differ significantly, that is, Yanchang mudrocks represent a balance-filled draining system dominated by extrabasinal detrital clays (other studies in this volume), and Lucaogou mudrocks in Santanghu Basin represent a sediment-starved under-filled to balance-filled chemical carbonate system dominated by intrabasinal sediment (Hackley and others, in prep.), comparison of relative quantities of detrital terrestrial Type III kerogens may be invalid.

Petrographic studies of immature (R_o 0.30%, HI 870 mg HC/g TOC) Green River Parachute Creek Member (Mahogany Ledge) lacustrine oil shale (Hackley and others, 2015) showed amorphous organic matter (oil-prone Type I) dominates. This material is not present in Yanchang samples because of oil window thermal maturity. As in the Yanchang, terrestrial

organics, including vitrinite and inertinite were sparse. However, the Mahogany Ledge is a chemical carbonate-dominated system. Previous studies (e.g., Cole, 1985) have suggested that open lacustrine, deep-water deposition of planktonic OM into permanently stratified, strongly reducing anoxic bottom sediments. However, more recent workers have interpreted preservation of OM in benthic microbial mats that accumulated in the photic zone (e.g., Schieber, 2007) and overturned the notion that low-energy, deep-water environments are required for mudstone deposition (Schieber and others, 2007). On the basis of these observations, we suggest that the Mahogany Ledge is not a proper analogue for immature Yanchang mudrocks.

Another proxy for immature Yanchang mudrocks may be the illite-rich Garden Gulch Member of the Green River Formation, which was deposited in "offshore" lacustrine environments (e.g., Johnson, 2012, although see Cole, 1985). The Garden Gulch Member contains a Type I kerogen with HI values also >800 mg HC/g TOC (Burnham and McConaghy, 2014; Birdwell and Washburn, 2015). Unpublished petrographic observations show that vitrinite and inertinite are rare in immature (R_o 0.28%) Garden Gulch samples (**figs. 7A and 7B**). The sample shown in **Figure 7** contains HI of 821 mg HC/g TOC that also may be a reasonable proxy for original HI in immature Yanchang Formation mudrocks. In **Figure 8**, we show the pseudo-Van Krevelen plot for Yanchang samples in comparison to the immature proxies that we have suggested herein. However, until immature Yanchang mudrock samples with clay-rich mineralogy become available, it is difficult to infer an original HI or kerogen type with any degree of confidence.

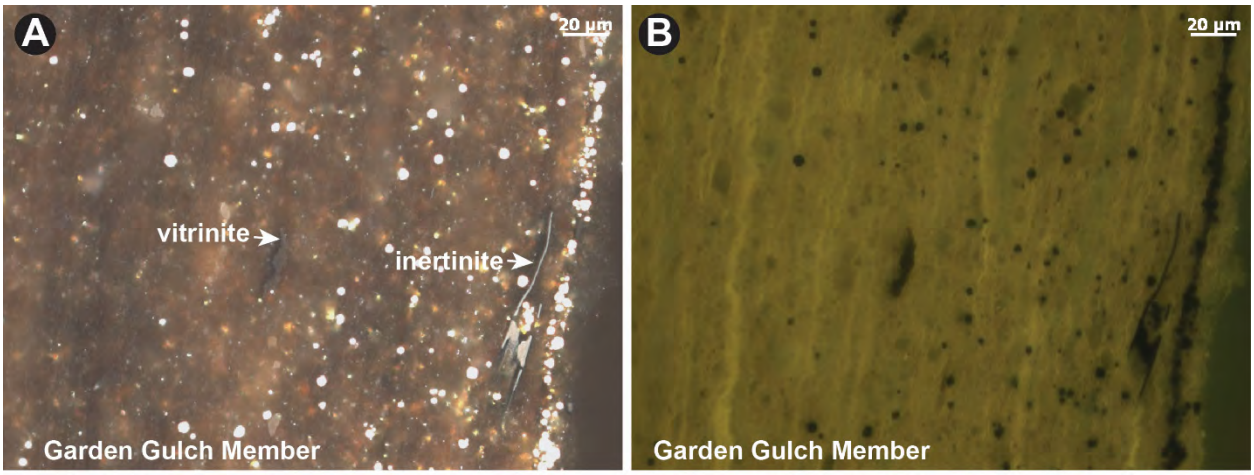

Figure 7. A. Garden Gulch Member of Green River Formation showing rare vitrinite and structured inertinite (white incident light, oil immersion). B. Same field as A illuminated with blue light showing fluorescent lamellar algal material. Sample from J. Birdwell, USGS.

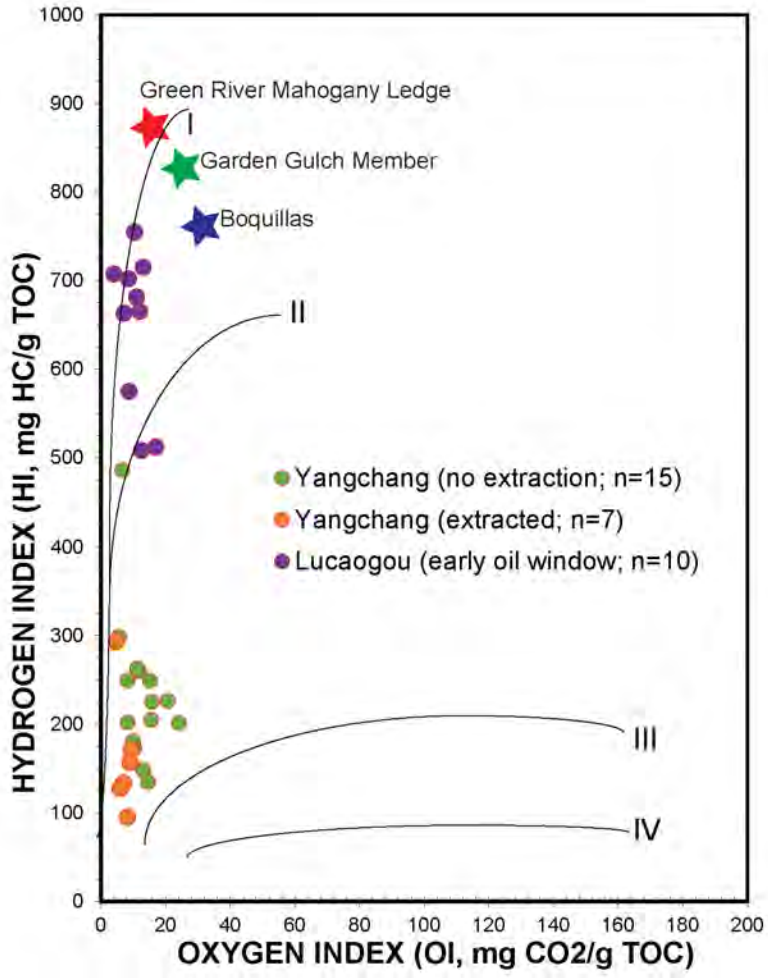

Figure 8. Pseudo van Krevelen diagram showing Yanchang samples, Lucaogou mudrocks (Hackley and others, in prep.), and immature lacustrine and marine mudrock proxies (data from Hackley and others, 2015, unpublished data, J. Birdwell, USGS).

Conclusions

We have evaluated herein the organic petrology and thermal maturity of Yanchang mudrocks from the Ordos Basin, north-central China “Kerogen typing” from Rock-Eval pyrolysis is misleading for Yanchang mudrocks because of peak oil window thermal maturity conditions determined from solid bitumen reflectance and pyrolysis parameters. Most of the TOC present is composed of solid bitumen, confirmed by petrography, high S1/TOC values, and comparison of pre- and post-extraction S1 values. Poor permeability suggests that solid bitumen is converted from original kerogen in situ. Terrestrial kerogens vitrinite and inertinite are scarce, suggesting a distal depositional environment. Immature Yanchang mudrocks are not available for identification of original kerogen type. However, the immature illite-rich Garden Gulch Member of the lacustrine Green River Formation or the early mature Boquillas Formation may be potential analogues for original kerogen type and geochemistry.

Acknowledgments

Brett Valentine (USGS) provided images from SEM. Owen Scholl (USGS) prepared samples for petrographic examination.

References

ASTM, 2015a, D2797 Standard practice for preparing coal samples for microscopical analysis by reflected light. Annual book of ASTM standards: Petroleum products, lubricants, and fossil fuels, Gaseous fuels, coal and coke, sec. 5, v. 5.06: ASTM International, West Conshohocken, PA, p. 528–532, http://www.astm.org/Standards/D2797.htm (Accessed December 21, 2015).

ASTM, 2015b, D7708 Standard test method for microscopical determination of the reflectance of vitrinite dispersed in sedimentary rocks: Annual book of ASTM standards: Petroleum products, lubricants, and fossil fuels, Gaseous fuels, coal and coke, sec. 5, v. 5.06: ASTM International, West Conshohocken, PA, p. 910–919, http://www.astm.org/Standards/D7708.htm (Accessed December 21, 2015).

Birdwell, J.E., and Washburn, K.E., 2015, Rapid analysis of kerogen hydrogen-to-carbon ratios in shale and mudrocks by laser-induced breakdown spectroscopy: Energy & Fuels, v. 29, p. 6999–7004.

Burnham, A.K., and McConaghy, J.R., 2014, Semi-open pyrolysis of oil shale from the Garden Gulch Member of the Green River Formation: Energy & Fuels, v. 28, p. 7246–7439.

Cardott, B.J., Landis, C.R., and Curtis, M.E., 2015, Post-oil solid bitumen network in the Woodford Shale, USA–a potential primary migration pathway. International Journal of Coal Geology, v. 139, p. 106–113.

Cole, R.D., 1985, Depositional environments of oil shale in the Green River Formation, Douglas Creek arch, Colorado and Utah. In: Picard, MD., (Ed.), Geology and energy resources, Uinta Basin of Utah: Utah Geological Association Publication 12, p. 211–224.

Dembicki, H., Jr., 2009, Three common source rock evaluation errors made by geologists during prospect or play appraisals: AAPG Bulletin, v. 93, p. 341–356.

Durand, B., 1980, Sedimentary organic matter and kerogen: definition and quantitative importance of kerogen. In: Durand, B., (Ed.), Kerogen: insoluble organic matter from sedimentary rocks: Paris, Editions Technip, p. 13–34.

Espitalié, J., Laporte, J.L., Madec, M., Marquis, F., Leplat, P., and Paulet, J., 1977, Méthode rapide de caractérisation des rochès, de leur potential pétrolier et de leur degree d'évolution: Revue de L'Institut Français du Pétrole, t. 32, p. 23–43.

Guo, H., Jia, W., Peng, P., Lei, Y., Luo, X., Cheng, M., Wang, X., Zhang, L., and Jiang, C., 2014, The composition and its impact on the methane sorption of lacustrine shales from the Upper Triassic Yanchang Formation, Ordos Basin, China. Marine and Petroleum Geology, v. 57, p. 509–520.

Guo, J., and Zhao, Z., 2012, China vigorously promoting shale gas exploration, development: Oil & Gas Journal, v. 110, no. 3, p. 60–62, 64–65.

Hackley, P.C., Araujo, C.V., Borrego, A.G., Bouzinos, A., Cardott, B., Cook, A.C., Eble, C., Flores, D., Gentzis, T., Gonçalves, P.A., Mendonça Filho, J.G., Hámor-Vidó, M., Jelonek, I., Kommeren, K., Knowles, W., Kus, J., Mastalerz, M., Menezes, T.R., Newman, J., Oikonomopoulos, I.K., Pawlewicz, M., Pickel, W., Potter, J. Ranainghe, P., Read, H., Reyes, J., Rodriguez, G.D.L.R., Fernandes de Souza, I.V.A., Suarez-Ruiz, I., Sýkorová, I., and Valentine, B.J., 2015, Standardization of reflectance measurements in dispersed organic matter: results of an exercise to improve interlaboratory agreement: Marine and Petroleum Geology, v. 59, p. 22–34.

Hackley, P.C., Fishman, N., Wu, T., and Baugher, G., in prep. Organic petrology of the lacustrine Lucaogou Formation, Santanghu Basin, northwest China: application to lake basin evolution. For submission to International Journal of Coal Geology.

Hackley, P.C., Guevara, E.H., Hentz, T.F., and Hook, R.W., 2009, Thermal maturity and organic composition of Pennsylvanian coals and carbonaceous shales, North-Central Texas: implications for coalbed gas potential: International Journal of Coal Geology, v. 77, p. 294–309.

Hanson, A.D., Ritts, B.D., and Moldowan, J.M., 2007, Organic geochemistry of oil and source rock strata of the Ordos Basin, north-central China. AAPG Bulletin, v. 91, p. 1273–1293.

IHS Energy Group, 2015 [includes data current as of December 2015], US Well and Production Data. IHS Energy Group, 15 Inverness Way East, D205, Englewood, CO 80112, USA (Accessed December 28, 2015).

Imbus, S.W., 1984, Organic petrography of the Green River Formation oil shales, Parachute Creek Member, Piceance Creek Basin, Colorado. West Virginia University, unpublished MS Thesis, 168 p.

Jacob, H., 1989, Classification, structure, genesis and practical importance of natural solid oil bitumen (“migrabitumen”): International Journal of Coal Geology, v. 11, p. 65–79.

Jarvie, D.M., Claxton, B.L., Henk, F., and Breyer, J.T., 2001, Oil and shale gas from the Barnett Shale, Fort Worth Basin, TX: American Association of Petroleum Geologists Annual Meeting Program 10, p. A100.

Jarvie, D.M., Hill, R.J., Ruble, T.E., and Pollastro, R.M., 2007, Unconventional shale-gas systems: the Mississippian Barnett Shale of North-Central Texas as one model for thermogenic shale gas assessment: AAPG Bulletin, v. 91, p. 475–499.

Johnson, R.C., 2012, The systematic geologic mapping program and a quadrangle-by-quadrangle analysis of time-stratigraphic relations within oil shale-bearing rocks of the Piceance Basin, western Colorado: U.S. Geological Survey Scientific Investigations Report 2012–5041, 28 p., http://pubs.usgs.gov/sir/2012/5041/report/SIR12-5041.pdf (Accessed January 3, 2015).

Katz, B.J., 1990, Controls on distribution of lacustrine source rocks through space and time. In: Katz, B.J., (Ed.), Lacustrine basin exploration: case studies and modern analogs: American Association of Petroleum Geologists Memoir 50, p. 61–76.

Katz, B.J., and Lin, F., 2014, Lacustrine basin unconventional resource plays: key differences. Marine and Petroleum Geology, v. 56, p. 255–265.

Landis, C.R., and Castaño, J.R., 1994, Maturation and bulk chemical properties of a suite of solid hydrocarbons: Organic Geochemistry, v. 22, p. 137–149.

Lin, S., Yuan, X., Tao, S., Yang, Z., and Wu, S., 2013, Geochemical characteristics of the source rocks in Mesozoic Yanchang Formation, central Ordos Basin: Journal of Earth Science, v. 24, p. 804–814.

Liu, Z., Shen, F., Zhu, X., Li, F., and Tan, M., 2015, Formation conditions and sedimentary characteristics of a Triassic shallow water braided delta in the Yanchang Formation, southwest Ordos Basin, China. PLoS ONE 10(6):e0119704.doi:10.1371/journal.pone.0119704 http://journals.plos.org/plosone/article?id=10.1371/journal.pone.0119704 (Accessed December 21, 2015).

Macquaker, H.S., Keller, M.A., and Davies, S.J., 2010, Algal blooms and "marine snow:" Mechanisms that enhance preservation of organic carbon in ancient fine-grained sediments: Journal of Sedimentary Research, v. 80, p. 934–942.

Mählmann, R.F., and Frey, M., 2012, Standardisation, calibration and correlation of the Kübler-index and the vitrinite/bituminite reflectance: an inter-laboratory and field related study: Swiss Journal of Geosciences, v. 105, p. 153–170.

Mukhopadhyay, P.K., 1989, Characterization of amorphous and other organic matter types by microscopy and pyrolysis-gas chromatography: Organic Geochemistry, v. 14, p. 269–284.

Mukhopadhyay, P.K., Hagemann, H.W., and Gormly, J.R., 1985, Characterization of kerogens as seen under the aspect of maturation and hydrocarbon generation: Erdöl Kohle, v. 38, p. 7–18.

Peters, K., 1986, Guidelines for evaluating petroleum source rock using programmed pyrolysis: AAPG Bulletin, v. 70, p. 318–329.

Petersen, H.I., Schovsbo, N.H., and Nielsen, A.T., 2013, Reflectance measurements of zooclasts and solid bitumen in Lower Paleozoic shales, southern Scandinavia: correlation to vitrinite reflectance: International Journal of Coal Geology, v. 114, p. 1–18.

Ren, Z., Zhang, S., Gao, S., Cui, J., Xiao, Y., and Xiao, H., 2007, Tectonic thermal history and its significance on the formation of oil and gas accumulation and mineral deposit in Ordos Basin: Science in China Series D: Earth Sciences 50, Supp. II, p. 27–38.

Ritts, B.D., Hanson, A.D., Darby, B.J., Nanson, L., and Berry, A., 2004, Sedimentary record of Triassic intraplate extension in north China: evidence from the nonmarine NW Ordos Basin, Helan Shan and Zhuozi Shan: Tectonophysics, v. 386, p. 177–202.

Robert, P., 1988, Organic metamorphism and geothermal history: microscopic study of organic matter and thermal evolution of sedimentary basins: Elf Aquitaine, Dordrecht, 311 p.

Schieber, J., 2007, Benthic microbial mats as an oil shale component: Green River formation (Eocene) of Wyoming and Utah. In: Schieber, J., Bose, P.K., Eriksson, P.G., Banerjee, S., Sarkar, S., Altermann, W., and Catuneau, O. (Eds.), Atlas of Microbial Mat Features Preserved within the Clastic Rock Record, v. 2.: Elsevier Atlases in Geosciences, p. 225–232.

Schieber, J., Southard, J., and Thaisen, K., 2007, Accretion of mudstone beds from migrating floccule ripples: Science, v. 318, p. 1760-–1763.

Sun, L., Tuo, J., Zhang, M., Wu, C., Wang, Z., and Zheng, Y., Formation and development of the pore structure in Chang 7 member oil-shale from Ordos Basin during organic matter evolution induced by hydrous pyrolysis. Fuel 158, 549—557.

Tang, X., Zhang, J. Wang X., Yu, B., Ding, W., and Zhang, L., 2013a, Geochemical characteristics and estimation of gas content of the low-middle mature continental shales: a case study from the Ordos Basin. AAPG Search and Discovery Article 10517, http://www.searchanddiscovery.com/documents/2013/10517tang/ndx_tang.pdf (Accessed December 23, 2015).

Tang, X., Zhang, J., Yu, B., and Ding, W., 2013b, Shale gas characteristics in the southeastern part of the Ordos Basin, China: implications for the accumulation condition and potential of continental shale gas. AAPG Search and Discovery Article 10481, http://www.searchanddiscovery.com/documents/2013/10481tang/ndx_tang.pdf (Accessed December 23, 2015).

Tao, S., Wang, Y., Tang, D., Wu, D., Xu, H., He, W., 2012, Organic petrology of the Fukang Permian Lucaogou Formation oil shales at the northern foot of Bogda Mountain, Junggar Basin, China. International Journal of Coal Geology 99, 27–34.

Taylor, G.H., Teichmüller, M., Davis, A., Diessel, C.F.K., Littke, R., and Robert, P., 1998, Organic Petrology. Gerbrüder Borntraeger, Berlin, 704 p.

van Gijzel, P., 1982, Characterization and identification of kerogen and bitumen and determination of thermal maturation by means of qualitative and quantitative microscopical techniques. In: Staplin, F.L., and others (Eds.), How to assess maturation and paleotemperatures. SEPM Short Course 7, p. 159–207.

Vandenbroucke, M. and Largeau, C., 2007, Kerogen origin, evolution and structure: Organic Geochemistry, v. 38, p. 719–833.

Wang, X., Zhang, L., Jiang, C., Sun, B., Gao, C., Fan, B., Guo, C., Wan, Y., Sun, J., and Hu, H., 2013. Lacustrine shale gas exploration in Yanchang exploratory block, China. AAPG Search and Discovery Article 10510, http://www.searchanddiscovery.com/documents/2013/10510wang/ndx_wang.pdf (Accessed December 21, 2015).

Wu, S., Zhu, R., Cui, J., Cui, J., Bai, B., Zhang, X., Jin, X., Zhu, D., You, J., and Li, X., 2015, Characteristics of lacustrine shale porosity evolution, Triassic Chang 7 Member, Ordos Basin, northwest China. Petroleum Exploration and Development, v. 42, p. 185–195.

Xie, X., Borjigin, T., Zhang, Q., Zhang, Z., Qin, J., Bian, L., and Volkman, J.K., 2015, Intact microbial fossils in the Permian Lucaogou Formation oil shale, Junggar basin, NW China: International Journal of Coal Geology, v. 146, p. 166–178.

Xiong, F., Jian, Z., Chen, J., Wang, X., Huang, Z., Liu, G., Chen, F., Li, Y., Chen, L., and Zhang, L., 2016, The role of the residual bitumen in the gas storage capacity of mature lacustrine shale: a case study of the Triassic Yanchang shale, Ordos Basin, China: Marine and Petroleum Geology, v. 69, p. 205–215.

Yang, H., and Zhang, W., 2005, Leading effect of the seventh member high-quality source rock of Yanchang Formation in Ordos Basin during the enrichment of low-penetrating oil-gas accumulation: geology and geochemistry: Geochimica, v. 34, p. 147–154 (in Chinese with English abstract).

Yang, W., Liu, G., and Feng, Y., 2016, Geochemical significance of 17α(H)-diahopane and its application in oil-source correlation of Yanchang formation in Longdong area, Ordos basin, China: Marine and Petroleum Geology, doi: 10.1016/j.marpetgeo.2015.10.016.

Yao, J., Deng, X., Zhao, Y., Han, T., Chu, M., and Pang, J., 2013, Characteristics of tight oil in Triassic Yanchang Formation, Ordos Basin: Petroleum Exploration and Development, v. 40, p. 161–169.

Yuan, X., Lin, S., Liu, Q., Yao, J., Wang, L., Guo, H., Deng, X., and Cheng, D., 2015, Lacustrine fine-grained sedimentary features and organic-rich shale distribution pattern: a case study of Chang 7 Member of Triassic Yanchang Formation in Ordos Basin, northwest China: Petroleum Exploration and Development, v. 42, p. 37–47.

Zhang, M., Ji, L., Wu, Y., and He, C., 2015, Palynofacies and geochemical analysis of the Triassic Yanchang Formation, Ordos Basin: implications for hydrocarbon generation potential and the paleoenvironment of continental source rocks: International Journal of Coal Geology, v. 152, p. 159–176.

Zhang, W., Yang, H., Li, J.F., and Ma, J., 2006, Leading effect of high class source rock of Chang 7 in Ordos Basin on enrichment of low permeability oil gas accumulation: Petroleum Exploration and Development, v. 33, p. 289-293 (in Chinese with English abstract).

Zhao, J., Mountney, N.P, Liu, C., Qu, H., and Lin, J., 2015, Outcrop architecture of a fluvio-lacustrine succession: Upper Triassic Yanchang Formation, Ordos Basin, China: Marine and Petroleum Geology, v. 68, p. 394–413.

Zhao, M., Behr, H., Ahrendt, H., Wemmer, K., Ren, Z., and Zhao, Z., 1996, Thermal and tectonic history of the Ordos basin, China: evidence from apatite fission track analysis, vitrinite reflectance, and K-Ar dating: AAPG Bulletin, v. 80, p. 1110–1134.

Zhao, W., Wang, H., Yuan, X., Wang, Z., and Zhu, G., 2010, Petroleum systems of Chinese nonmarine basins: Basin Research, v. 22, p. 4–16.

Zhao, W.Z., Wang, X.M., and Guo, Y.R., 2006, Restoration and tectonic reworking of the Late Triassic basin in western Ordos Basin: Petroleum Exploration and Development, v. 33, p. 6–13.

TASK 4.3

Liquid Hydrocarbon Characterization of Lacustrine Yanchang Formation

Xun Sun[1] and Daniel Enriquez[1]
Bureau of Economic *Geology[1], Jackson School of Geosciences, The University of Texas at Austin, Austin, TX*

Introduction

The Mesozoic and Cenozoic Eras were the main periods of the development of lacustrine facies around the world. Especially in China, at least 130 m of lacustrine and fluvial sedimentary rocks was deposited during the Late Triassic (Yanchang Formation) when the largest area of the lake was 100,000 km^2 (Wang and others, 1995). The humid and warm climates, along with a fresh water body, provide a favorable condition for the growth of nomarine aquatic organisms and preservation of organic matter (Li, 1986; Yang and Zhang, 1988). The Yanchang Formation is further divided into 10 subsections from top to bottom (Chang 1 to Chang 10) and primarily consist of lacustrine, deltaic, and fluvial deposits (Duan and others, 2008). Among these subsections, Chang 7 was deposited in a semideep to deep lacustrine environment. The Chang 7 member has been defined as high clay content (~ 40%) fine grained, organic-rich mudstones and oil shales. The Chang 7 subsection is thought to be the best source rocks in Ordos Basin (Duan and others, 2008). Despite the long history of oil and gas exploration and production, and the studies of the source rocks from Ordos Basin, the variation of the kerogen type, which is controlled by the lake facies, remains unclear in this study area. Furthermore, the hydrocarbon preservation and generation would largely be affected by the organic matter (OM) type and its preservation condition. Two core well samples and 12 different location core samples were selected in this study to (1) investigate the OM origin of the source rock; (2) evaluate their organic source and the semi-deep depositional environment of the source rocks; (3) determine their thermal maturity; and (4) understand how the kerogen type varies and associates with varied depositional facies, and its nature of maturation

Methods and Samples

Eighteen core samples from YY1 and YY22 two vertical wells were used in our study. A total of 15 cores samples were selected from YY1, and 3 core samples from YY22. Samples from YY1 cover three organic-rich intervals with total organic content (TOC) greater than 6%, and the depth ranges from 1372 m to 1397 m, 1451 m to 1458 m, and 1500 m to 1511 m, corresponding to Chang 7, 8, and 9 members. YY22 only has one high-TOC interval, Chang 7, with a TOC value larger than 6% (**Table 1**).

Table 1. Rock-Eval bulk geochemical data for samples from YY1 and YY22

Sample ID	ID	Depth	Carbonate	TOC	S1	S2	S3	Tmax	%Ro	Index	Index	Conc.	Norm. Oil	Index
Project /	Rock	Upper	Percent	Leco	Rock-Eval 2	Rock-Eval 2	Rock-Eval 2	Rock-Eval 2	Calculated	Hydrogen	Oxygen	S2/S3	S1/TOC	Production
		(m)	(wt%)	(wt%)	(mg HC/g)	(mg HC/g)	(mg CO2/g)	(°C)	(RE TMAX)	(S2x100/TOC)	(S3x100/TOC)	(mg HC/mg CO2)	Content	(S1/(S1+S2)
RBEG-140201-040	YY22-2560	1317.88	5.89	5.64	5.28	10.10	1.02	441	0.78	179	18	10	94	0.34
RBEG-140201-043	YY22-2746	1336.03	2.28	8.07	7.59	21.20	0.91	451	0.96	263	11	23	94	0.26
RBEG-140201-046	YY22-2858	1346.87	11.21	3.92	3.51	7.88	0.95	451	0.96	201	24	8	90	0.31
RBEG-140201-005	YY1-934	1364.69	10.36	5.84	2.22	11.10	0.61	451	0.96	190	10	18	38	0.17
RBEG-140201-006	YY1-992	1370.77	36.10	2.44	3.37	5.03	0.66	428	0.54	206	27	8	138	0.40
RBEG-140201-007	YY1-1005	1372.07	9.27	5.43	4.09	10.20	0.78	445	0.85	188	14	13	75	0.29
RBEG-140201-008	YY1-1030	1374.44	7.28	7.94	5.59	17.70	0.63	448	0.90	223	8	28	70	0.24
RBEG-140201-009	YY1-1070	1378.51	26.08	8.20	5.28	20.44	0.68	447	0.89	249	8	30	64	0.21
RBEG-140201-010	YY1-1145	1386.35	6.01	7.80	7.06	16.41	0.73	452	0.98	210	9	22	91	0.30
RBEG-140201-011	YY1-1209	1392.75	3.56	5.06	6.09	13.14	0.60	451	0.96	260	12	22	120	0.32
RBEG-140201-012	YY1-1257	1397.66	15.01	3.79	7.56	8.53	0.60	434	0.65	225	16	14	199	0.47
RBEG-140201-013	YY1-1408	1408.26	16.21	2.19	4.16	3.77	0.72	453	0.99	172	33	5	190	0.52
RBEG-140201-014	YY1-1418	1409.26	4.67	3.98	3.20	6.86	0.71	456	1.05	172	18	10	80	0.32
RBEG-140201-015	YY1-1447	1411.92	5.04	4.19	3.50	7.80	0.65	454	1.01	186	16	12	84	0.31
RBEG-140201-025	YY1-1775	1451.02	6.08	6.62	5.71	11.47	0.69	455	1.03	173	10	17	86	0.33
RBEG-140201-029	YY1-1907	1469.08	19.46	0.39	0.25	0.20	0.62	468	1.26	52	160	0	64	0.56
RBEG-140201-034	YY1-2103	1504.98	10.70	7.08	4.24	12.77	0.71	455	1.03	180	10	18	60	0.25
RBEG-140201-036	YY1-2244	1534.86	5.62	2.08	0.58	1.63	0.64	466	1.23	78	31	3	28	0.26

Another set of 12 core samples with different depths of Yanchang Formation from 10 wells was also analyzed. Ten core samples are from the Chang 7 organic-rich section and 2 core samples are from the Chang 9 interval. The TOC contents range from 1.72% to 13.72%, and the depth from 407 m to 2,297.05 m (**Table 2**). **Figure 1** shows the locations of 12 core samples in the study area. One sample (YCYWV1112) was from the delta-front depositional environment, and 11 samples represented the lacustrine semi-deep to deep lake depositional settings.

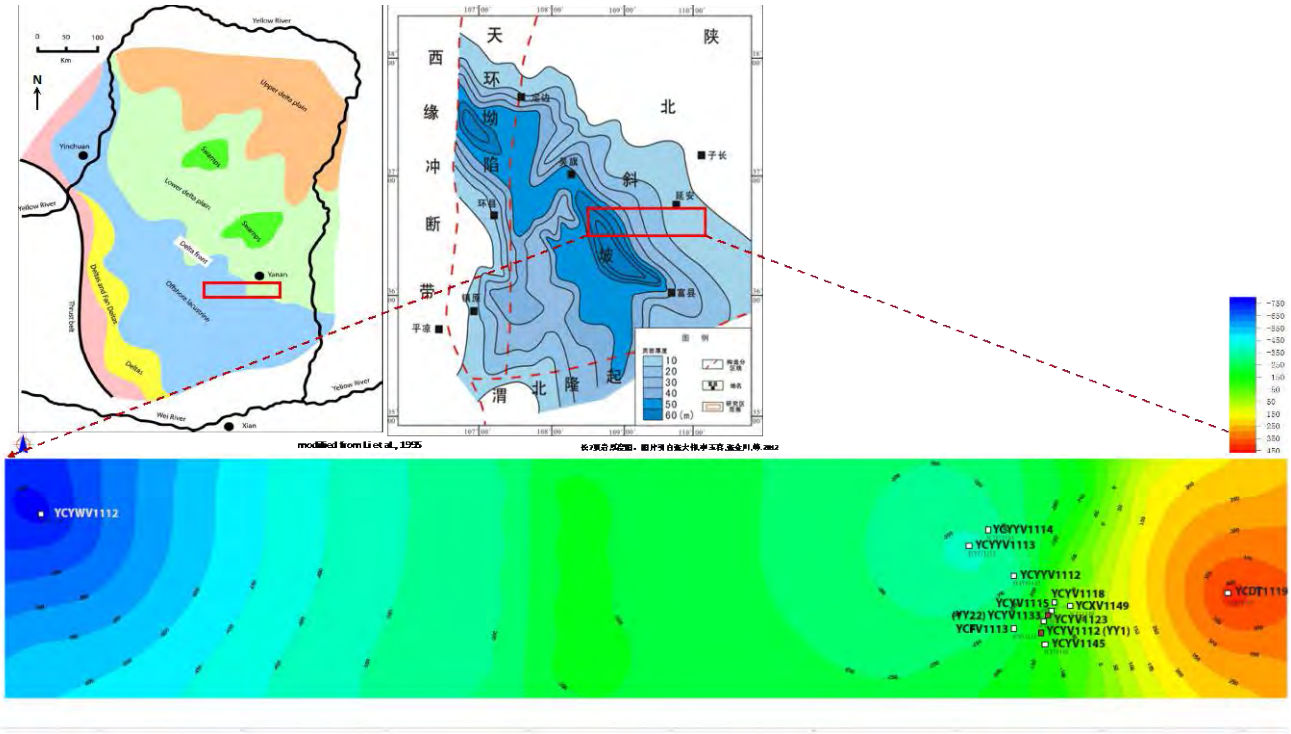

Figure 1. Geologic setting of the Ordos Basin and locations of the study area and core-sampled wells.

Table 2. Rock-Eval bulk geochemical data for samples from different depths in the Yanchang Formation.

Sample ID	Section	Depth	Carbonate	TOC	S1	S2	S3	Tmax	%Ro	Index	Index	Conc.	Norm. Oil	Index
Project /	Rock	Upper	Percent	Leco	Rock-Eval-2	Rock-Eval-2	Rock-Eval-2	Rock-Eval-2	Calculated	Hydrogen	Oxygen	S2/S3	S1/TOC	Production
		(m)	(wt%)	(wt%)	(mg HC/g)	(mg HC/g)	(mg CO2/g)	(°C)	(RE TMAX)					

All the samples were extracted with dichloromethane in Foss Sextec extraction systems for 3 hr. The extractable organic matter (EOM) was deasphaltened by precipitation with n-pentane, and the deasphaltened extracts were separated into saturate, aromatic, and NSO polar compounds fractions with different solvents. GC-MS was performed on a Shimadzu GC-2010 connected to a Shimadzu QP2010S Mass Spectrometer to determine the distributions of n-alkanes, isoprenoids,

terpenoids, and steranes. The GC was equipped with a 30 m×0.25 mm internal diameter DB-5ms Capillary Columns, fused silica capillary column coated with a thickness of 0.25 μm diphenyl dimethyl polysiloxane. The GC oven starting temperature was 50°C, programmed to rise from 50°C to 140°C at 12°C/minute and then from 140°C to 310°C at 3°C/minute and held for 15 minutes at 310°C for saturated hydrocarbon fraction analysis. For aromatic hydrocarbon fraction analysis, starting temperature of the oven was 60°C, programmed to rise from 50°C to 310°C at 3°C/minute, and held for 15 minutes at 310°C.

Results and Discussion

Bulk Geochemical Analysis

Bulk geochemical analysis shows some variations of OM source input for all the samples. Most of samples are dominated by Type II kerogen in plots of HI vs. OI and HI vs. Tmax (**figs. 2a and 2b**); some of the samples from the Chang 7 deep-lake depositional setting show the signature of mixed Type I and Type II kerogens; and one sample from delta front depositional setting is dominated by Type III kerogen. All the samples are in the oil window even they showed a wide range of present burial depths. HI (hydrogen index) ranges from 135 to 486 (mg HC/g TOC) (see **Table 2, fig. 2**), and the large variation of HI seems inconsistent with maturity level. Two samples from the Chang 7 deep-lake depositional setting (at present burial depths of 1,745.32 m and 1,917.2 m) have abnormally high HI index values corresponding to the burial depth, indicating the oil-prone Type I/II kerogen might be developed. The variation of OM type reflects the complexity of OM source input and preservation in the Triassic Yanchang lacustrine system (see **Tables 1 and 2**).

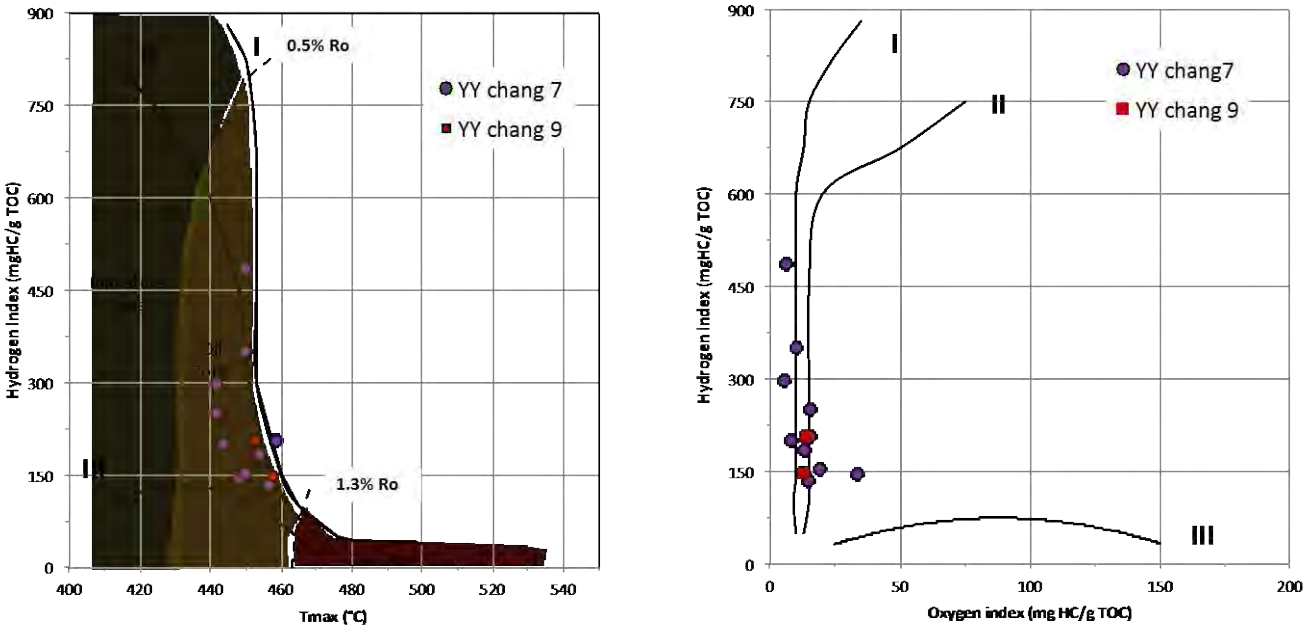

Figure 2. Rock-Eval analysis result for 12 samples.

Distribution of saturated, aromatics, polar, and asphaltene fractions for the residual oil from YY1 and YY22 fall into the same region in the ternary plot. This suggests that the organic matter source and thermal maturity are similar, except in two samples from low-TOC intervals. The enrichment of NSO and asphaltene fractions in the residual oil of these two low-TOC samples implies they might originate from organic-rich intervals or from different sources (**fig. 3**).
The ternary plot of the SARA separation of the residual oil from the 12 samples distributed in different locations showed a very complex result (**fig. 4**). The shallowest sample (YCDT 1119, 407 m) contains the highest proportion of NSO and asphaltene fractions, which corresponds to its low maturity. Two deeper samples (YCYYV 1113, 1114) contain moderate proportions of heavier fractions (NSO and asphaltene ~50%), which are higher than all the other samples except the shallowest one. This appears to conflict with the general increasing trend of thermal maturity with present burial depth. SARA variations in these two samples suggest that there is a range of depositional conditions in which OM preservation and conversion differ, resulting from a varied OM type or source input in different lacustrine depositional settings. The two deeper samples (YCYYV 1113, 1114) were deposited in the semi-deep to deep lake environment, in which OM source input is dominated by aquatic organisms, and resulted in oil-prone kerogen (Type I/II kerogen) being extensively reworked as a result of Type I/II kerogen. This explains their high HI values. The higher paraffin composition of Type I/II kerogen requires higher thermal stress for OM conversion than does Type II kerogen, causing a higher onset temperature for OM conversion to oil and gas.

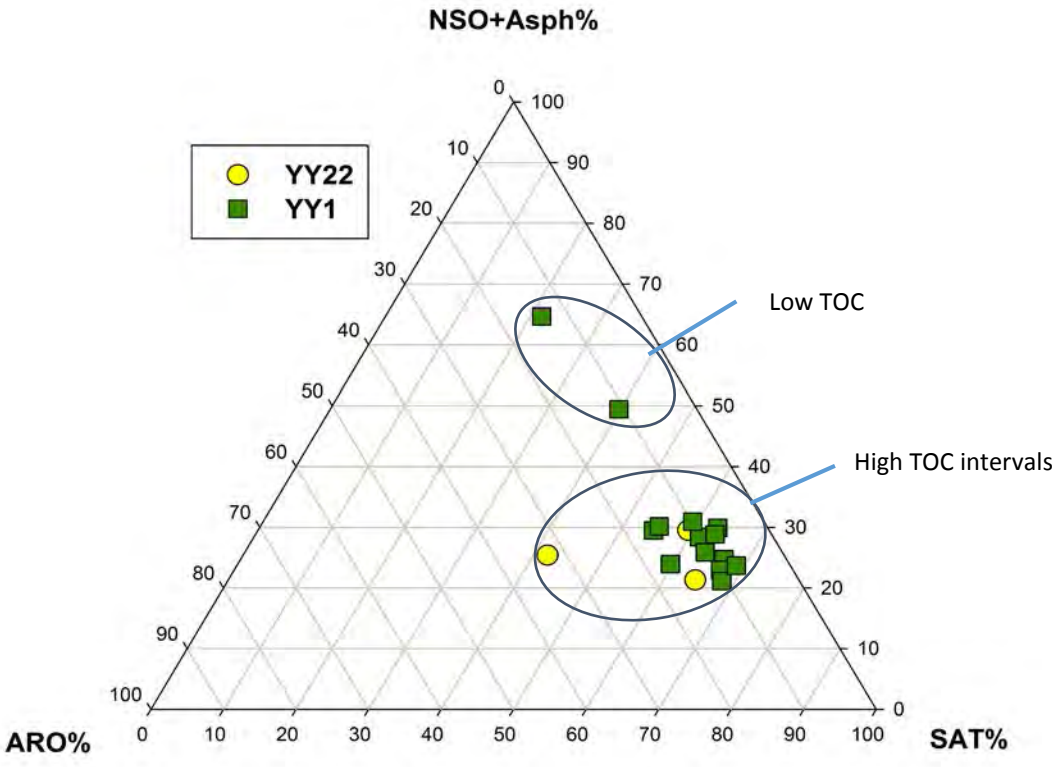

Figure 3. SARA fraction ternary plot for YY1 and YY22 samples.

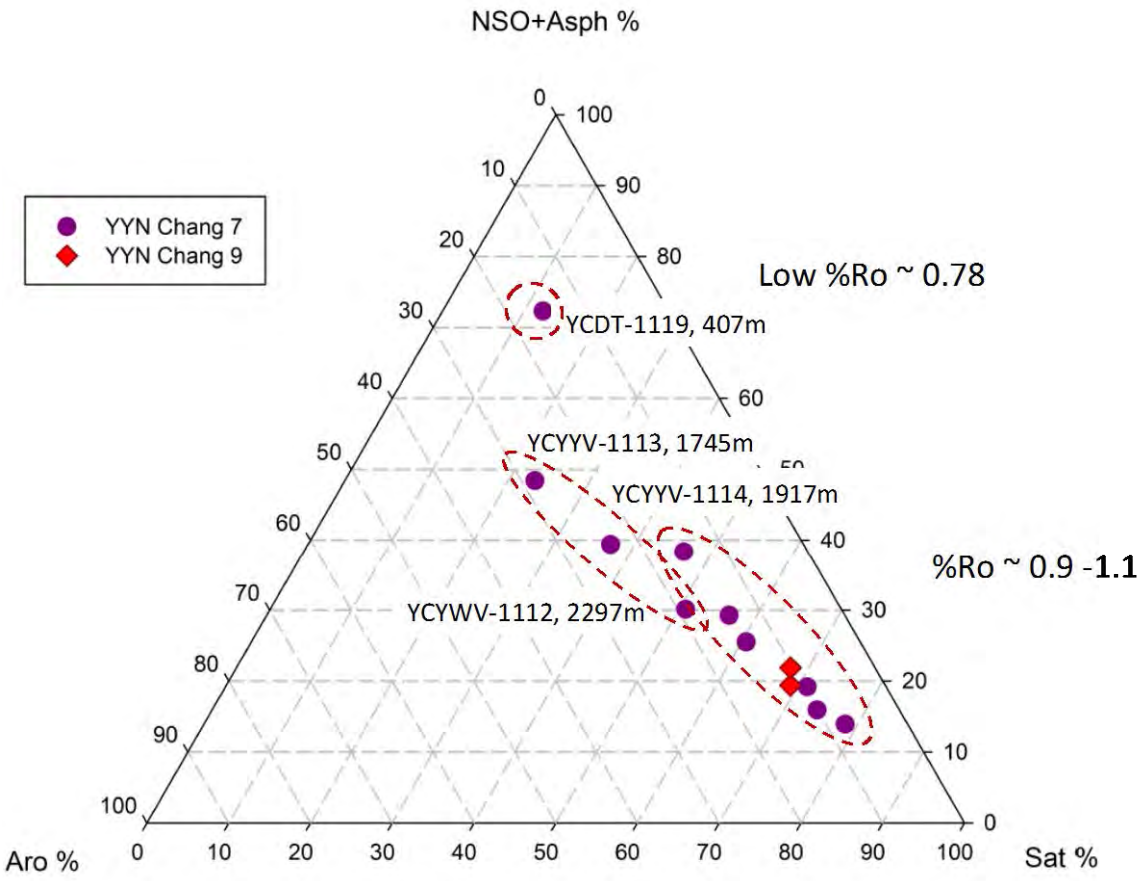

Figure 4. SARA fraction ternary plot for 12 samples.

Organic Matter Source Input

The total ion scan chromatograms (TIC) of saturated fractions are all similar, except for two samples from low-TOC intervals above and below Chang 9 subsections (YY1-1907 and YY1-2244). TIC exhibits a typical oil-window n-alkane distribution with a maximum peak at n-C_{19}. An overwhelmingly high concentration of n-alkane compared with the branched alkanes indicates relatively pristine non-marine algae input (**fig. 7**). All samples can be divided into two groups in the plot of Pr/C_{17} versus Ph/C_{18}. Organic-rich mudstone shows lower values than that of organic-lean siltstone. That most of the data fall into the non-marine OM source indicates limited OM source variation for YY1 organic-rich intervals (**fig. 5**). The total ion scans chromatograms of saturated fractions from residual oils for the 12 samples distributed in different locations are shown in **Figure 9**. There seems to be systematic variations in the composition of the extractable OM with depositional facies, which reflects variations in depositional conditions as the lake evolved. The saturated hydrocarbon from the edge of the lake sequence shows a little bimodal distribution of n-alkanes with maxima at C_{19} and C_{25} with a pronounced odd-to-even predominance (see **fig. 9a**). The proportion of pristane and phytane relative to the n-alkanes is high. Steranes are dominated by C_{29} components of possible higher plant or benthic algal origin (see **fig. 9a**). These features reflect the organic matter input from land plants mixed with algae. In the central deep-lake facies, there is an increase in the

proportion of waxy n-alkanes with no odd-to-even predominance (see **fig. 9b**). Thus, the composition of OM may be attributed to a higher plant and algae mixed source, which has been substantially modified and supplemented by contribution from bacterial biomass (Bohacs and others, 2000; Powell, 1986). In this study area, the OM types vary from Type III at the edge of the lake to Type I/II in the deep-lake facies.

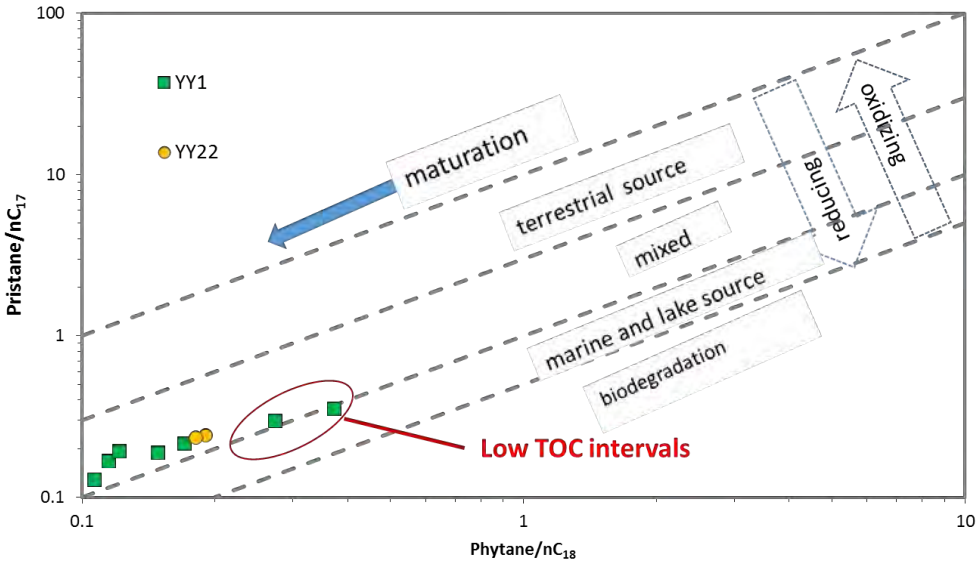

Figure 5. Pr/C17 vs. Ph/C18 plot for samples from YY1 and YY22.

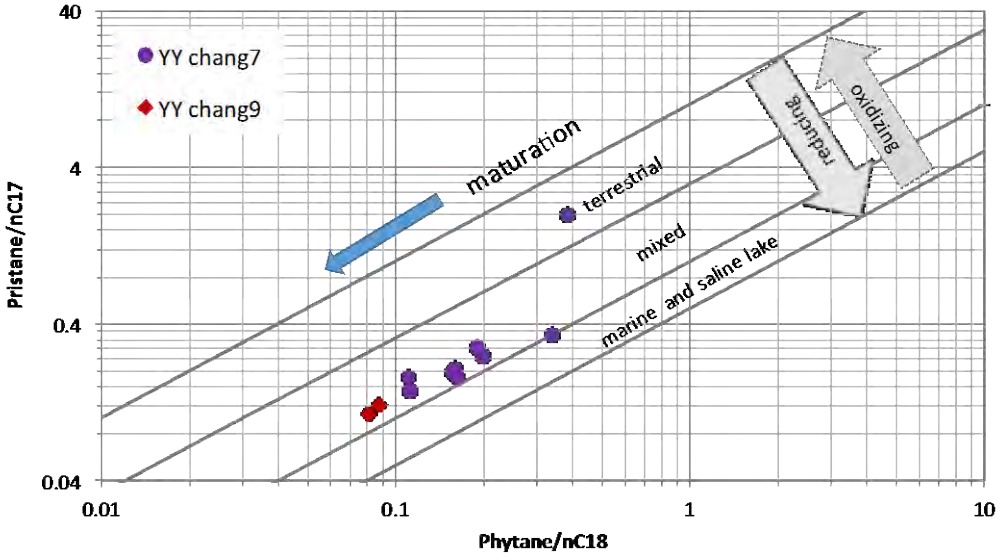

Figure 6. Pr/C17 vs. Ph/C18 plot for 12 samples.

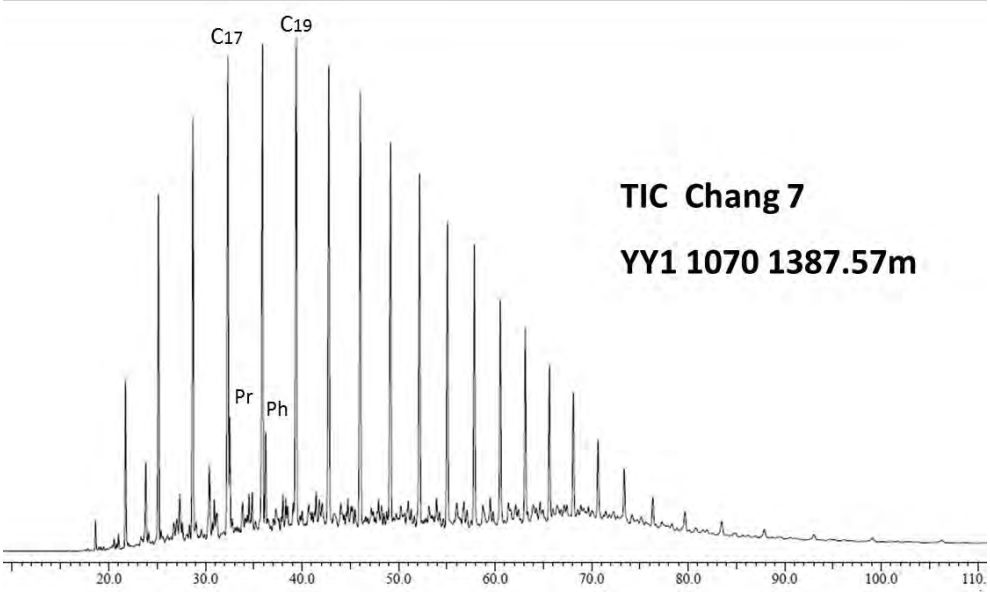

Figure 7. TIC spectrum of saturated fraction from YY1 1070, which is in the Chang 7 interval at a depth of 1387.57 m.

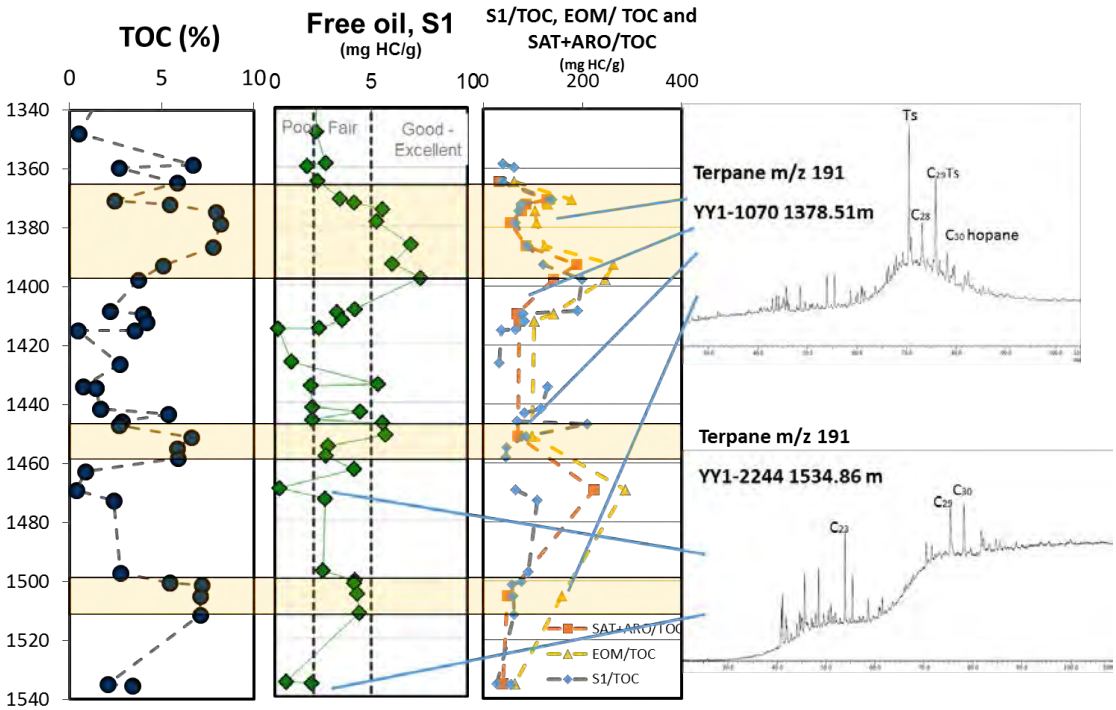

Figure 8. TOC, S1, and S1/TOC, EOM/TOC, (SAT+ARO)/TOC vertical profiles of samples from YY1 well. The m/z 191 streams are from YY1 1070 and YY1 2244.

Depositional Environment

The depositional oxidation and reducing conditions of all the samples can be determined in the plot of Pr/nC_{17} and Ph/nC_{18} (see **figs. 5 and 6**). High pristane to phytane ratios (>3) of the shallowest sample from delta front facies is associated with terrestrial source input in flood plains (Powell, 1984). It is characteristic of oils derived from organic matter of higher plant origin, which had undergone some oxidation before preservation (Powell, 1986). For all the other samples, a consistent reducing depositional environment has been identified, an environment that was beneficial in organic matter accumulation in the Yanchang Formation. The terpane streams for all the other samples show the character of moderate Pr/Ph ratios, poorly preserved higher homohopanes, low gammacerane indexes, and low C_{35} homohopane indexes; this suggests that the source rock from the Yanchang Formation was deposited under a weakly reducing to sub-oxic, freshwater depositional environment (see **figs. 8 and 9**) (Duan and others, 2006; Fu and others, 1986; Philip and others, 1991).

Abnormally high concentrations of Ts and diahopane have been detected in organic-rich mudstones except YCYYV 1113 and 1114. The abnormality could be related to an acidic environment and to a catalyst of clay minerals at the thermal maturity of oil window for those samples (Moldowan and others, 1991). The terpane stream from organic-lean siltstones has extremely low Ts and diahopane concentrations (see **fig. 8**), suggesting that the oil in siltstones probably has a different source compared with the residual oil of adjacent organic-rich intervals. According to the N_2 absorption analysis result, different from the other samples, YCYYV 1113 and 1114 show almost no small pores (Zhang and others, Task 3.2 of this report). As many studies point out that the minerals can physically protect associated organic matter from “attack,” especially clay minerals (Hedges and Oades, 1997). The starvation of small pores in the clay minerals and OM limited the acidic reactions’ condition, consequently inhibiting the rearrangement reactions from hopanes to diahopane. This might be the reason that no significant diahopanes have been identified from these two samples.

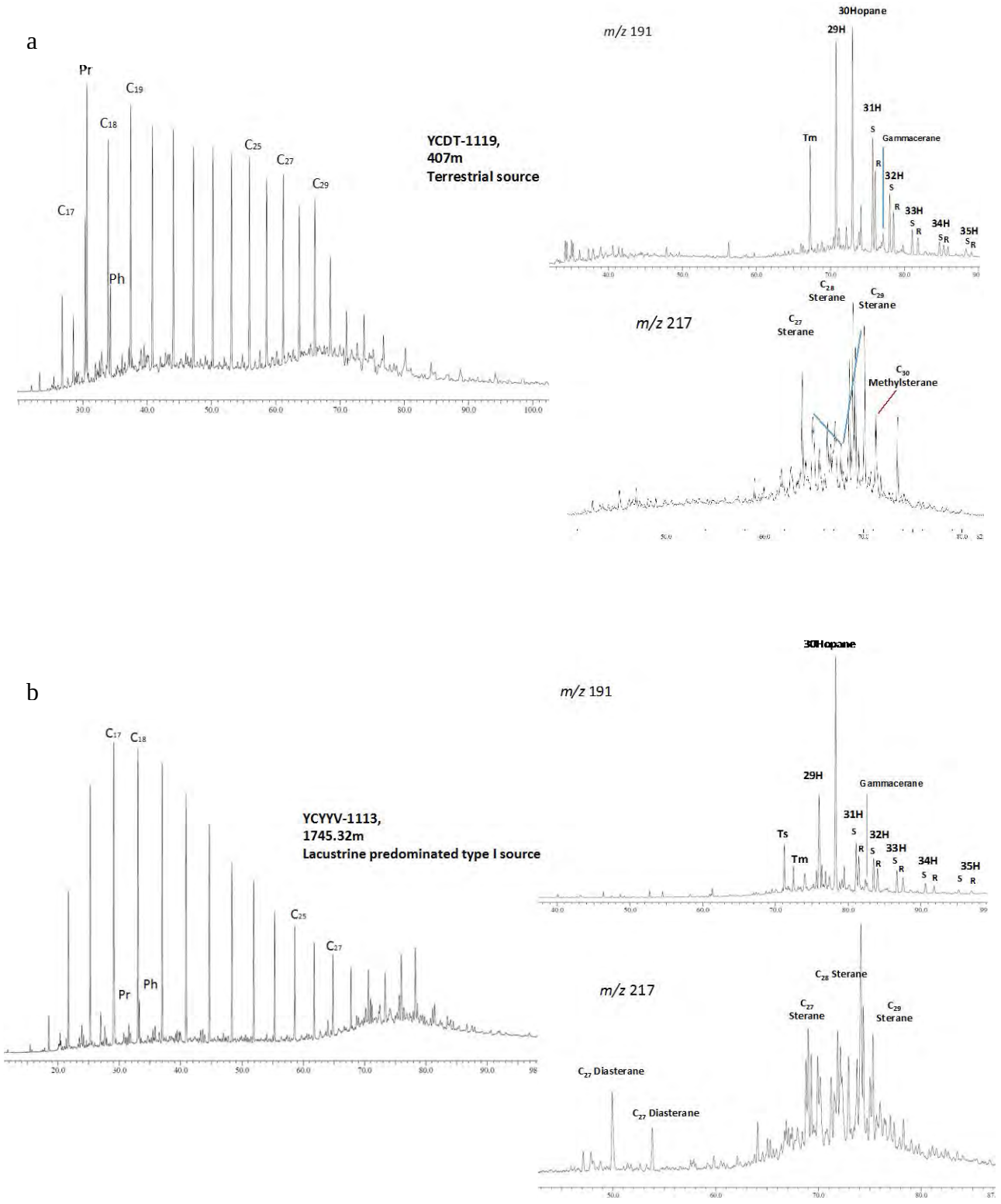

Figure 9. TIC spectra of the saturated fraction, trepan streams (*m/z* 191), and sterane streams (*m/z* 217) for (a) YCDT-1119, 407 m and (b) YCYYV-1113, 1745.32 m.

Thermal Maturity

The methylphenanthrene indexes (MPI-1) in aromatic fractions were defined initially by Radke and others (1982) for correlating with vitrinite reflectance values for sediments containing predominantly Type II and III kerogen. The MPI-1 calculated Roc% ranges from 0.89% to 1.05% for YY1, and increases with burial depth. The calculated Roc% for YY22 is from 0.9% to 0.95%, and it shows a slight increase with depth. The determined thermal maturity of Chang 7, 8, and 9 members is 0.93%, 1.01%, and 1.05%, respectively, for our two studied vertical wells. The methylphenanthrene indexes (MPI-1) calculated Roc% is less scattered than the calculated Roc% based on Tmax values (0.65 ~1.11% forYY1, 0.78~ 0.96% for YY22) (**fig. 10**).

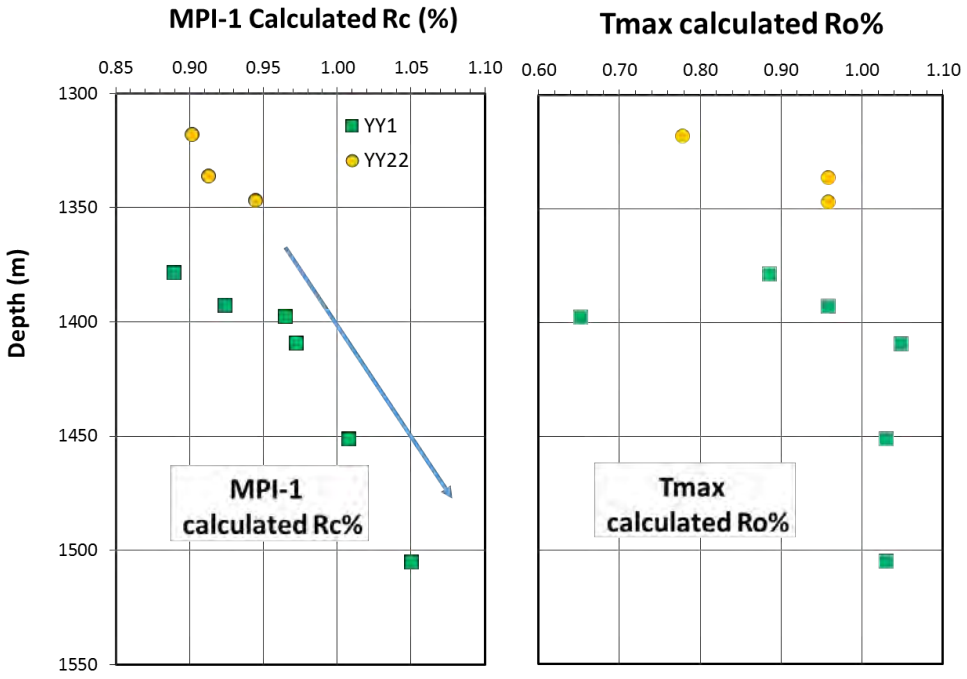

Figure 10. Calculated Roc based on MPI-1 and T_{max} according to the empirical equations.

The MPI-1 calculated Roc% for all 12 samples distributed in different locations ranges from 0.8% to 1.05% (**fig. 11**). The maturities of the source rocks are in the oil window, and a crudely increasing trend with current burial depth appears, except for three samples (YCYYV1113, YCYYV1114, and YCYWV 1112). The thermal maturities of these three samples do not correspond to their present burial depths when compared with the other samples. The inconsistencies of burial depth and thermal maturation of these three samples are possibly related to the variation in OM type in different depositional settings: the organic-rich mudstones distributed in the deep lake are dominated by Type I kerogen or the mixing of Type I and Type II kerogen, whereas the mudstones deposited in the delta plain and delta front have a mixed kerogen source input character between Type II and Type III kerogen. This inconsistency of thermal maturity with the burial depth is not related to maturity, but rather to a combination of source variations and depositional conditions. There is a gradual decrease in the contribution of Type III OM from the delta front to the deep-lake facies (fig. 1). The wide variety of kerogen

types occurs in the lacustrine basin; source facies do not fully follow the formulation of any general rules of OM maturation. Type I kerogens from lacustrine sequences (e.g., Uinta Basin) yield hydrocarbons at somewhat higher levels of thermal maturation than those in Type II kerogens (Tissot and Welte, 1984). This is because of the highly aliphatic nature of the kerogen. Thus, the organic-rich mudstone distributed in the deep lake is dominated by Type I kerogen, and it shows a higher onset temperature or "lower" maturity value than the organic-rich mudstone with a mixed type kerogen in the prodelta or delta front.

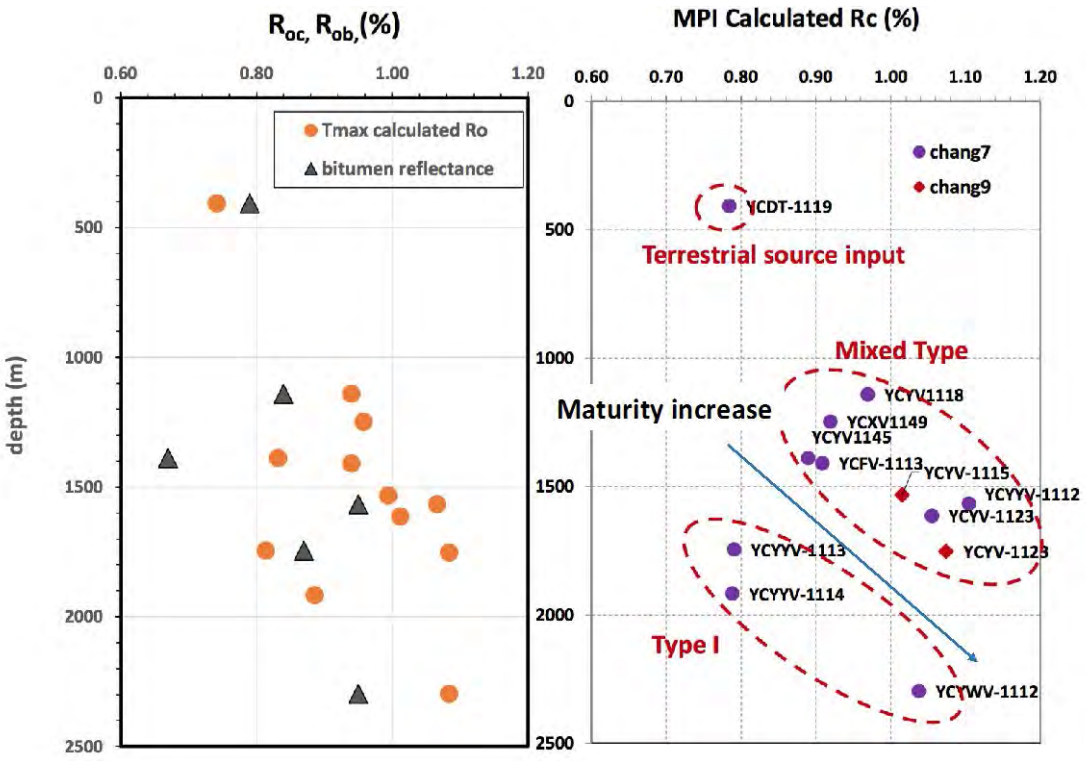

Figure 11. Vitrinite reflectance values of 12 samples and calculated Roc based on Tmax. Roc based on MPI-1 according to the empirical equations.

Conclusions

- The OM types from the Yangchang organic-rich mudstone range from Type III to Type I/II, and vary from Type III kerogen at the edge of the lake to Type I/II mixed kerogen in the deep lake facies. The shallowest well, YCDT-1119, is dominated by Type III kerogen, which was deposited in the oxidizing delta-front environment. Samples from YCYYV 1113, YCYYV 1114, and YCYWV-1112 are dominated by Type I/II kerogen, which was deposited in more reducing deep-lake environments.

- Moderate Pr/Ph ratios, poorly preserved higher homohopanes, low gammacerane indexes, and low C_{35} homohopane indexes for most of the samples suggest that the source rock from the Yanchang Formation was deposited under a weakly reducing to suboxic, fresh- water depositional environment that was beneficial to OM accumulation in the Yanchang Formation.

- The MPI-1 calculated Roc% is more accurate than the T_{max} calculated Ro%, which ranges from 0.8% to 1.05% and increases with burial depth in YY1 and YY22. Differences in hydrocarbon generation and oil cracking kinetics for a different kerogen type result in different maturation patterns. Type I/II kerogen shows a higher onset temperature or "late" oil generation when compared with the mixed type OM source.

References

Bohacs, K.M., Carroll, A.R., Neal, J.E., and Mankiewicz, P.J., 2000, Lake-basin type, source potential, and hydrocarbon character: an integrated sequence-stratigraphic-geochemical framework: AAPG Studies in Geology #46, p. 3–33.

Duan, Y., 2000, Organic geochemistry of recent marine sediment from Nansha Sea, China: Organic Geochemistry 2/3, p. 159–167.

Duan, Y., and Ma, L.H., 2001, Lipid geochemistry in a sediment core from Ruoergai Marsh deposit (Eastern Qinghai-Tibet Plateau, China): Organic Geochemistry 32, p. 1429–1442.

Duan, Y., Wang, Z.P., Zhang, H., Zhang, X.B., Qian, Y.R., and Zheng, G.D., 2006, Biomarker geochemistry of crude oils from Qaidam basin, northwestern China: Journal of Petroleum Geology, v. 29, p. 175–188.

Duan Y., Wang, C.Y., Zheng, C.Y., Wu, B.X., and Zheng, G.D., 2008, Geochemical study of crude oils from the Xifeng oilfield of the Ordos basin, China: Journal of Asian Earth Sciences, v. 31, no. 4, p. 341–356.

Fu, J.G., Sheng, P., Peng, S.C., Brassell, S.C., and Eglington, G., 1986, Peculiarities of salt lake sediments as potential source rocks in China: Organic Geochemistry 10, p. 119–126.

Han, J., and Calvin, M., 1969, Hydrocarbon distribution of algae and bacteria, and microbial activity in sediments: Proceedings of the National Academy of Sciences (USA), v. 64, p. 436–443.

Hanson, A.D., Ritts, B.D., Zinniker, D., Moldowan, J.M., and Biffi, U., 2001, Upper Oligocene lacustrine source rocks and petroleum systems of the northern Qaidam basin, northwest China: AAPG Bulletin, v. 85, p. 601–619.

Hedges, J., and Oades, J., 1997, Comparative organic geochemistries of soils and marine sediments: Organic Geochemistry 27, p. 319–361.

Li, K.Q., 1986, Late Triassic deltas in the Shanganning Basin: Acta Sedimentologica Sinica, v. 4, no. 1, p. 86–95 (in Chinese).

Moldowan, J.M., Fago, F.J., Carlson, R.M.K., Young, D.C., Duvne, G., Clardy, J., Schoell, M., Pillinger, C.T., and Watt, D.S., 1991, Rearranged hopanes in sediments and petroleum: Geochimica et Cosmochimica Acta, v. 55, p. 3333–3353.

Peters, K.E., Fraser, T.H., Amris, W., Rustanto, B., and Hermanto, E., 1999, Geochemistry of crude oils from eastern Indonesia: AAPG Bulletin, v. 83, p. 1927–1942.

Philip, R.P., Fan, P., Lewis, C.A., Li, J., Zhu, H., and Wang, H., 1991, Geochemical characteristics of oils from Chaidamu, Shanganning and Jianghan basins, China: Journal of Southeast Asian Earth Science, v. 5, p. 351–358.

Powell, T.G., 1984, Developments in concepts of hydrocarbon generation from terrestrial organic matter: Beijing Petroleum Symposium 20-24 Sept. 1984, Beijing China, Preprint, 40 p.

Powell, T.G., 1986, Petroleum geochemistry and depositional setting of lacustrine source rocks: Marine and Petroleum Geology, v. 3, p. 200–219.

Radke, M., Willsch, H., and Leythaeuser, D., 1982, Aromatic components of coal: relation of distribution pattern to rank: Geochimica et Cosmochimica Acta, v. 46, p. 1831–1848.

Radke, M., Willsch, H., and Leythaeuser, D., 1986, Maturity parameters based on aromatic hydrocarbon: Influence of organic matter type. In: Leythaeuser, D., and Rullkotter, J. (Eds.), Advance in Organic Geochemistry 1985. Organic Geochemistry, v. 10, p. 51–63.

Tissot, B., and Welte, D.H., 1984, Petroleum Formation and Occurrence, 2nd edn.:Springer-Verlag, Berlin, 699 p.

Volkman, J.K., Farrington, J.W., Gasgosian, R.B., and Wakeham, S.G., 1981, Lipid composition of coastal marine sediments from the Peru upwelling region. In: Bjoroy, M. and others. (Eds.), Advance in Organic Geochemistry 1981: Wiley, New York, p. 228–240.

Wang, H.D., Allen, J., and Philp, R.P., 1995, An organic geochemical investigation of oils and source rocks from two Mesozoic formations of Shanganning basin, China: Journal of Southeast Asian Earth Sciences, v. 11, p. 277–288.

Yang, J.J., and Zhang, B.R., 1988, Region Shanganning petroliferous basin and its reservoir sequence: Acta Petrologica Sinica, v. 9, no. 1, p. 1–8 (in Chinese).

Yang, J.J. (Ed.), 2002, Tectonic Evolution and Oil–Gas Reservoirs Distribution in Ordos Basin: Petroleum Industry Press, Beijing.

TASK 5.1

High Pressure CH_4 Adsorption and Gas Storage in Oil-bearing Argillaceous Mudstones, Yanchang Formation

Tongwei Zhang[1] and Jianfeng Zhang[2]

Bureau of Economic Geology[1], Jackson School of Geosciences, The University of Texas at Austin, Austin, TX
Shaanxi Yanchang Petroleum (Group) Co. Ltd.[2], Xi'an, Shaanxi, China

Introduction

Natural gas (primarily methane) stored in shale gas reservoirs is sourced from the organic matter (OM) through biogenic or thermogenic processes (Hill and others, 2007; Strapoc and others, 2010) and is thought to exist in one of three forms: (1) free gas in pores and fractures; (2) sorbed gas in OM and inorganic minerals; and (3) dissolved gas in bitumen, oil, and/or water. Characterization of shale-gas reservoirs can be helpful in understanding gas-in-place (GIP) predictions and estimated ultimate recovery (EUR); however, the heterogeneous nature of shale reservoirs presents a challenge for such characterization because key properties, including porosity, permeability, and pore connectivity, vary in scale from play to play.

The presence of pore fluids, including water and oil, can greatly affect gas storage in oil-bearing argillaceous mudstones of the Yanchang Formation. Water and oil pore fluids occupy a proportion of available pore spaces, resulting in a reduction of pore volume for gas storage. A sequential pore fluid removal method described in Task 3.2 (Zhang and others, this report) provides a way to determine gas, oil, and water saturation, and pore fluid distribution with the respect to pore size. The change of BET surface area for the same sample at moisture and oil-contained, dry and oil-contained, dry and oil-clean conditions provides a measure to gas storage to subtract the effect of the presence oil and water pore fluids on gas storage.

The Ordos Basin is an exhumed basin. In the EarlyTertiary, approximately 68 Ma ago, the entire basin was uplifted more than 1,000 m, resulting in a significant temperature decrease (~50°C). A large portion of generated oil and gas retained in pore spaces of organic-rich source rocks or sorbed in or on kerogens, and becomes the oil and gas sources produced from unconventional shale reservoirs after hydraulic fracturing. If the source rock is rapidly exhumed to shallower depths during a tectonic event, it may become overpressured relative to adjacent carrier beds that have equilibrated more rapidly to the new hydrostatic conditions. This pressure differential between the source rock and carrier beds is then able to drive further primary migration as the source rock pore pressure equilibrates to the new ambient conditions. This is a risk for shale gas resources assessment in exhumed basin. We quantify here the gas loss that occurs as a consequence of exhumation of the source rocks within the Ordos Basin.

Samples and Methods

Seven samples were selected for high-pressure CH_4 adsorption. A detailed geochemical characterization of the studied samples is listed in **Table 1**. TOC contents vary from 1.36% to 8.07%, and the hydrogen index ranges from 149 mgHC/g rock to 263 mgHC/g rock. T_{max} ranges from 448°C to 456°C, indicating the peak of oil generation. All the samples were crushed into

Table 1. The bulk geochemical characterization of the samples in this study

Sample ID	Depth	Carbonate	TOC	S1	S2	S3	Tmax	%Ro	HI	OI	Norm. Oil	PI
	(m)	(wt%)	(wt%)	(mg HC/g)	(mg HC/g)	(mg CO2/g)	(°C)	(RE TMAX)	(mg HC/gTOC)	(mgCO2/gTOC)	S1*100/TOC	(S1/(S1+S2)
YY22-2676	1329.17	82.26	1.36	1.90	2.60	1.04	448	0.90	191	76	140	0.42
YY1-1610	1426.15	4.40	2.72	0.86	4.05	0.51	453	0.99	149	19	32	0.18
YY1-1418	1409.26	4.67	3.98	3.20	6.86	0.71	456	1.05	172	18	80	0.32
YY1-934	1364.69	10.36	5.84	2.22	11.10	0.61	451	0.96	190	10	38	0.17
YY1-1775	1451.02	6.08	6.62	5.71	11.47	0.69	455	1.03	173	10	86	0.33
YY1-2103	1504.98	10.70	7.08	4.24	12.77	0.71	455	1.03	180	10	60	0.25
YY22-2746	1336.03	2.28	8.07	7.59	21.20	0.91	451	0.96	263	11	94	0.26

20 meshes to 50 meshes in size, and then were cleaned with CH_2Cl_2 solvent with Soxtex extraction system for 3 hours to remove oil. The solvent-cleaned samples were stored in a 10-ml glass vial filled with N_2 gas to prevent it from adsorbing moisture from atmosphere. Degassing occurred at 110°C for 12 hours. It was applied before CH_4 adsorption to activate the surface by removing moisture and other retained gases.

Results and Discussion

The excess CH_4 adsorption isotherms at 35°C, 50°C, and 65°C were measured under a dry and oil-clean condition for all seven samples. A modified Langmuir equation was used to fit the experimental observation; the detailed fitting method refers to Hu and others (2015). As shown in **Figure 1**, a nice fit is achieved between the experimental measured CH_4 adsorption and the theoretically calculated one at a given pressure and temperature condition. Three parameters, including a Langmuir maximum, Langmuir constant, and the density of adsorbed phase, can be obtained from the experimental fitting. Those parameters provide useful information to relate rock properties to gas adsorption.

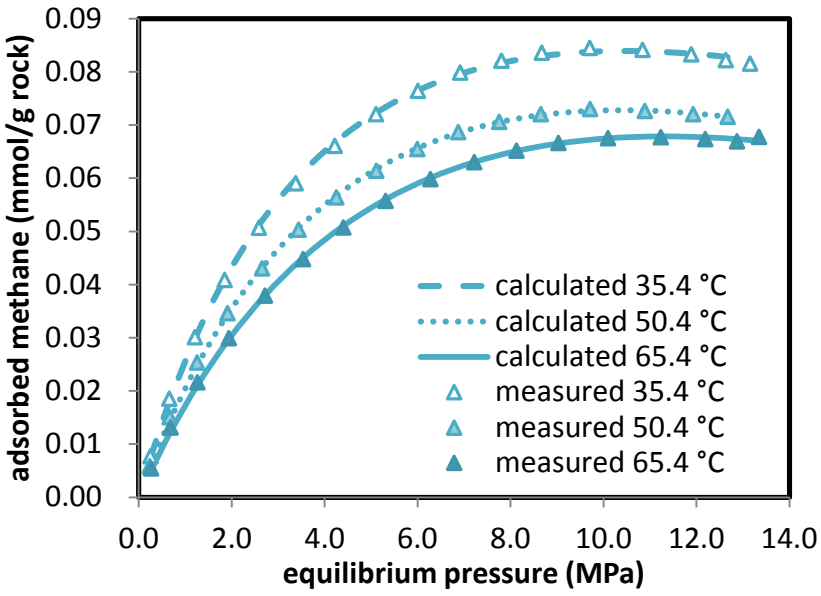

Figure 1. Excess CH4 adsorption isotherms on YY1-1610 at three different temperatures.

Key Factors in CH_4 Adsorption

Total OM total organic content (TOC) is considered an important factor to gas adsorption in shale gas system (Zhang and others, 2012); however, the controls to CH_4 adsorption for the Triassic-aged Yanchang shale are more complicated. As shown in **Figure 2**, the increase in the gas adsorption capacity does not follow the order of increasing the TOC. The sample with the highest CH_4 adsorption has the lowest TOC (1.36%), and the sample with the lowest CH_4 adsorption contains 3.78% TOC. This result indicates that TOC is not only the control on gas adsorption, and mineral compositions and pore structures also play a role in gas adsorption.

A BET-specific surface area is a measure of the availability of pore surfaces for CH_4 adsorption. The surface area is primarily affected by the small pores, in particular the pores with widths of less than10 nm. The greater the BET surface area, the smaller the pores developed in shales. Those small pores develop in both OM and clay minerals. The correlation between BET surface area and rock properties (TOC and mineralogy) provides indirect evidence where those small pores are allocated. As shown in **Figure 3a and 3b**, there is no direct correlation between TOC content and Langmuir maximum adsorbed CH_4, which is the maximum of adsorbed CH_4 capacity for a specific sample, indicating that OM is not the only available source for adsorbed gas storage. In contrast, a linear positive correlation appears in the plot of BET surface area and the maximum of adsorbed CH_4 capacity, thereby suggesting that both clay minerals and OM provide available spaces for adsorbed gas storage.

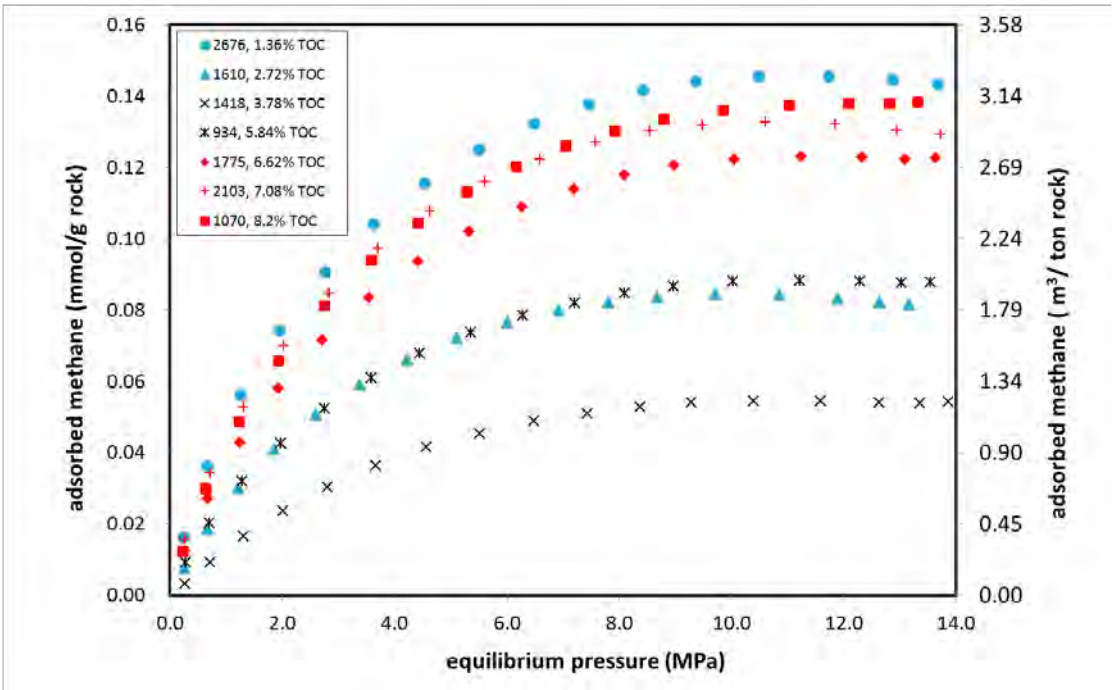

Figure 2. Excess CH_4 adsorption isotherms for the Triassic-aged Yanchang shales at 35°C.

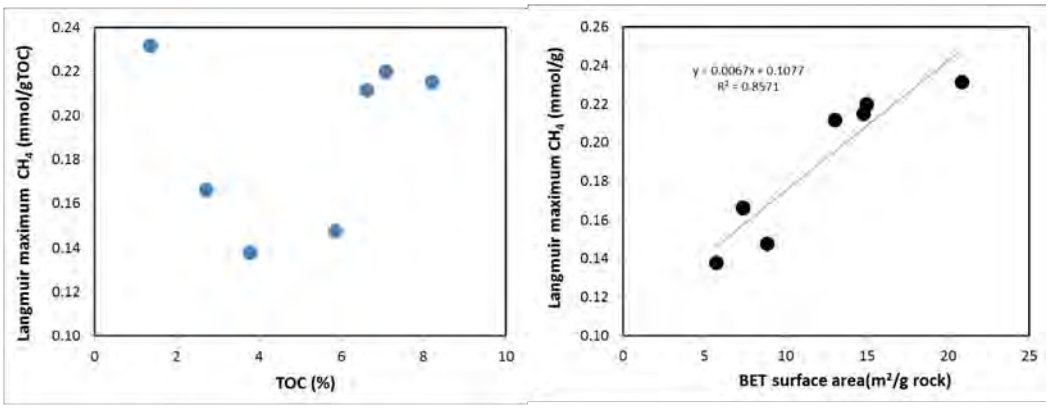

Figure 3. Correlation of Langmuir maximum CH_4 adsorption to TOC (a) and BET surface area (b) for the Triassic-aged Yanchang.

The linear regression line between Langmuir maximum of adsorbed gas and BET surface area was obtained and shown in **Equation 1** as follows:

$$Q_{max} = 0.0067V_{BET} + 0.1077 \qquad R^2 = 0.857 \qquad (1)$$

where Qmax, in mmol/g rock, is the Langmuir maximum of adsorbed CH_4 capacity, VBET, in m^2/g rock, is the measured BET surface area of specific sample, and R^2 is the regression error.

Thermal Dynamic Parameters of CH_4 Adsorption

When compared with Barnett Shale, Alum Shale, and Posidonia Shale, the Yanchang Triassic-aged shale shows a slightly high Langmuir pressure, which is the reciprocal of the Langmuir constant. In other words, the affinity of adsorbed CH_4 is weaker because of the presence of available clay mineral surfaces, resulting in readily releasing of adsorbed CH_4 in pressure reduction. The isosteric heat of adsorption and the standard entropy for the Triassic-aged shale samples ranged from 6.8 kJ/mol to 16.1 kJ/mol and from -59.1 J $mol^{-1}K^{-1}$ to -84.1 J $mol^{-1}K^{-1}$, respectively. Two of seven samples have larger values similar to the values of Barnett Shale, Alum Shale (**fig. 4**). Four of seven samples have intermediate values similar to the those of the Posidonia Shale, which contains a relatively high clay mineral content. One sample has low values similar to pure clay minerals. But the isosteric heat of adsorption and the standard entropy for the Triassic-aged shale samples are lower than Type II kerogen.

In terms of gas adsorption capacity after normalized to per unit of TOC, Yanchang shale shows greater gas adsorption capacity per gram of TOC than Barnett Shale and Alum Shale of the same thermal maturity. High clay mineral content of Yanchang Triassic-aged shale provide additional storage spaces for adsorbed gas, and compensates the less extensively development of OM hosted-pores.

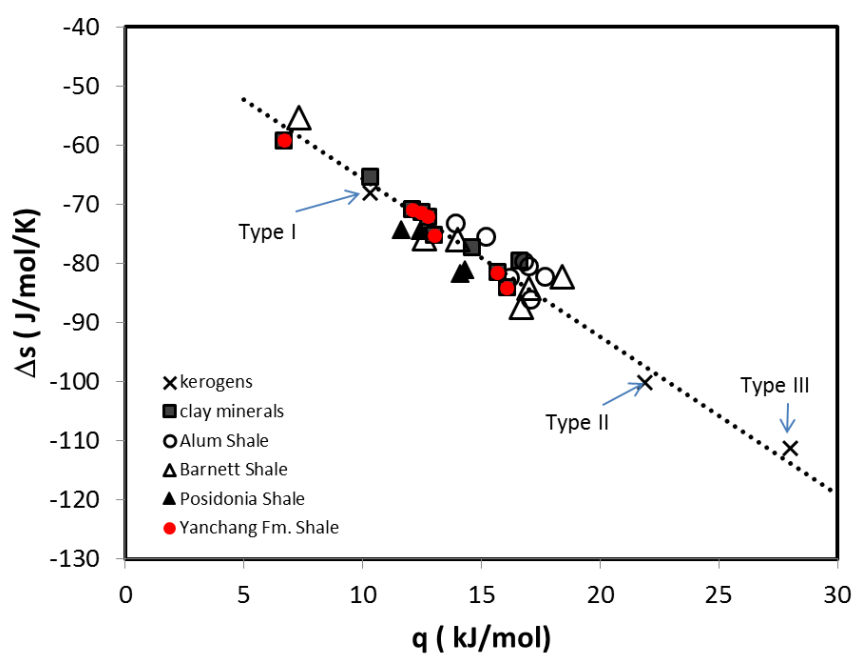

Figure 4. Plot of isosteric heat of adsorption (q) and the standard entropy (Δs) for the Triassic-aged shale.

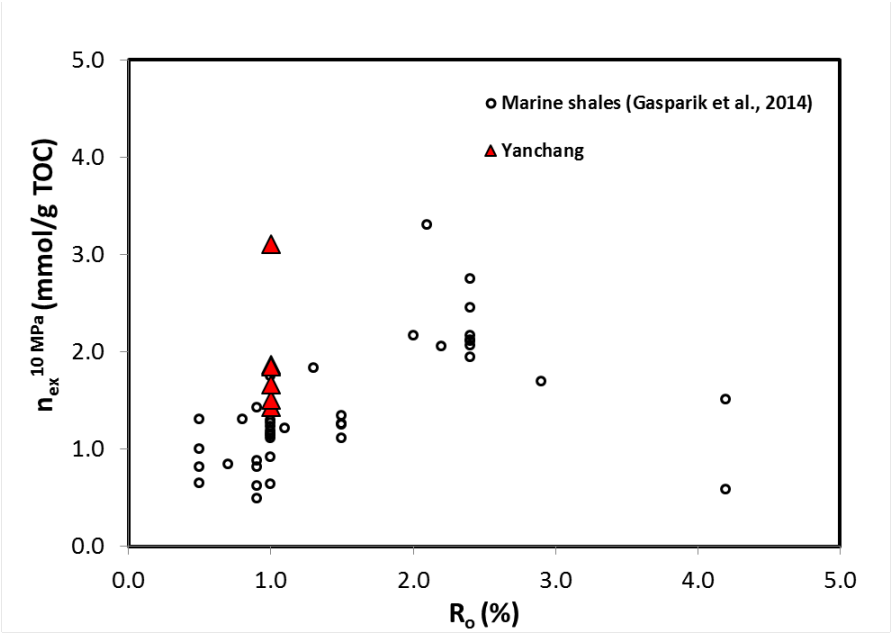

Figure 5. Comparison of adsorbed gas capacity (normalized to TOC) of Triassic-aged shale and marine shales (Barnett Shale, Alum Shale, and Posidonia Shale).

Effect of the Presence of Oil and Water Pore Fluids on CH_4 Adsorption

Oil and water pore fluids occupy a portion of available pore spaces, therefore greatly reducing the value of the BET surface area. As a result, CH_4 adsorption on oil-bearing argillaceous

mudstones is lower than that on oil-cleaning ones. The sequential pore fluid removal method provides a method for quantifying the surface area reduction before and after oil cleaning.

As shown in **Figure 6**, the BET surface area dramatically reduces in the presence of both water and oil. Compared with the value of BET surface area for the samples at dry and oil cleaning condition, there is an approximately 90% total surface area reduction for moisture- and oil-containing samples. The reduction in the BET surface area in the presence of oil and water pore fluids can be used as a measure of the decrease of adsorbed CH_4 capacity in oil-bearing mudstones.

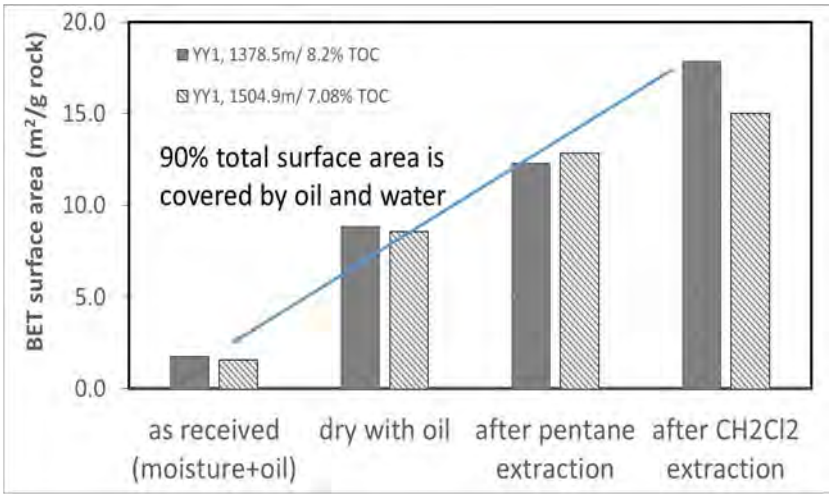

Figure 6. Comparison of BET surface area for Yanchang oil-bearing shales under four different conditions: moisture + oil, dry + oil, dry + asphaltene, and dry + no oil.

As shown in **Figure 7**, a CH_4 adsorption isotherm in oil-bearing mudstones can be estimated at a given temperature based on the previously discussed sequential pore fluid removal method. Simply assuming that the Langmuir maximum of adsorbed CH_4 capacity is a function of available surface area for the same samples at moisture- and oil-contained, dry- and oil-contained, and dry- and oil-clean conditions, the comparison of CH_4 adsorption isotherms was made in the presence of oil and water pore fluids, as shown in **Figure 7.** Compared with the dry and oil clean condition, an approximately 50% reduction in adsorbed CH_4 capacity is estimated in the presence of oil and gas for organic-rich argillaceous mudstones of the Chang 7 member in the YY1 well. In the presence of oil, gas, and water, an approximately 90% reduction in adsorbed CH_4 capacity occurs, indicating that moisture mainly occupies the pores less than 10 nm, which makes a significant contribution to total surface area. In addition, oil and water pore fluids occupy the pore spaces, resulting in a decrease in gas saturation. Therefore, the presence of oil and water pore fluids can greatly affect shale gas resources estimates, including both free gas and adsorbed gas.

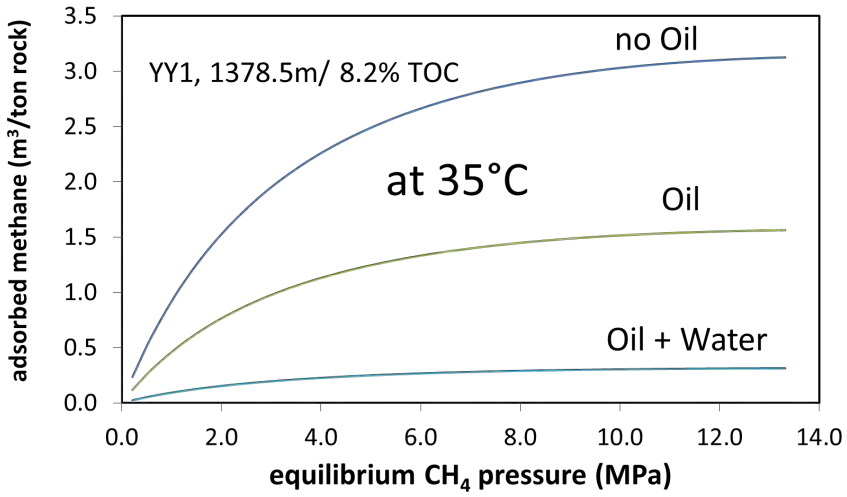

Figure 7. Plot showing estimation of pore fluids on adsorbed gas.

Estimate of Gas Storage in the Yanchang Formation

During times of petroleum generation, kerogens in organic-rich source rocks expel petroleum to form a fluid phase in the pore system. The relative timing of petroleum charge and trapping formation is a vital component in the accumulation of petroleum deposits. Exhumed basins have been historically viewed as higher-risk targets for conventional petroleum exploration because of the switch-off of petroleum generation in the source rock at the commencement of cooling during exhumation. However, even at the switch-off point, the source rock may retain a significant volume of petroleum sorbed in kerogen and within its pore system. English and others (2016) demonstrated that if the source rock is exhumed to shallower depths after peak burial, pore pressure reduction and the associated volumetric expansion of the petroleum—particularly of the gaseous—phase in the pore system will result in the discharge of additional petroleum into the adjacent carrier bed or reservoir formations. The high-grade shale plays may be associated with systems where the magnitude or rate of relative overpressure dissipation has limited the exhumation charge from the unconventional to conventional reservoirs within the basin.

The Ordos Basin is an exhumed basin. Burial and thermal history of the Y2 well in the Ordos basin is shown in **Figure 8**. The organic-rich Yanchang Formation reached the deepest burial depth of around 2600 m at 100 Ma, and the temperature was as hot, from 110°C to 140°C, which is a favorable temperature range for OM conversion to oil and gas. The temperature gradient is approximately 50°C/km, indicating that the Ordos Basin is a low-pressure and high-temperature basin (English and others, 2016). In the Early Tertiary, approximately 68 Ma ago, the entire basin was uplifted more than 1000 m, as shown in the Y2 well, resulting in significant temperature decrease (~50°C). The decrease in temperature during exhumation (a period of 32 Ma) can greatly reduce the fluid pore pressure in the carrier beds dominated by more permeable sandstone and siltstone. The re-equilibration of pore fluids in the carrier beds with hydrostatic system can be readily reached at a given pressure and temperature after exhumation. For organic-rich mudstone, some portion of the generated oil and gas expels during primary migration by way of bulk flow occurred both upward and downward by local fluid potential gradients (Mackenzie and Quigley, 1988), and lateral migration if either an interconnected

fracture network or a more permeable interbed is developed within the source rock. A large portion of generated oil and gas retains in pore spaces of organic-rich source rocks or sorbed in or on kerogens, and becomes the oil and gas sources produced from unconventional shale reservoirs after hydraulic fracturing. If the source rock is rapidly exhumed to shallower depths during a tectonic event, it may become overpressured relative to adjacent carrier beds that have equilibrated more rapidly to the new hydrostatic conditions. This pressure differential between the source rock and carrier beds is then able to drive further primary migration as the source rock pore pressure equilibrates to the new ambient conditions. This is a risk for shale gas resources assessment in an exhumed basin. We quantify the gas loss that occurs as a consequence of exhumation of the source rocks within the Ordos Basin.

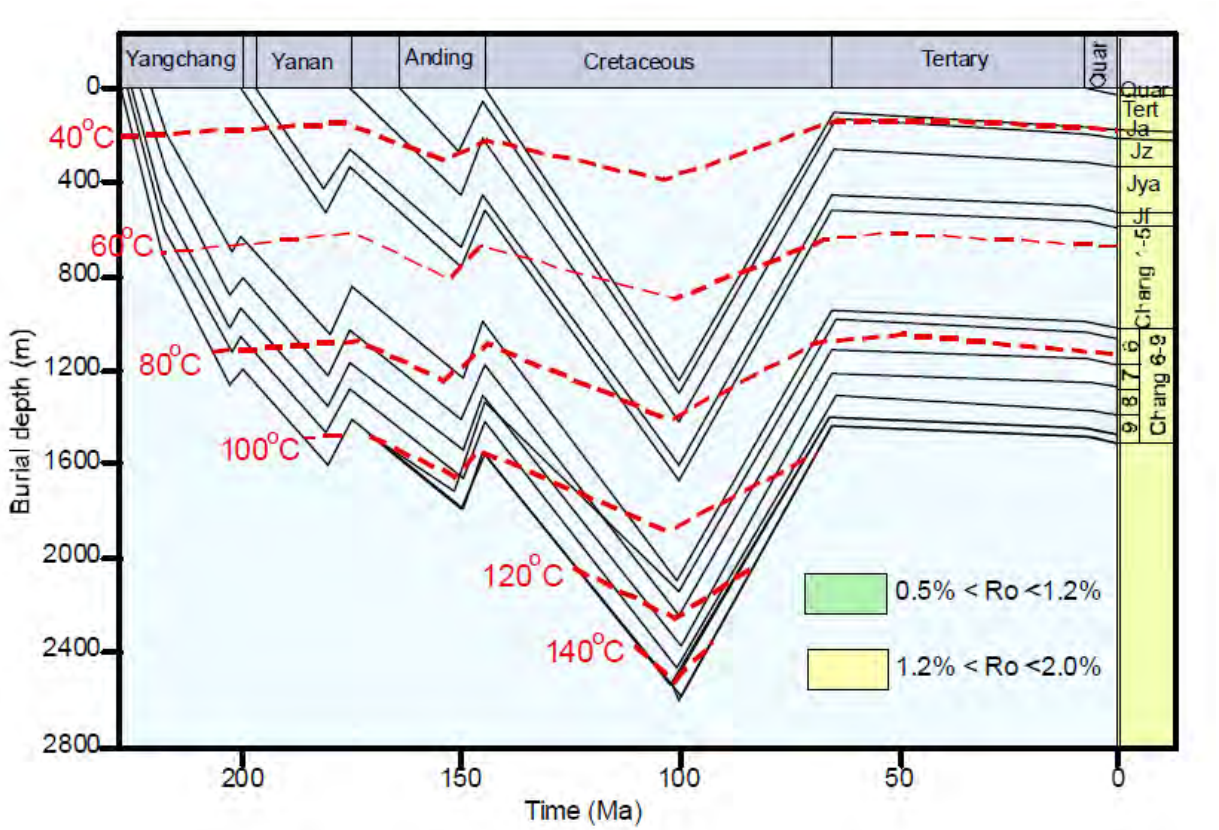

Figure 8. Burial and thermal history of Y2 well in the Ordos Basin. Diagram from Wang, X. and others (2016).

We used a simple analytical solution for pressure diffusion in a semi-infinite medium, assuming an instantaneous and uniform pressure drop along a planar surface, and followed the method of English and others (2016) and modeled how the pore pressure within a source rock responds when in contact with a lower-pressure carrier bed, sandstone. Conceptually, the model assumes a relatively overpressured source rock with homogeneous permeability (for a given petroleum fluid) situated over a more permeable water-bearing sandstone that has rapidly equilibrated with hydrostatic conditions in an open system during, or after, exhumation. No pressure buildup exists below the interface over time as the petroleum is efficiently removed within the permeable carrier bed. As expected, the reduction in pressure within the source rock occurs most rapidly at short distances from the lower-pressure interface (**fig. 9**), and the rate of pressure decline is

primarily controlled by the matrix permeability of the source rock. It is also apparent from the model that the re-equilibration of pressure within a source rock in close proximity to a permeable carrier bed occurs in geologically short time periods, that is, mostly within tens of thousands of years for matrix permeabilities in the range of 10 nd to 100 nd.

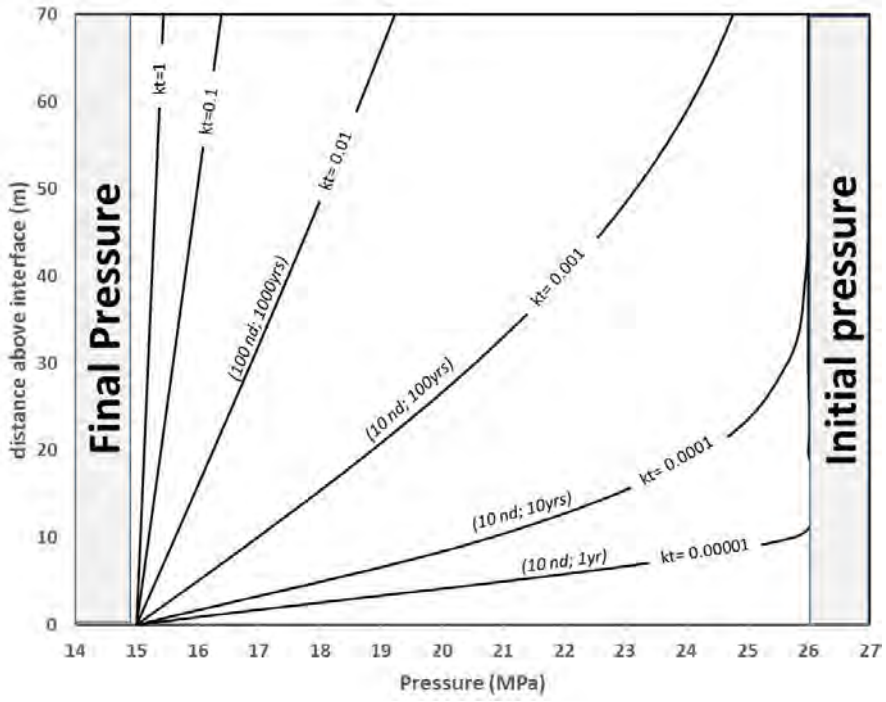

Figure 9. Vertical pressure depletion profiles in a source rock during exhumation. The model is based on the method of English and others (2016). Assumed parameters: porosity = 5%; temperature = 96°C; and permeability = 10 nd.

Figure 10 showed the variation in free gas, adsorbed gas, and total gas storage capacity for a source rock per square kilometer area and a meter thickness during exhumation from a 2600-m depth along a pressure-temperature-time path. With respect to the mudstone reservoir with only gas as pore fluid, constant source rock parameters were assumed: gas-filled porosity, 4%; total organic matter, 8.2 wt.%; rock grain density, 2.5 g/cc; temperature gradient, 0.05°C/m; pressure gradient, 10 kPa/m. The Langmuir maximum of adsorbed gas is 12 m^3/m^3 rock; adsorbed gas density, 403 kg/m^3. For a general calculation of free gas, the incremental volume of retained gas per 1-km^2 area, 1-m source rock thickness, and 1% gas-filled porosity is 0.01 MMcm (million cubic meter gas at standard condition). The relationship between Langmuir constant and temperature follows the equation:

$$\ln(k) = \frac{1458.9}{T} - 6.2858 \qquad (1)$$

Here T is temperature in Kevin, and k is Langmuir constant in Pa^{-1}. The empirical relation is based on the measured results of the sample of organic-rich mudstone at a 1378.1 m-depth in the YY1 well. As shown in **Figure 10**, absorbed gas capacity reaches a maximum at the depth range from 400 m to 1000 m, and a significant decrease occurs at the depth shallower than 200 m.

Adsorbed gas capacity even increases from depths of 2600 m to 1000 m. Therefore, the exhumation does not affect absorbed gas capacity for areas where the burial depth is shallower than 400 m.

The free gas loss during the exhumation varies with present burial depth of the Yanchang Formation. The exhumation causes a significant free gas loss in the area where the burial depth of organic-rich mudstone is less than 500 m (**fig. 10**). More than 70% free gas is gone during exhumation when Yanchang organic-rich mudstone at the peak of oil generation depth (2600 m) uplifted to the present burial depth of 500 m. Less than 40% free gas is lost during exhumation where the present burial depth of Yanchang organic-rich mudstone is deeper than 1100 m. The organic-rich interval of the Chang 7 member in the YY1 well is from 1350 m to 1410 m, and estimation of free gas loss is about 34% during exhumation. If less permeable, organic-lean mudstone layers develop in organic-rich mudstones, free gas loss should be insignificant during exhumation, resulting in overpressure under current hydrostatic conditions. High total gas concentration in the lower part of the organic-rich interval of the Chang 7 member in the YY1 well is an indication of gas retention in an organic-rich thick layer during exhumation (See Task 4-1 in this report). Low total gas concentration in the upper part of the Chang 7 member and the organic-rich mudstone intervals of Chang 8 and Chang 9 members in YY1 well might result from free gas loss during exhumation charge. The increases in pressure gradient from 0.44 psi/ft to 0.65 psi/ft is expected if no gas loss occurs during the exhumation.

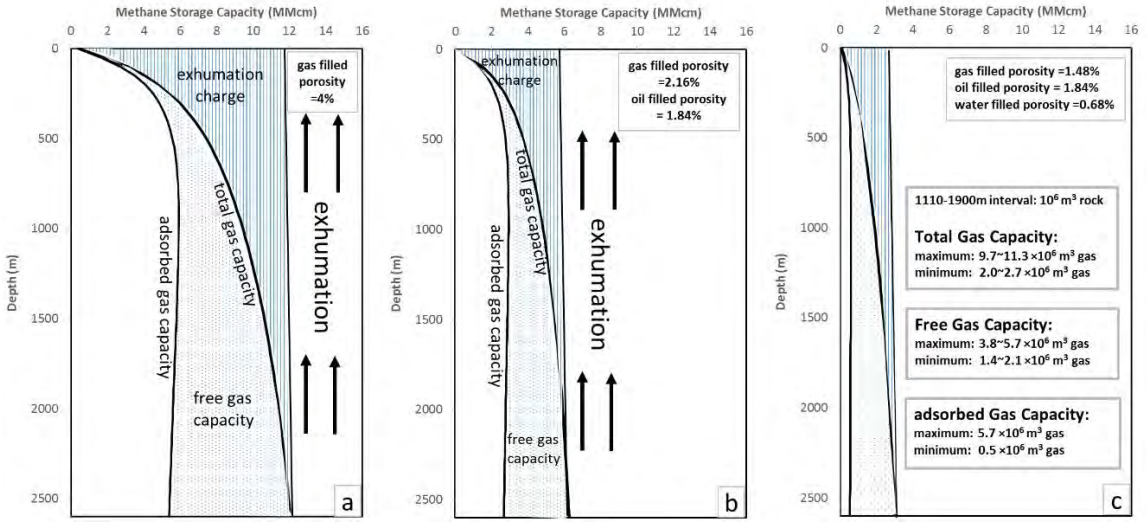

Figure 10. The variation in free gas, adsorbed gas, and total gas storage capacity for a source rock per square kilometer area and a meter thickness during exhumation from a 2600-m depth along pressure-temperature-time path. (a): gas only, gas filled porosity is 4.0%; (b): oil + gas, gas and oil filled porosity are 2.16% and 1.84%, respectively; and (c): oil + gas + water, gas, oil and water filled porosity are 1.48%, 1.84%, and 0.68%, respectively.

Free gas, adsorbed gas, and total gas capacity can also be calculated. The sequential fluid removal method presented in Task 3.2 allows us to determine gas-filled porosity, water-filled porosity, and oil-filled porosity by using N_2 adsorption. CH_4 gas specific gravity is 0.554. Then, free gas capacity can be calculated based on the P-V-T-z equation:

$$PVz = nRT \quad (2)$$

where P (MPa), V (m^3) and T (Kevin) are pressure, volume and temperature, and R is 8.3144 $m^3PaK^{-1}mol^{-1}$. The z-factor for gas was calculated using the pressure–volume–temperature (PVT) Prop add-in for Microsoft Excel (http://www.enrg.lsu.edu/energydata/past/pvtprop). The adsorbed gas capacity is calculated based on the modified Langmuir equation as follows:

$$Q_{ads} = Q_{max} \times \frac{kP}{1+kp}(1 - \frac{\rho}{\rho_{ads}}) \quad (3)$$

where Q_{ads} is adsorbed gas capacity at given temperature T (in Kevin) and pressure P (MPa) condition; ρ and ρ_{ads} are gas density at given T and P condition and adsorbed gas phase density, which is constant value of 403 kg/m^3 in our calculation; k, Langmuir constant, is calculated according to Eq. 1. Q_{max}, Langmuir maximum of adsorbed gas, is a function of total BET surface area. The measured BET surface area for as-received, dried, oil-cleaning conditions was used in our calculation. Total gas capacity at a given temperature and pressure condition is a sum of free gas and adsorbed gas capacity.

The presence of oil and water pore fluids can greatly reduce total gas capacity in the organic-rich mudstones of the Yanchang Formation. For a source rock per square kilometer area and a meter thickness, the comparison of free gas , adsorbed gas and total gas capacity in MMcm (10^6 m^3) in the presence of only gas, oil + gas, and oil + gas + water as pore fluids is shown in **Figure 10**. At the burial depth of 2600 m, the peak of oil generation, the total gas capacity deceases from 12.1 MMcm in gas alone to 6.26 MMcm in oil + gas, to 2.99 MMcm in oil + water + gas. Free gas capacity decreases from 6.65 MMcm in gas alone to 3.59 MMcm in oil + gas, to 2.46 MMcm in oil + water + gas. Adsorbed gas capacity decreases from 5.39 MMcm in gas alone to 2.67 MMcm in oil + gas and 0.53 MMcm in oil + gas + water. The reduction percentage of free gas and adsorbed gas capacity in the presence of oil is 46% and 41%, respectively. In contrast, the reduction of free gas and adsorbed gas in the presence of oil and water is 53% and 91%. Therefore, the presence of water reduces adsorbed gas capacity more significantly than in the presence of oil because water occupies a large portion of < 10 nm pores.

Total gas, free gas, and adsorbed gas in the organic-rich interval (1350 m to 1410 m in depth) of the Chang 7 member in the YY1 well is able to be estimated. Total gas capacity in the presence of gas alone is considered as the maximum gas storage capacity, and that in the presence of oil, gas and water is as the minimum gas storage capacity. For a 1 MMcm (10^6 m^3) rock block with 8.2% TOC, 4% total porosity and current burial depth ranging from 1350 m to 1410 m, the total gas capacity ranges from 2.35 MMcm to 10.5 MMcm. Of these, the free gas capacity is from 1.75 MMcm to 4.75 MMcm, and the adsorbed gas capacity ranges from 0.5 MMcm to 5.7 MMcm.

Conclusions

1. Both clay minerals and organic matter provide spaces for adsorbed gas storage in Triassic-aged Yanchang Formation mudstones, resulting in greater gas adsorption capacity per gram of TOC than Barnett Shale and Alum Shale at the same thermal maturity.

2. The Ordos Basin is an exhumed basin; exhumation doesn't affect absorbed gas capacity for areas where the burial depth is shallower than 400 m. However, exhumation causes a significant amount of free gas loss, and gas loss extent varies with the burial depth. Less than 40% free gas is lost during exhumation where the present burial depth of Yanchang organic-rich mudstone is deeper than 1100 m.
3. If no gas loss occurs during the exhumation, the overpressure could develop in Chang 7 organic-rich thick mudstone. The estimated pressure gradient varies from 0.44 psi/ft to 0.65psi/ft, or pressure factor is from 1 to 1.47.

4. Oil and water pore fluids occupy a portion of available pore spaces, and they greatly reduce the value of the BET surface area, resulting in the reduction of both free gas and adsorbed gas capacity. Using sequential pore fluid removal methods allows quantification of the oil, gas, and water-filled porosity and surface area reduction, both before and after oil cleaning.

5. The free gas and adsorbed gas in oil-bearing mudstones can be estimated by the method used in this study. The free gas capacity is from 1.75 MMcm to 4.75 MMcm, and adsorbed gas capacity is from 0.5 MMcm to 5.7 MMcm in 1 MMcm (10^6 m^3) in the Chang 7 organic-rich mudstone reservoir having 4% total porosity.

References

English, J.M., English, K.L., Corcoran, D.V., and Toussaint, F., 2016, Exhumation charge: The last gasp of a petroleum source rock and implications for unconventional shale resources: AAPG Bulletin, v. 100, p. 1–16.

Hill, R.J., Jarvie, D.M., Zumberge, J., Henry, M., and Pollastro, R.M., 2007, Oil and gas geochemistry and petroleum systems of the Fort Worth Basin. AAPG Bulletin, v. 91, p. 445–473.

Hu, H., Zhang, T., Wiggins-Camacho, J.D., Ellis, G.S., Lewan, M.D.; and Zhang, X., 2015, Experimental investigation of changes in methane adsorption of bitumen-free Woodford Shale with thermal maturation induced by hydrous pyrolysis: Marine and Petroleum Geology, v. 59, p. 114–128.

Mackenzie, A.S., and Quigley, T.M., 1988, Principles of geochemical prospect appraisal: AAPG Bulletin, v. 72, p. 399–415.

Strapoc, D.; Mastalerz, M.; Schimmelmann, A.; Drobniak, A.; and Hasenmueller, N.R., 2010, Geochemical constraints on the origin and volume of gas in the New Albany Shale (Devonian–Mississippian), eastern Illinois Basin. AAPG Bulletin, v. 94, p. 1713–1740.

Wang, X.; Zhang, L.; Jiang, C.; and Fan, B., 2016, Hydrocarbon storage space within lacustrine gas shale of the Triassic Yanchang Formation, Ordos Basin: Interpretation, in press.

Zhang, T.; Ellis, G.S.; Ruppel, S.C.; Milliken, K.; and Yang, R., 2012, Effect of organic-matter type and thermal maturity on methane adsorption in shale-gas systems: Organic Geochemistry, v. 47, p. 120–131.

TASK 5.2

Modeling of Liquid Flow in Shale

Ali Afsharpoor and Farzam Javadpour[1]

Bureau of Economic Geology[1], Jackson School of Geosciences, The University of Texas at Austin, Austin, TX

Problem Statement and Objectives

Modeling the liquid flow in shale has recently attracted extensive attention. To understand and optimize many processes such as liquid hydrocarbon production, determining how liquid flows in shale systems is the first step. Nanoscale pores in shale make the interaction of fluid molecules and pore walls more important than interactions in conventional reservoirs, in which the pores are orders of magnitude larger. Vast experimental observation in recent literature shows higher-than-expected fluid flow in nanopore systems. Therefore, conventional flow equations, such as Darcy's law, may not be valid for shale systems because of the difference in the controlling physics of liquid flow. Two main characteristics of liquid flow in shale are pore geometry and liquid slip at the inner pore wall. By looking more closely at scanning electron microscopy (SEM) images of shale samples, many different pore shapes have been observed. Fluid-flow behavior in noncircular geometry significantly deviates from the flow behavior in circular geometry used in many models. Additionally, liquid flow in microscale porous media reasonably assumes no fluid slippage on inner walls of pores, although this is not the case in nanoscale systems because of the difference in scale.

In this report, we examined numerous SEM images to summarize different pore shapes and sizes. We then used computational fluid dynamic (CFD) modeling for various geometric and slip conditions to develop a generalized flow equation to capture pore geometry and slip effect. The developed flow equation is used in pore-network modeling simulation to study effective liquid permeability in a shale system. Our study confirms that a simplified circular pores assumption causes apparent permeability to be significantly overestimated. The discrepancy between the realistic multigeometry pore model and the simplified circular pore model becomes more pronounced when pore sizes reduce and liquid slip on the inner pore wall is taken into account. The developed pore-network models is based on pore-size distribution, total organic content (TOC), porosity, surface area, pore geometry, and slip length obtained from the experimental measurements conducted at the Bureau of Economic Geology (BEG).

Introduction

Recently, shales have attracted renewed attention because of their importance as commercial hydrocarbon reservoirs in North America (Curtis, 2002; Montgomery and others, 2005; Pollastro, 2007; U.S. Energy Information Administration, 2015). For several decades, the main focus of the oil and gas industry has been on conventional reservoirs and the investigation of different approaches to optimizing hydrocarbon production. One of the basic tools for these purposes has been reservoir simulators developed based on physics principles and empirical equations from experimental works. Reservoir simulation predicts how fluid flows through porous media, which consist of pores connected by pore throats in microscale. In a shale system,

however, pores and throats are at nanoscale (Nelson, 2009), which applies different physics for fluid flow. As a result, several well-known correlations, such as Darcy's law, cannot be applied precisely to shale systems. The Darcy equation is as follows:

$$Q = \frac{KA}{\mu L}\Delta p \qquad (1)$$

where Q is volumetric flow rate, K is permeability, A is cross-sectional area, μ is viscosity, L is length, and Δp is pressure drop. Permeability in shale is very low (on the order of nanoDarcy) such that with typical pressure gradient in reservoirs, we do not expect any flow based on conventional flow equations; however, gas and liquid production have been observed in shale (Javadpour and others, 2007). Javadpour (2009) introduced the Knudsen diffusion and slip condition for gas flow in shale systems. Liquid flow in shale turned out to be even more surprising, because the liquid viscosity is an order of magnitude greater than the gas viscosity. The slip on the pore wall is negligible compared with the advection of microscale liquid flow in porous media, however, as we show in our Results and Discussions section, slip has an impressive effect on liquid flow at the nanoscale, which is an important discovery about liquid flow in tight porous media, such as shale.

Slip length is an extrapolated length at which the tangential component of the velocity vector vanishes and is a measure of slip effect in liquid flow in a duct. Figure 1 schematically illustrates the flow in a single duct in microscale (**fig. 1a**) and nanoscale (**fig. 1b**). Because the slip length is negligible compared to micrometer-scale pore geometry, slip effect can generally be ignored in a microscale system. In a nanoscale system, however, the slip length is comparable to pore size, and its effect must be considered.

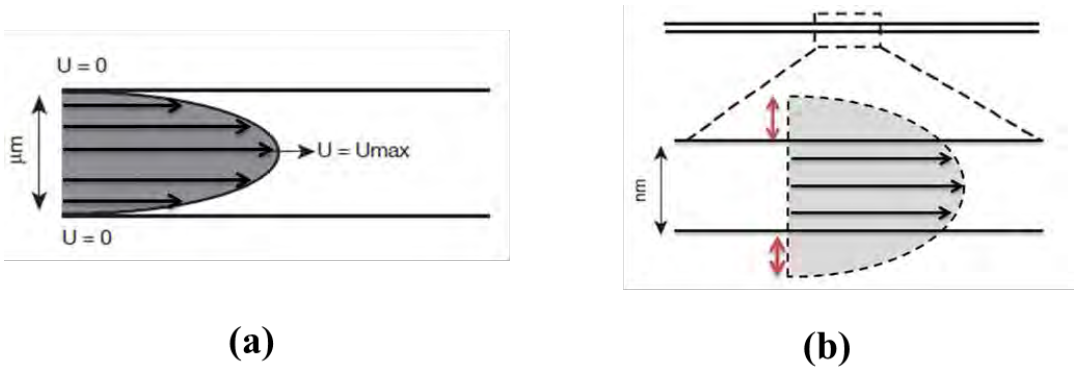

Figure 1. Schematic figures of slip condition in microscale (a) and nanoscale (b) systems. *Ls* is slip length.

Generally, pore geometry includes a wide range of possible shapes, from circular duct to slit, in shale (Loucks and others, 2009; Curtis and others, 2010; Sondergeld and others, 2010; Bernard and others, 2012; Chalmers and others, 2012; Milliken and others, 2013; Pommer and Milliken, 2015). Approximation of circular duct for pore throat geometry is reasonable in many applications of conventional reservoirs. However, for shale systems, fluid flow depends more on the shape of the pore throat, especially because slip condition must necessarily be considered. Extensive SEM image studies of pores in shale samples suggest a vast number of pore shapes deviating from circular, as shown in **Figures 2 and 3**. **Figure 2** shows SEM images of a sample

(sample 1) from the Eagle Ford Shale in different resolutions—circular-, angular-, and slit-type pores. **Figure 3** has more SEM images from the same shale sample (sample 2), but it was taken a few micrometers apart from sample 1. Pores in **Figure 3** are more noncircular and are slit type. Comparison of pore geometry in samples 1 and 2, as well as in many other SEM images, illustrates the variety of possible pore shapes in shale.

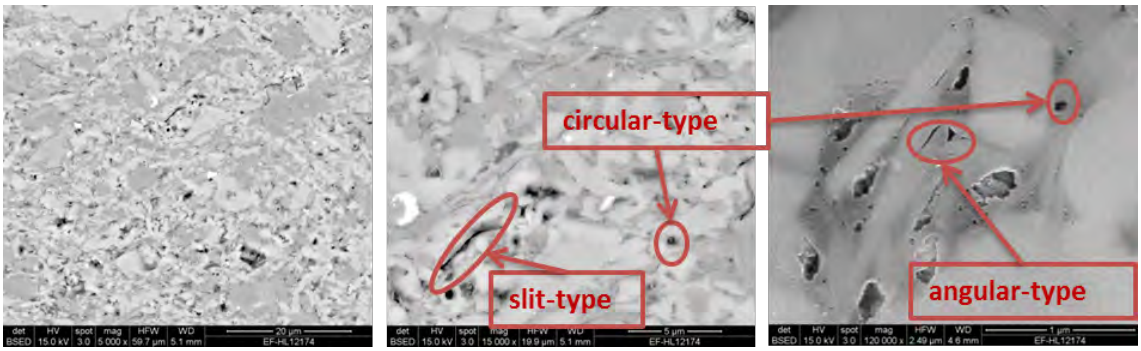

Figure 2. SEM images of Eagle Ford Shale systems (sample 1) in 5000X, 15000X, and 120000X, respectively, from left to right. Several circular-, slit, and angular-type pores are illustrated in the images.

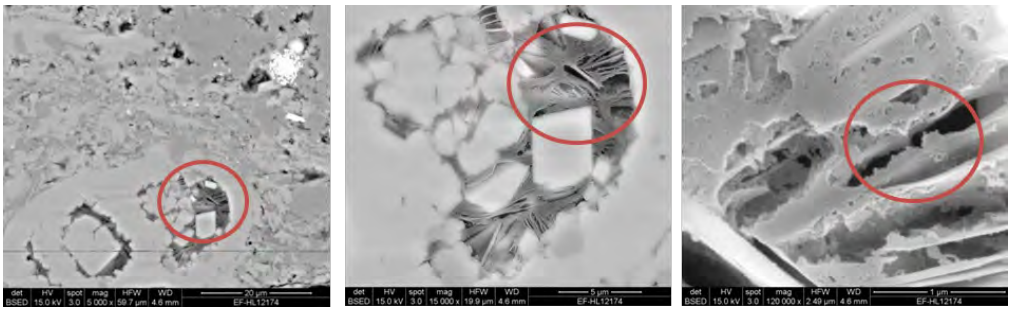

Figure 3. SEM images of Eagle Ford Shale systems (sample 2) in 5000X, 15000X, and 120000X, respectively, from left to right. Circles show many noncircular pores in samples that approximate slit shape.

Two input parameters required for the new flow equation are shape factor and slip length. Shape factor quantifies geometry and can be calculated from results of different methods, such as the nitrogen adsorption test and mercury injection capillary pressure (MICP) (Ross and Bustin, 2009; Chalmers and others, 2012; Mastalerz and others, 2012; Kuila and Prasad, 2013; Schmitt and others, 2013). The nitrogen adsorption test is a widely used technique to characterize porous media using the concept of adsorption of nitrogen by rocks. This technique provides important porous-media characteristics, such as pore-size distribution, wetted surface area, and pore volume (Naraghi and Javadpour, 2015). The second parameter, slip length for liquid flow, has been measured by atomic force microscopy (AFM) (Javadpour and others, 2015).

In this report, dimensional analysis has been conducted to find complete and independent dimensionless groups to ensure that the developed universal flow equation takes all dependent variables into account. Then, we performed CFD modeling of Newtonian fluid flow for various regular and irregular cross sections within the wide range of slip length. In CFD modeling, the principal equations are solved using the finite element method (FEM) to investigate the effect of geometry and slip on liquid-flow behavior. All sensitivity analysis on different parameters has been completed. Next, using regression analysis, we developed a generalized flow equation in a

duct with no constraint on cross-section shape and including slip effect. The generalized flow equation can be used for different models of shale systems, with the shape and slip effects now included. In this study, network modeling has been developed as a model for liquid flow in porous media, and the generalized flow equation has been implemented in this model. Then, we performed sensitivity analysis to investigate the effect of pore geometry and slip condition in pore scale on flow behavior in macroscale (that is, porous media).

Methodology

Liquid Flow in a Single Duct

The closed-form, fluid-flow equation for Newtonian flow in regular- and irregular-shaped ducts has been developed in this study using CFD modeling. For Newtonian fluid flow in a circular straight tube, the Hagen–Poiseuille equation is as follows:

$$Q = \frac{\pi R^4}{8\mu L}\Delta p \tag{2}$$

where $\frac{\pi R^4}{8\mu L}$ is hydraulic conductivity (g) for a circular tube. First, we performed dimensional analysis to solve the problem for appropriate dimensionless groups to make the generalized equation applicable in different scales. The three complete and independent dimensionless groups are as follows:

$$\pi_1 = G = \frac{A}{PL_c} \tag{3}$$

$$\pi_2 = \tilde{g} = \frac{g\mu}{A^2} \tag{4}$$

$$\pi_3 = L_{sd} = \frac{L_s}{\sqrt{A}} \tag{5}$$

where A is cross-section area, P is perimeter, L_c is characteristic length (L_c is perimeter [P] in a straight single duct), g is hydraulic conductivity, μ is viscosity, and L_s is slip length. The π_1 is a shape-factor dimensionless group named G, π_2 is dimensionless hydraulic conductivity ($\tilde{g}$), and π_3 is dimensionless slip length (L_{sd}). Shape factor is the ratio of area to flow to square-wetted perimeter for a constant cross-section straight tube. Greater value of the shape factor represents more circular geometry, and lower value means deviation from circular geometry, which can be either angular shapes or slit-type shapes. The shape factor definition, first expressed by Mason and Morrow (1991) for a constant cross-section straight duct, is generalized in this study for other complicated geometry.

Significant CFD modeling has been performed for a wide range of G, $\tilde{g}$, and L_{sd} values in three-dimensional (3D) simulation schemes to ensure that the correlation is valid for a wide range of parameter values. All calculation has been conducted in a dimensionless system to develop a flow to be used at different scales. The Momentum (**Equation 6**) and Continuity (**Equation 7**) equations have been solved using the FEM. COMSOL Multiphysics modeling software has been used to solve the FEM problems as follows:

Navier-Stokes

$$\rho\left[\frac{\partial \boldsymbol{u}}{\partial t} + \boldsymbol{u}\cdot\nabla\boldsymbol{u}\right] = -\nabla\rho + \nabla\cdot\boldsymbol{\tau} \quad (6)$$

$$\nabla\cdot\boldsymbol{u} = 0 \quad (7)$$

where $\boldsymbol{u}$ is velocity vector, and $\boldsymbol{\tau}$ is stress tensor. Sensitivity analysis on various parameters, such as mesh configuration has been performed for different cases to ensure the CFD modeling results are robust. For each geometry, we performed a comprehensive investigation to determine how hydraulic conductivity is sensitive to various geometrical parameters, such as the aspect ratio of a duct. Aspect ratio is the ratio of smallest to largest dimensions (that is, as the aspect ratio decreases), and the geometry deviates from a circular toward a slit-type shape.

Network Modeling

Network modeling is an efficient way to investigate flow in porous media at the microscopic level. Network models have been shown to be quantitative and predictive in certain instances (Bryant and others, 1993; Bakke and Oren, 1997; Lopez and others, 2003; Balhoff and Thompson, 2004, 2006), but to use the models, they must be: (1) physically representative of the morphology of the porous medium from which they are mapped, and (2) first-principle flow equations that correctly describe the physics in each pore throat that must be used as an input.

Herein, the porous media studied are packed beds of granular media. Computer-generated media are formed using a collective rearrangement algorithm, as described by Balhoff and Thompson (2004, 2006). The porosity and grain size can be defined *a priori*. Boundaries can be either periodic or fixed; herein, the boundaries are periodic, to minimize edge effects. The porous medium is mapped to a network model by way of a Delaunay tessellation algorithm, as described by Al-Raoush and others (2003). Pores connected by throats comprise the resulting network model. The connectivity in the network varies, and the volume of the conductivity of each pore and throat is unique and dependent on the pore/throat geometry. The conductivities are computed, as defined by Al-Raoush and others (2003).

Information about the pore and throat radii, shape factors, aspect ratios, etc., is also extracted, which requires the calculation of geometric parameters described in the developed flow equation for a single duct. Capturing the varying cross sections that occur in shale systems is essential for proper modeling of complex fluid flow. The porous media studied in this work were computer-generated random sphere packs. Each pore throat is a converging/diverging duct with an irregular-shaped cross section. Differences in the cross-sectional shapes depend on the random spheres' arrangement in the network. Various ranges of cross-sectional geometry existed in the network, leading to various flow behaviors for each pore throat, as discussed in the subsequent Results and Discussions section. The shape-factor parameter calculated for each pore throat using **Equation 3** requires the perimeter and cross-sectional area of a given pore throat, which comes from the Delaunay tessellation step in transforming sphere packing into a pore network.

The general approach to pore-network modeling is to impose mass conservation on the N pores and obtain pore pressures by solving the resultant system of $N\times N$ equations, subject to specified boundary conditions. Herein, a constant pressure drop is applied in one direction, and periodic boundary conditions are imposed in the other two directions. For an incompressible fluid, mass

conservation on pore *i* must be satisfied. For a simple case of Newtonian fluid, the continuity equation applies, producing the following:

$$\sum_j q_{ij} = \sum_j \frac{g_{ij}}{\mu}\left(P_i - P_j\right) = 0 \qquad (8)$$

For each pore, q_{ij} in **Equation 8** is the volumetric rate of flow from an adjacent pore *j* into pore *i* through their interconnected throat. P_i is the pressure in pore *i*, and g_{ij} is the hydraulic conductivity for the pore throat that connects pores *i* and *j*. Equation 8 states that the net accumulation of fluid in pore *i* is zero. **Figure 4** summarizes the methodology used in this study to simulate liquid flow in the shale pore-network model and calculate apparent permeability. First, as shown in **Figure 4**, a computer-generated sphere packing has been produced. Then, using 3-D Delaunay tessellation, we transformed the random sphere packing to the network of pores and pore throats. In the next step, we used the generalized flow equation developed in this study into the pore network and solved the system of equations to calculate pressure at each pore and flow rate at each pore throat. The generalized flow equation includes slip and geometry effects as important effects in shale systems. Finally, the apparent permeability is calculated for the network.

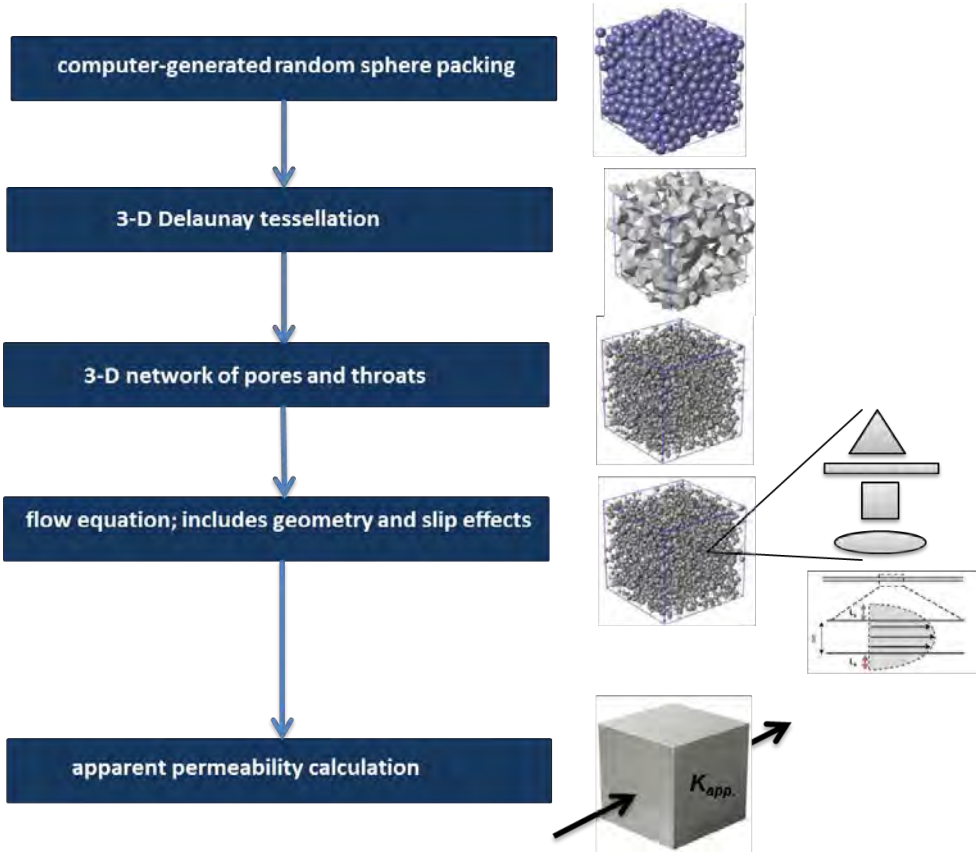

Figure 4. Flowchart of the methodology used in this study to calculate apparent permeability of the pore-network. First, a computer-generated sphere packing arrangement has been produced. Next, 3-D Delaunay tessellation is used to transform the random sphere packing to the network of pores and pore throats. Then the generalized flow equation developed in this study is used in the pore network and solves the system of equations to calculate pressure at each pore and flow rate at each pore throat. The generalized flow equation includes slip and geometry components as important effects in shale systems. Finally, the apparent permeability is calculated for the network.

Results and Discussions

CFD Modeling in a Single Duct

In this study, we developed a generalized flow equation for a Newtonian flow in a single duct with any cross-sectional shape. We examined the effect of two geometrical parameters on flow behavior in a single duct: first, the effect of angles on a cross-sectional shape (angle effect), and second, the effect of proportionality of maximum-to-minimum dimensions of the cross-sectional geometry (aspect ratio effect).

Figure 5 compares the dimensionless hydraulic conductivity in an equilateral triangular duct with that in a circular duct. Figure 5 also shows the velocity profile for circular and equilateral triangular ducts; note that the cross-sectional surface area, fluid properties, and injection rate are identical for all cases and some differ in shape and slip condition only, as illustrated in the figure. The circular duct with a no-slip condition is considered a base case for comparison. Dimensionless hydraulic conductivity for the base case is labeled $\tilde{g}_{base}$. For no-slip cases, as shown in **Figure 5**, stagnant film at the corner of the triangular duct is observed, however, the stagnant film is uniform around the wall for the circular duct. Dimensionless hydraulic conductivity calculated for the triangular duct is 30% less than for the circular duct with the same condition in the no-slip case.

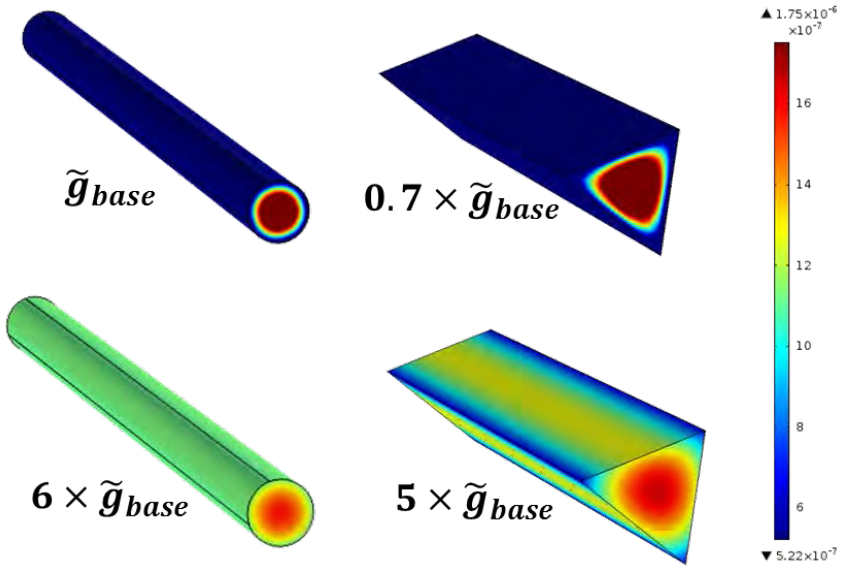

Figure 5. Velocity profile (m/s) comparison of equilateral, triangular duct hydraulic conductivity with a circular duct. The velocity profiles for a no-slip condition (top) are compared with profiles for a slip condition (bottom). Dimensionless hydraulic conductivities for circular-geometry and no-slip conditions are considered as the base case, and other cases with dimensionless hydraulic conductivities are compared using the base case.

Next, we applied the slip for the fluid flow in both the triangular and circular ducts (same slip length for both cases), thereby observing even more discrepancy in hydraulic conductivity between these two geometries. In cases with a slip condition, no stagnant film has been observed for circular geometry; however, stagnant flows still existed at the corners for triangular

geometry. Because stagnant flow causes an increase in flow resistance, less conductivity has been observed for cases with larger stagnant flow.

In summary, angular geometric shapes, such as triangles, have less hydraulic conductivity because of slow (sometimes stagnant) flow at corners. The discrepancy between angular geometry and circular geometry is more pronounced as the slip condition is applied, which is one reason that oversimplified assumptions of a circular shape for pore geometry underestimate fluid-flow behavior in shale, especially when the slip condition of the shale is not negligible.

Another geometric parameter that has a large effect on fluid flow in single duct is aspect ratio. **Figure 6** compares dimensionless hydraulic conductivity in a slit-type ellipse duct with that in a circular duct. **Figure 6** shows the velocity profile for circular and slit-type ellipse ducts; note that the cross-sectional surface area, fluid properties, and injection rate are identical in all cases and some differ in shape and slip condition only, as illustrated in the figure. In no-slip cases, the flow at the corner of ellipse geometry is stagnant; therefore, less area open to flow exists for slit-type ducts as compared to circular-shaped ducts. The calculated dimensionless hydraulic conductivity for the slit-type duct is 80% less than that for the circular duct—a significant reduction in flow capacity.

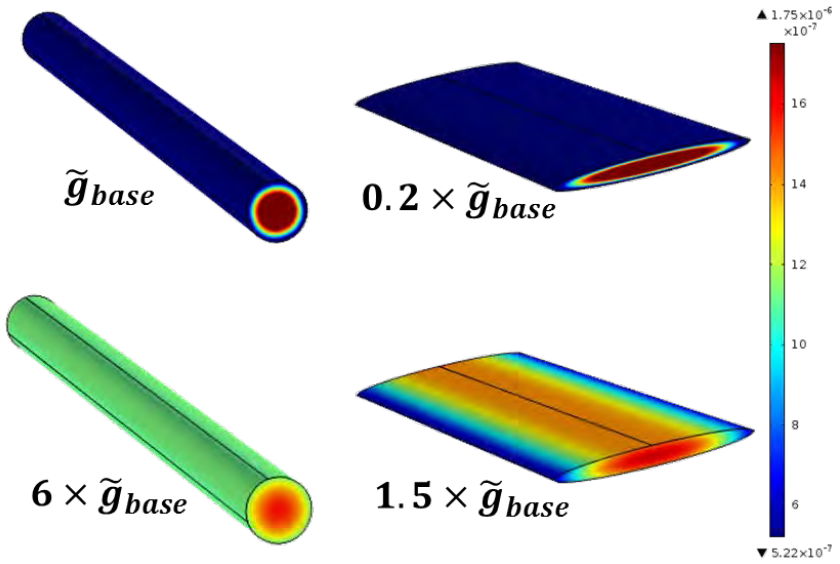

Figure 6. Velocity profile (m/s) comparison of slit-type ellipse duct hydraulic conductivity with circular duct. The velocity profiles for a no-slip condition (on top) compared with the ones with a slip condition (on bottom). Dimensionless hydraulic conductivity for circular geometry and a no-slip condition considered as the base case and other cases with dimensionless hydraulic conductivities compared based on the base case.

The difference between angle effect and aspect ratio effect becomes more pronounced when slip condition is applied. Both angle and aspect-ratio-effect comparisons show that ignoring slip and geometry effects in liquid flow in a single duct leads to significant error in flow-behavior analysis. Consequently, neglecting slip and pore-geometry effects in modeling of liquid flow in shale leads to an overestimation or underestimation of liquid flow in the shale system.

As shown in **Figure 7**, the dimensionless hydraulic conductivity ($\tilde{g}$) for the same cross-section area is different for different shapes. The differences become more pronounced with greater slip effect, implying that the flow equation needs to take into account the shape of the pores. **Figure 7** shows that as the pore shape approaches a slit shape (lower *G*), hydraulic conductivity decreases, in contrast, as it approaches a circular shape (higher *G*), hydraulic conductivity increases. As the geometry becomes more circular, less resistance to flow is observed.

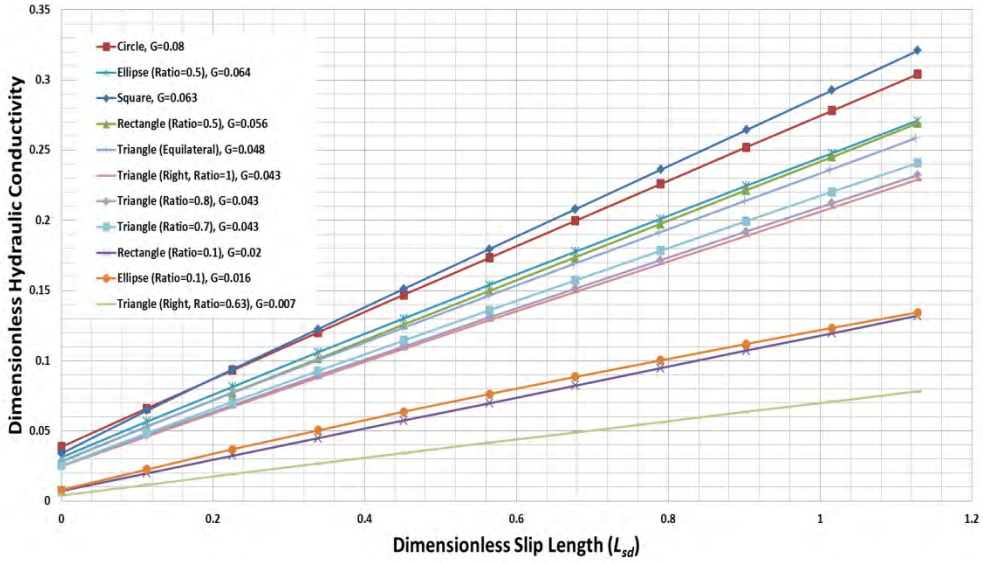

Figure 7. Dimensionless hydraulic conductivity for a different shape of the same cross-section area. Higher *G* (for shapes closer to circular) has more hydraulic conductivity than does lower *G* (shapes closer to slit shape).

Figure 8 shows the dimensionless hydraulic conductivity ($\tilde{g}$) versus shape factor for different dimensionless slip length (L_{sd}). As shown in this figure, the higher the *G* value, the more hydraulic conductivity for a given dimensionless slip length, except when a square has higher $\tilde{g}$ compared to a circle at high L_{sd} (the circle has a higher shape factor). This discrepancy occurs here because at high-slip length, the slip effect overrides the shape effect.

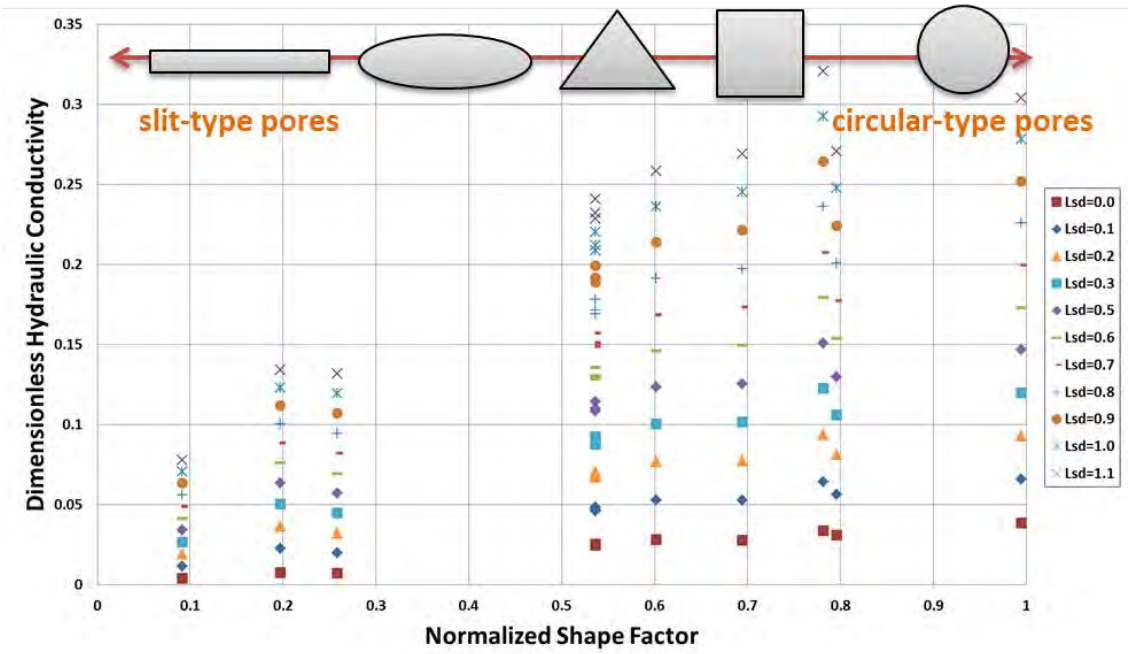

Figure 8. Dimensionless hydraulic conductivity versus normalized shape factor (G/G_{circle}) for different dimensionless slip lengths (L_{sd}) and same cross-section area.

In this study, we performed CFD modeling for many different geometric shapes. Results have been used to develop a closed-form generalized fluid-flow equation (**Equation 9**) for Newtonian fluid in a duct, with different cross-sectional shapes (including irregular) and slip effects included, as follows:

$$Q = \frac{A^2}{\mu L}[a + bL_{sd} + cG + dL_{sd}^2 + eG^2 + fL_{sd}G]\Delta p \qquad (9)$$

where coefficients *a*–*f* are empirical constants (as listed in **Table 1**), Q is volumetric flow rate, A is cross-sectional area, L is duct length, and Δp is pressure drop. The equation has two sets of constants: one for G values higher than 0.4, which represents the geometry closer to circular, and one for G values lower than 0.4, which represents the geometry closer to slit shape (**Table 1**).

Table 1. Coefficients of the closed-form generalized fluid flow equation.

Coefficient	Value (G >= 0.4)	Value (G < 0.4)
a	-0.16	-1.2×10^{-2}
b	0.12	5.7×10^{-2}
c	6.4	2
d	-5.5×10^{-3}	-5.2×10^{-3}
e	-50.0	-38.0
f	1.7	3.2

Using SEM images, we observed different pore geometry in real shale. We used JMicrovision software to extract the area open to flow and the wetted perimeter of each pore from SEM images, and then we defined a shape factor for each pore. The higher *G* value represents the geometry closer to circular, and the lower *G* value represents the one closer to slit shape. **Figures 9 and 10** show histograms of shape factors of pores in SEM images (120,000X resolution) of **Figures 2 and 3**, respectively. A comparison of **Figures 9 and 10** shows more slit-shape geometry (lower *G* value) in image 2 than in image 1 (120,000X resolution).

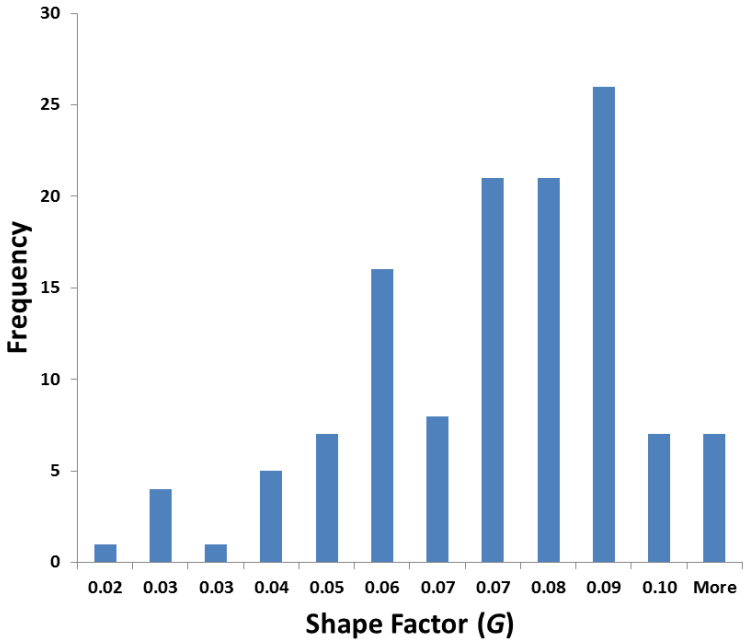

Figure 9. Histogram of shape factor (*G*) for SEM image of sample 1 (**fig. 2**) at 120000X resolution.

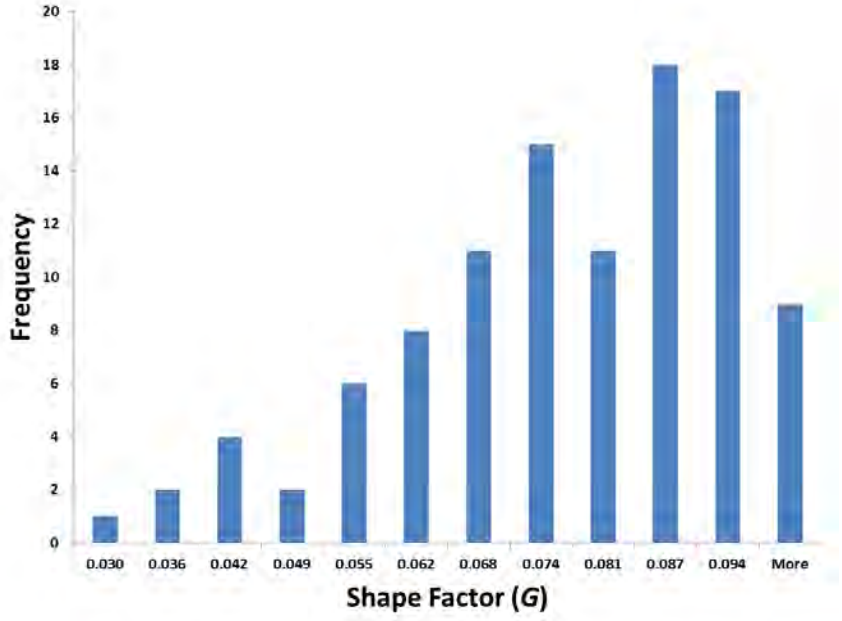

Figure 10. Histogram of shape factor (*G*) for SEM image of sample 2 (**fig. 3**) at 120000X resolution.

Finally, after analyzing the importance of slip and shape effect on liquid-flow behavior in a single duct, we investigated the effect of slip and pore geometry in porous media. The flow equation (**Equation 9**) is useful in analyzing shale systems using macroscopic measurements. Shape factor can be calculated from analysis of SEM images and nitrogen adsorption data.

Pore Network

In this study, we developed the pore network and performed a sensitivity analysis to investigate the effect of geometry and slip on liquid flow in porous media. We used computer-generated porous media from a sphere-packing model with grain sizes of 100 nm in diameter. Pore-network dimensions are 4400 nm for each side. The number of pores is 410, and the number of throats is 1892 (pore network 1). The periodic-pressure boundary condition is applied in *x*-direction; the no flow-boundary condition is applied in *y*-direction and *z*-direction. We used a multidimensional Newton–Raphson algorithm to solve the nonlinear system of equations. In the case of the no-slip condition using a circular duct to model the pore throat (case 1), the apparent permeability K_{ideal} is considered a basis of comparison for other cases. For the ideal case (case 1) using circular pore-geometry assumption, we first solved the pore network for no-slip condition. **Figure 11** shows the histogram of equivalent radius of each pore throat. The range of equivalent radius is roughly between 100 and 300 nm, and the average pore-throat radius is 164 nm. In many pore-network models, pore throats are assumed to be cylindrical duct (that is, circular cross section), similar to case 1 in this study.

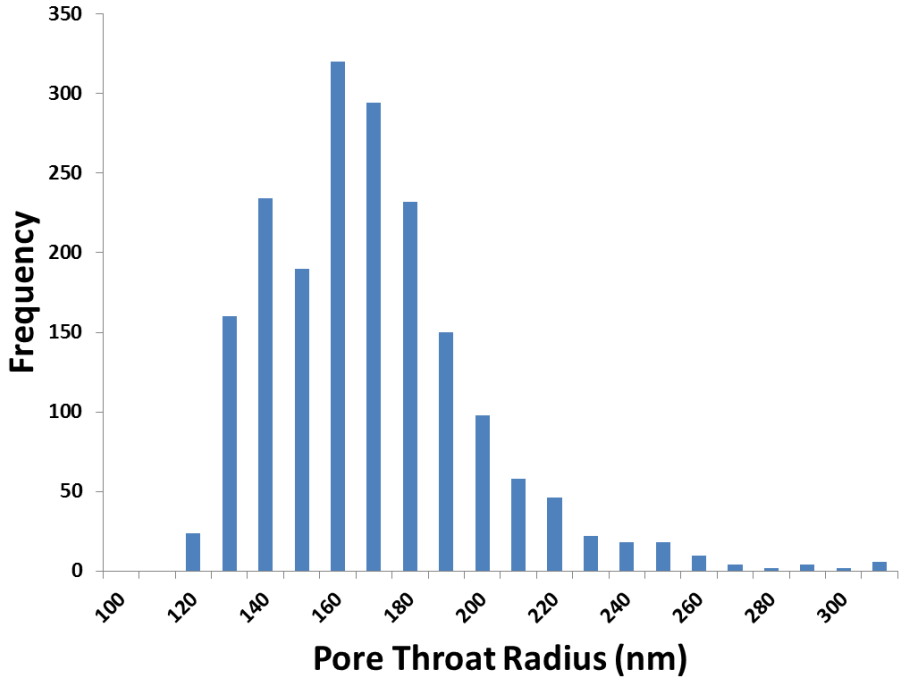

Figure 11. Pore-throat radius histogram of sphere-packing pore network (pore-network 1), L_s = 0.0 cm, circular duct assumption for pore throats (case 1), average radius is 164 nm, and the standard deviation is 30 nm.

Equation 9 is implemented as a flow equation to take into account both shape effect and slip effect. First, we extracted the perimeter of each pore throat from the structure of the pore network, knowing that the cross-sectional area of each pore throat allows its shape factor (G) to be calculated. Because case 2 uses the same pore network as case 1, all the real pore-structure features of porous media are the same. In case 2, however, the shape of pore throats is also taken into account by using **Equation 9**, which was developed from CFD results.

The slip length remains zero for case 2 (L_{sd} = 0.0, no slip condition). **Figure 12** shows the histogram of the calculated shape factor for the pore network, which ranges from 0.02 to 0.08. This shape-factor range implies a wide variety of pore geometry in the network; considering this, the shape effect is recommended because flow behavior depends significantly on pore geometry, as shown in CFD modeling results (**fig. 8**). As shown in **Figure 12**, as shape factor increases, the pores are close to circular-type pores, and decreasing the shape factor represents slit-type pores.

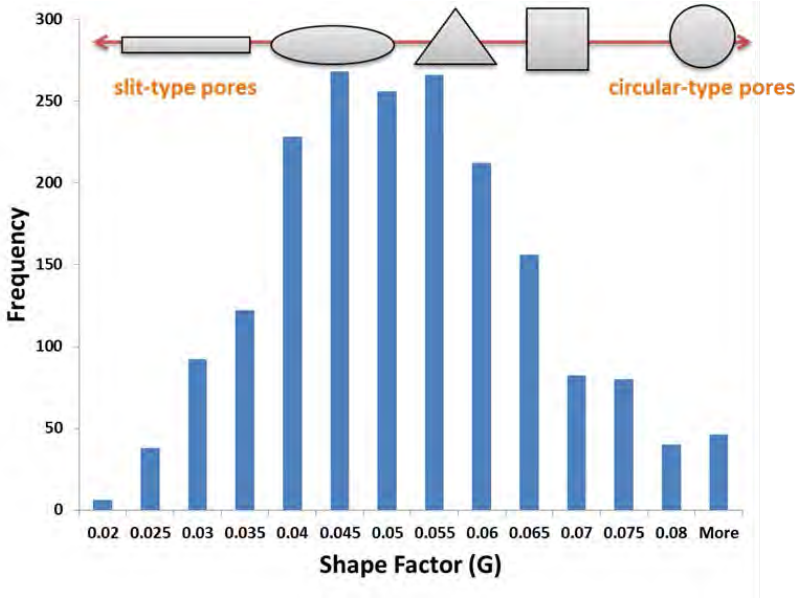

Figure 12. Shape-factor histogram of sphere-packing pore network (pore-network 1) (case 2), the average shape factor value is 0.05, and the standard deviation is 0.016.

In short, cases 1 and 2 have exactly the same conditions, except that in case 1, the Hagen–Poiseuille equation is used as the flow equation, and in case 2, the generalized flow equation (**Equation 9**) is used. Normalized permeability (K_n) defined in this study is the ratio of an apparent permeability to ideal apparent permeability (K_{ideal}). The normalized permeability of case 2 is 0.021 (that is, the apparent permeability of porous media using the Hagen-Poiseuille flow equation overestimates by almost 50 times the realistic apparent permeability of porous media). As a result, pore shape has an important effect on apparent-permeability calculation, especially for shale systems, whose pores have a wide range of possible shapes, as shown in SEM images (**figs. 2 and 3**).

In case 3, pore-network simulation includes slip effect to investigate its effect on Newtonian fluid flow in porous media. Case 3 uses the same pore-network and fluid-flow equation (**Equation 9**) as case 2, but the case 3 slip length is not zero. In shale, slip plays an important role in liquid-flow behavior because the slip length is comparable to the pore sizes. Pore size and slip length are in nanoscale. In case 3, the slip length is assumed to be equal to the average pore-throat radius (L_s=164 nm) to keep the slip length in the range of pore sizes, which is a condition in shale systems. The calculated normalized permeability for case 3 is 2.35. A comparison of cases 2 and 3 shows that including a slip effect increases the apparent permeability by 110 times. In case 3, each pore throat has less resistance to flow because of the slip effect, which reflects

more conductivity for the porous media. Many shale models underestimate apparent permeability because they ignore the slip effect. **Figure 13** is the histogram of the dimensionless slip length for case 3, with a slip length of 164 nm (average pore radius of pore network 1). In **Figure 13**, larger pore throats have less slip effect than smaller ones because the ratio of slip length to pore size is smaller. In **Figure 14**, normalized permeability between the ideal and realistic models is compared for different slip length. The ideal model, with its assumption of cylindrical ducts (that is, straight duct with a constant circular cross section) for pore throats, overestimates the apparent permeability of porous media; the discrepancy is more pronounced as the slip effect increases. The dashed line in **Figure 14** shows the difference in normalized permeability between the ideal and realistic models, as dimensionless slip length increases, the deviation of the ideal model from the realistic is higher. In summary, because the slip effect is significant in shale, the apparent permeability is overestimated by the ideal model.

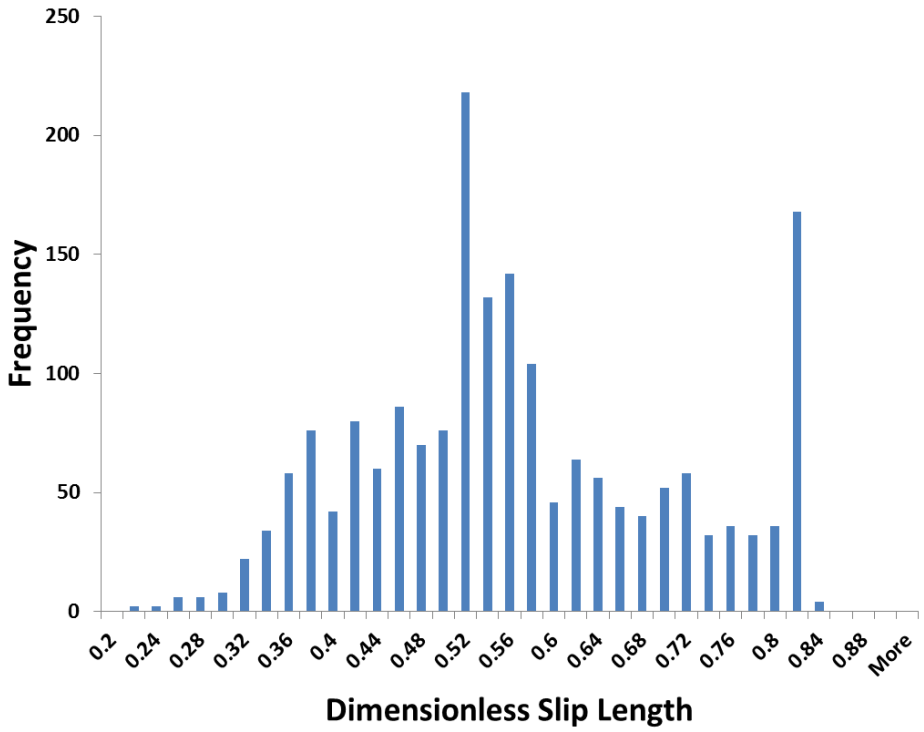

Figure 13. Dimensionless slip-length (L_{sd}) histogram of sphere-packing pore network (pore-network 1), with L_s = 164 nm (case 3).

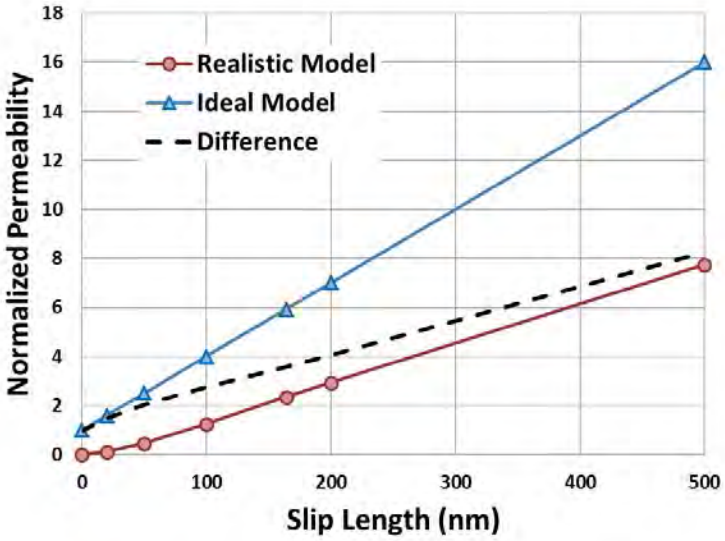

Figure 14. Normalized permeability versus slip length for pore-network 1 with circular assumption for pore throats (ideal model) and the model with considering the shape of pore throats (realistic model), the dashed line is the difference of normalized permeability between realistic and idea models. Notably, the average pore-throat radius is 164 nm.

We generated a new pore network with a smaller pore size to investigate the effect of pore size on apparent permeability of a porous media when slip and shape effects are included. We generated, by computer, a sphere packing of 1,000 grains in a cube size of 1,000 nm. Then, using the Delaunay tessellation algorithm, we mapped the new pore-network model (pore network 2) from the sphere packing. The total number of pores is 4,092, and the total number of pore throats is 18,770. **Figure 15** shows the pore-throat size distribution for pore network 2, with an average radius of 0.0174 and a standard deviation of 0.003. Periodic-pressure boundary condition is used in the *x*-direction and no-flow boundary condition in the *y*- and *z*-directions. The new pore-network permeability is approximately 75 times lower than that of pore network 1. The normal permeability of pore network 2 is 0.0133.

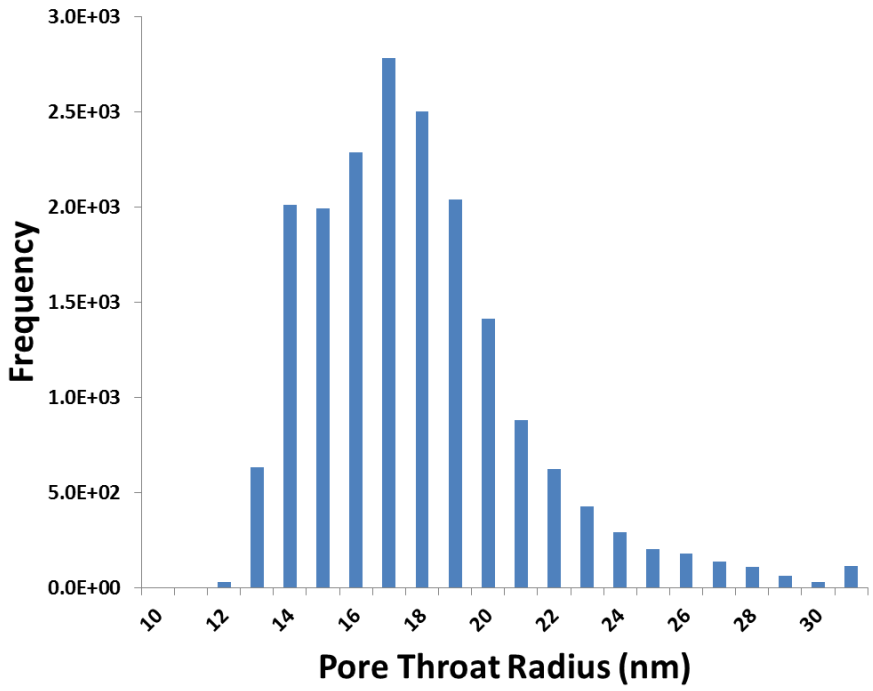

Figure 15. Pore-throat radius histogram of sphere-packing pore network (pore-network 2), average radius is 17.4 nm, and the standard deviation is 3 nm.

Figure 16 compares normalized permeability and slip length of the model assuming a circular shape for pore throats (ideal model), with the model considering the actual shapes of the pore throats (realistic model). **Figure 17** compares two pore networks based on the deviation of the realistic from the ideal model. Pore network 1 has an average pore-throat radius of 164 nm, which is almost 10 times higher than that of pore network 2, which has an average of 17.4 nm. **Figure 17** shows that as the porous media gets tighter (as in a shale system), the deviation of the ideal model from actual porous media is higher. Additionally, nitrogen adsorption tests show a bimodal trend for pore-size distribution in shale. These trends can be divided into two pore-size distributions: (1) for organic matter (smaller pore-size distribution) and (2) for inorganic matter (larger pore-size distribution). As shown in **Figure 17**, overestimation of apparent permeability for smaller pore-size distribution (such as organic matter in shale) is higher than for larger pore-size distribution (such as inorganic matter). However, in working with both organic and inorganic matter, using the ideal model (the circular cross-section assumption) can cause significant errors.

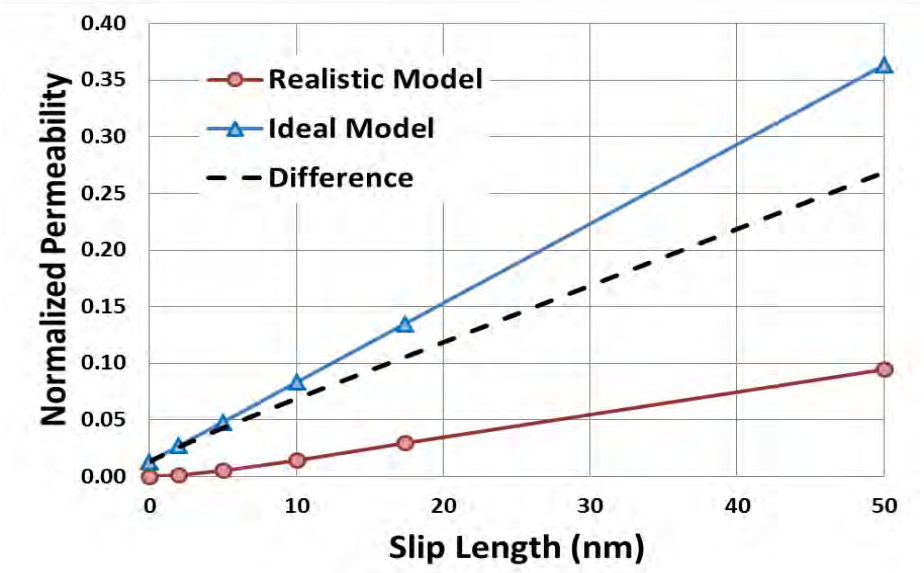

Figure 16. Normalized permeability versus slip length for pore-network 2 (1,000 grains) with circular assumption for pore-throats (ideal model) and the model with considering the shape of pore throats (realistic model), the dashed line is the difference between realistic and idea models. Notably, the average pore-throat radius is 17.4 nm.

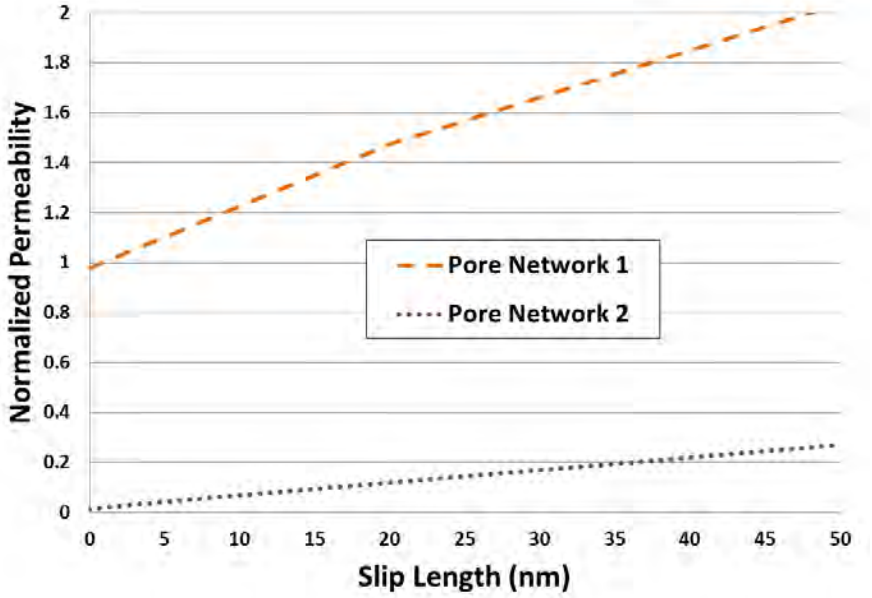

Figure 17. Differences between normalized permeability of realistic and ideal models for two pore networks versus slip length (nm). Pore-network 1 has an average pore-throat radius of 164 nm, and pore-network 2 has an average pore-throat radius of 17.4 nm.

Next, a more realistic pore-network model has been developed, based on the laboratory measurement of shale properties. Using nitrogen absorption experiments the pore-size distribution and surface area has been measured and used in the model to generate the

equivalent shale samples. And, from an SEM image analysis, the pore-geometry histogram has been extracted and used in the model. Two samples are analyzed in this report. Sample (case 1) YY1-1070 with TOC of 8.2% and porosity of 4.3%, and sample (case 2) YCYV1118-1141 with TOC of 5.19 % and porosity of 9.7%. **Figure 18** shows the apparent permeability calculated for given samples. **Figure 18** shows for sample YY1-1070 with higher TOC, as slip length increases, the apparent permeability increases because the slip length in for organic matter assumes 10 times higher than slip length of inorganic matter. The measurement of slip length using AFM shows that the organic matter has a higher slip length than does the inorganic matter.

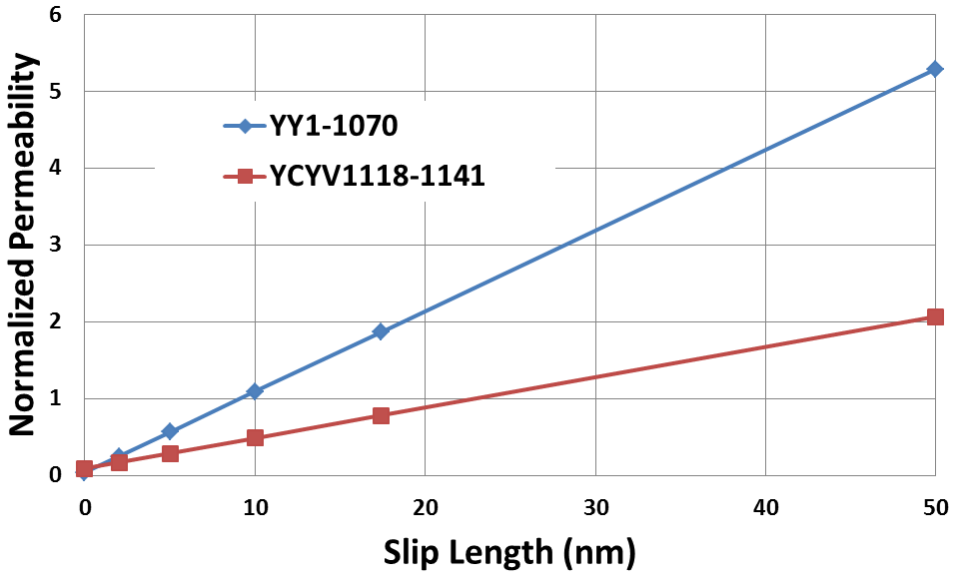

Figure 18. Normalized permeability versus slip length in inorganic matter for shale samples YY1-1070 with TOC of 8.2 percent and porosity of 4.3 percent, and YCYV1118-1141 with TOC of 5.19 percent and porosity of 9.7 percent.

Summary

In this study, two important characteristics of liquid flow in shale—pore geometry and slip condition—were examined and modeled.

- SEM images of the Yanchang shale show the wide range of pore geometry in both organic and inorganic matter.
- CFD modeling shows that for different cross-sectional geometries of a single constant cross-section duct, liquid-flow behavior changes significantly, with the differences becoming more pronounced as slip condition is applied. With the CFD simulation results, the generalized flow equation for liquid flow in a single tube has been developed for various cross-sectional geometries (circular and noncircular).
- We developed two pore-network models for the Yanchang shale samples to simulate slip-corrected liquid flow to determine apparent fluid permeability. Study of Sample 1 suggests an effective permeability of twice the Darcy permeability for realistic noncircular pore geometries. The effective permeability of Sample 2 suggests an effective permeability that is six times larger than Darcy permeability. These conclusions are based on a 50 nm slip length. We need to measure more slip length for Yanchang samples to have more accurate values of slip length.
- If we ignore noncircularity of pores and assume that all pores are circular, our estimates for Samples 1 and 2 would be erroneous by 900% and 250%, respectively.
- Pore-networks simulation results reveal that pore geometry and slip effect play important roles in fluid flow in Yanchang shale samples and that neglecting these characteristics causes error in fluid flow predictions.

References

Al-Raoush, R., Thompson, K.E., and Willson, C.S., 2003, Comparison of network generation techniques for unconsolidated porous media: Soil Science Society of America Journal, v. 67, p. 1687–1700.

Bakke, S., and Oren, P.E., 1997, 3-D pore-scale modelling of sandstones and flow simulations in the pore networks: SPE Journal, v. 2, p. 136–149.

Balhoff, M., and Thompson, K., 2004, Modeling the steady flow of yield-stress fluids in packed beds: American Institute of Chemical Engineers Journal, v. 50, p. 3034–3048.

Balhoff, M., and Thompson, K., 2006, A macroscopic model for shear-thinning flow in packed beds based on network modeling: Chemical Engineering Science, v. 61, p. 698–719.

Bernard, S., Wirth, R., Schreiber, A., Schulz, H.M., and Horsfield, B., 2012, Formation of nanoporous pyrobitumen residues during maturation of the Barnett Shale (Fort Worth Basin): International Journal Coal Geology, v. 103, p. 3–11.

Bryant, S.L., Mellor, D.W., and Cade, C.A., 1993, Physically representative network models of transport in porous media: American Institute of Chemical Engineers Journal, v. 39, p. 387–396.

Chalmers, G.R., Bustin, R.M., and Power, I.M., 2012, Characterization of gas shale pore systems by porosimetry, pycnometry, surface area, and field emission scanning electron microscopy/transmission electron microscopy image analyses: examples from the Barnett, Woodford, Haynesville, Marcellus, and Doig units: AAPG Bulletin, v. 96, p. 1099–1119.

Curtis, J.B., 2002, Fractured shale-gas systems: AAPG Bulletin, v. 86, p. 1921–1938.

Curtis, M.E., Ambrose, R.J., and Sondergeld, C.H., 2010, Structural characterization of gas shales on the micro- and nano-scales: SPE 137693, presented at Canadian Unconventional Resources and International Petroleum Conference, Reservoir Description and Dynamics, Society of Petroleum Engineers, Calgary, Alberta, Canada.

Javadpour, F., Fisher, D., and Unsworth, M., 2007, Nanoscale gas flow in shale sediments. Journal of Canadian Petroleum Technology, v. 46, p. 55–61.

Javadpour, F., 2009, Nanopores and apparent permeability of gas flow in mudrocks (shales and siltstone): Journal of Canadian Petroleum Technology, v. 48, p. 16–21.

Javadpour, F., McClure, M., and Naraghi, M.E., 2015, Slip-corrected liquid permeability and its effect on hydraulic fracturing in shale: Fuel, v. 160, p. 549–559.

Kuila, U., and Prasad, M., 2013, Specific surface area and pore-size distribution in clays and shales: Geophysical Prospecting, v. 61, p. 341–362.

Lopez, X., Valvatne, P.H., and Blunt, M.J., 2003, Predictive network modeling of single-phase non-Newtonian flow in porous media: Journal of Colloid and Interface Science, v. 264, p. 256–265.

Loucks, R.G., Reed, R.M., Ruppel, S.C., and Jarvie, D.M., 2009, Morphology, genesis, and distribution of nanometer-scale pores in siliceous mudstones of the Mississippian Barnett Shale: Journal of Sedimentary Research, v. 79, p. 848–861.

Mason, G., and Morrow, N.R., 1991, Capillary behavior of perfectly wetting liquid in irregular triangular tubes: Journal of Colloid and Interface Science, v. 141, p. 262–274.

Mastalerz, M., He, L., Melnichenko, Y.B., and Rupp, J.A., 2012, Porosity of coal and shale: insights from gas adsorption and SANS/USANS techniques: Energy & Fuels, v. 26, p. 5109–5120.

Milliken, K.L., Rudnicki, M., Awwiller, D.N., and Zhang, T., 2013, Organic matter-hosted pore system, Marcellus formation (Devonian), Pennsylvania: AAPG Bulletin, v. 97, p. 177–200.

Montgomery, S.L., Jarvie, D.M., Bowker, K.A., and Pollastro, R.M., 2005, Mississippian Barnett Shale, Fort Worth Basin, north-central Texas: gas-shale play with multitrillion cubic foot potential: AAPG Bulletin, v. 89, p. 155–175.

Naraghi, M.E., and Javadpour, F., 2015, A stochastic permeability model for the shale-gas systems: International Journal of Coal Geology, v. 140, p. 111–124. doi: 10.1016/j.coal.2015.02.004

Nelson, P.H., 2009, Pore throat sizes in sandstones, tight sandstones, and shales: AAPG Bulletin, v. 93, p. 1–13.

Pollastro, R.M., 2007, Total petroleum system assessment of undiscovered resources in the giant Barnett Shale continuous (unconventional) gas accumulation, Fort Worth Basin, Texas: AAPG Bulletin, v. 91, p. 551–578.

Pommer, M., and Milliken, K., 2015, Pore types and pore-size distributions across thermal maturity, Eagle Ford Formation, southern Texas: AAPG Bulletin, v. 99, p. 1713–1744.

Ross, D.J.K., and Bustin, R.M., 2009, The importance of shale composition and pore structure upon gas storage potential of shale gas reservoirs: Marine Petroleum Geology, v. 26, p. 916–927.

Schmitt, M., Fernandes, C.P., da Cunha Neto, J.A.B., Wolf, F.B., and dos Santos, V.S.S., 2013, Characterization of pore systems in seal rocks using nitrogen gas adsorption combined with mercury injection capillary pressure techniques: Marine Petroleum Geology, v. 39, p. 138–149.

Sondergeld, C.H., Ambrose, R.J., Rai, C.S., and Moncrieff, J., 2010, Micro-structural studies of gas shales. SPE 131771, presented at SPE Unconventional Gas Conference, Pittsburgh, Pennsylvania, USA.

U.S. Energy Information Administration, Drilling Productivity Report, 2015, http://www.eia.gov/petroleum/drilling/pdf/dpr-full.pdf (August 2015).

TASK 6.1

Preconditioning Extremely Noisy Seismic Data for Reservoir Characterization in a Loess Mountain Area, Southeastern Ordos Basin, China

Wei Wang[1,2], Hongliu Zeng[2]

1-Shaanxi Yanchang Petroleum (Group) Corp. Ltd., Xi'an, Shaanxi 710075, China
2-Bureau of Economic Geology, The University of Texas at Austin, Austin, Texas 78713, US

Abstract

The study area is located in the southeastern Ordos Basin, where abundant oil and gas resources are developed in Mesozoic and Paleozoic strata. The surface in this region is covered by a thick loess layer with several variations in tomography, thickness and velocity. These differences result in serious seismic challenges, such as complicated interferences and serious absorption of high frequencies. In addition, two extensively distributed shale layers in the Mesozoic formation also lead to serious interbed multiples. Conventional seismic data interpretation and inversion always suffer from residual noise and low seismic resolution. In 2013, a 3D full-azimuth and high-density seismic survey was acquired in this area by using the Schlumberger UniQ integrated point-receiver land seismic system. A targeted seismic data processing workflow was designed, using the Omega system, to deliver significant improvements in the finally migrated seismic image compared with conventional seismic data. However, both prestack seismic gathers and full-fold stacked seismic data are still contaminated by residual noise leaking from the seismic processing flow. Heavy scattering ground-roll noise is present at the near offsets of seismic gathers, whereas apparent random noise and stretch effects are encountered at large offsets. As is known, the near-offset amplitudes relate to changes in impedance of subsurface rocks, and far-offset amplitudes relate to changes in P-wave velocity, density, and S-wave velocity. The quality of prestack seismic inversion therefore can dramatically decrease. In fully stacked seismic data, residual noise causes serious jittering artifacts and inconsistent reflections, and it can completely submerge stratigraphic features such as channels. We developed respective composite workflows to perform data conditioning prior to seismic poststack interpretation and simultaneous prestack inversion. For fully stacked data, we first attenuated the residual scattering noise by using a pseudo f-x Cadzow filtering method. Then we diminished the random noise by applying structure-oriented filtering. Finally, we extended the seismic bandwidth on the basis of continuous wavelet transforms to obtain high-quality seismic data for attribute analyzing and stratigraphic interpretation. For prestack seismic gathers, we started by attenuating the near offset scattering noise and residual multiples with an f-x-y Cadzow filtering method. We enhanced the reflection coherence by rearranging seismic gathers as Offset Vector Tiling (OVT) to use the pseudo f-x Cadzow filtering. Then, we partially stacked prestack seismic gathers into angle gathers and improved the signal-to-noise ratio by applying a local dip filter to remove residual random noise. Last, we performed spectral balancing to alleviate NMO stretch and to compensate for the frequency loss by employing the angle-dependent bandwidth extending operators in the continuous wavelet transform domain. We applied the proposed workflows respectively to poststack seismic data and prestack seismic gathers of the 3D full-azimuth and

high-density seismic survey. Compared to the conventional time-migrated full stack data, the stratigraphic features and fracture zones can be more clearly identified from the conditioned full-stack data. Meanwhile, the inverted results from the conditioned prestack gathers show higher resolution and better correlation coefficients with well logs when compared to those inverted from conventional time-migrated gathers.

Introduction

The study area is located in the Southern Ordos Basin, the surface of which is covered by extremely thick and unconsolidated deposits of loess. Seismic exploration in this region has always been considered as one of the greatest challenges to petroleum exploration. The poor surface condition can cause serious seismic static problems and strong scattering noise present in the raw data. Poor-quality seismic images are thus delivered, commonly with low signal-to-noise ratio (SNR) and low dominant frequency (Chen and others, 2009; Liu, 2014). In recent years, vertical drills in the shale/mudstone layers in the Mesozoic formation have obtained considerable oil and gas production through fracturing. This indicates good prospects to explore and develop these resource rocks (Tang and others, 2014; Wang and others, 2013; Wang and others, 2014). For the purpose of characterizing the mudrock hydrocarbon system well, a point-source/point-receiver, high-density 3D seismic survey was performed to produce better seismic images. The most advanced seismic acquisition technologies (e.g., small-bin, full-azimuth, high-coverage, broadband energization) were employed, and a targeted amplitude preserved seismic processing workflow was used to produce significantly improved imaging results (Xiao and others, 2014; Wang and others, 2014).

Advanced seismic techniques have been found to be very valuable in improving the efficiency of shale gas development (Chopra and others, 2012; Coopersmith and others, 2013). Poststack attributes including coherence and curvature analysis for fault and fracture swarm detection can also be incorporated with fracture mapping. Prestack seismic inversion and azimuthal analysis are now routinely adopted for quantitative reservoir characterization of rock properties and fracture indicators (Gray and others, 2012; Perez and Marfurt, 2013; Trinchero and Vernengo, 2013). However, the quality of the input seismic data is critical to such advanced analysis. Although poststack attributes are sensitive to lateral changes in geology, they are also sensitive to lateral changes in types of noise. Even when the data have been migrated reasonably well and are multiples free, poststack seismic data are usually contaminated by both random and coherent noise. Certain types of noise have to be addressed before effectively interpreting the data. Another problem that degrades the interpretation is the relatively low bandwidth. Since processors don't pay special attention to the targets of interest during processing, the frequency content of the data commonly needs be enhanced to achieve interpretation consistent results. Chopra (2011) discussed alternative methods to suppress random noise and acquisition footprint and then to enhance frequency content of seismic data and evaluated their impacts on several seismic attributes. Chopra and Marfurt (2013) performed 5D interpolation to retrieve unrecorded offsets and azimuths in the prestack gathers to result in more geologically accurate geometric attributes. Bonar and Sacchi (2013) incorporated the ideas of f-x-y deconvolution within the sparse spectral decomposition to generate a spatially smooth time-frequency representation.

Al-Dossary compared the effectiveness of three noise reduction filters and chose two of them to reduce random noise and improve the detectability of channel edges.

The results of prestack inversion and fracture analysis are also ultimately dependent on the quality of the input seismic data. An optimal result is produced when the seismic data are rich in frequencies (both high and low), are relatively noise free, and have consistent amplitude, and the signal events are aligned to the expected AVO modeled response. Singleton (2009) quantified the advantages of performing prestack data conditioning prior to simultaneous impedance inversion. The addressed aspects there include (1) signal-to-noise ratio, (2) offset-dependent frequency loss, and (3) gather alignment. Darren Schmidt and others (2013) addressed frequency content, random and coherent noise, amplitude-preserving processing and gather flatness at the preconditioning stage to improve reservoir characterization results of rock properties and fracture indicators. Zhang and others improved the quality of simultaneous prestack inversion by developing a three-step workflow which includes minimizing the hockey sticks and stretch effects at large offsets and applying prestack structure-oriented filtering to suppress random noise. Mutlu and Marfurt (2015) improved the seismic vertical resolution through a cascade of an inverse NMO correction and a nonstretch NMO correction. Improved resolution of inverted results and geometric attributes were obtained from their case.

In this paper, we developed two processing workflows devoted to preconditioning poststack and prestack seismic data, respectively. These workflows are particularly designed for, first, suppressing the strong and resistant residual noise and then balancing the frequency spectrum. For fully stacked data, we combined f-x Cadzow filtering and structure-oriented filtering to deliver relatively noise-free data. Then, we performed a frequency-enhancement method to enhance depositional feature detection. For the prestack seismic gathers, we addressed the residual scattered noise with a cascaded two-step Cadzow filtering method, and further suppressed random noise through a prestack local dip filter. Next, we balanced the spectra of angle range limited data to compensate for the frequency loss. The efficiency of the proposed workflows is illustrated on the high-density data volumes from Southern Ordos Basin, China.

Methodology

Rank-Reducing Noise Suppression

The filters described here use a noise-suppression strategy called “matrix-rank reduction” (Trickett, 2003), also called truncated singular-value decomposition, principal-component analysis, or subspace filtering. The singular-value decomposition allows one to decompose a *p*-by-*p* matrix **A** into the sum of *p* matrices of rank one, named weighted eigenimages:

$$\mathbf{A} = \mathbf{I}_1 + \mathbf{I}_2 + ... + \mathbf{I}_p, \quad \|\mathbf{I}_i\|_2 \geq \|\mathbf{I}_{i+1}\|_2$$

A rank-*k* approximation to matrix **A** can be found by summing the first $k<p$ weighted eigenimages:

$$F_k(\mathbf{A}) = \mathbf{I}_1 + \mathbf{I}_2 + ... + \mathbf{I}_k$$

Rank reduction is a useful tool for noise suppression as coherent energy tends to fall into the first few eigenimages, whereas random energy is more evenly distributed across all eigenimages. Thus a rank-*k* approximation preserves coherency while eliminating randomness. Here we describe a family of rank reduction filters that work on constant-frequency slices (Table 1). For a multi-dimensional grid of traces, the general method is given in Table 1. The only difference among the various techniques we will discuss is how matrix **A** is formed in step 1.

Table 1. Steps for processing the rank-reducing filters.

Take the Discrete Fourier Transform (DFT) of each trace in the grid.
For each frequency within the signal band...
{
1. Place the complex trace values for this frequency into a matrix **A** (somehow).
2. Reduce the matrix to rank *k*.
3. Recover each trace value from the rank-reduced matrix by averaging all elements where that value was originally placed in matrix **A**.

}
Take the inverse DFT of each trace.

Ulrych and others (1999) described seismic applications for eigenimage filtering. Trickett (2003) applied eigenimage filtering in the f-x-y domain, where f represents frequency, x and y represents two spatial dimensions. Suppose we have an n-by-n grid of traces. To simplify the discussion we assume square grids. For a given frequency, let the complex values from a constant frequency slice of this grid have values $c_{i,j}$, i=1,...n, j=1,...n. In the method shown in Table 1, set

$$\mathbf{A} = \begin{bmatrix} c_{1,1} & c_{1,2} & \cdots & c_{1,n} \\ c_{2,1} & c_{2,2} & \cdots & c_{2,n} \\ \vdots & \vdots & \ddots & \vdots \\ c_{n,1} & c_{n,2} & \cdots & c_{n,n} \end{bmatrix}.$$

Averaging in step 3 of Table 1 is unnecessary because each trace has only one entry in the matrix.

Trickett (2002) proposed seismic applications for Cadzow filtering. Suppose we have a one-dimensional series of n traces whose values along a constant-frequency slice are c_i, i=1,...n. F-x Cadzow filtering is achieved by setting

$$\mathbf{A} = \begin{bmatrix} c_1 & c_2 & \cdots & c_{n-m+1} \\ c_2 & c_3 & \cdots & c_{n-m+2} \\ \vdots & \vdots & \ddots & \vdots \\ c_m & c_{m+1} & \cdots & c_n \end{bmatrix}$$

The rank reduction is performed on matrix **A,** as described in Table 1. Variable *m* is usually set to half of *n*, making the matrix as square as possible. This is a Hankel matrix, meaning that it is constant along each antidiagonal. Cadzow filtering was independently discovered several times, and is also known as Singular Spectrum Analysis (SSA) and the Caterpillar method (Golyandina, and others, 2001; Sacchi, 2009).

Trickett (2008) extended f-x Cadzow filtering to two spatial dimensions by forming a Hankel matrix of Hankel matrices:

$$\mathbf{A} = \begin{bmatrix} \mathbf{H}_1 & \mathbf{H}_2 & \cdots & \mathbf{H}_{n-m+1} \\ \mathbf{H}_2 & \mathbf{H}_3 & \cdots & \mathbf{H}_{n-m+2} \\ \vdots & \vdots & \ddots & \vdots \\ \mathbf{H}_m & \mathbf{H}_{m+1} & \cdots & \mathbf{H}_n \end{bmatrix}$$

where

$$\mathbf{H}_i = \begin{bmatrix} c_{i,1} & c_{i,2} & \cdots & c_{i,n-m+1} \\ c_{i,2} & c_{i,3} & \cdots & c_{i,n-m+2} \\ \vdots & \vdots & \ddots & \vdots \\ c_{i,m} & c_{i,m+1} & \cdots & c_{i,n} \end{bmatrix}.$$

F-x-y filtering is better than f-x filtering because it works with more data in a more local area, resulting in simultaneously more noise suppression and better signal preservation. Cadzow filtering has some advantages over eigenimage. The matrix configuration of Cadzow can be used in any number of spatial dimensions, as opposed to only two for eigenimage. It can also be made far stronger than eigenimage while still preserving conflicting dips. As a rough rule of thumb, Cadzow filtering gives a four-fold improvement in signal-to-noise ratio with each additional spatial dimension, assuming that typical parameters are used (Fig. 1). Thus higher-dimensional Cadzow filtering is of great interest for very noisy areas. Unfortunately, Cadzow becomes much more computationally expensive with each added dimension.

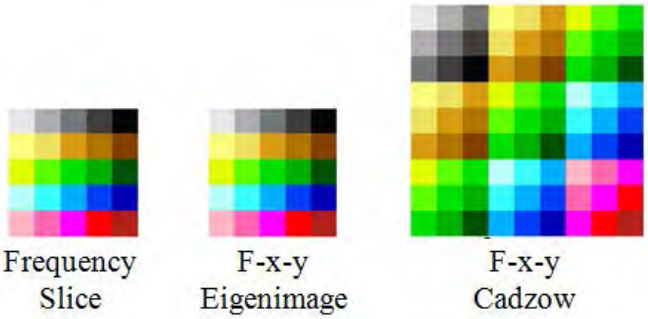

Figure 1. A frequency slice in two spatial dimensions and corresponding eigenimage and Cadzow matrices.

Local Dip Filtering

In seismic imaging of the earth's subsurface, we often describe the orientations of locally planar features by dip angles θ and, for 3D data, azimuthal angles ϕ. Dip filters attenuate or enhance planar features based on their dips and azimuths, and local dip filters are those that can adapt locally to sample-to-sample changes in those parameters.

Assume that **k** is a wave-number vector representing a wave-number component of the 3D data (full stacks or angle-limited stacks), and **n** is a unit vector defining a direction in 3D space. If $k_{\mathbf{n}}$ is the component of k parallel to **n**,

$$k_n = \mathbf{n} \cdot \mathbf{k} = \cos(\Delta\alpha)|\mathbf{k}|,$$

where Δα is the angle between k and n, then the projection ratio equals

$$\frac{k_n^2}{|\mathbf{k}|^2} = \cos^2(\Delta\alpha)$$

which can be used to weight any wave-number component of the data according to the angle Δα between the wave-number vector **k** and the direction defined by **n**, irrespective of the length of **k**. If we now assume **n** to the a function of space, **n**=**n**(**x**), we can no longer compute $k_{\mathbf{n}}$ directly in the wave-number domain. However, we can make use of the fact that multiplication by k_n^2 in the wave-number domain corresponds to the application of a negative second derivative along the direction defined by **n** in the space domain:

$$k_n^2 \leftrightarrow -\frac{\partial^2}{\partial n^2}.$$

This means that dip weighting with $\cos^2(\Delta\alpha)$, relative to a space-dependent direction vector **n** (associated with a previously calculated dip field), can be applied to an image $I(\mathbf{x})$ by numerically implementing the following expression:

$$\cos^2(\Delta\alpha)I(\mathbf{x}) = -\frac{\partial^2}{\partial n^2}\int |\mathbf{k}|^{-2}\left[\int I(\mathbf{x})e^{i\mathbf{k}\cdot\mathbf{x}}d^3x\right]e^{-i\mathbf{k}\cdot\mathbf{x}}d^3k.$$

In other words, the local dip filter can be implemented with the following simple steps:

(1) Apply a global 3D FFT to the image volume, scale by $|\mathbf{k}|^{-2}$ and apply an inverse 3D FFT.

(2) Apply a negative second derivative in space along the spatially varying direction **n**(**x**).

Ignoring spatial derivatives of the components of **n** itself, the second spatial derivative along **n** can be written as

$$\frac{\partial^2}{\partial n^2} = \mathbf{n}\cdot\nabla(\mathbf{n}\cdot\nabla) \approx n_x^2\frac{\partial^2}{\partial x^2} + n_y^2\frac{\partial^2}{\partial y^2} + n_z^2\frac{\partial^2}{\partial z^2} + 2\left(n_x n_y\frac{\partial}{\partial x}\frac{\partial}{\partial y} + n_x n_z\frac{\partial}{\partial x}\frac{\partial}{\partial z} + n_y n_z\frac{\partial}{\partial y}\frac{\partial}{\partial z}\right).$$

This second spatial derivative can be implemented numerically by using centered second-derivative finite-difference operators for the non-mixed second derivatives, and combinations of centered first-derivative finite-difference operators for the mixed second derivatives. To obtain sufficient accuracy up to high wave numbers, high-order finite-difference approximations need to be employed. This is essential for ensuring that the resulting weight only depends on the angle between n and k, and not on the length of k. Figure 2 shows examples of the wave-number response of the resulting filter for the 2D case, computed for selected directions n. The local dip filter can also be applied repeatedly to yield a narrower pass region of the filter response. If applied m times, the resulting filter response as a function of the angle Δα between n and k becomes $\cos^{2m}(\Delta\alpha)$. Corresponding wave-number responses for m=4 are shown in Figure 3.

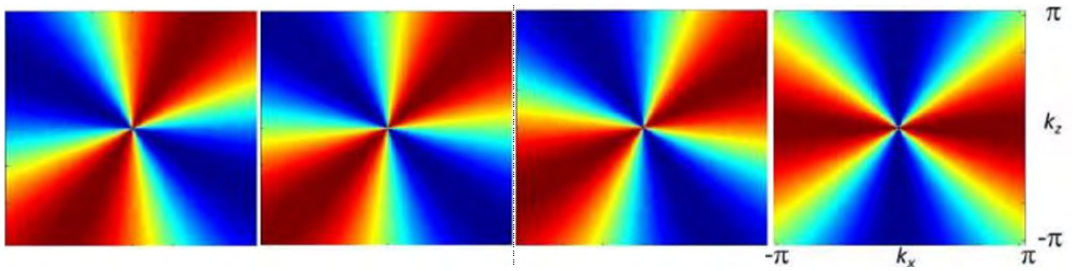

Figure 2. 2D amplitude spectra of local dip filter computed for various reference dip directions. From left to right: 30°, 45°, 60°, and 90° reference dip angle.

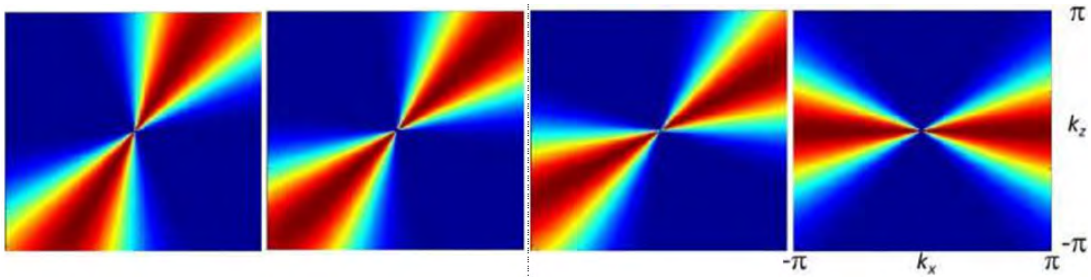

Figure 3. 2D amplitude spectra of local dip filter applied 4 times (m=4) computed for various reference dip directions. From left to right: 30°, 45°, 60°, and 90° reference dip angle.

Seismic Spectral Bandwidth Extension

The traditional method of analyzing a seismic trace in the frequency domain uses the Fourier transform or the fast Fourier transform (FFT). The problem with using a FFT is that it transforms local information into global information. The solution of using a short Fourier transform alleviates some of the problem by preserving some local information. However, the short window restricts frequencies that can be analyzed, and the extent of localization is limited by the single window length chosen. The wavelet transform does not have these same limitations and allows the analysis of both local information and large-extent information simultaneously.

Here, we use the continuous wavelet transform (CWT) to perform a time-series analysis of a seismic trace that decomposes the trace into its respective amplitude and phase components in both frequency and time domains. The CWT is defined as the convolution of a time series *f*(*t*) with a scaled (*s*) and translated (τ) wavelet $\psi(t)$:

$$W(\tau, s) = \int_{-\infty}^{+\infty} f(t) \frac{1}{\sqrt{|s|}} \psi^* \left(\frac{t-\tau}{s} \right) \mathrm{d}t$$

where (*) indicates the complex conjugate. The scaled wavelets are called daughter wavelets as they are scaled from the mother wavelet ψ.

The CWT is infinitely redundant in theory. Many researchers have found ways of rapidly extracting the essential information from these redundant transforms (Hubbard, 1998). Because the implementations of the CWT is a discrete operator and not a truly continuous operator, a choice needs to be made as to how many daughter wavelets will be used, thus how much redundancy to employ. A minimum of 10 scales per octave is sufficient to recreate the input time series from the transform by computing its reconstruction. Furthermore, the mother wavelet ψ must also meet the admissibility condition (Qian, 2002) as the analyzing wavelet is going to be used to reconstruct the original time series after bandwidth is extended.

We chose to use the Morlet wavelet as the mother wavelet. The Morlet wavelet is a complex function representing a plane wave modulated by a Gaussian function. The complex nature of the wavelet allows the calculation of amplitude and phase for each scale at distinct times. The choice of this wavelet was driven by the nature of the problem we are analyzing. In our case, we are analyzing a seismic trace, and a Gaussian modulated plane wave would be a good match for seismic time-series analysis. The Morlet wavelet is given by:

$$\Psi_\sigma(t) = \pi^{-\frac{1}{4}} \mathrm{e}^{-\frac{1}{2}t^2} \left(\mathrm{e}^{j\sigma t} - \kappa_\sigma \right)$$

where $\kappa_\sigma = \mathrm{e}^{-\frac{1}{2}\sigma^2}$ is defined by the admissibility criterion.

The CWT provides a very redundant, but also a very finely detailed, description of a signal in terms of both time and frequency. These properties are utilized to predict the harmonics and sub-harmonics used for bandwidth extension. Because the CWT operates in the time-frequency domain, it is limited by the uncertainty principle that states that we cannot know time and frequency with the same accuracy at the same time. This obviously limits the amount of information usable to predict the higher and lower order harmonics at any given time. This is

why the redundant nature of the CWT was chosen as our transform in contrast with the discrete wavelet transform (DWT), which uses an orthonormal basis and thus has no redundancy. The fuzzy nature of the CWT allows us to compute harmonics and sub-harmonics in a fuzzy way, that is, with incomplete information in both the time and frequency domains.

The time and frequency resolutions vary with scales by the standard deviations of the mother wavelet in the time domain (Δ_t) and the frequency domain (Δ_ω) as $s\Delta_t$ and Δ_ω/s. So the time resolution increases and the frequency resolution decreases with smaller scales (higher frequencies), and the time resolution decreases and the frequency resolution increases with larger scales (lower frequencies). In other words, in the low end of the spectrum frequency resolution is more important than time resolution, and at the high end of the spectrum time resolution is more important. The result is that the product of the standard deviations of time and frequency are constant for the entire frequency spectrum analyzed (Qian, 2002). This gives us the most optimal picture of the time-frequency domain.

By using the time-series analysis of the CWT, Smith and others computed harmonics and sub-harmonics from the available bandwidth in the seismic wavelet. Harmonics are referred to an integer multiple of a fundamental frequency, and sub-harmonics as a ratio of one over an integer multiple like 1/2. Since we are using a complex wavelet, amplitude and phase information is available for this computation. By convolving harmonic and sub-harmonic frequencies onto the seismic trace, we can recover this information and better reveal reflectivity that otherwise is difficult to detect. This unmasking of reflectivity is accomplished by increasing the bandwidth of the seismic wavelet with harmonic and/or sub-harmonic frequencies added to the seismic trace. Since this is a convolution-like process, harmonic or sub-harmonic frequencies, which correspond to reflectivity in the seismic trace, will be added to the seismic wavelet, but harmonics that do not correspond to reflectivity will effectively fall out of the transform.

The final step is reconstruction of the modified time series from the CWT domain of time and scale to a function of time only, which is the obtained seismic trace with extended bandwidth. The reconstruction formula is given by:

$$f(t) = \frac{1}{C_\Psi}\int_0^{+\infty}\int_{-\infty}^{+\infty} W(\tau, s)\psi\left(\frac{t-\tau}{s}\right)\frac{ds d\tau}{s^2}C_\Psi$$

where C_Ψ is given by the admissibility condition.

In implementation, the seismic trace is transformed by the CWT. The fundamental frequencies are chosen from user input as to the frequency range to use for computing harmonics and sub-harmonics. The frequency points representing the range of frequencies to use are called the pivot frequencies. Each pivot frequency is chosen from analyzing the seismic spectrum, and an octave below this pivot is used for computing harmonic frequencies or scales. For sub-harmonics, a different pivot frequency is chosen from the seismic spectrum, and an octave above this pivot is used for computing sub-harmonics frequencies or scales. The harmonics and/or sub-harmonics can extend upward/downward 1-2 octaves between the Nyquist and 0 Hz limit.

Energy density adjustments are made so that the harmonic and sub-harmonic scales produce a better shaped amplitude spectrum. These adjustments are made prior to adding back the

harmonic scales to the spectrum of the seismic wavelet. The transformed seismic trace, with added harmonics and/or sub-harmonics, is then reconstructed to give the new bandwidth extended seismic trace.

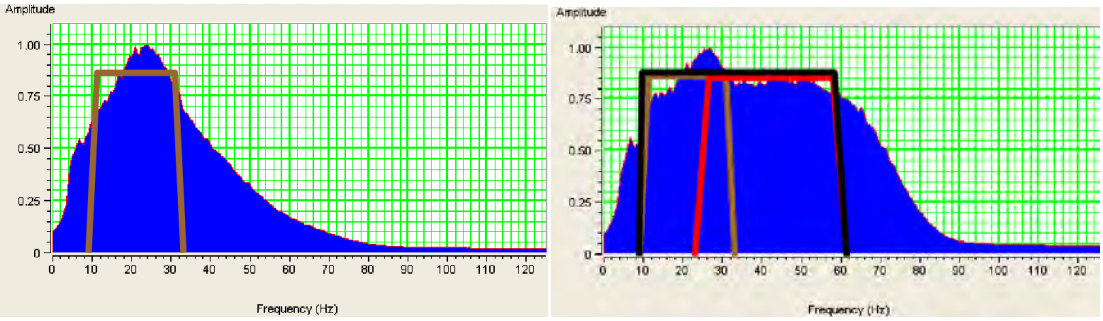

Figure 4. A nominal example to show the performance of bandwidth extension using CWT (left: input, right: bandwidth extended upward and downward 1 octave simultaneously).

Applications

Post-Stack Preconditioning and Stratigraphic Interpretation

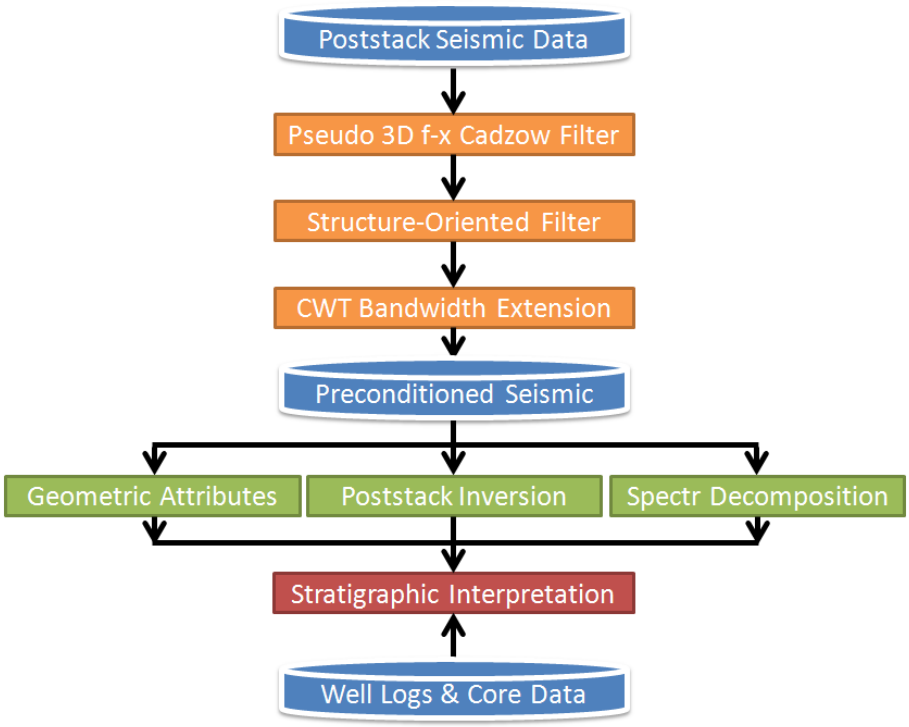

Figure 5. A workflow chart to precondition poststack seismic data and eventually generate seismic attributes for stratigraphic interpretation. The integration of Cadzow filtering and structure-oriented filtering is made to suppress residual noise sufficiently. The CWT bandwidth-extension method is adopted recovery reasonable seismic spectra.

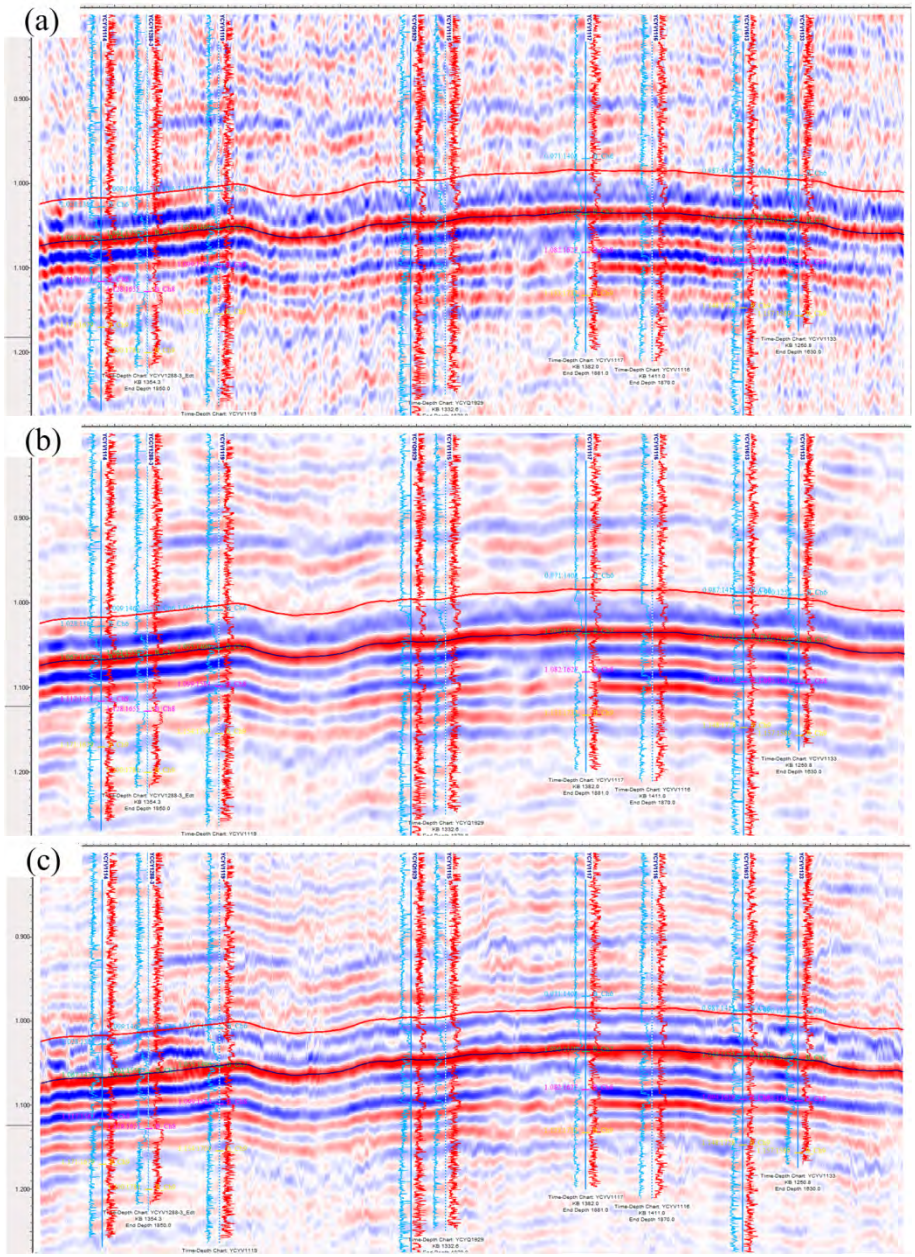

Figure 6. Intermediate results generated in the poststack preconditioning workflow. (a) An arbitrary line across multiple wells from the PSTM migrated data, (b) the corresponding filtered data after structure-oriented filtering, and (c) the corresponding bandwidth extended data. The blue logs along the well track are GR, and the red logs are AC.

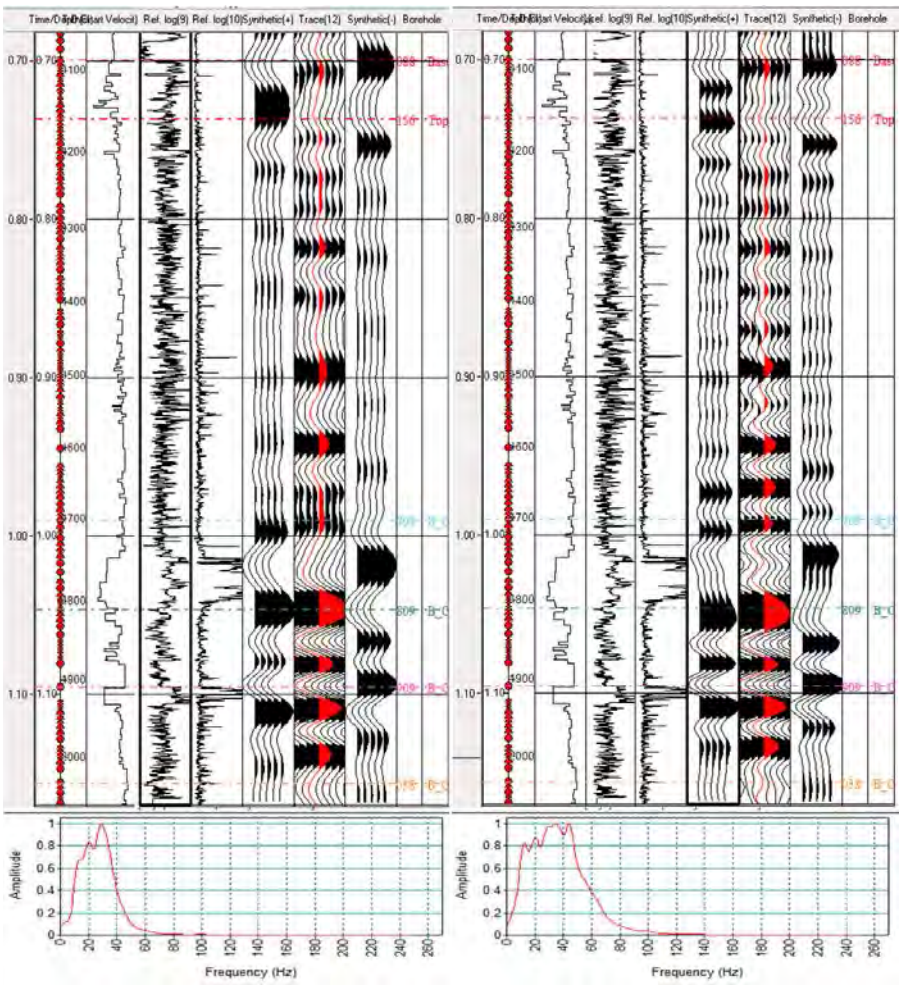

Figure 7. Synthetic seismograms comparison at the selected well before and after bandwidth extension. The left side is the synthetic trace composed by using a 25Hz Ricker wavelet compared to the filtered data. The right side shows the synthetic trace composed by using a 35Hz Ricker wavelet. At the bottom of each side, the average spectra of corresponding data are shown.

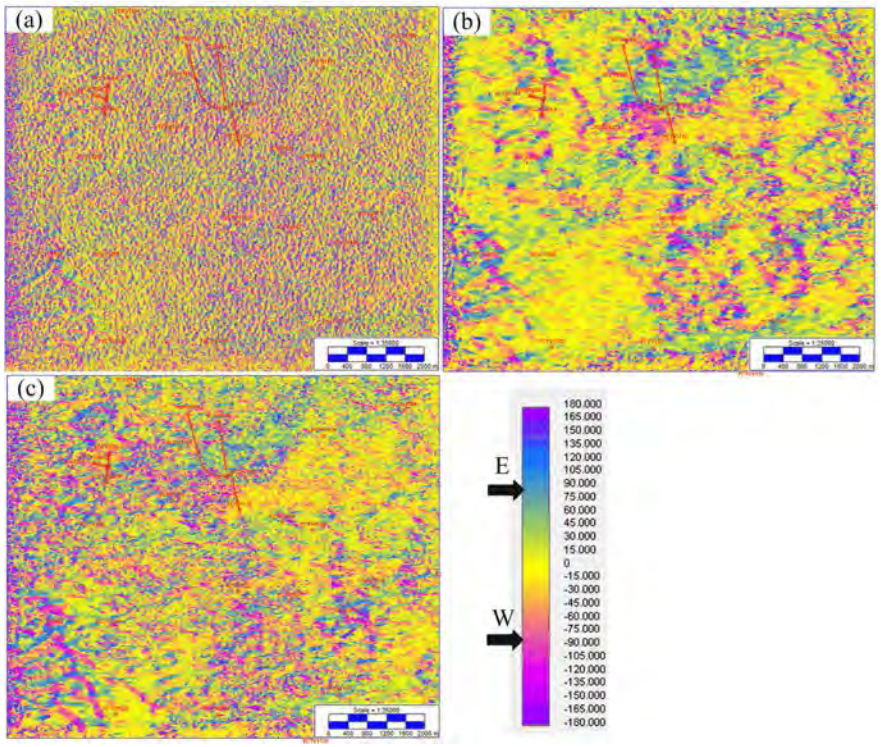

Figure 8. Dip/azimuth attributes comparison extracted from (a) the PSTM migrated data, (b) the integrated filtering data, and (c) the high-resolution data. Some fractured regions are more clearly depicted in the high resolution data.

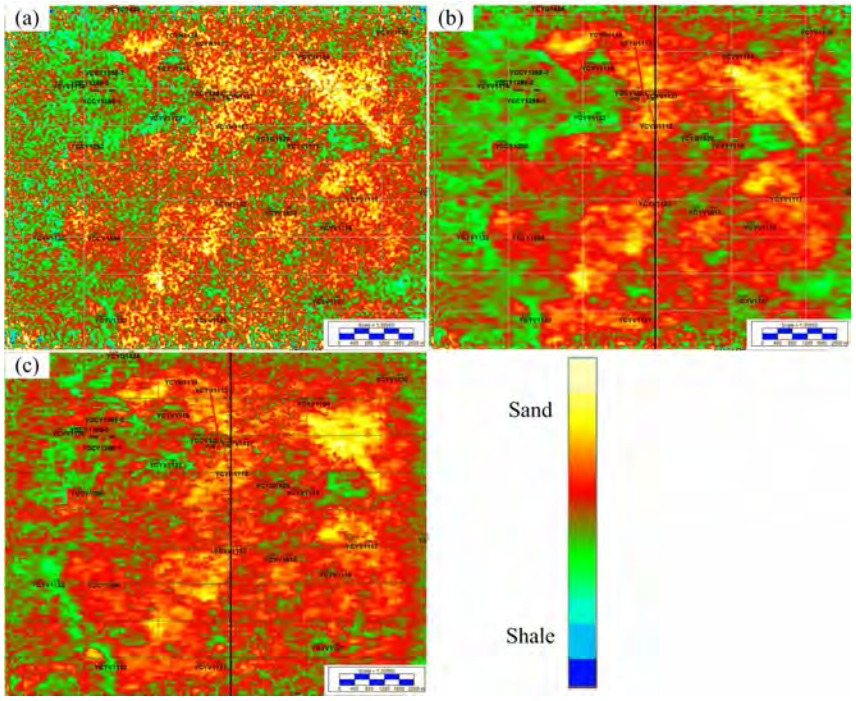

Figure 9. The 90-degree phase-rotated data (equivalent to poststack inverted impedance as a lithology indicator) from (a) the PSTM migrated data, (b) the integrated filtering data; (c) the high-resolution data. The depositional features are more clearly identified in the high-resolution result.

Pre-Stack Preconditioning and Simultaneous Pre-stack Inversion

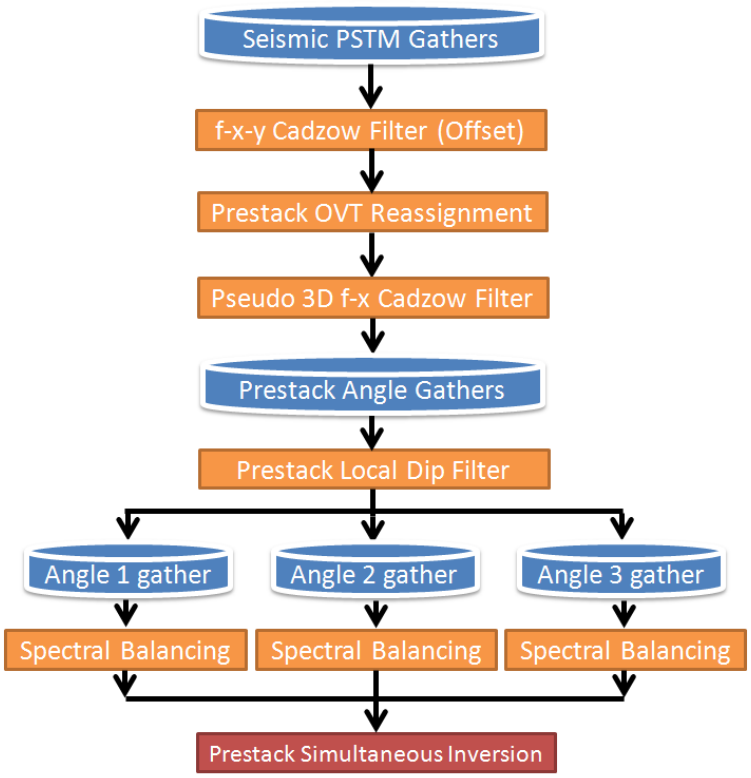

Figure 10. A workflow chart with three major precondition steps are shown to improve the quality of prestack gathers for simultaneous prestack inversion: (1) A combination of Cadzow filtering methods to suppress coherent noise; (2) A prestack local dip filter to suppress random noise; (3) An angle-dependent spectral balancing method to compensate the frequency loss.

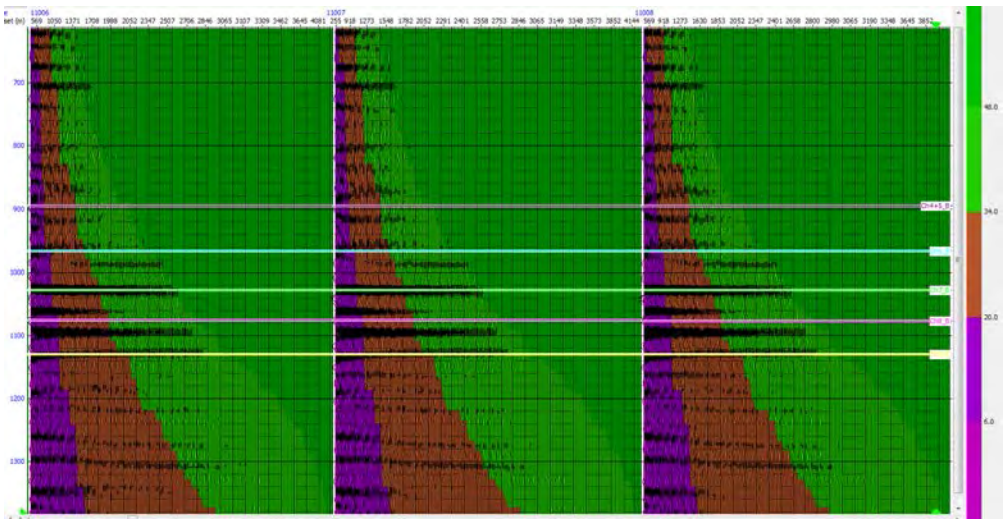

Figure 11. Three-angle division scheme evaluated on prestack gathers after coherent noise attenuation. The near angle stacks with 6-18 degree data, the middle angle stacks with 18-30 degree data, and the far angle stacks with 30-42 degree data.

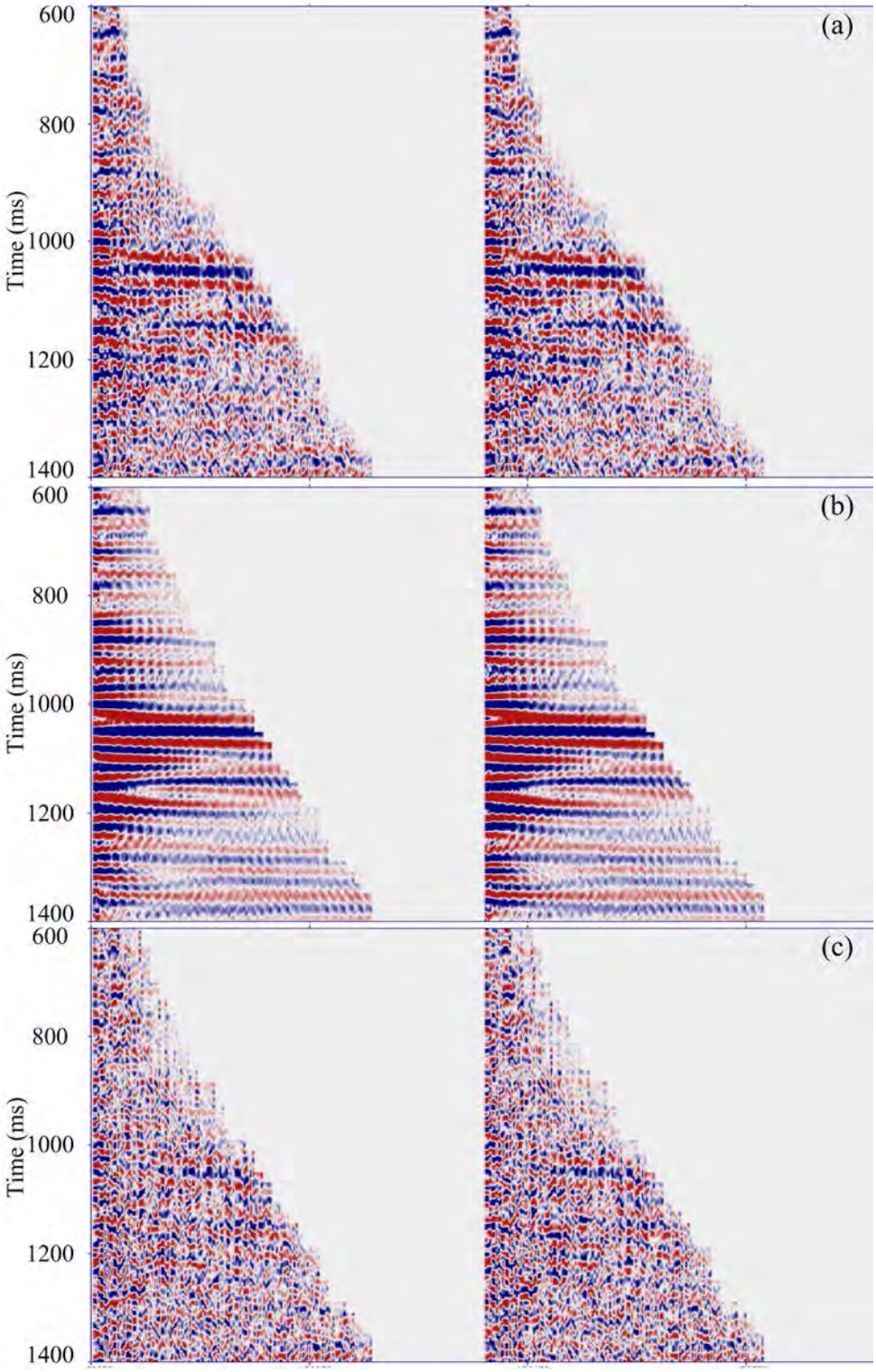

Figure 12. Intermediate filtered results generated by combining Cadzow filters. (a) The PSTM migrated original CRP gathers, and (b) the corresponding filtered gathers after pseudo 3D f-x Cadzow filtering, (c) the corresponding removed noise. The SNR is significantly improved and the gather is much flatter. Note that the far offsets emerge from the noisy background and that the AVO phenomena are clearly identified.

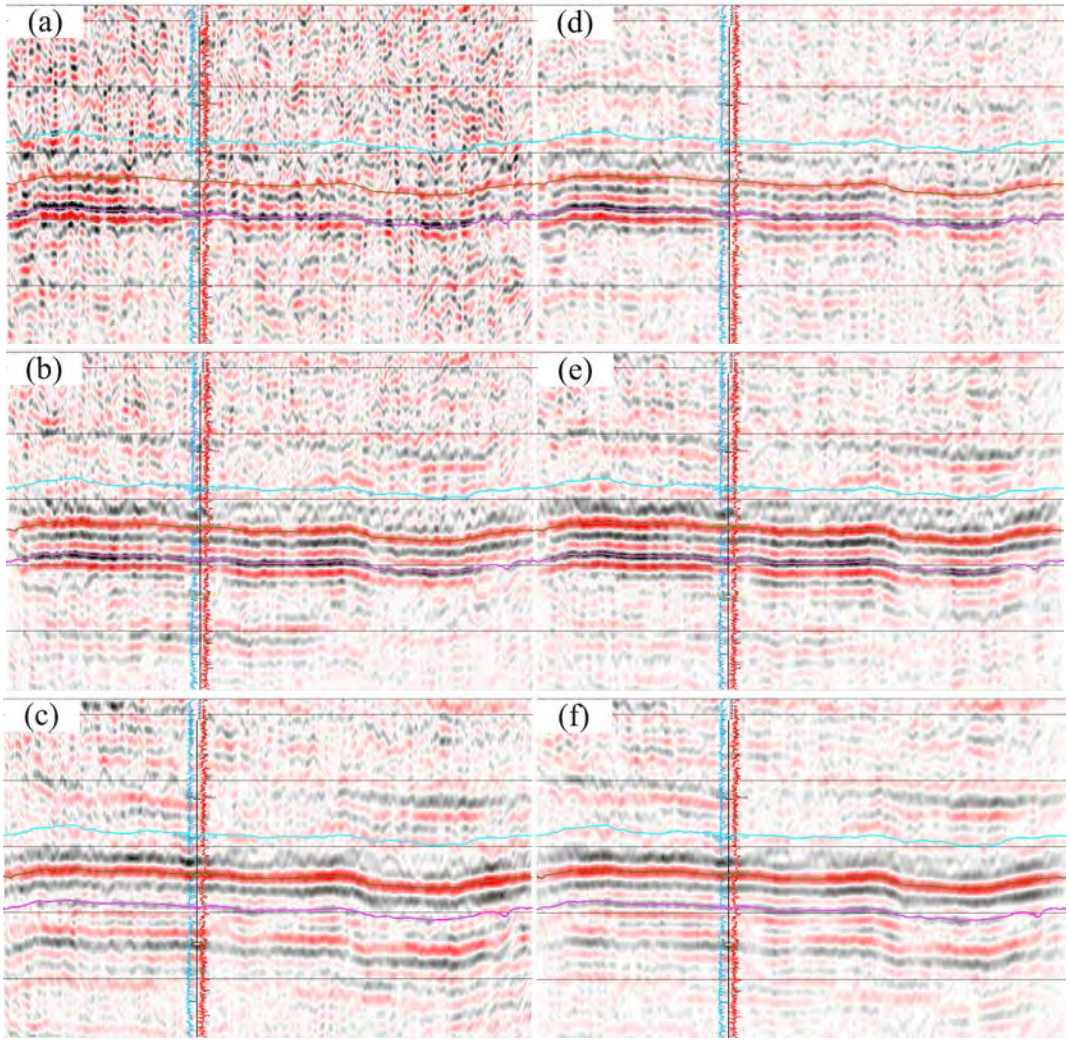

Figure 13. Intermediate filtered results generated by prestack local dip filtering. (a), (b) and (c) are respectively the near angle stacks, middle angle stacks, and the far angle stacks directly from the original CRP gathers. (d), (e) and (f) are the corresponding filtered version after prestack local dip filtering. The SNR of the near angle stacks is significantly improved.

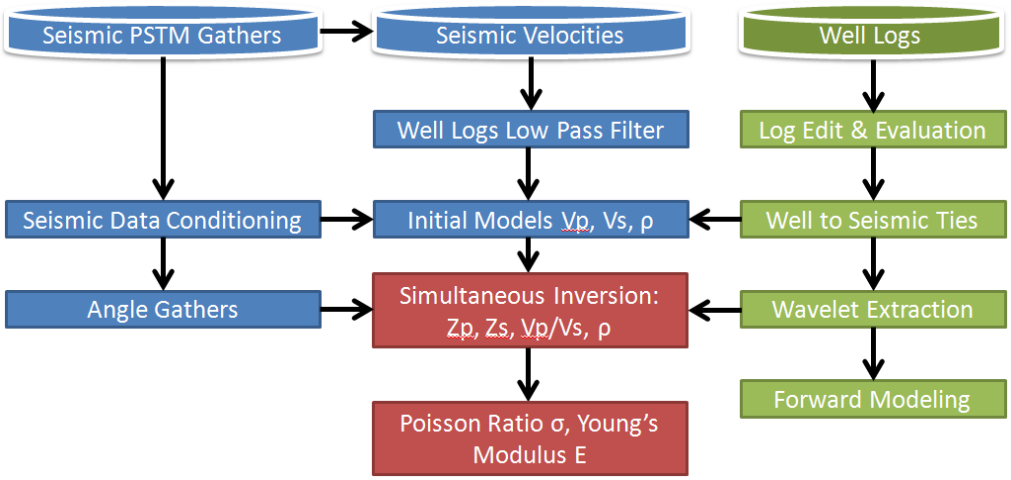

Figure 14. Flowchart showing three major preparations for simultaneous inversion, including: (1) preconditioning prestack gathers; (2) building initial models; (3) tying well logs to seismic data.

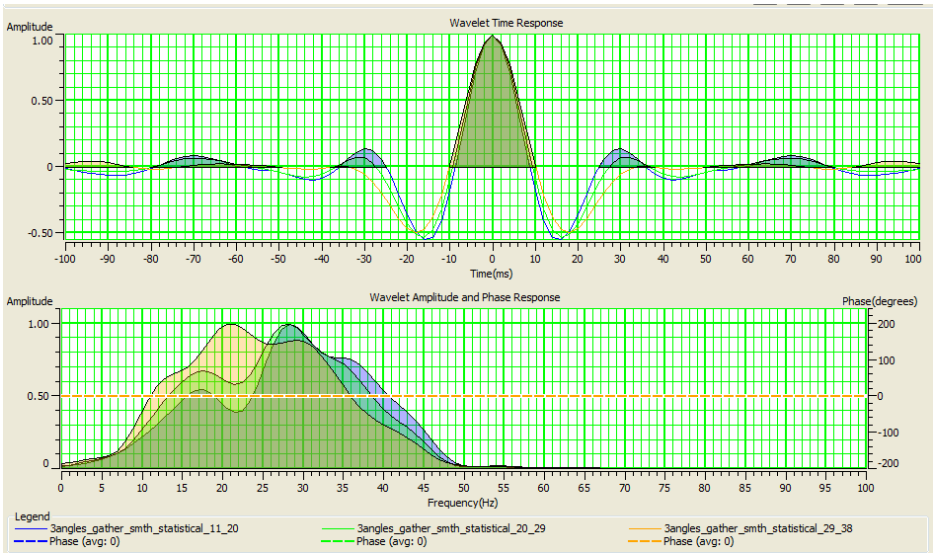

Figure 15. Three angle-dependent statistical wavelets for simultaneous inversion: Blue - 6/18 degree, green - 18/30 degree, yellow - 30/42 degree.

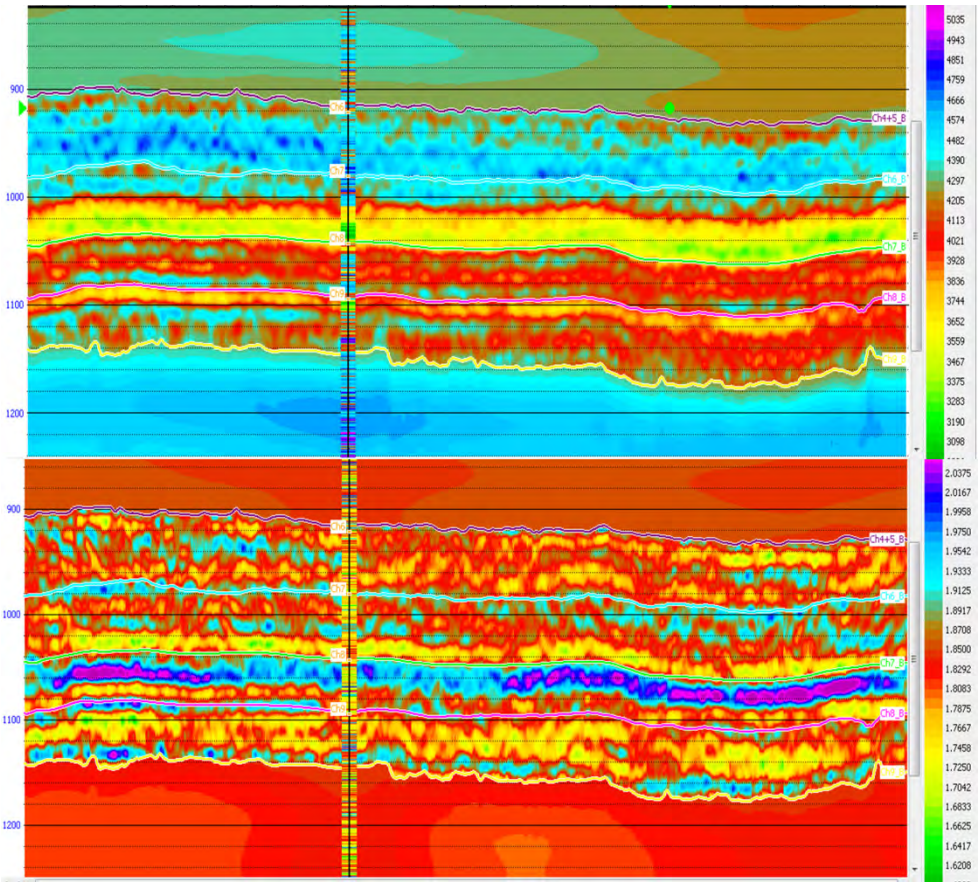

Figure 16. The inverted Zp and Young's modulus for the Mesozoic shale gas reservoirs. The computed Zp and Young's modulus from well logs are inserted for comparison.

Conclusions

The processed data—either migrated poststack data or prestack gathers—are dramatically impaired by the extremely low SNR and significant frequency loss because of the complex surface condition of the loess mountain area. Improving the data quality is critical to obtaining reliable stratigraphic interpretations and prestack inverted results. The main tasks for migrated poststack data are to (1) suppress coherent noise such as acquisition footprints; (2) remove residual random noise; and (3) extend the bandwidth. Main tasks for prestack gathers are to (1) suppress residual scattering noise and multiples; (2) enhance the coherence of reflections; and (3) balance the spectra to compensate frequency loss and stretch artifacts.

We here take advantage of the Cadzow filtering methodology to attenuate coherent noise in both prestack and poststack domains. We utilize the structure-oriented filtering to remove random noise in poststack data, and we propose a prestack local dip filtering to remove random noise and significantly enhance the coherence of angle stacks. We explore the frequency characteristics of seismic data in the CWT domain and perform spectra extensions both for poststack and prestack data, where the prestack performance is also AVO-compliant. Because unwanted noise is

rejected and frequency contents are well recovered, more information is now available for obtaining much more accurate stratigraphic interpretation and better inverted results.

References

Al-Dossary, S., 2015, Preconditioning seismic data for channel detection: Interpretation, v. 3, no. 1, p. T1–T4.

Bo Zhang, Chang, D., Tengfei Lin, and Marfurt, K. J., 2015, Improving the quality of prestack inversion by prestack data conditioning: Interpretation, v. 3, no. 1, p. T5–T12.

Bo Zhang, Tengfei Lin, and Marfurt, K. J., 2015, Noise suppression of time migrated gathers using prestack structure oriented filtering: SEG Technical Program Expanded Abstracts 2015, p. 4678–4682.

Bonar, D., and Sacchi, M., 2013, Spectral decomposition with f-x-y preconditioning: Geophysical Prospecting, v. 61, p. 152–165.

Chen, J.Y., Li, N., Hou, S.N., Yang, G.M., and Zhang, X.R., 2009, Development status overview of seismic prospecting technology in Loess Tableland: Coal Geology of China, v. 21, no. 12, p. 72–76.

Chopra, S., 2011, Extracting meaningful information from seismic attributes: CSEG RECORDER, 36(03).

Chopra, S., Sharma, R.K., Keay, J. and Marfurt, K.J., 2012, Shale gas reservoir characterization workflows. 82nd Annual International Meeting, SEG Expanded Abstracts, p. 1–5.

Chopra, S., and Marfurt, K.J., 2013, Preconditioning seismic data with 5D interpolation for computing geometric attributes: SEG Technical Program Expanded Abstracts 2013, p. 1368–1373.

Coopersmith, E., Burkholder, K. and Schulze, J., 2013. Valuing seismic at the drilling program level for sweet spot identification in unconventional resource plays: A tutorial via a representative example: Interpretation, v. 1(2), SB125-SB130.

Duveneck, E., 2015, A local dip filtering approach for removing noise from seismic depth images: SEG Technical Program Expanded Abstracts 2015, p. 4683-4687.

Fornberg, B., 1988, Generation of finite difference formulas on arbitrarily spaced grids: Mathematics of Computation, v. 51, no. 184, p. 699–706.

Golyandina, N., Nekrutkin, V., and Zhigljavsky, A., 2001, Analysis of time series structure: SSA and related techniques: CRC Press.

Gray, D., Anderson, P., Logel, J., Delbecq, F., Schmidt, D. and Schmid, R., 2012. Estimation of stress and geomechanical properties using 3D seismic data: First Break, v. 30, p. 59–68.

Hale, D., 2007, Local dip filtering with directional Laplacians: Colorado School of Mines, Center for Wave Phenomena Report CWP-567.

Hubbard, B.B., 1998, The world according to wavelets - the story of a mathematical technique in the making. 2nd Edition, A. K. Peters.

Igor, L. S., Braga, F., Moraes, S., and do Amaral de Almeida, M., 2011, Combining seismic data preconditioning, AVO inversion and geometrical attributes for high resolution reservoir delineation: 12th International Congress of the Brazilian Geophysical Society & EXPOGEF, p. 1417–1421.

Liu, B. G., 2014, The key technologies of 3D seismic exploration in loess plateau area of Southern Ordos Basin: Geophysical Prospecting for Petroleum, v. 53, no. 3, p. 330–337.

Michael Smith, Gary Perry, Jaime Stein, and others, 2008, Extending seismic bandwidth using the continuous wavelet transform: First Break, 26, 97-102.

Mutlu, O., and Marfurt, K.J., 2015, Improving seismic resolution of prestack time-migrated data: Interpretation, v. 3, no.4, p. T245–T255.

Perez, R., and Marfurt, K. J., 2013, Brittleness estimation from seismic measurements in unconventional reservoirs: Application to the Barnett Shale, 83rd Annual International Meeting, SEG Expanded Abstracts, p. 2258–2263.

Qian, S., 2002, Introduction to time-frequency and wavelet transforms: Prentice-Hall.

Sacchi, M., 2009, FX Singular Spectrum Analysis, CSPG CSEG CWLS Convention Abstracts, p. 392–395.

Schmidt, D., Veronesi, A., Delbecq, F., and Durand J., 2013, Seismic Data Preconditioning for Improved Reservoir Characterization: GeoConvention 2013 - Integration.

Singleton, S., 2009, The effects of seismic data conditioning on prestack simultaneous impedance inversion: The Leading Edge, v. 28, no. 7, p. 772–781.

Tang, X., Zhang, J. C., Wang, X. Z., Yu, B. S., Ding, W. L., Xiong, J. Y., Yang, Y. T., Wang, L. and Yang C., 2014, Shale characteristics in the southeastern Ordos Basin, China: Implications for hydrocarbon accumulation conditions and the potential of continental shales: International Journal of Coal Geology, v. 128-129, p. 32–46.

Trickett, S. R., 2002, F-x Eigenimage Noise Suppression: 72nd Annual International Meeting, SEG, Expanded Abstracts, p. 2166–2169.

Trickett, S. R., 2003, F-xy eigenimage noise suppression: Geophysics, v. 68, p, 751–759.

Trickett, S. R., 2008, F-xy Cadzow Noise Suppression: 78th Annual International Meeting, SEG, Expanded Abstracts, p. 2586–2590.

Trinchero, E., and Vernengo, L., 2013, Geomechanical and geometric seismic attributes in an interpretation workflow for characterization of unconventional reservoirs. The Leading Edge, v. 32(4), p. 386–392.

Ulrych, T. J., Sacchi, M. D., and Freire, S. L. M., 1999, Eigenimage processing of seismic sections, in Kirlin, R. L., and Done, W. J., Eds., Covariance analysis for seismic processing: Soc. Expl. Geophys., p. 241–274.

Vermeer, G. J. O., 1988, 3-D symmetric sampling: Geophysics, v. 63, p. 1629–1647.

Wang, F. Q., Wang, X. Z., Zhang, L. X., Liu, H. J., and Lei, Y., 2013. The shale gas resources estimation: An example from Mesozoic Triassic Yanchang Formation Member Chang 7, Ordos Basin. Earth Science Frontiers, v. 20(3), p. 240–246.

Wang, X.Z., 2014. Major breakthrough of gas exploration in Yangchang blocks and its significance. Oil and Gas Geology, v. 35(1), p. 1–9.

Wang, X. Z., Zhang, L. X., Liang, Q. S., Jiang, C. F., Wang, W., Yao, X. L., Shi, H., Zhao , C. L., Hinz, K., Liu, Q. L., van Barren P., Zhang, M., Zou X. H., and Liang, B., 2014, -azimuth, high-density, 3D point-source/point-receiver seismic survey for shale gas exploration in a loess plateau: a case study from the Ordos Basin, China: First Break, v. 32, p. 105–112.

Xiao, F. S., Yang, J. L., Liang, B., Zhang, M., Li, R., Li, F., Xiao, H.P., Lei, X., Liu, Q.L., and Heesom, T., 2014, High-density 3D point receiver seismic acquisition and processing - a case study from the Sichuan Basin, China. First Break, v. 32, p. 81–90.

TASK 6.2

3D Seismic Interpretation and Sweet-Spot Prediction

Hongliu Zeng[1] and Wei Wang[2]

1-Bureau of Economic Geology, Jackson School of Geosciences, The University of Texas at Austin, Austin, Texas
2-Research Institute of Shaanxi Yanchang Petroleum (Group) Co. Ltd.

Abstract

In this task, we conducted a seismic-sedimentological study in a newly acquired 3D survey in the study area to advance interpretation and prediction of lacustrine shale-gas reservoirs in Yanchang Formation. The seismic volume was converted into a log-lithology volume at the thin-bed level. Inverted acoustic impedance volume was stratal-sliced to extract seismic geomorphologic information. Deltaic facies and depositional history were interpreted by using lithologic and planoform morphology of seismic attributes on stratal slices. Detailed core analysis data on TOC, mineral composition, and mechanical properties of sandstones and shales were correlated to seismic-derived lithology and facies. Microseismic data were evaluated for reservoir performance in production wells. Finally, shale-gas sweet spots were predicted by mapping relatively high-brittleness lithofacies in 3D using seismic attributes. The high-TOC Chang 7-1 shale unit is not ideal for shale-gas development because of its ductile nature and tunnel effect in hydraulic fracturing. Chang 7-2 prodelta sediments are optimal drilling targets because of their large thickness, relatively high brittleness, and proximity to Chang 7-1.

Introduction

The Yanchang Formation has been the major hydrocarbon producer in the Erdos Basin for many years. Oil and gas are produced from conventional sandstone reservoirs in shallow-water deltas and fluvial systems. In recent years, the potential for finding unconventional shale-gas plays in the Chang 7 member and other lacustrine shale units in the Yanchang Formation is getting increased attention. In the study area, shale-gas exploration activities have recently increased, with some success.

Lack of high-quality 3D seismic data in much of the basin has long hindered exploration and production activities. Covered by thick, loose soil and vegetation, the Loess Plateau in the study area brings strong surface-wave noise and prevents effective statics correction, presenting difficult surface conditions for seismic data acquisition. Recently, this situation has changed with the introduction of new technologies. A 3D acquisition project based on UniQ high-density 3D survey technology (Pecholcs and others, 2012; Zubay and others, 2013) and following-up reprocessing efforts (this report) successfully improved data quality, making a genuine interpretation of lithology, depositional facies, and rock brittleness in the Yanchang Formation possible for this project.

With much of the study interval being composed of sandstones and shale units near or below seismic resolution, however, limited seismic- signal bandwidth still makes it difficult to interpret thin sandstones and gas-shale beds, which are key for the success of this project. Seismic geomorphology (Posamentier, 2000) has proven to be a valuable tool for high-resolution seismic facies imaging using stacked and migrated 3D seismic data. Integrated with seismic-lithology study, such seismic-facies signals can be converted to sedimentary-rock signals, depositional processes, and depositional systems. This work flow is called seismic sedimentology (Zeng and others, 1998b; Zeng and Hentz, 2004). By applying this technology, typical resolution of reservoir mapping by using seismic data is about 10 m, and it can be as thin as 1 m (e.g., Zeng and others, 2011).

In this study, we first attempted to map detailed lithofacies and depositional facies in Chang-7 and surrounding formations. Then we analyzed the relationships between lithology/facies and TOC and rock brittleness, and we evaluated fracking performance in wells using microseismic data. Finally, we made a prediction of sweet spots for future drilling.

Data

A 100-km^2 3D seismic data set was available for the study (**fig. 1**). The seismic data were acquired with a UniQ integrated point-receiver land seismic system, which is an extreme channel-count acquisition scheme (Pecholcs and others, 2012). Applied to acquiring a genuine signal in this difficult loess plateau area, this highly flexible system can be deployed in fast-moving, low-density exploration surveys and in full-azimuth, broad-bandwidth, point-source/point-receiver reservoir surveys. The first-round processing results provided by the contractor (Schlumberger) revealed reflection signals from the Yanchang Formation, and a follow-up reprocessing effort (Task 6.1) greatly improved data quality.

The new data demonstrate realistic amplitude, frequency, and continuity characteristics related to subsurface stratigraphy and reservoirs (**fig. 2a**), which are characterized by a frequency bandwidth of 10 to 50 Hz, with a dominant frequency of 30 Hz (**fig. 2b**). Synthetic seismograms at wells (e.g., well YCYV1133, **fig. 3**) illustrate a strong tie between major geologic surfaces and seismic events.

There are 29 wells available for this study. All wells have gamma-ray, spontaneous potential, and resistivity logs, and at least one porosity log (sonic, density, or neutron); key wells have sonic and/or dipole acoustic logs. An additional well, YY1, is a key site for core analysis and laboratory study. Although the well is located outside the 3D survey to the south, the stratigraphy and lab results (TOC, petrology, reservoir properties [porosity, pore networks], and mechanical properties [Young's modulus, Poison's ratio, bambino and UCS]) in this well can be easily tied to seismic data by wireline-log correlation. Microseismic data are available in five inclined or horizontal wells (**fig. 1**) for us to study rock responses to fracking and the relationship between reservoir performance and rock brittleness.

In addition, the data reprocessing workflow (Task 6.1) provided volumes of acoustic impedance (AI) and elastic properties (V_p, V_s, density, Young's modulus, and Poison's ratio), which are useful for lithologic, facies and brittleness evaluations and sweet-spot prediction.

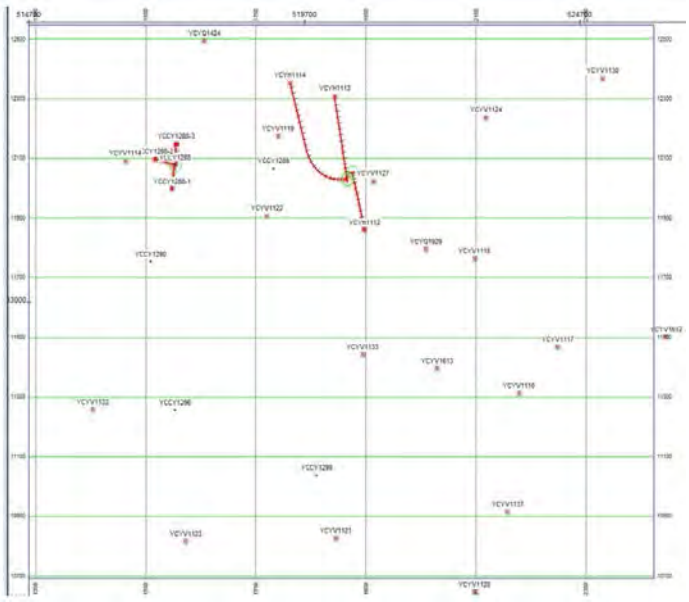

Figure 1. 3D seismic survey and location of wells used in study, except YY1 well.

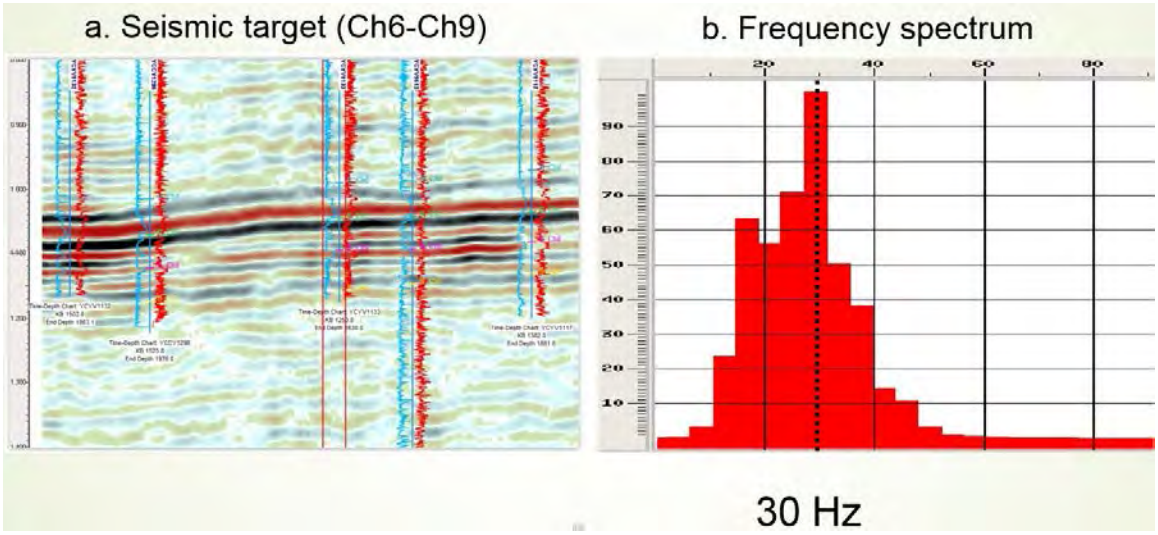

Figure 2. Quality of the seismic data. (a). A well-seismic section at the study interval. (b) Frequency spectrum showing a bandwidth of 10 to 50 Hz, with a dominant frequency of 30 Hz.

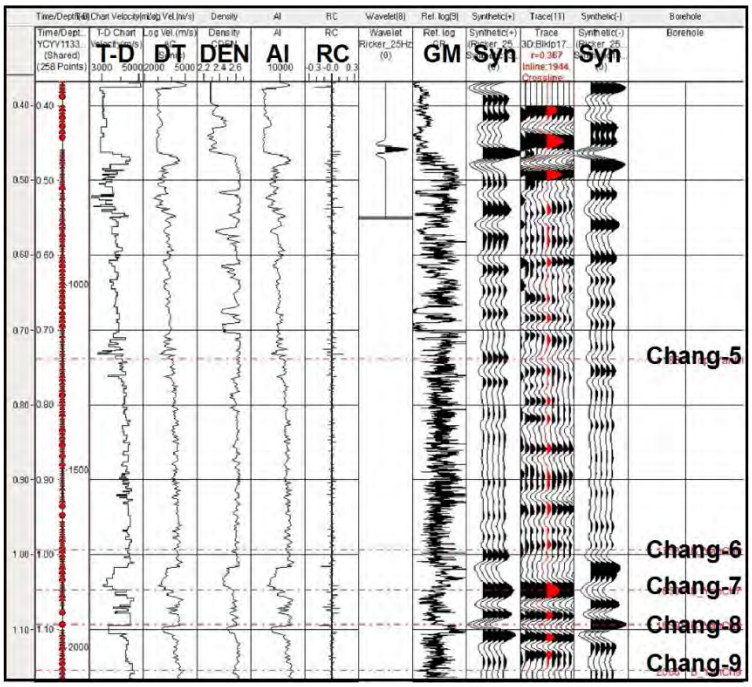

Figure 3. Synthetic seismogram from YCYV1133 well.

Methodology

We applied an integrated approach that combined core analysis, wireline-log correlation, and seismic interpretation to investigate lithology, facies, and rock brittleness before making a prediction of sweet spots. A 6-step workflow was implemented for this study:

Step 1: Seismic lithology. The purpose is to convert the 3D seismic volume into a log-lithology volume at the thin-bed level, ensuring a good correlation between lithology-indicative wireline logs (e.g., GR [gamma ray] and SP [spontaneous potential]) and well-site seismic attribute traces, making it possible to assign lithologic meanings to thin-bed seismic geomorphologic features on stratal slices. The key is to find a seismic attribute, either single or combined, that has a simple, near-linear relationship with lithology. Inversion, 90° phased traces, trace attributes, and AVO attributes are all possible candidates.

Step 2: Stratal slicing. To maximize the usefulness of seismic geomorphologic information, seismic attributes must be picked on a depositional surface (geologic-time surface or stratal slice) so that any attribute extractions on such a surface can represent a lithogenetic depositional unit. Typically, stratal slices are made proportionally between geologic-time equivalent, seismic-reference events (Zeng and others, 1998a, 1998b).

Step 3: Interpreting seismic geomorphology, facies and depositional history by using stratal slices and well calibration. In doing so, the planform morphology of seismic attributes on stratal slices can be viewed as representing depositional patterns preserved in the geologic record, in the same way as satellite pictures image modern depositional systems. Because they have been

conditioned to lithology, the seismic-attribute patterns on stratal slices also highlight lithofacies distributions, making the geometrical mapping of depositional systems more reliable and accurate. Facies analysis of core and wireline-log patterns provide necessary calibration to seismic interpretation. The major differences are that seismic images are pictures averaged over geologic time windows (typically $\lambda/4$ or one seismic event at high-frequency sequence level). The limited bandwidth of seismic data prohibits point-in-time imaging of paleogeography. Also, the seismic images are made from preserved depositional units after post-depositional processes. All those should be considered before a realistic interpretation of facies and depositional history can be achieved. Nonetheless, studies have shown the resolution of sand bodies recognized on stratal slices can be well below seismic resolution limits (e.g., Zeng and others, 2011; Cheng and others, 2015).

Step 4: Link seismic lithology and facies to TOC and rock brittleness. In this study, we made use of detailed core analysis data on TOC, mineral composition, and mechanical properties of sandstones and shales. Correlating these core-based parameters to seismic-derived lithology and facies is essential in using 3D seismic data to evaluate fracking performance and, more importantly, to predict sweet spots for future exploration and production. The correlation can be quantitative or qualitative in nature. For this study, only qualitative analysis was conducted, which provided adequate assurance for us to use seismic information directly for key rock mechanical properties and fracability analysis.

Step 5: Evaluate reservoir performance by using microseismic data. Assuming that the strength of microseismic events is a good measure of rock response (density and size of fractures) to fracking operations, we studied the size and distribution of microseismic events in inclined and horizontal wells and their relationship to well track position, stratigraphy, lithology, and facies. These factors enhanced our analysis of control factors on reservoir performance.

Step 6: Predict shale-gas sweet spots. By mapping relatively high-brittleness lithofacies in 3D using seismic attributes, future drilling targets can be evaluated on the basis of their thickness and proximity to high-TOC beds.

Seismic expression of lithology

One fundamental limiting factor in our ability to interpret stratigraphy and reservoirs is the low resolution of the seismic data. Considering a dominant frequency of 30 Hz and an average interval velocity of 3,500 m/s to 4,000 m/s, the calculated resolvable limit at the study interval (Chang 6 through Chang 9 members) is about 30 m to 35 m (16.7 ms). Except for the main shale unit in the lower Chang 7, which is 20-m- to 40-m-thick and is above resolvable limit in some areas, most of the reservoirs in the formation are thinner than the resolvable limit. In these thin units, it is unrealistic to measure thickness by directly tracking the top and base of a reservoir unit. Amplitude tuning is a better parameter for tracking relative thickness variation in thin beds.

Rock petrophysics controls the link between seismic signal and rock properties. In the study interval, there is a linear relationship between the velocity of sandstone and of shale (**fig. 4**). In general, the velocity (and acoustic impedance, or AI) increases with increasing sand content (or decreasing gamma-ray API reading) and decreasing clay content (or increasing API). There is a

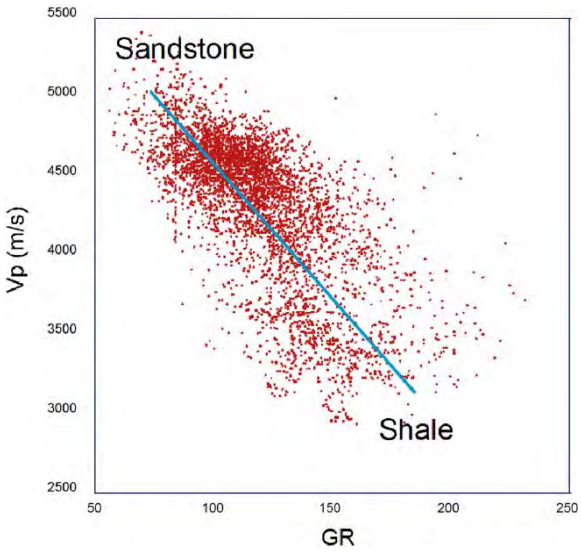

Figure 4. A linear relationship between Vp and lithology-indicative GR log in study interval in a well.

difference of 1,100 m/s between the peak velocities of sandstone and shale, which is capable of generating strong seismic reflections (average RC = 0.14) for lithology identification.

In this data set, a simple process of 90° phasing greatly improved lithologic interpretation in the Yanchang Formation (**fig. 5**). Sandstones are characterized by AI higher than that of shale. In the zero-phase data (fig. 5a), the same lithology of the same AI is tied to opposite polarities (peak–trough, or red–black couplet). The correlation between lithology-indicative curves (DT/GM) and seismic traces is typically poor. In the 90° data (**fig. 5b**), however, seismic responses are symmetric to the sandstone or shale beds in logs, causing the main seismic event (peak or trough) to coincide with the geologically defined thin beds (sandstone or shale, respectively). As a result, seismic polarity better ties to lithology, and the correlation between lithology-indicative logs and seismic traces is improved. This improvement should make a seismic section look more like a geologic section, and make an amplitude extraction on stratal slices more closely represent lithologic distribution of a depositional system.

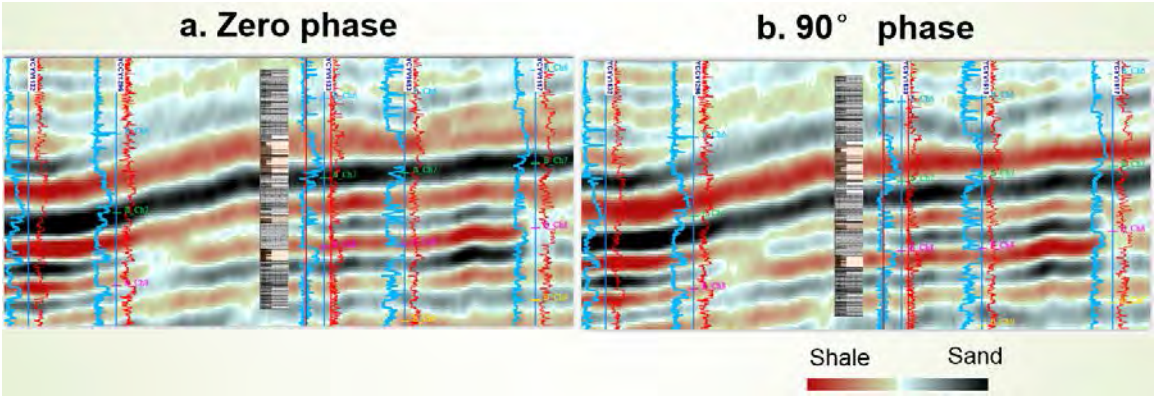

Figure 5. Well-seismic section showing advantages of 90° data for lithologic interpretation. (a) Zero-phase data. (b) 90° data. Logs displayed are DT on the left and gamma ray (GR) on the right. A deflection to the left in the logs indicates sandstone; to the right, shale.

In this study, a process of acoustic inversion further improved lithology-seismic correlation (**fig. 6**). Although the general correlation between the inverted AI and 90° data is high (compare **fig. 5b** and **fig. 6**), by measuring absolute AI, the inverted AI is a more direct representation of rock shaliness. As a result, at least three lithologic types, sandstone, shale, and shaly sandstone, can be recognized and mapped with inverted AI volume.

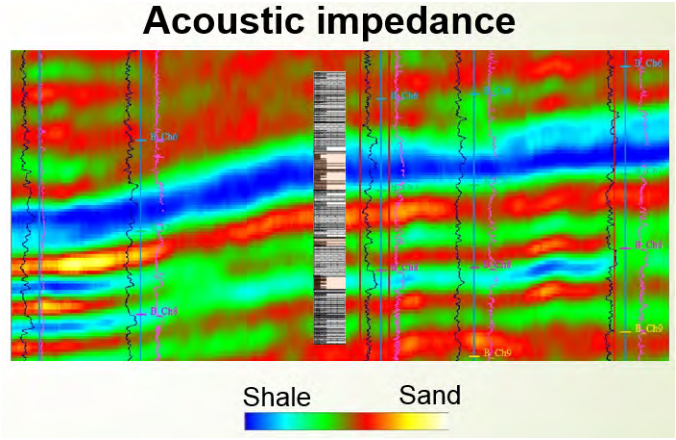

Figure 6. A section of inverted AI from seismic data in **Figure 5.**

Seismic expression of facies and depositional systems

The study interval is structurally simple. However, minor to moderate lateral thickness variations, and seismic stratal slices, have to be made between multiple (at least 2) time-significant reference seismic events. Three horizons (Chang 6, Chang 7, and Chang 9, **fig. 7**) were traced for this purpose. Both 90° phase data and inverted AI volume were sliced between these events using a linear interpolation algorithm. Eventually the inverted AI slices were chosen for analysis for finer detection of lithology and fewer wavelet effects.

Selected stratal slices (**figs. 8 through 15**) illustrate lithology- indicative, seismic-geomorphologic patterns in typical depositional facies in the Yanchang Formation. Calibrated to sandstone-prone or shale-prone end members, the warm-hued (yellow to red) AI in these slices tends to represent more sandy units, and cold-hued (blue and green) AI is more indicative of shaly units.

Developed in a complete cycle of lacustrine expansion and shrinking, the Yanchang Formation is a third-order sequence composed of multiple higher-order (probably 4th-order) sequences indicative of frequent lake-level rises and falls (e.g., lake-level curve, **fig. 8**). Arranged in stratigraphic and relative geologic-time order (e.g., well/seismic section and red arrow, **fig. 8**), these stratal slices demonstrate cyclical changes in lithology and seismic geomorphologic patterns:

- Among multiple shaly-then-sandy cycles, three cycles in Chang 9 through Chang 7 are displayed in **Figures 9 and 10**, **Figures 11 and 12**, and **Figures 13 and 14**, respectively (see C1 – C3 in **fig. 8** for position). **Figure 8** and **Figure 15** are two sandy units in Chang 10 and Chang 6 members, respectively.

- Among the three shaly-then-sandy cycles, the sandy units (**Figures 10, 12, and 14**) are characterized by multiple lobate-shaped high-sand content patterns. Various channel forms occur within and between those lobes. The lobe systems grade into more shaly, featureless zones to the southwest. Among the shaly units, two reveals multiple northeasterly-oriented lobes in smaller scale (**figs. 9 and 11**); the shaly unit in **Figure 13** (main high-TOC shale unit in Chang 7) is sheet-like and feature-less. The two slices at Chang 10 (**fig. 8**) and Chang 6 (**fig. 15**) are dominated by channel-shaped and arc-shaped sandy anomalies.

The significance of the depositional facies of these stratal slices was interpreted as a result of integrating core, wireline-log, and seismic data (lithology and geomorphology). The interpretation was tied to the lake-level curve and a box depositional model from regional study:

- Chang 10 (**fig. 8**): Deposited in lowstand before the lacustrine expansion, the sandy, sinuous channel forms and arc forms were interpreted as meander channels and amalgamated point-bar sandstone complexes in a fluvial system.

- Cycle 1 (C1) in upper Chang 9 and lower Chang 8 (**figs. 9 and 10**): The whole cycle is recorded as an upward-coarsening trend in GR logs. The transgression-regression cycle started with shaly unit (**fig. 9**) deposited in a prodelta and lake environment. The small lobes are probably prodelta sand bars. It was followed by a significant deltaic progradational event characterized by sandy, lobate delta plain and delta front deposits sourced from northeast.

- Cycle 2 (C2) in upper Chang 8 (**figs. 11 and 12**): Being revealed as another upward-coarsening trend in gamma-ray logs, this is a transgression-regression cycle with a deltaic environment similar to cycle 1. Some sandy channel complexes in the transgressive, prodelta environment might represent turbidite fans, a deep-water facies type common in the Yanchang Formation in the area.

- Cycle 3 (C3) in Chang 7 (**figs. 13 and 14**): This transgression-regression cycle was at the maximum lake expansion. Thick deep-lake deposits (**fig. 13**) were followed by a major influx of deltaic sandy sediments composed of delta plain, delta front, and prodelta facies (**fig. 14**).

- Chang 6 (**fig. 15**): Deposited at the end of lacustrine expansion cycle and the beginning of a long period of lowstand fluvial deposition, this unit is characterized by numerous sandy, sinuous channel forms tied to upward-fining grain-size trends in wells and can be interpreted as fluvial plain.

In summary, the sequential display of stratal slices from Chang 10 to Chang 6 members demonstrated a depositional history from fluvial (Chang 10) to lacustrine deltaic (Chang 9 to Chang 8), deep lake (lower Chang 7), deltaic (upper Chang 7), and back to fluvial depositional systems (Chang 6). The general sediment dispersal was from the source area to the northeast to the deep-lake zone to the southwest.

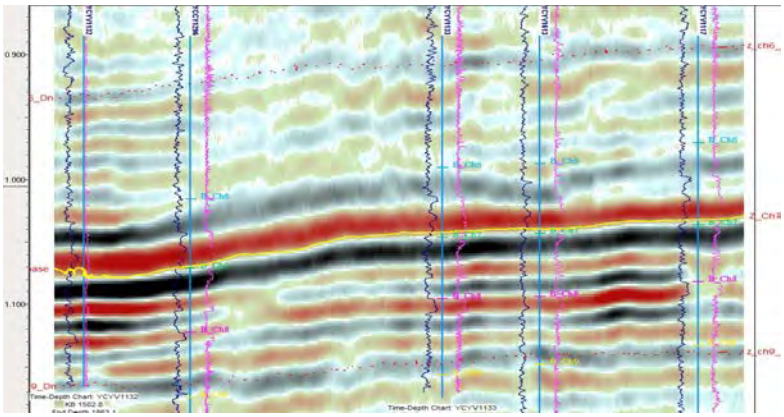

Figure 7. Three horizons used in stratal slicing. From top down: Chang 6, Chang 7, and Chang 9.

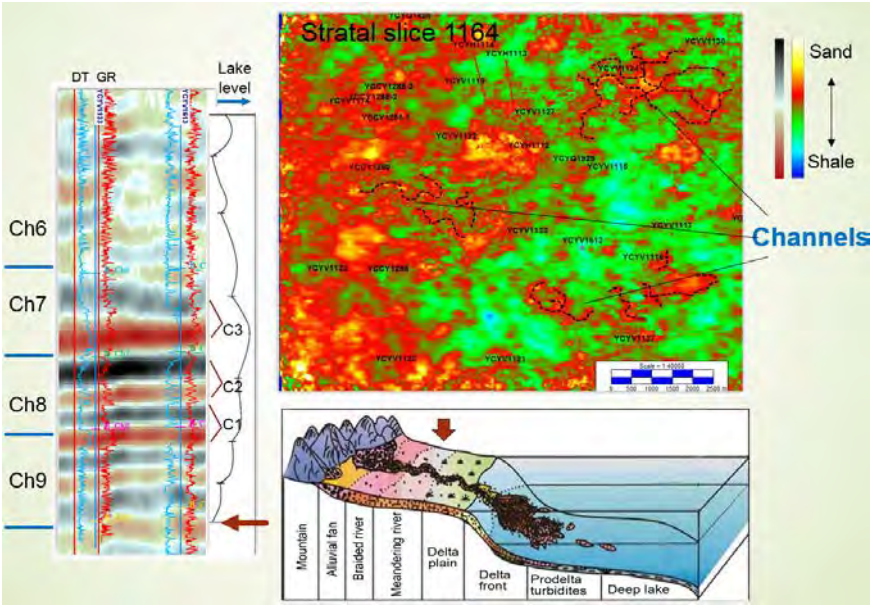

Figure 8. A representative stratal slice at the top of Chang 10 member and its stratigraphic, interpreted lake-level, and general depositional model position. C1, C2, and C3 denote three transgressive-regressive high-frequency sequence cycles.

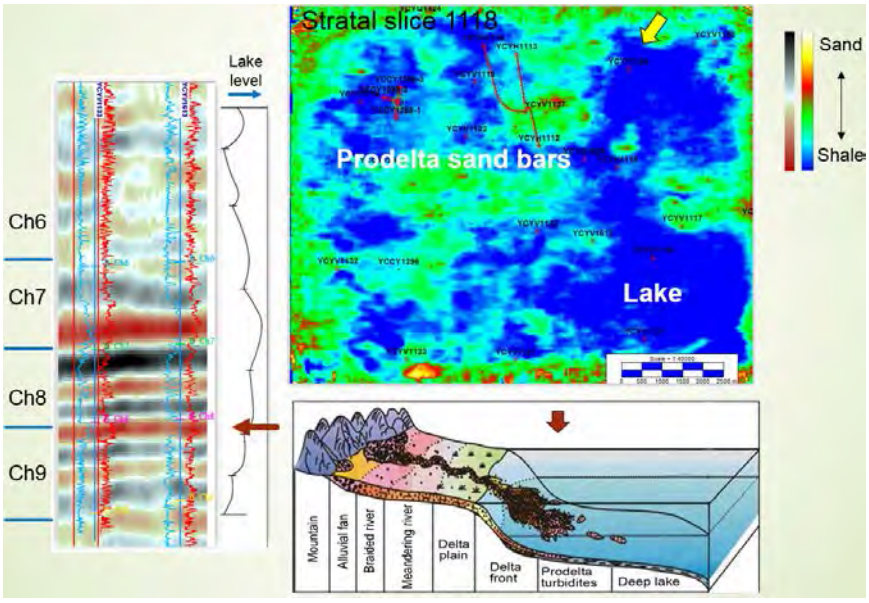

Figure 9. A representative stratal slice at the top of Chang 9 member and its stratigraphic, interpreted lake-level, and general depositional model position.

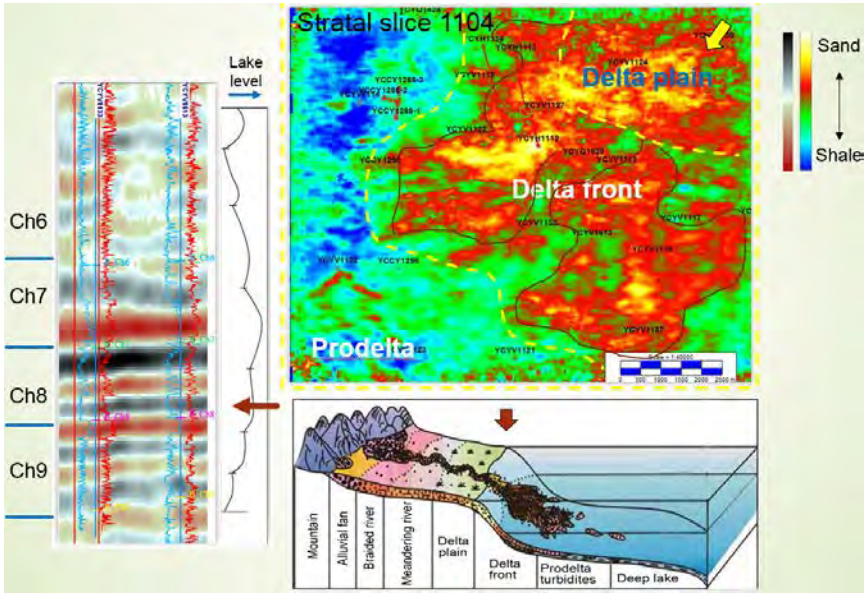

Figure 10. A representative stratal slice at lower Chang 8 member and its stratigraphic, interpreted lake-level, and general depositional model position.

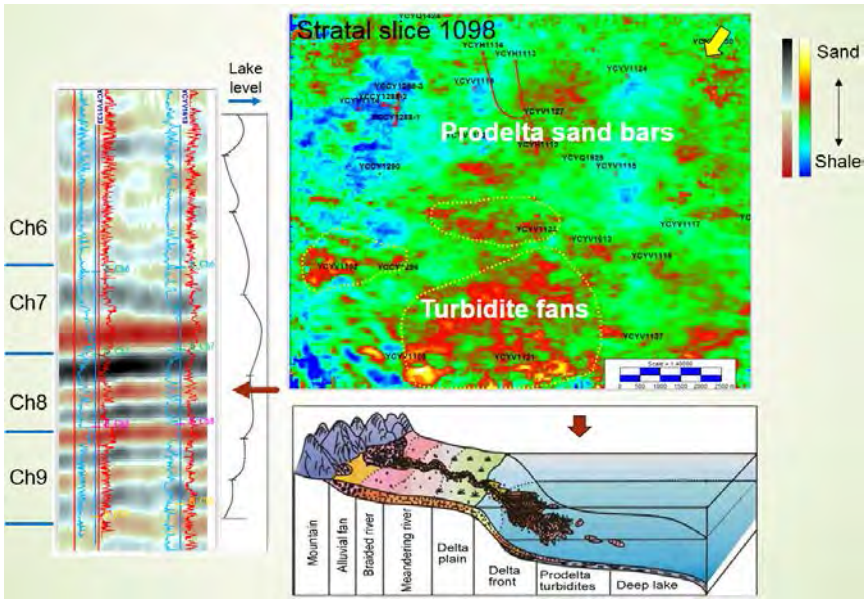

Figure 11. A representative stratal slice at mid-Chang 8 member and its stratigraphic, interpreted lake-level, and general depositional model position.

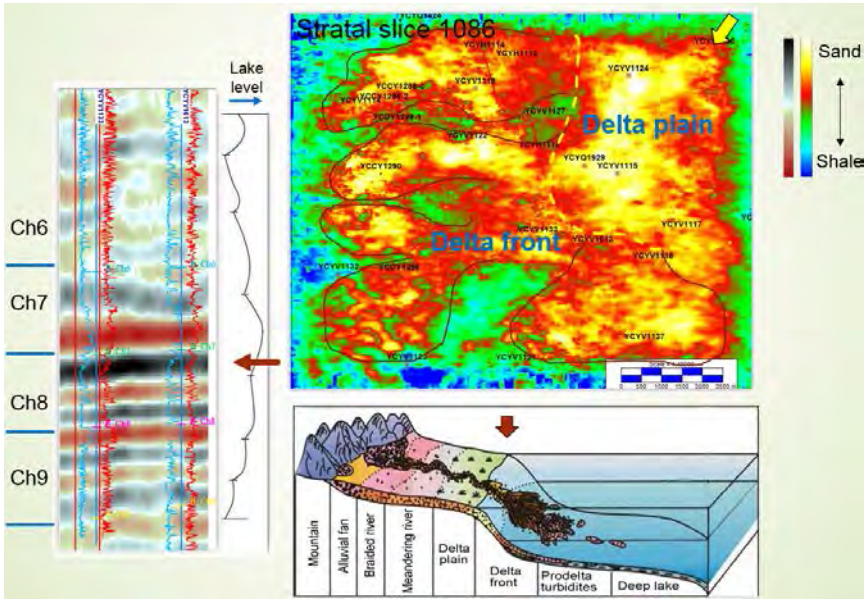

Figure 12. A representative stratal slice at upper Chang 8 member and its stratigraphic, interpreted lake-level, and general depositional model position.

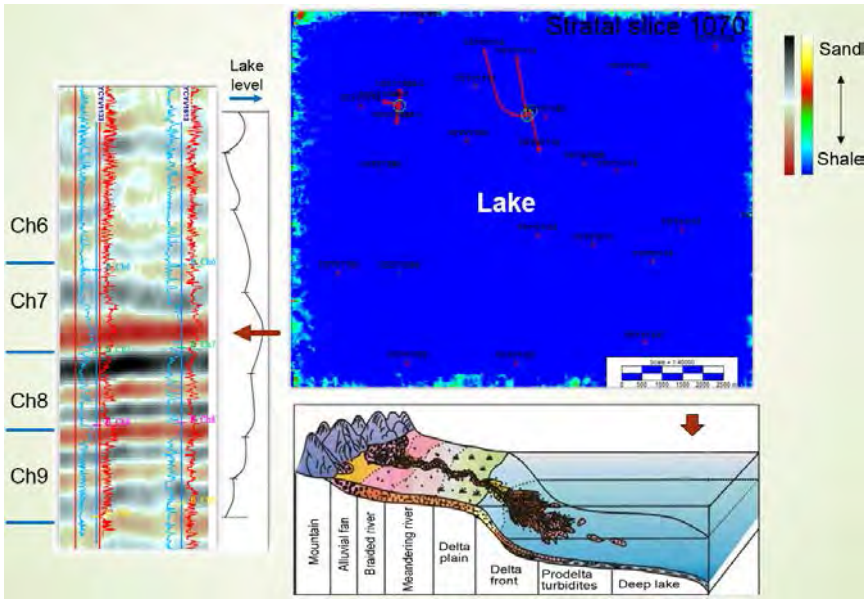

Figure 13. A representative stratal slice at lower Chang 7 member and its stratigraphic, interpreted lake-level, and general depositional model position.

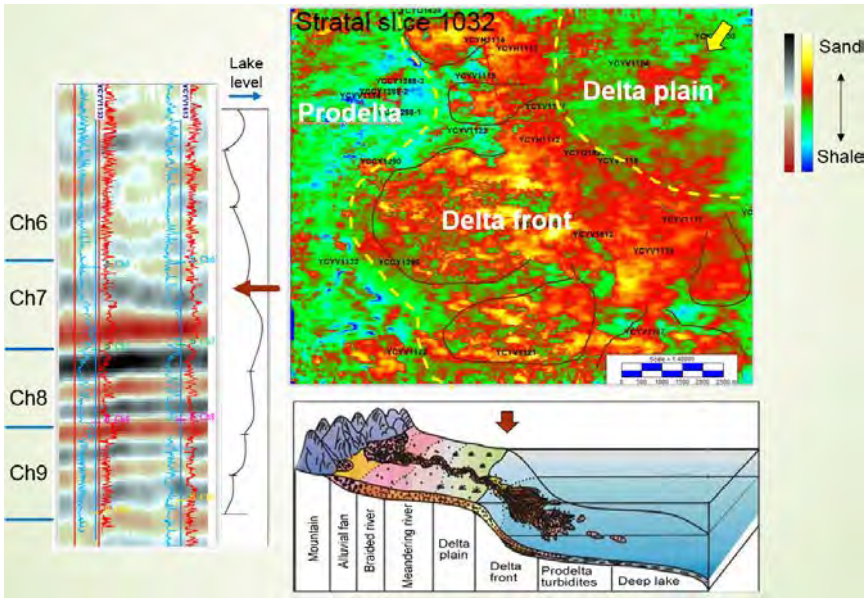

Figure 14. A representative stratal slice at upper Chang 7 member and its stratigraphic, interpreted lake-level, and general depositional model position.

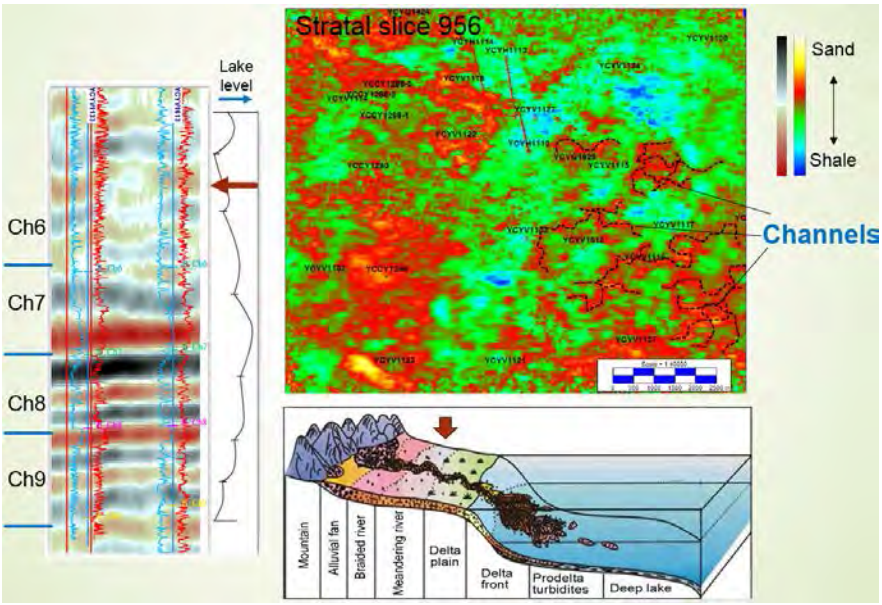

Figure 15. A representative stratal slice in Chang 6 member and its stratigraphic, interpreted lake-level, and general depositional model position.

Facies model of Chang 7 deltaic system in the study area

Developed at maximum lake expansion period, the Chang 7 member demonstrated all necessary components of a lacustrine deltaic system. In a dip well-seismic AI section (**fig. 16a**), AI traces are of enough resolution to divide the Chang 7 member into three submembers (from bottom to top): Chang 7-3, Chang 7-2, and Chang 7-1.

- These submembers are characterized by distinctive log patterns in an upward-coarsening trend: Chang 7-3 is high-gamma, low-velocity unit, followed by moderate-gamma and velocity in Chang 7-2, and low-gamma, high-velocity Chang 7-1. Correlating to the core descriptions (Task? Kitty), these submembers were identified as shale, thinly interbedded sandstones and shale beds, and thick sandstones, respectively, in YCYV1133 and YY1 wells (core section inserts, **fig. 16b and 16c**).

- These submembers were also detected as having quite different AI trends. AI values consistently increase from Chang7-3 to Chang 7-1, with clear boundaries. Whereas Chang 7-3 and Chang 7-1 are more or less sheetlike, the Chang 7-2 submember thickens significantly to the source direction (NE).

In the previous section, we interpreted the Chang 7-3 submember as deep lake facies (**fig. 13**), and the Chang 7-1 submember as delta plain, delta front, and prodelta facies (**fig. 14**). In between, the **Chang 7-2** submember should be predominantly prodelta facies. As summarized in **Figure 16d**, all three submembers are necessary components of a deltaic system. Interpreted depositional time lines (super-high-frequency depositional episodes) should cut through the

facies boundaries. Apparently, seismic reflections (and AI units) do not necessarily follow these depositional time lines.

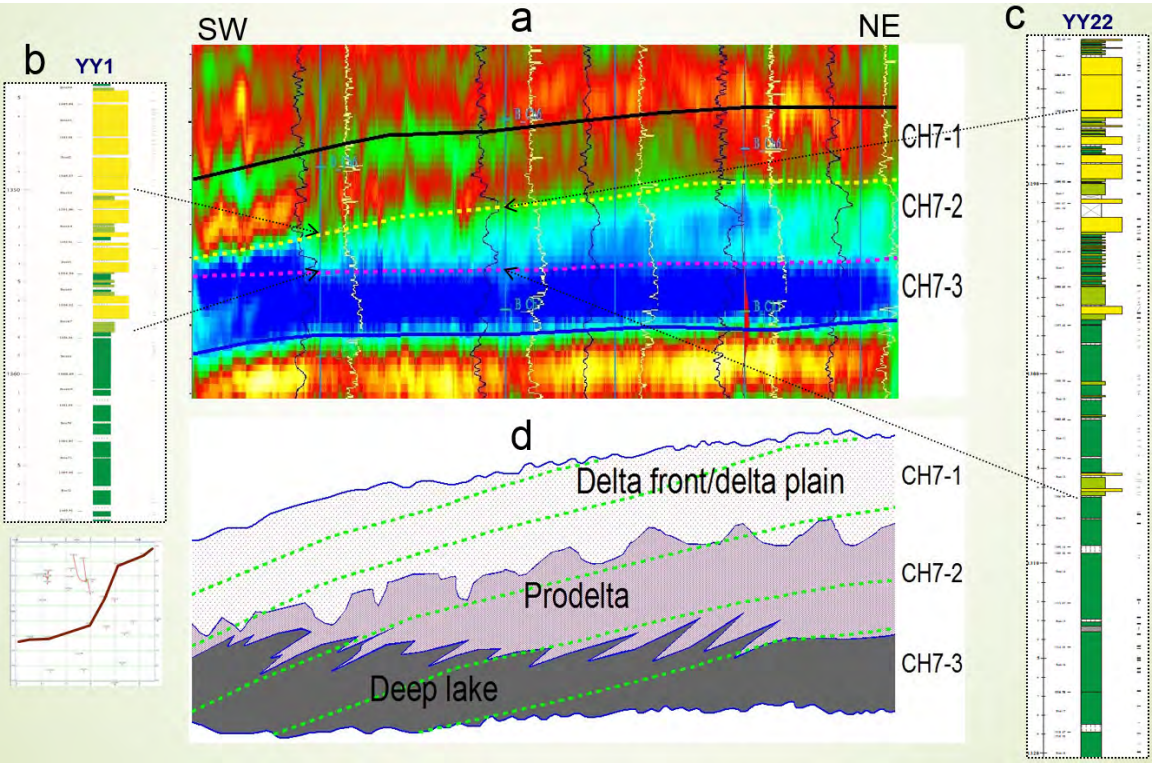

Figure 16. Facies model of the Chang 7 member. (a) Well-seismic AI section (see inserted base map for location). (b) Core section in the YY1 well. (c) Core section in the YCYV1133 well. (d) Facies model interpreted from (a). Green lines denote depositional time lines.

Link seismic lithology and facies to TOC and rock brittleness

In previous sections, we discussed seismic expression of lithology and facies. However, this information cannot be used to evaluate shale-gas reservoir quality before being linked to rock mechanical properties. Fortunately, the wireline lithology log (GR) demonstrated an excellent correlation to 90° and AI traces (**figs. 5b and 6**). As a result, the GR log could be ideal for serving as a bridge between the seismically-derived lithology and facies maps and core-derived TOC, contents of clay and brittle minerals (XRD), and mechanical measurements, which are readily available from the YY1 well.

- TOC measurements and the GR log fit quite well (**fig. 17a**). In general, high TOC correlates to API, and vice versa. The intervals with super-high GR values (>140 API) are exceptions, within which no correlation was observed. As shown in Figure 17b and c, both uranium and potassium contents do not increase in those intervals. Therefore, those zones are not highly radioactive volcanic ash layers. Although still mysterious to us at the present, those high-API zones should be disregarded when calculating clay content using GR (e.g., set 140 API as 100% shale volume).

- Content of clay minerals (sum of illite/mica, kaolinite, and chlorite) has a fair correlation to GR log (**fig. 18**). Except at the three high-API zones, API increases with content of clays (**fig. 18a**). If high API values are removed, a linear trend between the two exists (**fig. 18b**).

- Similarly, content of brittle minerals (sum of quartz and carbonates) has a reasonable correlation to the GR log (**fig. 19**). Except at the three high-API zones, API decreases with content of brittle minerals (**fig. 19a**). Similarly, if high API values are removed, linear trend exists between the two variables (**fig. 19b**).

- Bambino and USC data from core samples correlate well to the GR log except at the three high-API zones (**fig. 20**). That is, sandy rocks are mechanically stronger than shales, and therefore are probably more brittle.

- Finally, a log-based classification of rock brittleness can be calculated by first computing Young's modulus (E) and Poisson's ratio (σ) from Vp, Vp, and bulk density logs and then cross-plotting the two parameters with color-coded AI (**fig. 21a**). Apparently the double-peak (shale and sand) E is a better parameter to define brittleness; the single mode σ is less effective. For practical purpose, we simply call brittle and sub-brittle rocks as brittle, and ductile and sub-ductile rocks as ductile. Those classes of brittleness fit to the lithology log (GR) quite well (**fig. 21b**), with sections of sandstone and shaly sandstone more brittle and sections of shale and sandy shale more ductile.

As a conclusion, seismically-derived lithology/facies can be reliably used to evaluate TOC, clay content, and brittleness in a qualitative sense.

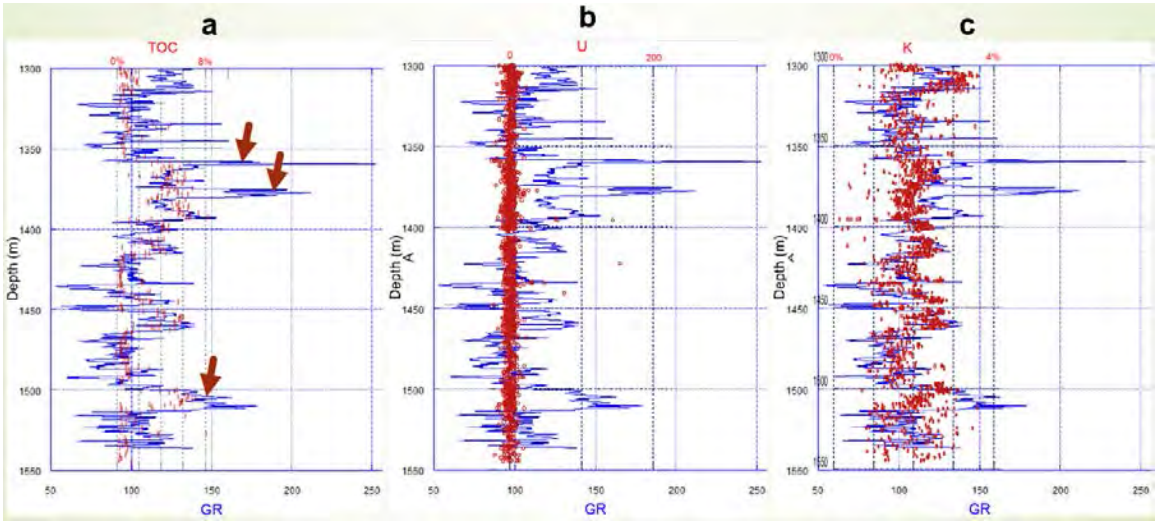

Figure 17. Relationship between the gamma-ray log and lab-measured TOC (a), and uranium (b) and potassium (c) contents in the YY1 well. Arrows refer to high-API zones.

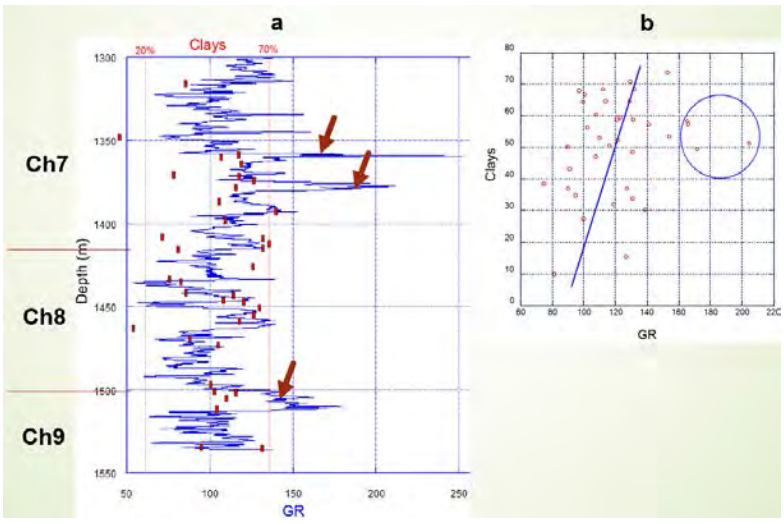

Figure 18. Relationship between gamma-ray log and lab-measured content of clay minerals. (a) Gamma-ray log and superimposed clay content. (b) Scattered plot.

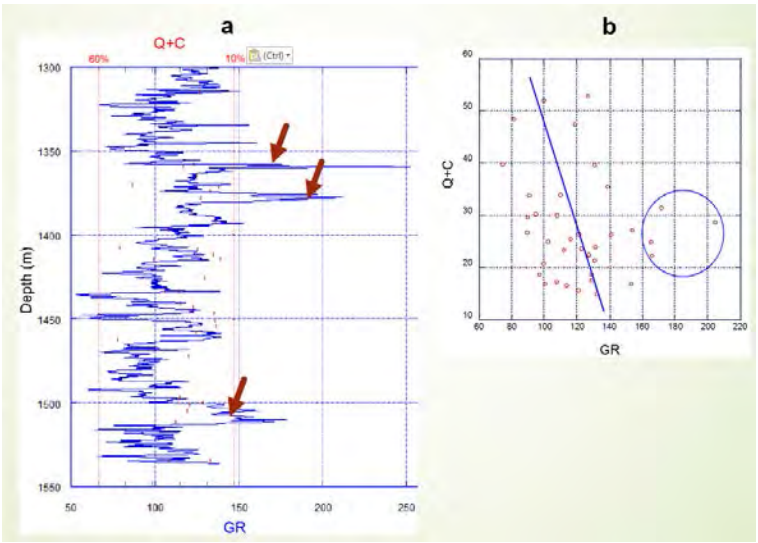

Figure 19. Relationship between gamma-ray log and lab-measured content of brittle minerals. (a) GR log and superimposed content of quartz and carbonate minerals. (b) Scattered plot.

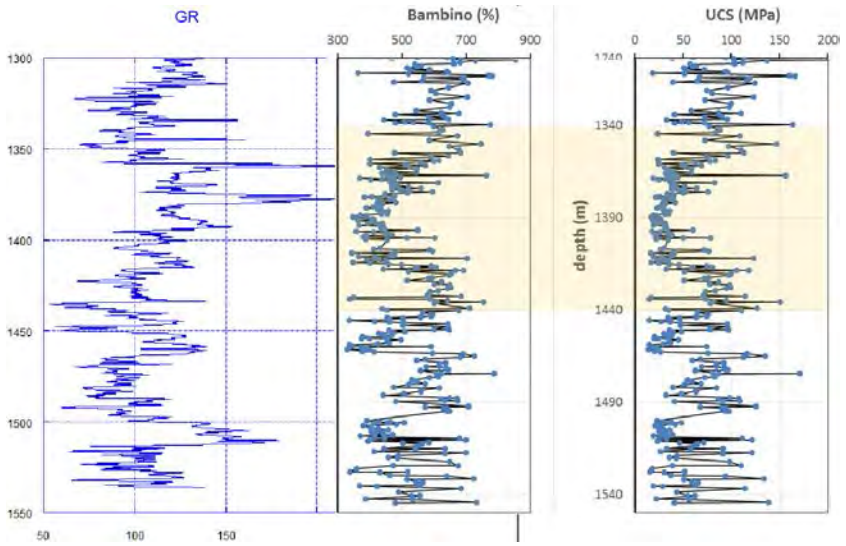

Figure 20. Relationship between gamma ray log and core-measured mechanical properties (Bambino and USC).

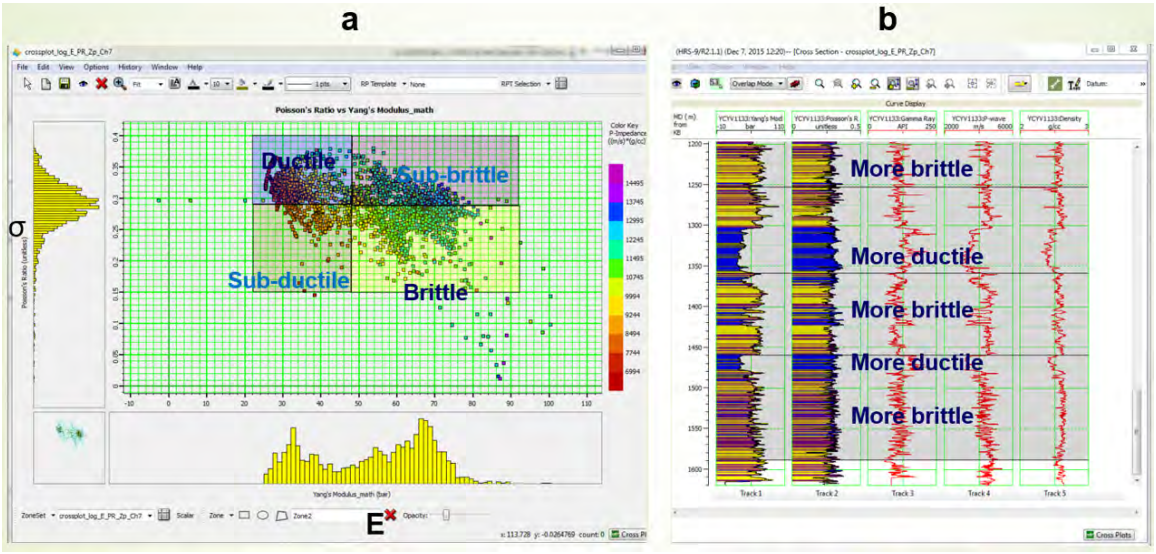

Figure 21. Wireline-log-based classification of rock brittleness and its relationship to the lithology curve gamma ray).

Reservoir performance as measured by microseismic data

In the study area, hydraulic fracturing work has been conducted in two inclined wells and three horizontal wells (**fig. 1**). In each of these wells, a microseismic survey was performed to record location and strength of microseismic events corresponding to multiple stages of high-pressure fluid injection along the well track. Those data were edited, magnitude-calibrated, and being tied to 3D seismic volume with proper time-to-depth curves.

In horizontal well YCYH1114 (**fig. 1**), the microseismic data were projected against, and plotted along, the well track on the AI section (**fig. 22**). The well track is at the center of Chang 7-3 high-TOC shale unit. It was surprising to observe that most of the microseismic events,

especially those stronger events (larger circles) are not located inside the Chang 7-3 shale unit near the borehole but instead are mostly in Chang 8 and Chang 7-1 units away from the borehole. Further analysis revealed that lithology has a significant influence on the strength and distribution of microseismic events. Along the borehole in the Chang 7-3 shale unit, the more sandy segment (left of the horizontal well track) has more microseismic events than the more shaly segment (right of the horizontal well track); away from the borehole in the Chang 8 and Chang 7-1 sandy units, number and strength of the microseismic events increase dramatically.

Because the rock brittleness is closely related to lithology, we also observed similar phenomena on the Young's modulus section (**fig. 23**). Along the borehole in the Chang 7-3 shale unit, the more brittle segment has more microseismic events than does the more ductile segment; away from the borehole in more brittle rocks in Chang 8 and Chang 7-1 sandy units, the microseismic events increase significantly.

These observations prompted us to surmise that the reservoir performance in the available wells have been controlled by what we call the "tunnel effect" (**fig. 24**). The thick, high-TOC Chang 7-3 shale unit is most ductile rock in the study area. A fracking operation conducted along the horizontal well track within this unit generated only a small number of fractures (tunnels or conduits); when those fractures reached the Chang 8 and Chang 7-1 sections away from the well track, more brittle rocks responded to the high-pressure fluid via these tunnels much more efficiently, leading to many more open fractures. Those open fractures, however, became idle when the fracture tunnels in the shale section healed themselves after the fracking, resulting in a low production rate in those wells.

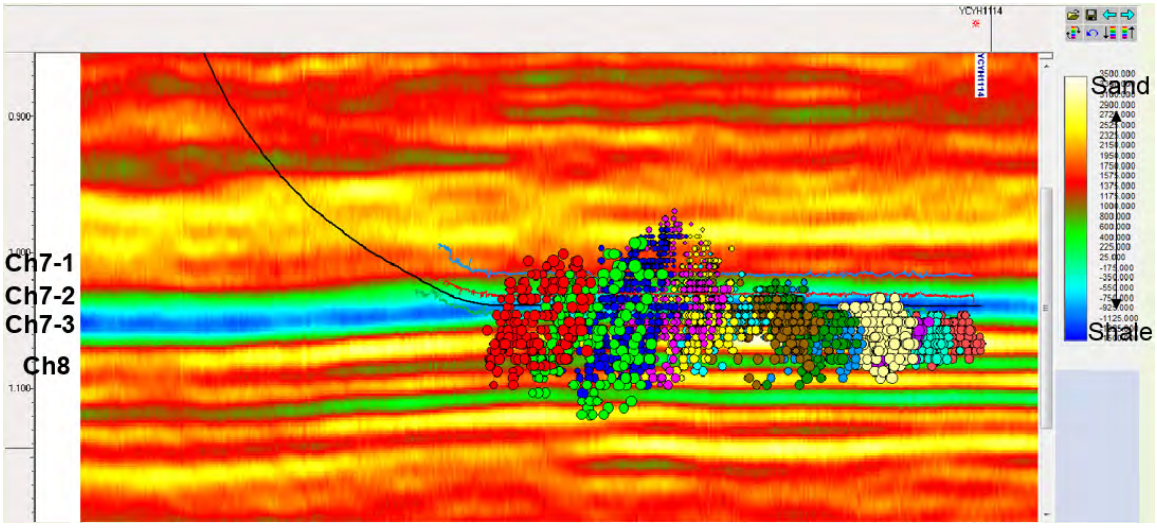

Figure 22. Density and strength of microseismic events in YCYH1114 well, displayed on AI section.

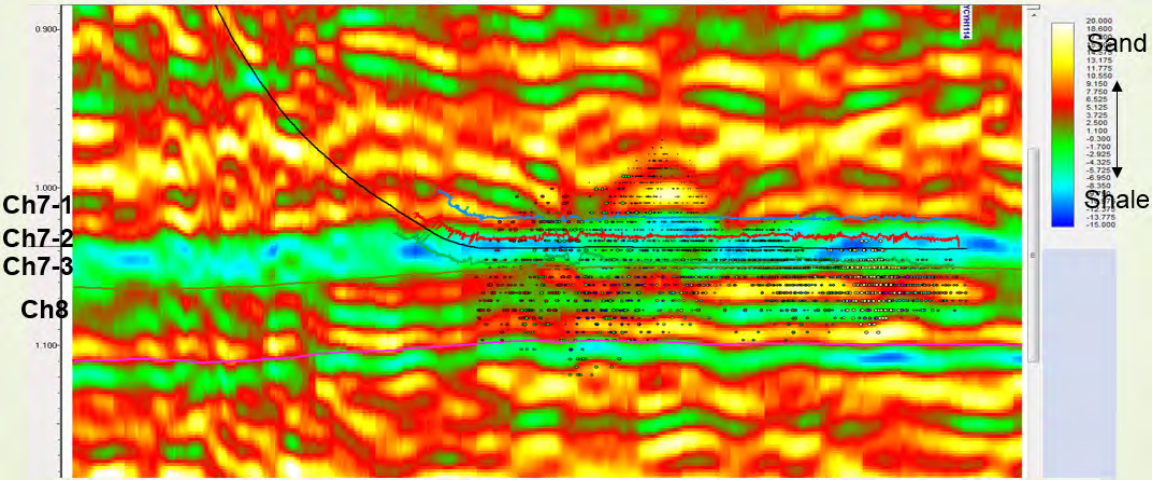

Figure 23. Distribution of microseismic events in the YCYH1114 well, displayed on the Young's modulus section.

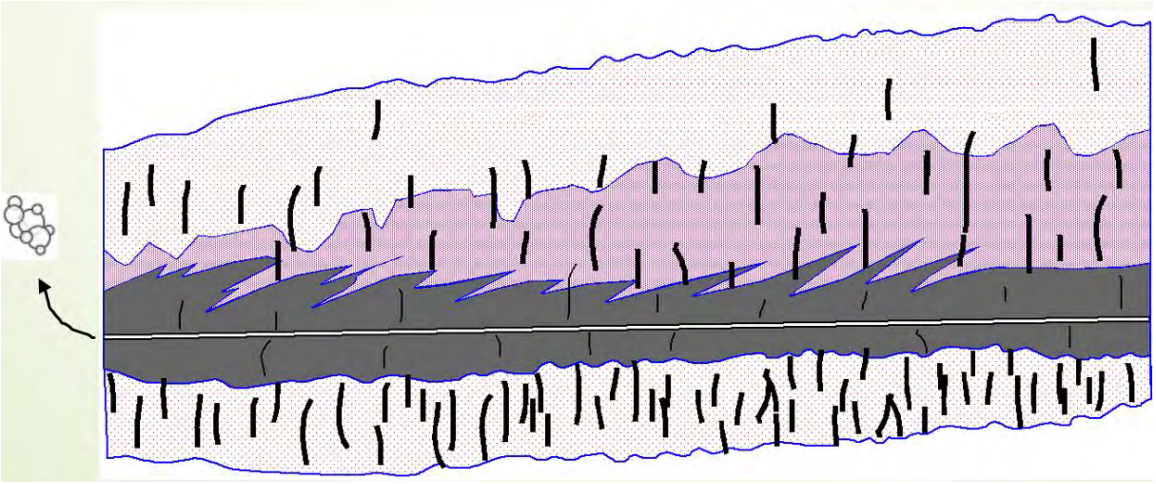

Figure 24. Tunnel effect.

Prediction of sweet spots

On the basis of core, log, and seismic analysis, we conclude that the thick, clay-rich, high-TOC shale in the Chang 7-3 submember is less ideal for shale-gas development in the study area. A more desired target, or sweet spot, should satisfy three conditions:

- 1. Proximity to high-TOC shale (Chang 7-3) for adequate supply of gas
- 2. A large volume (thickness) of rock mass for adequate gas reserve and space for the fracking operations
- 3. A unit dominated by brittle rocks, ideally thinly interbedded sand/shale sections, similar to those in the Marcellus or Bakken shale plays in the US.

Fortunately, Chang 7-2 prodelta sediments in the study area (**fig. 16**) meet these conditions. The Chang 7-2 unit immediately overlies Chang 7-3, the high-TOC unit, which is 20 m to 40 m thick in most of the study area (**fig. 25**); thickening to the northeastern corner, Chang 7-2 unit can be as thick as 50 m (fig. 26); more important, this unit is dominated by thinly interbedded prodelta sandstone, siltstone, and shale (core sections, **fig. 16**), presenting more brittle rocks that are more responsive to fracking, as shown in the YCYH1114 well (**figs. 22 and 23**). A stratal slice (**fig. 27**) in the Chang 7-2 unit illustrates multiple prodelta sand bars in the NE study area. Specifically, the drilling should be concentrated in the area where the Chang 7-2 unit is thicker than 30 m.

There are other favorable new drilling targets in the sandier Chang 8, Chang 7-1, and Chang 6 submembers. However, they do not meet current definitions of shale gas plays.

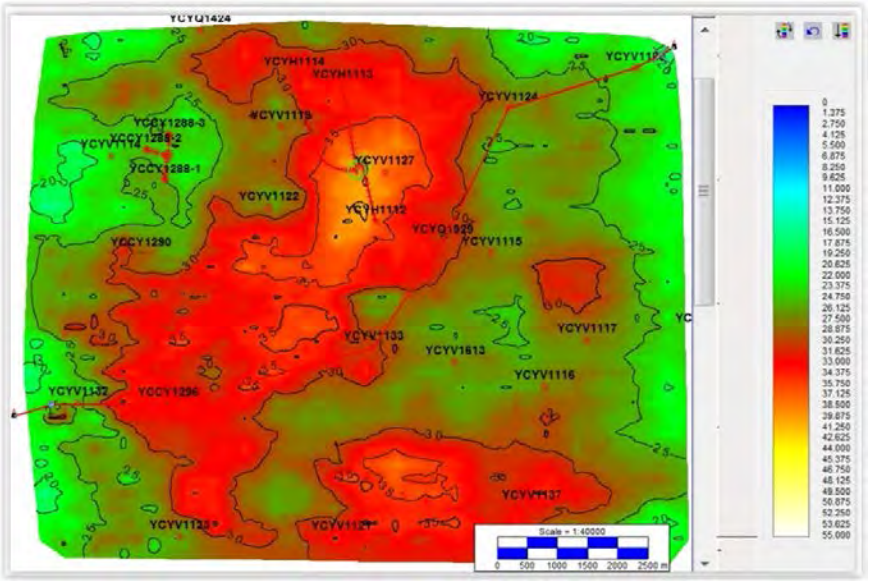

Figure 25. Thickness (m) of the CH7-3 submember. See **Figure 16** for position.

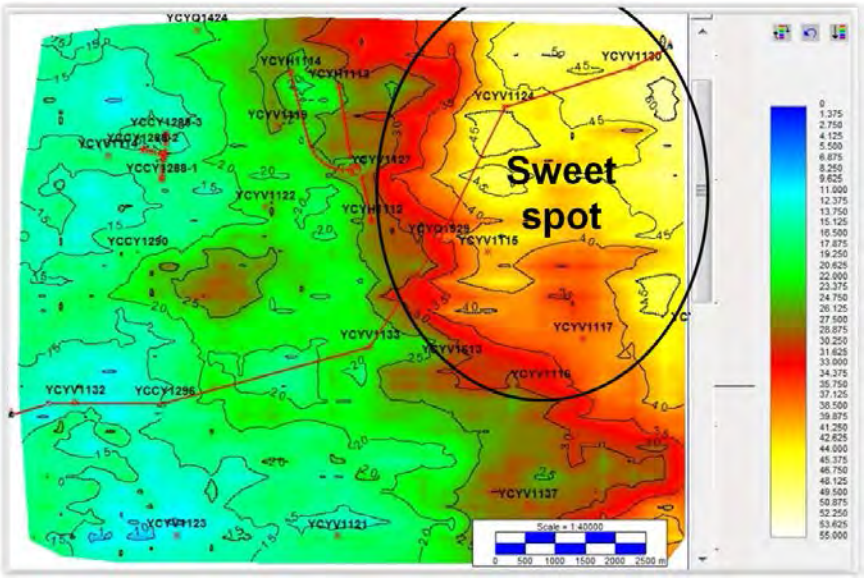

Figure 26. Thickness (m) of the CH7-2 submember. See **Figure 16** for position.

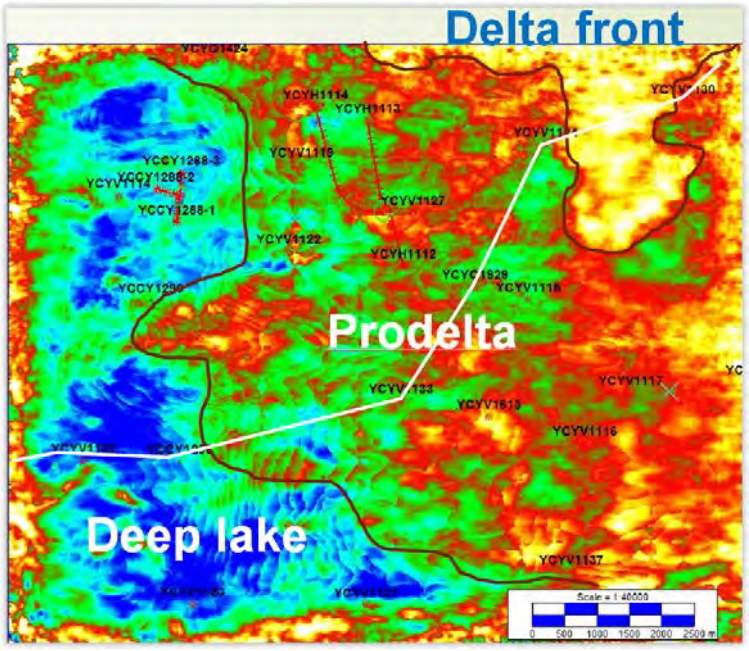

Figure 27. Facies interpreted on stratal slice in the Chang 7-2 unit.

Conclusions

1. Seismic amplitude and AI can be correlated to log lithology at a resolution of approximately 10 m.

2. Log lithology can be correlated to content of brittle/clay minerals.

3. The Chang 7 member is interpreted as a deltaic sequence, including three seismic units (from top): delta plain/delta front (Chang 7-1), prodelta (Chang 7-2), and deep lake (Chang 7-3) facies.

4. Analysis of stratal slices and microseismic data suggests that the Chang 7-3 shale unit is less favorable for shale-gas drilling and fracking because of its ductile nature and tunnel effect. Most of the induced fractures are in sandy sections (Chang 8, Chang 7-1, and Chang 6)

5. The more brittle, sandy Chang 7-2 interval thickens to as much as 50 m to the northeast and is the sweet spot for future exploration

Acknowledgments

We acknowledge the use of results in other tasks completed by team members. We thank Shaanxi Yanchang Petroleum (Group) for providing well and seismic data and for permitting us to present this study. IHS provided Kingdom software for interpretation and display of seismic data.

References

Cheng, S., Jiang, Y., Li, J., Li, C., Wang, Y., and Xu, L., 2015, Reservoir prediction in a development area with a high-density well pattern using seismic sedimentology: an example from the BB2 block, Changyuan LMD oil field, Songliao Basin, China: Interpretation, v. 3, no. 3, p. SS87–SS99.

Pecholcs, P. I., Al-Saad, R., Al-Sannaa, M., Quigley, J., Bagaini, C., Zarkhidze, May, R., Guellili, M., Sinanaj, S., and Membrouk, M., 2012, A broadband full azimuth land seismic case study from Saudi Arabia using a 100,000 channel recording system at 6 terabytes per day: acquisition and processing lessons learned (ext. abs.), *in* SEG Annual Meeting, Las Vegas, 5 p.

Posamentier, H. W., 2000, Seismic stratigraphy into the next millennium: a focus on 3D seismic data (abs.): AAPG Annual Convention Program, v. 9, p. A118.

Zeng, H., Backus, M. M., Barrow, K. T., and Tyler, N., 1998a, Stratal slicing, part I: realistic 3-D seismic model: Geophysics, v. 63, no. 2, p. 502–513.

Zeng, H., Henry, S. C., and Riola, J. P., 1998b, Stratal slicing, part II: real seismic data: Geophysics, v. 63, no. 2, p. 514–522.

Zeng, H., and Hentz, T. F., 2004, High-frequency sequence stratigraphy from seismic sedimentology: applied to Miocene, Vermilion Block 50, Tiger Shoal area, offshore Louisiana: AAPG Bulletin, v. 88, p. 153–174.

Zeng, H., Zhu, X., Zhu, R., and Zhang, Q., 2011, Ultra-thin, lacustrine sandstones imaged on stratal slices in the Cretaceous Qijia Depression, Songliao Basin, China (ext. abs.), *in* SEG Annual Meeting, San Antonio, p. 951−955.

Zubay, E., Cunnell, C., Zarkhidze, A., Baioumy, M., Viertel, H., and Al Qadi, A., 2013, Complex depth imaging using reverse time migration for an integrated high-density point-source and receiver survey onshore U.A.E.—a case study (ext. abs.), *in* SEG Annual Meeting, San Antonio, p. 3872−3876.

Conclusions Summary

During the past 2 years, researchers from Bureau of Economic Geology (BEG) and Yanchang Petroleum Group (Yanchang) worked closely to conduct an integrated research project titled "Lacustrine Shale Gas Reservoir Characterization in the Yanchang Formation by Integrated Geological Facies, Geochemistry, Chemostratigraphy, SEM Pore Imaging, Petrography, and Geophysics." Project objectives were to provide integrated studies of geological facies, hydrocarbon geochemical characterization, chemical stratigraphy, SEM pore imaging, and detailed petrographic study. These aspects were to be integrated to yield broader concepts on hydrocarbon generation and storage, as well as on the distribution of geological facies and fundamental rock attributes. In addition, models were to be developed for evaluating sweet spots for shale gas that can be applied in making economic decisions.

A large amount of new data collection has been conducted during the 2 years of the project. More than 60,000 raw data for 23 new analytical items, 15 GB of petrographic data (light microscope, X-ray elemental mapping, and cathodoluminescence imaging), 25 GB of SEM pore imaging data, and 216 core pictures were collected. Twenty oral presentations, 9 poster presentations, three reports, and five abstracts were given in annual and final project review meetings. Key results will be published in an Interpretation Special Section titled "Lacustrine Shale Characterization and Shale Resource Potential in Ordos Basin, China," in May 2017.

The following new and significant discoveries and concepts were produced from the integrated study:

1. A depositional model of the lithofacies of the Triassic Yanchang Formation was established. Four lithofacies, including (1) OM-rich argillaceous mudstone, 2) OM-lean argillaceous mudstone, (3) quartzose feldspathic arkose (siltstone and sandstone), and (4) feldspathic quartzose arkose (siltstone and sandstone) were determined for Yanchang Formation based on high-resolution XRF and XRD data. The organic-lean and organic-rich argillaceous mudstones were deposited in a deeper water lacustrine setting during lake highstands. Arkosic sandstone at the top of Chang 7 in Chang 6 were likely deposited in a more proximal deltaic setting.
2. Four flooding surfaces were defined, each of which represents basin deepening and serves as a possible correlation event. Each event is marked by the superposition of OM-rich mudstones over more proximal arkosic siltstones and sandstones. In addition to the surfaces that form the base and top of Chang 7, two surfaces were defined in Chang 8.
3. General facies types can be interpreted from most wireline logs but detailed correlations require consideration of all log responses. Variations in organic matter are well defined by density and resistivity wireline logs. Chemostratigraphy and TOC results indicate a significant linkage between TOC and %Al (a proxy for clay mineral content), and a positive relationship between enhanced TOC and %S (a proxy for pyrite content). Rock strength varies inversely with clay mineral and organic matter abundance. Because of their high clay mineral content, mudstones are relatively ductile and probably poor candidates for hydraulic fracturing.

4. The argillaceous mudstones and siltstones are immature mineralogically. The siltstones are lithic arkoses and/or arkosic litharenites. The high clay-mineral content, generally greater than 40%, has promoted extensive compaction of the sediments, occluding nearly all the primary interparticle pores, thus greatly reducing reservoir quality. The high clay-mineral content does not favor hydraulic fracturing of the mudstone reservoir.
5. The dominant diagenetic processes in the mudstones are compaction and organic maturation. Texturally, the mudstones of the Yanchang Formation are silt-bearing and silt-rich argillaceous mudstones. Greater silt content in the mudstones is correlated with the preservation of larger pores. Compositionally, mudstones of the Yanchang Formation are rich in quartz, feldspars, and clay minerals. The Yanchang mudstones have little cement, and the cement that is present is located primarily in anomalously large intragranular pores.
6. The pore network within the mudstones is dominated by intraparticle pores with a lesser abundance of OM-hosted pores. Interparticle pores are rare. Mean Gas Research Institute (GRI) porosity is 4.19%. Because the pore network is dominated by intraparticle pores and because the average pore size is very small, permeability is low (GRI estimated geometric mean permeability = 9.86 nd). The dominance of ineffective intraparticle pores creates a very weak correlation between GRI porosity and permeability.
7. Compaction and organic maturation are the main controls on porosity evolution in the lacustrine Yanchang Formation. Variation in texture, as expressed by silt content, and OM-content affect the pathways of porosity modification during compaction and maturation. Silt content is associated with the preservation of intergranular mineral-hosted, larger pores (> 20 nm). OM content, which is higher in relatively silt-poor samples, is associated with the loss of large pores and the generation of very small (< 10 nm), spongy, OM-hosted pores.
8. The OM-rich mudstone is a good-to-excellent source for oil generation potential. Carbon isotope data suggest that mudstones contain primarily aquatic organic matter, whereas arkoses contain terrestrial organic matter. Organic matter type varies in different depositional facies, and organic matter type is dominated by oil-prone Type I and II kerogens in deep lake facies, a mixture of Type II and III kerogens in prodelta facies, and Type III kerogen in delta plain/delta front. Its thermal maturity is in the oil window. The lower part of the Chang 7 member, a 25-m-thick organic-rich interval, contains a large amount of free oil and gas. It is the target for shale gas/oil exploration in terms of potential resources.
9. Models for gas storage in OM-rich mudstones show that both clay minerals and organic matter provide spaces for adsorbed gas and free gas storage. The Ordos basin is an exhumed sedimentary basin, and the exhumation causes a significant amount of free gas loss, and the extent of gas loss varies with burial depth. The presence of oil and water greatly reduce gas saturation. The estimated free gas capacity is from 1.75 million cubic meter (MMcm) to 4.75 MMcm in per million cubic meters of the Chang 7 organic-rich mudstone reservoir, which as a 4% total porosity.

10. Pore-network models were developed to simulate slip-corrected liquid flow and thus to determine apparent fluid permeability. Pore-network simulation results reveal that pore geometry and slip effect play important roles in fluid flow. If we ignore noncircularity of pores and assume that all pores are circular, our estimates of apparent permeability would be incorrect by factors of 2.5 to 9.0.
11. Field seismic data were reprocessed to fit the needs for high-resolution, high-fidelity prediction of lithology, rock properties, and fracking performance. A novel and creative workflow was adopted to suppress noise and to improve resolution, post and prestack inversion, and microseismic data analysis.
12. Integration of seismic, chemostratigraphy, and lithology from wireline logs was used to predict sweet spots. Seismic amplitude and acoustic impedance can be correlated to log lithology at a resolution approximating 10 m. The Chang 7 member includes three seismic units (from top to bottom): (1) delta plain/delta front (Ch 7-1), (2) prodelta (Ch 7-2), and (3) deep lake (Ch 7-3) facies. The Ch 7-3 mudrock unit is unsuitable for shale-gas drilling and fracking because of its low porosity and permeability, ductile properties, and interbedded sandy/muddy layers, which produce varied frackability (a tunnel effect). The more brittle, sandy Ch 7-2 interval, which thickens to as much as 50 m to the northeast, is recommended as the target zone, with a possible sweet spot to the northeast.

Appendix: Presentations and Publications Related to This Project

Oral presentations given at annual project review meeting in Xi'an, China, January 6–7, 2015:

1. Eric Potter, Brief Introduction to Research Progress of the Project
2. Eric Potter, U.S. Unconventional Resources
3. Harry Rowe and Bojiang Fan: Yanchang Formation: Elemental Geochemistry, Chemostratigraphy, and Mineralogy
4. Kitty Milliken and Ying Shen: Petrography of Units Chang 7, 8, and 9
5. Kitty Milliken: Predicting Mudrock Properties: Lessons from Conventional Reservoirs and a Look to the Future in Fine-Grained Systems
6. Bob Loucks and Patrick Smith: Yanchang Pore Network Investigation Update
7. Tongwei Zhang and Jianfeng Zhang: Pore Size Distribution of Yanchang Formation Lacustrine Shale by Using N2 Adsorption and Desorption Isotherms
8. Tongwei Zhang, Xun Sun, Daniel Enriquez, and Jianfeng Zhang: Organic Matter Type, Thermal Maturity, Oil and Gas Expulsion in Yanchang Formation
9. Chao Gao and Hongliu Zeng: Wireline Logs Analysis for Shale Properties
10. Hongliu Zeng and Wei Wang: 3D Seismic Acquisition, Processing, and Preliminary Interpretation

Poster presentations given at annual project review meeting in Xi'an, China, January 6–7, 2015:

1. Harry Rowe and Bojiang Fan: Chemostratigraphy of the Yanchang YY1 Core, Ordos Basin, China
2. Kitty Milliken and Ying Shen: Assessing Grain Assemblages by EDS X-Ray Mapping
3. Kitty Milliken and Ying Shen: Assessing Quartz Cementation with Scanned Cathodoluminescence Imaging
4. Tongwei Zhang, Jianfeng Zhang, and Daniel Enriquez: Pore Characterization of Triassic Organic-Rich Yanchang Mudstone by Using N2 Adsorption and Desorption Isotherms
5. Chao Gao and Hongliu Zeng: Wireline Logs Interpretation of YCYV1133 Well
6. Hongliu Zeng and Wei Wang: 3D Seismic Interpretation

(continued)

Oral presentations given at final project review meeting in Austin, Texas
December 15 -16, 2015:

1. Harry Rowe et al., Mineralogy, Elemental Chemistry, and Chemostratigraphy of the Triassic Yanchang Formation
2. Kitty Milliken et al., Petrology and Diagenesis in Organic-rich Mudstones Dominated by Extrabasinal Sediment Sources, Yanchang Formation (Triassic), Ordos Basin, China
3. Bob Loucks et al., Investigation of Yanchang Pore Types, Pore Networks, and Reservoir Quality
4. Patrick Smith, High-Resolution Microscopic Analysis of YY Shale
5. Sheng Peng, Porosity, Permeability, Pore Size Distribution and Fluid Pore Filling
6. Tongwei Zhang, Pore Characterization and Oil Storage in Yanchang Formation
7. Paul Hackley, Organic Petrography and Organic Matter Studies
8. Tongwei Zhang et al., Gas and Organic Geochemistry, Thermal Maturity, Organic Matter Type in Yanchang Formation
9. Ali Afsharpoor et al., Pore-Scale Modeling of Liquid Flow in Shale
10. Hongliu Zeng et al., 3D Seismic Interpretation and Sweet-Spot Prediction

Poster presentations given at final project review meeting in Austin, Texas
December 15 -16, 2015:

1. Kitty Milliken et al., YY1 core description
2. Kitty Milliken et al., YY22 core description
3. Tongwei Zhang et al., Insights into Reservoir Development Based on Integrated Studies of Organic Matter and Pores

Reports:

Annual report: 100 pages

Research progress report from January 2015 to July 2015: 30 pages

Final report: 312 pages

Publications (including manuscripts and abstracts):

Kitty L. Milliken, Xiangzeng Wang, Ying Shen, Quansheng Liang, Tongwei Zhang, Bob Loucks, and Harry Rowe, 2015: Grain Assemblages in Organic-Rich Mudstones Dominated by Extrabasinal Sediment Sources, Yanchang Formation (Triassic), Ordos Basin, China. Abstract submitted to AAPG 2015 International Convention and Exhibition, Melbourne, Australia.

Tongwei Zhang, Xiangzeng Wang, Jianfeng Zhang, Kitty L. Milliken, Harry Rowe, Ying Shen, and Bojiang Fan, 2014: Insights into reservoir development based on integrated studies of organic matter and pore size in a lacustrine shale: Triassic Yanchang Formation, Ordos Basin, China. Abstract submitted to AAPG 2015 Annual Convention and Exhibition, Denver, Colorado.

Harry Rowe, Xiangzeng Wang, Bojiang Fan, Tongwei Zhang, Kitty Milliken, Ying Shen, and Jianfeng Zhang, 2015: Chemostratigraphy of the Triassic Yanchang Fluvio-Lacustrine Succession, Ordos Basin, Shaanxi Province, China. Abstract submitted to AAPG 2015 International Convention and Exhibition, Melbourne, Australia.

Hongliu Zeng, Xiangzeng Wang, and Wei Wang, 2015, Applying sedimentology to high-resolution depositional-facies mapping in Triassic Yanchang Formation, Erdos Basin, China. 2015 SEG Conference.

Interpretation Special Section: Lacustrine shale characterization and shale resource potential in Ordos Basin, China

Manuscript submission deadline:	1 July 2016
Peer review complete:	26 November 2016
All files submitted for production:	9 December 2016
Publication of issue:	May 2017

Acknowledgments

This project is financially supported by the Yanchang Petroleum Group, under joint research agreement UTA13-000690 between The University of Texas at Austin and the Research Institute of Shaanxi Yanchang Petroleum (Group) Company, Ltd.

The Chemostratigraphy Laboratory, Gas Geochemistry Laboratory, Petrophysics Laboratory, and SEM Laboratory at the Bureau of Economic Geology at The University of Texas at Austin have provided XRF-analysis, fast XRD-analysis, gas and residual oil compositional analysis, and lithology and pore imaging, N_2 pore size distribution, and He GRI porosity and permeability data for the project. Five researchers from Yanchang worked in these laboratories and collected firsthand analytical data sets.

The Research Institute of Shaanxi Yanchang Petroleum has provided tremendous help in core sampling, XRF on-site core scanning, and gas sampling from production wells. The Research Institute has also provided 3D seismic survey data and well-logging data, which are the foundations for Tasks 5 and 6.

Paul Hackley from the Organic Petrography Laboratory of the U.S. Geological Survey measured bitumen reflectance and wrote the Task 4.2 section of this report. Zeiss, Inc., provided Low-Voltage High-Resolution SEM pore images. Whole-rock and clay-fraction XRD analyses were conducted by K-T GeoServices, Inc., and RockEval analyses were conducted by GeoMark Services.

In particular, we would like to acknowledge the helpful work by the administrators of both organizations for contract management and for arranging UT-Austin researchers' travel logistics in Xi'an and the Yanchang Petroleum Group researchers' logistics to and in Austin.

At the Bureau of Economic Geology, Amanda R. Masterson edited the manuscript, assisted by Jamie H. Coggin formatted the report. Cathy J. Brown, Manager of the Media section, coordinated production and distribution of this report.